

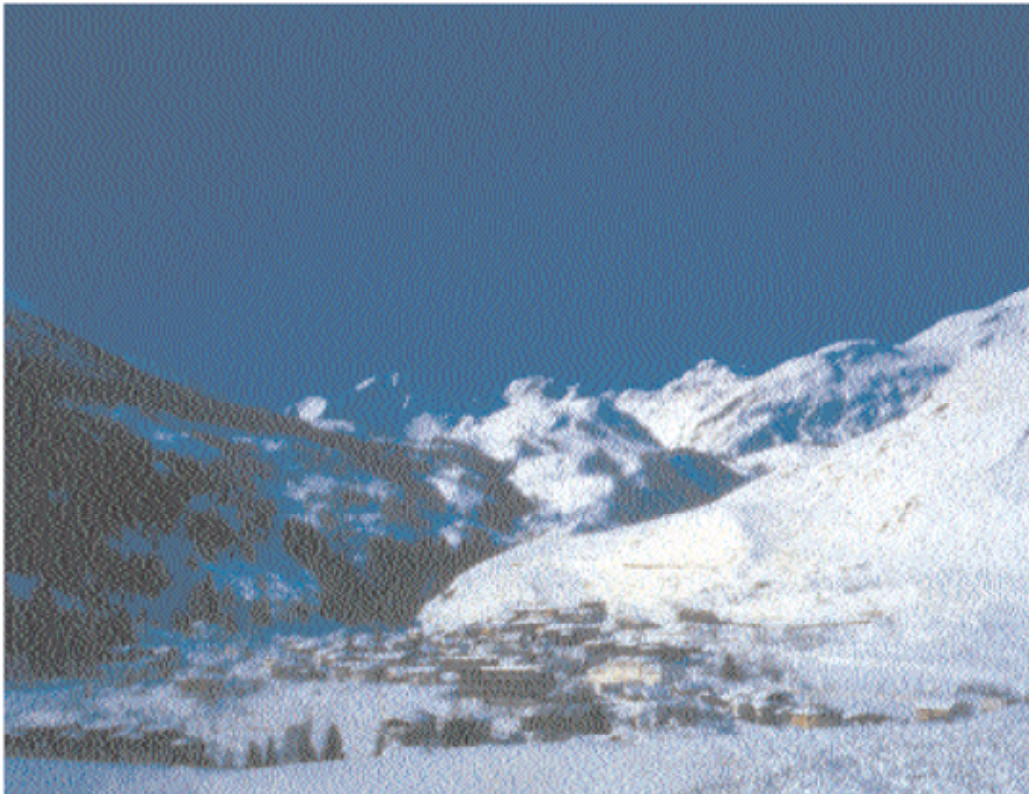
Les Rencontres de Physique de la Vallée d'Aoste

Results and Perspectives in Particle Physics

Edited by M. Greco

La Thuile, Aosta Valley

February 27 - March 5, 2005



ISTITUTO NAZIONALE DI FISICA NUCLEARE
Laboratori Nazionali di Frascati

Les Rencontres de Physique de la Vallée d'Aoste

Results and Perspectives in Particle Physics

FRASCATI PHYSICS SERIES

Series Editor

Stefano Bianco

Technical Editor

Luigina Invidia

Volume XXXIX — Special Issue

*Istituto Nazionale di Fisica Nucleare – Laboratori Nazionali di Frascati
Divisione Ricerca – SIS – Ufficio Pubblicazioni
P.O. Box 13, I-00044 Frascati (Roma) Italy
email: sis.publications@lnf.infn.it*

FRASCATI PHYSICS SERIES

Les Rencontres de Physique de la Vallée d'Aoste

RESULTS AND PERSPECTIVES IN PARTICLE PHYSICS

Copyright © 2005, by INFN Laboratori Nazionali di Frascati
SIS – Ufficio Pubblicazioni

All rights reserved. No part of this publication may be reproduced, stored in a retrieval system or transmitted, in any form or by any means, electronic, mechanical, photocopying, recording or otherwise, without the prior permission of the copyright owner.

ISBN – 88–86409–45–1

Printed in Italy by Poligrafica Laziale, P.le della Stazione 1, 00044 Frascati

FRASCATI PHYSICS SERIES

Volume XXXIX

**Les Rencontres de Physique
de la Vallée d'Aoste**

Results and Perspectives in Particle Physics

Editor
Mario Greco

La Thuile, Aosta Valley, February 27 – March 5, 2005

Conference Organizers

Giorgio Bellettini	<i>Pisa</i>
Giorgio Chiarelli	<i>Pisa</i>
Mario Greco	<i>Roma III</i>

List of Chairpersons

Giorgio Bellettini	<i>Pisa</i>
Albert Bramon	<i>Barcelona</i>
Rino Castaldi	<i>Pisa</i>
Giorgio Chiarelli	<i>Pisa</i>
Arnon Dar	<i>Haifa</i>
Fernando Ferroni	<i>Roma</i>
Harald Fritsch	<i>Münich</i>
Mario Greco	<i>Roma III</i>
Clemens Heusch	<i>Santa Cruz</i>
Robert Kephart	<i>Fermilab</i>
Peter Minkowski	<i>Bern</i>
Giancarlo Moneti	<i>Syracuse</i>
Lawrence Sulak	<i>Boston</i>

FOREWORD

The 2005 Rencontres de Physique de la Vallée d'Aoste were held at the Planibel Hotel of La Thuile, Aosta Valley, on February 27 – March 5, with the nineteenth edition of "Results and Perspectives in Particle Physics".

The physics programme included various topics in particle physics, also in connection with present and future experimental facilities, as cosmology, astrophysics and neutrino physics, CP violation and rare decays, electroweak and hadron physics with e^+e^- and hadron colliders, heavy flavours and prospects at future facilities.

The Session on "Physics and Society" included special colloquia on the "Energy Problem", in particular on energy from fusion, geothermal, solar and renewable sources.

Also a Round Table discussion on the Physics and Feasibility of the High Intensity, Medium Energy Accelerators was organized with the participation of F. Cervelli, F. Forti, R. Garoby, G. Isidori and P. Raimondi.

Giorgio Bellettini, Giorgio Chiarelli and I should like to warmly thank the session chairpersons and the speakers for their contribution to the success of the meeting.

The regional government of the Aosta Valley, in particular through the Minister of Public Education and Culture Teresa Charles, has been very pleased to offer its financial support and hospitality to the Rencontres of La Thuile, also contributing to the publication of these Proceedings. Also on behalf of the participants, representatives of some major Laboratories and Institutes in the world, we would like to thank all the Regional Authorities. Special thanks are also due to Bruno Baschiera, local coordinator of the Rencontres.

We are grateful to the former President of INFN Enzo Iarocci, the Directors of INFN Laboratori Nazionali di Frascati, Sergio Bertolucci and INFN Sezione di Pisa, Rino Castaldi, for the support in the organization of the Rencontres. We would like to thank also Paolo Caponera, Lucia Lilli, Cristina D'Amato, Claudia Tofani and Paolo Villani for their help in both planning and running the meeting. We are also grateful to Alessandra Miletto for her valuable contribution to the local organization of the meeting. The excellent assistance provided by Giovanni Nicoletti and Mauro Giannini made it possible to set up the computer link to the international network. Special thanks are due to Luigina Invidia for valuable help in the technical editing of the Proceedings.

Finally we would like to thank the Mayor Gilberto Roullet and the local authorities of La Thuile and the "Azienda di Promozione Turistica del Monte Bianco" for their warm hospitality, and the Planibel Hotel staff for providing us an enjoyable atmosphere.

CONTENTS

SESSION I – ASTROPHYSICS AND COSMOLOGY		1
Alan Wiseman	The startup of LIGO	3
Bruno Khélifi	Gamma Ray Astronomy on the Ground: Results and Perspectives	5
Dimitri Kazakov	Galactic Gamma Rays from Dark Matter Annihilation	15
Alvaro de Rujula	On the Origin of Cosmic Rays	17
Alexander Dolgov	Neutrino, Cosmos, and New Physics.....	19
Rita Bernabei	Particle Dark Matter	37
Aldo Morselli	Searching for Dark Matter in Space	63
Antonio Masiero	Dark Energy and (new?) Particle Physics	83
Andreas Eckart	The Role of Black Holes in the Universe	85
 SESSION II – NEUTRINO PHYSICS		 87
Kurt Woschnagg	Exploring the High-Energy Neutrino Universe Results from the South Pole – Results from AMANDA and Status of IceCube	89
Jeanne Wilson	New Results from the Salt Phase of the Sudbury Neutrino Observatory	107
Takeshi Nakadaira	Results from K2K	119
M. Patrick Decowski	KamLAND: Studying Neutrino Oscillation with Reactors	121
Alexander Studenikin	Quantum Theory of Neutrino Spin Light in Dense Matter	127
Tass Belias	The Startup of MINOS	145
Eugenio Coccia	The CNGS Program: a Status Report	147
Guido Altarelli	Normal and Special Models of Neutrino Masses and Mixings	149

SESSION III – QCD	167
Mario Martinez	Studies of Jet Properties at the Tevatron 169
Davide Boscherini	Hadron Spectroscopy and Heavy Flavours Production at HERA 181
Michail Danilov	Experimental Review on Pentaquarks 193
Andrei L. Kataev	Renormalons at the Boundaries Between Perturbative and Non-Perturbative QCD 211
SESSION IV – HEAVY FLAVOUR PHYSICS	231
Mario Antonelli	$ V_{us} $ and Rare K_s Decays at KLOE 233
Fabio Ambrosino	KLOE Results on the $f_0(980)$, $a_0(980)$ Scalars and Decays 241
Gang Li	Recent Results on Charmonium Physics at BES 249
Ping Wang	χ - χ' Phases and Impact on Measurements in Charmonium 257
Alex Smith	Recent Results from CLEO-c 259
Michael D. Hildreth	Production, Lifetimes, and Masses of B and C Hadrons 269
A. Kuzmin	Charm Physics at BELLE 281
Steven Robertson	Rare Decays and Exotic States at BaBar 299
Vittorio Lubicz	Determination of V_{us} : Recent Progresses from Theory 311
Victor Novikov	Binary Systems in QM and in QFT: CTP 321
SESSION V – CP VIOLATION AND RARE DECAYS	333
Marco S. Sozzi	Search for Direct CP Violation in Charged K Decays 335
Sasha Glazov	Klong in e-e-gamma 349
Thomas E. Latham	Unitary Triangle Angle Measurement at Babar 351
Rolf Dubitzky	Measurements of $ V_{ub} $ and $ V_{cb} $ at BaBar 371
Alan Schwartz	Angles of the CKM Unitarity Triangle Measured at BELLE 373

Isamu Nakamura	Sides of the Unitarity Triangle from BELLE	387
Stephanie Menzemer	B_s Oscillations and Prospects for m_s at the Tevatron	395
Eugenij Shabalin	How Large are CP Effects Produced by Different Mechanisms of CP Violation in $K_{\pm} \rightarrow 3$ Decays	411
Amarjit Soni	CP Violation Highlights: Circa 2005	417
SESSION VI – EW AND TOP PHYSICS		443
Giovanni Abbiendi	Running of the QED Coupling in Small-Angle Bhabha Scattering at LEP	457
Luca Trentadue	Measuring α_{QED} in e^+e^- : An Alternative Approach	455
Chris Parkes	W Boson Properties at LEP	461
Oliver Stelzer–Chilton	W Boson Production and Mass at the Tevatron	471
George Velev	Top Mass Measurements at the Tevatron RUN II	483
Frank Fiedler	Top Quark Production and Properties at the Tevatron	503
V. Daniel Elvira	Di-Boson Production and SM/SUSY Higgs Searches at the Tevatron	521
SESSION VII – SEARCH FOR PHYSICS BEYOND THE SM		537
Isabel Trigger	Search for Physics Beyond the Standard Model at LEP	539
Judith Katzy	Electroweak Physics and Searches for New Physics at HERA	547
Arnaud Duperrin	Searches for SuperSymmetry at the Tevatron	559
Kaori Maeshima	Non SUSY Searches at the Tevatron	569
Andrea Romanino	Ignoring the Hierarchy Problem	571

SESSION VIII – FUTURE SCENARIOS	583
Tamas Budavari	Findings and Prospects for the Sloan Digital Sky Survey Search 585
Carlo Pagani	The On-Going Effort Towards a Global Linear Collider 587
Jerome Faure	Laser Wakefield Acceleration of High Energy Quasi-Monoenergetic Electron Beams 593
Fabiola Gianotti	Preparing for Physics at the LHC 601
 SPECIAL SESSION – PHYSICS AND SOCIETY – The Energy Problem	
Duarte Borba	Energy from Fusion, from Dream to ITER 619
 Participants	 633

SESSION I — ASTROPHYSICS AND COSMOLOGY

- *Alan Wiseman* The startup of LIGO
- *Bruno Khélifi* Gamma Ray Astronomy on the Ground: Results and Perspectives
- *Theofisti Dafni* Galactic Gamma Rays from Dark Matter Annihilation
- *Alvaro de Rujula* On the Origin of Cosmic Rays
- *Alexander Dolgov* Neutrino, Cosmos, and New Physics
- *Rita Bernabei* Particle Dark Matter
- *Aldo Morselli* Searching for Dark Matter in Space
- *Antonio Masiero* Dark Energy and (new?) Particle Physics
- *Andreas Eckart* The Role of Black Holes in the Universe

THE STARTUP OF LIGO

Alan Wiseman
Madison, USA

Written contribution not received

GAMMA RAY ASTRONOMY ON THE GROUND: RESULTS AND PERSPECTIVES

Bruno Khélifi^a for the H.E.S.S. collaboration^b

^a*Max-Planck-Institute für Kernphysik, Saupfercheckweg 1,
D 69117 Heidelberg, Germany*

^b*<http://www.mpi-hd.mpg.de/HESS/collaboration>*

Abstract

Very high energy gamma-ray astronomy above 50 GeV has strongly evolved recently with the building and the operation of the third generation of Cherenkov atmospheric detectors on the ground. H.E.S.S., one such detector, is rapidly unveiling the very high energy sky, allowing one to study fundamental questions such as the origin of cosmic rays and the emission mechanisms of active galactic nuclei.

The latest results from the gamma-ray astronomy on the ground are reported here. The experimental techniques of the current generation detectors are described with the example of the H.E.S.S. array. The observational results of very high energy gamma-rays from different source classes are presented.

1 Introduction

γ -ray astronomy at very high energies (VHE, >100 GeV) allow us to explore the production and propagation of high-energy particles in the Nonthermal Universe. The first physics goals of this astronomy are to have a better understanding of the acceleration mechanisms of charged particles and of the mystery of the Cosmic Ray origin. For this task, observations of VHE γ -rays from Supernova Remnants, Starburst Galaxies, clusters of galaxies and from (un)identified galactic sources are under way. Among the physics goals, VHE observations of active galactic nuclei, microquasars, pulsars and γ -ray bursts allow to study the astrophysics around compact objects, e.g. the particle acceleration mechanisms within jets. Some fields of cosmology can be studying in the VHE range, in particular the spectral energy distribution of the extragalactic background light by observing distant AGNs. Finally, the detection of VHE γ -rays could constrain phenomena of cosmological origin, such as annihilations of dark matter particles (neutralinos) or relics of the Big Bang (e.g. monopoles of cosmic strings).

After describing the detection technique of VHE γ -rays with atmospheric Cherenkov detectors, the observational results of the High Energy Stereoscopic System (H.E.S.S.) detector are presented within the light of the latest results of VHE γ -ray observations. These results are reported for different types of sources, i.e. pulsar wind nebulae, unidentified VHE sources, SNRs, the Galactic Centre and AGN.

2 Atmospheric Cherenkov Technique

The techniques used to detect VHE γ -rays led to the first source detection in 1989 ⁴⁾ by the Whipple collaboration. They have evolved (see Tab. 1), such that the performance of the current detectors (third generation) are close to that of the former generation of X-ray satellites (e.g. ROSAT). The current generation of γ -ray detectors are using Imaging Atmospheric Cherenkov telescopes (IACT) in stereoscopy and the basic method to detect γ -rays is the following (see also Fig. 1-a). A γ -ray entering into the atmosphere creates an electromagnetic shower. The charged particles radiate Cherenkov photons (mostly between 400 nm and 600 nm), that are detected by optical telescopes on the ground. These telescopes record simultaneously Cherenkov images of the shower, which allow one to have good angular and energy resolution, and to have good sensitivity. The experimental techniques and the typical performances of the stereoscopic IACTs are illustrated with the example of the H.E.S.S. detector.

The H.E.S.S. array is situated in the Khomas highland of Namibia, at

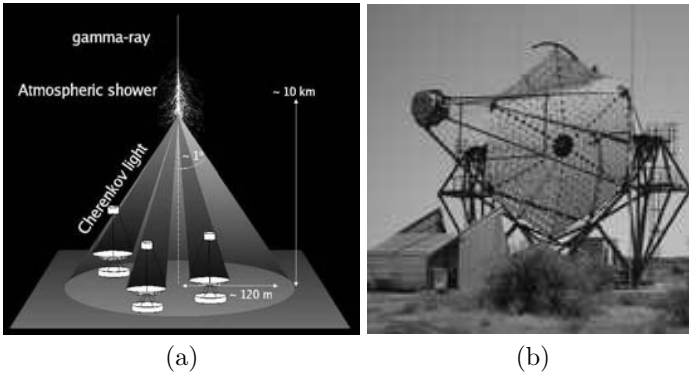


Figure 1: (a) Scheme of principle of the detection of VHE γ -rays by IACT. (b) Picture of a telescope of H.E.S.S.

an elevation of 1800 metres above sea level. The four telescopes are placed in a square formation with a side length of 120 metres. The telescopes, of steel construction, have an effective mirror area of 107 m^2 . Figure 1-b shows a picture of one of the telescopes. The H.E.S.S. cameras each consist of a hexagonal array of 960 pixels, each consisting of a photo-multiplier tube (PMT) and a Winston cone light collector. Each pixel covers an area of 0.16° in diameter projected onto the sky¹⁾. The total field of view on the sky is 5° in diameter. All triggering and read-out electronics are contained inside the camera body. The first telescope was completed in June 2002 and the full array is now operational since December 2003.

Table 1: IACT detectors of the second and third generations. The number of telescopes ($\# \text{ CT}$) is given, the diameter of the telescope dish, the field of view (FoV, diameter), the energy threshold in TeV (E_{th}) and the detector status (C=Closed, R=Running, B=Building).

Name	Location	$\# \text{ CT}$	Diameter	FoV	E_{th}	Status
CANGAROO	Australia	1	3.8 m	3°	1.5	C
CAT	France	1	5 m	3°	0.25	C
HEGRA	Canaries	5	3.5 m	3°	0.5	C
Whipple	U.S.A.	1	10 m	4°	0.3	R
CANGAROO III	Australia	4	10 m	4°	0.1	R
H.E.S.S.	Namibia	4	12 m	5°	0.1	R
MAGIC	Canaries	1	17 m	4°	0.03	R
VERITAS	U.S.A.	4 \rightarrow 7	12 m	3.5°	0.05	B

The data analysis permits efficient rejection of the background events

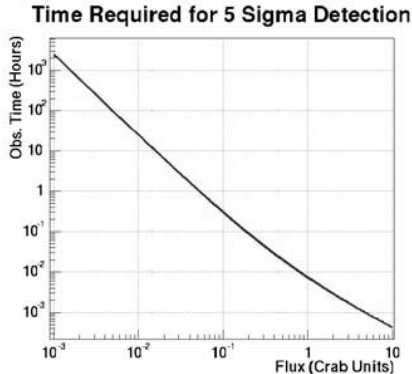


Figure 2: *Point-source sensitivity of H.E.S.S. at a zenith angle of 20°*

induced by Cosmic Ray (CR) showers. This analysis uses the morphological differences of the Cherenkov images of atmospheric showers in order to discriminate γ -rays from CRs. Details of the data analysis procedures may be found in Ref. 2) and Ref. 3). Monte-Carlo simulations predict a sensitivity for the H.E.S.S. array of $\sim 1\%$ of the flux of the Crab nebula (5σ , 50 hours, zenith angle of 20°) and an energy threshold of ~ 100 GeV at the zenith (see Fig. 2). The typical angular resolution is 0.1° and the energy resolution is about 15% up to tens of TeV.

3 The H.E.S.S. Observations

This section presents the main results of the H.E.S.S. observations up to early 2005, including the commissioning phase. The results are presented by source type, with a comparison of the results of other IACT detectors.

3.1 Pulsar Wind Nebula

Some young neutron stars are surrounded by a synchrotron nebula detected in radio and X-rays. The Crab nebula is an example of one such pulsar wind nebula (PWN). The central source, with a typical surface magnetic field of 10^{12} G and an initial rotational period between 10 and 100 ms, powers the surrounding nebula. The total energy available can range up to 10^{49} erg, and is a potential power source for production of VHE γ -rays. Electrons and positrons (probably with an additional hadronic component) are accelerated up to 100 TeV by a mechanism not well identified. And these leptons produce VHE γ -rays by inverse Compton (IC) scattering on target photons (CMBR and local Galactic IR background) 5). Alternatively, p-p collisions may also produce VHE photons (e.g. Ref. 6)).

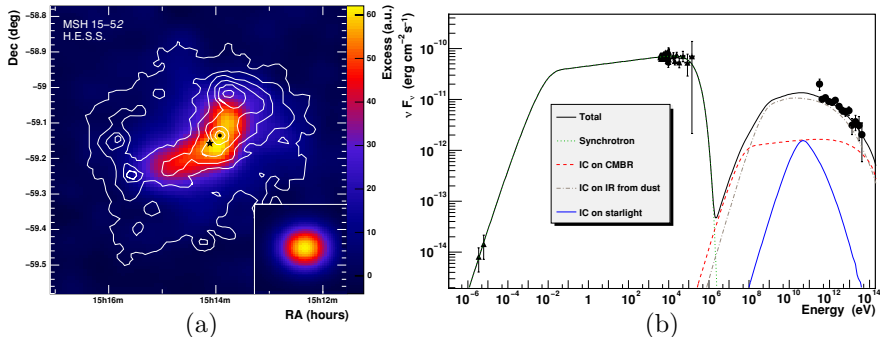


Figure 3: *H.E.S.S.* results on MSH 15-52: (a) Smoothed excess map above ~ 900 GeV. The right-bottom inset shows the simulated PSF smoothed identically. The white contour lines are the X-ray count rate levels as seen by ROSAT (0.1–2.4 keV). (b) Spectral energy distribution with radio ¹³⁾ and X-ray ¹⁴⁾ data. The lines are the best model fit of the one zone IC model.

The Crab nebula is a PWN and is conventionally used as a standard reference source of TeV γ -rays, due to its relative stability and high flux. Observations were made of this source in 2004. A strong signal was seen in ~ 27 hours of observations at a confidence level of more than 100σ . The flux of $\Phi(1 \text{ TeV}) = (1.71 \pm 0.04) \times 10^{-11} \text{ cm}^{-2} \text{ s}^{-1}$ above 1 TeV and the photon index of $\Gamma = 2.67 \pm 0.04$ are consistent with those seen by other experiments ^{7, 8, 9)}. The errors quoted are statistical, there is an estimated systematic error of 0.1 on the photon index and 20% on the flux. Before the H.E.S.S. observations, only this object has been firmly confirmed to be a VHE pulsar wind nebula.

MSH 15-52 is a composite SNR, containing a 150-ms pulsar (PSR B1509-58) that powers a PWN, a surrounding supernova shell (SNR) shell (G 320.4-1.2) and an H_α nebula (RCW 89), as seen in radio and X-rays (Ref. ¹⁰⁾ and references within). This region has been observed between March and June 2004, yielding 22.1 hours (live time) of good quality data with an average energy threshold of ~ 280 GeV. An excess above 25σ is detected around the pulsar position and appears to be elongated in the NW-SE direction, as seen in Fig. 3-a. The energy spectrum is compatible with a pure power law between ~ 280 GeV and ~ 40 TeV. The spectral index is $\Gamma = 2.67 \pm 0.04$, and the integral flux above ~ 280 GeV corresponds to $\sim 15\%$ of the Crab flux above the same threshold. This spectrum can be well reproduced by a simple one zone IC model described in Ref. ¹⁰⁾ (see Fig. 3-b).

One should note that two other PWN have been detected by H.E.S.S., within G 0.9+0.1 ¹¹⁾ and the system PSR B1259-63/SS 2883 ¹²⁾.

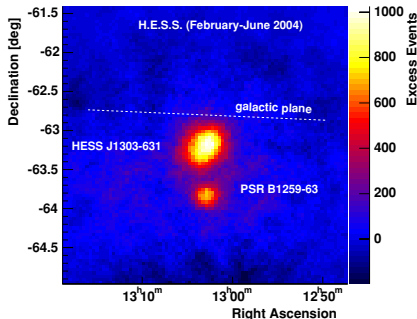


Figure 4: *Excess map showing both the unidentified source HESS J1303-631 and PSR B1259-63/SS 2883.*

3.2 VHE Unidentified sources

The HEGRA detector discovered an unidentified TeV γ -ray source in the Cygnus region ¹⁵⁾. This object, TeVJ2032+4130, appears to be extended ($r \sim 6'$), and its spectrum is compatible with a power law with $\Gamma = 1.90 \pm 0.10$. This unknown source lies within an OB association (Cygnus OB2). A possible origin of this TeV emission could be a hadron acceleration within stellar wind shocks in interaction with molecular clouds.

During the observation of the binary system PSR B1259-63/SS 2883, H.E.S.S. serendipitously discovered a new VHE source, HESS J1303-631, in the same field of view ¹⁶⁾ (see Fig. 4). This source has been detected at more than 20σ , after ~ 49 hours of observation, and appears to be extended ($\sigma \sim 0.15^\circ$). Its energy spectrum is compatible with a pure power law ($\Gamma = 2.44 \pm 0.05$) and the integral flux above ~ 380 GeV corresponds to $\sim 17\%$ of the Crab flux. Up to now, no counterpart at other wavelengths was found. Among all the possible candidates of VHE emitters, it is interesting to note that an OB association, Cen OB1, lies close to this new source.

3.3 Supernova Remnants

SNRs are thought to be the site of acceleration of CRs up to 10^{15} eV by Fermi acceleration. However, the naive picture according to which the VHE spectrum would give a clear signature of π° decay has not turned out to be true, and the situation is still under debate (e.g. Ref. ¹⁷⁾). Before the H.E.S.S. observations, three SNRs had been claimed by the CANGAROO collaboration, and one had been detected by the HEGRA collaboration.

H.E.S.S. detected two SNRs, RXJ 1713.7-3946 ¹⁸⁾ that has been also

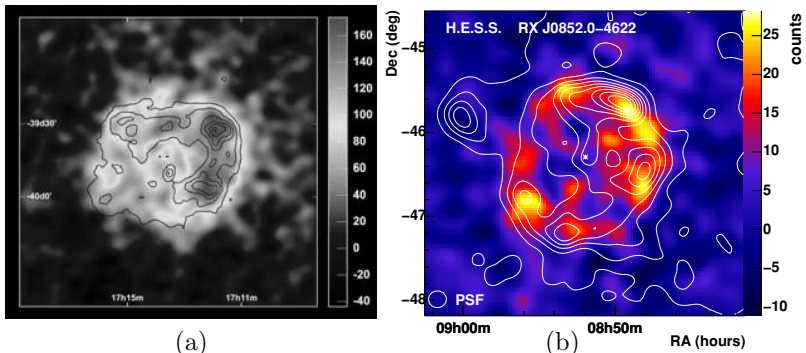


Figure 5: *Smoothed excess maps of (a) RXJ 1713.7–3946 and of (b) RXJ 0852.0–4622. The overlaid contours in both plots indicate ASCA X-ray observations of the same source.*

detected by CANGAROO, and RXJ 0852.0–4622¹⁹⁾). Our observations of SN 1006²⁰⁾, detected by CANGAROO, lead to constraining flux upper limits, well below the previous detection. Figure 5 shows smoothed excess maps of RXJ 1713.7–3946 and RXJ 0852.0–4622. The SNR shells are clearly resolved for the first time in the VHE range. Their integral fluxes above 1 TeV are around 65% and 100% of the Crab flux, respectively. Their spectra are compatible with power laws up to 10 TeV with $\Gamma=2.19\pm0.09$ and $\Gamma=2.10\pm0.10$, respectively.

3.4 The Galactic Centre

The Galactic Centre (GC) is an interesting candidate at most wavelengths and was observed by H.E.S.S. in 2003 with two telescopes and in 2004 with the full array. γ -ray emission from a direction consistent with the black hole Sagittarius A*, within their angular resolution, had been previously claimed by CANGAROO²¹⁾ and the Whipple collaboration²²⁾. Several types of potential VHE emitters lie in this region, such as the massive black hole, the SNR Sgr A Est, molecular clouds and perhaps dark matter.

A strong excess was seen by H.E.S.S. at a confidence level above 35σ ²³⁾. Figure 6-a shows a sky map of γ -ray candidates in the direction of the GC. The upper excess is the PWN G0.9+0.1, and the lower one is from the GC. The centre of gravity of the emission is consistent with both the black hole Sgr A* and the SNR Sgr A East, within the source position reconstruction accuracy of $40''$. The differential energy spectrum of the emission is measured by H.E.S.S. to have a photon index of 2.21 ± 0.09 and the integral flux above ~ 165 GeV corresponds to $\sim 5\%$ of the Crab flux. From this photon index, a lower limit of the neutralino mass can be derived, assuming that this signal is entirely due to neutralino annihilation. This limit is about 15 TeV, a value disfavoured on

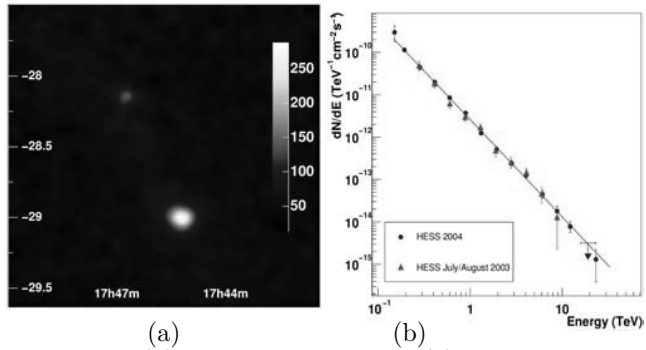


Figure 6: *Smoothed sky map (a) and energy spectrum (b) of the signal from the Galactic Centre.*

cosmological grounds.

3.5 Active Galactic Nuclei

Almost all known extragalactic VHE sources are AGN belonging to the class of blazars. They consist of supermassive ($\sim 10^9 M_{\odot}$) black holes surrounded by accretion disks, from which giant ultrarelativistic jets of plasma emerge. For blazars, one of these jets points towards the Earth, which boosts (via the Doppler effect) the electromagnetic radiation towards higher energies. They are also characterized by extreme variability on all time scales.

The blazar PKS 2155–304 ($z=0.117$) has been observed by H.E.S.S. since 2002. Here, the results of the 2003 campaign are reported. A clear signal at more than 45σ is detected after ~ 55 hours of observations³⁾. The time average spectrum is statistically compatible with a pure power law ($\Gamma=3.32\pm 0.06$) and there is no clear evidence for a spectral cutoff at high energies (see Fig. 7-a). The fitted photon index, that is relatively soft, is the result of γ -ray absorption by the extragalactic background light or/and the result of absorption within the blazar. In this dataset, the integral flux changes significantly with time between $\sim 10\%$ and $\sim 60\%$ of the Crab flux above ~ 300 GeV, but there is no evidence of spectral variability.

During the 2003 campaign, coordinated multiwavelength observations²⁴⁾ were made of PKS 2155–304 with H.E.S.S., the X-ray satellite RXTE, the optical telescope ROTSE-III and the radio-telescope of Nançay. Figure 7-b shows the correlation between the X-ray flux in the band 2–10 keV and the γ -ray flux above 300 GeV. Even though flux variations are apparent in the two energy ranges, no correlation is apparent, imposing constraints on the

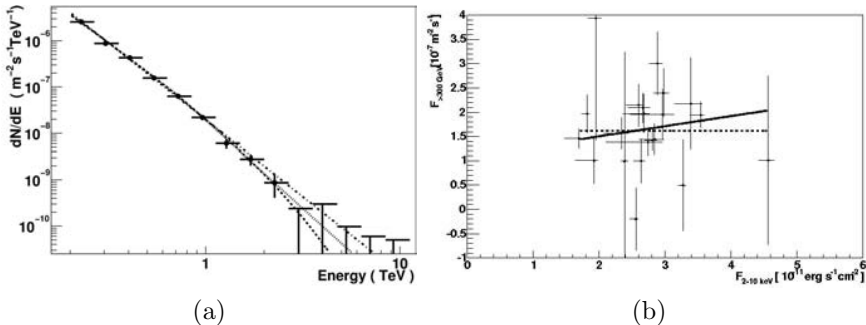


Figure 7: *Energy spectrum (a) and correlation between γ -rays and X-rays (b) for PKS 2155–304.*

acceleration and emission processes.

4 Conclusions and Perspectives

The H.E.S.S. experiment has been fully operational with four telescopes since January of 2004 and has achieved its design sensitivity and operational characteristics. Useful scientific results have been produced throughout the construction phase with two, three and four telescopes and exciting discoveries have been made. An extensive campaign of observations of galactic sources is underway and more exciting results are expected. Sources discussed here will be re-observed with the improved sensitivity and resolution of the full array. Such deeper observations are expected to provide further interesting insights from these sources, especially with the use of data from the whole electromagnetic spectrum.

5 Acknowledgements

The support of the Namibian authorities and of the University of Namibia in facilitating the construction and operation of H.E.S.S. is gratefully acknowledged, as is the support by the German Ministry for Education and Research (BMBF), the Max-Planck-Society, the French Ministry for Research, the CNRS-IN2P3 and the Astroparticle Interdisciplinary Programme of the CNRS, the U.K. Particle Physics and Astronomy Research Council (PPARC), the IPNP of the Charles University, the South African Department of Science and Technology and National Research Foundation, and by the University of Namibia. We appreciate the excellent work of the technical support staff in Berlin, Durham, Hamburg, Heidelberg, Palaiseau, Paris, Saclay, and in Namibia in the construction and operation of the equipment. I would like to thank the organizers of the conference for their warm welcome.

References

1. P. Vincent, J.-P. Denance, J.-H. Huppert *et al.*, Proc. 28th ICRC, Tsukuba, Univ. Academy Press, Tokyo, p. 2887 (2003).
2. F. Aharonian *et al.*, *Astropart. Phys.*, **22**, 109 (2004).
3. F. Aharonian *et al.*, *Astron. & Astrophys.*, **430**, 865 (2005).
4. T. C. Weekes *et al.*, *Astrophys. Journ.*, **342**, 379 (1989).
5. F.A. Aharonian, A.M. Atoyan and T. Kifune, *MNRAS*, **291**, 162 (1997).
6. E. Amato, D. Guetta, P. Blasi, *Astron. & Astrophys.*, **402**, 827 (2003).
7. G. Mohanty *et al.*, *Astropart. Phys.*, **9**, 15 (1998).
8. F.A. Aharonian *et al.* (HEGRA Collaboration), *Astrophys. J.*, **539**, 317 (2000).
9. C. Masterson *et al.*, *Proc. High Energy Gamma-Ray Astronomy*, **558**, 753 (AIP 1999).
10. F. Aharonian *et al.*, *Astron. & Astrophys.*, **435**, L17 (2005).
11. F. Aharonian *et al.*, *Astron. & Astrophys.*, **432**, L25, (2005).
12. S. Schlenker *et al.*, *Proc. High Energy Gamma-Ray Astronomy*, **745**, 341 (AIP 2005).
13. B.M. Gaensler *et al.*, *Astrophys. Journ.*, **569**, 878 (2002).
14. T. Mineo *et al.*, *Astron. & Astrophys.*, **380**, 695 (2001).
15. F. Aharonian *et al.*, *Astron. & Astrophys.*, **393**, L37, (2002).
16. M. Beilicke *et al.*, *Proc. High Energy Gamma-Ray Astronomy*, **745**, 347 (AIP 2005).
17. Y.M. Butt *et al.*, *Nature*, **418**, 499 (2002).
18. Aharonian *et al.*, *Nature*, **432**, 75 (2004).
19. F. Aharonian *et al.*, *Astron. & Astrophys.*, **437**, L7 (2005).
20. F. Aharonian *et al.*, *Astron. & Astrophys.*, **437**, 135 (2005).
21. K. Tsuchiya *et al.*, *Astrophys. Journ.*, **606**, L115 (2004).
22. K. Kosack *et al.*, *Astrophys. Journ.*, **608**, L97 (2004).
23. F. Aharonian *et al.*, *Astron. & Astrophys.*, **425**, L13 (2004).
24. F. Aharonian *et al.*, accepted by *Astron. & Astrophys.* (2005), astro-ph/0506593.

**GALACTIC GAMMA RAYS FROM DARK MATTER
ANNIHILATION**

Dimitri Kazakov

ITEP, Institute for Theoretical and Experimental Physics, Moscow

Written contribution not received

ON THE ORIGIN OF COSMIC RAYS

Alvaro de Rujula
CERN, Switzerland

Written contribution not received

NEUTRINO, COSMOS, AND NEW PHYSICS

A.D. Dolgov

INFN, Ferrara 40100, Italy and ITEP, 117218, Moscow, Russia

Abstract

Observational manifestations of possible breaking of spin-statistics relation for neutrinos are considered. It is argued that bosonic neutrinos may form cosmological cold dark matter, improve agreement of BBN predictions with observations, make operative Z-burst model of ultra-high energy cosmic rays, etc. Restrictions for an admixture of bosonic component to neutrino which follow from double beta decay are discussed.

1 Introduction

There is an impressive symbiosis of the “weakest” and lightest of the known massive particles, neutrino, and Cosmos. Cosmology and astrophysics allow to study neutrino properties with an accuracy which, in many cases, is inaccessible in direct terrestrial experiments and, vice versa, neutrino helps to resolve some cosmological and astrophysical mysteries ^{1, 2)}.

Cosmology allows to put a very stringent upper bound on neutrino mass at the level of about 1 eV, for a review see e.g. papers ³⁾. The bound on the amplitude of possible right handed currents and the mass of right intermediate bosons found from the analysis of Big Bang Nucleosynthesis (BBN) is orders of magnitude better than those obtained in laboratories. The same is true for neutrino magnetic moments and mixing of the usual active neutrinos with hypothetical sterile ones which are restricted by BBN ¹⁾ and stellar evolution ⁴⁾.

On the other hand, neutrino contributes to cosmology providing hot dark matter, but not the necessary cold one, if physics is normal. Neutrino may be related to dark energy ⁵⁾, and be responsible, at least partly, for ultra-high energy cosmic rays beyond GZK cut-off through the Z -burst mechanism ⁶⁾. The large mixing angle solution to the solar neutrino anomaly excludes noticeable lepton asymmetry of the universe ⁷⁾.

These lists are far from being complete but this is not the main subject of this talk. Instead of these rather well known topics I would like to talk about new, though quite speculative issues, related to effects of possible breaking of neutrino statistics in cosmology. The content of the talk is strongly based on ref. ⁸⁾.

The first question is why neutrino? First of all, neutrino is the only known particle indicating to new physics. As is known from observation of neutrino flavor oscillations leptonic flavor charges, electronic, muonic, and tauonic, are not conserved. Neutrino is the only observed particle for which Majorana mass is possible and, as a result total leptonic charge could be non-conserved. There are experimental indications to a possible leptonic charge non-conservation from neutrinoless double beta decay ⁹⁾. It may mean that neutrino communicates with a hidden sector of the particle world and is a messenger of new physics from the hidden sector. It could be that no sacred principles are respected in the hidden world and neutrinos brings us exotic possibilities of breaking CPT theorem ¹⁰⁾ or Lorentz invariance, which are actively discussed in the recent years. Since at the present days cosmology is quickly becoming precise science, maybe cosmos will bring through neutrinos new surprising physics.

The most exciting possibility which, in particular, may lead to violation of CPT and Lorentz invariance and even to much more drastic consequences is

a breaking of the spin-statistics relation for neutrinos. Ironically the particle brought to this world by Pauli may violate Pauli exclusion principle. In fact Pauli and Fermi repeatedly asked the question if spin-statistics relation could be not exact and electrons were a little bit different.

Possible violation of exclusion principle for the usual matter, i.e. for electrons and nucleons was discussed in a number of papers at the end of the 80th ¹¹⁾. Efforts to find a more general than pure Fermi-Dirac or Bose-Einstein statistics ¹²⁾ were taken but no satisfactory theoretical frameworks had been found. Experimental searches of the Pauli principle violation for electrons ¹³⁾ and nucleons ¹⁴⁾ have also given negative results.

If one assumes that spin-statistics relation is broken while otherwise remaining in the frameworks of the traditional quantum field theory then immediately several deep theoretical problems would emerge:

- 1) non-locality;
- 2) faster-than-light signals;
- 3) non-positive energy density and possibly unstable vacuum;
- 4) maybe breaking of unitarity;
- 5) broken CPT and Lorentz invariance (as mentioned above).

Either these consequences (if they indeed were realized) exclude any violation of spin-statistics theorem and discussion of this violation should be forbidden or they open an exciting space for further research and development. An answer to that is first of all a matter of experiment which may either exclude or confirm the drastic assumption of breaking the spin-statistics relation. As for observational manifestations of the mentioned phenomena they should be weak because they are induced by weakly interacting neutrinos and, moreover, in higher orders of perturbation theory.

Perturbative expansion of the scattering matrix has the well known form:

$$S = 1 + \sum_n \frac{(-i)^n}{n!} \int \Pi d^4 x_j T \{ \mathcal{H}(x_1) \dots \mathcal{H}(x_n) \} \quad (1)$$

where $T\{\dots\}$ means time-ordered product of operators inside brackets. Lorentz invariance is ensured if Hamiltonian, \mathcal{H} , is bosonic operator, i.e. it commutes with itself if separated by the light cone, see e.g. ¹⁵⁾. However, for bosonic or partly bosonic neutrinos the effective Hamiltonian responsible even for the simple reaction $e + p \leftrightarrow n + \nu$ is not bosonic and observables do not commute for space-like separation and locality breaks. Presumably unitarity is maintained because Hamiltonian remains Hermitian.

Another possibility that Hamiltonian/Lagrangian approach and least action principle are applicable only approximately and theory is drastically modified, while the observable effects may still be small.

So let us postpone discussion of (non-existing) theory and consider phenomenology of neutrinos obeying Bose or mixed statistics⁸⁾. What can we buy for this price?

2 Dark matter.

It is well known that the usual fermionic neutrinos cannot form cosmological cold dark matter for any spectrum of primordial fluctuations and arbitrary self-interaction. This conclusion is based on the Tremain-Gunn bound¹⁶⁾ which does not allow to fill galaxies with sufficiently many light fermions (satisfying the Gerstein-Zeldovich bound¹⁷⁾) to account for the observed hidden mass. Thus we face the following dark matter dilemma:

- 1) new particles and old (normal) physics
- 2) old particles (neutrinos) and very new physics.

To make the cosmological cold dark matter neutrinos must form Bose condensate in the early universe. To this end a very large lepton asymmetry is necessary with

$$\frac{|n_\nu - n_{\bar{\nu}}|}{n_\gamma} \sim 100 \quad (2)$$

Such asymmetry might be created in a version of the Affleck and Dine¹⁸⁾ scenario.

A large asymmetry allows to fill up the present day universe by a huge number of cosmic neutrinos such that they would be able to make all CDM, $\Omega_{CDM} \approx 0.25$, if

$$n_\nu \sim 10^4 \text{ cm}^{-3} \quad (3)$$

The spectrum of cosmic background neutrinos, if they are bosonic, would be very much different from the fermionic ones because the Bose equilibrium distribution has the form:

$$f_{\nu_b} = \frac{1}{\exp[(E - \mu_\nu)/T - 1]} + C\delta(k), \quad (4)$$

where $\mu = m_\nu$ is the maximum value of chemical potential of bosonic neutrinos equal to their mass. The condensate amplitude C does not depend upon neutrino energy but may depend upon time. One sees that the bulk of the condensed neutrinos is cold. In galaxies the neutrino number density would be about 6 orders of magnitude larger than the average cosmological number density, i.e.

$$n_\nu^{(gal)} \sim 10^{10} (m_\nu/0.1 \text{ eV}) \text{ cm}^{-3}. \quad (5)$$

Structure formation with Bose condensed light bosons with the usual integer spin was considered in ref.¹⁹⁾. The model well reproduces the essential

features of the observed large scale structure. Since the picture is spin independent the same must be true as well for bosonic neutrinos.

The results and numerical estimates presented in this section are true for purely bosonic neutrinos however, as we see below, experiments on two neutrino double beta decay seem to exclude 100% breaking of statistics and at least some fermionic fraction must be present in a neutrino. It makes the model noticeably more cumbersome, but less vulnerable.

3 Equilibrium distribution for mixed statistics

The statistics dependent term in kinetic equation for the reaction $1 + 2 \leftrightarrow 3 + 4$ has the form

$$F = f_1(p_1)f_2(p_2)[1 \pm f_3(p_3)][1 \pm f_4(p_4)] - f_3(p_3)f_4(p_4)[1 \pm f_1(p_1)][1 \pm f_2(p_2)] \quad (6)$$

where f_j is the distribution function of particle j . This expression is valid in the case of T-invariant theory when the detailed balance condition is fulfilled. Since T-invariance is broken, kinetic equation is modified but the equilibrium distributions $f_j^{(eq)}$ remain the same canonical Bose and Fermi ones as in T-invariant theory (20). This statement is based on the unitarity of S -matrix. If the spin-statistics relation is broken, as a result the unitarity may also be broken. If this is the case, then a breaking of T -invariance may create large deviations from the standard equilibrium distribution functions of neutrinos.

In what follows we neglect complications related to a violation of T-invariance. In the case that neutrino obeys pure Bose statistics its equilibrium distribution is given by the standard Bose form (4). Indeed, it is easy to see that for this distribution F vanishes and together with it the collision integral vanishes too. However, the form of equilibrium distribution for mixed statistics is not so evident. It depends upon an assumption about F for particles obeying mixed statistics. We do not have rigorous arguments in favor of one or other form for F and as a reasonable guess assume that the factor depending upon the neutrino statistics in F changes as

$$(1 - f_\nu) \rightarrow c^2(1 - f_\nu) + s^2(1 + f_\nu) \quad (7)$$

where $c = \cos \gamma$, $s = \sin \gamma$ and γ is some mixing angle characterizing admixture of wrong statistics.

Another possibility for description of mixed statistics in kinetic equation could be

$$(1 - f_\nu) \rightarrow c^2(1 - c^2 f_\nu) + s^2(1 + c^2 f_\nu). \quad (8)$$

However, it is easy to see that these two seemingly reasonable possibilities (7) and (8) are identically equivalent. In both cases

$$(1 - f_\nu) \rightarrow (1 - \kappa f_\nu) \quad (9)$$

where

$$\kappa = c^2 - s^2 = \cos 2\gamma \quad (10)$$

We call κ the Fermi-Bose mixing parameter ²¹⁾. One can check that in the case of mixed statistics introduced to kinetic equation according to (9) the equilibrium distribution takes the form ²¹⁾:

$$f_\nu^{(eq)} = [\exp(E/T) + \kappa]^{-1} . \quad (11)$$

where κ runs from +1 to -1 corresponding respectively to Fermi and Bose limits. The intermediate value $\kappa = 0$ corresponds to Boltzmann statistics.

If $-1 < \kappa < 0$, the maximum value of the chemical potential may be bigger than the neutrino mass:

$$\mu^{(max)} = m_\nu - T \ln(-\kappa) \quad (12)$$

Bose condensation might take place for negative κ only.

Another possible form of a modification of statistics dependent factor in kinetic equation would emerge if we assume that there are two neutrino fields with the same mass and different statistics, fermionic and bosonic. The Lagrangian would always depend upon two independent field operators in the combination:

$$\psi_\nu = c\psi_b + s\psi_f, \quad (13)$$

where $\psi_{f,b}$ are respectively bosonic and fermionic operators. In this case kinetic equation would contain two different terms:

$$c^2 f_f(1 - f_f) \quad (14)$$

and

$$s^2 f_b(1 - f_b) \quad (15)$$

Equilibrium distributions would be canonical ones, e.g. for vanishing chemical potential they are:

$$f_{f,b} = 1/[\exp(E/T) \pm 1] \quad (16)$$

but the number of states in equilibrium becomes doubled. On the other hand, the probability of e.g. neutron beta-decay remains the same as in the standard theory because $c^2 + s^2 = 1$.

4 Big Bang Nucleosynthesis

The impact of purely bosonic neutrinos on BBN was considered earlier in paper ²²⁾. The effects of mixed statistics described by the equilibrium distribution (11) were calculated in our work ²¹⁾. The equilibrium energy density of bosonic

neutrinos at $T \gg m_\nu$ is $8/7$ of the energy density of fermionic neutrinos and thus the change of statistics would lead to an increase of the effective number of neutrino species at BBN by $\Delta N_\nu = 3/7$ (for three neutrinos). On the other hand, a larger magnitude of the neutrino distribution function and the fact that it enters kinetic equation (see (6)) as $(1 + f_\nu)$ instead of $(1 - f_\nu)$ makes the weak reactions of neutron-proton transformations faster and hence the n/p freezing temperature becomes lower. This effect dominates and as a result the effective number of massless species becomes smaller than 3. According to the calculations of ref. ²¹⁾ the effective number of neutrino species in the case of pure Bose statistics becomes $N_{eff} = 2.43$, practically independently on the value of the baryon-to-photon ratio $\eta = n_B/n_\gamma$.

The effective number of neutrino species determined by the comparison of the calculated abundance of primordial ${}^4\text{He}$ with the standard result is presented in the upper panel of fig. 1 as a function of κ . However, the effect of change of statistics cannot be described by a simple change in N_ν if other light elements are included. In the lower panel of fig. 1 the relative changes of the abundances of ${}^2\text{H}$, ${}^4\text{He}$, and ${}^7\text{Li}$ are presented. As expected the mass fraction of ${}^4\text{He}$ drops down, while the amount of ${}^2\text{H}$ goes up. A higher deuterium abundance can be explained by a slower conversion of deuterium to heavier elements due to fewer neutrons and faster cosmological expansion at $T \approx 0.8 \cdot 10^9$ when the light elements have been formed.

At $\kappa = -1$ we find for ${}^4\text{He}$: $Y_p = 0.240$, which makes much better agreement with the value extracted from observations (for a review of the latter see *e.g.* ²³⁾). Different helium observations yield different results, *e.g.*, ref. ²⁴⁾ finds $Y = 0.238 \pm 0.002$, and ref. ²⁵⁾ finds $Y = 0.2421 \pm 0.0021$ (1σ , only statistical error-bars). These results are shown in figure 2 as the skew hatched (yellow) region. Whether the existing helium observations are accurate or slightly systematically shifted will be tested with future CMB observations ²⁶⁾.

The amount of ${}^2\text{H}$ rises at most to $X_{2H}/X_H = 2.5 \cdot 10^{-5}$ and the agreement between BBN and WMAP data remains good, bearing in mind the observational uncertainties. Primordial ${}^7\text{Li}$ drops down to $X_{7Li}/X_H = 4.55 \cdot 10^{-10}$, again slightly diminishing the disagreement between theory and observations.

We see that at the present time BBN does not exclude even a pure bosonic nature of all three neutrinos. Furthermore, the agreement between the value of the baryonic mass density, η , inferred from CMBR and the predicted abundances of ${}^4\text{He}$, ${}^2\text{H}$, and ${}^7\text{Li}$ becomes even better. In other words, in the standard BBN model there is an indication of disagreement between observations of ${}^4\text{He}$ and ${}^2\text{H}$ - they correspond to different values of η with the observed abundances of ${}^4\text{He}$ indicating a smaller value than given by CMBR, while ${}^2\text{H}$ agrees with CMBR. Motivated by these results the value of $\Delta N_\nu = -0.7 \pm 0.35$ was suggested in ref. ²⁷⁾. In the case of predominantly bosonic neutrinos, as discussed

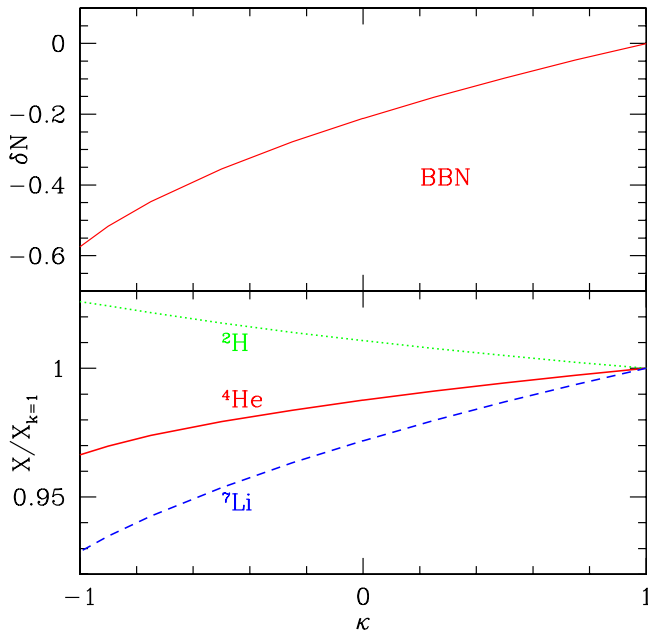


Figure 1: *Upper panel: the change in the effective number of degrees of freedom which corresponds to the change of the ${}^4\text{He}$ abundance as a function of the effective Fermi-Bose parameter κ . Lower panel: the relative change of the primordial abundances of deuterium, helium-4, and lithium-7, as functions of κ . We take $\eta = n_B/n_\gamma = 6.5 \cdot 10^{-10}$*

above, the discrepancy between ${}^2\text{H}$, ${}^4\text{He}$, and CMBR disappears.

The results presented in this section are obtained for negligible chemical potential of electronic neutrinos. On the other hand, formation of cosmological neutrino condensate discussed in sec. 2 demands the maximum value of μ_ν given by eq. (12). As is known ⁷⁾, BBN allows at most $\mu/T = 0.07$ for any neutrino flavor. This implies $\kappa > 0.9$. Such a large admixture of a wrong bosonic state to ν_e is most probably excluded by the data on double beta decay (see below, sec. 7). However, one may still hope to save the neutrino cold dark matter (νCDM) if the mixing angle determined from the decay is different from that that enters neutrino kinetics (see discussion in sec. 8. Another possibility to save νCDM is to assume that the chemical potentials of ν_μ or ν_τ are much larger than that of ν_e . The latter are very weakly restricted by BBN and only the large mixing between neutrino flavors equalizes all chemical potentials. However, the change of neutrino statistics may lead to a different

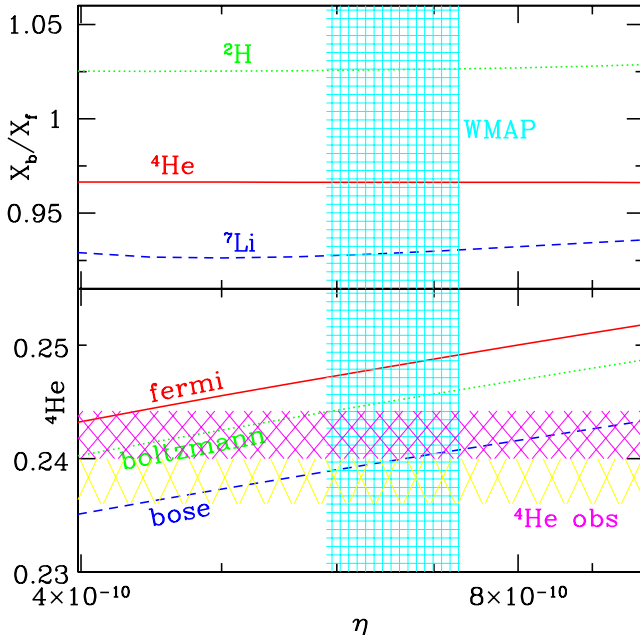


Figure 2: *Upper panel:* the ratios of abundances of different elements in the cases of purely bosonic neutrinos with respect to the standard fermionic case as functions of the baryon number density, η . The vertically hatched (cyan) region shows the WMAP 2σ determination of η . *Lower panel:* the absolute abundance of ${}^4\text{He}$ as a function of η for the purely bosonic, Boltzmann, and fermionic neutrino distributions, corresponding to $\kappa = -1, 0, +1$ respectively. The two skew hatched regions show the observation of primordial helium from ref. ²⁴⁾ (lower, yellow) and ref. ²⁵⁾ (upper, magenta), which marginally overlap at 1σ .

refraction index in the primeval plasma and to suppression of the transformation of $\nu_{\mu,\tau}$ into ν_e . There is also a more conventional way to suppress neutrino flavor oscillations in the primeval plasma introducing neutrino coupling to light pseudo-goldstone boson, Majoron. The effective potential of neutrinos induced by the Majoron exchange would suppress flavor transformations in the cosmological plasma ²⁸⁾. This would allow to have large chemical potentials of $\nu_{\mu,\tau}$ and small chemical potential of ν_e .

5 Astrophysical consequences

Neutrino statistics plays key role in the environments where neutrinos form dense degenerate gases. Direct test of the “bosonic” nature of neutrinos can be provided by precise measurements of the neutrino energy spectrum from supernova. Generically, the spectrum of bosonic neutrinos should be more narrow. To establish the difference one needs to measure the spectrum both in the low, $E < 3T$, and in the high, $E > 3T$ energy parts.

A violation of the exclusion principle can influence dynamics of the SN collapse. According to the usual scenario at the initial stages (formation of the hot proto-neutron star) the neutronization leads to production of high concentration of the electron neutrinos which are trapped in the core. The chemical potential of these neutrinos (due to the Pauli principle) can reach 70 - 100 MeV. These neutrinos heat the medium and diffuse from the core. Violation of the Pauli principle allows for the neutronization neutrinos to be produced with lower energies. These neutrinos escape easier the star leading to faster cooling and lower central temperatures. The evolution of the lepton number would change as well.

High neutrino density in the condensate (especially if an additional clustering occurs) enhances the rate of the Z^0 -bursts produced by the annihilation of the ultra high energy (UHE) cosmic neutrinos on the relic neutrinos⁶⁾. This in turn, enhances production of the UHE cosmic rays, and may help to explain the cosmic ray evens above the GZK cut-off.

Charge asymmetric neutrino condensate may produce a strong refraction of the high energy neutrinos from remote sources (active galactic nuclei, gamma ray bursters). Apart from lensing, one may expect a substantial impact on neutrino oscillations²⁹⁾.

Since the density of dark matter in galaxies is about 6 orders of magnitude larger than their average cosmological energy density, a condensation of cold neutrinos around the Earth might have an effect on the end point of the beta decay spectra, in particular, in the tritium decay experiments on search for neutrino mass³⁰⁾.

6 Double beta decay

In contrast to electrons and nucleons which form atoms and nuclei, where the effects of statistics are of primary importance, it is difficult to observe processes with identical neutrinos. A realistic reaction for the test of neutrino statistics can be the two-neutrino double beta decay,

$$A \rightarrow A' + 2\bar{\nu} + 2e^- \quad (17)$$

(or similar with production of antineutrinos and positrons). The probability of the decay as well as the energy spectrum and angular distribution of electrons should be affected by the change of neutrino statistics.

To have a formalism for description of identical neutrinos one needs to specify operators of neutrino creation/annihilation. We assume that they consist of two parts, fermionic, \hat{f} , and bosonic \hat{b} for operators of annihilation, $\hat{a} = \hat{f} + \hat{b}$. Its Hermitian conjugate could naturally be the operator of neutrino

creation. Correspondingly we define one neutrino state as:

$$|\nu\rangle = \hat{a}^+|0\rangle \equiv c_1\hat{f}^+|0\rangle + s_1\hat{b}^+|0\rangle = c|f\rangle + s|b\rangle \quad (18)$$

where $|f\rangle$ and $|b\rangle$ are respectively one particle fermionic and bosonic states and $c_1 = \cos\delta$ and $s_1 = \sin\delta$. It would be natural to expect that δ is equal to γ introduced above in eq. (7) but we cannot prove it formally.

To describe the two-neutrino state one needs to specify the relevant commutators which, we postulate, have the following form:

$$\hat{f}\hat{b} = e^{i\phi}\hat{b}\hat{f}, \quad \hat{f}^+\hat{b}^+ = e^{i\phi}\hat{b}^+\hat{f}^+, \quad \hat{f}\hat{b}^+ = e^{-i\phi}\hat{b}^+\hat{f}, \quad \hat{f}^+\hat{b} = e^{-i\phi}\hat{b}\hat{f}^+, \quad (19)$$

where ϕ is an arbitrary phase. The two neutrino state is natural to define as

$$|k_1, k_2\rangle = \hat{a}_1^+\hat{a}_2^+|0\rangle \quad (20)$$

The matrix element of the decay of nucleus A into $2\nu + 2e + A'$ may be possibly taken in the usual way:

$$A_{2\beta} = \langle k_1, k_2, 2e, A' \left| \int d^4x_1 d^4x_2 \psi_\nu(x_1)\psi_2(x_2)\mathcal{M}(x_1, x_2) \right| 0, A \rangle. \quad (21)$$

After making the necessary commutating according to eq. (19) we obtain:

$$A_{2\beta} = A_- [c_1^4 + c_1^2s_1^2(1 - \cos\phi)] + A_+ [s_1^4 + c_1^2s_1^2(1 + \cos\phi)]. \quad (22)$$

where A_- and A_+ are respectively antisymmetric (fermionic) and symmetric (bosonic) parts of two neutrino emission. It is easy to see that the amplitude can be parametrized as

$$A_{2\beta} = \cos^2\chi A_- + \sin^2\chi A_+, \quad (23)$$

where $\cos^2\chi = c_1^4 + c_1^2s_1^2(1 - \cos\phi)$ and $\sin^2\chi = s_1^4 + c_1^2s_1^2(1 + \cos\phi)$. The probability of the double beta decay integrated over neutrino momenta evidently does not contain interference between A_+ and A_- and is equal to:

$$W_{tot} = \cos^4\chi W_- + \sin^4\chi W_+, \quad (24)$$

where W_\pm are proportional to $|A_\pm|^2$.

The probability of decay into unusual bosonic neutrinos is proportional to the bi-linear combinations of the type K_mK_n , K_mL_n , L_mL_n , where

$$\begin{aligned} K_m^b &\equiv [E_m - E_i + E_{e1} + E_{\nu1}]^{-1} - [E_m - E_i + E_{e2} + E_{\nu2}]^{-1}, \\ L_m^b &\equiv [E_m - E_i + E_{e2} + E_{\nu1}]^{-1} - [E_m - E_i + E_{e1} + E_{\nu2}]^{-1}. \end{aligned} \quad (25)$$

Here the upper index b indicates that the results are applicable to bosonic neutrinos, E_i is the energy of the initial nuclei, E_m is the energy of the intermediate

nucleus state m , E_{ei} , and $E_{\nu i}$ are the energies of electrons and neutrinos respectively. The minus signs between the two terms in the above expressions are due to the bosonic character of neutrinos; in the case of fermionic neutrinos we would have plus signs³¹⁾. For electrons we assume the normal Fermi statistics.

In the case of $0^+ \rightarrow 0^+$ transitions the combinations K_m and L_m can be approximated by

$$K_m^b \approx \frac{E_{e2} - E_{e1} + E_{\nu 2} - E_{\nu 1}}{(E_m - E_i + E_0/2)^2}, \quad L_m^b \approx \frac{E_{e1} - E_{e2} + E_{\nu 2} - E_{\nu 1}}{(E_m - E_i + E_0/2)^2}, \quad (26)$$

whereas for the fermionic neutrinos

$$K_m^f \approx L_m^f \approx \frac{2}{E_m - E_i + E_0/2}. \quad (27)$$

Here $E_0/2 = E_e + E_\nu$ is the average energy of the leptonic pair. Appearance of the differences of the electron and neutrino energies in eq. (26) leads to a suppression of the total probability. It also modifies the energy distributions of electrons. The probabilities of the transitions $0^+ \rightarrow 2^+$ are proportional to the combinations $(K_m - L_m)(K_n - L_n)$, where

$$(K_m^b - L_m^b) \approx \frac{2(E_{e2} - E_{e1})}{(E_m - E_i + E_0/2)^2}. \quad (28)$$

In the case of fermionic neutrinos the combination has an additional factor $(E_{\nu 2} - E_{\nu 1})/(E_m - E_i + E_0/2)$ and the suppression is stronger.

A simple estimate shows that the probability of $0^+ \rightarrow 0^+$ -transition for bosonic neutrinos is suppressed by 1/250 for ^{56}Ge and by 1/10 for ^{100}Mo . Theoretically the total decay rate is known with the accuracy within a factor of few. This probably allows to exclude a 100% bosonic neutrino. However, the fraction of bosonic neutrino can still be very high. According to our preliminary calculations^{8, 32)} the value of the mixing angle can be as large as:

$$\sin^2 \chi \leq 0.7 \quad (29)$$

For $0^+ \rightarrow 2^+$ the situation is opposite: bosonic neutrinos are more efficiently produced. However, no interesting bound is obtained in this case because the statistics for these decays is much lower.

One can use the data on the spectrum of the emitted electrons, either single electron spectrum or distribution over the total energy of both electrons. The spectra do not have any noticeable ambiguity related to unknown nuclear matrix elements and the present day accuracy is at the level of 10%. Potentially their analysis may improve the above quoted limit (29) or indicate the existence

of a “bosonic” admixture to neutrinos. Some already observed anomalies may be interpreted as hints supporting the latter.

Unfortunately we cannot say at the present stage how the Fermi-Bose parameter introduced above (10) is related to the mixing angle χ . Even if we assume that the mixing angle in neutrino kinetics (7) is the same as in the definition of neutrino states (18), the unknown value of the angle ϕ which enters the commutation relations (19) and upon which depends the angle χ (23) makes the relation between κ and χ rather arbitrary.

7 Theoretical problems and discussion

Mentioned above ambiguities are related to intrinsic problems of formulation a theory with mixed statistics. Working at a naive level, as we did above, it is even difficult to define the properly normalized particle number operator. According to eqs. (18) and (20) it is natural to define the n identical neutrino state as

$$|n\rangle = (c_1 f^+ + s_1 b^+)^n |0\rangle \quad (30)$$

The normalization of this state is

$$\langle n|n\rangle = s_1^{2(n-1)} \left[n! s_1^2 + (n-1)! c_1^2 \left(\frac{\sin(n\phi/2)}{\sin(\phi/2)} \right)^2 \right] \quad (31)$$

If we introduce the particle number operator in the usual way:

$$\hat{n} = a^+ a, \quad (32)$$

then its diagonal matrix elements would be

$$\langle n|\hat{n}|n\rangle = s_1^{2(n-1)} \left[n n! s_1^4 + 2n! c_1^2 s_1^2 \cos \frac{\phi(n-1)}{2} \frac{\sin n\phi/2}{\sin \phi/2} + c_1^2 (n! s_1^2 + (n-1)! (c_1^2 - s_1^2)) \left(\frac{\sin(n\phi/2)}{\sin(\phi/2)} \right)^2 \right] \quad (33)$$

The particle number operator, as introduced above, has reasonable and self-consistent interpretation only for the case of pure statistics, while for mixed statistics it even does not commute with Hamiltonian if the latter, or operator \hat{n} , or both are not somehow modified.

There are no problems with reactions where only one neutrino is involved, but serious difficulties may arise with two neutrino reactions, as e.g. $\nu l \rightarrow \nu l$ or $\bar{\nu} \nu \rightarrow \bar{l} l$, even if the participating neutrinos are not in an identical state. The amplitude of νe -elastic scattering in the usual approach is given by the expansion of the T-exponent of the action and is described by two diagrams differing

by an interchange of emission and absorption points. If taken literally, the diagrams with W^\pm -exchange would give vanishing amplitude for purely bosonic neutrinos¹. In this case only Z -exchange would contribute to $\nu_e e$ -scattering and the cross-sections of $\nu_\mu e$ and $\nu_e e$ -scattering would be equal. Reactor neutrino experiments are consistent with the standard value of $\nu_e e$ cross-section and seem to exclude the possibility of purely bosonic ν_e . Using these data one can put a rather strong bound on bosonic admixture to electronic neutrino. On the other hand, perturbation theory with non-bosonic Hamiltonian may need to be modified and the above conclusion of vanishing of the amplitude of scattering of pure bosonic neutrinos on electrons would be invalid.

It is unclear if all these problems can be resolved in a simple way or drastic modifications of the underlying theory is necessary, which is a nontrivial task because the observed consequences of the theory must not be destroyed.

The presentation in the previous sections and in the original paper⁸⁾ was on pure (and poor) phenomenological level. For example if neutrinos have mixed statistics then in double beta decay the symmetry of the final state of neutrinos is mixed: symmetric with weight a_+ and antisymmetric with the weight a_- . It seems plausible that these weights are respectively $\cos^4 \chi$ and $\sin^4 \chi$ as argued in the previous section, eq. (24), simply on the basis on the normalization arguments.

Similar reasoning is possible for kinetic effects, eqs. (7,8). There are no rigorous theoretical arguments in favor of such description but the result (11) for the equilibrium distribution in the case of mixed statistics looks quite beautiful. Moreover, the fact that two “reasonable” (or natural) ways of description (7) and (8) give the same result is an argument in favor of their validity.

8 Conclusion

There is no consistent theoretical frameworks for description of mixed neutrino statistics and even in the case of purely bosonic neutrinos the fermionic property of the Hamiltonian would make a possible future theory quite unusual if it will ever be formulated. Still independently on theory there could be some predictions testable by experiment. So to summarize we will conclude that:

1. The suggestion of bosonic or mixed statistics for particles (neutrinos) with half integer spin looks exciting but opens a Pandora box of serious theoretical problems, which may be impossible to resolve without revolutionary modification of the standard theory. Such modification looks especially difficult in the case of mixed statistics.

¹This was noticed also by F. Vissani at this Conference.

2. The suggested mixture of statistics allows to break plenty of sacred principles, as e.g. Lorentz invariance, CPT-theorem, locality, etc, which are actively discussed now.
3. Bosonic neutrinos open a possibility of making all cosmological dark matter out of neutrinos in accordance with Occam's razor: "Plurality should not be posited without necessity."
4. "Bosonization" of neutrinos leads to effective number of neutrino species at BBN smaller than 3 and makes an agreement of the BBN calculations with the data noticeably better.
5. Analysis of accumulated and accumulating data on two neutrino double beta decay could restrict the admixture of wrong statistics to neutrinos or to indicate a violation of spin-statistics relation.
6. Last, but not the least, if the validity of spin-statistics theorem has been studied for the usual matter, electrons and nucleons it surely worth studying for neutrinos. The possibility that statistics is modified for neutrinos seems more plausible because neutrino is a natural particle to be a messenger from hidden sector of physics where some principles respected in our world can be violated.

References

1. A.D. Dolgov, *Phys. Rept.* **370** (2002) 333, hep-ph/0202122;
A.D. Dolgov, *Surveys High Energ. Phys.* **17** (2002) 91, hep-ph/0208222.
2. G.G. Raffelt, *AIP Conf. Proc.* **721** (2004) 130;
S. Hannestad, *New J. Phys.* **6** (2004) 108, hep-ph/0404239.
3. S. Hannestad, Talk given at NOW 2004: Neutrino Oscillation Workshop, Conca Specchiulla, Otranto, Italy, 11-17 Sep 2004, hep-ph/0412181;
R.H. Brandenberger, A. Mazumdar, M. Yamaguchi, *Phys. Rev.* **D69** (2004) 081301, hep-ph/0401239.
4. G.G. Raffelt, *Stars as laboratories for fundamental physics: the astrophysics of neutrinos, axions, and other weakly interacting particles*, Chicago, USA: Univ. Press. (1996);
G.G. Raffelt, astro-ph/0302589.
5. D.B. Kaplan, A.E. Nelson, N. Weiner, *Phys. Rev. Lett.* **93** (2004) 091801, hep-ph/0401099;
see also a talk by A. Masiero at this Conference, *Varying neutrino mass and dark energy*.
6. D. Fargion, B. Mele, A. Salis, *Astrophys. J.* **517** (1999) 725, astro-ph/9710029;
T. J. Weiler, *Phys. Rev. Lett.* **49** (1982) 234; *Astropart. Phys.* **11** (1999) 303, hep-ph/9710431;
Z. Fodor, S.D. Katz, A. Ringwald, "Oulu 2002, Beyond the desert" p. 567, hep-ph/0210123;
D.V. Semikoz, G. Sigl, *JCAP* **0404** (2004) 003, hep-ph/0309328.
7. A.D. Dolgov, S.H. Hansen, S. Pastor, S.T. Petcov, G.G. Raffelt, D.V. Semikoz, *Nucl. Phys.* **B632** (2002) 363, hep-ph/0201287.
8. A.D. Dolgov, A.Yu. Smirnov, hep-ph/0501066.
9. H.V. Klapdor-Kleingrothaus, et al, *Eur. Phys. J.* **A12** (2001) 147; H.V. Klapdor-Kleingrothaus, A. Dietz, I.V. Krivosheina, O. Chkvorets *Nucl. Instrum. Meth.* **A522** (2004) 371;
The NEMO Collaboration (R. Arnold et al.) *JETP Lett.* **80** (2004) 429; [*JETP Lett.* **80** (2004) 377; hep-ex/0410021].
10. V.A. Kostelecky, M. Mewes, *Phys. Rev.* **D70** (2004) 031902, hep-ph/0308300, *Phys. Rev.* **D69** (2004) 016005 hep-ph/0309025;
N.E. Mavromatos, hep-ph/0402005, Talk given at 2nd International Workshop on Neutrino Oscillations in Venice (NO-VE 2003), Venice, Italy, 3-5 Dec 2003. "Venice 2003, Neutrino oscillations" 405.

11. A.Yu. Ignatiev, V.A. Kuzmin, *Yad. Fiz.* **46** (1987) 786 [*Sov. J. Nucl. Phys.* **46** (1987) 786]; *JETP Lett.* **47** (1988) 4;
L.B. Okun, *Pis'ma ZhETF*, **46** (1987) 420 [*JETP Lett.* **46** (1987) 529];
Yad. Fiz. **47** (1988) 1192;
O.W. Greenberg, R.N. Mohapatra, *Phys. Rev. Lett.* **59** (1987) 2507, **62** (1989) 712, *Phys. Rev. D***39** (1989) 2032;
A.B. Govorkov, *Theor. Math. Phys.* **54** (1983) 234;
A.B. Govorkov, *Phys. Lett. A***137** (1989) 7;
L.B. Okun, *Uspekhi Fiz. Nauk*, **158** (1989) 293 [*Sov. Phys. Usp.* **32** (1989) 543], *Comments Nucl. Part. Phys.* **19** (1989) 99.
12. H.S. Green, *Phys. Rev.* **90** (1953) 270;
O.W. Greenberg, *Phys. Rev. Lett.* **13** (1964) 598;
O.W. Greenberg, A.M.L. Messiah, *Phys. Rev.* **138** (1965) B1155;
R.N. Mohapatra, *Phys. Lett B***242** (1990) 407;
O.W. Greenberg, A.K. Mishra, *Phys. Rev. D***70** (2004) 125013, math-ph/0406011.
13. M. Goldhaber, G. Scharff-Goldhaber, *Phys. Rev.* **73** (1948) 1472;
E. Fishbach, T. Kirsten and O. Shaeffer, *Phys. Rev. Lett.* **20** (1968) 1012;
F. Reines, H.W. Sobel, *Phys. Rev. Lett.* **32** (1974) 954;
B.A. Logan, A. Ljubicic, *Phys. Rev. C***20** (1979) 1957;
R.D. Amado, H. Primakoff, *Phys. Rev. C***22** (1980) 1338;
E. Ramberg, G. Snow, *Phys. Lett. B***238** (1990) 438;
K. Deilamian, J. D. Gillaspay, D. Kelleher, *Phys. Rev. Lett.* **74** (1995) 4787;
V. M. Novikov, A. A. Pomansky, E. Nolte, *JETP Lett.* **51** (1990) 1;
V.M. Novikov, et al., *Phys. Lett. B***240** (1990) 227.
14. R. Plaga, *Z. Phys. A* **333** (1990) 397; A.C. Barabash, V.N. Kornoukhov, Yu.M. Tsipenyuk, V.A. Chapyzhnikov, *Pis'ma ZhETF*, **68** (1998) 104 [*JETP Lett.* **68** (1998) 112];
The NEMO Collaboration (R. Arnold et al.) *Eur. Phys. J. A***6** (1999) 361;
E. Baron, R.N. Mohapatra, V.L. Teplitz, *Phys. Rev. D***59** (1999) 036003;
Borexino collaboration, H.O.Back, et al, hep-ph/0406252, *European Physical Journal C* **37** (2004) 421.
15. C. Itzykson, J.-B. Zuber, *Quantum Field Theory*, p. 150; McGraw-Hill, 1985;
S. Weinberg, *The Quantum Theory of Fields*, pp. 144, 236; Cambridge University Press, 1995.
16. S. Tremaine, J.E. Gunn, *Phys. Rev. Lett.* **42** (1979) 407.
17. S.S. Gerstein, Ya.B. Zeldovich, *Pisma Zh. Eksp. Teor. Fiz.* **4** (1966) 174 [*JETP Lett.* **4** (1966) 120].

18. I. Affleck, M. Dine, *Nucl. Phys.* **B249** (1985) 361.
19. J. Madsen, *Phys. Rev. Lett.* **69** (1992) 571.
20. A.D. Dolgov, *Pisma Zh. Eksp. Teor. Fiz.* **29** (1979) 254.
21. A. D. Dolgov, S. H. Hansen, A. Yu. Smirnov, astro-ph/0503612.
22. L. Cucurull, J.A. Grifols, R. Toldra, *Astropart. Phys.* **4**, (1996) 391.
23. Eidelman S *et al*, 2004 *Phys. Lett.* **B592** 1
24. Fields B D and Olive K A, 2005 arXiv:astro-ph/9803297.
25. Izotov Y I and Thuan T X, 2004, *Astrophys. J.* **602**, 200
26. Trotta R and Hansen S H, 2004 *Phys. Rev. D* **69** 023509
27. Steigman G, astro-ph/0501591, To appear in the Proceedings of the ESO/Arcetri Workshop on "Chemical Abundances and Mixing in Stars in the Milky Way and its Satellites", eds., L. Pasquini and S. Randich (Springer-Verlag Series, "ESO Astrophysics Symposia").
28. A.D. Dolgov, F. Takahashi, *Nucl. Phys.* **B688** (2004) 189, hep-ph/0402066; A.D. Dolgov, F. Takahashi, Talk given at 12th International Conference on Supersymmetry and Unification of Fundamental Interactions (SUSY 04), Tsukuba, Japan, 17-23 Jun 2004, hep-ph/0409299.
29. C. Lunardini and A.Yu. Smirnov, *Phys. Rev. D***64** (2001) 073006.
30. V.M. Lobashev *et al*, *Phys. Lett.* **B460** (1999) 227; Ch. Weinheimer *et al*, *Phys. Lett.* **B460** (1999) 219.
31. W. C. Haxton, G. J. Stephenson Jr., *Prog. in Part. and Nucl. Phys.* **12** (1984) 409; M. Doi *et al.*, *Prog. of Theor. Phys. Suppl.* **83** (1985); J. D. Vergados *Phys. Rep.* **133** (1986) 1; F. Boehm and P. Vogel, *Physics of massive neutrinos*, Cambridge Univ. Press. 1987.
32. A. Barabash, A. Dolgov, P. Domin, F. Simkovic, A. Smirnov (in progress).

PARTICLE DARK MATTER

R. Bernabei

DAMA collaboration *

*Dipartimento di Fisica, Università di Roma "Tor Vergata"
and INFN, Sezione di Roma2, I-00133 Rome, Italy*

Abstract

Experimental observations and theoretical considerations have shown that a large part of the Universe is made of Cold Dark Matter particles, relics from the Big Bang; this has currently motivated a large experimental effort to investigate them both by direct and indirect detection methods. In particular, the DAMA/NaI experiment ($\simeq 100$ kg highly radiopure NaI(Tl)) had the unique feature to effectively investigate the presence of a Dark Matter particle component in the galactic halo in a model independent way by exploiting the so-called annual modulation signature. With a total exposure of more than 10^5 kg · day, collected over seven annual cycles deep underground at the Gran Sasso National Laboratory of the I.N.F.N., it has pointed out – at 6.3σ C.L. – an effect which satisfies all the many peculiarities of the signature and neither systematic effects nor side reactions able to mimic the signature were found. Moreover, several (but still few with respect to the possibilities) corollary model dependent quests for the candidate particle have been carried out. In this paper the obtained results are summarized and some perspectives are discussed at some extent. Comparisons with other searches and their future possible projections are addressed as well.

* DAMA collaboration:

R. Bernabei, P. Belli, F. Cappella, F. Montecchia, F. Nozzoli

*Dipartimento di Fisica, Università di Roma "Tor Vergata"
and INFN, Sezione di Roma2, I-00133 Rome, Italy*

A. d'Angelo, A. Incicchitti, D. Prosperi

*Dipartimento di Fisica, Università di Roma "La Sapienza"
and INFN, Sezione di Roma, I-00185 Rome, Italy*

R. Cerulli

INFN - Laboratori Nazionali del Gran Sasso, I-67010 Assergi (Aq), Italy

C.J. Dai, H.H. Kuang, H.L. He, J.M. Ma, Z.P. Ye

IHEP, Chinese Academy, P.O. Box 918/3, Beijing 100039, China

1 Introduction

The problem of the existence of Dark Matter in our Universe dates back to the astrophysical observations at the beginning of past century ^{1, 2)}, but the presence of Dark Matter in our Universe has been definitively accepted by the scientific community only about 40 years later, when two groups performed systematic measurements of the rotational velocities of celestial bodies in spiral galaxies ³⁾. After the '70 many other observations have further confirmed the presence of Dark Matter in the Universe and, at present, the measurements are mainly devoted to the investigation of the quantity, of the distribution (from the cosmological scale down to the galactic one) and of the nature of the Dark Matter in the Universe. Recent measurements of the CMB temperature anisotropy by WMAP ⁴⁾, analysed in the framework of the *Big Bang* cosmological scenario, support a density of the Universe: $\Omega = 1$, further crediting that most of the Universe is dark. Recently, observations on the supernovae Ia at high red-shift as standard candles have suggested that about 73% of Ω might be in form of a *dark energy* ⁵⁾; the argument is still under investigation and presents some problems on possible theoretical interpretations. However, even in this scenario – where the matter density in the Universe would be $\Omega_m \sim 0.3$ ^{4, 6)} – large space for Dark Matter particles in the Universe exists. In fact, the luminous matter can only account for a density $\simeq 0.005$ and the baryonic Dark Matter for $\simeq 0.04$. On the other hand, the contribution of Dark Matter particles relativistic at the decoupling time (such as light neutrinos) is also restricted to be $\lesssim 0.01$ by considerations on large scale structure formations ⁷⁾. Thus, most of the Dark Matter particles in the Universe, relics from the Big Bang, were either produced at rest or non relativistic at decoupling time; they are named Cold Dark Matter particles (CDM). The CDM candidates have to be neutral, stable or quasi-stable (e.g. with a time decay of order of the age of the Universe) and have to be elusive in the interaction with ordinary matter. These features are respected by the axions (also already investigated by DAMA/NaI ⁸⁾), by the axion-like candidates with mass up to tens keV, by a class of candidates named WIMPs (Weakly Interacting Massive Particles) and by some other candidates which cannot properly be classified as WIMP, but which offer similar phenomenology.

Since in the Standard Model of particle Physics no suitable particle as CDM candidate exists, a window beyond the Standard Model is investigated. At present, a widely considered candidate for CDM is the lightest supersymmetric particle named neutralino. In fact, in the supersymmetric theories where the R-parity is conserved, the lightest supersymmetric particle must be stable and can interact neither by electromagnetic nor by strong interactions, otherwise it would be detected in the galactic halo as the ordinary matter is. However,

other candidates are also considered, such as e.g. a heavy neutrino of the 4th family or a sneutrino (the spin-0 supersymmetric partner of the neutrino) in a multi-component Dark Matter scenario. Moreover, a dominant contribution of a sneutrino candidate remains still possible in supersymmetric models with violation of lepton number, where two mass states and a small energy splitting is present, as reported in ref. ⁹⁾; a similar sneutrino can only inelastically scatter off nuclei, after its excitation to the low lying energy level. Other possible candidates are the particles from multi-dimensional Kaluza-Klein-like theories, the mirror Dark Matter particles ¹⁰⁾, the self-interacting dark matter particles ¹¹⁾, etc. Moreover, in principle even whatever particle with suitable characteristics, not yet foreseen by theories, can be a good candidate as CDM.

Several observations have pointed out that our Galaxy should also be embedded in a dark halo with mass at least 10 times larger than that of the luminous matter. The CDM particles of this dark halo can be investigated either by direct (deep underground) or by indirect (in space or underwater or underground) approaches. In the first case, their interaction on target nuclei can be detected by means of the signal induced by the recoiling nucleus or, in case of inelastic scattering, also by the successive de-excitation gamma's; moreover, other possibilities which directly involve ionization/excitation phenomena in the detector remain still open. In the other case, the flux of secondary particles - mainly neutrinos, positrons, anti-protons, gamma's - produced by possible annihilation of some of the CDM candidates either in the Sun or in the Earth or in the halo may be detected. Most of the approaches are limited by the possibility to give only a model dependent result; relate discussions can be found e.g. in refs. ^{12, 13)} and references therein.

2 A direct detection experiment exploiting a model independent signature: DAMA/NaI

The DAMA/NaI experiment was proposed in 1990 ¹⁴⁾, designed and realized having the main aim to investigate in a model independent way the presence of a Dark Matter particle component in the galactic halo ^{15, 16, 17, 18, 19, 20, 21, 22, 12, 13)}. For this purpose, we planned to exploit the effect of the Earth revolution around the Sun on the Dark Matter particles interactions on a suitable underground set-up. In fact, as a consequence of its annual revolution, the Earth should be crossed by a larger flux of Dark Matter particles in June (when its rotational velocity is summed to the one of the solar system with respect to the Galaxy) and by a smaller one in December (when the two velocities are subtracted).

In fact, the expected differential rate as a function of the recoil energy, dR/dE_R (see ref. ¹²⁾ for detailed discussion), depends on the CDM velocity

distribution and on the Earth's velocity in the galactic frame, $\vec{v}_e(t)$. Projecting $\vec{v}_e(t)$ on the galactic plane, one can write: $v_e(t) = v_\odot + v_\oplus \cos\gamma \cos\omega(t - t_0)$. Here v_\odot is the Sun's velocity with the respect to the galactic halo ($v_\odot \simeq v_0 + 12$ km/s and v_0 is the local velocity whose value is in the range 170-270 km/s ^{17, 23}); $v_\oplus = 30$ km/s is the Earth's orbital velocity around the Sun on a plane with inclination $\gamma = 60^\circ$ with the respect to the galactic plane. Furthermore, $\omega = 2\pi/T$ with $T=1$ year and roughly $t_0 \simeq 2^{nd}$ June (when the Earth's speed is at maximum). The Earth's velocity can be conveniently expressed in unit of v_0 : $\eta(t) = v_e(t)/v_0 = \eta_0 + \Delta\eta \cos\omega(t - t_0)$, where – depending on the assumed value of the local velocity – $\eta_0=1.04-1.07$ is the yearly average of η and $\Delta\eta = 0.05-0.09$. Since $\Delta\eta \ll \eta_0$, the expected counting rate in a k -th energy interval can be expressed by the first order Taylor approximation:

$$S_k[\eta(t)] = S_k[\eta_0] + \left[\frac{\partial S_k}{\partial \eta}\right]_{\eta_0} \Delta\eta \cos\omega(t - t_0) = S_{0,k} + S_{m,k} \cos\omega(t - t_0), \quad (1)$$

with the contribution from the highest order terms less than 0.1%. This annual modulation signature is very distinctive since a seasonal effect induced by CDM particles must simultaneously satisfy all the following requirements: (i) the rate must contain a component modulated according to a cosine function; (ii) with one year period; (iii) a phase that peaks roughly around $\simeq 2^{nd}$ June; (iv) this modulation must only be found in a well-defined low energy range, where CDM particles can induce signals; (v) it must apply to those events in which just one detector of many actually "fires", since the probability that CDM particles would have multiple interactions is negligible; (vi) the modulation amplitude in the region of maximal sensitivity must be $\lesssim 7\%$ for usually adopted halo distributions, but it can be significantly larger in case of some possible scenarios such as e.g. those in refs. ^{9, 24}). Only systematic effects able to fulfil these requirements and to account for the whole observed modulation amplitude could mimic this signature; thus, no other effect investigated so far in the field of rare processes offers a so stringent and unambiguous signature. With the present technology, the annual modulation signature remains the main signature of a CDM signal in the galactic halo, offering an efficient model independent signature, able to test a large interval of cross sections and of halo densities; it was originally suggested in the middle of '80 by ²⁵).

The DAMA/NaI experiment was located deep underground in the Gran Sasso National Laboratory of I.N.F.N. ^{26, 27, 28, 29}); it has been part of the DAMA project, which is also composed by several other low background set-ups, such as: i) DAMA/LXe ($\simeq 6.5$ kg pure liquid Xenon scintillator, using Kr-free enriched Xenon) ^{30, 31}); ii) DAMA/R&D, set-up devoted to tests on prototypes and small scale experiments ³²); iii) the new second generation larger mass NaI(Tl) radiopure set-up DAMA/LIBRA (see later); iv)

DAMA/Ge detector for sample measurements.

In particular, the NaI(Tl) scintillator was chosen as the best target material to investigate the process since it offers several competing advantages with the respect to every other technique considered so far, such as: well known technology; large mass; high duty cycle; feasible well controlled operational conditions and monitoring; routine calibrations feasible down to keV range in the same conditions as the production runs; high light response, that is keV threshold reachable; absence of the necessity of re-purification or cooling down/warming up procedures (implying high reproducibility, high stability, etc.); absence of microphonic noise and an effective noise rejection at threshold (time decay of NaI(Tl) pulses is hundreds ns, while that of noise pulses is tens ns); reachable high radiopurity by material selections and protocols, by chemical/physical purifications, etc.; sensitivity to spin-independent (SI), spin-dependent (SD), mixed (SI&SD) couplings as well as to many other existing scenarios; sensitivity to both high (by Iodine target) and low (by Na target) mass candidates; possibility to effectively investigate the annual modulation signature in all the needed aspects; pulse shape discrimination feasible at reasonable level; possibility to achieve significant results on several other rare processes; no safety problems; necessity of a relatively small underground space; the lowest cost with the respect to every other considered technique; etc.

Considering its main goal, DAMA/NaI has been designed by employing and further developing all the necessary low-background techniques and procedures. A detailed description of the set-up, of its radiopurity, of its performance, of the used hardware procedures, of the determination of the experimental quantities and of the data reduction has been given in refs. 33, 18, 19, 12, 13). Here only few arguments are addressed.

The nine 9.7 kg highly radiopure DAMA/NaI crystals are encapsulated in radiopure Cu housings; moreover, 10 cm long Tetrasil-B light guides act as optical windows on the two end faces of each crystals and are coupled to specially developed low background photomultipliers (PMT). The measured light response is 5.5 – 7.5 photoelectrons/keV depending on the detector. The two PMTs of a detector work in coincidence with hardware thresholds at the single photoelectron level in order to assure high efficiency for the coincidence at few keV level. The energy threshold of the experiment, 2 keV, is instead determined by means of X-rays sources and of keV range Compton electrons on the basis also of the features of the noise rejection procedures and of the efficiencies when lowering the number of available photoelectrons 33).

The detectors are enclosed in a sealed copper box, continuously maintained in HP Nitrogen atmosphere in slightly overpressure with respect to the external environment.

A suitable low background hard shield against electromagnetic and neutron background was realized using very high radiopure Cu and Pb bricks 33),

Cd foils and 10/40 cm polyethylene/paraffin; the hard shield is also sealed in a plexiglas box and maintained in the high purity (HP) Nitrogen atmosphere. Moreover, about 1 m concrete (made from the Gran Sasso rock material) almost fully surrounds the hard shield outside the barrack and at its bottom, acting as a further neutron moderator.

A three-level sealing system from environmental Radon is effective. In fact, in addition to the previous sealed boxes in HP Nitrogen atmosphere, the inner part of the barrack, where the set-up is allocated, has also the floor (above the concrete) and all the walls sealed by Supronyl (permeability: $2 \cdot 10^{-11}$ cm²/s ³⁴) plastic and the entrance door is air-tight. A low level oxygen alarm informs the operator before entering the inner part of the barrack since the HP Nitrogen which fills both the inner Cu box and the external plexiglas box is released in this closed environment. The Radon level inside the (sealed) barrack is continuously monitored and recorded with the production data ^{15, 16, 33, 18, 19, 12, 13}; it is at the level of sensitivity of the used radonmeter.

On the top of the shield a glove-box (also maintained in the HP Nitrogen atmosphere and equipped with a compensation chamber) is directly connected to the inner Cu box, housing the detectors, through Cu pipes. The pipes are filled with low radioactivity Cu bars (covered by 10 cm of low radioactive Cu and 15 cm of low radioactive Pb) which can be removed to allow the insertion of the holders of the radioactive sources for calibrating the detectors in the same running condition, without any contact with external environment ³³).

The whole installation is air-conditioned and the operating temperature as well as many other parameters are continuously monitored and acquired with the production data. Moreover, self-controlled computer processes automatically monitor several parameters and manage alarms ^{33, 19, 12}).

The electronic chain and the data acquisition system operative up to summer 2000 have been described in ref. ³³), while the new electronics and DAQ installed in summer 2000 have been described in ref. ¹²). Moreover, the experiment took data up to MeV energy region despite the optimization was done for the keV energy range.

The following part of this paper will summarize the final model independent result, some of the corollary quests for the candidate particle, comparisons, implications and perspectives. However, it is worth to remind that - thanks to its radiopurity and features - DAMA/NaI has also investigated other approaches for Dark Matter particles in ref. ^{35, 36}) and several other rare processes such as: possible processes violating the Pauli exclusion principle ³⁷), CNC processes in ²³Na and ¹²⁷I ³⁸), electron stability ³⁹), searches for neutral SIMPs ⁴⁰), for neutral nuclearites ⁴⁰), for Q-balls ⁴¹) and for solar

axions⁸⁾; moreover, DAMA/NaI allowed also the study of nuclear transition to a possible superdense nuclear state⁴²⁾ and possible two-body cluster decay of ^{127}I ⁴³⁾.

2.1 The 6.3σ C.L. model-independent evidence for a Dark Matter component in the galactic halo

The DAMA/NaI set-up has exploited the annual modulation signature over seven annual cycles^{15, 16, 17, 18, 19, 20, 21, 22, 12, 13)}. The presence of a model independent positive evidence in the data of DAMA/NaI has been firstly reported by the DAMA collaboration at the TAUP conference in 1997⁴⁴⁾ and published also in¹⁵⁾, confirmed in^{16, 17)}, further confirmed in^{18, 19, 20, 21, 22)} and conclusively confirmed, at end of experiment, in 2003^{12, 13)}.

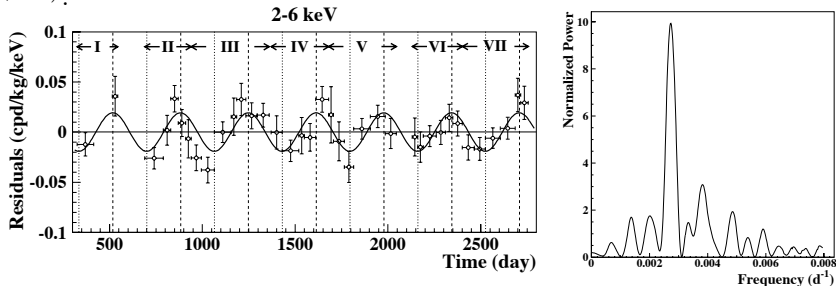


Figure 1: On the left: *experimental residual rate for single-hit events in the cumulative (2–6) keV energy interval as a function of the time over 7 annual cycles (total exposure $107731 \text{ kg} \times \text{day}$); end of data taking July 2002. The experimental points present the errors as vertical bars and the associated time bin width as horizontal bars. The superimposed curve represents the cosinusoidal function behaviour expected for a Dark Matter particle signal with a period equal to 1 year and phase exactly at 2nd June; the modulation amplitude has been obtained by best fit. See ref. ^{12, 13)}. On the right: *power spectrum of the measured single-hit residuals for the cumulative (2–6) keV energy interval calculated including also the treatment of the experimental errors and of the time binning. As it can be seen, the principal mode corresponds to a frequency of $2.737 \cdot 10^{-3} \text{ d}^{-1}$, that is to a period of $\simeq 1$ year.**

During seven independent experiments of one year each one, it has pointed out the presence of a modulation satisfying the many peculiarities of a particle Dark Matter induced effect, reaching an evidence at 6.3σ C.L.. In fact, a model-independent approach on the data collected by DAMA/NaI over seven annual cycles offers an immediate evidence of the presence of an annual modu-

lation of the measured rate of the *single-hit* events in the lowest energy region. In particular, in Fig. 1 – *left* the time behaviour of the residual rate of the *single-hit* events in the cumulative (2-6) keV energy interval is reported. The data favour the presence of a modulated cosine-like behaviour at 6.3σ C.L. and their fit for this cumulative energy interval offers modulation amplitude equal to (0.0200 ± 0.0032) cpd/kg/keV, a phase $t_0 = (140 \pm 22)$ days and a period $T = (1.00 \pm 0.01)$ year, all parameters kept free in the fit. The period and phase agree with those expected in the case of an effect induced by Dark Matter particles of the galactic halo ($T = 1$ year and t_0 roughly at $\simeq 152.5^{th}$ day of the year). The χ^2 test on the (2–6) keV residual rate disfavors the hypothesis of unmodulated behaviour giving a probability of $7 \cdot 10^{-4}$ ($\chi^2/d.o.f. = 71/37$). The same data have also been investigated by a Fourier analysis as shown in Fig. 1 – *right*, where a clear peak corresponding to a period of $\simeq 1$ year is present. Modulation is not observed above 6 keV¹²⁾. Finally, a suitable statistical analysis has shown that the modulation amplitudes are statistically well distributed in all the crystals, in all the data taking periods and considered energy bins. More arguments can be found in ref. 12, 13) and references therein. A careful quantitative investigation of all the known possible sources

Table 1: *Summary of the results obtained by investigating the possible sources of systematics or of side reactions*^{12, 13)}. *No systematics or side reaction has been found able to give a modulation amplitude different from zero; thus very cautious upper limits (90% C.L.) have been calculated and are shown here in terms of the measured model independent modulation amplitude, S_m^{obs} . As it can be seen, they cannot account for the measured modulation amplitude and, in addition, cannot satisfy the peculiar requirements of the signature*^{19, 12, 13)}.

Source	Cautious upper limit (90%C.L.)
Radon	$< 0.2\% S_m^{obs}$
Temperature	$< 0.5\% S_m^{obs}$
Noise	$< 1\% S_m^{obs}$
Energy scale	$< 1\% S_m^{obs}$
Efficiencies	$< 1\% S_m^{obs}$
Background	$< 0.5\% S_m^{obs}$
Side reactions	$< 0.3\% S_m^{obs}$
In addition: no effect can mimic the signature	

of systematic and side reactions has been regularly carried out and published at time of each data release; in particular, quantitative detailed discussions can

be found in refs. 19, 12, 13). No systematic effect or side reaction able to account for the observed modulation amplitude and to satisfy all the requirements of the signature has been found. Thus, very cautious upper limits (90% C.L.) on the possible contributions to the modulated amplitude have been calculated as summarized in Table 1; for a detailed quantitative discussion see ref. 19, 12, 13).

As a further relevant investigation, the *multiple-hits* events collected during the DAMA/NaI-6 and 7 running periods (when each detector was equipped with its own Transient Digitizer with a dedicated renewed electronics) have been studied and analysed by using the same identical hardware and the same identical software procedures as for the case of the *single-hit* events (see Fig. 2). The *multiple-hits* events class – on the contrary of the *single-hit* one –

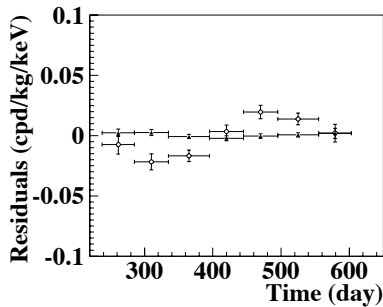


Figure 2: *Experimental residual rates over seven annual cycles for single-hit events (open circles) – class of events to which Dark Matter particle events belong – and over the last two annual cycles for multiple-hits events (filled triangles) – class of events to which Dark Matter particle events do not belong – in the (2–6) keV cumulative energy interval. They have been obtained by considering for each class of events the data as collected in a single annual cycle and using in both cases the same identical hardware and the same identical software procedures. The initial time is taken on August 7th. See text.*

does not include events induced by Dark Matter particles since the probability that a Dark Matter particle interacts in more than one detector is negligible. The fitted modulation amplitudes are: $A = (0.0195 \pm 0.0031)$ cpd/kg/keV and $A = -(3.9 \pm 7.9) \cdot 10^{-4}$ cpd/kg/keV for *single-hit* and *multiple-hits* residual rates, respectively. Thus, evidence of annual modulation with proper features is present in the *single-hit* residuals (events class to which the CDM particle-induced recoils belong), while it is absent in the *multiple-hits* residual rate (event class to which only background events belong). Since the same identical hardware and the same identical software procedures have been used to analyse the two classes of events, the obtained result offers an additional strong

support for the presence of Dark Matter particles in the galactic halo further excluding any side effect either from hardware or from software procedures or from background.

In conclusion, the presence of a Dark Matter particle component in the galactic halo is supported by DAMA/NaI at 6.3σ C.L. and the modulation amplitude measured over those 7 annual cycles in NaI(Tl) at the location of the Gran Sasso Laboratory for the (2 – 6) keV energy region is (0.0200 ± 0.0032) cpd/kg/keV. This is the experimental result of DAMA/NaI. It is model independent; no other experiment whose result can be directly compared with this one is available so far in the field of Dark Matter investigation.

2.2 Corollary results: quests for a candidate particle in some of the many possible model frameworks

On the basis of the obtained 6.3σ model-independent result, corollary investigations can also be pursued on the nature of the Dark Matter particle candidate. This latter investigation is instead model-dependent and – considering the large uncertainties which exist on the astrophysical, nuclear and particle physics assumptions and on the theoretical and experimental parameters needed in the calculations – has no general meaning (as it is also the case of exclusion plots and of the Dark Matter particle parameters evaluated in indirect detection experiments). Thus, it should be handled in the most general way as we have pointed out with time passing 15, 16, 17, 18, 19, 20, 21, 22, 12, 13).

Candidates, kinds of Dark Matter particle couplings with ordinary matter and implications, cross sections, nuclear form factors, spin factors, scaling laws, halo models, priors, etc. are discussed in ref. 12). The reader can find in this latter paper and in references therein devoted discussions to correctly understand the results obtained in corollary quests and the real validity of any claimed model-dependent comparison in the field. Here, we just remind that the results briefly summarized here are not exhaustive of the many scenarios possible at present level of knowledge, including those depicted in some more recent works such as e.g. refs. 24, 45).

DAMA/NaI is intrinsically sensitive both to low and high Dark Matter particle mass having both a light (the ^{23}Na) and a heavy (the ^{127}I) target-nucleus; in previous corollary quests for the candidate, dark matter particle masses above 30 GeV (25 GeV in ref. 15)) have been presented 16, 18, 20, 21, 22) for few (of the many possible) model frameworks. However, that bound holds only for neutralino when supersymmetric schemes based on GUT assumptions are adopted to analyse the LEP data 46). Thus, since other candidates are possible and also other scenarios can be considered for the neutralino itself as recently

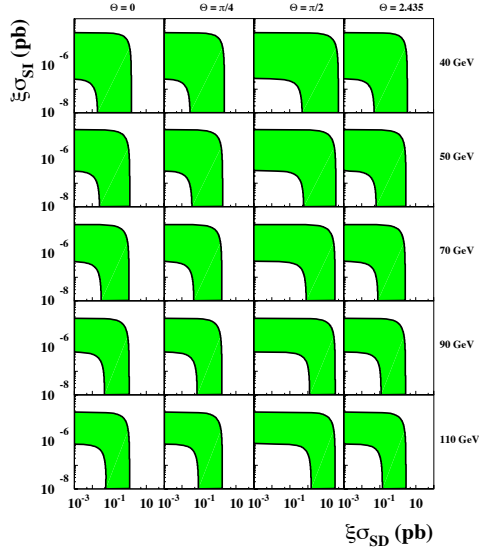


Figure 3: Case of a Dark Matter particle with mixed SI&SD interaction in the model frameworks of ref. 12). Coloured areas: example of slices (of the 4-dimensional allowed volume) in the plane $\xi\sigma_{SI}$ vs $\xi\sigma_{SD}$ for some of the possible m_W and θ values. Four SD couplings are reported as examples: *i*) $\theta = 0$ ($a_n = 0$ and $a_p \neq 0$ or $|a_p| \gg |a_n|$) corresponding to a particle with null SD coupling to neutron; *ii*) $\theta = \pi/4$ ($a_p = a_n$) corresponding to a particle with the same SD coupling to neutron and proton; *iii*) $\theta = \pi/2$ ($a_n \neq 0$ and $a_p = 0$ or $|a_n| \gg |a_p|$) corresponding to a particle with null SD couplings to proton; *iv*) $\theta = 2.435$ rad ($\frac{a_n}{a_p} = -0.85$) corresponding to a particle with SD coupling through Z_0 exchange. The case $a_p = -a_n$ is nearly similar to the case *iv*). Inclusion of other existing uncertainties on parameters and models would further extend the regions; for example, the use of more favourable form factors and/or of more favourable spin factors than the considered ones would move them towards lower cross sections.

pointed out¹, the present model-dependent lower bound quoted by LEP for the neutralino in the supersymmetric schemes based on GUT assumptions is simply marked in the following figures. It is worth to note that this model dependent LEP limit – when considered – selects the CDM particle-Iodine elastic scatterings as dominant.

¹In fact, when the assumption on the gaugino-mass unification at GUT scale is released, neutralino masses down to $\simeq 6$ GeV are allowed (47, 48).

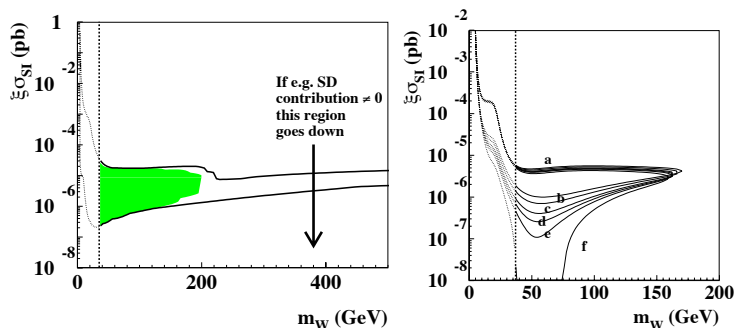


Figure 4: On the left : Case of a Dark Matter particle with dominant SI interaction for the model frameworks of ref. ¹²⁾. *Region allowed in the plane (m_W , $\xi\sigma_{SI}$).* The vertical dotted line represents a bound in case of a neutralino candidate when supersymmetric schemes based on GUT assumptions are adopted to analyse the LEP data; the low mass region is allowed for neutralino when other schemes are considered and for every other candidate; see text. While the area at Dark Matter particle masses above 200 GeV is allowed only for few configurations, the lower one is allowed by most configurations (the colored region gathers only those above the vertical line) ¹²⁾. The inclusion of other existing uncertainties on parameters and models would further extend the region; for example, the use of more favourable SI form factor for Iodine alone would move it towards lower cross sections. On the right : Example of the effect induced by the inclusion of a SD component different from zero on allowed regions given in the plane $\xi\sigma_{SI}$ vs m_W . In this example the Evans' logarithmic axisymmetric C2 halo model with $v_0 = 170$ km/s, ρ_0 equal to the maximum value for this model and a given set of the parameters' values (see ¹²⁾) have been considered. The different regions refer to different SD contributions for the particular case of $\theta = 0$: $\sigma_{SD} = 0$ pb (a), 0.02 pb (b), 0.04 pb (c), 0.05 pb (d), 0.06 pb (e), 0.08 pb (f). Analogous situation is found for the other model frameworks.

For simplicity, here the results of these corollary quests for a candidate particle are presented in terms of allowed regions obtained as superposition of the configurations corresponding to likelihood function values *distant* more than 4σ from the null hypothesis (absence of modulation) in each of the several (but still a limited number) of the possible model frameworks considered in ref. ¹²⁾. These allowed regions/volumes take into account the time and energy behaviours of the single-hit experimental data and have been obtained by a maximum likelihood procedure (for a formal description see e.g. refs. 15, 16, 18)) which requires the agreement: i) of the expectations for the mod-

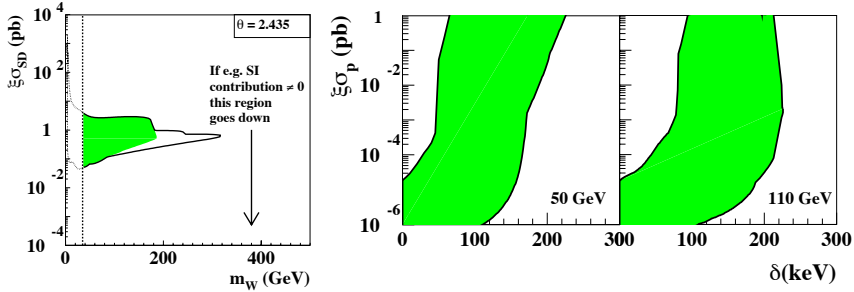


Figure 5: On the left: Case of a Dark Matter particle with dominant SD interaction in the model frameworks of ref. ¹²⁾. *Example of a slice (of the 3-dimensional allowed volume) in the plane (m_W , $\xi\sigma_{SD}$) at a given θ value (θ is defined in the $[0, \pi)$ range); here $\theta = 2.435$ (Z_0 coupling). For the definition of the vertical line and of the coloured area see the caption of Fig. 4. Inclusion of other existing uncertainties on parameters and models (as discussed in ref. ^{12, 13)}) would further extend the SD allowed regions. For example, the use of more favourable SD form factors and/or more favourable spin factors would move them towards lower cross sections. Values of $\xi\sigma_{SD}$ lower than those corresponding to this allowed region are possible also e.g. in case of an even small SI contribution (see ref. ^{12, 13)}). On the right: Case of a Dark Matter particle with preferred inelastic interaction in the model frameworks of ref. ¹²⁾. *Examples of slices (coloured areas) of the 3-dimensional allowed volume ($\xi\sigma_p$, δ , m_W) for some m_W values. Inclusion of other existing uncertainties on parameters and models would further extend the regions; for example, the use of more favourable form factors and of different escape velocity would move them towards lower cross sections. For details see ref. ^{12, 13)}.**

ulated part of the signal with the measured modulated behaviour for each detector and for each energy bin; ii) of the expectations for the unmodulated component of the signal with the respect to the measured differential energy distribution and - since ref. ¹⁸⁾ - also with the bound on recoils obtained by pulse shape discrimination from the devoted DAMA/NaI-0 data ³⁵⁾. The latter one acts in the likelihood procedure as an experimental upper bound on the unmodulated component of the signal and - as a matter of fact - as an experimental lower bound on the estimate of the background levels. Thus, the C.L.'s, we quote for the allowed regions, already account for compatibility with the measured differential energy spectrum and with the measured upper bound on recoils. Finally, it is worth to note that the best fit values of cross

sections and Dark Matter particle mass span over a large range when varying the considered model framework, thanks also to the different sensitivity due to the light (Sodium) and heavy (Iodine) target-nuclei.

Fig. 3, 4, 5 show some of the allowed regions or slices of the allowed volumes in the frameworks considered in ref. 12); details and descriptions of the symbols are given in ref. 12). Here we only remind that $tg\theta$ is the ratio between the Dark Matter particle-neutron and the Dark Matter particle-proton effective spin-dependent coupling strengths and that θ is defined in the $[0, \pi)$ interval. Obviously, larger sensitivities than those reported in the following figures would be reached when including the effect of other existing uncertainties on the astrophysical, nuclear and particle Physics assumptions and related parameters; similarly, the set of the best fit values would also be enlarged as well. For details see ref. 12).

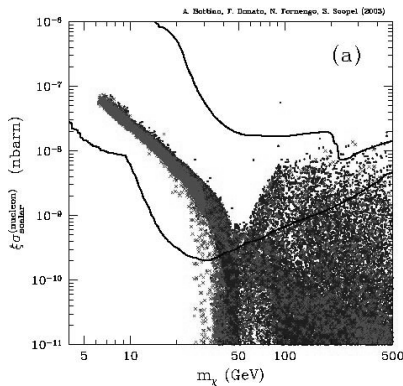


Figure 6: Figure taken from ref. 48): theoretical expectations of $\xi\sigma_{SI}$ versus m_χ in the purely SI coupling for the particular case of a neutralino candidate in MSSM with gaugino mass unification at GUT scale released; the curve surrounds the DAMA/NaI purely SI allowed region as in Fig. 4-left.

In Fig. 6 the theoretical expectations in the purely SI coupling for the particular case of a neutralino candidate in MSSM with gaugino mass unification at GUT scale released 48) are shown. The marked curve surrounds the DAMA/NaI purely SI allowed region as in Fig. 4 – left. However, it is worth to remind that many other possibilities exist also in the supersymmetric scenario, since e.g. the neutralino itself has mixed SI&SD coupling with ordinary matter and the supersymmetric theories have in their general extension much more involved free parameters than those generally considered. Moreover, other analyses have been and are performed in terms of other Dark Matter particle candidates (see literature).

3 The present situation in the field

3.1 Direct detection

As already mentioned, no other experiment, whose result can be directly compared in a model independent way with that of DAMA/NaI, is available so far in the field of Dark Matter direct detection.

In fact, most of the activities, started in the 90's, are still at R&D stage and/or have released marginal exposures with the respect to the many years of existence and to the several used detectors. This is the case of CDMS, EDELWEISS and CRESST experiments, while the Zeplin experiment is more recent (49, 50, 51, 52). Since these experiments have claimed to have "excluded" DAMA/NaI, we will briefly point to the attention of the reader only few arguments, while Table 2 summarizes some items for comparison.

Firstly, let us preliminarily assume as fully correct the "selected" number of events, the energy threshold, the energy scale, etc. quoted by those experiments (see Table 2) and let us consider if – at least under this hypothesis – their claims might be justified. The answer is obviously not; in fact: i) they give a single model dependent result using ^{nat}Ge or ^{nat}Xe target, while DAMA/NaI gives a model independent result using ^{23}Na and ^{127}I targets; ii) in the single (of the many possible) model scenario, they consider, they "fix" all the astrophysical, nuclear and particle physics assumptions at a single questionable choice; the same is even for the experimental and theoretical parameters values needed in the calculations.

In particular, a comparison among experiments using different target-nuclei can only be model dependent, since several aspects must be considered, such as: i) the nature of the Dark Matter particle; ii) its real coupling with ordinary matter (mixed SI&SD, purely SI, purely SD, *preferred inelastic*) etc.; iii) the choice of the nuclear SI and SD form factors and the relative parameters for each involved target-nucleus; iv) the choice of the spin factor for each involved target-nucleus; v) the real scaling laws for the nuclear cross sections (see for instance ref. 45); vi) the real halo model and the related parameters; vii) the real values of the experimental and theoretical parameters within their uncertainties; etc. As an example we remind that not only large differences in the measured rate can be expected when using target-nuclei sensitive to the SD component of the interaction (such as e.g. ^{23}Na and ^{127}I) with respect to those largely insensitive to such a coupling (such as e.g. ^{nat}Ge , ^{nat}Si , ^{nat}Ar , ^{nat}Ca , ^{nat}W , ^{nat}O), but also when using different target-nuclei although all – in principle – sensitive to such a coupling, depending on the unpaired nucleon (compare e.g. the odd-spin isotopes – with neutron unpaired – of ^{129}Xe , ^{131}Xe , ^{125}Te and those with small abundance of ^{73}Ge , ^{29}Si , ^{183}W with the proton unpaired ^{23}Na and ^{127}I cases) (12, 13). Hence, most of the regions/volumes –

Table 2: Features of the DAMA/NaI results on the Dark Matter particle annual modulation signature over the seven annual cycles 12, 13) with those of refs. 49, 50, 52, 51).

	DAMA/NaI	CDMS-II	Edelweiss-I	Zepplin-I	Cressi-II
Signature	Annual modulation	None	None	None	None
Target-nuclei	^{23}Na , ^{127}I	^{76}Ge	^{76}Ge	^{136}Xe	CaWO_4
Technique	well known	poorly experienced	poorly experienced	critical optical liquid/gas interface in this realization	poorly experienced
Target mass	≈ 100 kg	0.75 kg	0.32 kg	≈ 3 kg	≈ 0.6 kg
Exposure	$\approx (1.1 \cdot 10^5)$ kg · day	19.4 kg · day	30.5 kg · day	280 kg · day	20.5 kg · day
Depth of the experimental site	1400 m	780 m	1700 m	1100 m	1400 m
Software energy threshold	2 keV e.e. (5.5 – 7.5 p.e./keV)	10 keV e.e.	20 keV e.e.	2 keV e.e. (but: $\sigma/E = 100\%$ mostly 1 p.e./keV; 52) (2.5 p.e./keV for 16 days; 53)	12 keV e.e.
Quenching factor	Measured	Assumed = 1	Assumed = 1 (see also 54)	Measured	Assumed = 1
Measured event rate in low energy range	≈ 1 cpd/kg/keV	??; claimed γ 's larger than CDMS-I (≈ 60 cpd/kg/keV, 10^5 events)	$\approx 10^4$ events total	≈ 100 cpd/kg/keV	??; ≈ 6 cpd/kg/keV above 35 keV
Claimed events after rejection procedures	either 0 or 1	2 (claimed taken in a noisy period)		≈ 20 -50 cpd/kg/keV after rejection and ?? after standard PSD 52, 53)	16
Events satisfying the signature in DAMA/NaI	modulation amplitude integrated over the given exposure $\approx 10^3$ events	insensitive	insensitive	insensitive	insensitive
Expected number of events from DAMA/NaI effect		from few down to zero depending on the models (and on quenching factor)	from few down to zero depending on the models (and on quenching factor)	depends on the models (even zero)	from few down to zero depending on the models (and on quenching factor)

already allowed by DAMA/NaI in the frameworks considered so far – are unexplorable e.g. by Ge, Si, Xe, CaWO_4 present experiments and by their future possible projection.

In addition, DAMA/NaI is generally quoted there in an uncorrect, partial and unupdated way and existing scenarios to which DAMA/NaI is fully sensitive – on the contrary of the others – are ignored.

Comments about the experimental aspects of those experiments can be found elsewhere (see e.g. 12, 13)).

In conclusion, those claims for contradiction have intrinsically no scientific bases.

In future, some complementary information to that achieved by DAMA/NaI and achievable by the present DAMA/LIBRA experiment could be obtained by experiments such as e.g. Genius-TF, CUORE and WARP at Gran Sasso Laboratory, provided that they would also have suitable long-term stability, low energy threshold, etc.

As regards the experiments planning to use, in the keV energy range, very large mass of liquid noble gases as target – in particular Xenon – we remind that several technical difficulties exist and sharply increase with the size of the detector 55).

Finally, the strategies to reject electromagnetic background from the data are limited by their statistical nature because of e.g. the tail effects from the different populations, of the noise, etc. and by the existence of well known side processes (such as e.g. end-range alphas, fission fragments, environmental neutrons and, in some cases, strummental effects as surface electrons, etc.), whose contributions cannot be estimated and subtracted at the level of precision required for their claimed reachable sensitivity (as it can be easily derived even by simple considerations). Moreover, these techniques are absolutely unsuitable if the CDM candidates would instead directly involve ionization/excitation phenomena in the detector.

3.2 Indirect detection

As mentioned, the Dark Matter particles, via their annihilation either in the celestial bodies (such as Earth and Sun) or in the Galactic halo could give rise to high energy neutrinos, positrons, antiprotons and gamma rays. Therefore, they could be *indirectly* detected by looking either for "upgoing" muons – produced by ν_μ – in underground, underwater or under-ice detectors or for antimatter and gamma rays in the space. However, it is worth to remark that no direct model independent comparison can be performed between the results obtained in direct and indirect searches; any comparison would depend on assumptions and on the considered model frameworks. In particular, a comparison would always require the calculation and the consideration of all the possible Dark

Matter particle configurations in the given particle model (e.g. for χ : in the allowed parameters space), since it does not exist a biunivocal correspondence between the observables in the two kinds of experiments: for example, WIMP-nucleus elastic scattering cross section (direct detection case) and flux of muons from neutrinos (indirect detection case, the same conclusion can be achieved for anti-matter and gamma's in the space). In fact, the counting rate in direct search is proportional to the SD and to the SI cross sections, while the muon flux is connected not only to them, but also to the WIMP annihilation cross section. In principle, the three cross sections can be correlated, but only when a specific model is adopted and by non directly proportional relations.

In the case of "upgoing" muons in terrestrial detectors, the expected μ flux is the key quantity. However, several sources of uncertainties are present in the related estimates (and, therefore, in the obtained results) such as e.g. the assumption that a "steady state" has been reached in the considered celestial body and the estimate and subtraction of the existing competing processes, offered by the atmospheric neutrinos. Model dependent analyses with a similar approach have been carried out by large experiments deep underground such as e.g. MACRO and Superkamiokande. In particular, the case of the neutralino candidate in MSSM has been discussed in ⁵⁶⁾, showing that their model dependent results were not in conflict with DAMA/NaI.

As we mentioned, the annihilation of CDM candidates in the galactic halo could also produce antimatter particles and gamma rays. The antimatter searches have to be carried out outside the atmosphere, i.e. on balloons or satellites. In particular, the Dark Matter particles annihilation would result in an excess of antiprotons or of positrons over an estimated background arising from other possible sources. The estimate and subtraction of such a background together with the influence of the Earth and of the galactic magnetic field on these particles plays a crucial role on the possibility of a reliable extraction of a signal. However, at present an excess of positrons with energy $\simeq 5 - 20$ GeV has been suggested by ⁵⁷⁾ and other experiments. Interpreted in terms of Dark Matter particles annihilation it gives a result not in conflict with the effect observed by DAMA/NaI ⁵⁷⁾.

As regards the possibility to detect γ 's from Dark Matter particles annihilation in the galactic halo, experiments in space are planned. However, at present it is difficult to estimate their possibilities considering e.g. the background level, the uncertainties in its reliable estimate and subtraction as well as the smallness of the expected signal (even more, if a subdominant component would be present) when properly calculated with rescaling procedure. However, in ref. ^{59, 60)} the presence of a γ excess from the center of the Galaxy in the EGRET data ⁶¹⁾ has already been suggested. This excess match with a possible Dark Matter particles annihilation in the galactic halo ^{59, 60)} and is

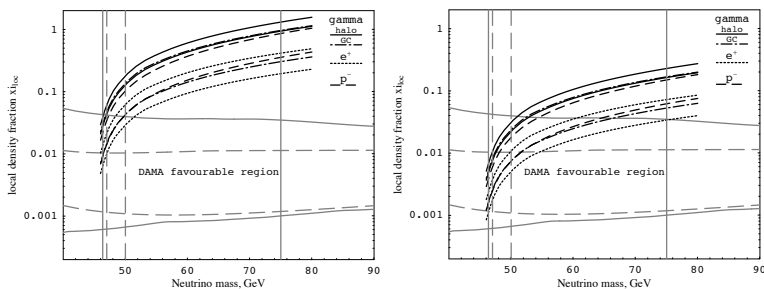


Figure 7: *Figures taken from ref. 58): Case of a subdominant heavy 4th neutrino candidate in the plane local density fraction versus the heavy neutrino mass. The favorable region obtained from the DAMA/NaI data (grey dashed line when using the Evan’s halo model; solid line when using the other halo models) and the best-fit density parameters deduced from cosmic gamma-radiation (from halo and galactic center), positron and antiproton analysis are shown (left panel). The effect of the inclusion of possible neutrino clumpiness is also reported (right panel). See ref. 58) for details.*

also not in conflict with the DAMA/NaI model independent result previously reported.

For completeness, we remind that recently it has been suggested 58) that the positive hints from the indirect detection – namely the excess of positrons and of gamma rays in the space – and the model independent effect observed by DAMA/NaI can also be described in a scenario with multi-component Dark Matter in the galactic halo, made of a subdominant component of heavy neutrinos of the 4th family and of a sterile dominant component. In particular (see Fig. 7), it has been shown that an heavy neutrino with mass around 50 GeV can account for all the observations, while the inclusion of possible clumpiness of neutrino density as well as new interactions in the heavy neutrino annihilation, etc. can lead to wider mass ranges: from about 46 up to about 75 GeV (see ref. 58) for details).

A new generation of experiments in the space is foreseen in the immediate future, such as AGILE, AMS-2, PAMELA, GLAST, They will certainly contribute to improve our knowledge.

4 Toward the future: from DAMA/NaI to DAMA/LIBRA and beyond

The large merits of highly radiopure NaI(Tl) set-up have been demonstrated in the practice by DAMA/NaI which has been the highest radiopure set-up available in this particular field. It has effectively pursued a model independent

approach to investigate Dark Matter particles in the galactic halo collecting an exposure several orders of magnitude larger than those available in the field and has obtained many other complementary or by-products results.

In 1996 DAMA proposed to realize a ton set-up ⁶²⁾ and a new R&D project for highly radiopure NaI(Tl) detectors was funded at that time and carried out for several years in order to realize as an intermediate step the second generation experiment, successor of DAMA/NaI, with an exposed mass of about 250 kg.

Thus, new powders and other materials have been selected, new chemical/physical radiopurification procedures in NaI and TlI powders have been exploited, new growing/handling protocols have been developed and new prototypes have been built and tested. As a consequence of the results of this second generation R&D, the new experimental set-up DAMA/LIBRA (Large sodium Iodide Bulk for RAre processes), $\simeq 250$ kg highly radiopure NaI(Tl) crystal scintillators (matrix of twenty-five $\simeq 9.70$ kg NaI(Tl) crystals), was funded at end 1999 and realised. In fact, after the completion of the DAMA/NaI data taking in July 2002, the dismantling of DAMA/NaI occurred and the installation of DAMA/LIBRA started. In particular, the experimental site as well as many components of the installation itself have been implemented (environment, shield of PMTs, wiring, HP Nitrogen system, cooling water of air conditioner, electronics and DAQ, etc.). In particular, all the Cu parts have been chemically etched before their installation following a new devoted protocol and maintained in HP Nitrogen atmosphere until the installation. All the procedures performed during the dismantling of DAMA/NaI and the installation of DAMA/LIBRA detectors have been carried out in HP Nitrogen atmosphere (see Fig.8).



Figure 8: Left: *the installation of the 25 NaI(Tl) crystals (9.70 kg each one) of DAMA/LIBRA in HP Nitrogen atmosphere. Right: One of the final stages of the detectors' installation. All the procedures as well as these photos have been carried out in HP Nitrogen atmosphere.*

DAMA/LIBRA is taking data since March 2003 and the first data release

will, most probably, occur when an exposure larger than that of DAMA/NaI will have been collected and analysed in all the aspects. The highly radiopure DAMA/LIBRA set-up is a powerful tool for further investigation on the Dark Matter particle component in the galactic halo having all the intrinsic merits already mentioned and a larger exposed mass, an higher overall radiopurity and improved performances with the respect to DAMA/NaI. Thus, DAMA/LIBRA will further investigate the 6.3σ C.L. model independent evidence pointed out by DAMA/NaI with increased sensitivity in order to reach even higher C.L.. Moreover, it will also offer an increased sensitivity to improve corollary quests on the nature of the candidate particle, trying to disentangle at least among some of the many different possible astrophysical, nuclear and particle physics models as well as to investigate other new possible scenarios. As an example, we remind the effects induced on the Dark Matter particles distribution by the contributions from satellite galaxies tidal streams, by the possible existence of caustics and by the possible existence of "solar wakes". In particular, recently it has been pointed out ²⁴⁾ that contributions to the Dark Matter particles in the galactic halo should be expected from tidal streams from the Sagittarius Dwarf elliptical galaxy. Considering that this galaxy was undiscovered until 1994 and considering galaxy formation theories, one has to expect that also other satellite galaxies do exist and contribute as well. In particular, the Canis Major satellite Galaxy has been pointed out as reported in 2003 in ref. ⁶³⁾; it can, in principle, play a very significant role being close to our galactic plane. At present, the best way to investigate the presence of a stream contribution is to determine more accurately the phase of the annual modulation, t_0 , as a function of the energy; in fact, for a given halo model t_0 would be expected to be (slightly) different from 152.5 d and to vary with energy (see Fig. 9).

Thanks to the higher sensitivity, DAMA/LIBRA will also allow to study the possible effects induced on the Dark Matter particles distribution in the galactic halo by the existence of caustics. It has been shown that the continuous infall of Dark Matter particles in the galactic gravitational field can form caustic surfaces and discrete streams in the Dark Matter particles halo ⁶⁴⁾. The phenomenology to point out a similar scenario is analogous to that in the previous item.

As an additional verification of the possible presence of contributions from streams of Dark Matter particles in our galactic halo, DAMA/LIBRA can investigate also the gravitational focusing effect of the Sun on the Dark Matter particle of a stream. In fact, one should expect two kinds of enhancements in the Dark Matter particles flow: one named "spike", which gives an enhancement of Dark Matter particle density along a line collinear with the direction of the incoming stream and of the Sun, and another, named "skirt", which gives a larger Dark Matter particle density on a surface of cone whose opening angle depends on the stream velocity.

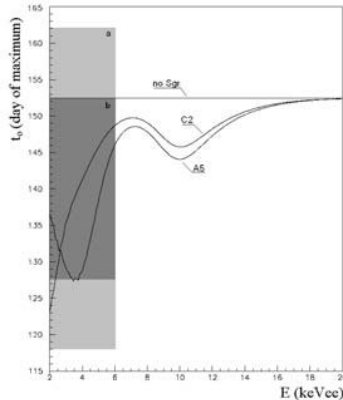


Figure 9: *Expected behaviours of the phase, t_0 , of the annual modulation signal as function of the energy when considering: i) only galactic halo (“no Sgr”); ii) galactic halo (C2 halo model with $v_0 = 220$ km/s, ρ_0 equal to the maximum value for this model) and a contribution from Sagittarius Dwarf galaxy (“C2”); iii) galactic halo (A5 halo model with $v_0 = 220$ km/s, ρ_0 equal to the maximum value for this model) and a contribution from Sagittarius Dwarf galaxy (“A5”). The contributions from Sagittarius Dwarf galaxy have been taken in both cases with a density equal to 4% of ρ_0 . The light shadow region is the final result of DAMA/NaI on the t_0 value for the cumulative energy interval (2 – 6) keV, while the dark shadow region is the expectation on t_0 assuming an experiment with the same features as DAMA/NaI, an exposure of $3 \cdot 10^5$ kg · day and the same central value for t_0 .*

Moreover, other interesting topics will be addressed by the highly radiopure DAMA/LIBRA, such as the study (i) on the velocity and spatial distribution of the Dark Matter particles in the galactic halo (for details see the discussions in ref. 12, 22); (ii) on possible structures as clumpiness with small scale size; (iii) on the coupling(s) of the Dark Matter particle with the ^{23}Na and ^{127}I target-nuclei; (iv) on the nature of the Dark Matter particles; (v) on scaling laws and cross sections (recently, it has been pointed out 45) that, even for the neutralino candidate, the usually adopted scaling laws could not hold); etc.

A large work will be faced by DAMA/LIBRA, which is in addition at present the intrinsically most sensitive experiment in the field of Dark Matter because of its radiopurity, exposed mass and high duty cycle. These qualities will also allow DAMA/LIBRA to further investigate with higher sensitivity several other rare processes.

Finally, at present a third generation R&D effort toward the possible NaI(Tl) ton set-up has been funded and related works have already been started.

5 Conclusion

The investigation of the Dark Universe is one of the main topics of the present-day Physics. In particular, experimental efforts to investigate the significant part of the Universe in form of Cold Dark Matter particles are carried out. The necessity to pursue a model independent signature is evident.

DAMA/NaI has been a pioneer experiment running at LNGS for several years and investigating as first the model independent annual modulation signature with suitable sensitivity and control of the running parameters. During seven independent experiments of one year each one, it has pointed out at 6.3σ C.L. the presence of a modulation satisfying all the many peculiarities of a Dark Matter particle induced effect. Neither systematic effects nor side reactions able to account for the modulation amplitude observed in this experimental set-up and to contemporaneously satisfy all the requirements of the signature have been found. DAMA/NaI has also pointed out the complexity of corollary investigations on the nature of the candidate particle, because of the present poor knowledge on the many astrophysical, nuclear and particle physics aspects; several scenarios have been considered and others are under investigation. A second generation experiment DAMA/LIBRA has been realized and put in operation since March 2003 to further investigate the Dark Matter particle component in the galactic halo and its properties. Moreover, further efforts towards the creation of ultimate radiopure NaI(Tl) set-ups are in progress with a third generation R&D towards a possible 1 ton set-up we proposed in 1996.

Some main aspects of the research in the field have also been summarized. In particular, complementary information could be foreseen from some other incoming experiments exploiting either the direct or the indirect detection methods.

References

1. F. Zwicky, *Helv. Phys. Acta* **6**, 110 (1933).
2. S. Smith, *Astrophys. J.* **83**, 23 (1936).
3. V.C. Rubin and W.K. Ford, *Astrophys. J.* **159**, 379 (1970); M. Roberts and A.H. Rots, *Astron. Astrophys.* **26**, 483 (1973).
4. D. N. Spergel *et al.*, *astro-ph/0302209*.

5. A. Riess *et al.*, *Astronom. J.* **116**, 1009 (1998); E.D. Perlmutter *et al.*, *Astrophys. J.* **517**, 565 (1999).
6. C. L. Bennett *et al.*, *astro-ph/0302207*.
7. R.A.C. Croft *et al.*, *Phys. Rev. Lett.* **83**, 1092 (1999); O. Elgaroy *et al.*, *astro-ph/0204152*.
8. R. Bernabei *et al.*, *Phys. Lett. B* **515**, 6 (2001).
9. D. Smith and N. Weiner, *Phys. Rev. D* **64**, 043502 (2001), *hep-ph/0402065*.
10. R. Foot, *hep-ph/0308254*.
11. S. Mitra, *astro-ph/0409121*.
12. R. Bernabei *et al.*, *La Rivista del Nuovo Cimento* **26** n.1, 1-73 (2003) [*astro-ph/0307403*].
13. R. Bernabei *et al.*, *Int. J. Mod. Phys. D* **13**, 2127 (2004).
14. P. Belli, R. Bernabei, C. Bacci, A. Incicchitti, R. Marcovaldi, D. Prospero, DAMA proposal to INFN Scientific Committee II, April 24th 1990.
15. R. Bernabei *et al.*, *Phys. Lett. B* **424**, 195 (1998).
16. R. Bernabei *et al.*, *Phys. Lett. B* **450**, 448 (1999).
17. P. Belli *et al.*, *Phys. Rev. D* **61**, 023512 (2000).
18. R. Bernabei *et al.*, *Phys. Lett. B* **480**, 23 (2000).
19. R. Bernabei *et al.*, *Eur. Phys. J. C* **18**, 283 (2000).
20. R. Bernabei *et al.*, *Phys. Lett. B* **509**, 197 (2001).
21. R. Bernabei *et al.*, *Eur. Phys. J. C* **23**, 61 (2002).
22. P. Belli *et al.*, *Phys. Rev. D* **66**, 043503 (2002).
23. P.J.T. Leonard and S. Tremaine, *Astrophys. J.* **353**, 486 (1990); C.S. Kochanek, *Astrophys. J.* **457**, 228 (1996); K.M. Cudworth, *Astron. J.* **99**, 590 (1990).
24. K. Freese *et al.*, *astro-ph/0309279*; *Phys. Rev. Lett.* **92**, 11301 (2004).
25. K.A. Drukier *et al.*, *Phys. Rev. D* **33**, 3495 (1986); K. Freese *et al.*, *Phys. Rev. D* **37**, 3388 (1988).
26. M. Ambrosio *et al.*, *Astrop. Phys.* **7**, 109 (1997).

27. P. Belli *et al.*, *Il Nuovo Cimento A* **101**, 959 (1989).
28. M. Cribier *et al.*, *Astrop. Phys.* **4**, 23 (1995).
29. C. Arpesella *et al.*, *Health Phys.* **72**, 629 (1997).
30. P. Belli *et al.*, *Astrop. Phys.* **5**, 217 (1996); P. Belli *et al.*, *Il Nuovo Cimento C* **19**, 537 (1996); P. Belli *et al.*, *Phys. Lett. B* **387**, 222 (1996); *Phys. Lett. B* **389**, 783 (1996)(err.); P. Belli *et al.*, *Phys. Lett. B* **465**, 315 (1999); P. Belli *et al.*, *Phys. Rev. D* **61**, 117301 (2000); R. Bernabei *et al.*, *New Journal of Physics* **2**, 15.1 (2000); R. Bernabei *et al.*, *Phys. Lett. B* **493**, 12 (2000); R. Bernabei *et al.*, *Nucl. Instr. & Methods A* **482**, 728 (2002); R. Bernabei *et al.*, *Eur. Phys. J. direct C* **11**, 1 (2001); R. Bernabei *et al.*, *Phys. Lett. B* **527**, 182 (2002); R. Bernabei *et al.*, *Phys. Lett. B* **546**, 23 (2002).
31. R. Bernabei *et al.*, *Phys. Lett. B* **436**, 379 (1998).
32. R. Bernabei *et al.*, *Astrop. Phys.* **7**, 73 (1997); R. Bernabei *et al.*, *Il Nuovo Cimento A* **110**, 189 (1997); P. Belli *et al.*, *Astrop. Phys.* **10**, 115 (1999); P. Belli *et al.*, *Nucl. Phys. B* **563**, 97 (1999); R. Bernabei *et al.*, *Nucl. Phys. A* **705**, 29 (2002); P. Belli *et al.*, *Nucl. Instr. & Methods A* **498**, 352 (2003); R. Cerulli *et al.*, *Nucl. Instr. & Methods A* **525**, 535 (2004).
33. R. Bernabei *et al.*, *Il Nuovo Cim. A* **112**, 545 (1999).
34. M. Wojcik, *Nucl. Instrum. & Methods B* **61**, 8 (1991).
35. R. Bernabei *et al.*, *Phys. Lett. B* **389**, 757 (1996).
36. R. Bernabei *et al.*, *Il Nuovo Cimento A* **112**, 1541 (1999).
37. R. Bernabei *et al.*, *Phys. Lett. B* **408**, 439 (1997).
38. P. Belli *et al.*, *Phys. Rev. C* **60**, 065501 (1999).
39. P. Belli *et al.*, *Phys. Lett. B* **460**, 236 (1999).
40. R. Bernabei *et al.*, *Phys. Rev. Lett.* **83**, 4918 (1999).
41. F. Cappella *et al.*, *Eur. Phys. J. direct C* **14**, 1 (2002).
42. R. Bernabei *et al.*, *Eur. Phys. J. A* **23**, 7 (2005).
43. R. Bernabei *et al.*, *Eur. Phys. J. A* **24**, 51 (2005).
44. R. Bernabei *et al.*, *Nucl. Phys. B (Proc. Suppl.)* **70**, 79 (1999).
45. G. Prezeau *et al.*, *Phys. Rev. Lett.* **91**, 231301 (2003).

46. D.E. Groom *et al.*, Eur. Phys. J. C **15**, 1 (2000).
47. D. Hooper and T. Plehn, MADPH-02-1308, CERN-TH/2002-29, *hep-ph/0212226*.
48. A. Bottino *et al.*, Phys. Rev. D **69**, 037302 (2004).
49. CDMS collaboration, *astro-ph/0405033*; Phys. Rev. Lett. **84**, 5699 (2000).
50. EDELWEISS collaboration, in the Proc. of NDM03, Japan (2003); Phys. Lett. B **513**, 15 (2001).
51. CRESST coll., Astrop. Phys. **23**, 325 (2005).
52. N. Smith, talk given at IDM02, York, september 2002.
53. R. Luscher, talk given at Moriond, march 2003.
54. E. Simon *et al.*, Nucl. Instrum. & Meth. A **507**, 643 (2003).
55. R. Bernabei *et al.*, in the volume "Cosmology and particle Physics", AIP ed. 189 (2001).
56. A. Bottino *et al.*, Phys. Lett. B **402**, 113 (1997); Phys. Lett. B **423**, 109 (1998); Phys. Rev. D **59**, 095004 (1999); Phys. Rev. D **59**, 095003 (1999); Astrop. Phys. **10**, 203 (1999); Astrop. Phys. **13**, 215 (2000); Phys. Rev. D **62**, 056006 (2000); Phys. Rev. D **63**, 125003 (2001); Nucl. Phys. B **608**, 461 (2001).
57. G.L. Kane *et al.*, *hep-ph/0108138*.
58. K. Belotsky, D. Fargion, M. Khlopov and R.V. Konoplich, *hep-ph/0411093*.
59. A. Morselli, talk given at Vulcano 2002.
60. A. Morselli *et al.*, *astro-ph/0211327*.
61. A. Strong *et al.*, Astrophys. J. **537**, 763 (2000).
62. R. Bernabei *et al.*, Astrop. Phys. **4**, 45 (1995); R. Bernabei, in The identification of Dark Matter, World Sc. Pub. (1997) 574.
63. R.A. Ibata *et al.*, Mon. Not. Roy. Astr. Soc. **348**, 12 (2004).
64. F.S. Ling, P. Sikivie, S. Wick, *astro-ph/0405231*.

SEARCHING FOR DARK MATTER IN SPACE

A. Morselli

INFN Roma II and Dept. of Physics, University of Roma "Tor Vergata"

Abstract

Experimental cosmology has been steadily progressing over the last few years. The emerging picture is of a cosmological average matter density of $\Omega_m = 0.27 \pm 0.04$ which is much larger than the baryon density $\Omega_b = 0.044 \pm 0.004$. The nature of the astronomical dark matter is still unresolved. The favoured candidate for the nonbaryonic component is a neutral weakly-interacting massive particle (WIMPs) with a mass in the range from tens of GeV to TeV. They would naturally appear as one of the thermal leftovers from the early Universe and their existence is predicted in several classes of extensions of the Standard Model of particle physics. The most popular case is that of the lightest neutralino in R -parity conserving supersymmetric models. Considerable effort has been put into the search for dark matter WIMPs in the last decade, with several complementary techniques applied. One route worth being explored is provided by indirect signatures. Neutralinos should pervade the Milky Way halo and be concentrated at the galactic centre and in the cores of the sun and earth. As they mutually annihilate, they should produce high energy photons and antimatter cosmic-rays and should therefore generate spectral distortions in the corresponding backgrounds. The direct detection of annihilation products in cosmic rays offers an alternative way to search for supersymmetric dark matter particles candidates. The study of the spectrum of gamma-rays, antiprotons and positrons in space has already showed some deviation from the expected signals but with weak statistical evidence. We will review the present situation and the achievable limits with the experiments PAMELA and GLAST.

1 Propagation of Cosmic Rays in the Milky Way and Its Uncertainties

The key problem in the quest for exotic signals in cosmic rays is to know the standard contributions.

The most complete equation for the propagation of cosmic rays that includes all the known physical processes is

$$\begin{aligned} \frac{\partial \psi(\mathbf{r}, p, t)}{\partial t} &= q(\mathbf{r}, p) + \nabla \cdot (D_{xx} \nabla \psi - \mathbf{V}_c \psi) + \frac{d}{dp} p^2 D_{pp} \frac{d}{dp} \frac{1}{p^2} \psi \\ &- \frac{\partial}{\partial p} \left[\dot{p} \psi - \frac{p}{3} (\nabla \cdot \mathbf{V}_c) \psi \right] - \frac{1}{\tau_f} \psi - \frac{1}{\tau_r} \psi, \end{aligned} \quad (1)$$

where $\psi(\mathbf{r}, p, t)$ is the total phase space density. We will shortly review here the main features of the physical processes described by this equation implemented in the Galprop code ^{1, 2)}.

The second term describes isotropic diffusion, defined by the coefficient that depends on the rigidity (momentum per unit of charge, $\rho = p/Z$)

$$D_{xx} = \beta D_0 (\rho / \rho_0)^\delta, \quad (2)$$

inspired by the Kolmogorov spectrum ($\delta = 1/3$) of the weak magnetohydrodynamic turbulence. In ³⁾ was first shown that the Kolmogorov spectrum best reproduces the sharp peak in B/C data. The convection velocity field \mathbf{V}_c , that corresponds to the Galactic wind, has a cylindrical symmetry. Its z-component is the only one different from zero. It increases linearly with the distance z from the Galactic plane. This is in agreement with magnetohydrodynamical models ⁴⁾. In the Galactic plane there should be no discontinuity in the convection velocity field and so we considered only $V_c(z = 0) = 0$. Reacceleration is determined by the diffusion coefficient in the momentum space D_{pp} . D_{pp} is a function of the corresponding configuration space diffusion coefficient D_{xx} and of the Alfvén velocity V_A in the framework of quasi-linear MHD theory ^{5, 6, 7)}

$$D_{pp}(D_{xx}, V_A) = \frac{4p^2 V_A^2}{3\delta(4 - \delta^2)(4 - \delta)w}, \quad (3)$$

where w characterizes the level of turbulence, and it is equal to the ratio of MHD wave energy density to magnetic field energy density. It is assumed $w = 1$, but the only relevant quantity is V_A^2/w .

The unknown values of parameters such as the Alfvén velocity, the convection velocity gradient in Milky Way and the height of the galactic

halo can be constrained by the B/C data. With the sets of the constrained parameters one can find all the possible spectra for the others cosmic rays. This procedure was already used in ⁸⁾ for another propagation code. Injected spectra of all primary nuclei are power laws

$$dq(p)/dp \propto p^{-\gamma}, \quad (4)$$

where the value of γ can, in principle, vary with species. This power law approximation as well as a small break in the injection indexes γ is allowed in the framework of diffusive shock acceleration models ^{9, 10, 11)}.

Source term $q(\mathbf{r}, p)$ for secondaries contains cross sections for their production from progenitors on H and He targets

$$q(\vec{r}, p) = \beta c \psi_p(\vec{r}, p) [\sigma_H^{ps}(p) n_H(\vec{r}) + \sigma_{He}^{ps}(p) n_{He}(\vec{r})], \quad (5)$$

where $\sigma_H^{ps}(p)$ and $\sigma_{He}^{ps}(p)$ are the production cross sections for the secondary from the progenitor on H and He targets, ψ_p is the progenitor density, and n_H, n_{He} are the interstellar hydrogen and helium number densities.

The last two terms in equation (1) are loss terms with characteristic times for fragmentation and radioactive decay.

The heliospheric modulation of the local interstellar spectra in the vicinity of the Earth and in the heliosphere hole has to be taken into account in order to obtain the realistic cosmic rays spectra in locations where they are/will be measured (balloon-born or satellite-borne experiments).

We made use of a widely used and tested model in which the transport equation is solved in the force field approximation ^{12, 13)}. That equation describes diffusion processes in the heliosphere and includes effects of heliospheric magnetic field and solar wind. In this case, solar modulation is a function of just a single parameter that describes the strength of the modulation. All the dynamical processes are simulated simply changing the interstellar spectra during the propagation inside the heliosphere:

$$\frac{\Phi^{toa}(E^{toa})}{\Phi^{is}(E^{is})} = \left(\frac{p^{toa}}{p^{is}}\right)^2, \quad (6)$$

$$E^{is} - E^{toa} = |Ze|\phi, \quad (7)$$

where E and p are energies and momenta of the interstellar and top of the atmosphere fluxes and ϕ is the unique parameter that determines the solar modulation.

In Galprop the model of the Galaxy is three dimensional with cylindrical symmetry; the coordinates are (R, z, p) , where R is Galactocentric radius, z is the distance from the Galactic plane, and p is the total particle momentum. The distance from the Sun to the Galactic centre is taken to be 8.5 Kpc. The

propagation region is bounded fixing $R_{max} \equiv R = 30$ Kpc and $z_{max} \equiv z$ beyond which free escape is assumed. The distribution of cosmic rays sources is chosen to reproduce (after propagation) the cosmic rays distribution determined by the analysis of EGRET gamma-ray data done in ¹¹). The code first computes propagation of primaries, giving the primary distribution as a function of (R, z, p) . Then the secondary source function is obtained from the gas density and cross sections. Finally, the secondary propagation is computed.

Secondary to primary CR ratios are the most sensitive quantities on variation of the propagation parameters. This can be verified numerically. Primary to primary and secondary to secondary ratios are not very sensitive to changes in the propagation parameters because they have similar propagation mechanisms. The most accurately measured secondary to primary ratio is boron to carbon ratio (B/C, see ¹⁴). Boron is secondary while, one of its progenitors, carbon is primary. The B/C data are used also because they have relatively well known cross sections. To estimate the quality of the data fit we used the standard χ^2 test

$$\chi^2 = \frac{1}{N-1} \sum_n \frac{1}{(\sigma_n^{B/C})^2} (\Phi_{n,exp}^{B/C} - \Phi_{n,teo}^{B/C})^2, \quad (8)$$

where $\sigma^{B/C}$ are statistical errors for $N = 46$ experimental points and $\Phi_{exp}^{B/C}$ are measured and $\Phi_{teo}^{B/C}$ are predicted values of the ratio.

We analyzed only the two extreme cases of the propagation models either without convection or without reacceleration. We did not succeed in obtaining satisfactory models with all the physical processes switched on. A possible explanation is that one of the processes is really subdominant in the Galaxy in such a way that the data require either reacceleration or convection to be well fitted. So in the first case we included diffusive and reacceleration effects (see equation (1) and we considered two sub-cases: (DR) without a break in the index of primary injection spectra and (DRB) with a break at the rigidity ρ^γ . The second case (DC) contains diffusion and convection terms from the same equation (1). In this model there are two breaks: one in the index of the primary injection spectra and the other in the spectra of the diffusion coefficient D_{xx} . The first break means that at some rigidity ρ^γ the index γ suffers a discontinuity (see equation (4) and ref. ¹⁰) for details), while the second one means that at some rigidity ρ_0 the diffusion index δ suffers a discontinuity (see equation (2) and discussion in ref. ²).

For the DR model we chose to vary the following parameters: the height of the Galactic halo z , the constant in the diffusion coefficient D_0 (from equation (2)), the index of the diffusion coefficient δ (from the same equation), the primary spectra injection index γ for all the energies (from equation (4)) and the Alfvén velocity v_A that determines the strength of reacceleration. In

order to find the allowed range of these parameters we have required a reduced χ^2 less than 2 for the fit of the B/C experimental data¹⁴). In figure 1 are presented the enveloping curves of all the good fits with solid lines around the best fit line for the same model, that is represented with dashed line. We took the experimental data with relatively small solar modulation parameter ϕ between 325 MV and 600 MV, where the force field approximation is better justified than for the high modulation parameters. The allowed ranges of propagation parameters of this model are given in the table 2. In the case

Table 1: Allowed values for diffusion and convection (DC) model parameters.

par./val.	$z[Kpc]$	$D_0[\frac{cm^2}{s}]$	δ_2	$\frac{dV_c}{dz}[\frac{Kkm}{skpc}]$	γ_1	γ_2
minimal	3.0	$2.3 \cdot 10^{28}$	0.48	5.0	2.42	2.14
best fit	4.0	$2.5 \cdot 10^{28}$	0.55	6.0	2.48	2.20
maximal	5.0	$2.7 \cdot 10^{28}$	0.62	7.0	2.50	2.22

Table 2: Allowed values for diffusion and reacceleration (DR) model parameters.

par./val.	$z[Kpc]$	$D_0[cm^2s^{-1}]$	δ	γ	$v_A[Kms^{-1}]$
minimal	3.0	$5.2 \cdot 10^{28}$	0.25	2.35	22
best fit	4.0	$5.8 \cdot 10^{28}$	0.29	2.47	26
maximal	5.0	$6.7 \cdot 10^{28}$	0.36	2.52	35

Table 3: Allowed values for DRB parameters.

par./val.	$z[Kpc]$	$D_0[\frac{cm^2}{s}]$	δ	γ_1	γ_2	$v_A[\frac{Kkm}{s}]$
minimal	3.5	$5.9 \cdot 10^{28}$	0.28	1.88	2.36	25
best fit	4.0	$6.1 \cdot 10^{28}$	0.34	1.92	2.42	32
maximal	4.5	$6.3 \cdot 10^{28}$	0.36	2.02	2.50	33

of the DC model we chose to vary the following parameters: D_0 , the diffusion index δ_1 below the reference rigidity $\rho_0 = 4$ GV and δ_2 above it (all those parameters are from equation (2)), the halo size z , the convection velocity V_c (from equation (1)) and the injection index for primary nuclei γ_1 below the reference rigidity $\rho_0^\gamma = 20$ GV and γ_2 above it (see equation (4)). Enveloping curves of B/C fits for the reduced χ^2 values less than 2.8 are given in figure 1.

Positive variations around $\delta_1 = 0$ gave unsatisfactory fit. In order to take the smallest possible break of this index we decided not to take negative δ_1 values. Allowed values for the propagation parameters can be found in table 1.

We found the spectra that correspond to the parameters of the best fit of B/C data for subFe/Fe ratio (see figure 2), protons, helium and electrons as well as the corresponding propagation parameters uncertainties. For DC model the obtained fits are good, while DR overestimates protons (figure 3), helium (figure 4) and electrons.

In order to improve those fits, we considered the DR model with a break in the injection index for the primary nuclei spectra with a rigidity of 10 GV (2, 10). We determined the allowed values of the propagation parameters (table 3) demanding the same reduced $\chi^2=2$ as for DR model (see figure 1). The positron and antiproton uncertainties are presented in figure 6. Even if positrons at low energies and protons and helium in all the energy range are fitted better (see figure 3 and figure 4), they remain overestimated. For the computation of B/C ratio, Galprop uses only one principal progenitor and compute weighted cross sections. Introducing the break in the index of the primary injection spectra in DR model give worst electron data fit than in the case without the break. On the other side, the antiproton spectra remain unchanged, still significantly and systematically underestimated in all the energy range.

We also calculated how the antiproton spectra change on variation of the most important antiproton production cross sections. Antiprotons are created in the interactions of primary cosmic rays (protons and other nuclei) with interstellar gas. Dominant processes are interactions of high energy primary protons with hydrogen, $p + p \rightarrow p + p + p + \bar{p}$. Parameterization of this cross section is given in (17). Other cross sections, those of primary protons with other nuclei, are studied in reference (18). From these, the most important are those that involve helium, and they contribute less than 20% of the total production of all the antiprotons. All the heavier nuclei together give just a few percents of the total production.

Uncertainties of cross sections influence the antiproton spectra uncertainties from 20% up to 25% depending on energy and the uncertainty in the measurements of helium to hydrogen ratio bring another 3% to 7%, depending on energy.

Total uncertainties of positrons and antiprotons are presented in figure 6. They vary from 35% up to 55% for antiprotons and from 20% up to 40% for positrons for both the models in the current experimental data energy range.

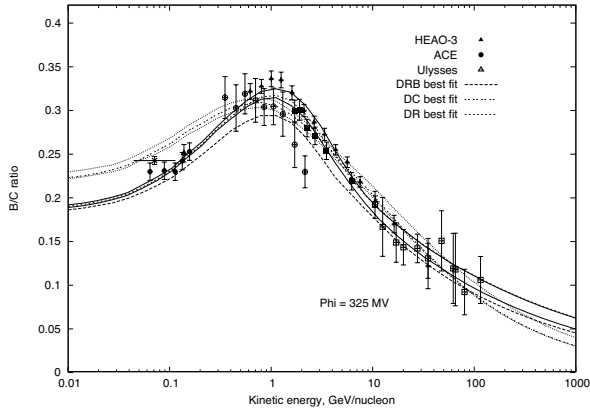


Figure 1: Propagation parameters uncertainty for B/C ratio: for DR model is given with solid lines around the best fit (dashed line), while for DC model is given with dotted lines around the best fit (dashed line). For DRB model we give the best fit (dashed line). For the complete list of the experimental data see 14).

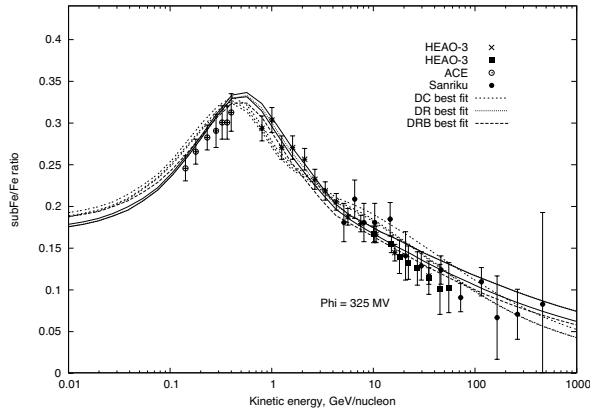


Figure 2: Ratio (Sc+Ti+V)/Fe that corresponds to the propagation parameters that give the best fits of B/C data for the DC model is given with dashed line and it is inside the corresponding uncertainty band given with dashed lines. The ratio for the DR model is given with dotted line and it is inside the uncertainty given with solid lines, while for DRB model is given with larger-step dashed line without the uncertainty band around. Experimental data are taken from 16).

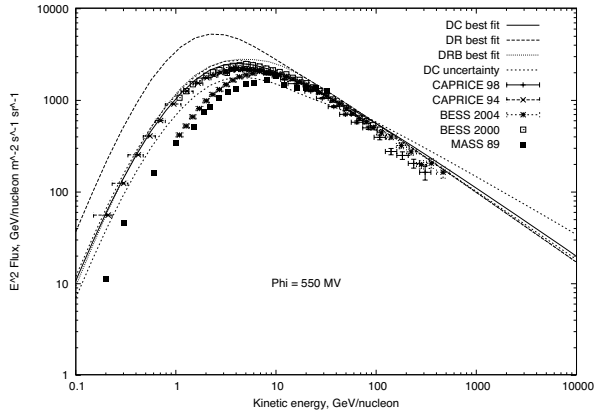


Figure 3: Upper and lower bounds of proton spectra due to the uncertainties of the propagation parameters for the DC model are represented with dashed lines. Spectra that correspond to the parameters of the best B/C fit are given for the DC model with solid line, for the DR model with dashed line and for the DRB model with dotted line. Experimental data are taken from ¹⁵⁾.

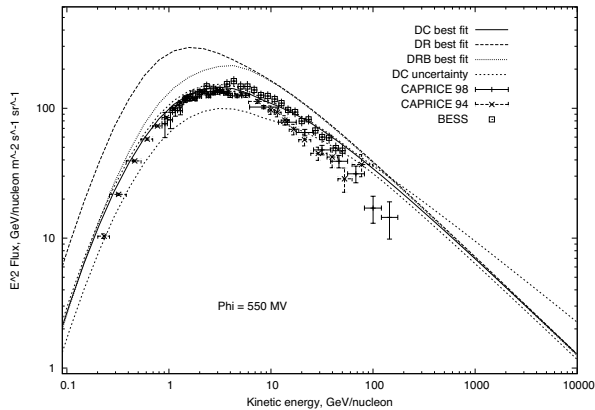


Figure 4: Upper and lower bounds of helium spectra due to the uncertainties of the propagation parameters for the DC model are represented with dashed lines. Spectra that correspond to the parameters of the best B/C fit are given for the DC model with solid line, for the DR model with dashed line and for the DRB model with dotted line. Experimental data are taken from ¹⁵⁾.

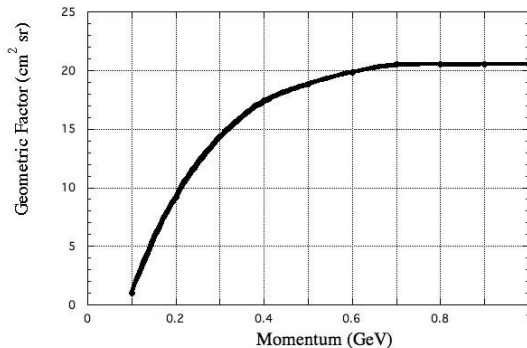


Figure 5: Geometric factor of PAMELA

2 Component of the Antiproton Spectra Induced by Neutralino Annihilations

In this section we take into account the possibility of a neutralino induced component in the \bar{p} flux. Our analysis is performed in the well known mSUGRA framework¹⁹⁾ with the usual gaugino mass universality at the grand unification scale M_{GUT} .

In the general framework of the minimal supersymmetric extension of the Standard Model (MSSM), the lightest neutralino is the lightest mass eigenstate obtained from the superposition of four interaction eigenstates, the supersymmetric partners of the neutral gauge bosons (the bino and the wino) and Higgs bosons (two Higgsinos). Its mass, composition and couplings with Standard Model particles and other superpartners are functions of several free parameters one needs to introduce to define such supersymmetric extension. In the mSUGRA model, universality at the grand unification scale is imposed. With this assumption the number of free parameters is limited to five

$$m_{1/2}, m_0, \text{sign}(\mu), A_0 \text{ and } \tan\beta,$$

where m_0 is the common scalar mass, $m_{1/2}$ is the common gaugino mass and A_0 is the proportionality factor between the supersymmetry breaking trilinear couplings and the Yukawa couplings. $\tan\beta$ denotes the ratio of the VEVs of the two neutral components of the SU(2) Higgs doublet, while the Higgs mixing μ is determined (up to a sign) by imposing the Electro-Weak Symmetry Breaking (EWSB) conditions at the weak scale. In this context the MSSM can be regarded as an effective low energy theory. The parameters at the weak

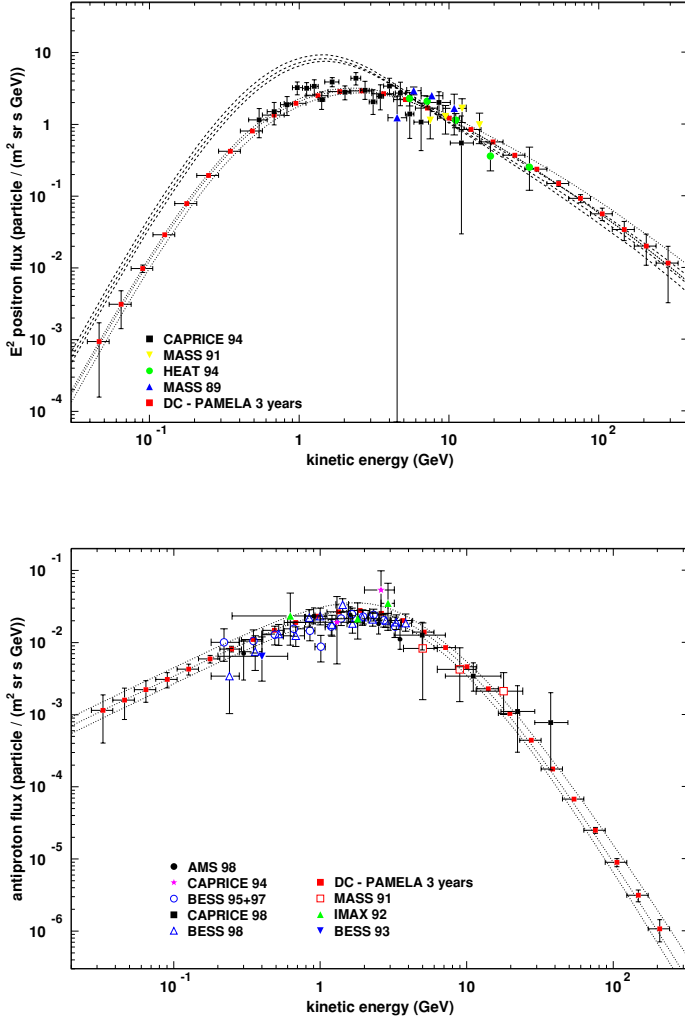


Figure 6: Experimental data (from ³²) confronted with PAMELA's expectations for positrons (top) and antiprotons (bottom) for DC model background. Total uncertainties and the spectra that correspond to the parameters of the best B/C fit for DC model are given with dotted lines while for DRB model with dashed lines.

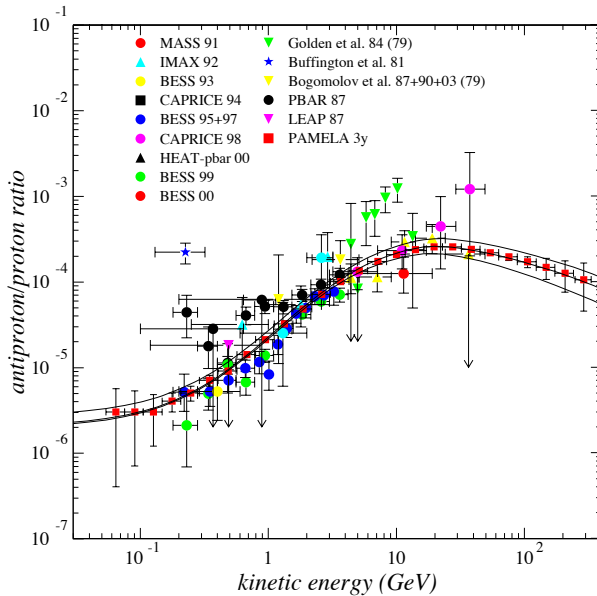


Figure 7: Experimental data (from ³²)) confronted with PAMELA's expectations for the antiproton proton ratio for the DC model background. The propagation uncertainty band of the antiproton proton ratio and the curve that corresponds to the parameters of the best B/C fit in the middle are given with solid lines.

energy scale are determined by the evolution of those at the unification scale, according to the renormalization group equations (RGEs) ²⁰).

For this purpose, we have made use of the ISASUGRA RGE package in the ISAJET 7.64 software ²¹). After fixing the five mSUGRA parameters at the unification scale, we extract from the ISASUGRA output the weak-scale supersymmetric mass spectrum and the relative mixings. Cases in which the lightest neutralino is not the lightest supersymmetric particle or there is no radiative EWSB are disregarded.

The ISASUGRA output is then used as an input in the DarkSUSY package ²²). The latter is exploited to:

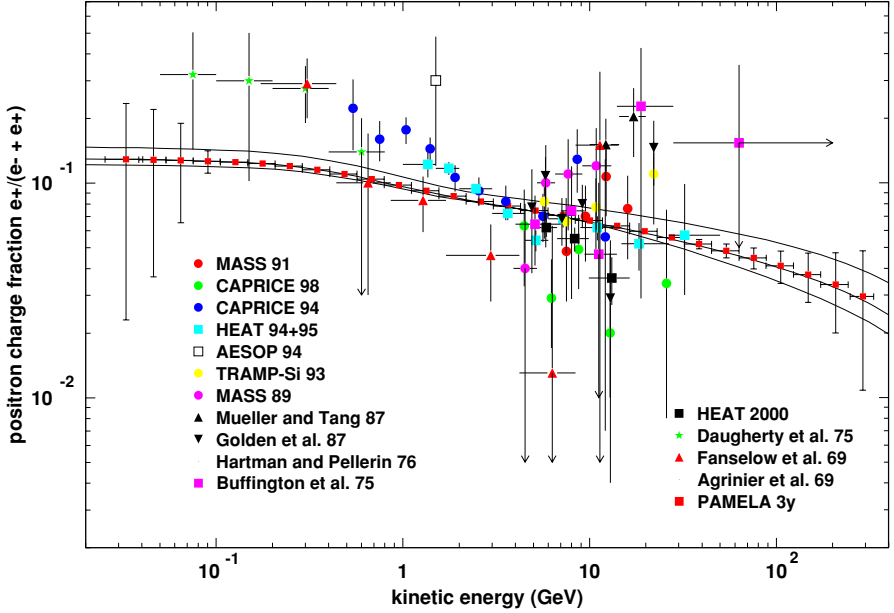


Figure 8: Experimental data (from ³²) confronted with PAMELA's expectations for positron charge fraction for the DC model background. The propagation uncertainty band of the positron charge fraction and the curve that corresponds to the parameters of the best B/C fit in the middle are given for a better comparison.

- reject models which violate limits recommended by the Particle Data Group 2002 (PDG) ²³);
- compute the neutralino relic abundance, with full numerical solution of the density evolution equation including resonances, threshold effects and all possible coannihilation processes ²⁴);
- compute the neutralino annihilation rate at zero temperature in all kinematically allowed tree-level final states (including fermions, gauge bosons and Higgs bosons);
- DarkSUSY estimates the induced antiproton yield by linking to the results

of the simulations performed with the Lund Monte Carlo program Pythia 25).

This setup as well as some other similar scenarios were already considered in the context of dark matter detection and of an improvement of the cosmic rays data fits (a list of references includes, for example 26, 27).

2.1 Clumpy Halo Models

In order to obtain a higher antiproton flux in the case of high neutralino masses we assumed a small clump scenario 28) for the dark matter halo in our Galaxy. In fact, in equation (10) the dependence of the antiproton flux is $\propto \rho^2/m_\chi^2$: without increasing the total halo mass by increasing the average density, there can be assumed a local density enhancement, that will also lead to the increasing of the antiproton flux.

By hypothesis the clump is a spherical symmetric compact object with mass M_{cl} and some density profile $\rho_{cl}(\vec{r}_{cl})$. We denote with f the dark matter fraction concentrated in clumps and we introduce the dimensionless parameter d

$$d = \frac{1}{\rho_0} \frac{\int d^3 r_{cl} [\rho_{cl}(\vec{r}_{cl})]^2}{\int d^3 r_{cl} \rho_{cl}(\vec{r}_{cl})} \quad (9)$$

that gives the overdensity due to a clump with respect to the local halo density $\rho_0 = \rho(r_0)$, where r_0 is our distance from the Galactic Center (GC). In a smooth halo scenario the total neutralino induced \bar{p} flux calculated for $r = r_0$ is given by 29)

$$\Phi_{\bar{p}}(r_0, T) \equiv (\sigma_{ann} v) \sum_f \frac{dN^f}{dT} B^f \left(\frac{\rho_0}{m_\chi} \right)^2 C_{prop}(T). \quad (10)$$

where T is the \bar{p} kinetic energy, $\sigma_{ann} v$ is the total annihilation cross section times the relative velocity, m_χ is the neutralino mass, B^f and dN^f/dT , respectively, the branching ratio and the number of \bar{p} produced in each annihilation channel f per unit energy and $C_{prop}(T)$ is a function entirely determined by the propagation model. In the presence of many small clumps the \bar{p} flux is given by

$$\Phi_{\bar{p}}^{clumpy}(r_0, T) = f d \cdot \Phi_{\bar{p}}(r_0, T) \quad (11)$$

For the smooth profile we assumed a Navarro, Frenck and White profile (NFW) 30).

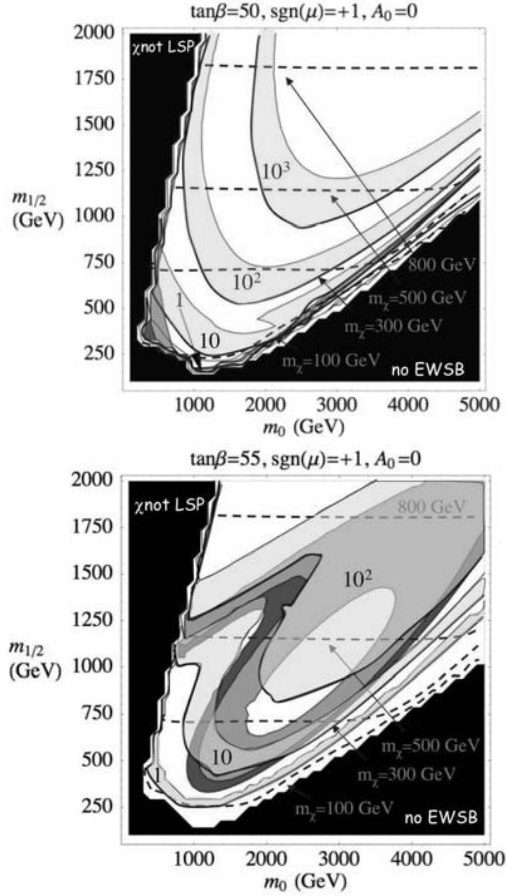


Figure 9: Contour plots for the minimum fd needed for a PAMELA disentanglement (upper bounds of the translucent bands) and for the maximum fd allowed by current experimental data (lower bounds of the translucent bands). In the upper panel $\tan\beta = 50$ while in the lower panel $\tan\beta = 55$. The other parameters (keep fixed) are $A_0 = 0$ and $\text{sgn}(\mu)=1$. Black color represents the regions in the parameter space that are excluded either by accelerator bounds or because electroweak symmetry breaking is not achieved or because the neutralino is not the lightest supersymmetric particle. Red (dark shaded) are domains with Ωh^2 in the WMAP region $0.09 < \Omega h^2 < 0.13$, while green (light shaded) are the parameter space domains with $0.13 < \Omega h^2 < 0.3$. We also show the equi-neutralino mass contours (blue dashed lines).

2.2 Propagation of the Neutralino Induced Component

The primary contribution to the antiproton flux is computed using the public code `DarkSUSY`³¹⁾. We modified the antiproton propagation in order to be consistent with the DC propagation model as implemented in `Galprop` code. We assumed diffusion coefficient spectra used in `Galprop` code with our best fit values for the diffusion constants D_0 and δ . In `DarkSUSY`, the convection velocity field is constant in the upper and the lower Galactic hemispheres (with opposite signs, and so it suffers unnatural discontinuity in the Galactic plane), while `Galprop` uses magnetohydrodynamically induced model, in which one component of velocity field along the Galactic latitude (the only one that is different from zero) increases linearly with the Galactic latitude⁴⁾. We assumed an averaged convection velocity calculated from the Galactic plane up to the Galactic halo height z .

2.3 Detection of the Secondary Components in the Positron and the Antiproton Fluxes by PAMELA

In this section we calculate the statistical errors for the PAMELA³²⁾ experiment for the positron and the antiproton background spectra calculated with `Galprop`¹.

The calculation is done for a three years mission assuming the geometric factor given in figure 5. PAMELA's statistical errors for positrons and antiprotons in the case of the DC model are given in figure 6. In figures 7 and 8 there are the PAMELA expectations together with the propagation uncertainties for the antiproton proton ratio and positron charge fraction respectively.

3 The Possibility of Disentanglement of the Neutralino Induced Component in the Antiproton Flux With PAMELA

In this section we present the results we found about the minimal values of the clumpiness factors fd needed to disentangle a neutralino induced component in the antiproton flux with PAMELA. We computed this factor as a function of the mSUGRA parameters, fixing A_0 , $\tan\beta$ and $\text{sign}(\mu) = 1$. In this way the clumpiness factor become a function of m_0 and $m_{1/2}$ parameters. Similar analysis were already made in the literature (see for example²⁷⁾).

For the discrimination we requested the following conditions:

¹The list of the people and the institutions involved in the collaboration together with the on-line status of the project is available at <http://wizard.roma2.infn.it/>.

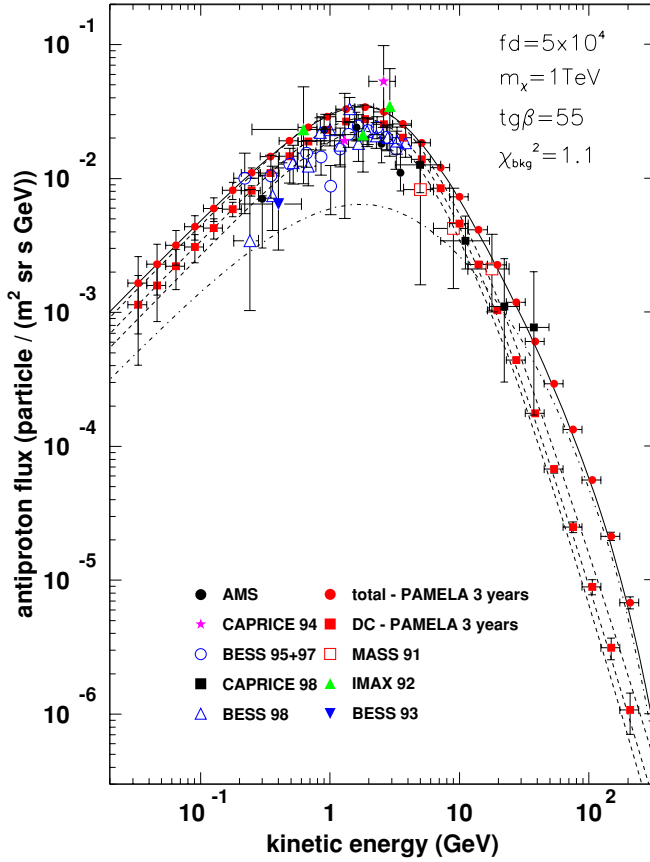


Figure 10: Antiproton absolute flux: theoretical predictions for total uncertainty and best B/C fit for DC model (dashed lines) . Experimental data are from [9]. The PAMELA expectations points (red squares) for DC background are for three years of data taking. The dash-dotted line is a neutralino induced contribution for a neutralino mass of 1 TeV (see text) and a clumpiness factor fd of $5 \cdot 10^4$ while the solid line is total contribution calculated with the addition of the DC background and the red circles are the corresponding PAMELA points.

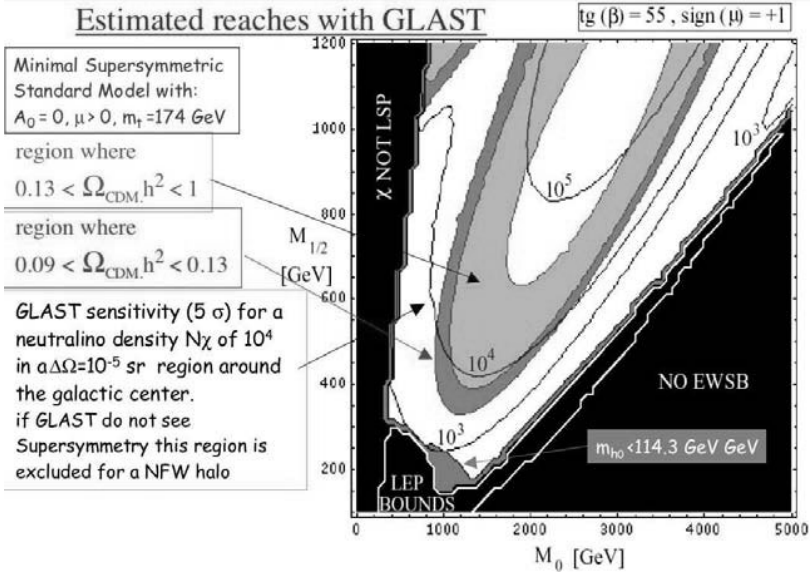


Figure 11: Contour plot in the mSUGRA ($m_0, m_{1/2}$) plane, for the value of the normalization factor N_χ , that allows the detection of the neutralino γ ray signal with GLAST. In the green region $0.13 \leq \Omega_\chi h^2 \leq 1$, while the red region corresponds to the WMAP range $0.09 \leq \Omega_\chi h^2 \leq 0.13$. The black region corresponds to models that are excluded either by incorrect EWSB, LEP bounds violations or because the neutralino is not the LSP. In the dark shaded region $m_{h_0} < 114.3 \text{ GeV}$ and h_0 is the lightest Higgs.

1. The total antiproton flux $\phi_{tot} = \phi_{bkg} + \phi_{susy}$ gives a good fit of the experimental data.
2. Difference between ϕ_{tot} and DC model ϕ_{bkg} is detectable by PAMELA.

The first condition is satisfied if

$$\chi_{fit}^2 = \frac{1}{N-1} \sum_n \frac{(\Phi_n^{exp} - \Phi_n^{tot})^2}{(\sigma_n^{exp})^2} \quad (12)$$

is less than the $\chi_{fit,0}^2 = 1.7$, for $N = 40$ experimental points. The second condition is satisfied if

$$\chi_{discr}^2 = \frac{1}{M-1} \sum_m \frac{(\Phi_m^{bkg} - \Phi_m^{tot})^2}{(\sigma_m^{P,bkg})^2} \quad (13)$$

is greater than the $\chi_{discr,0}^2 = 1.8$, for $M = 29$ points, where $\sigma_m^{P,bkg}$ are the PAMELA statistical errors associated to the background flux (those presented in figure 6).

Figure 10 shows an example of good model satisfying both conditions. The SUSY contribution to the \bar{p} flux is for a neutralino mass of 1 TeV (obtained from a particular choice of mSUGRA parameters) and a clumpiness factor fd of $5 \cdot 10^4$. Higher neutralino masses improve high energy data fit but only with the increase of the clumpiness factor because of the dependence from the inverse neutralino mass squared m_χ in the \bar{p} flux.

For each model we found the minimal value of the clumpiness factor fd needed to satisfy both conditions. As the clumpiness factor is a function of m_0 and $m_{1/2}$ parameters we made contour plots calculating equi-clumpiness factors lines. The results for $\tan\beta=50$ and $\tan\beta=55$ is presented in figure 9. The regions in parameter space that are excluded either by accelerator bounds or because electroweak symmetry breaking is not achieved or because the neutralino is not the lightest supersymmetric particle are represented with black color. Red (dark shaded) color indicates the $(m_0, m_{1/2})$ domains with Ωh^2 in the WMAP ³³⁾ region $0.09 < \Omega h^2 < 0.13$. Green (light shaded) color indicates the parameter space regions with values of $0.13 < \Omega h^2 < 0.3$. In figures 9 the equi-clumpiness factors lines for the maximal allowed (by the present experimental data) fd are represented by the lower bound of the translucent light blue (very light shaded) regions. The translucent regions denote the parameter space domains that correspond to models that satisfy both the conditions (12) and (13), keeping fixed values of fd (those indicated inside the regions).

It can be seen that even small clumpiness factors (of order 10) are sufficient for PAMELA detection. This is very important, because, even if we consider a DC model as the background flux (that alone already gives a good fit of the experimental data) it is still possible to disentangle a supersymmetric component in a wide region of the parameter space (in comparison with the WMAP allowed zone). For higher value of $\tan\beta$ the situation is even more favourable ³⁵⁾.

The search for supersymmetric signal with PAMELA will be complementary to the search for neutralinos looking at the distortion of the gamma-ray flux that will be performed with GLAST.

Figure 11 show the GLAST capability for $\tan\beta=55$ to probe in two years the supersymmetric dark matter hypothesis ²⁰⁾. The figures show in the $(m_0, m_{1/2})$ plane, the iso-contour regions for the minimum allowed value of the neutralino density in a $\Delta\Omega = 10^{-5} sr$ region around the galactic center. The density depends from the halo shape of the neutralino distribution, that is still matter of debate and can vary from a value of $N_\chi = 3 \times 10^1$ for an

isothermal profile up to $N_\chi = 10^4$ for a NFW profile ³⁰⁾ and up to $N_\chi = 10^7$ for a Moore profile ³⁶⁾. GLAST indeed can explore a good portion of the supersymmetric parameter space especially at large values of $\tan\beta$ and if the halo has a NFW (or steeper) profile. This is a very steep ($1/r$) profile but consistent with available dynamical constraints on the Galaxy ²⁰⁾.

References

1. Strong A W and Moskalenko I V 1998 *ApJ* **509** 212
Moskalenko I V and Strong A W 1998 *ApJ* **493** 694-707
2. Moskalenko I V, Strong A W, Ormes et al. 2002 *ApJ* **565** 280
3. Heinbach U and Simon M 1995 *ApJ* **441** 209-221
4. Zirakashvili V N, Breitschwerdt D, Ptuskin V S and Volk H J 1996 *A&A* **311** 113
5. Fermi E 1949 *Phys. Rev.* **75** 1169
6. Seo E S and Ptuskin V S 1994 *ApJ* **431** 705
7. Berezhinskii V S, Bulanov S V, Dogiel V A, Ginzburg V L, Ptuskin V S 1990 *Astrophysics of Cosmic Rays* (North Holland, Amsterdam)
8. Donato F et al. 2001 *ApJ* **536** 172
Donato F, et al. 2003 *Phys. Rev. D* **69** 06350
9. Blandford R D and Ostriker J P 1980 *ApJ* **237** 793
10. Ellison D C et al. 2001 *ApJ* **563** 191-201
11. Strong A W and Mattox J R 1996 *A & A* **308** L21
12. Gleeson L J and Axford W I 1968 *ApJ* **154** 1011
13. Perko J S 1987 *A&A* **184** 119
14. Davis A J et al. 2000 *AIP Conf. Proc. 528*, ed. Mewaldt R A et al (AIP, New York)
Lukasiak A et al. 1999 *Proc. 26th Int. Cosmic-Ray Conf.* (Salt Lake City) **3** 41
15. Boezio M et al. 2003 *Astroparticle Physics* **19** 583-604
16. Davis A J et al. 2000 *On the low energy decrease in Galactic cosmic ray* *Proc ACE-2000 Symp.* ed. Mewald R A et al. (NY: AIP) AIP Conf. Proc. **528** 421-424

17. Tan L C and Ng L K 1983 *J. Phys. G* **9** 227
18. Gaisser T K and Schaefer R K 1992 *ApJ* **394** 174
19. Hall L J, Lykken J, and Weinberg S 1983 *Phys. Rev. D* **27** 2359
20. Cesarini A, Fucito F, Lionetto A, Morselli A and Ullio P 2004 *Astropart. Phys.* **21** 267
21. Baer H, Paige F E, Protopopescu S D and Tata X *Preprint* hep-ph/0001086
22. Gondolo P, et al. 2004 *JCAP* **07** 008 *Preprint* astro-ph/0211238
23. Hagiwara K et al. 2002 *Phys. Rev.* **D66** 010001
24. Edsjo J, Schelke M, Ullio P and Gondolo P 2003 *JCAP* **04** 001
25. Sjöstrand T 1994 *Comp. Phys. Comm.* **82** 74
26. Feng J L, Matchev K T and Wilczek F 2001 *Phys. Rev. D* **63** 045024
Bottino A, et al. 2001 *Phys. Rev.* **D63** 125003
Ellis J, Ferstl A and Olive K A 2002 *Phys. Lett.* **B532** 318
Bertin V, Nezri E and Orloff J 2002 *Eur. Phys. J.* **C26** 111
27. Profumo S and Ullio P 2004 *JCAP* **07** 006
Bottino A et al. 2004 *Phys. Rev. D* **69** 063501
de Boer W et al. 2003 *Preprint* IEKP-KA/2003-17, [hep-ph/0309029]
28. Bergstrom L, Edsjö J, Gondolo P and Ullio P 1999 *Phys. Rev. D* **59** 043506
29. Bergstrom L, Edsjo J and Ullio P Bergstrom L, Edsjo J, Ullio P 1999 *ApJ* **526** 215 [astro-ph/9902012]
30. Navarro J F, Frenk C S and White S D M 1996 *ApJ* **462** 563
31. Gondolo P, Edsjo J, Ullio P, Bergstrom L, Schelke M and Baltz E A 2004 *JCAP* **07** 008
32. Picozza P and Morselli A 2003 *J. Phys. G: Nucl. Part. Phys* **29** 903-911
33. Bennet C L et al. 2003 *ApJ Suppl.* **148** 1
34. Chan K L, Chattopadhyay U, Nath P 1997 *Phys. Rev. D* **58** 096004
Feng J L, Matchev K T, Moroi T 2000 *Phys. Rev. D* **61** 075005
Baer H et al. 2003 *J. High Energy Phys.* **0306** 054
35. A.M.Lionetto, A.Morselli, V.Zdravkovic, astro-ph/0502406 submitted to JCAP
36. S. Ghigna et al., *Astrophys. J.* **544** (2000) 616.

DARK ENERGY AND (NEW?) PARTICLE PHYSICS

Antonio Masiero
INFN, Sezione di Padova, Italy

Written contribution not received

THE ROLE OF BLACK HOLES IN THE UNIVERSE

Andreas Eckart

Institute of Physics, University of Cologne, Cologne, Germany

Written contribution not received

SESSION II – NEUTRINO PHYSICS

- *Kurt Woschnagg* Exploring the High–Energy Neutrino Universe Results from the South Pole – Results from AMANDA and Status of IceCube
- *Jeanne Wilson* New Results from the Salt Phase of the Sudbury Neutrino Observatory
- *Takeshi Nakadaira* Results from K2K
- *M. Patrick Decowski* KamLAND: Studying Neutrino Oscillation with Reactors
- *Alexander Studenikin* Quantum Theory of Neutrino Spin Light in Dense Matter
- *Tass Belias* The Startup of MINOS
- *Eugenio Coccia* The CNGS Program: a Status Report
- *Guido Altarelli* Normal and Special Models of Neutrino Masses and Mixings

**EXPLORING THE HIGH-ENERGY NEUTRINO UNIVERSE
FROM THE SOUTH POLE –
RESULTS FROM AMANDA AND STATUS OF ICECUBE**

Kurt Woschnagg

Dept. of Physics, University of California, Berkeley, CA 94720, USA

for the AMANDA collaboration ?)

Abstract

The Antarctic Muon And Neutrino Detector Array (AMANDA) is a neutrino telescope embedded deep in the 2.8 km-thick polar icecap at the South Pole. AMANDA aims to detect high-energy cosmic neutrinos from sources where the highest-energy cosmic rays are produced and accelerated. We present recent results from AMANDA on searches for high-energy neutrinos of extraterrestrial origin. We have searched for a diffuse flux of neutrinos, neutrino point sources, and neutrinos from GRBs and from WIMP annihilations in the Sun or the center of the Earth. We also present a preliminary result on the first energy spectrum above a few TeV for atmospheric neutrinos. The status of IceCube, the km³-sized successor to AMANDA, is reviewed after its first successful construction season.

1 Introduction

In observational astronomy and astrophysics, the properties of cosmological objects are studied through the detection of cosmic information carriers emitted by the objects. Three types of messengers have been used to date: electromagnetic radiation (photons), cosmic rays, and neutrinos (figure ??).

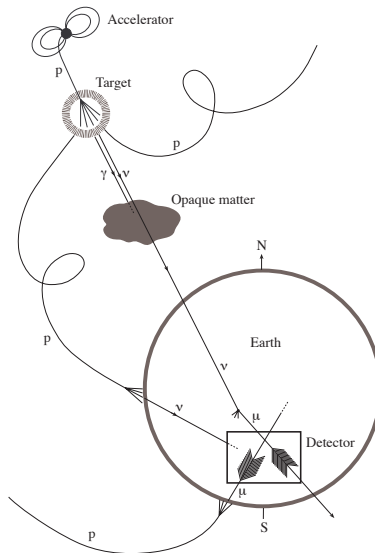


Figure 1: *High-energy astrophysical information carriers: cosmic rays (p) are deflected by magnetic fields; photons (γ) are absorbed by intervening matter; neutrinos (ν) point back to their source and can traverse great distances. For neutrino detection, Earth is used as a filter against cosmic rays.*

The electrically neutral photons are not deflected by intergalactic magnetic fields and therefore point back to their origin, but are absorbed by intervening matter and interactions with the microwave and infrared backgrounds. Furthermore, photons cannot yield any information on the internal processes of the sources since they are produced in their outer regions. Cosmic rays, composed of nuclei, are deflected by magnetic fields, and suffer energy losses during propagation which deforms their energy spectrum. Neutrinos, which

have no electric charge and a low interaction cross-section with matter, can travel cosmological distances un-deflected by magnetic fields, and the distance at which the Universe can be observed is limited only by the strength of the source. They can thus retain the complete source flux and spectral information when reaching the Earth. On the other hand, due to the low interaction cross-section, neutrino detection requires very large detector volumes and long exposure times.

The existence of high-energy cosmic neutrinos is suggested by the observation of high-energy cosmic rays and gamma rays. Observation of cosmic neutrinos could shed light on the production and acceleration mechanisms of cosmic rays, which are not understood for energies above the “knee” at 10^{15} eV. Neutrinos with energies in the TeV range and higher may be produced by a variety of sources. Candidate cosmic accelerators include supernova remnants, the accretion disk and jets of Active Galactic Nuclei (AGN), and the violent processes behind Gamma Ray Bursts (GRB). In these environments, neutrinos are expected to be produced in the decays of pions created through proton-proton or proton-photon collisions. The expected neutrino energy spectrum from such accelerators is typically predicted to be E^{-2} . The AMANDA detector was built to explore the high-energy universe in neutrinos, using the advantages of neutrinos as cosmic messengers. In January 2005, construction began on IceCube ^{?)}, the km³-sized successor to AMANDA.

2 The AMANDA Neutrino Telescope

The AMANDA detector ^{?)} consists of 677 optical modules arranged along 19 vertical strings buried deep in the glacial ice at the South Pole, mainly at depths between 1500 and 2000 m (figure ??). Each module consists of a photomultiplier tube (PMT) housed in a spherical glass pressure vessel. PMT pulses are transmitted to the data acquisition electronics at the surface via coaxial cables (inner 4 strings), twisted pair cables (6 strings) or optical fibers (outer 9 strings). The geometric outline of the bulk of the array is a cylinder which is 500 m high and with a radius of 100 m. The typical vertical spacing between modules is 10–20 m, and the horizontal spacing between strings 30–50 m.

The optical modules record Cherenkov light generated by secondary charged leptons (e , μ , τ) created in neutrino interactions near the detector. Events are

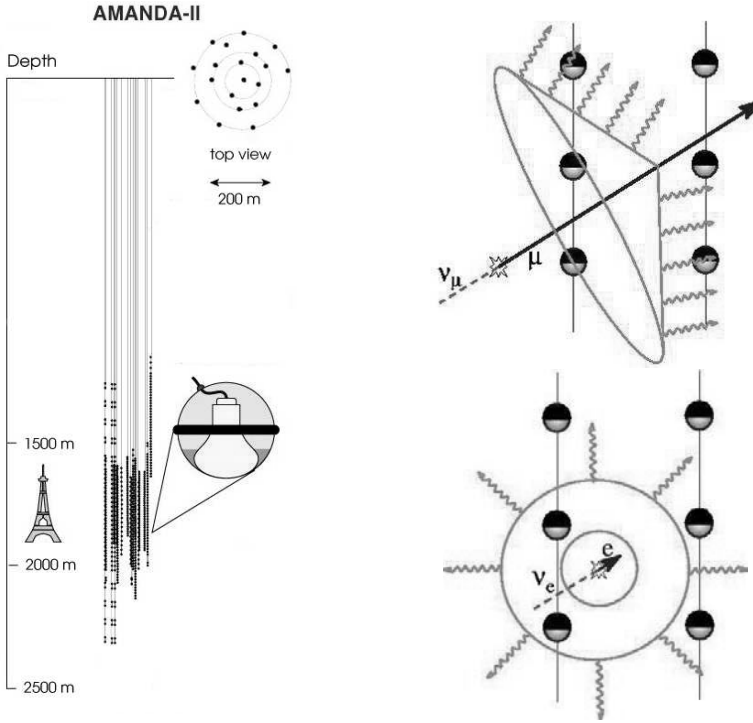


Figure 2: Schematic view of the AMANDA neutrino telescope and event signatures for ν_μ -induced muon tracks and ν_e -induced cascades.

reconstructed ^{?)} by maximizing the likelihood that the timing pattern of the recorded light is produced by a hypothetical track or cascade¹ (see figure ??). The angular resolution is between 1.5° and 2.5° for muon tracks, depending on declination, and $\sim 30^\circ$ for cascades, the difference reflecting the fact that muon tracks yield a long lever arm whereas cascades produce more spherical light patterns. On the other hand, the energy resolution, which is correlated to the amount of detected light, is better for cascades, 0.15 in $\log(E)$, than for muon tracks, 0.4 in $\log(E)$.

Using calibration light sources deployed with the strings and a YAG laser

¹A cascade is an electromagnetic or hadronic shower.

at the surface connected to diffusing balls in the ice via optical fibers, we have mapped ^{?)} the optical properties of the ice over the full relevant wavelength- and depth range (figure ??). The glacial ice is extremely transparent for Cherenkov wavelengths near the peak sensitivity of the modules: at 400 nm, the average absorption length is 110 m and the average effective scattering length is 20 m. Below a depth of 1500 m, both scattering and absorption are dominated by dust, and the optical properties vary with dust concentration. The depth profile is in good agreement with variations of dust concentration measured in ice cores from other Antarctic sites ^{?, ?, ?)}. These dust layers reflect past variations in climate. Implementation of the detailed knowledge of ice properties into our detector simulation and reconstruction tools reduces systematic uncertainties and improves track and cascade reconstruction.

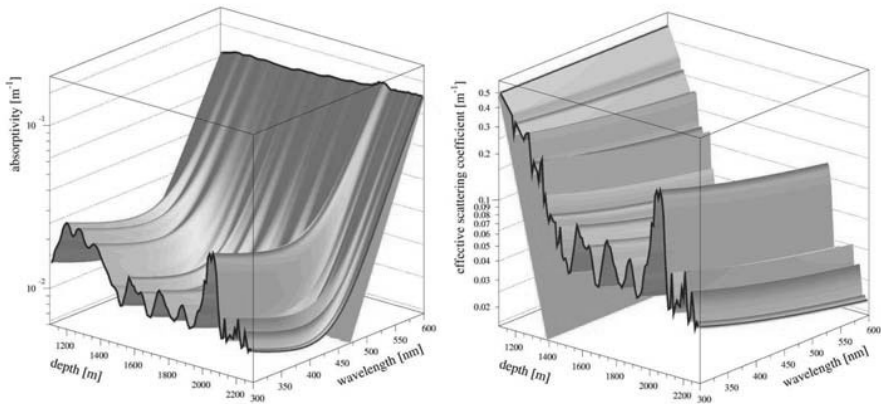


Figure 3: *Optical properties of deep South Pole ice: absorptivity (left) and scattering coefficient (right) as function of depth and wavelength. The green (partially obscured) tilted planes show the contribution from pure ice to absorption and from air bubbles to scattering, respectively. If these contributions are subtracted, the optical properties vary with the concentration of insoluble dust, which tracks climatological variations in the past ^{?, ?, ?)}.*

The full 19-string array, named AMANDA-II, started taking data in 2000. An earlier 10-string stage (comprising the inner 10 strings), called AMANDA-B10, took data in the period 1997–1999. In the 2003/04 field season, the data

acquisition system was upgraded with Transient Waveform Recorders on all channels, digitizing the PMT pulses in the electronics on the surface. Waveform digitization will increase the effective dynamic range of individual channels by about a factor 100 and will lead to an improvement in energy reconstruction, especially at high energies.

3 Physics Topics and Analysis Strategies

AMANDA is used to explore a variety of physics topics, ranging from astrophysics to particle physics, over a wide range of energies. At the low energy end, in the MeV range, AMANDA is sensitive to bursts of antineutrinos from supernovae (which would be detected by a collective rate increase in all PMTs). For higher energies, GeV to TeV, the detector is used to study atmospheric neutrinos and to conduct indirect dark matter searches. In the energy range for which AMANDA has been primarily optimized, TeV to PeV, the aim is to use neutrinos to study AGN and GRBs, looking both for a diffuse flux and for point sources of high-energy neutrinos. Using special analysis techniques, the array is also sensitive to the ultra-high energies in the PeV to EeV range.

For most analysis channels, AMANDA uses the Earth as a filter and looks down for up-going neutrinos. The main classes of background are up-going atmospheric neutrinos and down-going atmospheric muons that are misreconstructed as up-going. Since AMANDA is located at the South Pole, an up-going event will have originated in the Northern sky.

We present all flux limits following the ordering scheme by Feldman and Cousins^{?)} and include systematic uncertainties in the limit calculations according to the method derived by Conrad *et al.*^{?)} The main sources of systematic uncertainty in the analyses presented here are the modelling of muon propagation and of optical ice properties in the detector simulation, adding up to roughly 25% uncertainty.

The AMANDA collaboration adheres strictly to a policy of performing all analyses in a “blind” manner to ensure statistical purity of the results. In practice, this means that selection criteria are optimized either on a sub-sample of the data set which is then excluded from the analysis yielding the final result, or on a time-scrambled data set which is only unscrambled after the selection criteria have been optimized and finalized.

4 Atmospheric Neutrinos

Neutrinos, and to some extent muons, created by cosmic ray interactions in the atmosphere constitute the main background in most analysis channels (the atmospheric muon flux is five orders of magnitude larger than the expected neutrino flux), but also serve as a test beam with which to study the detector response. Since the overwhelming majority of up-going neutrinos detected by AMANDA, even in the presence of a signal from an extraterrestrial source, are generated in the atmosphere by cosmic rays, we can study atmospheric neutrinos with high statistics at energies that have been out of reach for other neutrino detectors. Using a neural net energy reconstruction, trained on a full detector and physics simulation, followed by regularized unfolding, we measure a preliminary energy spectrum for up-going neutrinos with year 2000 AMANDA-II data (figure ??). This is the first atmospheric neutrino spectrum above a few

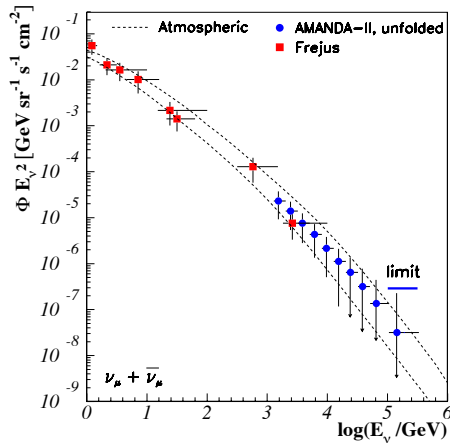


Figure 4: Atmospheric neutrino energy spectrum (preliminary) from regularized unfolding of AMANDA data, compared to the Fréjus spectrum^{?)} at lower energies. The two dashed curves are model predictions (based on separate parametrizations below^{?)} and above^{?)} 100 GeV) for the horizontal (upper) and vertical (lower) flux. The thick solid horizontal line indicates the limit we derive (section ??) on an E^{-2} flux of extraterrestrial muon neutrinos.

TeV, and it extends up to 300 TeV. It is in good agreement with theoretical predictions and smoothly extends the spectrum measured at lower energies by Fréjus ^{?)}.

5 Searches for a Diffuse Flux of Cosmic Neutrinos

The ultimate goal of AMANDA is to find and study the properties of cosmic sources of high-energy neutrinos. Should individual sources be too weak to produce an unambiguous directional signal in the array, the integrated neutrino flux from all sources could still produce a detectable diffuse signal. We have searched several years of data for such a diffuse signal using complementary techniques in different energy regimes.

5.1 Atmospheric neutrino spectrum

The atmospheric neutrino spectrum (fig. ??) was used to set a preliminary upper limit on a diffuse E^{-2} flux of extraterrestrial muon neutrinos for the energy range covered by the highest bin, 100–300 TeV, by calculating the maximal non-atmospheric contribution to the flux in the bin given its statistical uncertainty. However, the bins in the unfolded spectrum are correlated and the uncertainty in the last bin can not a priori be assumed to be Poissonian. The statistics in the bin were therefore determined with a Monte Carlo technique used to construct confidence belts following the definition by Feldman and Cousins ^{?)}. Given the unfolded number of experimental events in the bin (a fractional number), a preliminary 90% C.L. upper limit of

$$E^2 \Phi_{\nu_\mu}(E) < 2.6 \times 10^{-7} \text{ GeV cm}^{-2} \text{ s}^{-1} \text{ sr}^{-1} \quad (1)$$

was derived for $100 \text{ TeV} < E_\nu < 300 \text{ TeV}$, which includes 33% systematic uncertainties.

5.2 Cascades

In the cascade channel, AMANDA has essentially 4π coverage, and is sensitive to all three neutrino flavors. The year 2000 data sample, corresponding to 197 days livetime, was searched for cascade events. Event selection was based on topology and energy, and optimized to maximize the sensitivity to an E^{-2} signal spectrum. After final cuts one event remains, with an expected background

of $0.90^{+0.69}_{-0.43}$ from atmospheric muons and $0.06^{+0.09}_{-0.04}$ from atmospheric neutrinos. Not having observed an excess over background, we calculate a limit on a signal flux. The 90% C.L. limit on a diffuse flux of neutrinos of all flavors for neutrino energies between 50 TeV and 5 PeV, assuming full flavor mixing so that the neutrino flavor ratios are 1:1:1 at the detector, is

$$E^2 \Phi_\nu(E) < 8.6 \times 10^{-7} \text{ GeV cm}^{-2} \text{ s}^{-1} \text{ sr}^{-1}. \quad (2)$$

Since the energy range for this analysis contains the energy of the Glashow resonance, a limit on the flux at 6.3 PeV can be derived:

$$E^2 \Phi_{\bar{\nu}_e}(6.3 \text{ PeV}) < 2 \times 10^{-6} \text{ GeV cm}^{-2} \text{ s}^{-1} \text{ sr}^{-1}. \quad (3)$$

These limits ^{?)} obtained with one year (2000) of AMANDA-II data are roughly a factor 10 lower than the limits from similar searches performed with AMANDA-B10 data from 1997 ^{?)} and 1999 ^{?)}.

5.3 Ultra High Energy neutrinos

At ultra-high energies (UHE), above 1 PeV, the Earth is opaque to electron- and muon-neutrinos. Tau neutrinos with such initial energies might penetrate the Earth through regeneration ^{?)}, in which the τ produced in a charged-current ν_τ interaction decays back into ν_τ , but they will emerge with much lower energies. The search for extraterrestrial UHE neutrinos is therefore concentrated on events close to the horizon and even from above. The latter is possible since the atmospheric muon background is low at these high energies due to the steeply falling spectrum. Our search for UHE events in 1997 AMANDA-B10 data (131 days of livetime) relies on parameters that are sensitive to the expected characteristics of an UHE signal: bright events, long tracks (for muons), low fraction of single photoelectron hits. A neural net was trained to optimize the sensitivity to an E^{-2} neutrino signal in data dominated by atmospheric neutrino background.

After final selection, 5 data events remain, with 4.6 ($\pm 36\%$) expected background. Thus, no excess above background is observed and we derive ^{?)} a 90% C.L. limit on an E^{-2} flux of neutrinos of all flavors, assuming a 1:1:1 flavor ratio at Earth, for energies between 1 PeV and 3 EeV, of

$$E^2 \Phi_\nu(E) < 0.99 \times 10^{-6} \text{ GeV cm}^{-2} \text{ s}^{-1} \text{ sr}^{-1}. \quad (4)$$

A similar analysis of AMANDA-II data from 2000 is under way. However, the bright UHE events also saturate the larger array, so a substantial gain in sensitivity will mainly be due to the additional exposure time and improved selection algorithms.

5.4 Summary of diffuse searches

Using different analysis techniques, AMANDA has set limits on the diffuse flux of neutrinos with extraterrestrial origin for neutrino energies from 6 TeV ^{?)} up to a few EeV (figure ??). With the exception of the limit from the unfolded atmospheric spectrum, which can be seen as a quasi-differential limit, the limits are on the integrated flux over the energy range which contains 90% of the signal. Our limits exclude, at 90% C.L., some models ^{?, ?)} predicting diffuse neutrino fluxes.

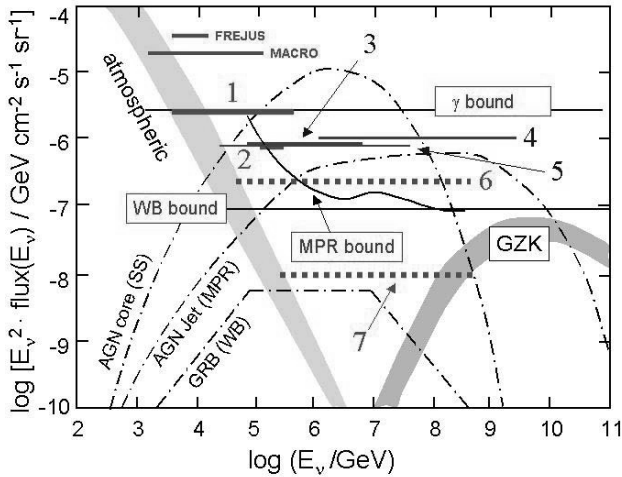


Figure 5: Limits on a diffuse flux of neutrinos of all flavors with an E^{-2} energy spectrum: (1) from ν_μ in 1997 AMANDA-B10 data; (2) from unfolded 2000 atmospheric neutrino spectrum; (3) from 2000 cascades; (4) from 1997 UHE events; (5) Baikal cascades 1998-2003; (6) sensitivity for 4 years of AMANDA data; (7) sensitivity for 3 years of IceCube data.

6 Point Source Searches

Searches for neutrino point sources require good pointing resolution and are thus restricted to the ν_μ channel. We have searched AMANDA-II data from 2000–2003 (corresponding to 807 days of livetime) for a point source signal. Events were selected to maximize the model rejection potential ^{?)} for a hypothetical E^{-2} neutrino spectrum convoluted with the background spectra due to atmospheric neutrinos and misreconstructed atmospheric muons. The selection criteria were optimized for the combined 4-year data set in each declination band separately since the geometry of the detector array introduces declination-dependent efficiencies. The *sensitivity* of the analysis, defined as the average upper limit one would expect to set on a non-atmospheric neutrino flux if no signal is detected, is shown in figure ?? for an E^{-2} signal spectrum.

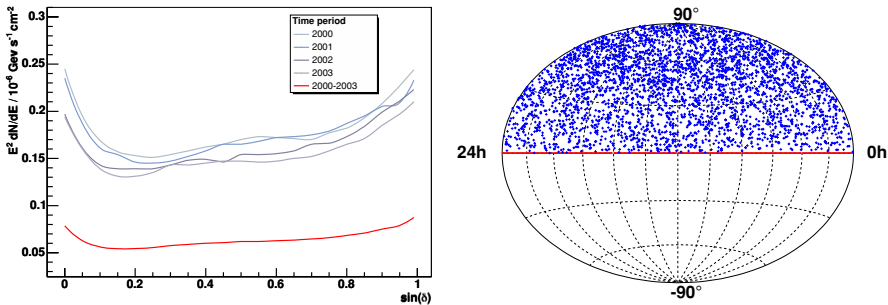


Figure 6: *Left: Sensitivity for an E^{-2} flux spectrum as function of declination. Right: Sky plot for 3329 up-going neutrino candidates in 4-year data sample.*

The final sample (figure ??, right) of 3329 neutrino candidates below the horizon, i.e. from the Northern sky, (with 3438 expected atmospheric neutrinos) was scanned for point sources with two methods. In the first, the sky is divided into a (repeatedly shifted) fine-meshed grid of overlapping bins which are tested for a statistically significant excess over the background expectation (estimated from all other bins in the same declination band). This search yielded no evidence for extraterrestrial point sources. The second method is an unbinned

search, in which the sky locations of the events and their uncertainties from reconstruction are used to construct a sky map of *significance* in terms of fluctuation (in σ) over background (figure ??). This map displays only one potential hot spot (above 3σ) with $\sigma = 3.4$, which is well within the expectation from a random event distribution. For comparison, similar significance maps were constructed after randomizing the right ascension for all events, thus simulating a truly random distribution (one such map is shown in the middle panel of figure ??). These scrambled maps are statistically indistinguishable from the real (upper) map. A full statistical analysis of many such scrambled maps proves that the sky map is fully compatible with a distribution expected from an atmospheric neutrino sample. The bottom panel in figure ?? shows the distribution of the highest significance found in 1000 scrambled maps. The probability for finding $\sigma_{max} = 3.4$ or higher in a random map is 92%. We thus see no evidence for point sources with an E^{-2} energy spectrum based on the first four years of AMANDA-II data. This preliminary result complements previously published results from point source searches with the AMANDA-B10 detector ?) and the first year ?) and first three years ?) of AMANDA-II data. Adding two more years of data to the one-year sample increased the sensitivity by a factor of 2.2.

7 Search for Neutrinos from GRBs

A special case of point source analysis is the search for neutrinos coincident with gamma ray bursts (GRBs) detected by satellite-borne detectors. For this search, the timing of the neutrino event serves as an additional selection handle which significantly reduces background. We have used samples of GRBs observed by two gamma ray detector systems: the BATSE instrument on board the CGRO satellite, which was decommissioned in 2000, and the Third Interplanetary Network (IPN3), a group of spacecraft equipped with gamma-ray burst detectors which uses triangulation to spatially locate the bursts.

For each burst, AMANDA data in a 10 min window around the GRB time (here defined as the start of T_{90} , the period which covers 90% of the γ -ray signal) was kept blind. The background was estimated by averaging over events in the on-source spatial bin within ± 1 hour of the burst (excluding the 10 min signal window). Data was then searched for a statistically significant excess over background within T_{90} (which is contained within the blind window).

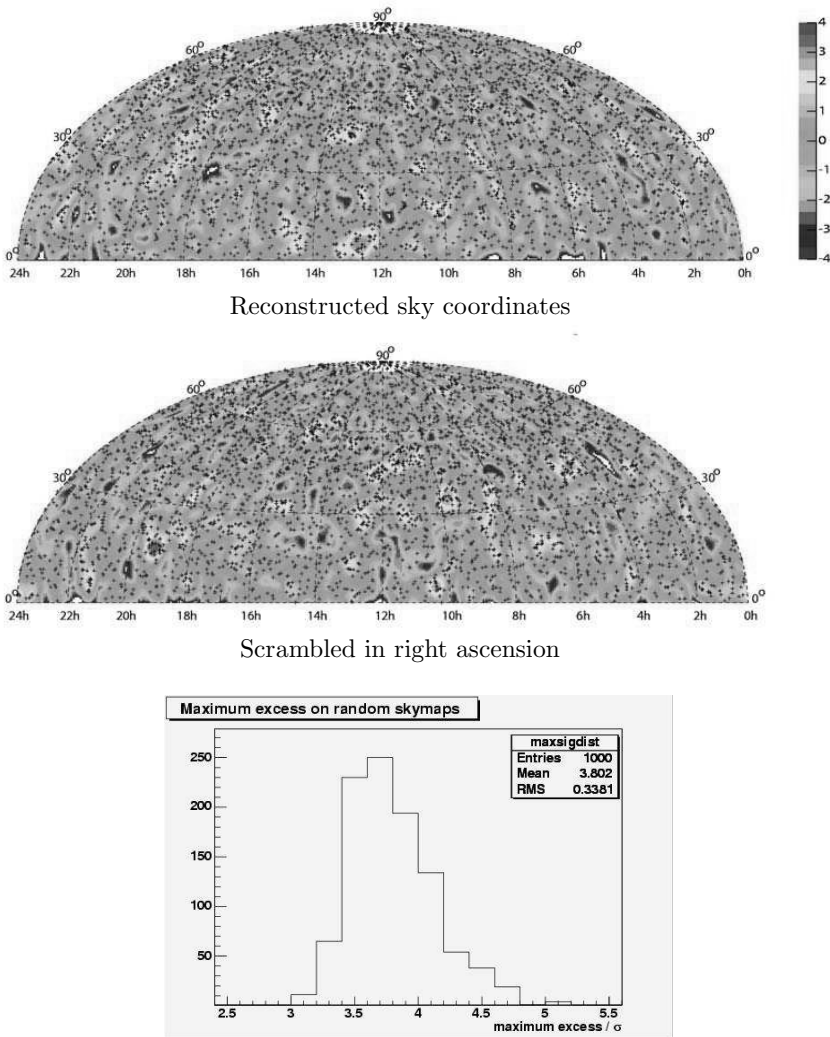


Figure 7: Significance map (top) constructed from 3329 up-going events in the final sample from a point source search with AMANDA-II data from 2000–2003. The points show the reconstructed sky positions (declination and right ascension) of the neutrino candidates. The color scale indicates the significance (in σ). The highest significance is $\sigma = 3.4$. The middle panel shows an example of a significance map based on the same events, but with randomized right ascension coordinates. The bottom panel shows the distribution of highest significance from 1000 scrambled sky maps.

We have initially analyzed a sample of only BATSE-triggered bursts. We found no neutrino event coincident with any of 312 bursts recorded between 1997, when AMANDA-B10 became operational, and 2000, when BATSE operations ended, and derived a preliminary limit on the muon neutrino flux ^{?)}. Recently, we have performed a similar search on a sample containing 139 bursts triggered by BATSE and/or IPN between 2000 and 2003. As in the previous analysis, no neutrino event was observed in coincidence with any of the bursts, in this case with an average of 1.25 expected from background fluctuations. Assuming a broken power-law energy spectrum as proposed by Waxmann and Bahcall ^{?)}, with $E_{\text{break}} = 100$ TeV and $\Gamma_{\text{bulk}} = 300$, we obtain a (preliminary) 90% C.L. upper limit on the expected muon neutrino flux at the Earth of

$$E^2 \Phi_\nu(E) < 3 \times 10^{-8} \text{ GeV cm}^{-2} \text{ s}^{-1} \text{ sr}^{-1} \quad (5)$$

based on the 139 burst sample.

We are currently expanding our GRB-neutrino searches to include cascade events. In the cascade analysis, the 4π coverage together with the temporal coincidence requirement compensate for the poor pointing resolution. In addition, an analysis modeling the flux of coincident neutrinos, based on the discrete set of electromagnetic parameters associated with individual GRBs, is being performed in the context of the fireball phenomenology ^{?)}.

8 Dark Matter Searches

Particle physics provides an interesting candidate for non-baryonic dark matter in the Weakly Interacting Massive Particle (WIMP). In particular, the Minimal Supersymmetric extension of the Standard Model (MSSM) provides a promising WIMP candidate in the neutralino, which could be the lightest supersymmetric particle. Neutralinos can be gravitationally trapped in massive bodies, and can then via annihilation and decay of the resulting particles produce neutrinos. AMANDA can therefore perform indirect dark matter searches by looking for fluxes of neutrinos from the center of the Earth or the Sun.

For the former, we present a preliminary update to our published limits obtained with one year of 10-string data ^{?)}. We have looked for vertically up-going tracks in AMANDA-B10 data from 1997 to 1999, corresponding to a total livetime of 422 days. No WIMP signal was found and a 90% C.L. upper

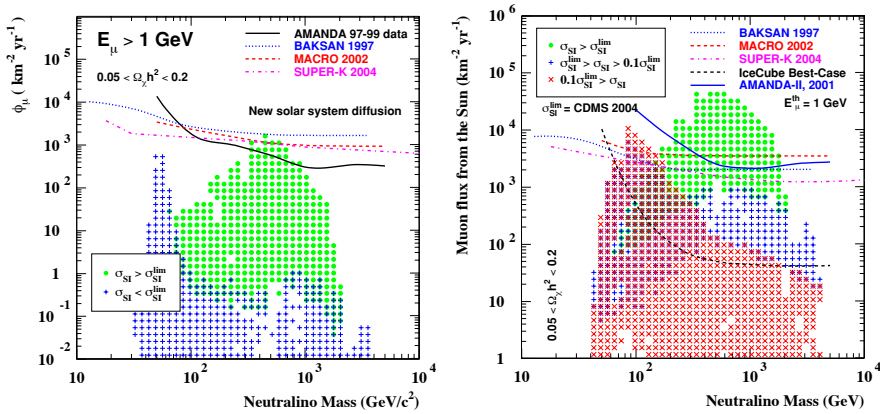


Figure 8: Preliminary limits on the muon flux due to neutrinos from neutralino annihilations in the center of the Earth (left) and the Sun (right). The colored symbols correspond to model predictions ^{?)} within the allowed parameter space of the MSSM. The green models are disfavored by direct searches with CDMS II ^{?)}.

limit on the muon flux from the center of the Earth was set for neutralino masses between 50 GeV and 5 TeV (figure ??, left panel).

Due to its larger mass (resulting in a deeper gravitational well) and a higher capture rate due to additional spin-dependent processes, the Sun can also be used for WIMP searches despite its much larger distance from the detector. Although the Sun is maximally 23° below the horizon at the South Pole, AMANDA-II can be used for a WIMP search thanks to its improved reconstruction capabilities for horizontal tracks. Analysis of 2001 data (0.39 years of livetime) yielded no WIMP signal. The preliminary upper limit on the muon flux from the Sun is compared to MSSM predictions ^{?)} in figure ?? (right panel).

For heavier neutralino masses, the limit obtained with less than one year of AMANDA-II data is already competitive with limits from indirect searches with detectors that have several years of integrated livetime. The green points

in figure ?? correspond to models that are disfavored by direct searches ?), which appear to set more severe restrictions on the allowed parameter space than indirect searches. However, it should be noted that the two methods are complementary in that they (a) probe the WIMP distribution in the solar system at different epochs and (b) are sensitive to different parts of the velocity distribution.

9 Status of IceCube

The successful operation of AMANDA has led to a cubic-kilometer extension to be built in the same location: the IceCube telescope ?). This array will comprise 4800 digital optical modules (DOM) on 80 strings, instrumenting one km³ of ice at depths between 1450 and 2450 m. The modules have digitizing electronics on-board, and only digital PMT waveform information is sent to the surface. In January 2005, the first string was deployed. All 60 DOMs are operational after refreeze of the hot-water-drilled hole containing the string. Construction will continue until 2010 when the array is expected to be fully commissioned.

Acknowledgements

We acknowledge the support of the following agencies: National Science Foundation – Office of Polar Programs, National Science Foundation – Physics Division, University of Wisconsin Alumni Research Foundation, Department of Energy and National Energy Research Scientific Computing Center (supported by the Office of Energy Research of the Department of Energy), UC-Irvine ANEAS Supercomputer Facility, USA; Swedish Research Council, Swedish Polar Research Secretariat and Knut and Alice Wallenberg Foundation, Sweden; German Ministry for Education and Research, Deutsche Forschungsgemeinschaft (DFG), Germany; Fund for Scientific Research (FNRS-FWO), Flanders Institute to encourage Scientific and Technological Research in Industry (IWT) and Belgian Federal Office for Scientific, Technical and Cultural affairs (OSTC), Belgium; D. F. C. acknowledges the support of the NSF CAREER program; E. R. acknowledges the support of the Marie-Curie fellowship program of the European Union; M. R. acknowledges the support of the Swiss National Science Foundation.

References

1. O. Botner *et al.*, Nucl. Phys. B (Proc. Suppl.) **143**, 367 (2005).
2. E. Andrés *et al.*, Nature **410**, 441 (2001).
3. J. Ahrens *et al.*, Nucl. Instrum. Meth. A **524**, 169 (2004).
4. K. Woschnagg *et al.*, in preparation.
5. J. R. Petit *et al.*, Nature **399**, 429 (1999).
6. L. Augustin *et al.*, Nature **429**, 623 (2004).
7. O. Watanabe *et al.*, Ann. Glaciol. **29**, 176 (1999).
8. G. J. Feldman and R. D. Cousins, Phys. Rev. D **57**, 3873 (1998).
9. J. Conrad *et al.*, Phys. Rev. D **67**, 012002 (2003).
10. W. Rhode *et al.*, Astropart. Phys. **4**, 217 (1996).
11. M. Honda *et al.*, Phys. Rev. D **52**, 4985 (1995).
12. L. V. Volkova and G. T. Zatsepin, Sov. J. Nucl. Phys. **37**, 212 (1980).
13. M. Ackermann *et al.*, Astropart. Phys. **22**, 127 (2004).
14. J. Ahrens *et al.*, Phys. Rev. D **67**, 012003 (2003).
15. F. Halzen and D. Saltzberg, Phys. Rev. Lett. **81**, 4305 (1998).
16. M. Ackermann *et al.*, Astropart. Phys. **22**, 339 (2005).
17. J. Ahrens *et al.*, Phys. Rev. Lett. **90**, 251101 (2003).
18. F. W. Stecker and M. H. Salamon, Space Sci. Rev. **75**, 341 (1996).
19. L. Nellen, Phys. Rev. D **47**, 5270 (1993).
20. G. C. Hill and K. Rawlins, Astropart. Phys. **19**, 393 (2003).
21. J. Ahrens *et al.*, Astrophys. J. **583**, 1040 (2003).
22. J. Ahrens *et al.*, Phys. Rev. Lett. **92**, 071102 (2004).
23. M. Ackermann *et al.*, Phys. Rev. D **71**, 077102 (2005).
24. R. Hardtke *et al.*, Proc. 28th Int. Cosmic Ray Conf. (ed. T. Kajita *et al.*, Tsukuba, August 2003), 2717 (University Academy Press, Tokyo, 2003).
25. J. Bahcall and E. Waxmann, Phys. Rev. D **64**, 023002 (2001).
26. M. Stamatikos *et al.*, AIP Conf. Proc. **727**, 146 (2004).

27. D. S. Akerib *et al.*, Phys. Rev. Lett. **93**, 211301 (2004).
 28. J. Ahrens *et al.*, Phys. Rev. D **66**, 032006 (2002).
 29. J. Edsjö, Nucl. Phys. B (Proc. Suppl.) **143**, 435 (2005).
 30. <http://icecube.wisc.edu>

* . The AMANDA collaboration:

M. Ackermann⁴, J. Ahrens¹¹, D. W. Atlee⁸, X. Bai¹, R. Bay⁹, M. Bartelt², S. W. Barwick¹⁰, T. Becka¹¹, K.-H. Becker², J. K. Becker⁷, E. Bernardini⁴, D. Bertrand³, D. J. Boersma⁴, S. Böser⁴, O. Botner¹⁷, A. Bouchta¹⁷, O. Bouhalil³, J. Braun¹⁵, C. Burgess¹⁸, T. Burgess¹⁸, T. Castermans¹³, D. Chirkin⁶, J. A. Coarasa⁸, B. Collin⁸, J. Conrad¹⁷, J. Cooley¹⁵, D. F. Cowen⁸, A. Davour¹⁷, C. De Clercq¹⁹, T. DeYoung¹², P. Desiati¹⁵, P. Ekström¹⁸, T. Feser¹¹, T. K. Gaisser¹, R. Ganugapati¹⁵, H. Geenen², L. Gerhardt¹⁰, A. Goldschmidt⁶, A. Groß⁷, A. Hallgren¹⁷, F. Halzen¹⁵, K. Hanson¹⁵, D. Hardtke⁹, R. Hardtke¹⁵, T. Harenberg², T. Hauschildt⁴, K. Helbing⁶, M. Hellwig¹¹, P. Herquet¹³, G. C. Hill¹⁵, J. Hodges¹⁵, D. Hubert¹⁹, B. Hughey¹⁵, P. O. Hulth¹⁸, K. Hultqvist¹⁸, S. Hundertmark¹⁸, J. Jacobsen⁶, K.-H. Kampert², A. Karle¹⁵, J. Kelley¹⁵, M. Kestel⁸, L. Köpke¹¹, M. Kowalski⁴, M. Krasberg¹⁵, K. Kuehn¹⁰, R. Lang⁴, H. Leich⁴, M. Leuthold⁴, J. Lundberg¹⁷, J. Madsen¹⁶, K. Mandli¹⁵, P. Marciniewski¹⁷, H. S. Matis⁶, C. P. McParland⁶, T. Messarius⁷, Y. Minaeva¹⁸, P. Miočinić⁹, R. Morse¹⁵, K. Münich⁷, R. Nahnauer⁴, J. W. Nam¹⁰, T. Neunhoffer¹¹, P. Niessen¹, D. R. Nygren⁶, Ph. Olbrechts¹⁹, C. Pérez de los Heros¹⁷, D. Pieloth⁴, A. C. Pohl⁵, R. Porrata⁹, P. B. Price⁹, G. T. Przybylski⁶, K. Rawlings¹⁵, E. Resconi⁴, W. Rhode⁷, M. Ribordy¹³, S. Richter¹⁵, H.-G. Sander¹¹, K. Schinarakis², S. Schlenstedt⁴, D. Schneider¹⁵, R. Schwarz¹⁵, S. H. Seo⁸, A. Silvestri¹⁰, M. Solarz⁹, G. M. Spiczak¹⁶, C. Spiering⁴, M. Stamatikos¹⁵, D. Steele¹⁵, P. Steffen⁴, R. G. Stokstad⁶, K.-H. Sulanke⁴, I. Taboada⁹, O. Tarasova⁴, L. Thollander¹⁸, S. Tilav¹, J. Vandenbroucke⁹, L. C. Voicu⁸, B. Voigt⁴, W. Wagner⁷, C. Walck¹⁸, M. Walter⁴, Y. R. Wang¹⁵, C. H. Wiebusch², R. Wischniewski⁴, H. Wissing⁴, K. Woschnagg⁹, G. Yodh¹⁰

- (1) Bartol Research Institute, University of Delaware, Newark, DE 19716, USA
 (2) Dept. of Physics, Bergische Universität Wuppertal, D-42097 Wuppertal, Germany
 (3) Université Libre de Bruxelles, Science Faculty CP230, B-1050 Brussels, Belgium
 (4) DESY-Zeuthen, D-15735 Zeuthen, Germany
 (5) Dept. of Technology, Kalmar University, S-39182 Kalmar, Sweden
 (6) Lawrence Berkeley National Laboratory, Berkeley, CA 94720, USA
 (7) Institute of Physics, University of Dortmund, D-44221 Dortmund, Germany
 (8) Dept. of Physics, Pennsylvania State University, University Park, PA 16802, USA
 (9) Dept. of Physics, University of California, Berkeley, CA 94720, USA
 (10) Dept. of Physics and Astronomy, University of California, Irvine, CA 92697, USA
 (11) Institute of Physics, University of Mainz, D-55099 Mainz, Germany
 (12) Dept. of Physics, University of Maryland, College Park, MD 20742, USA
 (13) University of Mons-Hainaut, B-7000 Mons, Belgium
 (15) Dept. of Physics, University of Wisconsin, Madison, WI 53706, USA
 (16) Physics Dept., University of Wisconsin, River Falls, WI 54022, USA
 (17) Division of High Energy Physics, Uppsala University, S-75121 Uppsala, Sweden
 (18) Dept. of Physics, Stockholm University, S-10691 Stockholm, Sweden
 (19) Vrije Universiteit Brussel, Dienst ELEM, B-1050 Brussels, Belgium

NEW RESULTS FROM THE SALT PHASE OF THE SUDBURY NEUTRINO OBSERVATORY

Jeanne Wilson, for the SNO Collaboration
University of Sussex, Brighton, BN1 9QH, UK

Abstract

Results are presented from the complete salt phase at the Sudbury Neutrino Observatory in which NaCl was dissolved in the pure D₂O target. In units of $10^6 \text{ cm}^{-2} \text{ s}^{-1}$, the total flux of active-flavour neutrinos from ⁸B decay in the Sun is found to be $4.94^{+0.21}_{-0.21}(\text{stat})^{+0.38}_{-0.34}(\text{syst})$ and the integral flux of electron neutrinos for an undistorted ⁸B spectrum is $1.68^{+0.06}_{-0.06}(\text{stat})^{+0.08}_{-0.09}(\text{syst})$. The electron recoil energy spectrum obtained from this 391 day data set is presented and a search for matter-effects in the Earth through a possible day-night asymmetry in the charged-current integral rate is consistent with no asymmetry.

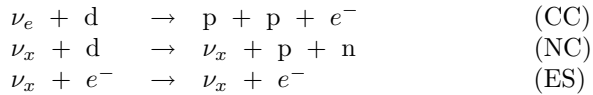
1 Introduction

Results from the completed Phase II of the Sudbury Neutrino Observatory (SNO) are summarised in this paper. From this 391 day data sample three new results have been obtained which confirm and improve upon previous SNO measurements from both Phase I and a subset of Phase II data. In Phase II neutron capture in the D₂O detecting medium was enhanced by the addition of ~ 2000 kg of NaCl. The salt additive enables a statistical separation of NC events from CC and ES events without using energy distributions but by measuring event isotropy, thus allowing measurement of the electron recoil energy spectrum. The first day-night asymmetry results are also presented for the Phase II data along with updated model-independent flux measurements. A full description of the analysis performed can be found in Ref. ²⁾.

2 The SNO Detector

SNO ¹⁾ is a water Čerenkov detector located at a depth of 2092 m (6010 m of water equivalent) in the Creighton mine near Sudbury, Ontario. The detector (shown in figure 1) is situated in a large, barrel-shaped cavity, 22 m in diameter and 34 m in height. The 1 kilotonne ultra-pure D₂O target is contained within a transparent acrylic vessel (AV), 12 m in diameter and 5.5 cm thick. A 17.8 m diameter, geodesic sphere surrounds the AV and supports 9456 inward-looking and 91 outward-looking 20 cm photomultiplier tubes (PMTs). The remaining volume is filled with ultra-pure H₂O that acts as a cosmic ray veto and as a shield from naturally occurring radioactivity from both the construction materials and the surrounding rock.

The D₂O target enables SNO to simultaneously measure both the flux of electron type neutrinos and the total flux of all active neutrinos from ⁸B decay in the Sun through the following interactions:



The charged-current (CC) interaction on the deuteron is sensitive exclusively to ν_e , and the neutral-current (NC) interaction has equal sensitivity to all active neutrino flavours (ν_x , $x=e,\mu,\tau$). Elastic scattering (ES) on the electron is also sensitive to all active flavours, but has ~ 6.5 times higher sensitivity to ν_e as the process can occur through W exchange for ν_e as well as Z exchange.

In Phase I (the Pure D₂O Phase) of the SNO experiment, neutrons produced by the NC interaction were observed through capture on deuterium nuclei. The excited state of tritium produced subsequently decays releasing a 6.25 MeV γ which Compton scatters to produce an electron. In June 2001

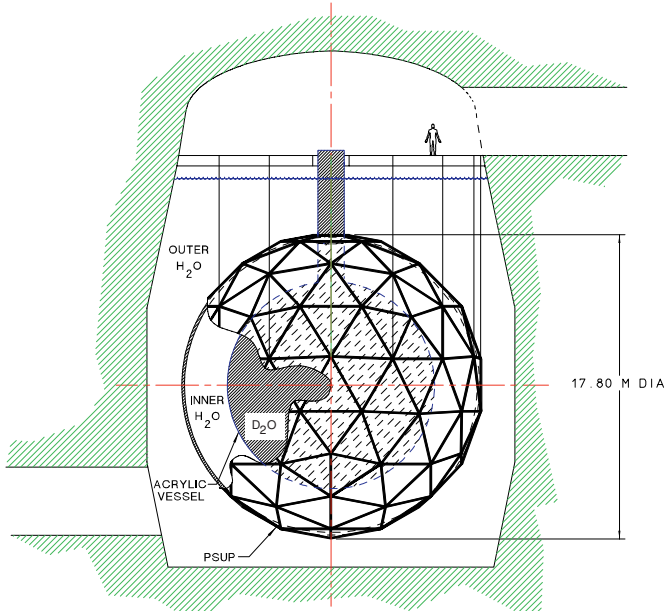


Figure 1: A cross-sectional view of the SNO detector.

~ 2000 kg of NaCl was added to the D_2O for Phase II (the Salt Phase). The addition of the salt enhanced SNO's ability to detect solar 8B neutrinos in three ways. The neutron efficiency in Phase I, volume weighted within the selected analysis region was 14.4% but in Phase II 40.7% efficiency was achieved due to the larger capture cross-section on ^{35}Cl . Secondly, the total energy of γ s released from neutron capture on ^{35}Cl is greater at 8.6 MeV so the observed energy peak for neutrons in the salt phase is higher than Phase I and more distinct from the low energy radioactive background. Finally, the hit distribution on the PMT array from the multiple γ rays emitted from capture on ^{35}Cl is significantly different from that produced by a single relativistic electron. This allows statistical separation of electrons created by CC interactions and neutrons from NC interactions without any assumptions on the underlying neutrino energy distribution.

3 Signal Extraction

Figure 2 shows the four characteristic observables used to statistically separate the signals due to the three types of neutrino interaction and also a background of external neutrons (EN) created outside the D_2O volume. Background neutrons created inside the D_2O volume, for example those from photo-disintegration of deuterium, produce events indistinguishable from the NC signal and are subtracted from the internal neutrons after the fit. The variables

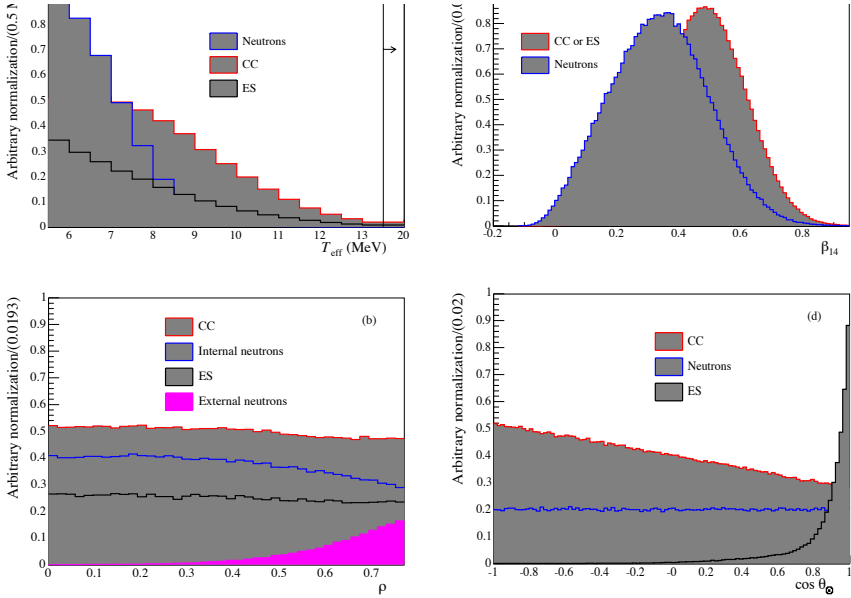


Figure 2: (a) T_{eff} and (b) ρ (c) β_{14} and (d) $\cos \theta_{\odot}$ distributions for CC, ES, NC and external neutron events. Where internal and external neutron distributions are identical the distribution is simply labelled neutrons. Note that the distribution normalisations are arbitrary and chosen to allow the shape differences to be seen clearly. The CC energy spectrum shape corresponds to an undistorted ${}^8\text{B}$ model.

used are the effective electron kinetic energy, T_{eff} , a parameterisation of event isotropy, β_{14} , a parameterisation of reconstructed event position, ρ , and the cosine of the reconstructed event direction with respect to the Sun, $\cos \theta_{\odot}$.

The vertex position, direction and isotropy of each event are reconstructed from the PMT trigger times and positions. The volume-weighted parameterisation of the event radial position:

$$\rho = \left(\frac{R}{R_{\text{AV}}} \right)^3 \quad (1)$$

is used for signal separation, where $R_{\text{AV}} = 600.5$ cm is the radius of the acrylic vessel. Isotropy refers to the uniformity of the spatial distribution of triggered PMTs in an event and was parameterised as

$$\beta_{14} = \beta_1 + 4\beta_4 \quad (2)$$

where

$$\beta_l = \frac{2}{N(N-1)} \sum_{i=1}^{N-1} \sum_{j=i+1}^N P_l(\cos\theta_{ij}). \quad (3)$$

Here P_l is the Legendre polynomial of order l , θ_{ij} is the angle between triggered PMTs i and j relative to the reconstructed event vertex, and N is the total number of triggered PMTs in the event.

The probability distributions shown are composed of Monte Carlo simulated events and were used in an extended maximum likelihood fit to the 4722-event data set to extract the electron neutrino energy spectrum, ^8B neutrino fluxes and day-night asymmetries. As some neutrino oscillation scenarios can distort the ν_e spectrum, the energy (T_{eff}) distribution of the CC and ES interactions was not assumed; for these two signals PDFs were created separately for each 0.5 MeV interval in the T_{eff} range 5.5–13.5 MeV. For $T_{\text{eff}} > 13.5$ MeV a single bin was used due to the low statistics in this energy region. A single PDF was used for both the NC and EN components whose T_{eff} spectra which result from the energy release of neutron capture on ^{35}Cl are independent of neutrino energy. The normalisation for each of these PDFs was allowed to vary in the fit giving a model-independent measurement of the neutrino energy spectrum.

Due to mild correlations between the four variables, multi-dimensional PDFs were used to avoid biases in the results of the likelihood fit. Statistical limitations prevent the use of 4-dimensional PDFs which would naturally accommodate all correlations between observables, so two different factorisations were considered.

$$P(T_{\text{eff}}, \beta_{14}, \rho, \cos\theta_{\odot}) = P(T_{\text{eff}}, \beta_{14}) \times P(\cos\theta_{\odot}) \times P(\rho) \quad (4)$$

$$P(T_{\text{eff}}, \beta_{14}, \rho, \cos\theta_{\odot}) = P(T_{\text{eff}}, \beta_{14}, \rho) \times P(\cos\theta_{\odot}|T_{\text{eff}}, \rho) \quad (5)$$

Both factorisations were tested by applying the signal extraction procedure to 100 simulated data sets, each generated to simulate the expected characteristics of the data. It was found that the parameterisation in equation 4 resulted in a small bias, which was reduced to an insignificant level through the explicit inclusion of correlations with ρ and $\cos\theta_{\odot}$ in the second parameterisation. In equation 5 the first factor is just the 3-dimensional PDF for the variables T_{eff} , β_{14} , and ρ , and the second factor is the conditional PDF for $\cos\theta_{\odot}$ given T_{eff} and ρ . When the expected bias from equation 4 was corrected for, both approaches gave consistent results when applied to the data.

4 Systematic Uncertainties

Systematic uncertainties in the observable parameters used in signal extraction were evaluated through detailed comparisons of Monte Carlo simulations and

calibration data. Detailed descriptions of these studies can be found in Ref. 2). The effects of these uncertainties on the extracted neutrino fluxes and spectra were evaluated by separately varying the PDFs according to the estimated 1σ uncertainty for each possible systematic effect. The signal extraction was then repeated and the difference between the nominal fit values and the shifted PDF fit values was taken as the systematic uncertainty.

For the current analysis a number of systematic uncertainties were re-evaluated for possible differential effects in energy. Non-linear contributions to the uncertainties in T_{eff} and β_{14} were parameterised based on calibration data obtained with ^8Li and ^{252}Cf sources. Small differential effects in the selection efficiency for neutrino events and uncertainty in the fiducial volume for analysis were also taken into account.

5 Solar Neutrino Energy Spectrum

Figure 3 shows the CC energy spectrum obtained from the maximum likelihood fit. Statistical uncertainties are shown around the data points and the systematic uncertainties are shown with respect to the prediction for an undistorted ^8B shape. Whilst some uncertainties may change the PDF shapes leading to a change in the fitted number of events, others simply affect the overall acceptance of events. Both must be accounted for as the latter can lead to errors in the translation of differential event counts into differential neutrino fluxes.

6 Day Night Asymmetry Measurements

Asymmetries between the day-time and night-time neutrino fluxes were tested for by performing the signal extraction separately for day and night data sets to extract an asymmetry ratio:

$$A_{\text{DN}} = \frac{2(\Phi_{\text{N}} - \Phi_{\text{D}})}{\Phi_{\text{N}} + \Phi_{\text{D}}} \quad (6)$$

where Φ_{N} and Φ_{D} are the measured day-time and night-time fluxes respectively. Matter-enhanced neutrino oscillations could cause ν_e regeneration inside the Earth for certain ranges of mixing parameters resulting in a day-night asymmetry in the CC and ES fluxes measured in SNO. The CC and ES asymmetries are predicted to be small for the favoured large mixing angle (LMA) parameter space, and for standard oscillations between active neutrino flavours the NC asymmetry should be zero. Under this assumption, the CC and ES asymmetries were measured while the NC asymmetry was constrained to zero through a simultaneous fit to both the day and night data sets. However, tests were made for an asymmetry in the NC flux as well since this could be evidence for

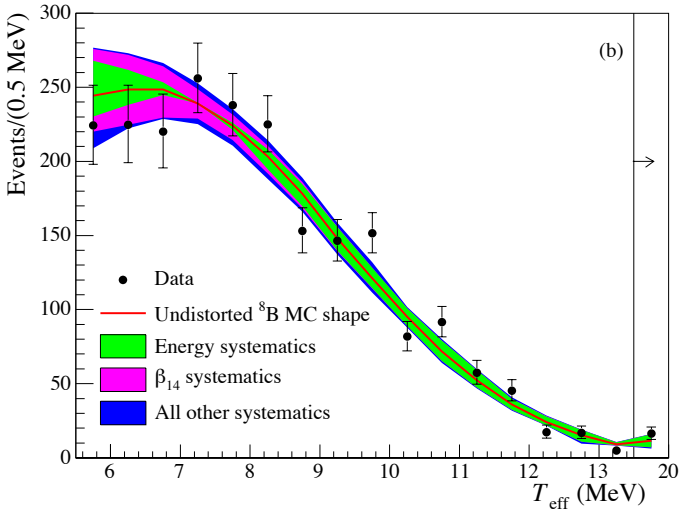


Figure 3: *The extracted CC T_{eff} spectrum with statistical error bars compared to predictions for an undistorted ${}^8\text{B}$ shape with combined systematic uncertainties.*

an admixture of sterile neutrinos, or for unexpected matter interactions inside the Earth.

The same technique of perturbing PDFs was used to evaluate systematic uncertainties in the day-night ratio. An advantage of forming the ratio is that many systematics will cancel so only systematic effects that scale the day and night fluxes differently were considered. Sources of background that are not expected to vary between day and night such as neutrons produced as spallation products of muons that traverse the SNO detector were used in order to evaluate the magnitude of such effects. These studies are described in detail in Ref. 2).

Due to the cancellation of systematic effects, the dominant uncertainties in the asymmetry ratio are statistical. To avoid introducing statistical bias, the analysis procedure was developed on only 20% of the available salt data set, sampled uniformly from each run. When the analysis procedure was finalised, it was applied to the full data set giving results statistically consistent with those obtained from the 20% data-set.

The fluxes and asymmetry ratios obtained for the CC, ES and NC signals with and without the $A_{\text{NC}} = 0$ constraint are given in table 1. In all cases the asymmetries measured are consistent with zero.

Table 1: *Day-night integral fluxes from a shape-unconstrained signal extraction, with and without the constraint $A_{\text{NC}} \equiv 0$. Fluxes are in units of 10^6 neutrinos $\text{cm}^{-2}\text{s}^{-1}$.*

Signal	Day flux	Night flux	A
$A_{\text{NC}} = 0$			
CC	$1.71 \pm 0.08 \pm 0.09$	$1.65 \pm 0.08 \pm 0.09$	$-0.037 \pm 0.063 \pm 0.032$
ES	$2.18 \pm 0.34 \pm 0.14$	$2.53 \pm 0.32 \pm 0.16$	$0.153 \pm 0.198 \pm 0.030$
NC	$4.93 \pm 0.21 \pm 0.36$		0
No constraint on A_{NC}			
CC	$1.73 \pm 0.09 \pm 0.10$	$1.64 \pm 0.08 \pm 0.09$	$-0.056 \pm 0.074 \pm 0.053$
NC	$4.81 \pm 0.31 \pm 0.39$	$5.02 \pm 0.29 \pm 0.41$	$0.042 \pm 0.086 \pm 0.072$
ES	$2.17 \pm 0.34 \pm 0.14$	$2.52 \pm 0.32 \pm 0.16$	$0.146 \pm 0.198 \pm 0.033$

7 Solar Neutrino Fluxes

The integral number of events of each signal type obtained from the energy-unconstrained maximum likelihood fit were used to calculate the equivalent ${}^8\text{B}$ fluxes (in units of $10^6 \text{ cm}^{-2} \text{ s}^{-1}$)

$$\begin{aligned}\phi_{\text{CC}} &= 1.68_{-0.06}^{+0.06}(\text{stat})_{-0.09}^{+0.08}(\text{syst}) \\ \phi_{\text{ES}} &= 2.35_{-0.22}^{+0.22}(\text{stat})_{-0.15}^{+0.15}(\text{syst}) \\ \phi_{\text{NC}} &= 4.94_{-0.21}^{+0.21}(\text{stat})_{-0.34}^{+0.38}(\text{syst}).\end{aligned}$$

The non- ν_e active neutrino component ($\phi_{\mu\tau}$) of the ${}^8\text{B}$ flux can be determined by subtracting the ϕ_e component, as measured by the CC flux, from the NC and ES fluxes. Whereas the NC measurement is equally sensitive to all active neutrinos, the ES measurement has reduced sensitivity to non-electron neutrinos in the form $\phi_{\text{ES}} = \phi_e + 0.1553\phi_{\mu\tau}$. The resulting $\phi_{\mu\tau}$ fluxes, in units of $10^6 \text{ cm}^{-2} \text{ s}^{-1}$, are

$$\begin{aligned}\phi_{\mu\tau}^{\text{NC}} &= 3.26 \pm 0.25 (\text{stat})_{-0.35}^{+0.40} (\text{syst}) \\ \phi_{\mu\tau}^{\text{ES}} &= 4.36 \pm 1.52 (\text{stat})_{-0.87}^{+0.90} (\text{syst}).\end{aligned}$$

Figure 4 shows the flux of non-electron flavour active neutrinos ($\phi_{\mu\tau}$) versus the flux of electron neutrinos (ϕ_e). The error ellipses shown are the 68%, 95% and 99% joint probability contours for $\phi_{\mu\tau}$ and ϕ_e .

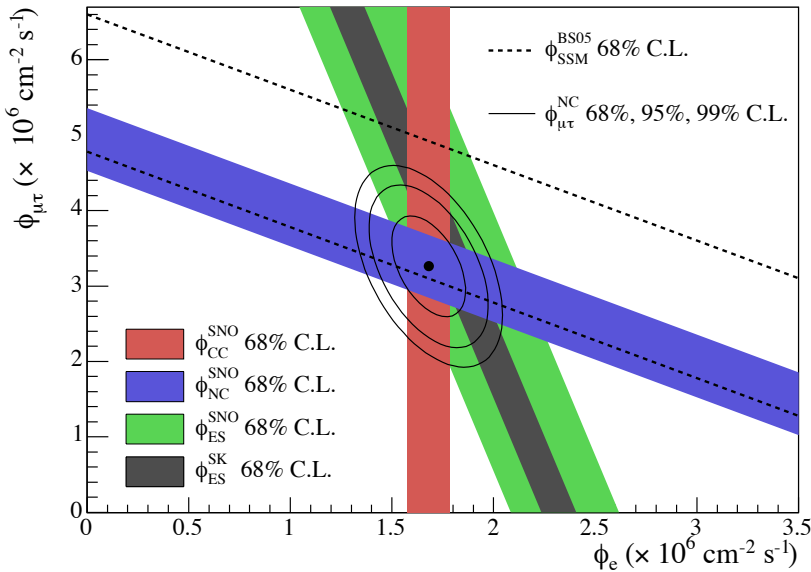


Figure 4: Flux of $\mu + \tau$ neutrinos versus flux of electron neutrinos. CC, NC and ES flux measurements are indicated by the filled bands. The total ${}^8\text{B}$ solar neutrino flux predicted by the Standard Solar Model ³⁾ is shown as dashed lines, and that measured with the NC channel is shown as the solid band parallel to the model prediction. The narrow band parallel to the SNO ES result corresponds to the Super-Kamiokande result in Ref. ⁴⁾.

8 Interpretation of Results

The fluxes, spectra and day-night asymmetries presented here were fitted to a two-flavour, active neutrino oscillation model, along with other available solar neutrino data including results from phase I of SNO ^{5, 6, 7)}, Cl ⁸⁾, Ga ^{9, 10)} and SuperK zenith spectra ⁴⁾. A global χ^2 minimisation, in which the total ${}^8\text{B}$ flux was allowed to vary was performed to obtain the most likely values of the mixing parameters Δm^2 and $\tan^2 \theta$. The top panel in Fig. 5 shows the allowed region of parameter space. The best-fit oscillation parameters, with 1σ uncertainties on the 2-dimensional parameter region given, are $\Delta m^2 = 6.5^{+4.4}_{-2.3} \times 10^{-5} \text{ eV}^2$, $\tan^2 \theta = 0.45^{+0.09}_{-0.08}$.

The global analysis was repeated including the 766 ton-year data from KamLAND ^{11, 12)} which improves the constraints on allowed Δm^2 as shown in the lower panel of figure 5. The resulting best-fit parameters from this combined global analysis are $\Delta m^2 = 8.0^{+0.6}_{-0.4} \times 10^{-5} \text{ eV}^2$ and $\tan^2 \theta = 0.45^{+0.09}_{-0.07}$.

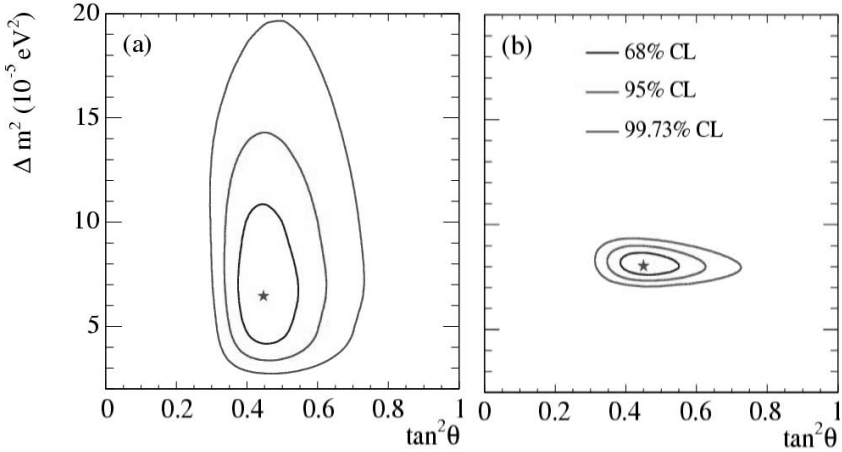


Figure 5: (a) Global neutrino oscillation analysis using only solar neutrino data, and (b) including KamLAND 766 ton-year data. The stars are plotted at the best-fit parameters from the χ^2 analysis.

9 Conclusions and Outlook

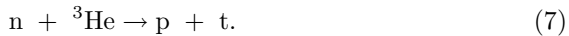
New results from the full Phase II data set including integral fluxes, energy spectral information from the CC reaction with complete statistical and systematic uncertainties, and day-night integrated-flux asymmetries have been presented. These results confirm and improve upon previous SNO data and provide further confirmation of flavour change for solar neutrinos and for the oscillation of massive neutrinos as the dominant flavour change mechanism.

Global analysis of solar neutrino and KamLAND data strongly favour LMA oscillations. The oscillation parameter space has now been tightly constrained to a region where the predicted distortion to the ${}^8\text{B}$ energy spectrum is small. The measured energy spectrum derived from the CC reaction is consistent with the expected spectrum assuming an undistorted ${}^8\text{B}$ shape and also with the predicted spectrum corresponding to the best-fit LMA parameters. The day-night flux asymmetries predicted for the LMA scenario are also small and the day-night asymmetries measured here are completely consistent with these predictions, as well as with no day-night effect.

The analysis presented here has been performed above an effective electron kinetic energy threshold of 5.5 MeV. Work is underway to reduce the

energy threshold for analysis of the existing SNO data in order to improve sensitivity for spectrum measurement at low energies where distortion of the ^8B spectrum is predicted to be largest. It is also hoped that some systematics will be significantly reduced through a combined analysis of the Phase I and Phase II data, resulting in improved precision of the spectral and day-night measurements.

Improved precision in the NC flux measurement is expected from Phase III data. The NaCl was removed from the D_2O in October 2003, in preparation for the installation of neutral current detectors (NCDs) for the third and final phase of the SNO experiment. ^3He proportional counters with a total active length of $\sim 350\text{ m}$ have been strung throughout the D_2O volume to provide an independent measurement of the NC flux on an event by event basis. The neutron capture mechanism of these ^3He proportional counters is



The commissioning period for the NCDs is now complete and production data taking for Phase III commenced at the beginning of 2005.

10 Acknowledgements

This research was supported by: Canada: Natural Sciences and Engineering Research Council, Industry Canada, National Research Council, Northern Ontario Heritage Fund, Atomic Energy of Canada, Ltd., Ontario Power Generation, High Performance Computing Virtual Laboratory, Canada Foundation for Innovation; US: Dept. of Energy, National Energy Research Scientific Computing Centre; UK: Particle Physics and Astronomy Research Council.

References

1. The SNO Collaboration, Nucl. Instr. and Meth., **A449**, 172 (2000).
2. The SNO Collaboration, Submitted to Phys. Rev. C (2005) arXiv:nucl-ex/0502021.
3. J. N. Bahcall, A. M. Serenelli, and S. Basu, arXiv:astro-ph/0412440
4. S. Fukuda *et al.*, Phys. Lett. **B539**, 179 (2002).
5. The SNO Collaboration, Phys. Rev. Lett., **87**, 071301 (2001).
6. The SNO Collaboration, Phys. Rev. Lett., **89**, 011301 (2002).
7. The SNO Collaboration, Phys. Rev. Lett., **89**, 011302 (2002).

8. B. Cleveland *et al.*, *Astrophys. J.*, **496**, 505, (1998).
9. V. Gavrin, *Results from the Russian American Gallium Experiment (SAGE)*, VIIIth International Conference on Topics in Astroparticle and Underground Physics (TAUP 2003), Seattle, September 5–9, 2003; J.N. Abdurashitov *et al.*, *J. Exp. Theor. Phys.* **95**, 181 (2002); the latest SAGE results were presented by C. Cattadori, *Results from Radiochemical Solar Neutrino Experiments*, XXIst International Conference on Neutrino Physics and Astrophysics (Neutrino 2004), Paris, June 14–19, 2004.
10. E. Bellotti, *The Gallium Neutrino Observatory (GNO)*, VIIIth International Conference on Topics in Astroparticle and Underground Physics (TAUP 2003), Seattle, September 5–9, 2003; M. Altmann *et al.*, *Phys. Lett. B* **490**, 16 (2000); W. Hampel *et al.*, *Phys. Lett. B* **447**, 127 (1999).
11. K. Eguchi *et al.*, *Phys. Rev. Lett.*, **90**, 021802, (2003).
12. T. Araki *et al.*, arXiv:hep-ex/0406035.

RESULTS FROM K2K

Takeshi Nakadaira

*High Energy Accelerator Research Organization, KEK
1-1 Oho, Tsukuba, Ibaraki 305-0801 Japan*

Written contribution not received

KamLAND: STUDYING NEUTRINO OSCILLATION WITH REACTORS

Michal Patrick Decowski for the KamLAND Collaboration
Department of Physics, University of California, Berkeley, CA 94720, USA

Abstract

The KamLAND experiment uses reactor anti-neutrinos to study the solar neutrino oscillation parameters. KamLAND recently updated the reactor neutrino measurement, with almost a factor of five more statistics than previously reported. The measured spectral distortion in the anti-neutrino spectrum strongly favors neutrino oscillation as the explanation for neutrino disappearance and provides the most accurate value of Δm_{12}^2 to date.

1 Introduction

Many reactor anti-neutrino experiments have been conducted in the past 50 years. In 1956, one of the first such experiments, at the Savannah River Reactor Plant, measured first evidence of the anti-neutrino and measured its proton cross section. The original experiments were located only a few meters from the reactor core, the source of anti-neutrinos. In the years since that first experiment, reactor neutrino experiments have steadily increased their baselines, with the goal to ultimately find neutrino disappearance. That goal was reached in 2002, when KamLAND reported first observation of reactor anti-neutrino disappearance at an average reactor-detector baseline of ~ 180 km¹⁾.

Nuclear reactors emit electron anti-neutrinos isotropically during the decay of fission products in the fission process. Without a disappearance mechanism, one expects to measure a $1/R^2$ neutrino flux decrease with distance R . If however, neutrinos are massive, they may oscillate into flavors undetectable to the detector, leading to an apparent disappearance of electron anti-neutrinos.

The $\bar{\nu}_e$ spectrum emitted by commercial reactors can be calculated with $\sim 2\%$ uncertainty from $\bar{\nu}_e$ spectra and the reactor fission rates provided by the power companies operating the reactors. The median reactor $\bar{\nu}_e$ energy is 4 MeV. The low energy of reactor anti-neutrinos make the experiments especially sensitive to low values of Δm^2 . In addition, since the oscillation probability function depends on L/E_ν , any oscillatory behavior should also manifest itself in a distortion of the neutrino energy spectrum.

2 The KamLAND Experiment

The most recent large reactor neutrino experiment is the KamLAND experiment in Japan. The experiment searches for neutrino oscillation using a baseline that is two orders of magnitude larger than previous experiments. Due to the long baseline, the $\bar{\nu}_e$ flux is significantly decreased relative to earlier experiments, necessitating a much larger detector volume to compensate for the loss in flux. The KamLAND experiment therefore uses a 1 kton fiducial mass. However, the increased volume of the detector also demands more shielding from cosmic backgrounds to avoid dead time, this effectively means that the detector has to be placed deep underground.

KamLAND is situated in the old Kamiokande cavity in a horizontal shaft mine in the Japanese Alps. The site is surrounded by 53 Japanese commercial power reactors, at a flux weighted average distance of 180 km from the reactors. This baseline makes KamLAND sensitive to the neutrino mass-splitting associated with the solar neutrino problem and in particular to the large mixing angle (LMA) solution.

KamLAND consists of a stainless steel sphere of 18 m diameter with 1879

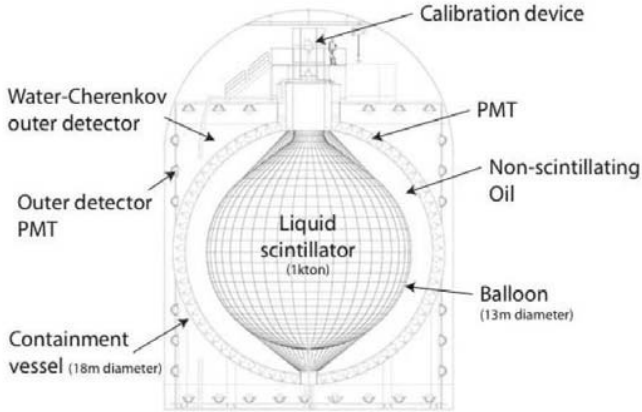


Figure 1: *Sketch of the KamLAND detector.*

photomultiplier tubes mounted to the inner surface, see fig. 1. Inside the sphere is a 13 m diameter nylon balloon filled with liquid scintillator. Outside of the balloon, non-scintillating, highly purified oil provides buoyancy for the balloon and acts as a shield against external radiation. The energy resolution of the detector is $6.2\%/\sqrt{E(\text{MeV})}$. Surrounding the detector outside of the stainless steel sphere is a water Cherenkov detector which provides a muon veto counter and acts as shielding from radioactivity in the rock.

Electron anti-neutrinos are detected via inverse β -decay, $\bar{\nu}_e + p \rightarrow e^+ + n$, with a 1.8 MeV $\bar{\nu}_e$ energy threshold. The prompt scintillation light from the e^+ gives an estimate of the incident $\bar{\nu}_e$ energy, $E_{\bar{\nu}_e} = E_{\text{prompt}} + \bar{E}_n + 0.8 \text{ MeV}$, where E_{prompt} is the prompt event energy including the positron kinetic energy and the annihilation energy, and \bar{E}_n is the average neutron recoil energy, which is typically a few tens of keV. The neutron captures on hydrogen $\sim 200 \mu\text{s}$ later, giving off a characteristic 2.2 MeV γ ray. This delayed coincidence is a powerful tool for reducing background.

The analysis presented here ²⁾ utilizes the following event selection cuts: (a) a radial fiducial volume cut of 5.5 m; (b) a time difference between the positron and delayed neutron of $0.5 \mu\text{s} < \Delta T < 1000 \mu\text{s}$; (c) a position difference of $\Delta R < 2 \text{ m}$ between the two; (d) a prompt event energy of $2.6 \text{ MeV} < E_{\text{prompt}} < 8.5 \text{ MeV}$ and (e) a delayed event energy of $1.8 \text{ MeV} < E_{\text{delayed}} < 2.6 \text{ MeV}$. The prompt energy threshold of 2.6 MeV significantly cuts backgrounds and avoids the effect of anti-neutrinos from uranium and thorium decaying in the Earth (geo-neutrinos). The efficiency of all cuts is $(89.8 \pm 1.5)\%$. The total systematic uncertainty is 6.5%, where the largest contribution is due

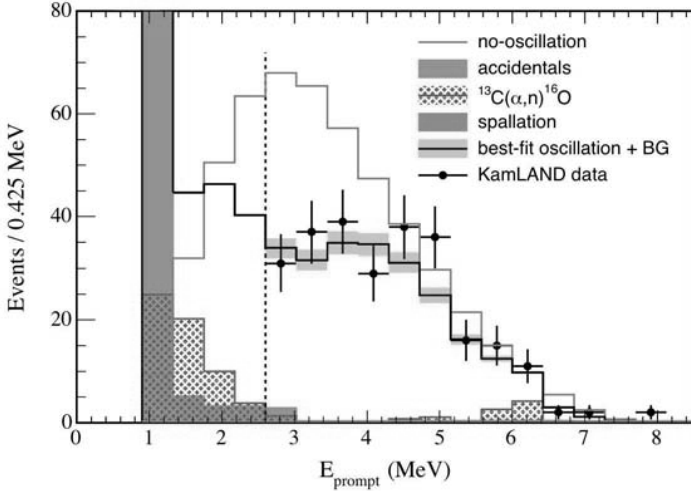


Figure 2: Prompt event energy spectrum of $\bar{\nu}_e$ candidate events with associated background spectra ²⁾. The shaded band indicates the systematic error in the best-fit reactor spectrum above 2.6 MeV. Events from the $^{13}\text{C}(\alpha,n)^{16}\text{O}$ reaction are the main background to the measurement.

to the systematic uncertainty of the fiducial volume. The total livetime of the data presented here is 515 days ²⁾.

Understanding backgrounds is vital in KamLAND. The background from accidental correlations of radioactive decays in KamLAND is estimated by employing an off-time coincidence window; it is 2.69 ± 0.02 events in the data sample. Fast neutrons coming from muon spallation interactions in the rock outside of KamLAND contribute 0.9 background events. Other cosmogenically produced background comes from the beta delayed-neutron emitter ^9Li . This background is suppressed by either tracking the preceding muon and vetoing a detector volume in a 3 m radius around the muon track for 2 s or vetoing the entire detector for the same amount of time in case of particularly energetic muon events or when the muon could not be tracked reliably. We estimate that the ^9Li background contributes 4.8 ± 0.9 events to the data sample.

Finally, the fourth and largest background contribution is an indirect background triggered by α -decay in ^{210}Po . The 5.3 MeV α has a small probability of interacting with ^{13}C in the scintillator (^{13}C has a 1.1% natural abundance in carbon). The subsequent neutron from the $^{13}\text{C}(\alpha,n)^{16}\text{O}$ reaction has a few MeV kinetic energy and will predominantly lose energy through elastic scat-

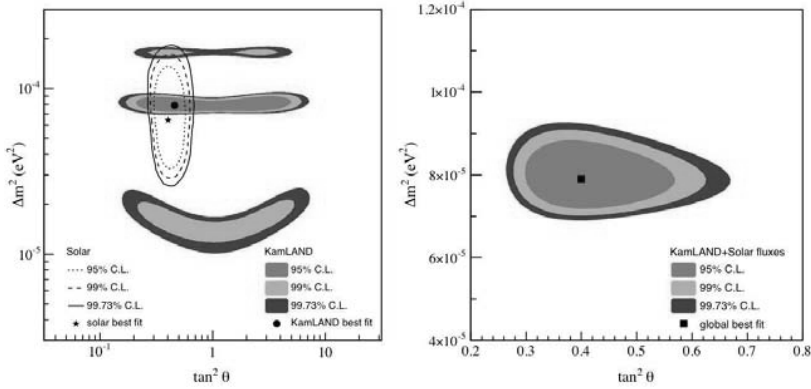


Figure 3: (left) Neutrino oscillation parameter allowed region from KamLAND anti-neutrino data (shaded regions) and solar neutrino experiments (lines)³⁾. (right) Result of a combined two-neutrino oscillation analysis of KamLAND and the observed solar neutrino fluxes under the assumption of CPT invariance.

tering on protons in the scintillator. The quenched proton energy will mostly be below the 2.6 MeV analysis threshold, however the neutron also has a small probability of inelastically interacting with ^{12}C in the scintillator, emitting a 4.4 MeV γ or exciting the ^{16}O to the 6 MeV state. The prompt neutron energy loss and the subsequent capture of the neutron makes the signature of these events similar to the $\bar{\nu}_e$ signature. These events contribute 10.3 ± 7.1 events to the total background of 17.8 ± 7.3 events. The observed prompt energy of the (α, n) background is shown in fig. 2.

3 Recent Results

In an exposure of 766 ton-year to reactor $\bar{\nu}_e$ and in the absence of $\bar{\nu}_e$ disappearance, KamLAND expects to observe 365.2 ± 23.7 (syst) events above 2.6 MeV. KamLAND observes only 258 $\bar{\nu}_e$ events, confirming $\bar{\nu}_e$ disappearance at the 99.998% significance level. The spectrum of the 258 $\bar{\nu}_e$ candidates, including all backgrounds is shown in fig. 2. Performing a two neutrino oscillation analysis, we find a best-fit of $\tan^2 \theta = 0.46$ and $\Delta m_{12}^2 = 7.9_{-0.5}^{+0.6} \times 10^{-5} \text{ eV}^2$, with a large uncertainty on $\tan^2 \theta$. A statistical analysis of the data²⁾ finds that the best-fit oscillation parameters have a goodness-of-fit of 11.1%, while the goodness-of-fit of the scaled no-oscillation spectrum where the normalization was fit to the data is only 0.4%.

The left panel of fig. 3 shows the allowed region contours in Δm^2 - $\tan^2 \theta$ parameter space derived from $\Delta\chi^2$ values. Superimposed on the shaded KamLAND regions, are the regions observed by solar neutrino flux experiments ³⁾. KamLAND disfavors the LMA0 region (at $\Delta m_{12}^2 \sim 10^{-5} \text{ eV}^2$) at 97.5% C.L. and also disfavors the LMA II region (at $\Delta m_{12}^2 \sim 2 \times 10^{-4} \text{ eV}^2$) at 98.0 C.L. Larger values of Δm_{12}^2 previously allowed by KamLAND are now disfavored at more than 99.73%.

A two neutrino oscillation analysis of a combination of KamLAND data and observed solar neutrino fluxes (right panel of fig. 3) yields $\tan^2 \theta = 0.40_{-0.07}^{+0.10}$ and $\Delta m_{12}^2 = 7.9_{-0.5}^{+0.6} \times 10^{-5} \text{ eV}^2$. With the recently updated full SNO salt analysis, a global analysis of solar neutrino fluxes and KamLAND data gives ⁴⁾ $\tan^2 \theta = 0.45_{-0.07}^{+0.09}$ and $\Delta m_{12}^2 = 8.0_{-0.4}^{+0.6} \times 10^{-5} \text{ eV}^2$. KamLAND is the only experiment to measure Δm_{12}^2 in the solar neutrino sector accurately in the foreseeable future.

4 Conclusion

The updated KamLAND results have confirmed reactor neutrino disappearance at 99.998% statistical significance. The observed energy spectrum disagrees with the expected spectral shape in the absence of neutrino oscillation at 99.6% significance and prefers the distortion expected from neutrino oscillation. The statistical and systematic uncertainties of the neutrino rate measurement are now comparable. The KamLAND collaboration is currently working to reduce the systematic uncertainty.

References

1. K. Eguchi *et al.* (KamLAND Collaboration), Phys. Rev. Lett. **90**, 021802 (2003).
2. T. Araki *et al.* (KamLAND Collaboration), Phys. Rev. Lett. **94**, 081801 (2005).
3. S.N. Ahmed *et al.* (SNO Collaboration), Phys. Rev. Lett. **92**, 181301 (2004).
4. B. Aharmim *et al.* (SNO Collaboration), arXiv:nucl-ex/0502021.

QUANTUM THEORY OF NEUTRINO SPIN LIGHT IN DENSE MATTER

Alexander Grigoriev ^{*}, Alexander Studenikin [†]

*Department of Theoretical Physics,
Moscow State University,
119992 Moscow, Russia*

Alexei Ternov [‡]

*Department of Theoretical Physics,
Moscow Institute for Physics and Technology,
141700 Dolgoprudny, Russia*

Abstract

We develop the quantum theory of the spin light of neutrino ($SL\nu$) exactly accounting for the effect of background matter. Contrary to the already performed studies of the $SL\nu$, in this paper we derive explicit and closed expressions for the $SL\nu$ rate and power and for the emitted photon energy, which are valid for an arbitrary matter density (including very high values). The spatial distribution of the radiation power and the dependence of the emitted photon energy on the direction of radiation are also studied in detail for the first time. We analyze the $SL\nu$ polarization properties and show that within a wide range of neutrino momenta and matter densities the $SL\nu$ radiation is circularly polarized. Conditions for effective $SL\nu$ photon propagation in the electron plasma are discussed. It is also shown that in dense matter the average energy of the emitted photon can reach values in the range from one third of the neutrino momentum up to one half of the neutrino energy in matter. The main features of the studied radiation are summarized, and possibilities for the $SL\nu$ production during different astrophysical and cosmology processes are discussed.

1 Spin light of a neutrino in matter

There exist various mechanisms for the production of electromagnetic radiation by a massive neutrino moving in a background environment (see, for instance, 1)¹). We have recently shown 2)²) within the quasi-classical approach, that a massive neutrino moving in background matter can emit a new type of electromagnetic radiation. This radiation has been termed the "spin light of neutrino" ($SL\nu$) in matter. In 3)³) we have also considered $SL\nu$ in gravitational fields of rotating astrophysical objects. Developing the quantum theory of this phenomenon 4, 5)^{4, 5}), we have demonstrated that $SL\nu$ arises owing to two underlying phenomena: (i) the shift of neutrino energy levels in matter, that are different for the two opposite neutrino helicity states, and (ii) the emission of an $SL\nu$ photon in the process of neutrino transition from the "excited" helicity state to the low-lying helicity state in matter. However, calculations of the transition rate and radiation power have been performed in the limit of a low matter density and, therefore, evaluation of a consistent quantum theory of $SL\nu$ still remains an open issue.

In this paper we develop the quantum theory of $SL\nu$, exactly taking into account the effect of background matter, and obtain expressions for the $SL\nu$ rate and power that are valid for any value of the matter density parameter (see also 6)⁶). In Section 2 we briefly discuss the modified Dirac equation and the neutrino energy spectrum in the presence of matter which are then used (Section 3) for derivation of the $SL\nu$ transition rate and power. We get an exact expression for the emitted photon energy as a function of the initial neutrino energy and the matter density parameter. The dependence of the photon energy on the direction of the photon propagation is analyzed, and a detailed study of the radiation spatial distribution is also performed. We also derive the exact and closed expressions for the rate and total radiation power of $SL\nu$ and analyze them for different limiting cases. The $SL\nu$ polarization properties are studied in Section 4, and the conclusion is made concerning the total circular polarization of the emitted photons. Section 5 is devoted to the discussion of restrictions on the propagation of $SL\nu$ photons that can be set by the electron plasma. In conclusion (Section 6) we give a summary of the investigated properties of $SL\nu$ in matter. The $SL\nu$ production during processes of collapse and coalescence of neutron stars or a neutron star being "eaten up" by the black hole at the center of our Galaxy are also discussed as one of possible mechanisms of gamma-rays production.

¹A brief classification of the known mechanisms of the electromagnetic radiation by a neutrino is given in the first paper of 2)²).

2 The modified Dirac equation in matter

To account for the influence of background matter on neutrinos we use the approach ⁴⁾ (similar to the Furry representation in quantum electrodynamics) that is based on the exact solutions of the modified Dirac equation for a neutrino in matter:

$$\left\{ i\gamma_\mu \partial^\mu - \frac{1}{2}\gamma_\mu(1 + \gamma_5)f^\mu - m \right\} \Psi(x) = 0. \quad (1)$$

In the case of matter composed of electrons

$$f^\mu = \frac{G_F}{\sqrt{2}}(1 + 4 \sin^2 \theta_W)j^\mu, \quad (2)$$

where the electron current j^μ is given by

$$j^\mu = (n, n\mathbf{v}). \quad (3)$$

Here θ_W , n and \mathbf{v} are, respectively, the Weinberg angle, the number density of background electrons and the speed of the reference frame in which the mean momentum of the electrons is zero. As it has been shown ⁴⁾ the solutions of Eq.(1) are given by

$$\Psi_{\varepsilon, \mathbf{p}, s}(\mathbf{r}, t) = \frac{e^{-i(E_\varepsilon t - \mathbf{p}\mathbf{r})}}{2L^{\frac{3}{2}}} \begin{pmatrix} \sqrt{1 + \frac{m}{E_\varepsilon - \alpha m}} \sqrt{1 + s \frac{p_3}{p}} \\ s \sqrt{1 + \frac{m}{E_\varepsilon - \alpha m}} \sqrt{1 - s \frac{p_3}{p}} e^{i\delta} \\ s\varepsilon \sqrt{1 - \frac{m}{E_\varepsilon - \alpha m}} \sqrt{1 + s \frac{p_3}{p}} \\ \varepsilon \sqrt{1 - \frac{m}{E_\varepsilon - \alpha m}} \sqrt{1 - s \frac{p_3}{p}} e^{i\delta} \end{pmatrix}, \quad (4)$$

where energy spectrum is

$$E_\varepsilon = \varepsilon \sqrt{\mathbf{p}^2 \left(1 - s\alpha \frac{m}{p}\right)^2 + m^2 + \alpha m}, \quad (5)$$

$$\alpha = \frac{1}{2\sqrt{2}} \tilde{G}_F \frac{n}{m}, \quad \tilde{G}_F = G_F(1 + 4 \sin^2 \theta_W). \quad (6)$$

In equations (4)-(6) m , \mathbf{p} and $s = \pm 1$ are the neutrino mass, momentum and helicity, respectively. The quantity $\varepsilon = \pm 1$ splits the solutions into two branches that in the limit of vanishing matter density, $\alpha \rightarrow 0$, reproduce the positive and negative-frequency solutions for the Dirac equation in vacuum.

Note that generalization to the case of matter composed of different types of fermions is straightforward ⁴⁾, and the correct value for the neutrino energy

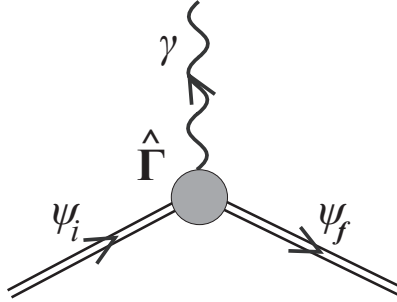


Figure 1: The effective diagram of the $SL\nu$ photon emission process. The broad lines correspond to the initial and final neutrino states in the background matter.

difference corresponding to the Mikheyev-Smirnov-Wolfenstein effect ⁷⁾ can be recovered from (5). The modified effective Dirac equations for a neutrino interacting with various background environments within different models were previously used ⁸⁾ in a study of the neutrino dispersion relations, neutrino mass generation and for derivation of the neutrino oscillation probabilities in matter. On the same basis, the neutrino decay into an antineutrino and a light scalar particle (majoron), as well as the corresponding process of the majoron decay into two neutrinos or antineutrinos, were studied in the presence of matter ⁹⁾.

3 The $SL\nu$ transition rate and power

The $SL\nu$ amplitude calculated within the developed quantum theory is given by (see also ⁴⁾)

$$S_{fi} = -\mu\sqrt{4\pi} \int d^4x \bar{\psi}_f(x)(\hat{\Gamma}\mathbf{e}^*) \frac{e^{ikx}}{\sqrt{2\omega L^3}} \psi_i(x), \quad (7)$$

$$\hat{\Gamma} = i\omega \{ [\boldsymbol{\Sigma} \times \boldsymbol{\varkappa}] + i\gamma^5 \boldsymbol{\Sigma} \},$$

where μ is the neutrino magnetic moment, ψ_i and ψ_f are the exact solutions of equation (1) for the initial and final neutrino states ⁴⁾, $k^\mu = (\omega, \mathbf{k})$ and \mathbf{e}^* are the photon momentum and polarization vector, $\boldsymbol{\varkappa} = \mathbf{k}/\omega$ is the unit vector pointing in the direction of the emitted photon propagation.

$$S_{fi} = -\mu \sqrt{\frac{2\pi}{\omega L^3}} 2\pi \delta(E' - E + \omega) \int d^3x \bar{\psi}_f(\mathbf{r})(\hat{\Gamma} \mathbf{e}^*) e^{i\mathbf{k}\mathbf{r}} \psi_i(\mathbf{r}), \quad (8)$$

where the delta-function stands for energy conservation, E and E' are the energies of the initial and final neutrino states in matter. Performing integration over the spatial co-ordinates, we can recover the delta-functions for the three components of the momentum. Finally, we get the law of energy-momentum conservation for the considered process,

$$E = E' + \omega, \quad \mathbf{p} = \mathbf{p}' + \boldsymbol{\varkappa}, \quad (9)$$

where \mathbf{p} and \mathbf{p}' are the initial and final neutrino momenta, respectively. From (9) it follows that the emitted photon energy ω exhibits a critical dependence on the helicities of the initial and final neutrino states. In the case of electron neutrino moving in matter composed of electrons α is positive. It follows that $SL\nu$ can arise only when the neutrino initial and final states are characterized by $s_i = -1$ and $s_f = +1$, respectively. One can also conclude that in the process considered the relativistic left-handed neutrino is converted to the right-handed neutrino. A discussion of the main properties of $SL\nu$ emitted by different flavor neutrinos moving in matter composed of electrons, protons and neutrons can be found in ⁴⁾ (see also ¹⁰⁾).

The emitted photon energy in the considered case ($s_i = -s_f = -1$), obtained as an exact solution of equations (9), is

$$\omega = \frac{2\alpha m p [(E - \alpha m) - (p + \alpha m) \cos \theta]}{(E - \alpha m - p \cos \theta)^2 - (\alpha m)^2}, \quad (10)$$

where θ is the angle between $\boldsymbol{\varkappa}$ and the direction of the initial neutrino propagation. The photon energy is a rather complicated function of the neutrino energy E and momentum p , the matter density parameter α and the angle θ . Fig.1 shows the angular dependence of the photon energy for different values of the neutrino momentum. From this figure one may expect that in the case of relativistic neutrinos ($p \gg m$) and not very dense matter ($\alpha \ll \frac{p}{m}$) $SL\nu$ is collimated along the direction of the neutrino momentum p (see the dashed and solid-dashed curves). On the contrary, in the case of non-relativistic neutrinos ($p \ll m$) and $\alpha \gg \frac{p}{m}$ (see solid line in Fig.1) the emitted photon energy in the direction of the neutrino momentum p is suppressed. It should also be noted that for all cases shown in Fig.1 the energies ω of the photons radiated at large angles θ are of the order of $\sim \alpha m$. In the case of a not very high density of matter, when the parameter $\alpha \ll 1$, one can expand the photon energy (10) over α and in the linear approximation get the result of ^{4, 5)}:

$$\omega = \frac{1}{1 - \beta \cos \theta} \omega_0, \quad (11)$$

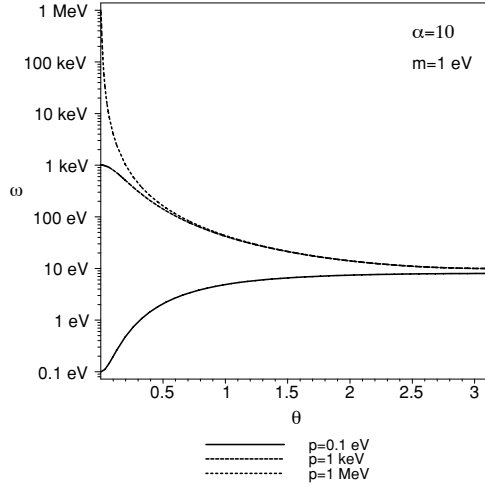


Figure 2: Angular dependence of photon energy for different values of the neutrino momentum: 1) the solid line corresponds to $p = 0.1 \text{ eV}$, 2) the dashed-solid line corresponds to $p = 1 \text{ keV}$ and 3) the dashed line corresponds to $p = 1 \text{ MeV}$. The matter density parameter is $\alpha = 10$.

where

$$\omega_0 = \frac{\tilde{G}_F}{\sqrt{2}} n\beta, \quad \beta = \frac{p}{\sqrt{p^2 + m^2}}. \quad (12)$$

Using the expressions for the amplitude (8) and for the photon energy (10) we calculate the spin light transition rate and total radiation power exactly accounting for the matter density parameter:

$$\Gamma = \mu^2 \int_0^\pi \frac{\omega^3}{1 + \tilde{\beta}'y} S \sin \theta d\theta, \quad (13)$$

$$I = \mu^2 \int_0^\pi \frac{\omega^4}{1 + \tilde{\beta}'y} S \sin \theta d\theta, \quad (14)$$

where

$$S = (\tilde{\beta}\tilde{\beta}' + 1)(1 - y \cos \theta) - (\tilde{\beta} + \tilde{\beta}')(\cos \theta - y). \quad (15)$$

Here we introduce the notations

$$\tilde{\beta} = \frac{p + \alpha m}{E - \alpha m}, \quad \tilde{\beta}' = \frac{p' - \alpha m}{E' - \alpha m}, \quad (16)$$

where the final neutrino energy and momentum are, respectively,

$$E' = E - \omega, \quad p' = K\omega - p, \quad (17)$$

and

$$y = \frac{\omega - p \cos \theta}{p'}, \quad K = \frac{E - \alpha m - p \cos \theta}{\alpha m}. \quad (18)$$

Performing the integration in (13), we obtain for the $SL\nu$ rate in matter

$$\begin{aligned} \Gamma = & \frac{1}{2(E-p)^2(E+p-2\alpha m)^2(E-\alpha m)p^2} \\ & \times \left\{ (E^2 - p^2)^2 (p^2 - 6\alpha^2 m^2 + 6E\alpha m - 3E^2) \left((E - 2\alpha m)^2 - p^2 \right)^2 \right. \\ & \times \ln \left[\frac{(E+p)(E-p-2\alpha m)}{(E-p)(E+p-2\alpha m)} \right] + 4\alpha m p [16\alpha^5 m^5 E (3E^2 - 5p^2) \\ & - 8\alpha^4 m^4 (15E^4 - 24E^2 p^2 + p^4) + 4\alpha^3 m^3 E (33E^4 - 58E^2 p^2 + 17p^4) \\ & - 2\alpha^2 m^2 (39E^2 - p^2) (E^2 - p^2)^2 + 12\alpha m E (2E^2 - p^2) (E^2 - p^2)^2 \\ & \left. - (3E^2 - p^2) (E^2 - p^2)^3 \right\}, \quad (19) \end{aligned}$$

where the energy of the initial neutrino is given by (5) with $\varepsilon = -s_i = 1$.

As it follows from (19), the $SL\nu$ rate is a rather complicated function of neutrino momentum p and mass m , it also non-trivially depends on the matter density parameter α . In the limit of a low matter density, $\alpha \ll 1$, we get

$$\Gamma \simeq \frac{64}{3} \frac{\mu^2 \alpha^3 p^3 m}{E_0}, \quad (20)$$

where $E_0 = \sqrt{p^2 + m^2}$. The obtained expression is in agreement with our results of (2, 4, 5). Note that the considered limit of $\alpha \ll 1$ can be appropriate even for a very dense media of neutron stars with $n \sim 10^{33} \text{ cm}^{-3}$ because $\frac{1}{2\sqrt{2}} \tilde{G}_F n \sim 1 \text{ eV}$ for a medium characterized by $n = 10^{37} \text{ cm}^{-3}$.

Performing also the integration in (14), we obtain the total $SL\nu$ radiation

power in matter

$$\begin{aligned}
I = & \frac{5}{2(E-p)^3(E+p-2\alpha m)^3 p^2} \times \left\{ (E+p)^2(E-m)^3(E+p-2\alpha m)^3 \right. \\
& \times (E-p-2\alpha m)^2 \left(2\alpha^2 m^2 - 2\alpha m(E + \frac{1}{5}p) + E^2 - \frac{3}{5}p^2 \right) \\
& \times \ln \left(\frac{(2\alpha m - p - E)(E-p)}{(2\alpha m + p - E)(E+p)} \right) \\
& - 4\alpha m p \left(32\alpha^6 m^6 \left(E^4 - pE^3 - \frac{5}{3}p^2 E^2 + \frac{5}{3}p^3 E + \frac{8}{15}p^4 \right) \right. \\
& - 96\alpha^5 m^5 \left(E^5 - \frac{23}{30}pE^4 - \frac{83}{45}p^2 E^3 + \frac{11}{9}p^3 E^2 + \frac{38}{45}p^4 E - \frac{1}{10}p^5 \right) \\
& + 128\alpha^4 m^4 \left(E^6 - \frac{47}{80}pE^5 - \frac{511}{240}p^2 E^4 + \frac{127}{120}p^3 E^3 + \frac{157}{120}p^4 E^2 \right. \\
& \quad \left. - \frac{89}{240}p^5 E - \frac{7}{48}p^6 \right) \\
& - 96(E^2 - p^2)\alpha^3 m^3 \left(E^5 - \frac{53}{120}pE^4 - \frac{3}{2}p^2 E^3 + \frac{89}{180}p^3 E^2 + \frac{47}{90}p^4 E - \frac{19}{360}p^5 \right) \\
& + 42(E^2 - p^2)^2 \alpha^2 m^2 \left(E^4 - \frac{32}{105}pE^3 - \frac{314}{315}p^2 E^2 + \frac{4}{21}p^3 E + \frac{17}{105}p^3 \right) \\
& - 10\alpha m(E^2 - p^2)^3 \left(E^3 - \frac{4}{25}pE^2 - \frac{17}{25}p^2 E + \frac{2}{25}p^3 \right) \\
& \left. + (E^2 - p^2)^4 \left(E^2 - \frac{3}{5}p^2 \right) \right\}. \tag{21}
\end{aligned}$$

In the case $\alpha \ll 1$, we get

$$I \simeq \frac{128}{3} \mu^2 \alpha^4 p^4 \tag{22}$$

in agreement with Refs. 2, 4, 5).

Let us consider the $SL\nu$ rate and power for the different limiting values of the neutrino momentum p and matter density parameter α . In the relativistic case $p \gg m$ from (19) we get

$$\Gamma = \begin{cases} \frac{64}{3} \mu^2 \alpha^3 p^2 m, \\ 4\mu^2 \alpha^2 m^2 p, \\ 4\mu^2 \alpha^3 m^3, \end{cases} \quad I = \begin{cases} \frac{128}{3} \mu^2 \alpha^4 p^4, \\ \frac{4}{3} \mu^2 \alpha^2 m^2 p^2, \\ 4\mu^2 \alpha^4 m^4, \end{cases} \quad \begin{cases} \text{for } \alpha \ll \frac{m}{p}, \\ \text{for } \frac{m}{p} \ll \alpha \ll \frac{p}{m}, \\ \text{for } \alpha \gg \frac{p}{m}, \end{cases} \tag{23}$$

and in the opposite case, $p \ll m$, we have

$$\Gamma = \begin{cases} \frac{64}{3}\mu^2\alpha^3p^3, \\ \frac{512}{5}\mu^2\alpha^6p^3, \\ 4\mu^2\alpha^3m^3, \end{cases} \quad I = \begin{cases} \frac{128}{3}\mu^2\alpha^4p^4, \\ \frac{1024}{3}\mu^2\alpha^8p^4, \\ 4\mu^2\alpha^4m^4, \end{cases} \quad \begin{array}{l} \text{for } \alpha \ll 1, \\ \text{for } 1 \ll \alpha \ll \frac{m}{p}, \\ \text{for } \alpha \gg \frac{m}{p}. \end{array} \quad (24)$$

One can see that in the case of a very high matter density the rate and radiation power are determined by the background matter density only. Note that the obtained $SL\nu$ rate and radiation power for $p \gg m$ and $\alpha \gg \frac{m}{p}$ are in agreement with 10).

From the expressions for the $SL\nu$ rate and total power it is possible to get an estimate for the average emitted photon energy:

$$\langle\omega\rangle = \frac{I}{\Gamma}. \quad (25)$$

In the relativistic case, $p \gg m$, we get

$$\langle\omega\rangle \simeq \begin{cases} 2\alpha\frac{p^2}{m}, & \text{for } \alpha \ll \frac{m}{p}, \\ \frac{1}{3}p, & \text{for } \frac{m}{p} \ll \alpha \ll \frac{p}{m}, \\ \alpha m, & \text{for } \alpha \gg \frac{p}{m}. \end{cases} \quad (26)$$

For the matter parameter $\alpha \gg \frac{m}{p}$ we again confirm, here, the result obtained in 10). In the non-relativistic case, $p \ll m$, we have for the average emitted photon energy

$$\langle\omega\rangle \simeq \begin{cases} 2\alpha p, & \text{for } \alpha \ll 1, \\ \frac{10}{3}\alpha^2 p, & \text{for } 1 \ll \alpha \ll \frac{m}{p}, \\ \alpha m, & \text{for } \alpha \gg \frac{m}{p}. \end{cases} \quad (27)$$

We should like to note that for a wide range of neutrino momenta p and density parameters α the $SL\nu$ power is collimated along the direction of the neutrino propagation. The shapes of the radiation power spatial distributions calculated with use of (14) in the case of $p > m$ for low and high matter density are shown in Figs.2 and 3, respectively. As it follows from these figures, the shape of the distribution depends on the density of matter. The shape of the spatial distribution of the radiation changes from projector-like to cap-like with increase of the matter density. From (14) it follows, that in the case of $p \gg m$ for a wide range of matter densities, $\alpha \ll \frac{p}{m}$, the direction of the maximum in the spatial distribution of the radiation power is characterized by the angle

$$\cos\theta_{max} \simeq 1 - \frac{2}{3}\alpha\frac{m}{p}. \quad (28)$$

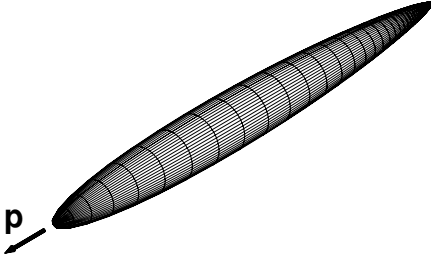


Figure 3: The spatial distribution of the $SL\nu$ radiation power for $p/m = 5$, $\alpha = 0.01$.

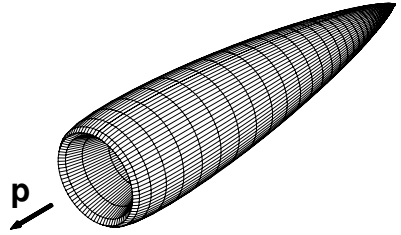


Figure 4: The spatial distribution of the $SL\nu$ radiation power for $p/m = 10^3$, $\alpha = 100$.

It follows that in a dense matter the $SL\nu$ radiation in the direction of the initial neutrino motion is strongly suppressed, whereas there is a luminous ring in the plane perpendicular to the neutrino motion. Note that the rate of the matter-induced neutrino majoron decay, as it was shown in the second paper of ⁹⁾, exhibits a similar angular distribution.

From analysis of the spatial distribution of the $SL\nu$ radiation and the emitted photon average energy we predict an interesting new phenomenon that can appear if a bunch of neutrinos propagates in a very dense matter. In the case of relativistic neutrinos $p \gg m$ and dense matter characterized by $\alpha \gg \frac{p}{m}$ we get that the average value of $\omega \cos \theta$ is negative and equals

$$\langle \omega \cos \theta \rangle = -\frac{1}{3}\alpha m. \quad (29)$$

This means that in the considered case a reasonable fraction of the $SL\nu$ photons are emitted in the direction opposite to the initial neutrino momentum p , as if the neutrinos of the bunch shake off the spin light photons. It also follows, that in this case the neutrino momentum p increases as the neutrinos radiate. To illustrate this phenomena we plot in Fig.4 the $SL\nu$ radiation power spatial distribution for relativistic neutrinos with $p/m = 10$ and the density parameter equal to $\alpha = 100$. The two-dimensional cut of the spatial distribution of the radiation is shown in Fig.5.

4 $SL\nu$ polarization properties

In our previous studies ^{4, 5)} we considered the $SL\nu$ in the low matter density limit, $\alpha \ll 1$, with account of the photon linear and circular polarizations. Here, we extend our previous consideration of the $SL\nu$ polarization properties

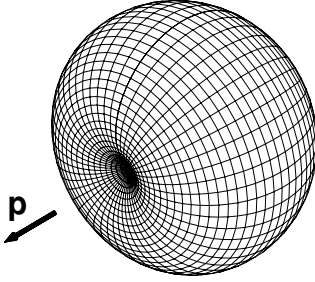


Figure 5: The spatial distribution of the $SL\nu$ radiation power for $p/m = 10$, $\alpha = 100$.

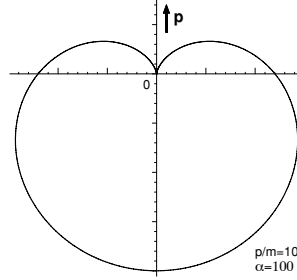


Figure 6: The two-dimensional cut of the spatial distribution of the $SL\nu$ radiation power shown in Fig.4, $p/m = 10$, $\alpha = 100$.

to the case of an arbitrary matter density that enables us to treat the emitted photon polarization in the limit of very high matter density.

We first consider the two different linear photon polarizations and introduce the two orthogonal vectors

$$\mathbf{e}_1 = \frac{[\boldsymbol{\kappa} \times \mathbf{j}]}{\sqrt{1 - (\boldsymbol{\kappa} \cdot \mathbf{j})^2}}, \quad \mathbf{e}_2 = \frac{\boldsymbol{\kappa}(\boldsymbol{\kappa} \cdot \mathbf{j}) - \mathbf{j}}{\sqrt{1 - (\boldsymbol{\kappa} \cdot \mathbf{j})^2}}, \quad (30)$$

where \mathbf{j} is the unit vector pointing in the direction of the initial neutrino propagation. Decomposing the neutrino transition amplitude (7) in contributions from the photons of the two linear polarizations determined by the vectors \mathbf{e}_1 and \mathbf{e}_2 , we get

$$I^{(1),(2)} = \mu^2 \int_0^\pi \frac{\omega^4}{1 + \beta'y} \left(\frac{1}{2} S \mp \Delta S \right) \sin \theta d\theta, \quad (31)$$

where

$$\Delta S = \frac{1}{2} \frac{m^2 p \sin^2 \theta}{(E' - \alpha m)(E - \alpha m) p'}. \quad (32)$$

In the low matter density case, $\alpha \ll 1$, the total radiation power of the linearly polarized photons is

$$I^{(1),(2)} \simeq \frac{64}{3} \left(1 \mp \frac{1}{2} \right) \mu^2 \alpha^4 p^4, \quad (33)$$

in agreement with (4, 5). Thus, the radiation powers for the two linear polarizations differ by a factor of three. Contrariwise, in all other cases the radiation

powers for the two polarizations, \mathbf{e}_1 and \mathbf{e}_2 , are of the same order,

$$I^{(1)} \simeq I^{(2)} \simeq \frac{1}{2}(I^{(1)} + I^{(2)}). \quad (34)$$

It is also possible to decompose the radiation power for the circularly polarized photons. The two orthogonal vectors

$$\mathbf{e}_l = \frac{1}{\sqrt{2}}(\mathbf{e}_1 + il\mathbf{e}_2) \quad (35)$$

describe the two photon circular polarizations ($l = \pm 1$ correspond to the right and left photon circular polarizations, respectively). For the radiation power of the circular-polarized photons we obtain

$$I^{(l)} = \mu^2 \int_0^\pi \frac{\omega^4}{1 + \beta'y} S_l \sin \theta d\theta, \quad (36)$$

where

$$S_l = \frac{1}{2} (1 + l\beta') (1 + l\beta) (1 - l \cos \theta) (1 + ly). \quad (37)$$

In the limit of low matter density, $\alpha \ll 1$, we get for the power

$$I^{(l)} \simeq \frac{64}{3} \mu^2 \alpha^4 p^4 \left(1 - l \frac{p}{2E_0} \right). \quad (38)$$

In this limiting case the radiation power of the left-polarized photons exceeds that of the right-polarized photons

$$I^{(-1)} > I^{(+1)}. \quad (39)$$

In particular, this result is also valid for non-relativistic neutrinos, $p \ll m$, for a low density with $\alpha \ll 1$.

It is remarkable that in the most interesting case of rather dense matter ($\alpha \gg \frac{m}{p}$ for $p \gg m$ and $\alpha \gg 1$ for $p \ll m$), the main contribution to the power is provided by the right-polarized photons, whereas the emission of the left-polarized photons is suppressed:

$$I^{(+1)} \simeq I, \quad (40)$$

$$I^{(-1)} \simeq 0. \quad (41)$$

Thus, we conclude that in a dense matter the $SL\nu$ photons are emitted with nearly total right-circular polarization. Note that if the density parameter changes sign, then the emitted photons will exhibit the left-circular polarization.

5 Propagation of $SL\nu$ photons in plasma

Finally, we should like to discuss in some detail restrictions on the propagation of $SL\nu$ photons, that are due to the presence of background electron plasma in the case of $p \gg m$ for the density parameter $\frac{m}{p} \ll \alpha \ll \frac{p}{m}$. Only photons with energy exceeding the plasmon frequency

$$\omega_{pl} = \sqrt{\frac{4\pi e^2}{m_e} n}, \quad (42)$$

can propagate in the plasma (here $e^2 = \alpha_{QED}$ is the fine-structure constant and m_e is the mass of the electron). From (10) and (28) it follows that the photon energy and the radiation power depend on the direction of the radiation. We can conclude that the maximal photon energy,

$$\omega_{max} = p, \quad (43)$$

and the energy of the photon emitted in the direction of the maximum radiation power,

$$\omega(\theta_{max}) = \frac{3}{4}p, \quad (44)$$

are of the same order in the case considered. For relativistic neutrinos and rather dense matter the angle θ_{max} , at which the radiation power (14) has its maximum, and the angle (43) corresponding to the maximal photon energy are both very close to zero (to illustrate this we show in Fig.6 the photon energy and radiation power angular distributions for the particular case of $m = 1 \text{ eV}$, $p = 100 \text{ MeV}$ and $n = 10^{32} \text{ cm}^{-3}$). In addition, as it follows from (26), the average photon energy $\langle \omega \rangle = \frac{1}{3}p$ is also of the order of ω_{max} and $\omega(\theta_{max})$. Therefore, the effective $SL\nu$ photon energy reasonably exceeds the plasmon frequency (42) if the following condition is fulfilled:

$$p \gg p_{min} = 3.5 \times 10^4 \left(\frac{n}{10^{30} \text{ cm}^{-3}} \right)^{1/2} \text{ eV}. \quad (45)$$

The $SL\nu$ photon emitted by a neutrino with momentum $p \gg p_{min}$ freely propagates through the plasma. For $n \sim 10^{33} \text{ cm}^{-3}$ we have $p_{min} \sim 1 \text{ MeV}$.

6 Summary of $SL\nu$ properties

To conclude, we should like to mention that the obtained equation (1) is the most general equation of motion for the neutrino in which the effective potential accounts for both the charged and neutral-current interactions with the background matter. Possible effects of the motion and polarization of matter can also be incorporated (4-6).

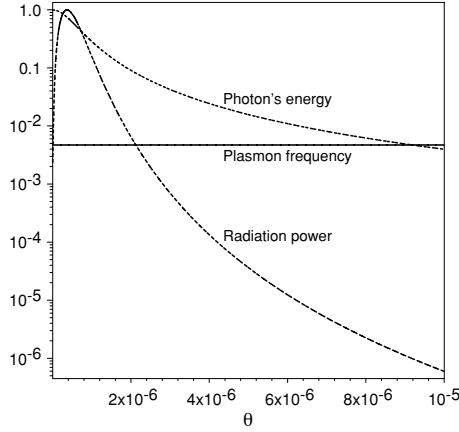


Figure 7: The angular dependence of the emitted photon energy and radiation power for the set of parameters: $m = 1 \text{ eV}$, $p = 100 \text{ MeV}$, $n = 10^{32} \text{ cm}^{-3}$. The solid line denotes the energy level that corresponds to the plasmon frequency (42).

The exact solutions obtained for the modified Dirac equation and the neutrino energy spectrum form a basis for a rather powerful method for studying different processes stimulated by neutrinos in the presence of background matter. For instance, from the neutrino energy spectrum (5) and from the matter density parameters for relativistic electron and muon neutrinos propagating in matter composed of electrons, protons and neutrons (see 4) we can get the following expressions for the two flavour neutrinos:

$$E_{\nu_e, \nu_\mu}^{s=-1} \approx E_0 + 2\alpha_{\nu_e, \nu_\mu} m_{\nu_e, \nu_\mu}, \quad (46)$$

where

$$\alpha_{\nu_e} = \frac{1}{2\sqrt{2}} \frac{G_F}{m} \left(n_e(1 + 4 \sin^2 \theta_W) + n_p(1 - 4 \sin^2 \theta_W) - n_n \right), \quad (47)$$

and

$$\alpha_{\nu_\mu} = \frac{1}{2\sqrt{2}} \frac{G_F}{m} \left(n_e(4 \sin^2 \theta_W - 1) + n_p(1 - 4 \sin^2 \theta_W) - n_n \right), \quad (48)$$

here $n_{e,p,n}$ are the electron, proton, and neutron number densities, respectively. From the above expressions, the electron energy shift with respect to the muon energy in matter is

$$\Delta E \equiv E_{\nu_e}^{s=-1} - E_{\nu_\mu}^{s=-1} = \sqrt{2} G_F n_e. \quad (49)$$

Thus, the correct value for the neutrino energy difference corresponding to the Mikheyev-Smirnov-Wolfenstein effect ⁷⁾ can be recovered.

Now, after the study of $SL\nu$ taking exactly into account matter effects, performed above, we can summarize the main features of the phenomena considered as follows:

1) a neutrino with nonzero mass and magnetic moment emits spin light when moving in dense matter,

2) in general, $SL\nu$ in matter is due to the neutrino energy dependence on the matter density and, in particular, to neutrinos of the same momentum p but of opposite helicities having different energies in matter;

3) in the particular case of electron neutrinos moving in matter composed predominantly of electrons, the matter density parameter α is positive; here the negative-helicity neutrino (the left-handed relativistic neutrino ν_L) is converted to the positive-helicity neutrino (the right-handed neutrino ν_R), giving rise to neutrino-spin polarization effect;

4) the matter density parameter α can, in general, be negative; therefore the types of initial and final neutrino states, conversion between which effectively produces the $SL\nu$ radiation, are determined by the matter composition;

5) the obtained expressions for the $SL\nu$ radiation rate and power, (13) and (14), exhibit non-trivial dependence on the density of matter and on the initial neutrino energy; in particular, as it follows from (23) and (24), in the low matter density limit the power is suppressed by an additional factor of $\frac{m}{p}$ (for $p \gg m$) or by $\frac{p}{m}$ (for $m \gg p$), in the high density limit, $\alpha \gg \frac{p}{m}$ ($p \gg m$) or $\alpha \gg \frac{m}{p}$ ($m \gg p$), the power acquires the increasing factor $\frac{p}{m}$ (for $p \gg m$) or $\frac{m}{p}$ (for $m \gg p$);

6) for a wide range of matter density parameters the $SL\nu$ radiation is beamed along the neutrino momentum p , however the actual shape of the radiation spatial distribution may vary from projector-like to cap-like, depending on the neutrino momentum-to-mass ratio and the value of α ;

7) it has been shown that for a certain choice of neutrino momentum and matter density a reasonable fraction of the emitted photons move in the direction opposite to the neutrino momentum (this interesting phenomenon arises, for instance, in the particular case of the neutrino parameter $\frac{p}{m} \sim 10$ and $\alpha \sim 100$);

8) in a wide range of matter density parameters α the $SL\nu$ radiation is characterized by total circular polarization;

9) the emitted photon energy is also essentially dependent on the neutrino energy and matter density; in particular, the photon energy increases from $\omega \sim 2p$ up to $\omega \sim \alpha m$ with the density; in the most interesting for astrophysical and cosmology applications case (when $p \gg m$ and $\frac{m}{p} \ll \alpha \ll \frac{p}{m}$) the average energy of the emitted photon is one third of the neutrino momentum p , in the case of very high density this value equals one half of the initial neutrino energy

in matter.

We argue that the investigated properties of neutrino-spin light in matter may be important for experimental identification of this radiation from different astrophysical and cosmological sources. The fireball model of GRBs (see [11] for recent reviews) is one of the examples. Gamma-rays can be expected to be produced during collapses or coalescence processes of neutron stars, owing to the $SL\nu$ mechanism in dense matter discussed. Another rather favorable situation for effective $SL\nu$ production can be realized during a neutron star being "eaten up" by the black hole at the center of our Galaxy. For estimation, let us consider a neutron star of mass $M_{NS} \sim 3M_{\odot}$ ($M_{\odot} = 2 \cdot 10^{33}g$ is the solar mass). The corresponding effective number density will be $n \sim 8 \cdot 10^{38} \text{ cm}^{-3}$ and for the matter density parameter we get $\alpha \sim 23$, if the neutrino mass is $m \sim 0.1 \text{ eV}$. For relativistic neutrino energies ($p \gg m$) the emitted $SL\nu$ photon energy, as it follows from (26), is $\langle \omega \rangle \sim 1/3p$, so that the energy range of this radiation may even extend up to energies peculiar to the spectrum of gamma-rays. Note that, as it is shown in Section 4, this radiation is characterized by the total circular polarization. This fact can be important for experimental observations.

7 Acknowledgements

The authors are thankful to Venyamin Berezhinsky, Alexander Dolgov, Carlo Giunti, Gil Pontecorvo, Victor Semikoz and Alexander Zakharov for very useful discussions. One of the authors (A.S.) thank Mario Greco for the invitation to participate in this Conference and also thanks all the organizers for their kind hospitality.

References

1. A. Ioannisian, G. Raffelt, Phys.Rev. **D 55**, 7038 (1997).
2. A. Lobanov, A. Studenikin, Phys.Lett. **B 564**, 27 (2003); Phys.Lett. **B 601**, 171 (2004).
3. M. Dvornikov, A. Grigoriev, A. Studenikin, Int.J.Mod.Phys. **D 14**, 308 (2005), hep-ph/0406114.
4. A. Studenikin, A. Ternov, Phys.Lett. **B 608**, 107 (2005), hep-ph/0410297, hep-ph/0412408.
5. A. Studenikin, A. Ternov, in: Proc. of the 13th Int. Seminar on High Energy Physics "Quarks-2004", (ed. D.Levkov, V.Matveev and V.Rubakov, Publ. Department of Institute of Nuclear Physics RAS, Moscow, 2004),

- hep-ph/0410296; A. Grigoriev, A. Studenikin, A. Ternov, Particle Physics in Laboratory, Space and Universe, in: Proc. Eleventh Lomonosov Conference on Elementary Particle Physics (ed. A.Studenikin, Moscow, 2005), p. 55 (World Scientific, Singapore, 2005), hep-ph/0502210.
6. A. Grigoriev, A. Studenikin, A. Ternov, in: Proceedings of the Int. Workshop Cosmion-2004, (ed. M. Khlopov, K. Bronnikov) Grav. & Cosm. **11**, 1 (2005); hep-ph/0502231.
 7. L. Wolfenstein, Phys.Rev. **D 17**, 2369 (1978); S. Mikheyev, A. Smirnov, Sov.J.Nucl.Phys. **42**, 913 (1985).
 8. L.N. Chang, R.K. Zia, Phys.Rev. **D 38**, 1669 (1988); V. Oraevsky, V. Semikoz, Ya. Smorodinsky, Phys.Lett. **B 227**, 255 (1989); J. Pantaleone, Phys.Lett. **B 268**, 227 (1991); Phys.Rev. **D 46**, 510 (1992); K. Kiers, N. Weiss, Phys.Rev. **D 56**, 5776 (1997); K. Kiers, M. Tytgat, Phys.Rev. **D 57**, 5970 (1998); P. Mannheim, Phys.Rev. **D 37**, 1935 (1988); D. Nötzold, G. Raffelt, Nucl.Phys. **B 307**, 924 (1988); J. Nieves, Phys.Rev. **D 40**, 866 (1989); W. Haxton, W-M. Zhang, Phys.Rev. **D 43**, 2484 (1991); M. Kachelriess, Phys.Lett. **B 426**, 89 (1998); A. Kusenko, M. Postma, Phys.Lett. **B 545**, 238 (2002).
 9. Z. Berezhiani, M. Vysotsky, Phys.Lett. **B 199**, 281 (1987); Z. Berezhiani, A. Smirnov, Phys.Lett. **B 220**, 279 (1989); C. Giunti, C.W. Kim, U.W. Lee, W.P. Lam, Phys.Rev. **D 45**, 1557 (1992); Z. Berezhiani, A. Rossi, Phys.Lett. **B 336**, 439 (1994).
 10. A. Lobanov, hep-ph/0411342.
 11. B. Zhang, P. Meszaros, Int.J.Mod.Phys. **A 19**, 2385 (2004); T. Piran, Rev.Mod.Phys. **76**, 1143 (2004).

THE STARTUP OF MINOS

Anastasios Belias

Rutherford Appleton Laboratory Chilton, Didcot, UK

Written contribution not received

THE CNGS PROGRAM: A STATUS REPORT

Eugenio Coccia

IINFN Gran Sasso and University of Rome "Tor Vergata "

Written contribution not received

NORMAL AND SPECIAL MODELS OF NEUTRINO MASSES AND MIXINGS

Guido Altarelli

CERN, Department of Physics, Theory Division
CH-1211 Geneva 23, Switzerland

and

Dipartimento di Fisica 'E. Amaldi', Università di Roma Tre
INFN, Sezione di Roma Tre, I-00146 Rome, Italy

Abstract

One can make a distinction between "normal" and "special" models. For normal models θ_{23} is not too close to maximal and θ_{13} is not too small, typically a small power of the self-suggesting order parameter \sqrt{r} , with $r = \Delta m_{sol}^2 / \Delta m_{atm}^2 \sim 1/35$. Special models are those where some symmetry or dynamical feature assures in a natural way the near vanishing of θ_{13} and/or of $\theta_{23} - \pi/4$. Normal models are conceptually more economical and much simpler to construct. Here we focus on special models, in particular a recent one based on A4 discrete symmetry and extra dimensions that leads in a natural way to a Harrison-Perkins-Scott mixing matrix.

1 Introduction

By now there is convincing evidence for solar and atmospheric neutrino oscillations. The Δm^2 values and mixing angles are known with fair accuracy. A summary, taken from Ref. ¹⁾ of the results is shown in Table 1. For the Δm^2 we have: $\Delta m_{atm}^2 \sim 2.5 \cdot 10^{-3} \text{ eV}^2$ and $\Delta m_{sol}^2 \sim 10^{-5} \text{ eV}^2$. As for the mixing angles, two are large and one is small. The atmospheric angle θ_{23} is large, actually compatible with maximal but not necessarily so: at 3σ : $0.31 \lesssim \sin^2 \theta_{23} \lesssim 0.72$ with central value around 0.5. The solar angle θ_{12} is large, $\sin^2 \theta_{12} \sim 0.3$, but certainly not maximal (by about 5-6 σ now ²⁾). The third angle θ_{13} , strongly limited mainly by the CHOOZ experiment, has at present a 3σ upper limit given by about $\sin^2 \theta_{13} \lesssim 0.08$.

Table 1: Square mass differences and mixing angles ¹⁾

	lower limit (3σ)	best value	upper limit (3σ)
$(\Delta m_{sun}^2)_{LA} (10^{-5} \text{ eV}^2)$	5.4	6.9	9.5
$\Delta m_{atm}^2 (10^{-3} \text{ eV}^2)$	1.4	2.6	3.7
$\sin^2 \theta_{12}$	0.23	0.30	0.39
$\sin^2 \theta_{23}$	0.31	0.52	0.72
$\sin^2 \theta_{13}$	0	0.006	0.054

In spite of this experimental progress there are still many alternative routes in constructing models of neutrino masses. This variety is mostly due to the considerable ambiguities that remain. First of all, it is essential to know whether the LSND signal ⁴⁾, which has not been confirmed by KARMEN ⁵⁾ and is currently being double-checked by MiniBoone ⁶⁾, will be confirmed or will be excluded. If LSND is right we probably need at least four light neutrinos; if not we can do with only the three known ones, as we assume here in the following. As neutrino oscillations only determine mass squared differences

a crucial missing input is the absolute scale of neutrino masses (within the existing limits from terrestrial experiments and cosmology ^{7), 8)}).

The following experimental information on the absolute scale of neutrino masses is available. From the endpoint of tritium beta decay spectrum we have an absolute upper limit of 2.2 eV (at 95% C.L.) on the mass of " $\bar{\nu}_e$ " ⁷⁾, which, combined with the observed oscillation frequencies under the assumption of three CPT-invariant light neutrinos, represents also an upper bound on the masses of all active neutrinos. Complementary information on the sum of neutrino masses is also provided by the galaxy power spectrum combined with measurements of the cosmic microwave background anisotropies. According to the recent analysis of the WMAP collaboration ⁸⁾, $\sum_i |m_i| < 0.69$ eV (at 95% C.L.). More conservative analyses give $\sum_i |m_i| < 1 - 1.8$ eV, still much more restrictive than the laboratory bound. But, to some extent, the cosmological bound depends on a number of assumptions (or, in fashionable terms, priors). However, for 3 degenerate neutrinos of mass m , depending on our degree of confidence in the cosmological bound, we can be sure that $m \lesssim 0.23 - 0.3 - 0.6$ eV. The discovery of $0\nu\beta\beta$ decay would be very important because it would directly establish lepton number violation and the Majorana nature of ν 's, and provide direct information on the absolute scale of neutrino masses. The present limit from $0\nu\beta\beta$ is $|m_{ee}| < 0.2$ eV or to be more conservative $|m_{ee}| < (0.3 \div 0.5)$ eV, where $m_{ee} = \sum U_{ei}^2 m_i$ in terms of the mixing matrix and the mass eigenvalues (see eq.(6)).

Given that neutrino masses are certainly extremely small, it is really difficult from the theory point of view to avoid the conclusion that L conservation is probably violated. In fact, in terms of lepton number violation the smallness of neutrino masses can be naturally explained as inversely proportional to the very large scale where L is violated, of order M_{GUT} or even M_{Pl} . Given for granted that neutrinos are Majorana particles, their masses can arise either from the see-saw mechanism or from generic dimension-five non renormalizable operators ⁹⁾ of the form:

$$O_5 = \frac{(Hl)_i^T \lambda_{ij} (Hl)_j}{M} + h.c. \quad , \quad (1)$$

with H being the ordinary Higgs doublet, l_i the SU(2) lepton doublets, λ a matrix in flavour space, M a large scale of mass and a charge conjugation matrix C between the lepton fields is understood. Neutrino masses generated by O_5 are of the order $m_\nu \approx v^2/M$ for $\lambda_{ij} \approx O(1)$, where $v \sim O(100 \text{ GeV})$ is the vacuum expectation value of the ordinary Higgs. A priori comparable masses are obtained in the see-saw mechanism: the resulting neutrino mass matrix reads:

$$m_\nu = m_D^T M^{-1} m_D \quad . \quad (2)$$

that is the light neutrino masses are quadratic in the Dirac masses and inversely proportional to the large Majorana mass. For $m_\nu \approx \sqrt{\Delta m_{atm}^2} \approx 0.05$ eV and $m_\nu \approx m_D^2/M$ with $m_D \approx v \approx 200$ GeV we find $M \approx 10^{15}$ GeV which indeed is an impressive indication for M_{GUT} . Thus neutrino masses are a probe into the physics at M_{GUT} .

2 The ν -Mixing Matrix

If we take maximal s_{23} ($s_{ij} = \sin\theta_{ij}$) and keep only linear terms in $u = s_{13}e^{i\varphi}$, from experiment we find the following structure of the U_{fi} ($f = e, \mu, \tau$, $i = 1, 2, 3$) mixing matrix, apart from sign convention redefinitions:

$$U_{fi} = \begin{pmatrix} c_{12} & s_{12} & u \\ -(s_{12} + c_{12}u^*)/\sqrt{2} & (c_{12} - s_{12}u^*)/\sqrt{2} & 1/\sqrt{2} \\ (s_{12} - c_{12}u^*)/\sqrt{2} & -(c_{12} + s_{12}u^*)/\sqrt{2} & 1/\sqrt{2} \end{pmatrix}, \quad (3)$$

(4)

Even for three neutrinos the pattern of the neutrino mass spectrum is still undetermined: it can be approximately degenerate, or of the inverse hierarchy type or normally hierarchical. Given the observed frequencies and the notation $\Delta m_{sun}^2 \equiv |\Delta m_{12}^2|$, $\Delta m_{atm}^2 \equiv |\Delta m_{23}^2|$ with $\Delta m_{12}^2 = |m_2|^2 - |m_1|^2 > 0$ and $\Delta m_{23}^2 = m_3^2 - |m_2|^2$, the three possible patterns of mass eigenvalues are:

$$\begin{aligned} \text{Degenerate} &: |m_1| \sim |m_2| \sim |m_3| \gg |m_i - m_j| \\ \text{Inverted hierarchy} &: |m_1| \sim |m_2| \gg |m_3| \\ \text{Normal hierarchy} &: |m_3| \gg |m_{2,1} \end{aligned} \quad (5)$$

Models based on all these patterns have been proposed and studied and all are in fact viable at present.

The detection of neutrino-less double beta decay would offer a way to possibly disentangle the 3 cases. The quantity which is bound by experiments is the 11 entry of the ν mass matrix, which in general, from $m_\nu = U^* m_{diag} U^\dagger$, is given by :

$$|m_{ee}| = |(1 - s_{13}^2)(m_1 c_{12}^2 + m_2 s_{12}^2) + m_3 e^{2i\phi} s_{13}^2|, \quad (6)$$

Starting from this general formula it is simple to derive the following bounds for degenerate, inverse hierarchy or normal hierarchy mass patterns.

- a) Degenerate case. If $|m|$ is the common mass and we take $s_{13} = 0$, which is a safe approximation in this case, because $|m_3|$ cannot compensate for the smallness of s_{13} , we have $m_{ee} \sim |m|(c_{12}^2 \pm s_{12}^2)$. Here

the phase ambiguity has been reduced to a sign ambiguity which is sufficient for deriving bounds. So, depending on the sign we have $m_{ee} = |m|$ or $m_{ee} = |m|\cos 2\theta_{12}$. We conclude that in this case m_{ee} could be as large as the present experimental limit but should be at least of order $O(\sqrt{\Delta m_{atm}^2}) \sim O(10^{-2} \text{ eV})$ unless the solar angle is practically maximal, in which case the minus sign option can be arbitrarily small. But the experimental $2\text{-}\sigma$ range of the solar angle does not favour a cancellation by more than a factor of about 3.

- b) Inverse hierarchy case. In this case the same approximate formula $m_{ee} = |m|(c_{12}^2 \pm s_{12}^2)$ holds because m_3 is small and s_{13} can be neglected. The difference is that here we know that $|m| \approx \sqrt{\Delta m_{atm}^2}$ so that $|m_{ee}| < \sqrt{\Delta m_{atm}^2} \sim 0.05 \text{ eV}$. At the same time, since a full cancellation between the two contributions cannot take place, we expect $|m_{ee}| > 0.01 \text{ eV}$.
- c) Normal hierarchy case. Here we cannot in general neglect the m_3 term. However in this case $|m_{ee}| \sim |\sqrt{\Delta m_{sun}^2} s_{12}^2 \pm \sqrt{\Delta m_{atm}^2} s_{13}^2|$ and we have the bound $|m_{ee}| < \text{a few } 10^{-3} \text{ eV}$.

Recently some evidence for $0\nu\beta\beta$ was claimed¹⁰⁾ corresponding to $|m_{ee}| \sim (0.2 \div 0.6) \text{ eV}$ ($(0.1 \div 0.9) \text{ eV}$ in a more conservative estimate of the involved nuclear matrix elements). If confirmed this would rule out cases b) and c) and point to case a) or to models with more than 3 neutrinos.

3 "Normal" versus "Special" Models

After KamLAND, SNO and WMAP not too much hierarchy in neutrino masses is indicated by experiments:

$$r = \Delta m_{sol}^2 / \Delta m_{atm}^2 \sim 1/35. \quad (7)$$

Precisely at 3σ : $0.018 \lesssim r \lesssim 0.053$. Thus, for a hierarchical spectrum, $m_2/m_3 \sim \sqrt{r} \sim 0.2$, which is comparable to the Cabibbo angle $\lambda_C \sim 0.22$ or $\sqrt{m_\mu/m_\tau} \sim 0.24$. This suggests that the same hierarchy parameters (raised to powers with $o(1)$ exponents) are at work for quark, charged lepton and neutrino mass matrices. This in turn indicates that, in absence of some special dynamical reason, we do not expect a quantity like θ_{13} to be too small. Indeed it would be very important to know how small the mixing angle θ_{13} is and how close to maximal is θ_{23} . Actually one can make a distinction between "normal" and "special" models. For normal models θ_{23} is not too close to maximal and θ_{13} is not too small, typically a small power of the self-suggesting order parameter \sqrt{r} , with $r = \Delta m_{sol}^2 / \Delta m_{atm}^2 \sim 1/35$. Special models are those where some symmetry or dynamical feature assures in a natural way the near vanishing of

θ_{13} and/or of $\theta_{23} - \pi/4$. Normal models are conceptually more economical and much simpler to construct. Typical categories of normal models are

- a) Anarchy: Models with approximately degenerate mass spectrum and no ordering principle, no approximate symmetry assumed in the neutrino mass sector (11)–(12). The small value of r is accidental, due to random fluctuations of matrix elements in the Dirac and Majorana neutrino mass matrices. The see-saw formula being a product of 3 matrices generates a broad distribution of r values resulting from random input in each factor. All mixing angles are generically large: so we do not expect θ_{23} to be maximal nor θ_{13} to be too small.
- b) Semianarchy: We have seen that anarchy is the absence of structure in the neutrino sector. Here we consider an attenuation of anarchy where the absence of structure is limited to the 23 sector. The typical texture is in this case (13)–(12):

$$m_\nu \approx m \begin{pmatrix} \delta & \epsilon & \epsilon \\ \epsilon & 1 & 1 \\ \epsilon & 1 & 1 \end{pmatrix}, \quad (8)$$

where δ and ϵ are small and by 1 we mean entries of $o(1)$ and also the 23 determinant is of $o(1)$. This texture can be realized for example with different U(1) charges for (l_1, l_2, l_3) , eg $(a, 0, 0)$ appearing in the dim. 5 operator of eq.(1). Clearly, in general we would expect two mass eigenvalues of order 1, in units of m , and one small, of order δ or ϵ^2 . This pattern does not fit the observed solar and atmospheric observed frequencies. However, given that the ratio r is not too small, we can assume that its small value is generated accidentally, as for anarchy. We see that, if by chance the second eigenvalue $\eta \sim \sqrt{r} \sim \delta + \epsilon^2$, we can then obtain the correct value of r with large but in general non maximal θ_{23} and θ_{12} and small $\theta_{13} \sim \epsilon$. The smallness of θ_{13} is the main advantage over anarchy, but the relation with \sqrt{r} normally keeps θ_{13} not too small (eg $\delta \sim \epsilon^2$ in simple U(1) models).

- c) In the limit of exact $L_e - L_\mu - L_\tau$ symmetry we have inverted hierarchy with $r = 0$ and bi-maximal mixing (both θ_{12} and θ_{23} are maximal) (14)–(12). Simple forms of symmetry breaking cannot sufficiently displace θ_{12} from the maximal value because typically $\tan^2 \theta_{12} \sim 1 + o(r)$. Viable normal models are obtained by arranging large contributions to θ_{23} and θ_{12} from the charged lepton mass diagonalization. But then, in order to obtain the measured value of θ_{12} the size of θ_{13} must be close to its present upper bound.

- d) Normal hierarchy models with 23 determinant suppressed by see-saw ¹²⁾: in the 23 sector one needs relatively large mass splittings to fit the small value of r but nearly maximal mixing. This can be obtained if the 23 sub-determinant is suppressed by some dynamical trick. Typical examples are lopsided models ¹⁵⁾ ¹³⁾ ¹⁶⁾ with large off diagonal term in the Dirac matrices of charged leptons and/or neutrinos (in minimal SU(5) the d-quark and charged lepton mass matrices are one the transposed of the other, so that large left-handed mixings for charged leptons correspond to large unobservable right-handed mixings for d-quarks). Another typical example is the dominance in the see-saw formula of a small eigenvalue in M_{RR} , the right-handed Majorana neutrino mass matrix ¹⁷⁾. When the 23 determinant suppression is implemented in a 33 context, normally θ_{13} is not protected from contributions that vanish with the 23 determinant, hence with r .

The fact that some neutrino mixing angles are large and even nearly maximal, while surprising at the start, was eventually found to be well compatible with a unified picture of quark and lepton masses within GUTs. The symmetry group at M_{GUT} could be either (SUSY) SU(5) or SO(10) or a larger group. For example, normal models based on anarchy, semianarchy, inverted hierarchy or normal hierarchy can all be naturally implemented by simple assignments of $U(1)_F$ horizontal charges in a semiquantitative unified description of all quark and lepton masses in SUSY SU(5) \times $U(1)_F$. Actually, in this context, if one adopts a statistical criterium, hierarchical models appear to be preferred over anarchy and among them normal hierarchy appears the most likely.

In conclusion we expect that experiment will eventually find that θ_{13} is not too small and that θ_{23} is sizably not maximal. But if, on the contrary, either θ_{13} very small or θ_{23} very close to maximal will emerge from experiment or both, then theory will need to cope with this fact. One can imagine other types of special models, for example one where, starting from the lagrangian basis where the symmetries of the model are specified, all neutrino mixings arise from the diagonalisation of the charged lepton mass matrix. In ref. ¹⁸⁾ we argue that, in presence of two large mixing angles, this dominance of charged lepton mass diagonalization does not "normally" happen, although we can devise special tricks to enforce this possibility. In particular we have constructed an example which is natural in the technical sense and moreover has a very small θ_{13} , so that it is a special model also in this respect. It is interesting to conceive and explore dynamical structures that could lead to special models in a natural way. Normal models have been extensively discussed in the literature ¹²⁾, so we concentrate here on examples of special models.

4 Some Special Models

We want to discuss here some particularly special models where both θ_{13} and $\theta_{23} - \pi/4$ exactly vanish¹. Then the neutrino mixing matrix U_{fi} ($f = e, \mu, \tau$, $i = 1, 2, 3$), in the basis of diagonal charged leptons, is given by, apart from sign convention redefinitions:

$$U_{fi} = \begin{pmatrix} c_{12} & s_{12} & 0 \\ -s_{12}/\sqrt{2} & c_{12}/\sqrt{2} & -1/\sqrt{2} \\ -s_{12}/\sqrt{2} & c_{12}/\sqrt{2} & 1/\sqrt{2} \end{pmatrix}, \quad (9)$$

where c_{12} and s_{12} stand for $\cos \theta_{12}$ and $\sin \theta_{12}$, respectively. It is much simpler to write natural models of this type with s_{12} small and thus many such attempts are present in the early literature. More recently, given the experimental value of θ_{12} , the more complicated case of s_{12} large was also attacked, using non abelian symmetries, either continuous or discrete (19, 20, 21, 23, 24, 26, 22). In the flavour basis the general form of the neutrino mass matrix for $\theta_{13} = 0$ (no CP violation!) and θ_{23} maximal is given by:

$$m_\nu = \begin{pmatrix} x & y & y \\ y & z & w \\ y & w & z \end{pmatrix}, \quad (10)$$

In eq. (10) 4 real parameters appear corresponding to 3 eigenvalues plus θ_{12} . In many examples the invoked symmetries are particularly ad hoc and/or no sufficient attention is devoted to corrections from higher dimensional operators that can spoil the pattern arranged at tree level and to the highly non trivial vacuum alignment problems that arise if naturalness is required also at the level of vacuum expectation values (VEVs).

An interesting special case of eq. (9) is obtained for $s_{12} = 1/\sqrt{3}$, i.e. the so-called tri-bimaximal or Harrison-Perkins-Scott mixing pattern (HPS)²⁴, with the entries in the second column all equal to $1/\sqrt{3}$ in absolute value:

$$U_{HPS} = \begin{pmatrix} \sqrt{\frac{2}{3}} & \frac{1}{\sqrt{3}} & 0 \\ -\frac{1}{\sqrt{6}} & \frac{1}{\sqrt{3}} & -\frac{1}{\sqrt{2}} \\ -\frac{1}{\sqrt{6}} & \frac{1}{\sqrt{3}} & \frac{1}{\sqrt{2}} \end{pmatrix}. \quad (11)$$

¹More precisely, they vanish in a suitable limit, with correction terms that can be made negligibly small.

This matrix is a good approximation to present data ². This is a most special model where not only θ_{13} and $\theta_{23} - \pi/4$ vanish but also θ_{12} assumes a particular value. Clearly, in a natural realization of this model, a very constraining and predictive dynamics must be underlying.

Interesting ideas on how to obtain the HPS mixing matrix have been discussed in refs ²⁴). The most attractive models are based on the discrete symmetry A_4 , which appears as particularly suitable for the purpose, and were presented in ref. ^{21, 22}). Here we discuss some general features of HPS models and present our version of an A_4 model ²⁵). There are a number of substantial improvements in our version with respect to Ma in ref. ²²). First, the HRS matrix is exactly obtained in a first approximation when higher dimensional operators are neglected, without imposing ad hoc relations among parameters (in ref. ²²). the equality of b and c is not guaranteed by the symmetry). The observed hierarchy of charged lepton masses is obtained by assuming a larger flavour symmetry. The crucial issue of the required VEV alignment in the scalar sector is considered with special attention and a natural solution of this problem was presented. We also keep the flavour scalar fields distinct from the normal Higgs bosons (a proliferation of Higgs doublets is disfavoured by coupling unification) and singlets under the Standard Model gauge group. Last not least, we study the corrections from higher dimensionality operators allowed by the symmetries of the model and discuss the conditions on the cut-off scales and the VEVs in order for these corrections to be completely under control.

5 Basic Structure of the Model

The HPS mixing matrix implies that in a basis where charged lepton masses are diagonal the effective neutrino mass matrix is given by $m_\nu = U_{HPS} \text{diag}(m_1, m_2, m_3) U_{HPS}^T$:

$$m_\nu = \left[\frac{m_3}{2} \begin{pmatrix} 0 & 0 & 0 \\ 0 & 1 & -1 \\ 0 & -1 & 1 \end{pmatrix} + \frac{m_2}{3} \begin{pmatrix} 1 & 1 & 1 \\ 1 & 1 & 1 \\ 1 & 1 & 1 \end{pmatrix} + \frac{m_1}{6} \begin{pmatrix} 4 & -2 & -2 \\ -2 & 1 & 1 \\ -2 & 1 & 1 \end{pmatrix} \right] \quad (12)$$

The eigenvalues of m_ν are m_1, m_2, m_3 with eigenvectors $(-2, 1, 1)/\sqrt{6}, (1, 1, 1)/\sqrt{3}$ and $(0, 1, -1)/\sqrt{2}$, respectively. In general, apart from phases, there are six parameters in a real symmetric matrix like m_ν : here only three are left after the values of the three mixing angles have been fixed à la HPS. For a hierarchical spectrum $m_3 \gg m_2 \gg m_1$, $m_3^2 \sim \Delta m_{atm}^2$, $m_2^2/m_3^2 \sim \Delta m_{sol}^2/\Delta m_{atm}^2$

²In the HPS scheme $\tan^2 \theta_{12} = 0.5$, to be compared with the latest experimental determination ²⁾: $\tan^2 \theta_{12} = 0.45_{-0.08}^{+0.09}$.

and m_1 could be negligible. But also degenerate masses and inverse hierarchy can be reproduced: for example, by taking $m_3 = -m_2 = m_1$ we have a degenerate model, while for $m_1 = -m_2$ and $m_3 = 0$ an inverse hierarchy case (stability under renormalization group running strongly prefers opposite signs for the first and the second eigenvalue which are related to solar oscillations and have the smallest mass squared splitting). From the general expression of the eigenvectors one immediately sees that this mass matrix, independent of the values of m_i , leads to the HPS mixing matrix. It is a curiosity that the eigenvectors are the same as in the case of the Fritzsche-Xing (FX) matrix²⁷⁾ but with the roles of the first and the third ones interchanged (so that for HPS θ_{23} is maximal while $\sin^2 2\theta_{12} = 8/9$, while for FX the two mixing angles keep the same values but are interchanged).

In ref. 25) (see also 28)) we show that if we want to reproduce $\theta_{23} = \pi/4$ in some limit of our theory, necessarily this limit cannot correspond to an exact symmetry in flavour space (we explicitly exclude symmetries that are broken by $o(1)$ terms, for example such that the difference between the μ and the τ masses is a breaking effect or is introduced by hand while the symmetry would prescribe them of the same order). Then a maximal atmospheric mixing angle can only originate from breaking effects as a solution of a vacuum alignment problem.

Our model is based on the discrete group A_4 following refs 21, 22), where its structure and representations are described in detail. Here we simply recall that A_4 is the discrete symmetry group of the rotations that leave a tetrahedron invariant, or the group of the even permutations of 4 objects. It has 12 elements and 4 inequivalent irreducible representations denoted 1, 1', 1'' and 3 in terms of their respective dimensions. Introducing ω , the cubic root of unity, $\omega = \exp i\frac{2\pi}{3}$, so that $1 + \omega + \omega^2 = 0$, the three one-dimensional representations are obtained by dividing the 12 elements of A_4 in three classes, which are determined by the multiplication rule, and assigning to (class 1, class 2, class 3) a factor (1, 1, 1) for 1, or (1, ω , ω^2) for 1' or (1, ω^2 , ω) for 1''. The product of two 3 gives $3 \times 3 = 1 + 1' + 1'' + 3 + 3$. Also $1' \times 1' = 1''$, $1' \times 1'' = 1$, $1'' \times 1'' = 1'$ etc. For $3 \sim (a_1, a_2, a_3)$, $3' \sim (b_1, b_2, b_3)$ the irreducible representations obtained from their product are:

$$1 = a_1 b_1 + a_2 b_2 + a_3 b_3 \quad (13)$$

$$1' = a_1 b_1 + \omega a_2 b_2 + \omega^2 a_3 b_3 \quad (14)$$

$$1'' = a_1 b_1 + \omega^2 a_2 b_2 + \omega a_3 b_3 \quad (15)$$

$$3 \sim (a_2 b_3, a_3 b_1, a_1 b_2) \quad (16)$$

$$3 \sim (a_3 b_2, a_1 b_3, a_2 b_1) \quad (17)$$

Following ref. ²²⁾ we assigns leptons to the four inequivalent representations of A_4 : left-handed lepton doublets l transform as a triplet 3, while the right-handed charged leptons e^c , μ^c and τ^c transform as 1, $1'$ and $1''$, respectively. The flavour symmetry is broken by two real triplets φ and φ' and by a real singlet ξ . At variance with the choice made by ²²⁾, these fields are gauge singlets. Hence we only need two Higgs doublets $h_{u,d}$ (not three generations of them as in ref. ²²⁾), which we take invariant under A_4 . We assume that some mechanism produces and maintains the hierarchy $\langle h_{u,d} \rangle = v_{u,d} \ll \Lambda$ where Λ is the cut-off scale of the theory ³. The Yukawa interactions in the lepton sector read:

$$\mathcal{L}_Y = y_e e^c(\varphi l) + y_\mu \mu^c(\varphi l)'' + y_\tau \tau^c(\varphi l)' + x_a \xi(ll) + x_d(\varphi' ll) + h.c. + \dots \quad (18)$$

In our notation, (33) transforms as 1, (33)' transforms as $1'$ and (33)'' transforms as $1''$. Also, to keep our notation compact, we use a two-component notation for the fermion fields and we set to 1 the Higgs fields $h_{u,d}$ and the cut-off scale Λ . For instance $y_e e^c(\varphi l)$ stands for $y_e e^c(\varphi l) h_d / \Lambda$, $x_a \xi(ll)$ stands for $x_a \xi(l h_u l h_u) / \Lambda^2$ and so on. The Lagrangian \mathcal{L}_Y contains the lowest order operators in an expansion in powers of $1/\Lambda$. Dots stand for higher dimensional operators. Some terms allowed by the flavour symmetry, such as the terms obtained by the exchange $\varphi' \leftrightarrow \varphi$, or the term (ll) are missing in \mathcal{L}_Y . Their absence is crucial and is guaranteed by an additional discrete Z_4 symmetry under which f^c transform into $-i f^c$ ($f = e, \mu, \tau$), l into il , φ is invariant and φ' changes sign. This symmetry also explains why φ and φ' cannot be interchanged.

We need a mechanism such that the fields φ' , φ and ξ develop a VEV along the directions:

$$\begin{aligned} \langle \varphi' \rangle &= (v', 0, 0) \\ \langle \varphi \rangle &= (v, v, v) \\ \langle \xi \rangle &= u \quad . \end{aligned} \quad (19)$$

Then at the leading order of the $1/\Lambda$ expansion, the mass matrices m_l and m_ν for charged leptons and neutrinos are given by:

$$m_l = v_d \frac{v}{\Lambda} \begin{pmatrix} y_e & y_e & y_e \\ y_\mu & y_\mu \omega & y_\mu \omega^2 \\ y_\tau & y_\tau \omega^2 & y_\tau \omega \end{pmatrix} , \quad (20)$$

³This is the well known hierarchy problem that can be solved, for instance, by realizing a supersymmetric version of this model.

$$m_\nu = \frac{v_u^2}{\Lambda} \begin{pmatrix} a & 0 & 0 \\ 0 & a & d \\ 0 & d & a \end{pmatrix} , \quad (21)$$

where

$$a \equiv x_a \frac{u}{\Lambda} , \quad d \equiv x_d \frac{v'}{\Lambda} . \quad (22)$$

Charged leptons are diagonalized by

$$l \rightarrow \frac{1}{\sqrt{3}} \begin{pmatrix} 1 & 1 & 1 \\ 1 & \omega^2 & \omega \\ 1 & \omega & \omega^2 \end{pmatrix} l , \quad (23)$$

and charged fermion masses are given by:

$$m_e = \sqrt{3} y_e v_d \frac{v}{\Lambda} , \quad m_\mu = \sqrt{3} y_\mu v_d \frac{v}{\Lambda} , \quad m_\tau = \sqrt{3} y_\tau v_d \frac{v}{\Lambda} . \quad (24)$$

We can easily obtain a natural hierarchy among m_e , m_μ and m_τ by introducing an additional $U(1)_F$ flavour symmetry under which only the right-handed lepton sector is charged. We assign F-charges 0, 2 and $3 \div 4$ to τ^c , μ^c and e^c , respectively. By assuming that a flavon θ , carrying a negative unit of F, acquires a VEV $\langle \theta \rangle / \Lambda \equiv \lambda < 1$, the Yukawa couplings become field dependent quantities $y_{e,\mu,\tau} = y_{e,\mu,\tau}(\theta)$ and we have

$$y_\tau \approx O(1) , \quad y_\mu \approx O(\lambda^2) , \quad y_e \approx O(\lambda^{3 \div 4}) . \quad (25)$$

In the flavour basis the neutrino mass matrix reads ⁴:

$$m_\nu = \frac{v_u^2}{\Lambda} \begin{pmatrix} a + 2d/3 & -d/3 & -d/3 \\ -d/3 & 2d/3 & a - d/3 \\ -d/3 & a - d/3 & 2d/3 \end{pmatrix} , \quad (26)$$

and is diagonalized by the transformation:

$$U^T m_\nu U = \frac{v_u^2}{\Lambda} \text{diag}(a + d, a, -a + d) , \quad (27)$$

with

$$U = \begin{pmatrix} \sqrt{2/3} & 1/\sqrt{3} & 0 \\ -1/\sqrt{6} & 1/\sqrt{3} & -1/\sqrt{2} \\ -1/\sqrt{6} & 1/\sqrt{3} & +1/\sqrt{2} \end{pmatrix} . \quad (28)$$

⁴Notice that a unitary change of basis like the one in eq. (23) will in general change the relative phases of the eigenvalues of m_ν .

The leading order predictions are $\tan^2 \theta_{23} = 1$, $\tan^2 \theta_{12} = 0.5$ and $\theta_{13} = 0$. The neutrino masses are $m_1 = a + d$, $m_2 = a$ and $m_3 = -a + d$, in units of v_u^2/Λ . We can express $|a|$, $|d|$ in terms of $r \equiv \Delta m_{sol}^2/\Delta m_{atm}^2 \equiv (|m_2|^2 - |m_1|^2)/|m_3|^2 - |m_1|^2$, $\Delta m_{atm}^2 \equiv |m_3|^2 - |m_1|^2$ and $\cos \Delta$, Δ being the phase difference between the complex numbers a and d :

$$\begin{aligned}\sqrt{2}|a|\frac{v_u^2}{\Lambda} &= \frac{-\sqrt{\Delta m_{atm}^2}}{2 \cos \Delta \sqrt{1-2r}} \\ \sqrt{2}|d|\frac{v_u^2}{\Lambda} &= \sqrt{1-2r} \sqrt{\Delta m_{atm}^2} .\end{aligned}\quad (29)$$

To satisfy these relations a moderate tuning is needed in our model. Due to the absence of (ll) in eq. (18) which we will motivate in the next section, a and d are of the same order in $1/\Lambda$, see eq. (22). Therefore we expect that $|a|$ and $|d|$ are close to each other and, to satisfy eqs. (29), $\cos \Delta$ should be negative and of order one. We obtain:

$$\begin{aligned}|m_1|^2 &= \left[-r + \frac{1}{8 \cos^2 \Delta (1-2r)} \right] \Delta m_{atm}^2 \\ |m_2|^2 &= \frac{1}{8 \cos^2 \Delta (1-2r)} \Delta m_{atm}^2 \\ |m_3|^2 &= \left[1 - r + \frac{1}{8 \cos^2 \Delta (1-2r)} \right] \Delta m_{atm}^2\end{aligned}\quad (30)$$

If $\cos \Delta = -1$, we have a neutrino spectrum close to hierarchical:

$$|m_3| \approx 0.053 \text{ eV} \quad , \quad |m_1| \approx |m_2| \approx 0.017 \text{ eV} \quad .\quad (31)$$

In this case the sum of neutrino masses is about 0.087 eV. If $\cos \Delta$ is accidentally small, the neutrino spectrum becomes degenerate. The value of $|m_{ee}|$, the parameter characterizing the violation of total lepton number in neutrinoless double beta decay, is given by:

$$|m_{ee}|^2 = \left[-\frac{1+4r}{9} + \frac{1}{8 \cos^2 \Delta (1-2r)} \right] \Delta m_{atm}^2 \quad .\quad (32)$$

For $\cos \Delta = -1$ we get $|m_{ee}| \approx 0.005$ eV, at the upper edge of the range allowed for normal hierarchy, but unfortunately too small to be detected in a near future. Independently from the value of the unknown phase Δ we get the relation:

$$|m_3|^2 = |m_{ee}|^2 + \frac{10}{9} \Delta m_{atm}^2 \left(1 - \frac{r}{2} \right) \quad ,\quad (33)$$

which is a prediction of our model.

It is also important to get some constraint on the mass scales involved in our construction. From eqs. (29) and (22), by assuming $x_d \approx 1$ $v_u \approx 250$ GeV, we have

$$\Lambda \approx 1.8 \times 10^{15} \left(\frac{v'}{\Lambda} \right) \text{ GeV} \quad . \quad (34)$$

Since, to have a meaningful expansion, we expect $v' \leq \Lambda$, we have the upper bound

$$\Lambda < 1.8 \times 10^{15} \text{ GeV} \quad . \quad (35)$$

Beyond this energy scale, new physics should come into play. The smaller the ratio v'/Λ , the smaller becomes the cut-off scale. For instance, when $v'/\Lambda = 0.03$, Λ should be close to 10^{14} GeV. A complementary information comes from the charged lepton sector, eq. (24). A lower bound on v/Λ can be derived from the requirement that the Yukawa coupling y_τ remains in a perturbative regime. By asking $y_\tau v_d < 250$ GeV, we get

$$\frac{v}{\Lambda} > 0.004 \quad . \quad (36)$$

Finally, by assuming that all the VEVs fall in approximately the same range, which will be shown in section 5, we obtain the range

$$0.004 < \frac{v'}{\Lambda} \approx \frac{v}{\Lambda} \approx \frac{u}{\Lambda} < 1 \quad , \quad (37)$$

that will be useful to estimate the effects of higher-dimensional operators. Correspondingly the cut-off scale will range between about 10^{13} and 1.8×10^{15} GeV.

6 Vacuum alignment in a A_4 model in an extra dimension

The problem of achieving the vacuum alignment of eq. (19) is not at all trivial. At the same time, to produce the desired mass matrices in the neutrino and charged lepton sectors, we should prevent, at least at some level, the interchange between the fields φ and φ' . There are several difficulties to naturally accomplish these requirements. By minimizing the scalar potential of the theory with respect to φ and φ' we get six equations that we would like to satisfy in terms of the two unknown v and v' . Even though we expect that, due to the symmetry A_4 , the six minimum conditions are not necessarily independent, such an expectation turns out to be wrong in the specific case, unless some additional relation is enforced on the parameters of the scalar potential. These additional relations are in general not natural. For instance, even by imposing them at the tree level, they are expected to be violated at the one-loop order.

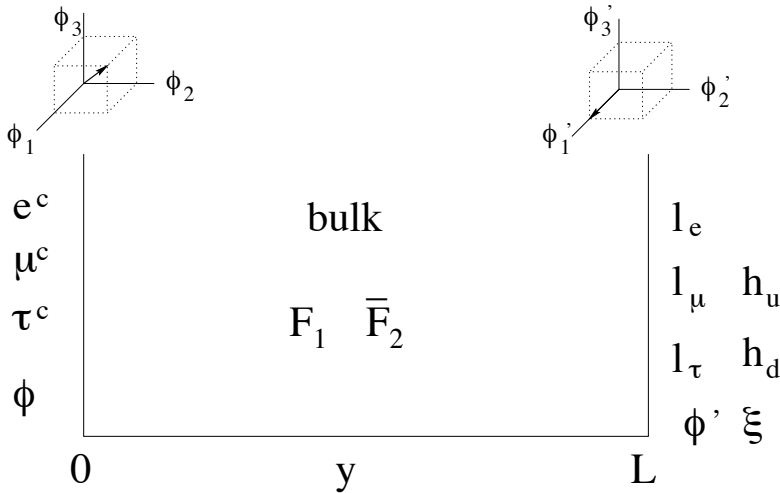


Figure 1: *Fifth dimension and localization of scalar and fermion fields. The symmetry breaking sector includes the A_4 triplets φ and φ' , localized at the opposite ends of the interval. Their VEVs are dynamically aligned along the directions shown at the top of the figure.*

Therefore it turns out that without some special trick the minimum conditions cannot be all satisfied by our vacuum configuration. We now discuss a solution to this problem.

One of the problems we should overcome in the search for the correct alignment is that of keeping neutrino and charged lepton sectors separate, including the respective symmetry breaking sectors. Here we show that such a separation can be achieved by means of an extra spatial dimension. The space-time is assumed to be five-dimensional, the product of the four-dimensional Minkowski space-time times an interval going from $y = 0$ to $y = L$. At $y = 0$ and $y = L$ the space-time has two four-dimensional boundaries, which we will call branes. Our idea is that matter $SU(2)$ singlets such as e^c, μ^c, τ^c are localized at $y = 0$, while $SU(2)$ doublets, such as l are localized at $y = L$ (see Fig.1). Neutrino masses arise from local operators at $y = L$. Charged lepton masses are produced by non-local effects involving both branes. The simplest possibility is to introduce a bulk fermion $F(x, y)$, depending on all space-time coordinates, that interacts with e^c, μ^c, τ^c at $y = 0$ and with l at $y = L$. The exchange of such a fermion can provide the desired non-local coupling between right-handed and left-handed ordinary fermions. We also impose the discrete

Z_4 symmetry introduced in the previous section under which $(f^c, l, F, \varphi, \varphi', \xi)$ transform into $(-if^c, il, iF, \varphi, -\varphi', -\xi)$. Finally, assuming that φ and (φ', ξ) are localized respectively at $y = 0$ and $y = L$, we obtain a natural separation between the two sectors and their respective scalar potentials are minimized by the desired field configurations, for natural values of the implied parameters.

Such a mechanism only works in the case of discrete symmetries, since in the continuous case the large symmetry of the total potential energy would make the relative orientations of the two scalar sectors undetermined.

Last but not least, the hierarchy of the charged lepton masses can be reproduced by the usual Froggatt-Nielsen mechanism within the context of an abelian flavour symmetry, which turns out to be fully compatible with the present scheme.

In ref. 25) we have extensively discussed how this lowest order picture is modified by the introduction of higher dimensional operators. The induced corrections are parametrically small, of second order in the expansion parameter VEV/Λ , Λ being the cut-off of the theory, and they can be made numerically negligible.

We believe that, from a purely technical point of view, we have fulfilled our goal to realize a completely natural construction of the HPS mixing scheme. But to construct our model we had to introduce a number of special dynamical tricks (like a peculiar set of discrete symmetries in extra dimensions). Apparently this is the price to pay for a “special” model where all mixing angles are fixed to particular values. Perhaps this exercise can be taken as a hint that it is more plausible to expect that, in the end, experiment will select a “normal” model with θ_{13} not too small and θ_{23} not too close to maximal.

Acknowledgment

I thank Giorgio Bellettini, Giorgio Chiarelli and Mario Greco for their kind invitation to this perfectly organised Conference

References

1. M. Maltoni et al., Phys. Rev. D68 (2003) 113010.
2. B. Aharmim *et al.* [SNO Collaboration], arXiv:nucl-ex/0502021.
3. A. Strumia and F. Vissani, arXiv:hep-ph/0503246; G. L. Fogli, E. Lisi, A. Marrone, A. Melchiorri, A. Palazzo, P. Serra and J. Silk, Phys. Rev. D **70** (2004) 113003 [arXiv:hep-ph/0408045]; J. N. Bahcall, M. C. Gonzalez-Garcia and C. Pena-Garay, JHEP **0408**, 016 (2004) [arXiv:hep-ph/0406294]; M. Maltoni, T. Schwetz, M. A. Tortola and J. W. F. Valle, New J. Phys. **6** (2004) 122 [arXiv:hep-ph/0405172].

4. The LSND collaboration, hep-ex/0104049.
5. The Karmen collaboration, Nucl. Phys. Proc. Suppl. 91, 191 (2000).
6. P. Spentzouris, Nucl. Phys. Proc. Suppl. **100**, 163 (2001).
7. C. Kraus *et al.*, arXiv:hep-ex/0412056; V. M. Lobashev, Phys. Atom. Nucl. **63** (2000) 962 [Yad. Fiz. **63** (2000) 1037].
8. C. L. Bennett *et al.*, Astrophys. J. Suppl. **148** (2003) 1; D. N. Spergel *et al.*, Astrophys. J. Suppl. **148** (2003) 175.
9. S. Weinberg, Phys. Rev. Lett. 59 (1987) 2607; see also C.J. Hogan, Rev. Mod. Phys. 72 (2000) 1149.
10. H.V. Klapdor-Kleingrothaus *et al.*, Mod. Phys. Lett., A37 2409 (2001); H. V. Klapdor-Kleingrothaus, A. Dietz, I. V. Krivosheina and O. Chkvorets, Nucl. Instrum. Meth. A **522** (2004) 371 and Phys. Lett. B **586** (2004) 198.
11. L. J. Hall, H. Murayama and N. Weiner, Phys. Rev. Lett. **84**, 2572 (2000);
12. For a review, see G. Altarelli and F. Feruglio, New J. Phys. **6** (2004) 106.
13. N. Irges, S. Lavignac and P. Ramond, Phys. Rev. D **58**, 035003 (1998);
14. R. Barbieri, L. J. Hall, D. R. Smith, A. Strumia and N. Weiner, JHEP **9812**, 017 (1998); R. Barbieri, L. J. Hall and A. Strumia, Phys. Lett. B **445**, 407 (1999);
15. C. H. Albright and S. M. Barr, Phys. Rev. D **58**, 013002 (1998); C. H. Albright, K. S. Babu and S. M. Barr, Phys. Rev. Lett. **81**, 1167 (1998); P. H. Frampton and A. Rasin, Phys. Lett. B **478**, 424 (2000).
16. G. Altarelli and F. Feruglio, Phys. Lett. B **439**, 112 (1998); G. Altarelli and F. Feruglio, JHEP **9811**, 021 (1998).
17. See for instance: S. F. King, JHEP **0209** (2002) 011.
18. G. Altarelli, F. Feruglio and I. Masina, Nucl. Phys. B **689** (2004) 157.
19. W. Grimus and L. Lavoura, JHEP **0107** (2001) 045; W. Grimus and L. Lavoura, Acta Phys. Polon. B **32** (2001) 3719; W. Grimus and L. Lavoura, Eur. Phys. J. C **28** (2003) 123; W. Grimus and L. Lavoura, Phys. Lett. B **572** (2003) 189; W. Grimus and L. Lavoura, arXiv:hep-ph/0305309. W. Grimus and L. Lavoura, Acta Phys. Polon. B **34** (2003) 5393; W. Grimus, A. S. Joshipura, S. Kaneko, L. Lavoura and M. Tanimoto, JHEP **0407** (2004) 078; W. Grimus, A. S. Joshipura, S. Kaneko, L. Lavoura, H. Sawanaka and M. Tanimoto, Nucl. Phys. B **713** (2005) 151; F. Caravaglios and S. Morisi, [arXiv:hep-ph/0503234]; S. Morisi and M. Picariello, [arXiv:hep-ph/0505113].

20. C. Wetterich, Phys. Lett. B **451** (1999) 397; R. Barbieri, L. J. Hall, G. L. Kane and G. G. Ross, arXiv:hep-ph/9901228; O. Vives, [arXiv:hep-ph/0504079].
21. E. Ma and G. Rajasekaran, Phys. Rev. D **64** (2001) 113012 [arXiv:hep-ph/0106291]; K. S. Babu, E. Ma and J. W. F. Valle, Phys. Lett. B **552** (2003) 207; M. Hirsch, J. C. Romao, S. Skadhauge, J. W. F. Valle and A. Villanova del Moral, arXiv:hep-ph/0312244; M. Hirsch, J. C. Romao, S. Skadhauge, J. W. F. Valle and A. Villanova del Moral, arXiv:hep-ph/0312265; E. Ma, arXiv:hep-ph/0404199.
22. E. Ma, Phys. Rev. D **70** (2004) 031901; E. Ma arXiv:hep-ph/0409075; E. Ma, New J. Phys. **6** (2004) 104.
23. S. L. Chen, M. Frigerio and E. Ma, arXiv:hep-ph/0404084.
24. P. F. Harrison, D. H. Perkins and W. G. Scott, Phys. Lett. B **530** (2002) 167 [arXiv:hep-ph/0202074]; P. F. Harrison and W. G. Scott, Phys. Lett. B **535** (2002) 163; [arXiv:hep-ph/0203209]. P. F. Harrison and W. G. Scott, Phys. Lett. B **547** (2002) 219; P. F. Harrison and W. G. Scott, Phys. Lett. B **557** (2003) 76; P. F. Harrison and W. G. Scott, arXiv:hep-ph/0402006; P. F. Harrison and W. G. Scott, arXiv:hep-ph/0403278.
25. G. Altarelli and F. Feruglio, Nucl. Phys. B **720** (2005) 64;
26. J. Kubo, A. Mondragon, M. Mondragon and E. Rodriguez-Jauregui, Prog. Theor. Phys. **109** (2003) 795; T. Ohlsson and G. Seidl, Phys. Lett. B **537** (2002) 95; Nucl. Phys. B **643** (2002) 247; S. F. King and G. G. Ross, Phys. Lett. B **520** (2001) 243; Very recent models are: S.F. King, [arXiv:hep-ph/0506297]; I. Varzielos and G.G. Ross, [arXiv:hep-ph/0507176].
27. H. Fritzsch, Z.Z. Xing, Phys. Lett. B372, 265 (1996); H. Fritzsch, Z.Z. Xing, Phys. Lett. B440, 313 (1998); H. Fritzsch, Z.Z. Xing, Prog. Part. Nucl. Phys. 45, 1 (2000); M. Fukugita, M. Tanimoto, T. Yanagida, Phys. Rev. D57 (1998) 4429; Phys. Rev. D59, 113016 (1999); M. Tanimoto, T. Watari, T. Yanagida Phys. Lett. B461, 345 (1999); S. K. Kang and C. S. Kim, Phys. Rev. D **59**, 091302 (1999); M. Tanimoto, Phys. Lett. B **483**, 417 (2000); N. Haba, Y. Matsui, N. Okamura, T. Suzuki, Phys. Lett. B489, 184 (2000). Y. Koide and A. Ghosal, Phys. Lett. B **488**, 344 (2000); E. K. Akhmedov, G. C. Branco, F. R. Joaquim and J. I. Silva-Marcos, Phys. Lett. B **498**, 237 (2001).
28. R. Gatto, G. Morchio, G. Sartori and F. Strocchi, Nucl. Phys. B **163** (1980) 221; J. I. Silva-Marcos, JHEP **0307** (2003) 012; C. I. Low and R. R. Volkas, Phys. Rev. D **68** (2003) 033007; C. I. Low, arXiv:hep-ph/0404017. Y. Koide, Phys. Rev. D **71** (2005) 016010; F. Feruglio, Nucl. Phys. Proc. Suppl. **143** (2005) 184;

SESSION III – QCD

- *Mario Martinez* Studies of Jet Properties at the Tevatron
- *Davide Boscherini* Hadron Spectroscopy and Heavy Flavours
Production at HERA
- *Michail Danilov* Experimental Review on Pentaquarks
- *Andrei L. Kataev* Renormalons at the Boundaries Between Perturbative
and Non-Perturbative QCD

STUDIES OF JET PROPERTIES AT THE TEVATRON

Mario Martínez

Instituto de Física de Altas Energías Universidad Autónoma de Barcelona

E-80193 Bellaterra (Barcelona) Spain

(On behalf of the CDF Collaboration)

Abstract

In this contribution, a number of new QCD results on jet production from the CDF and DØ experiments in Run II are discussed in detail.

1 Introduction

The Run II at the Tevatron will define a new level of precision for QCD studies in hadron collisions. Both collider experiments, CDF and D0, expect to collect up to 8 fb^{-1} of data in this new run period. The increase in instantaneous luminosity, center-of-mass energy (from 1.8 TeV to 2 TeV) and the improved acceptance of the detectors will allow stringent tests of the Standard Model (SM) predictions in extended regions of jet transverse momentum, P_T^{jet} , and jet rapidity, Y^{jet} . The hadronic final states in hadron-hadron collisions are characterized by the presence of soft contributions (the so-called *underlying event*) from initial-state gluon radiation and multiple parton interactions between remnants, in addition to the jets of hadrons originated by the hard interaction. A proper comparison with pQCD predictions at the parton level requires an adequate modeling of these soft contributions which become important at low P_T^{jet} . In this letter, a review of some of the most important QCD results from Run II is presented.

2 Inclusive Jet Production at the Tevatron

The measurement of the inclusive jet production cross section for central jets constitutes one of the pillars of the jet physics program at the Tevatron. It provides a stringent test of perturbative QCD predictions over almost nine orders of magnitude and probes distances up to $\sim 10^{-19} \text{ m}$. Thanks to the increase in the center-of-mass energy in Run II the jet production rate has been multiplied (by a factor of five for jets with $P_T^{\text{jet}} > 600 \text{ GeV}$) and the first measurements have already extended the P_T^{jet} coverage by 150 GeV compared to Run I. In addition, both CDF and D0 experiments explore new jet algorithms following the theoretical work that indicates that the cone-based jet algorithm employed in Run I is not infrared safe and compromises a future meaningful comparison with pQCD calculations at NNLO. Figure 1 shows the measured inclusive jet cross section by CDF using the longitudinally invariant K_T algorithm ¹⁾ and based on the first 145 pb^{-1} of Run II data. Measurements have been performed using values for the D parameter in the K_T expression,

$$K_{ij} = \min(p_{T,i}^2, p_{T,j}^2) \cdot \frac{(y_i - y_j)^2 + (\phi_i - \phi_j)^2}{D}, \quad (1)$$

equal to 0.5, 0.7 and 1.0. The measurements are compared to pQCD NLO calculations ²⁾ using CTEQ6 ³⁾ parton density functions in the proton and antiproton and the renormalization and factorization scales set to $p_T^{\text{max}}/2$. The measured cross section is reasonably well described by the predictions for $P_T^{\text{jet}} > 150 \text{ GeV}$ within the present uncertainties. The systematic errors on

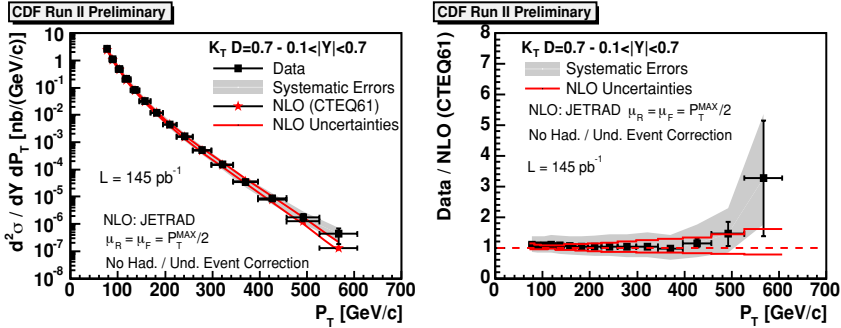


Figure 1: *The measured inclusive jet cross section compared to pQCD NLO predictions. Jets are searched for using the longitudinally invariant K_T algorithm.*

the data are dominated by the uncertainty on the jet energy scale determination while the theoretical predictions suffer from our limited knowledge of the gluon distribution at high x . At lower P_T^{jet} , the data is systematically above the predictions and the effect increases as D increases (see Figure 2). This indicates the presence of soft-gluon contributions and fragmentation effects that have not been taken into account yet.

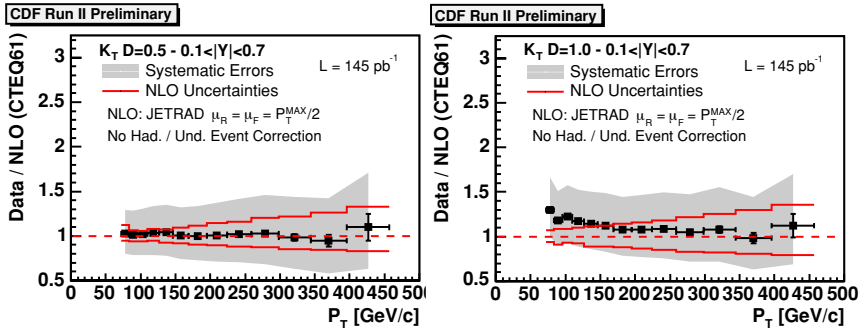


Figure 2: *Ratio between the measured inclusive jet cross section and the pQCD NLO predictions using the K_T algorithm with $D=0.5$ and $D=0.7$, respectively.*

Figure 3 shows the measured inclusive jet cross section by D0 based on the first 143pb^{-1} of Run II data. The new midpoint⁴⁾ jet algorithm has been used with a cone size $R=0.7$. This algorithm constitutes an improved version of the cone-based algorithm used in Run I and it is shown to be infrared safe when used in fixed-order parton-level calculations. The data is in good agreement

with the pQCD NLO predictions using CTEQ6 parton density functions and $R_{\text{sep}} = 1.3$. However, the measurement is dominated by a relatively large uncertainty on the absolute jet energy scale. Figure 4 shows the measured

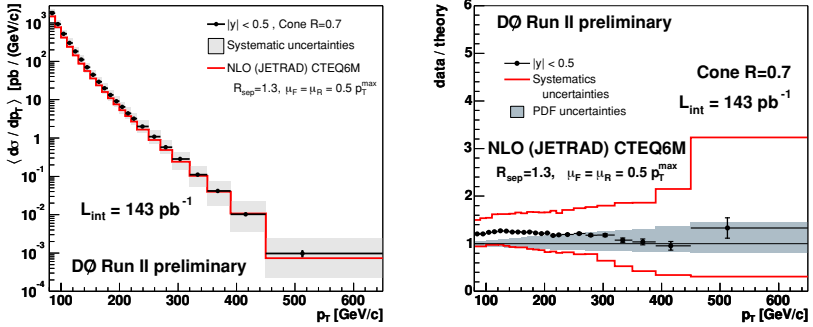


Figure 3: *The measured inclusive jet cross section by D0 compared to pQCD NLO predictions. Jets are searched for using the midpoint jet algorithm.*

cross section by D0 as a function of the dijet invariant mass in dijet production of central jets. This measurement is particularly sensitive to the presence of narrow resonances decaying into jets of hadrons up to masses of 1.3 TeV. The data is well described by pQCD NLO predictions.

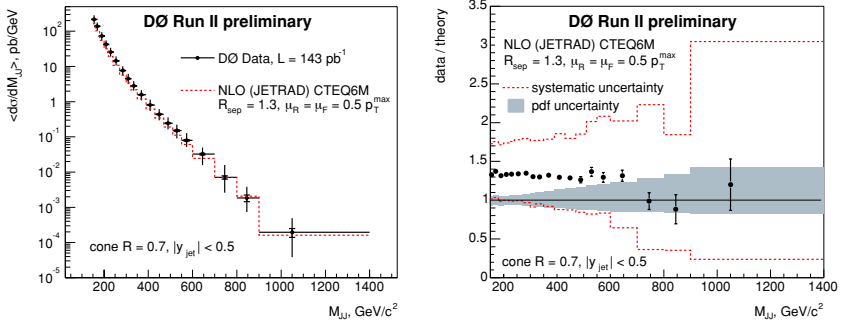


Figure 4: *The measured inclusive dijet cross section by D0 as a function of the dijet mass compared to pQCD NLO predictions.*

Nowadays, the Tevatron high- P_T^{jet} jet data is used, together with prompt-photon data from fixed target experiments, to constrain the gluon distribution at high- x . Jet measurements at large rapidities are important because they

constrain the gluon density in a region in P_T^{jet} where no effect from new physics is expected. The D0 experiment has already extended the jet cross section measurements to the forward region for jets with $|y| < 2.4$ (see Figure 5). At

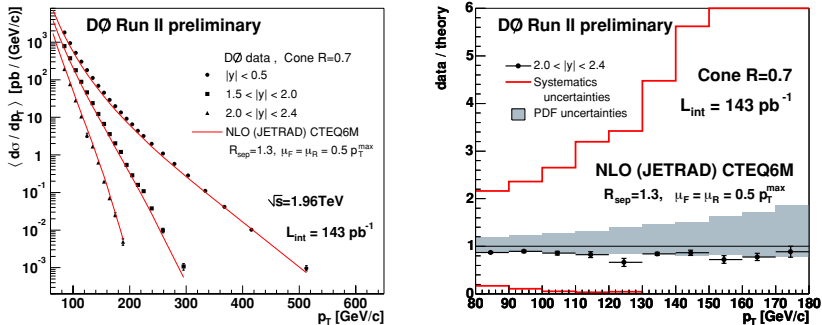


Figure 5: (Left) measured inclusive jet cross section by D0 in different regions of rapidity compared to pQCD NLO predictions. (Right) ratio between the measurements and the pQCD NLO predictions for jets with $2.0 < |y| < 2.4$.

the moment, the results are affected by large systematic errors. In the near future the experiments will highly reduce their uncertainties and precise cross section measurements will allow to further constrain the gluon distribution and thus enhance their sensitivity to new physics at very high P_T^{jet} .

3 Study of the Underlying Event

As mentioned in previous section, the hadronic final states at the Tevatron are characterized by the presence of soft underlying emissions, usually denoted as *underlying event*, in addition to highly energetic jets coming from the hard interaction. The underlying event contains contributions from initial- and final-state soft gluon radiation, secondary semi-hard partonic interactions and interactions between the proton and anti-proton remnants that cannot be described by perturbation theory. These processes must be approximately modeled using Monte Carlo programs tuned to describe the data. The jet energies measured in the detector contain an underlying event contribution that has to be subtracted in order to compare the measurements to pQCD predictions. Hence, a proper understanding of this underlying event contribution is crucial to reach the desired precision in the measured jet cross sections. In the analysis presented here, the underlying event in dijet production has been studied by looking at regions well separated from the leading jets, where the underlying event contribution is expected to dominate the observed hadronic

activity. Jets have been reconstructed using tracks with $p_T^{\text{track}} > 0.5$ GeV and $|\eta^{\text{track}}| < 1$ and a cone algorithm with $R=0.7$. The ϕ space around the leading jet is divided in three regions: *towards*, *away* and *transverse* (see Figure 6-left), and the transverse region is assumed to reflect the underlying event contribution. Figure 6-right shows the average track density in the transverse region

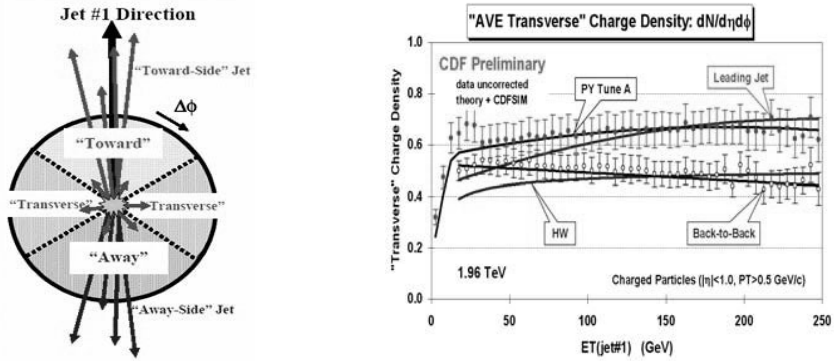


Figure 6: (Left) Scheme of the different ϕ regions defined around the leading jet. (Right) Measured average track density in the transverse region as a function of the E_T^{jet} of the leading jet. The measurements are compared to different Monte Carlo models.

as a function of E_T^{jet} of the leading jet for the dijet inclusive sample and for events where the leading jets are forced to be back-to-back in ϕ , in order to further reduce extra hard-gluon radiation. The observed plateau indicates that the underlying event activity is, to a large extent, independent from the hard interaction. The measurements have been compared to the predictions from PYTHIA ⁵⁾ and HERWIG ⁶⁾ Monte Carlo programs including leading-order QCD matrix elements plus initial and final parton showers. The PYTHIA samples have been created using a special tuned set of parameters, denoted as PYTHIA-Tune A, which includes an enhanced contribution from initial-state soft gluon radiation and a tuned set of parameter to control secondary parton interactions. It was determined as a result of similar studies of the underlying event performed using CDF Run I data ⁷⁾. PYTHIA-Tune A describes the hadronic activity in transverse region while HERWIG underestimates the radiation at low E_T^{jet} . Similar measurements in Z+jet(s) events would allow to explore the univesality of the underlying event contribution in events with a very different colour configuration in the final state.

4 Jet Shapes

The internal structure of jets is dominated by multi-gluon emissions from the primary final-state parton. It is sensitive to the relative quark- and gluon-jet fraction and receives contributions from soft-gluon initial-state radiation and beam remnant-remnant interactions. The study of jet shapes at the Tevatron provides a stringent test of QCD predictions and tests the validity of the models for parton cascades and soft-gluon emissions in hadron-hadron collisions. The CDF experiment has presented results on jet shapes for central jets with transverse momentum in the region $37 \text{ GeV} < P_T^{\text{jet}} < 380 \text{ GeV}$, where jets are searched for using the midpoint¹ algorithm and a cone size $R = 0.7$. The integrated jet shape, $\Psi(r)$, is defined as the average fraction of the jet transverse momentum that lies inside a cone of radius r concentric to the jet cone:

$$\Psi(r) = \frac{1}{N_{\text{jet}}} \sum_{\text{jets}} \frac{P_T(0, r)}{P_T(0, R)}, \quad 0 \leq r \leq R \quad (2)$$

where N_{jet} denotes the number of jets. The measured jet shapes have been compared to the predictions from PYTHIA-Tune A and HERWIG Monte Carlo programs.

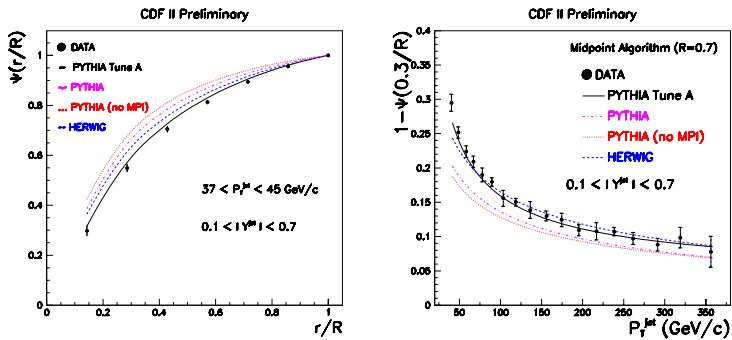


Figure 7: The measured integrated jet shape compared to different Monte Carlo predictions.

In addition, two different PYTHIA samples have been used with default parameters and with and without the contribution from multiple parton interactions (MPI) between proton and antiproton remnants, the latter denoted as PYTHIA-(no MPI), to illustrate the importance of a proper modeling of soft-gluon radiation in describing the measured jet shapes. Figure 7(left) presents

¹A 75% merging fraction has been used instead of the default 50%.

the measured integrated jet shapes, $\Psi(r/R)$, for jets with $37 < P_T^{\text{jet}} < 45$ GeV, compared to HERWIG, PYTHIA-Tune A, PYTHIA and PYTHIA-(no MPI) predictions. In addition, Figure 7(right) shows, for a fixed radius $r_0 = 0.3$, the average fraction of the jet transverse momentum outside $r = r_0$, $1 - \Psi(r_0/R)$, as a function of P_T^{jet} where the points are located at the weighted mean in each P_T^{jet} range. The measurements show that the fraction of jet transverse momentum at a given fixed r_0/R increases ($1 - \Psi(r_0/R)$ decreases) with P_T^{jet} , indicating that the jets become narrower as P_T^{jet} increases. PYTHIA with default parameters produces jets systematically narrower than the data in the whole region in P_T^{jet} . The contribution from secondary parton interactions between remnants to the predicted jet shapes (shown by the difference between PYTHIA and PYTHIA-(no MPI) predictions) is relatively small and decreases as P_T^{jet} increases. PYTHIA-Tune A predictions describe all of the data well. HERWIG predictions describe the measured jet shapes well for $P_T^{\text{jet}} > 55$ GeV but produces jets that are too narrow at lower P_T^{jet} . Figure 8(left) shows the

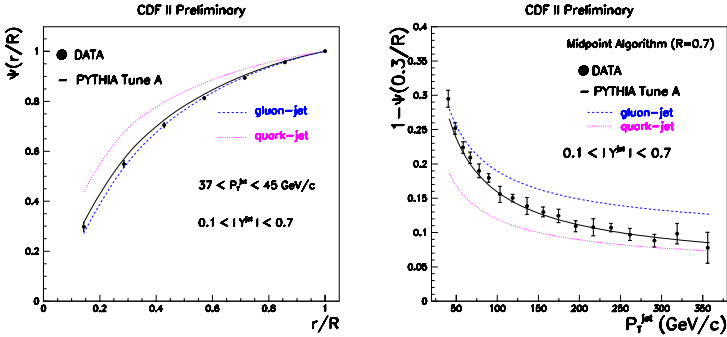


Figure 8: *The measured integrated jet shape compared to the predictions of PYTHIA-Tune A and the separated contributions from quark- and gluon-jets.*

measured integrated jet shapes, $\Psi(r/R)$, for jets with $37 < P_T^{\text{jet}} < 45$ GeV, compared to PYTHIA-Tune A and the predictions for quark- and gluon-jets² separately. Figure 8(right) shows the measured $1 - \Psi(r_0/R)$, $r_0 = 0.3$, as a function of P_T^{jet} . The Monte Carlo predictions indicate that the measured jet shapes are dominated by contributions from gluon-initiated jets at low P_T^{jet} while contributions from quark-initiated jets become important at high P_T^{jet} .

²Each hadron-level jet from PYTHIA is classified as a quark- or gluon-jet by matching ($y - \phi$ plane) its directions with that of one of the outgoing partons from the hard interaction.

This can be explained in terms of the different partonic contents in the proton and antiproton in the low- and high- P_T^{jet} regions, since the mixture of gluon- and quark-jet in the final state partially reflects the nature of the incoming partons that participate in the hard interaction. For a given type of parton-jet in the Monte Carlo (quark- or gluon-jet), the observed trend with P_T^{jet} shows the running of the strong coupling constant, $\alpha_s(P_T^{\text{jet}})$. Jet shape measurements thus introduce strong constraints on phenomenological models describing soft-gluon radiation and the underlying event in hadron-hadron interactions. Similar studies with b-tagged jets will be necessary to test our knowledge of b-quark jet fragmentation processes in hadronic interactions, which is essential for future precise Top and Higgs measurements.

5 $\Delta\phi_{\text{dijet}}$ Decorrelations

The D0 experiment has employed the dijet sample to study azimuthal decorrelations, $\Delta\phi_{\text{dijet}}$, between the two leading jets. The normalized cross section:

$$\frac{1}{\sigma_{\text{dijet}}} \frac{d\sigma}{d\Delta\phi_{\text{dijet}}} \quad (3)$$

is sensitive to the spectrum of the gluon radiation in the event. The measurements has been performed in different regions of the leading jet P_T^{jet} starting at $P_T^{\text{jet}} > 75$ GeV and the second jet is required to have at least $P_T^{\text{jet}} > 40$ GeV.

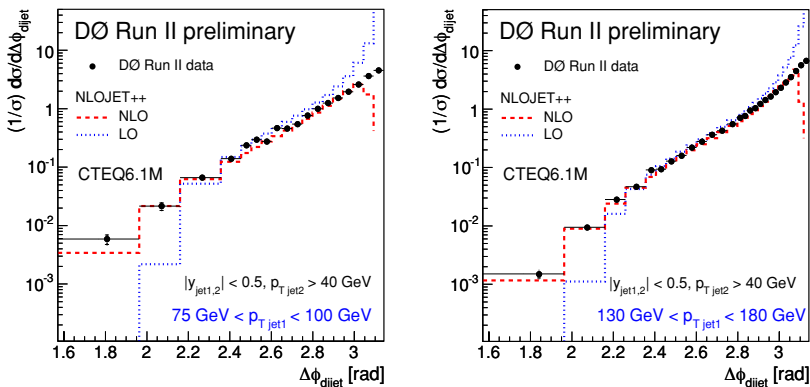


Figure 9: Measured azimuthal decorrelations in dijet production for central jets compared to p QCD predictions in different regions of P_T^{jet} of the leading jet.

Figure 9 shows the measured cross section compared to LO and NLO predictions from NLOJET++ program ⁸⁾. The LO predictions, with at most

three partons in the final state, is limited to $\Delta\phi_{\text{dijet}} > 2\pi/3$, for which the three partons define a *Mercedes-star* topology. It presents a prominent peak at $\Delta\phi_{\text{dijet}} = \phi$ corresponding to the soft limit for which the third parton is collinear to the direction of the two leading partons. The NLO predictions, with four partons in the final state, describes the measured $\Delta\phi_{\text{dijet}}$ distribution except at very high and very low values of $\Delta\phi_{\text{dijet}}$ where additional soft contributions, corresponding to a resummed calculation, are necessary. A reasonable approximation to such calculations is provided by parton shower Monte Carlo programs.

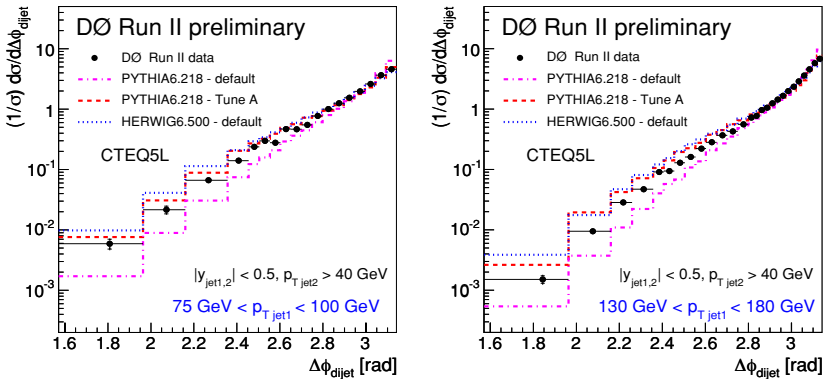


Figure 10: Measured azimuthal decorrelations in dijet production for central jets compared to PYTHIA and HERWIG predictions in different regions of leading P_T^{jet} .

Figure 10 presents the measured cross section compared to PYTHIA-Tune A, PYTHIA and HERWIG predictions in different regions of P_T^{jet} . PYTHIA with default parameters underestimates the gluon radiation at large angles. PYTHIA-Tune A predictions, which include an enhanced contribution from initial-state soft gluon radiation and secondary parton interactions, describe the azimuthal distribution. HERWIG also describes the data although tends to produce less radiation than PYTHIA-Tune A close to the direction of the leading jets.

6 Summary and Conclusions

Both CDF and D0 experiments have carried out measurements of the inclusive jet production cross section in Run II at the Tevatron using different jet algorithms. The measurements are in agreement with pQCD NLO predictions. Dedicated studies of the underlying event, jet shapes and azimuthal decorrela-

tions in dijet final states allowed to establish the validity of the Monte Carlo models used to describe the soft-gluon contributions in the final state.

7 Acknowledgements

I thank the organizers for their kind invitation to the conference and for the exciting program of talks and discussions they made possible.

References

1. Stephen D. Ellis, Davision E. Soper, *Phys.Rev.* **D 48** 3160-3166 (1993).
2. W.T. Giele, E.W.N. Glover, D.A. Kosower, *Nucl. Phys.***B 403** 633 (1993).
3. J. Pumplin et al., *JHEP* **0207** 012 (2002).
4. G. C. Blazey, et al., hep-ex/0005012.
S.D. Ellis, J. Huston and M. Toennesmann, hep-ph/0111434.
5. H.-U. Bengtsson and T. Sjöstrand, *Comp. Phys. Comm.* **46** 43 (1987).
6. G. Marchesini et al., *Comp. Phys. Comm.* **67** 465 (1992).
7. D. Acosta et al., CDF Collaboration, *Phys. Rev.* **D65**, 092002 (2002).
8. Zoltán Nagy, Zoltán Trócsányi, *Phys.Rev.Lett.* **79** 3604 (1997).

HADRON SPECTROSCOPY AND HEAVY FLAVOUR PRODUCTION AT HERA

Boscherini Davide

INFN - Bologna

on behalf of the H1 and ZEUS Collaborations

Abstract

Studies of charm and beauty production in ep collisions with a center-of-mass energy of 318 GeV are reported from the two HERA collaborations, H1 and ZEUS. The results are from data collected during the HERA phase I and are compared to the available next-to-leading order QCD calculations. Results on the search for pentaquark states are also shown for the same data taking period.

1 Heavy Flavour Production

The study of heavy flavour processes in ep collisions at HERA is a powerful tool for exploring the dynamics of the strong interactions described by the Quantum Chromodynamics (QCD) and for testing the proton structure function.

The production of heavy quarks in ep collisions at HERA mainly occurs via the process of boson-gluon fusion. The kinematic region covers photoproduction, in which the exchanged photon is quasi-real ($Q^2 \sim 0$), to the region of deep inelastic scattering (DIS), with photon virtualities much larger than the c - or b -quark mass. The large value of the heavy quark mass provides a scale for perturbative calculations which are therefore expected to give reliable results. Two schemes are available for next-to-leading order (NLO) QCD calculations:

- *massive scheme* ¹⁾, where u , d and s are the only active flavours in the proton and the photon, and charm and beauty are produced dynamically in the hard scattering
- *massless scheme* ²⁾ where charm and beauty are treated as active flavours in both the proton and the photon, in addition to u , d and s . In this scheme, so-called *excitation processes* occur in which the beauty quark is a constituent of the resolved photon or of the proton.

The former scheme is expected to give better results for transverse momenta of the b -quark of the order of its own mass, while the latter is more reliable for larger transverse momenta.

1.1 Inclusive Production of D^+ , D^0 , D_s^+ and D^{*+} Mesons in DIS

The production of charm quarks is expected to be well described by perturbative QCD (pQCD) calculations due to the hard scale provided by the charm mass. However, the hadronization of a charm quark into a cluster of hadrons involves non-perturbative processes. Therefore, a theoretical description of the production of charmed hadrons contains a phenomenological, non-perturbative part, which is expected to be process independent.

The visible cross sections of D^+ , D^0 , D_s^+ and D^{*+} have been measured by H1 ³⁾ making use of the following decay channels: $D^+ \rightarrow K^- \pi^+ \pi^+$, $D^0 \rightarrow K^- \pi^+$, $D_s^+ \rightarrow \phi \pi^+ \rightarrow (K^+ K^-) \pi^+$ and $D^{*+}(2010) \rightarrow D^0 \pi^+ \rightarrow (K^- \pi^+) \pi^+$. The relatively large life time of the weakly-decaying D -mesons makes it possible to reconstruct the displacement of their decay point with respect to the primary vertex, using the central silicon tracker and to apply selection cuts on the reconstructed secondary vertices. The number of signal events is determined for each D-meson individually, by fitting the invariant mass distribution with an appropriate background function and a Gaussian to describe the signal.

The measured cross sections are reported in table 1. The comparison with a LO Monte Carlo is quite satisfactory. Preliminary results ⁴⁾ have been obtained by ZEUS on the same subject and they show a good agreement with NLO QCD predictions.

Cross section [nb]	D^+	D^0	D_s^+	D^{*+}
$\sigma_{vis}(ep \rightarrow eDX)$	2.16	6.53	1.67	2.90
Stat. error	± 0.19	± 0.49	± 0.41	± 0.20
Syst. error	+0.46 -0.35	+1.06 -1.30	+0.54 -0.54	+0.58 -0.44
AROMA LO prediction σ_{vis}	2.45	5.54	1.15	2.61
Prediction uncertainty	± 0.30	± 0.69	± 0.30	± 0.31
Estimated beauty contribution	10%	9%	17%	7%

Table 1: *Inclusive charmed meson electroproduction cross sections for the four meson states in the visible kinematic range, defined by $2 \leq Q^2 \leq 100 \text{ GeV}^2$, $0.05 \leq y \leq 0.7$, $p_t(D) \geq 2.5 \text{ GeV}$ and $|\eta(D)| \leq 1.5$. Also given are the predictions for D meson production (including the beauty contribution) based on a LO Monte Carlo simulation.*

The fragmentation fractions $f(c \rightarrow D)$ are defined as the ratio of the total cross section of a given charmed meson to the one for a charm quark. Using a Monte Carlo model to extrapolate from the visible to the total cross section for the charmed meson, the fragmentation factors shown in fig.1, together with the LEP results, were obtained.

These results agree well with the measurements performed in e^+e^- and thus support the assumption of a universal fragmentation.

1.2 Measurement of $F_2^{c\bar{c}}$ and $F_2^{b\bar{b}}$ at High Q^2

Inclusive c and b cross sections have been measured by H1 for $Q^2 > 150 \text{ GeV}^2$. Events containing heavy quarks can be distinguished from light quark events exploiting the long lifetimes of c and b flavoured hadrons, which lead to displacements of tracks from the primary vertex. The distance of a track to the primary vertex is reconstructed using precise spatial information from the vertex detector. The measurement of $F_2^{c\bar{c}}$ and $F_2^{b\bar{b}}$ has been done in a kinematic region where there is little extrapolation needed to correct to the full phase space; therefore the model dependent uncertainty due to the extrapolation is small. In fig.2 the ratios $F_2^{c\bar{c}}/F_2$ and $F_2^{b\bar{b}}/F_2$ are shown. The measurement of $F_2^{b\bar{b}}$ has been performed by H1 for the first time ¹²⁾. The contribution of charm to F_2 can be estimated to be around 10-30% in the kinematic region

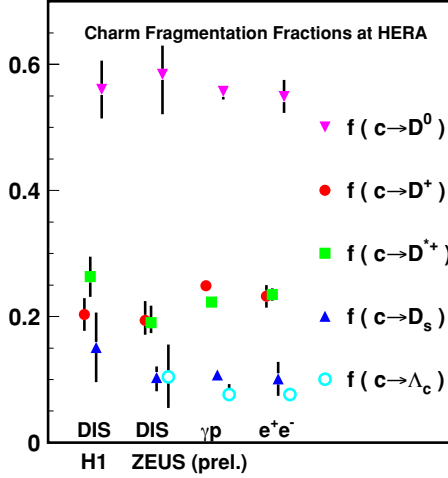


Figure 1: *Fragmentation factors for the different D mesons (and Λ_c). Measurements from H1 and ZEUS are shown together with e^+e^- results.*

considered, while the contribution from beauty is approximately an order of magnitude lower.

1.3 Measurement of Beauty Production Using Events with Muons and Jets

For beauty production, pQCD calculations are expected to give reliable predictions, as the mass of the b quark ($m_b \sim 5$ GeV) provides a hard scale. The first measurements of beauty cross section at HERA ⁷⁾ were higher than pQCD predictions calculated at next-to-leading order (NLO). Similar observations were made in hadron-hadron collisions ⁸⁾ and also in two-photon interactions ⁹⁾.

The cross section for the process $ep \rightarrow e\bar{b}bX \rightarrow ejj\mu X'$ in photoproduction and $ep \rightarrow e\bar{b}bX \rightarrow ejj\mu X'$ in deep inelastic scattering have been measured. To discriminate events containing beauty from those with charm or light quarks, H1 ¹¹⁾ has used two distinct features of the B-hadrons simultaneously, for the first time at HERA: the large mass and the long lifetime. The B-hadron mass leads to a broad distribution of the transverse momentum p_t^{rel} of the decay muon relative to the beauty quark jet direction. The B-hadron lifetime is reflected in the large impact parameters $\delta \sim 200 \mu m$ of the decay muon tracks relative to the primary vertex. Only the first method has been used by ZEUS ¹⁰⁾ because of the lack of a precision vertex detector during HERA I. The results obtained by the two experiments are shown in fig.3, together with the NLO predictions in the respective kinematic range of

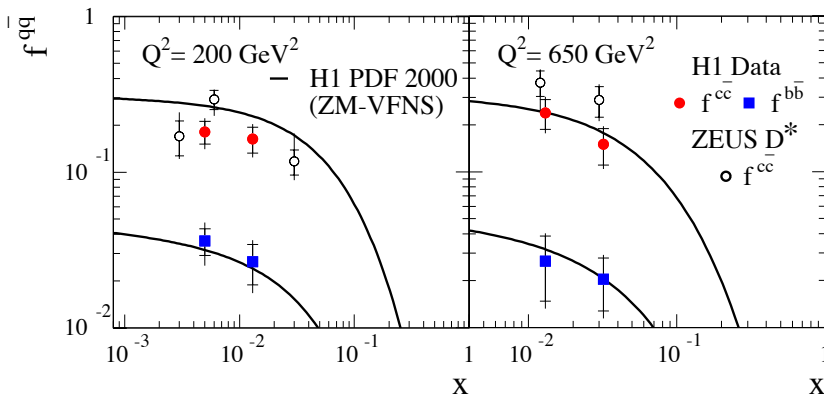


Figure 2: The contributions to the total cross section $f^{c\bar{c}}$ and $f^{b\bar{b}}$ shown as a function of x for two different Q^2 values. The inner error bars show the statistical error, the outer error bars represent the statistical and systematic errors added in quadrature. The $f^{c\bar{c}}$ from ZEUS obtained from measurements of D^* mesons ⁵⁾ and the prediction of the H1 NLO QCD fit ⁶⁾ are also shown.

the measurements. The data tends to be above the theory, but the agreement is considerably improved with respect to the previous measurements.

1.4 Summary on Heavy Flavour Production

The results shown on charm DIS cross sections are in good agreement with the NLO QCD predictions. The charm fragmentation factors measured at HERA are compatible with those obtained in e^+e^- collisions. In the beauty sector, the production cross section is in much better agreement with NLO QCD predictions with respect to the previous measurements, but there is still present a tendency for data to be above the theory. The first measurement of $F_2^{b\bar{b}}$ for $Q^2 > 150 \text{ GeV}^2$ has been performed by H1.

2 Pentaquark Searches

Several experiments have recently reported the observation of a narrow resonance with mass in the region of 1540 MeV, decaying to K^+n or K_s^0p ¹³⁾. This state has both baryon number and strangeness +1, such that its minimal composition in the constituent quark model is $uudds$. It has thus been interpreted as a pentaquark, the Θ^+ . There is also evidence for two related

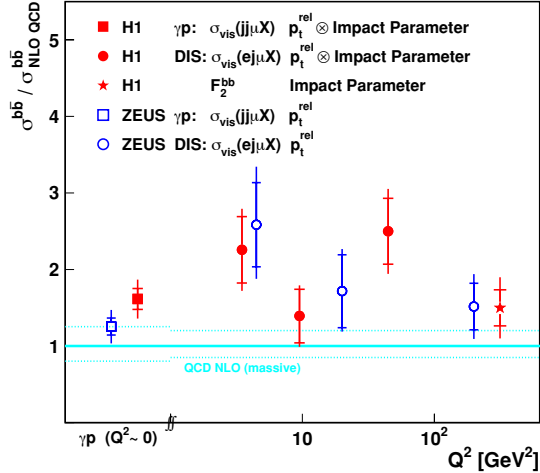


Figure 3: *Cross section ratios (data over theory) as a function of Q^2 for the processes $ep \rightarrow ebbX \rightarrow ejj\mu X'$ in photoproduction and $ep \rightarrow ebbX \rightarrow ej\mu X'$ in DIS, as measured by H1 and ZEUS.*

states with strangeness -2¹⁶⁾. Various models have been put forward to explain the nature of these states and the structure of the multiplet that contains them¹⁴⁾. The possibility of pentaquark states in the charm sector has also been considered¹⁵⁾, following the observation of strange pentaquarks.

2.1 Search for a Narrow Baryonic State Decaying to $K_S^0 p$ and $K_S^0 \bar{p}$

The luminosity of the data sample used by ZEUS is 121 pb^{-1} ¹⁷⁾. The events are selected in the kinematic range $Q^2 > 1 \text{ GeV}^2$. K_S^0 mesons are reconstructed via the decay mode $K_S^0 \rightarrow \pi^+ \pi^-$. Accepting only K_S^0 candidates with transverse momentum $p_t(K_S^0) \geq 0.3 \text{ GeV}$ and pseudorapidity $|\eta(K_S^0)| \leq 1.5$ in the laboratory frame, the number of reconstructed candidates is 866800 ± 1000 . Proton (or anti-proton) candidates are selected using the measurement of the ionization loss dE/dx in the central tracker and applying cuts based on the Bethe-Bloch equation. The purity of the proton sample, estimated from MC simulation, is around 60%. The selected K_S^0 and proton candidates are com-

binned and the invariant mass is reconstructed fixing the K_S^0 mass to the PDG value. A peak around 1520 MeV in the invariant-mass spectrum is visible for $Q^2 > 20 \text{ GeV}^2$ as shown in fig.4, while it is less pronounced in different kinematic regions. A Σ bump at 1480 MeV is reported in the PDG, therefore the invariant-mass distribution is fitted with a three-parameter background function and two Gaussians, obtaining a signal peak position of $1521 \pm 1.5(\text{stat.})$ MeV, with a width of $6.1 \pm 1.6(\text{stat.})$ MeV. The fit gives 221 ± 48 events above the background, corresponding to 4.6σ . Fitting with only one Gaussian similar results are obtained.

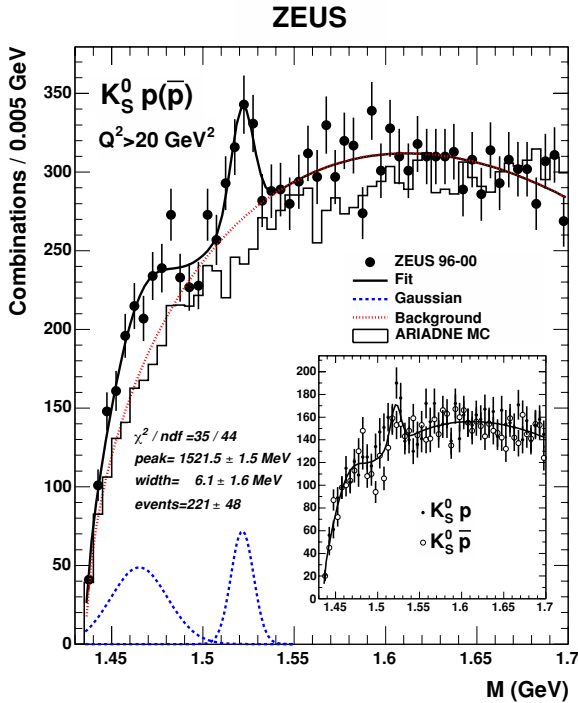


Figure 4: Invariant-mass spectrum for the $K_S^0 p(\bar{p})$ channel for $Q^2 > 20 \text{ GeV}^2$, as obtained by ZEUS. The solid line is the result of a fit to the data using a three-parameter background function plus two Gaussians. The dashed line shows the Gaussian components and the dotted line the background according to this fit. The histogram shows the prediction of the ARIADNE MC simulation normalised to the data in the mass region above 1650 MeV. The inset shows the $K_S^0 \bar{p}$ (open circles) and the $K_S^0 p$ (black dots) candidates separately, compared to the result of the fit to the combined sample scaled by a factor of 0.5.

2.2 Search for a Narrow Charmed Baryonic State Decaying to $D^{*+}\bar{p}(D^{*-}p)$

The data analysed by the H1 collaboration correspond to an integrated luminosity of 76 pb^{-1} (18). The events are selected in the kinematic range $Q^2 > 1 \text{ GeV}^2$ and $0.05 < y < 0.7$. The D^* mesons are reconstructed via the decay channel $D^* \rightarrow D^0\pi^+ \rightarrow (K^-\pi^+)\pi^+$. D^* candidates with $p_t(D^*) > 1.5 \text{ GeV}$ and $-1.5 < \eta(D^*) < 1$ are combined with oppositely charged proton candidates selected according to the proton likelihood based on the particle energy loss dE/dx in the central trackers. A clear peak is visible in the invariant mass distribution $M(D^*p)$, as shown in fig.5, where a fit with a Gaussian distribution added to an appropriate background function is superimposed. The result of the fit for the peak position is $M(D^*p) = 3099 \pm 3(\text{stat.}) \text{ MeV}$ with a root-mean-square width for the Gaussian of $12 \pm 3(\text{stat.})$.

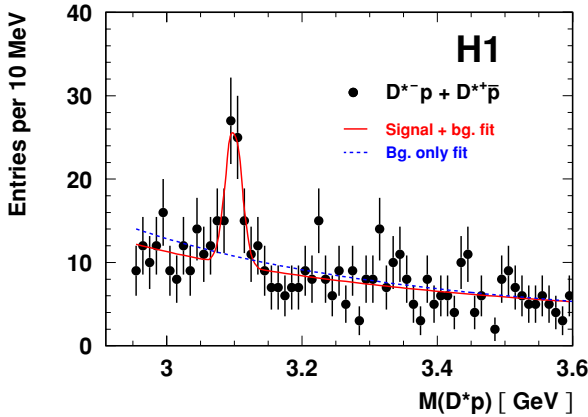


Figure 5: $M(D^*p)$ distribution from opposite-charge D^*p combinations, as obtained by H1. The data are compared with the result of a fit in which both signal and background components are included (solid line) and with the result of a fit in which only the background component is included (dashed line).

The signal consists of $N_s = 50.6 \pm 11.2$ events, from which the observed D^*p resonance is estimated to contribute roughly to 1% of the total D^* production rate in the kinematic region studied.

A similar analysis (19) has been performed by ZEUS using an integrated luminosity of 126 pb^{-1} . No resonance structure was observed in the $M(D^{*\pm}p^\mp)$ spectrum from more than 60 000 reconstructed $D^{*\pm}$ mesons. An upper limit of 0.23% (95% C.L.) has been set on the fraction of D^* mesons originating from Θ_c^0 decays. The upper limit for DIS with $Q^2 > 1 \text{ GeV}^2$ is 0.35% (95% C.L.), not compatible with the value of around 1% found by H1.

2.3 Search for Pentaquarks Decaying to $\Xi\pi$ in DIS

Recently, the experiment NA49 at the CERN SPS reported the observation of the $\Xi_{3/2}^{--}$ and $\Xi_{3/2}^0$ members of the $\Xi_{3/2}$ multiplet¹⁶⁾. These states would lie at the bottom of the hypothetical antidecuplet of pentaquarks with the Θ^+ at the apex, and, while $\Xi_{3/2}^0$ would have an ordinary charge assignment, $\Xi_{3/2}^{--}$ is manifestly exotic with minimal quark content $ddss\bar{u}$. ZEUS used an integrated luminosity of 121 pb^{-1} to search for new baryonic states in the $\Xi^-\pi^\pm$ and $\Xi^+\pi^\pm$ invariant-mass spectra²⁰⁾. The Ξ^- (Ξ^+) states were reconstructed via the $\Lambda\pi^-$ ($\bar{\Lambda}\pi^+$) decay channel. The Λ baryons were identified by their charged decay mode, $\Lambda \rightarrow p\pi^-$, using pairs of tracks from secondary vertices. The resulting $\Xi\pi$ invariant-mass spectrum is shown in fig.6(a) where a clean $\Xi^0(1530)$ state is observed, while no pentaquark signal is found in the region predicted by NA49. In fig.6(b) the invariant-mass spectrum is shown for $Q^2 > 20 \text{ GeV}^2$, the kinematic region where the Θ^+ signal was best seen by ZEUS. No pentaquark signal is seen in this restricted kinematic region.

ZEUS

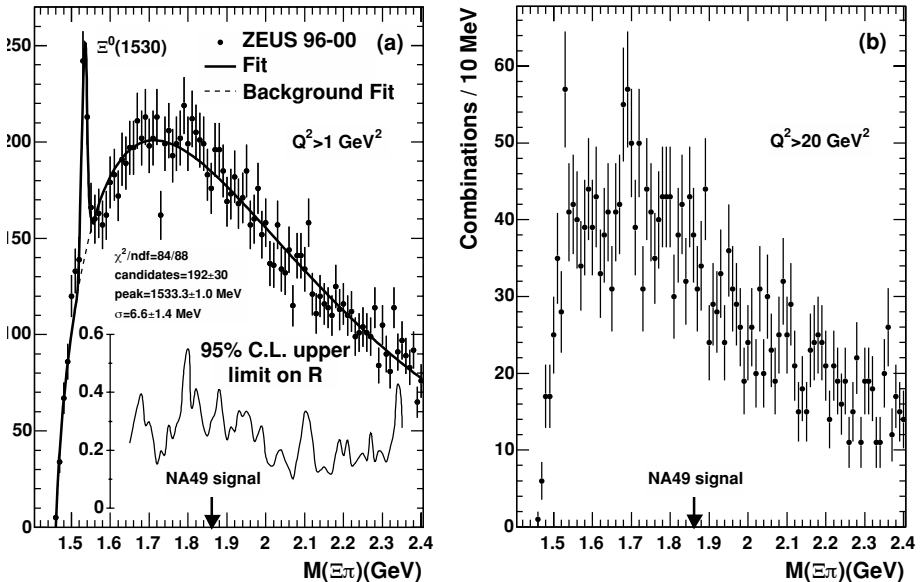


Figure 6: The $\Xi\pi$ invariant-mass spectrum for: (a) $Q^2 > 1 \text{ GeV}^2$ and, (b) $Q^2 > 20 \text{ GeV}^2$, as measured by ZEUS. The solid line in (a) is the result of a fit to the data using a Gaussian plus a three-parameter background function. The dashed line shows the background according to this fit.

2.4 Summary on Pentaquark Searches

The hypothetical pentaquark state $\Theta^+(1530)$ has been searched for by ZEUS. A signal with a statistical significance of 4.6σ has been observed in the kinematic region of $Q^2 > 20 \text{ GeV}^2$.

A clear signal has been found by H1 in searching for the charmed pentaquark state $\Theta_c^0(3100)$. This signal has not been confirmed by ZEUS, despite the larger statistical sample available.

ZEUS also has a negative result for searching for the pentaquark state $\Xi^{--}(1860)$ whose observation was recently reported by the NA49 collaboration.

References

1. S. Frixione, P. Nason and G. Ridolfi, Nucl. Phys. B **454**, 3 (1995) [hep-ph/9506226];
M. Cacciari, S. Frixione and P. Nason, JHEP **0103**, 006 (2001);
B.W. Harris and J. Smith, Nucl. Phys. B **452**, 109 (1995).
2. B.A. Kniehl *et al*, Phys. Lett. B **356**, 539 (1995) [hep-ph/9505410];
B.A. Kniehl, M. Krämer and M.Spira, Z. Phys. C **76**, 689 (1997) [hep-ph/9610267];
J. Binnewies, B.A. Kniehl and G. Kramer, Z. Phys. C **76**, 677 (1997) [hep-ph/9702408];
J. Binnewies, B.A. Kniehl and G. Kramer, Phys. Rev. D **58**, 014014 (1998) [hep-ph/9712482];
3. A. Aktas *et al* [H1 Collaboration], [hep-ex/0408149].
4. S. Chekanov *et al* [ZEUS Collaboration], paper submitted to ICHEP-2004, abstract: 5-0344, 11-0345.
5. S. Chekanov *et al* [ZEUS Collaboration], Phys. Rev. D **69**, 012004 (2004) [hep-ph/0308068].
6. C. Adloff *et al* [H1 Collaboration], Eur. Phys. J. C **30**, 1 (2003) [hep-ex/0304003].
7. C. Adloff *et al* [H1 Collaboration], Phys. Lett. B **467**, 156 (1999) [hep-ex/9909029]; [Erratum-ibid. B **518**, 331 (2001)];
J. Breitweg *et al* [ZEUS Collaboration], Eur. Phys. J. C **18**, 625 (2001) [hep-ex/0011081].
8. F. Abe *et al* [CDF Collaboration], Phys. Rev. Lett. **71**, 2396 (1993);
F. Abe *et al* [CDF Collaboration], Phys. Rev. D **53**, 1051 (1996) [hep-ex/9508017];

- S. Abachi *et al* [D0 Collaboration], Phys. Rev. Lett. **74**, 3548 (1995);
S. Abachi *et al* [D0 Collaboration], Phys. Rev. Lett. B **370**, 239 (1996).
9. M. Acciarri *et al* [L3 Collaboration], Phys. Lett. B **503**, 10 (2001) [hep-ex/0011070].
10. J. Breitweg *et al* [ZEUS Collaboration], Phys. Lett. B **599**, 173 (2004);
Phys. Rev. D **70**, 012008 (2004)
11. C. Adloff *et al* [H1 Collaboration], hep-ex/0502010.
12. C. Adloff *et al* [H1 Collaboration], DESY 04-209.
13. T. Nakano *et al* [LEPS Collaboration], Phys. Rev. Lett. **91**, 012002 (2003);
J. Barth *et al* [SAPHIR Collaboration], Phys. Lett. B **572**, 127 (2003);
V. Kubarovskiy *et al* [CLAS Collaboration], Phys. Rev. Lett. **91**, 252001 (2003);
V. Kubarovskiy *et al* [CLAS Collaboration], Phys. Rev. Lett. **92**, 032001 (2004); [Erratum-ibid. **92**, 049902 (2004)];
V.V. Barmin *et al* [DIANA Collaboration], Phys. Atom. Nucl. **66**, 1715 (2003);
A.E. Asratyan, A.G. Dolgolenko and M.A. Kubantsev, [hep-ex/0309042]
A. Aleev *et al* [SVD Collaboration], [hep-ex/0401024]
A. Airapetian *et al* [HERMES Collaboration], Phys. Lett. B **585**, 213 (2004);
M. Abdel-Bary *et al* [COSY-TOF Collaboration], hep-ex/0403011.
14. D. Diakonov, V. Petrov and M.V. Polyakov, Z. Phys. A **359**, 305 (1997);
15. R.L. Jaffe and F. Wilczek, Phys. Rev. Lett. **91**, 232003 (2003) [hep-ph/0307341].
16. C. Alt *et al* [NA49 Collaboration], Phys. Rev. Lett. **92**, 042003 (2004).
17. S. Chekanov *et al* [ZEUS Collaboration], Phys. Lett. B **591**, 7 (2004).
18. C. Adloff *et al* [H1 Collaboration], Phys. Lett. B **588**, 17 (2004).
19. S. Chekanov *et al* [ZEUS Collaboration], Eur. Phys. J. C **38**, 29 (2004).
20. S. Chekanov *et al* [ZEUS Collaboration], DESY 05-018.

EXPERIMENTAL REVIEW ON PENTAQUARKS

Michael Danilov
Institute for Theoretical and Experimental Physics
B.Chermushkinskaya 25
117218 Moscow
Russia

Abstract

The experimental evidence for pentaquarks is reviewed and compared with the experiments that do not see any sign of pentaquarks.

1 Observation of pentaquarks

Until recently, all existing baryons could be interpreted as bound states of three quarks. Observations of a pentaquark state Θ^+ in nK^+ ¹⁾ and pK^0 ²⁾ modes created a lot of excitement. The corresponding invariant mass distributions obtained by the LEPS and DIANA collaborations are shown in Fig. 1 , 2.

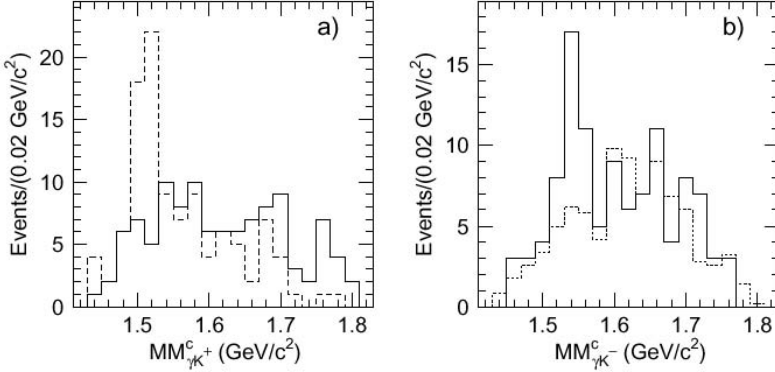


Figure 1: *Missing mass spectra for the γK^+ (left) and γK^- (right) for the reaction $\gamma C \rightarrow K^+ K^- X$ ¹⁾. The dashed (solid) histogram shows events with (without) additional detected proton. The $\Lambda(1520)$ signal is seen on the left and evidence for Θ^+ is seen on the right.*

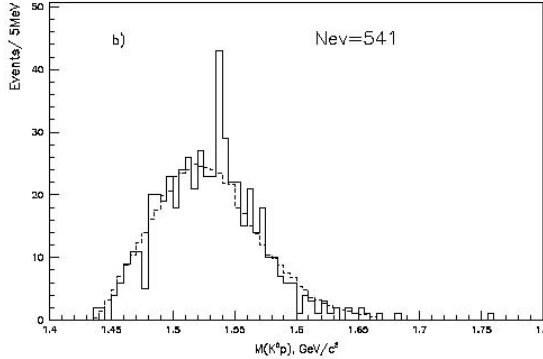


Figure 2: *Invariant mass of pK^0 in the reaction $K^+ Xe \rightarrow pK_S X$ ²⁾. The dashed histogram is the expected background.*

The minimal quark content of the Θ^+ is $uudd\bar{s}$. Thus for the first time unambiguous evidence was obtained for hadrons with an additional quark-

antiquark pair.

Analysis of the DIANA data demonstrates that the width of the Θ^+ is very small $\Gamma = 0.9 \pm 0.3 \text{ MeV}$ ³⁾. A similar small width was obtained from the analysis of the K^+d cross section ^{4) - 8)}. Such a narrow width is extremely unusual for hadronic decays and requires reassessment of our understanding of quark dynamics. Properties of the Θ^+ were in the excellent agreement with the theoretical predictions ⁹⁾ based on the chiral quark soliton model. This paper motivated both experimental searches although later on the accuracy of these predictions was questioned ¹⁰⁾. In the quark soliton model the Θ^+ belongs to an antidecuplet of baryons (see Fig. 3). Octet, decuplet, 27-plet, and 35-plet of pentaquarks are also expected.

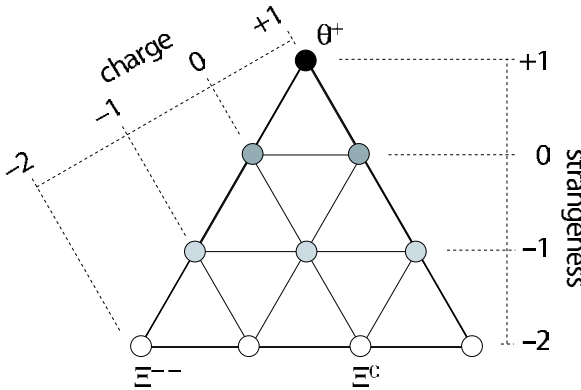


Figure 3: The predicted anti-decuplet ⁹⁾ of pentaquark baryons. Experimental evidence for three indicated particles has been presented.

Many experiments promptly confirmed the existence of the Θ^+ ^{11) - 24)} in different processes: photoproduction, deep inelastic scattering, hadroproduction, and neutrino interactions. Table 1 shows properties of the observed peaks.

There is some spread in the mass values obtained by different experiments. In particular masses in the pK_S final state are lower than in the nK^+ one. The accuracy of the mass determination is not high in most of the experiments and therefore the disagreement is not very serious statistically. However the DIANA and ZEUS measurements are quite precise and contradict each other by more than 4 sigma. Several experiments observe finite width of the Θ^+ that is much larger than 1 MeV. However, the accuracy is again not high and within 3 sigma all width measurements are consistent with the instrumental resolution.

Table 1: *Experiments with evidence for the Θ^+ baryon.*

Reference	Group	Reaction	Mass (MeV)	Width (MeV)
1)	LEPS(1)	$\gamma C \rightarrow K^+ K^- X$	1540 ± 10	< 25
2)	DIANA	$K^+ X e \rightarrow K^0 p X$	1539 ± 2	< 9
11)	CLAS(d)	$\gamma d \rightarrow K^+ K^- p(n)$	1542 ± 5	< 21
12)	SAPHIR	$\gamma d \rightarrow K^+ \bar{K}^0(n)$	1540 ± 6	< 25
13)	νBC	$\nu A \rightarrow K_s^0 p X$	1533 ± 5	< 20
14)	CLAS	$\gamma p \rightarrow \pi^+ K^+ K^-(n)$	1555 ± 10	< 26
15)	HERMES	$e^+ d \rightarrow K_s^0 p X$	1526 ± 3	13 ± 9
16)	ZEUS	$e^+ p \rightarrow K_s^0 p X$	1522 ± 3	8 ± 4
17)	COSY-TOF	$pp \rightarrow K^0 p \Sigma^+$	1530 ± 5	< 18
18)	SVD	$pA \rightarrow K_s^0 p X$	1526 ± 5	< 24
19)	LEPS(2)	$\gamma d \rightarrow K^+ K^- X$	~ 1530	
20)	$\nu BC2$	$\nu A \rightarrow K_s^0 p X$	1532 ± 2	< 12
21)	NOMAD	$\nu A \rightarrow K_s^0 p X$	1529 ± 3	< 9
22)	JINR	$p(C_3H_8) \rightarrow K_s^0 p X$	1545 ± 12	16 ± 4
23)	JINR(2)	$CC \rightarrow K_s^0 p X$	1532 ± 6	< 26
24)	LPI	$np \rightarrow np K^+ K^-$	1541 ± 5	< 11

The spread in mass and width may indicate that some experiments observe not a signal but a statistical fluctuation.

If the pentaquark interpretation of observed peaks is correct one expects many other exotic (or cripto exotic) baryons belonging to the same antidecuplet or other multiplets. Indeed several experiments observe additional peaks in the vicinity of the Θ^+ mass (20, 22, 24). For example 3 peaks with the estimated statistical significance of 7.1, 5.0, and 4.5 sigma are seen in neutrino interactions (20).

The NA49 collaboration claims an observation of a double strange pentaquark (25). Two observed narrow resonances Ξ_{10}^{--} and Ξ_{10}^0 (see Fig. 4) fit naturally into the same antidecuplet as the Θ^+ (see Fig. 3).

An evidence for an anti-charmed pentaquark was obtained by the H1 collaboration (26) (see Fig. 5).

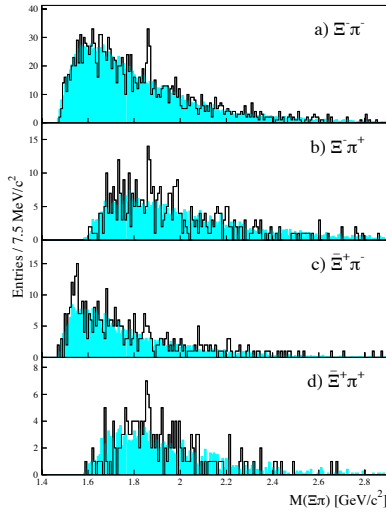


Figure 4: Invariant mass spectra for $\Xi^- \pi^-$ (a), $\Xi^- \pi^+$ (b), $\Xi^+ \pi^-$ (c), and $\Xi^+ \pi^+$ (d) in the NA49 experiment. The shaded histograms are the normalized mixed-event backgrounds.

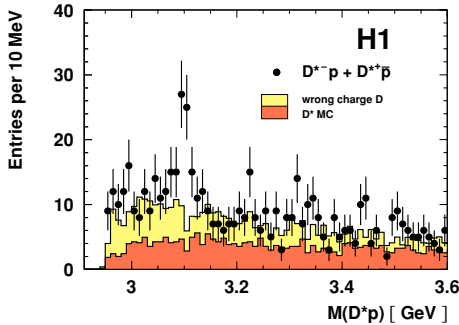


Figure 5: Invariant mass distribution of $D^{*-}p$ and $D^{*+}\bar{p}$ combinations in the H1 experiment. Two background components are shown as the shaded histograms.

2 Reliability of pentaquark observations

The evidence for pentaquarks was criticized by several authors (for a review see 27). They considered kinematic reflections, ghost tracks and arbitrary selection criteria as possible explanations for the observed peaks. The first

two worries were shown to be not important at least in some experiments (for a review see ²⁸). The last point is especially serious since statistical significance of the positive experiments is not high and thus they are vulnerable to a psychological bias. This problem is illustrated by the JINR analysis ²²) in which authors without any reason discard the momentum range where they do not see the signal. The ZUES collaboration does not see the signal in data with $Q^2 < 20 \text{ GeV}^2$. Their justification for discarding these data is also not too convincing. There are other examples of experiments with not well justified cuts. On the other hand there are experiments (for example DIANA) in which event selection criteria have high efficiency and reasonably justified.

The statistical significance of peaks is overestimated in all experiments since the shape of the background is not known. This looks obvious if one removes the fit curves and plot the data points with error bars (see Fig. 6 taken from ²⁷).

Nevertheless the number of experiments is large and the combined significance is high if we disregard for a moment the spread in the peak position and width. So one can not prove that all observed peaks are fakes or statistical fluctuations. Only high statistics experiments can confirm or disprove the claim for pentaquarks.

3 Non-observation experiments

Experiments which do not observe pentaquarks are shown in Table 2. Many of them are high statistics experiments which observe by far larger number of conventional resonances than the experiments which observe pentaquarks, and have much better mass resolution. The first significant negative result was published by the HERA-B collaboration ³³). HERA-B does not see any evidence for the Θ^+ but observes a clear $\Lambda(1520)$ and $\bar{\Lambda}(1520)$ signals of about 2 thousand events. HERA-B obtains an upper limit on the ratio of production cross sections for the Θ^+ and $\Lambda(1520)$ of $R_{\Lambda^*} < 2.7\%$ at the 95% CL for $M_{\Theta^+} = 1530 \text{ MeV}$. In the whole range of reported Θ^+ masses from 1522 MeV to 1555 MeV the limit varies up to 16%.

The ratio of the Θ^+ and $\Lambda(1520)$ production cross sections R_{Λ^*} is often used for the comparison of different experiments since $\Lambda(1520)$ is narrow and easily reconstructed, it has a mass similar to the Θ^+ mass and one can draw similar diagrams for $\Lambda(1520)$ and Θ^+ production by exchanging an \bar{K} meson into a K meson. The existence of similar diagrams unfortunately does not prove that production mechanisms for Θ^+ and $\Lambda(1520)$ are similar. The ratio R_{Λ^*} is of the order of unity in several experiments which observe the Θ^+ and less than a few percent in many experiments which do not see Θ^+ (see Table 2).

In order to resolve this discrepancy many authors assume that the Θ^+ production drops very fast with energy and is heavily suppressed in e^+e^- an-

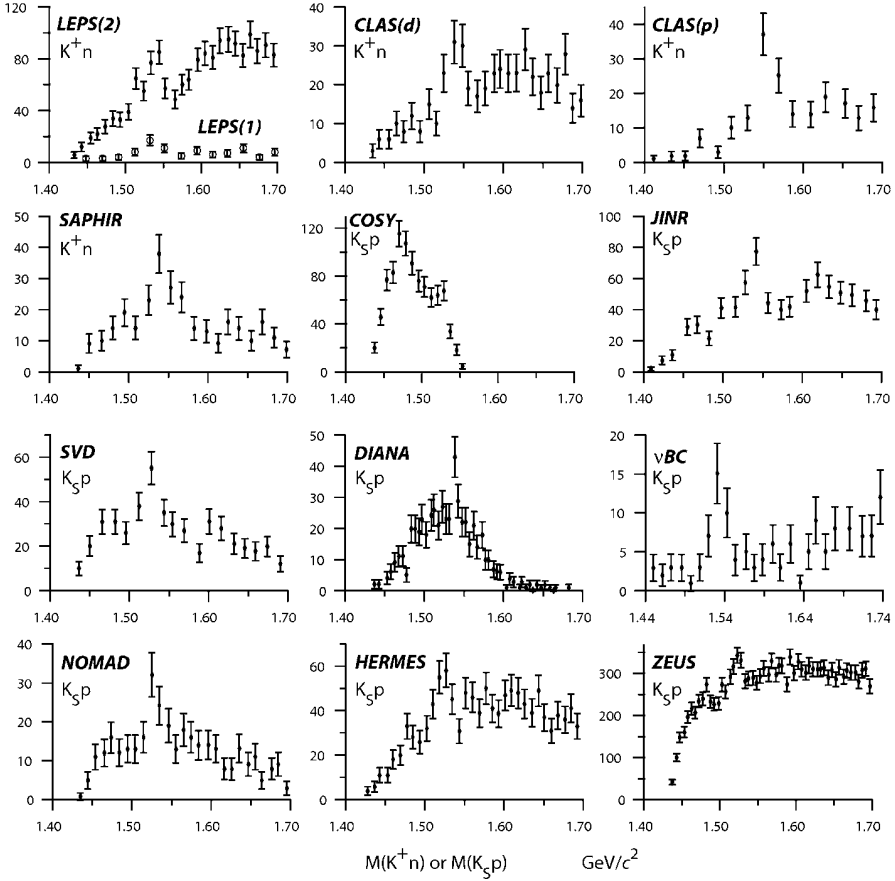


Figure 6: *Mass spectra of nK^+ and pK_S pairs in the experiments which provide evidence for the Θ^+ .*

niihilation. A model exists in which the Θ^+ production cross section is strongly suppressed at high energies in the fragmentation region ⁴⁴). It is not clear how reliable this model is. In any case it is not applicable for the central production for example in the HERA-B experiment where some models predict the Θ^+ yield much higher than the experimental limits ⁴⁵).

However, the Θ^+ production mechanism is not known and therefore it is important to have a high statistics experiment at low energies where most evidence for pentaquarks comes from. This goal was achieved by the BELLE collaboration which analyzed interactions of low momentum particles produced

Table 2: *Experiments with non-observation of the Θ^+ baryon.*

Reference	Group	Reaction	Limit
29)	BES	$e^+e^- \rightarrow J/\Psi \rightarrow \Theta\Theta$	$< 1.1 \times 10^{-5}$ B.R.
30)	BaBar	$e^+e^- \rightarrow \Upsilon(4S) \rightarrow pK^0X$	$< 1.0 \times 10^{-4}$ B.R.
31)	Belle	$e^+e^- \rightarrow B^0\bar{B}^0 \rightarrow p\bar{p}K^0X$	$< 2.3 \times 10^{-7}$ B.R.
33)	HERA-B	$pA \rightarrow K_S^0pX$	$< 0.02 \times \Lambda^*$
34)	SPHINX	$pC \rightarrow \Theta^+X$	$< 0.1 \times \Lambda^*$
35)	HyperCP	$\pi, K, pCu \rightarrow K_S^0pX$	$< 0.3\%$ K^0p
36)	CDF	$p\bar{p} \rightarrow K_S^0pX$	$< 0.03 \times \Lambda^*$
37)	FOCUS	$\gamma BeO \rightarrow K_S^0pX$	$< 0.02 \times \Sigma^*$
38)	Belle	$\pi, K, pA \rightarrow K_S^0pX$	$< 0.02 \times \Lambda^*$
39)	PHENIX	$Au + Au \rightarrow K^-\bar{n}X$	(not given)
32)	ALEPH	$e^+e^- \rightarrow K_s^0pX$	$< 0.07 \times \Lambda^*$
40)	COMPASS	$\mu^+A \rightarrow K_s^0pX$	–
41)	DELPHI	$e^+e^- \rightarrow K_s^0pX$	$< 0.5 \times \Lambda^*$
42)	E690	$pp \rightarrow K_s^0pX$	$< 0.005 \times \Lambda^*$
43)	LASS	$K^+p \rightarrow K^+n\pi^+$	–
41)	L3	$\gamma\gamma \rightarrow K_s^0pX$	$< 0.1 \times \Lambda$

in e^+e^- interactions with the detector material. We will discuss this experiment after reviewing the situation with the anti-charmed and doubly strange pentaquarks.

4 The anti-charmed pentaquark

The anti-charmed pentaquark was observed in the pD^{*-} and $\bar{p}D^{*+}$ channels by the H1 collaboration both in DIS and photo production ²⁶⁾. After many experimental checks H1 concludes that the signal is real and self consistent. Still the signal has very unusual properties. The Θ_c^0 measured width of (12 ± 3) MeV is consistent with the experimental resolution of (7 ± 2) MeV. So its intrinsic width is very small although its mass is 151 MeV above the pD^{*-} threshold and 292 MeV above pD^- threshold. Its decay into pD^{*-} is clearly visible although naively one would expect much larger branching fraction for the pD^- channel where energy release is twice larger. Finally it is produced with an enormous cross section. About 1.5% of all charged D^* mesons are coming from decays of this new particle! These properties are very surprising

but we can not a priori exclude such a possibility.

However, the ZEUS experiment which works at the same electron-proton collider HERA does not see Θ_c^0 and gives an upper limit of 0.23% at the 95% CL on the fraction of charged D^* coming from Θ_c^0 decays (46). We denote this fraction $R_{\Theta_c^0/D^*}$. For DIS events with $Q^2 > 1 \text{ GeV}^2$ the upper limit is 0.35% at the 95% CL. This is a clear contradiction with the H1 result. We are not aware of any convincing explanation of this discrepancy. One can try to explain the difference using following arguments. ZEUS detects more soft D^* than H1. If one assumes that pentaquarks are produced with high momenta only, than D^* mesons from their decays should be also energetic. In this case soft D^* that are more efficiently detected by ZEUS should not be used in the comparison with H1. However such an assumption does not resolve the discrepancy since ZEUS does not see the signal also in the kinematic range very similar to the H1 one.

The CDF collaboration also does not see any sign of Θ_c^0 (36). CDF has two orders of magnitude more reconstructed D^* mesons. They reconstruct $6247 \pm 1711 D_2^{*0} \rightarrow D^{*+}\pi^-$ and $3724 \pm 899 D_1^0 \rightarrow D^{*+}\pi^-$ decays which have the event topology very similar to Θ_c^0 . Majority of charm particles at HERA and Tevatron are produced in the fragmentation process. It is impossible to reconcile the results of the two experiments if Θ_c^0 is produced in the fragmentation process as well. No other mechanism was proposed so far. There are also upper limits on Θ_c^0 production in e^+e^- collisions by ALEPH (32) and in photo production by FOCUS (37).

We conclude that the evidence for Θ_c^0 is by far weaker than the evidence against it.

5 Doubly strange pentaquark.

The NA49 claim for the observation of the doubly strange pentaquark was not supported by several experiments which tried to find it. HERA-B has 8 times more Ξ^- hyperons and slightly better mass resolution. There is no $\Xi(1862)$ signal in the $\Xi^-\pi^-$ or $\Xi^-\pi^+$ mass distributions (see Fig. 7) while there is a clear $\Xi(1530)^0$ peak with about 1000 events (including charge conjugate combinations). HERA-B sets an upper limit of 4%/B($\Xi(1862)^{--} \rightarrow \Xi^-\pi^-$) at the 95%CL on the ratio of production cross section for $\Xi(1862)^{--}$ and $\Xi(1530)^0$. We denote this ratio $R_{\Xi(1862)/\Xi(1530)}$. $R_{\Xi(1862)/\Xi(1530)}$ is about 18%/B($\Xi(1862)^{--} \rightarrow \Xi^-\pi^-$) in the NA49 experiment (33, 47). The center of mass energy in HERA-B is about 2 times larger than in NA49. However the arguments about a very fast drop of the pentaquark production cross section in the fragmentation region (44) do not apply to the central production where the signal is observed by NA49 (25, 48) and where it is searched for at

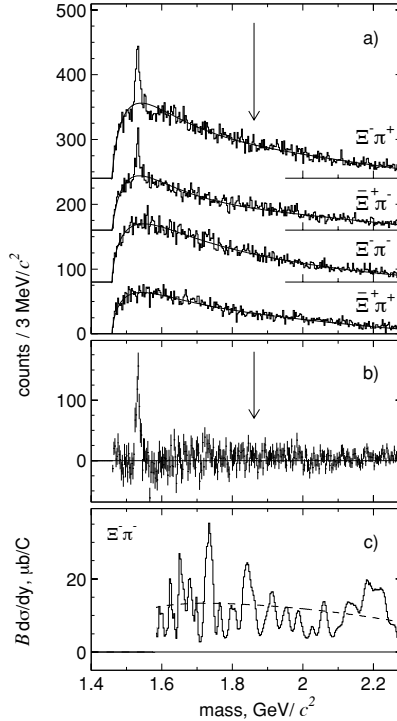


Figure 7: The $\Xi\pi$ invariant mass spectra for $p + C$ collisions in the HERA-B experiment (a); sum of all four $\Xi\pi$ spectra with the background subtracted (b); upper limit at 95%CL for mid-rapidity (c) .

HERA-B. The E690 experiment has even smaller limit on the $R_{\Xi(1862)/\Xi(1530)}$ of $0.2\%/B(\Xi(1862)^{-} \rightarrow \Xi^{-}\pi^{-})$ at the 95% CL ⁴²⁾. E690 studies proton - proton interactions at 800 GeV i.e. the same process as NA49 but at the twice larger CM energy. The WA89 experiment has about 300 times larger number of Ξ^{-} hyperons but does not observe $\Xi(1860)$ ⁴⁹⁾. However this experiment uses a Σ^{-} beam and a straightforward comparison is not possible. The ALEPH, BaBar, CDF, COMPASS, FOCUS and ZEUS experiments also do not see $\Xi(1862)$ in a variety of initial processes ^{32, 30, 36, 40, 37, 46)}.

We conclude that the evidence for $\Xi(1862)$ is by far weaker than the evidence against it.

6 The Belle experiment

As discussed above many high statistics experiments do not see the Θ^+ and set stringent limits on its production cross section in different processes. It was argued, however, that the Θ^+ production can be suppressed at high energies or in specific processes like e^+e^- annihilation. Therefore Belle decided to study interactions of low momentum particles produced in e^+e^- interactions with the detector material. This allows to achieve production conditions similar to the experiments which observe the Θ^+ . For example the most probable kaon momentum is only 0.6 GeV (see Fig. 8). The Belle kaon momentum spectrum has a large overlap with the DIANA spectrum ²).

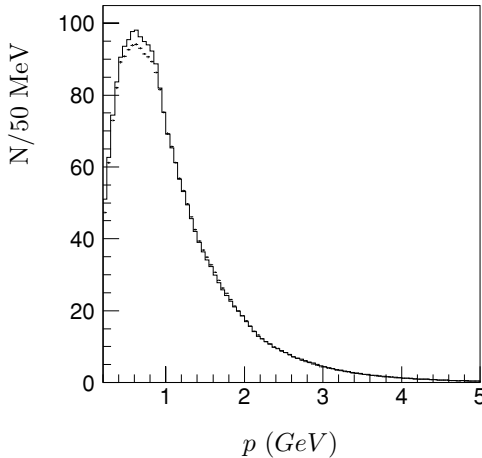


Figure 8: *Momentum spectra of K^+ (solid histogram) and K^- (dashed histogram) in the Belle experiment.*

The analysis is performed by selecting pK^- and pK_S secondary vertices. The protons and kaons are required not to originate from the region around the run-averaged interaction point. The proton and kaon candidate are combined and the pK vertex is fitted. The xy distribution of the secondary pK^- vertices is shown in Fig. 9 for the barrel part (left) and for the endcap part (right) of the detector. The double wall beam pipe, three layers of SVD, the SVD cover and the two support cylinders of the CDC are clearly visible. The xy distribution for secondary pK_S vertices is similar.

The mass spectra for pK^- and pK_S secondary vertices are shown in Fig. 10. No significant structures are observed in the $M(pK_S)$ spectrum, while in the $M(pK^-)$ spectrum a $\Lambda(1520)$ signal is clearly visible.

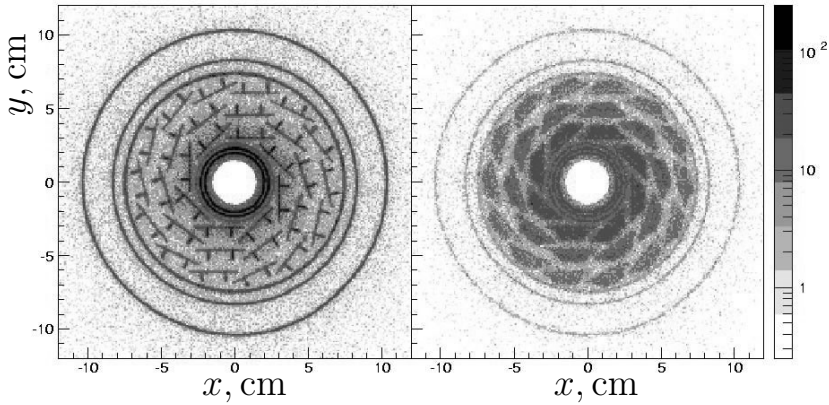


Figure 9: The xy distribution of secondary pK^- vertices for the barrel (left) and endcap (right) parts of the Belle detector.

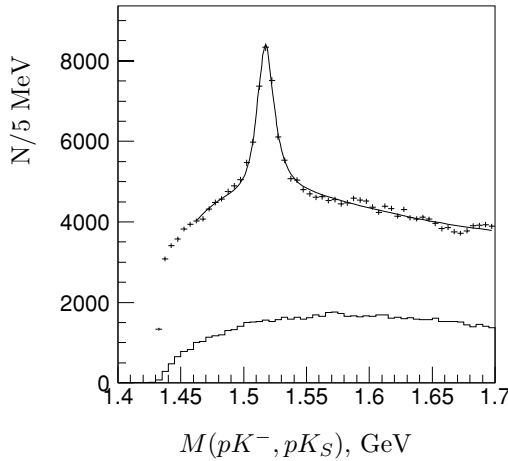


Figure 10: Mass spectra of pK^- (points with error bars) and pK_S (histogram) secondary pairs in the Belle experiment.

The $\Lambda(1520)$ yield is 15.5 thousand events. The $\Lambda(1520)$ momentum spectrum is relatively energetic (see Fig. 11). $\Lambda(1520)$ produced in a formation channel should be contained mainly in the first bin of the histogram even in the presence of the Fermi motion. Therefore most of $\Lambda(1520)$ are produced in

the production channel.

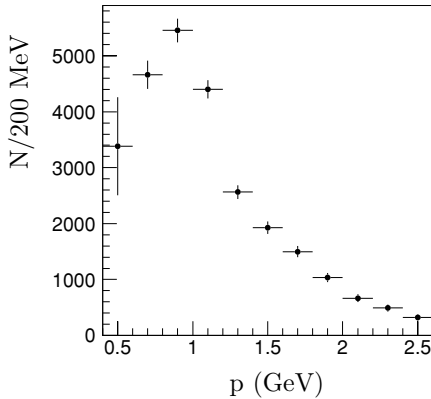


Figure 11: $\Lambda(1520)$ momentum spectrum in the Belle experiment.

The upper limit for the narrow Θ^+ yield is 94 events at the 90% CL for $M_{\Theta^+} = 1540$ MeV. This leads for the upper limit of 2% at the 90%CL on the ratio of Θ^+ and $\Lambda(1520)$ production cross sections. For other reported Θ^+ masses the limit is even smaller.

Projectiles are not reconstructed in the Belle approach. Therefore the Θ^+ and $\Lambda(1520)$ can be produced by any particle originating from the e^+e^- annihilation: K^\pm , π^\pm , K_S^0 , K_L^0 , p , Λ , etc. Belle shows that $\Lambda(1520)$ are seldom accompanied by K^+ mesons from the same vertex. This means that $\Lambda(1520)$ are produced mainly by particles with negative strangeness. The fraction of energetic Λ hyperons in e^+e^- annihilation is too small to dominate $\Lambda(1520)$ production.

The Belle limit is much smaller than the results reported by many experiments which observe the Θ^+ . For example it is two orders of magnitude smaller than the value reported by the HERMES Collaboration¹⁵⁾. The Θ^+ and $\Lambda(1520)$ are produced in inclusive photoproduction at HERMES. Photons produce hadrons dominantly via (virtual) pions or Kaons. Therefore the production conditions are quite similar in the two experiments. We do not know any physical explanation for the huge difference between the Belle and HERMES results.

The expected number of reconstructed Θ^+ in the formation reaction $K^+n \rightarrow pK_S^0$ can be estimated knowing the Θ^+ width, the number of K^+ mesons with appropriate momentum, amount of material and the reconstruction efficiency. The Θ^+ width was estimated using the DIANA data to be 0.9 ± 0.3 MeV³⁾. Using this value of the Θ^+ width we estimate the number of

expected Θ^+ events at Belle to be comparable with their upper limit. If so the Belle result disagrees with the DIANA observation. However we should wait for a quantitative statement from the Belle Collaboration.

A comparison of the Belle upper limit on R_{Λ^*} with the exclusive photoproduction experiments is not simple. However, it is very strange to have about two orders of magnitude difference in R_{Λ^*} since the Belle kaon (and pion) momentum spectrum is quite soft and comparable with the momentum spectrum of virtual kaons (or pions) in the low energy photoproduction experiments.

7 Conclusions

The NA49 claim for the observation of $\Xi(1862)$ pentaquarks is hard to reconcile with the results of many experiments which have up to 300 times larger statistics of usual Ξ^- and $\Xi(1530)$ hyperons and a better mass resolution. In particular E690 investigated the same production process at about twice larger CM energy and obtained hundred times lower limit on the ratio of $\Xi(1862)$ and $\Xi(1530)$ production cross sections.

The H1 claim for the anti-charmed pentaquark contradicts the ZEUS study made at almost identical conditions. CDF sets a very stringent limit on the Θ_c^0 yield although they observed 178 times more D^* than H1. CDF reconstructed also about 10 thousand $D_2^{*0} \rightarrow D^{*+}\pi^-$ and $D_1^0 \rightarrow D^{*+}\pi^-$ decays (including charge conjugate states). These decays are very similar in kinematics and efficiency to $\Theta_c^0 \rightarrow pD^{*-}$ decays (the H1 signal is observed mainly with energetic protons for which the particle identification does not play an important role). Three other experiments do not see any sign of the Θ_c^0 in different production processes [32, 31, 37]. It is hard to reconcile the H1 claim with this overwhelming negative evidence.

The claims for observation of the Θ^+ in inclusive production at medium and high energies are not supported by many high statistics experiments which reconstruct by far larger number of ordinary hyperons with negative strangeness. Even if one assumes that the Θ^+ production is strongly suppressed at high energies there is still a contradiction between several of these results with the Belle upper limit obtained with low momentum kaons.

However, even if some claims for the Θ^+ observation are wrong it does not mean that all observations are wrong. The DIANA and exclusive photoproduction experiments are not in contradiction with the high energy experiments if one assumes that the Θ^+ production drops very fast with the energy. There is a qualitative disagreement of these experiments with the Belle data. However here we should wait for the quantitative analysis of the Belle data. Results of high statistics exclusive photoproduction experiments are expected very soon. We hope that the situation with the pentaquark existence will be clarified already this year.

8 Acknowledgements

We are grateful to A.Dolgolenko, A.Kaidalov, R.Mizuk, and P.Pakhlov for the fruitful discussions.

References

1. T. Nakano *et al.*, (LEPS), Phys. Rev. Lett. **91**:012002 (2003); hep-ex/0301020.
2. V.V. Barmin *et al.*, (DIANA), Phys. Atom. Nuclei **66**, 1715 (2003); hep-ex/0304040.
3. R.N. Cahn and G.H. Trilling, Phys. Rev. **D69**, 011501 (2004).
4. S. Nussinov, hep-ph/0307357.
5. R.A. Arndt *et al.*, Phys. Rev. **C68**, 042201 (2003); Erratum **C69**, 019901 (2004).
6. J. Haidenbauer and G. Krein, Phys. Rev. **C68**, 052201 (2003).
7. A. Sibirtsev *et al.*, Phys. Lett. **B599**, 230 (2004).
8. W.R. Gibbs, Phys. Rev. **C70**, 045208 (2004).
9. D. Diakonov, V. Petrov and M. Polyakov, Z. Phys. A **359**, 305 (1997).
10. J. Ellis, M. Karliner and M. Praszalowicz, JHEP **0405**, 2 (2004); hep-ph/0401127.
11. S. Stepanyan *et al.*, (CLAS), Phys. Rev. Lett. **91**:25001 (2003); hep-ex/0307018.
12. J. Barth *et al.*, (SAPHIR), Phys. Lett. **B572**, 127 (2003); hep-ex/0307083.
13. A.E. Asratyan, A.G. Dolgolenko and M.A. Kubantsev, Phys. Atom. Nucl. **67**, 682 (2004); hep-ex/0309042.
14. V. Kubarovsky *et al.*, (CLAS), Phys. Rev. Lett. **92**:032001 (2004); hep-ex/0311046.
15. A. Airapetian *et al.*, (HERMES), Phys. Lett. **B585** (2004) 213; hep-ex/0312044.
16. The ZEUS collaboration, Phys. Lett. **B591** (2004) 7; hep-ex/0403051.
17. M. Abdel-Barv, *et al.*, (COSY-TOF), Phys. Lett. **B595**, 127 (2004); hep-ex/0403011.

18. A. Aleev *et al.*, (SVD), submitted to Yad. Fiz.; hep-ex/0401024.
19. T. Nakano, QNP2004 Conference, www.qnp2004.org.
20. A. Asratyan, A. Dolgolenko and M. Kubantsev, Nucl. Phys. B (Proc.Suppl.) **142** 79 (2005).
21. L. Camilleri, Presented at Neutrino 2004, Paris, neutrino2004.in2p3.fr.
22. P. Aslanyan *et al.*, , hep-ex/0403044.
23. R.Togoo *et al.*, , Proc. Mongolian Acad. Sci. 4(2003)2.
24. Yu.Troyan *et al.*, , hep-ex/0404003.
25. C. Alt *et al.*, (NA49), Phys. Rev. Lett. **92**, 042003 (2004); hep-ex/0310014.
26. A. Aktas *et al.*, , Phys. Lett. B **588**, 17 (2004); hep-ex/0403017.
27. A.Dzierba, C.Mayer, A.Szczepanek, hep-ex/0412077.
28. K. Hicks *et al.*, , submitted to Phys. Rev. D; hep-ph/0411265.
29. J.Z. Bai *et al.*, (BES), Phys. Rev. D **70**:012004 (2004); hep-ex/0402012.
30. The BaBar Collaboration, hep-ex/0408064.
31. The Belle Collaboration, hep-ex/0409010.
32. S.R. Armstrong, hep-ex/0410080; S. Schael *et al.*, (ALEPH), Phys. Lett. B **599**, 1 (2004).
33. I. Abt *et al.*, (HERA-B), Phys. Rev. Lett. **93**:212003 (2003); hep-ex/0408048.
34. Yu.M. Antipov *et al.*, (SPHINX), Eur. Phys. J. **A21**, 455 (2004); hep-ex/0407026.
35. M.J. Longo *et al.*, (HyperCP), Phys. Rev. D **70**:111101 (2004); hep-ex/0410027.
36. I. Gorelov *et al.*, (CDF), hep-ex/0408025;
D. Litvintsev *et al.*, (CDF), hep-ex/0410024.
37. K. Stenson *et al.*, (FOCUS), hep-ex/0412021.
38. K. Abe *et al.*, (Belle), hep-ex/0411005.
39. C. Pinkerton *et al.*, (PHENIX), J. Phys. G **30**:S1201 (2004); nucl-ex/0404001.

40. G. Brona and B. Baddek (COMPASS), 2004
www.compass.cern.ch/compass/notes/2004-5.
41. S. Armstrong, hep-ex/0410080.
42. D. Cristian *et al.*, (E690) www.qnp2004.org.
43. J. Napolitano *et al.*, , hep-ex/0412031.
44. A.I. Titov, A. Hosaka, S. Date and Y. Ohashi, Phys. Rev. C **70**:042202 (2004).
45. F. Becattini *et al.*, , Phys.Rev. C69, 024905(2004).
46. S. Chekanov *et al.*, (ZEUS), Eur. Phys. J. **C38**, 29 (2004); hep-ex/0409033.
47. H.G. Fischer and S. Wenig, Eur. Phys. J. **C37**, 133 (2004); hep-ex/0401014.
48. D. Barna PhD Thesis, NA49 note 294 at <http://na49info.cern.ch>.
49. M.I. Adamovich *et al.*, (WA89), Phys. Rev. C **70**:022201 (2004); hep-ex/0405042.

RENORMALONS AT THE BOUNDARIES BETWEEN PERTURBATIVE AND NON-PERTURBATIVE QCD

A.L. Kataev

Institute for Nuclear Research, 117312 Moscow, Russia

Abstract

The basis of renormalon calculus is briefly discussed. This method is applied to study the QCD predictions for three different sum rules of deep-inelastic scattering, namely for the Gross–Llewellyn Smith, Bjorken polarized and unpolarized sum rules. It is shown that the renormalon structures of these a posteriori different physical quantities are closely related. These properties are giving us the hint that theoretical expressions of these three sum rules are similar both in the perturbative and non-perturbative sectors. Some phenomenological consequences of the new relations are discussed.

1 Introduction

The modern theoretical basis of renormalon calculus was first built in the rather inspiring work of Ref. ¹⁾, devoted to the consideration of $e^+e^- \rightarrow \text{hadrons}$ process, and in the important work of Ref. ²⁾, devoted to the consideration of deep-inelastic scattering processes. After these studies the number of theoretical and practical developments appeared in the literature (see reviews of Refs. ^{3)–5)}).

In what is discussed below, we will consider definite several subjects, related to deep-inelastic scattering (DIS) sum rules.

It is commonly expected that in the canonical renormalization schemes, say the $\overline{\text{MS}}$ scheme, perturbative expansions in small QCD coupling constant $a_s = \alpha_s/(4\pi)$ of theoretical expressions for physical quantities, defined in the Euclidean region, are asymptotic ones. This means that the difference of the total sums

$$D(a) = 1 + \sum_{n \geq 1} d_n a^n \quad (1)$$

and their finite sums

$$D_k(a) = 1 + \sum_{n=1}^k d_n a^n \quad (2)$$

satisfy the following property

$$\lim_{a \rightarrow 0} \left| \frac{D(a) - D_k(a)}{a^k} \right| \rightarrow 0 \quad . \quad (3)$$

In other words the difference between the total series and their finite sum are expressed as

$$D(a) - D_k(a) = O(a^{k+1}) \quad . \quad (4)$$

In this case the error of the truncation of the asymptotic series can be estimated by the last term of $D_k(a)$, namely $d_k a^k$ ⁶⁾.

In QCD one expects that in the $\overline{\text{MS}}$ scheme the coefficient function for DIS sum rules, normalized to unity can be approximated by the following asymptotic series ⁷⁾:

$$D_k(a) = 1 + \sum_{k \geq 1} (\beta_0)^k k! \left(K_D^{\text{UV}} (-1)^k k^a + K_D^{\text{IR}} k^b \right) a_s^{k+1} \quad , \quad (5)$$

where sign-alternating series with the coefficient K^{UV} is generated by the ultraviolet renormalons (UVR), sign-constant asymptotic series with coefficient K^{IR} result from the consideration of infrared renormalons (IRR), and a and b are the known numbers, that depend from the ratio of the first two coefficients of the QCD β -function.

Working within renormalon calculus we will demonstrate that the perturbative and non-perturbative contributions to definite DIS sum rules are related. In other words we will show that the renormalon approach is working at the boundaries between these two regimes in QCD.

The aim of this article is three fold:

- to explain the basic stages of renormalon calculus in QCD, using the simple language;
- to show that in the asymptotic perturbative expansion of three DIS sum rules, namely of the Gross–Llewellyn Smith (GLS), Bjorken- polarized (Bjp) and Bjorken- unpolarized (Bjup) sum rules, may be universal. We will present arguments, based on the consideration of the results given in Refs. 8), 9), that these expansions are defined by the poles in the closely related Borel images of all three sum rules.
- We will explain the features, which follow from the consideration of the IRR poles in the Borel images of the three DIS sum rules. Moreover our aim is to outline new consequences of the IRR calculus. They indicate the existence of relations between twist-4 $1/Q^2$ non-perturbative contributions to the sum rules we are interested in ¹⁰⁾. These results form the basis of the new QCD relations between theoretical expressions for these three sum rules ¹⁰⁾, which seem to be supported by the experimental data within existing error bars. More critical tests of these relations are proposed.

2 Renormalon calculus and DIS sum rules

Let us first express a perturbative QCD series in terms of a Borel integral as

$$D(a_s) = \sum_{n=0}^{\infty} d_n a_s^n \quad (6)$$

$$\begin{aligned}
&= \sum_{n=0}^{\infty} d_n \frac{n!}{\Gamma(n+1)} \delta^n \\
&= \int_0^{\infty} \exp(-\delta/\beta_0 a_s) \sum_{n=0}^{\infty} d_n \frac{\delta^n}{n!} d\delta \\
&= \int_0^{\infty} \exp(-\delta/\beta_0 a_s) B[D](\delta) d\delta \ , \quad (7)
\end{aligned}$$

where $\beta_0 = (11/3)C_A - (4/3)T_f N_f$ is the first coefficient of the QCD β -function, with $C_A = 3$, $T_f = 1/2$, and $B[D](\delta)$ is the image of the Borel integral.

At this stage we define the DIS sum rules we will be interested in. The GLS sum rule of the νN DIS ¹¹⁾ has the following form

$$\begin{aligned}
\text{GLS}(Q^2) &= \frac{1}{2} \int_0^1 dx \left[F_3^{\nu n}(x, Q^2) + F_3^{\nu p}(x, Q^2) \right] \\
&= 3C_{\text{GLS}}(Q^2) - \frac{\langle\langle O_1 \rangle\rangle}{Q^2} - O\left(\frac{1}{Q^4}\right) \ . \quad (8)
\end{aligned}$$

In the Born approximation, this “measures” the number of valence quarks, that are contained in the nucleon and can thus be considered as the **baryon sum rule**. In the $\overline{\text{MS}}$ scheme, the twist-2 perturbative coefficient function $C_{\text{GLS}}(Q^2)$ is calculated explicitly, including a_s^2 and a_s^3 terms ¹²⁾, ¹³⁾. The twist-4 matrix element of the $O(1/Q^2)$ non-perturbative contribution to the GLS sum rule is related to the matrix element calculated in Ref. ¹⁴⁾ to be

$$\langle\langle O_1 \rangle\rangle = \frac{8}{27} \langle\langle O^S \rangle\rangle \ , \quad (9)$$

where $\langle\langle O^S \rangle\rangle$ is defined by the dimension-2 operator

$$O_\mu = \bar{u} \tilde{G}_{\mu\nu} \gamma_\nu \gamma_5 u + (u \rightarrow d) \ , \quad (10)$$

where

$$\tilde{G}_{\mu\nu} = \frac{1}{2} \epsilon_{\mu\nu\alpha\beta} G_{\alpha\beta}^a \frac{\lambda^a}{2} \quad (11)$$

and

$$\langle P | O_\mu^S | P \rangle = 2p_\mu \langle\langle O^S \rangle\rangle \ . \quad (12)$$

The second sum rules, actively studied both in theory and experiment, is the BjP sum rule ¹⁵⁾, having the physical meaning of **polarized isospin sum**

rule. Its theoretical expression can be defined as

$$\begin{aligned} \text{Bjp}(Q^2) &= \int_0^1 dx \left[g_1^{lp}(x, Q^2) - g_1^{ln}(x, Q^2) \right] \\ &= \frac{g_A}{6} C_{\text{Bjp}}(Q^2) - \frac{\langle\langle O_2 \rangle\rangle}{Q^2} - O\left(\frac{1}{Q^4}\right). \end{aligned} \quad (13)$$

Here $g_A = 1.26$ is the known β -decay constant. At the a_s^3 level its perturbative part differs from the one of the GLS sum rule by the absence of small “light-by-light”-type terms, proportional to the colour structure $d^{abc}d^{abc}$ 13). The structure of the power corrections to the matrix element of the leading $O(1/Q^2)$ power correction was analytically calculated in Ref. 16), with the useful correction input from the considerations of Ref. 17). The final expressions are presented in a simple-form in the review of Ref. 18), from which we can get:

$$\langle\langle O_2 \rangle\rangle = \frac{1}{6} \frac{8}{9} \left[\langle\langle U^{\text{NS}} \rangle\rangle - \frac{M_N^2}{4} \langle\langle V^{\text{NS}} \rangle\rangle \right], \quad (14)$$

where

$$\begin{aligned} \langle P, S | U_\mu^{\text{NS}} | P, S \rangle &= 2M_N S_\mu \langle\langle U^{\text{NS}} \rangle\rangle \\ \langle P, S | V_{\mu\nu, \sigma}^{\text{NS}} | P, S \rangle &= 2M_N \langle\langle V^{\text{NS}} \rangle\rangle \{ (S_\mu P_\nu - S_\nu P_\mu) P_\delta \}_{S\{\nu, \sigma\}} \end{aligned} \quad (15)$$

and $\langle\langle U^{\text{NS}} \rangle\rangle$ and $\langle\langle V^{\text{NS}} \rangle\rangle$ are the reduced matrix elements of the local operators from Ref. 16), namely

$$\begin{aligned} U_\mu^{\text{NS}} &= g_s [\bar{u} \tilde{G}_{\mu, \nu} \gamma^\nu u - (u \rightarrow d)] \\ V_{\mu\nu, \sigma}^{\text{NS}} &= g_s \{ \bar{u} \tilde{G}_{\mu\nu} \gamma_\delta u - (u \rightarrow d) \}_{S\{\nu, \delta\}}, \end{aligned} \quad (16)$$

where $S\{\nu, \sigma\}$ stand for symmetrization over the given subscripts and $\tilde{G}_{\mu, \nu}$ is defined in Eq. (11). In Ref. 19) the definition of Eq. (14) was used for the estimates of $O(1/Q^2)$ corrections to Bjp sum rule, using the three-point function QCD sum rules technique. These calculations were then re-analysed with the same method in Ref. 20). The numerical results of these calculations will be discussed later. In the work of Ref. 21) a similar analysis was done with the help of the same method for the first term in the r.h.s. of Eq. (14), while the term, proportional to $(M_N^2/4)\langle\langle V \rangle\rangle$ was included into an $O(M_N^2/Q^2)$ kinematical power correction to the Bjp sum rule, which involves the second x^2

moments of the leading-twist contribution to $g_1^{p-n} = g_1^p - g_1^n$ and the twist-3 matrix element, defined through the combination of x^2 -weighted moments of the difference of structure functions g_1^{p-n} and of $g_2^{p-n} = g_2^p(x, Q^2) - g_2^n(x, Q^2)$ as

$$d_2^{p-n} = \int_0^1 dx x^2 \left(2g_1^{p-n}(x, Q^2) + 3g_2^{p-n}(x, Q^2) \right) , \quad (17)$$

Taking into account this decomposition, it is possible to rewrite a theoretical expression for the numerator of the $1/Q^2$ contribution, in the way it was done say, in the most recent experimental work of Ref. 22)

$$\mu_4^{p-n} = \frac{M_N^2}{9} (a_2^{p-n} + 4d_2^{p-n} + 4f_2^{p-n}) , \quad (18)$$

where

$$a_2 = \int_0^1 dx x^2 [g_1^p(x, Q^2) - g_1^n(x, Q^2)] \quad (19)$$

is the target mass correction and

$$2m_N^2 f_2^{p-n} S_\mu = -4M_N S_\mu \langle \langle U^{\text{NS}} \rangle \rangle \quad (20)$$

is the twist-4 contribution, which is related to the definition used by us as

$$\langle \langle O_2 \rangle \rangle = \frac{1}{6} \frac{8}{9} \langle \langle U^{\text{NS}} \rangle \rangle = -\frac{1}{6} \frac{4}{9} M_N^2 f_2^{p-n} . \quad (21)$$

In other words we have the following relation

$$M_N^2 f_2^{p-n} = -2 \langle \langle U^{\text{NS}} \rangle \rangle . \quad (22)$$

It should be stressed that in the region where the perturbative theory is working well enough and the application of the operator-product expansion method is valid (say at $Q^2 \geq 2 \text{ GeV}^2$), we expect that both target mass corrections and twist-3 terms are small and will neglect them in our further considerations ¹.

The third sum rule, which was originally derived for purely theoretical purposes, is the Bjorken unpolarized sum rule ²³⁾. It can be written down as:

$$\begin{aligned} \text{Bj unp}(Q^2) &= \int_0^1 dx \left[F_1^{\nu p}(x, Q^2) - F_1^{\nu n}(x, Q^2) \right] \\ &= C_{\text{Bj unp}}(Q^2) - \frac{\langle \langle O_3 \rangle \rangle}{Q^2} - O\left(\frac{1}{Q^4}\right) . \end{aligned} \quad (23)$$

¹For completeness we note that there is a minor difference between the the $O(M_N^2/Q^2)$ coefficients of the $\int_0^1 dx x^2 g_1^{p-n}$ terms in Ref. 19) and Ref. 22). In the former and latter cases they are equal to (10/9) and 1 respectively.

It may be also studied in future as the valuable test of QCD both in perturbative and non-perturbative sectors.

As in the previous two cases, the coefficient function $C_{\text{Bjump}}(Q^2)$ is calculated up to next-to-next-to-leading order a_s^3 -corrections^{24), 25)}. The twist-4 matrix element to this sum rule was evaluated in Ref.¹⁴⁾; with the following result:

$$\langle\langle O_3 \rangle\rangle = \frac{8}{9} \langle\langle O^{\text{NS}} \rangle\rangle \quad , \quad (24)$$

where the matrix element $\langle\langle O^{\text{NS}} \rangle\rangle$ is related to the dimension-2 operator

$$O_\mu^{\text{NS}} = \bar{u} \tilde{G}_{\mu\nu} \gamma_\nu \gamma_5 u - \bar{d} \tilde{G}_{\mu\nu} \gamma_\nu \gamma_5 d \quad , \quad (25)$$

its matching over nucleon states

$$\langle P | O_\mu^{\text{NS}} | P \rangle = 2p_\mu \langle\langle O^{\text{NS}} \rangle\rangle \quad (26)$$

and application of Eq. (24).

Let us now return to the renormalon calculus. The basic theoretical problem is how to define the Borel image $B[D](\delta)$ (or the Borel sum) of the integral in Eq. (7) for the quantities we are interested in. In QCD this problem is usually solved using perturbative methods and calculating the corresponding multiloop Feynman diagrams with a one-gluon line, dressed by the chains of fermion bubbles (so called renormalon chain insertion). These chains are generating sign-alternating asymptotic perturbative series, typical of the quantities under consideration, in powers of the expansion parameter $N_f a_s$ (where N_f is the number of quarks flavours). The contributions of these chains are gauge-invariant, but they do not reflect the whole picture of renormalon effects in QCD. The latter begin to manifest themselves after application of the naive non-abelianization (NNA) ansatz²⁶⁾ only, namely after the replacement $N_f \rightarrow -(3/2)\beta_0 = N_f - (33/2)$ in the leading terms of the large- N_f expansion. This procedure transforms a large- N_f expansion into a large- β_0 expansion, which in addition to quark bubbles insertions into the renormalon chain, is taking into account the contributions of the gluon- and ghost-bubbles insertions as well (though neglecting definite one-loop insertions into the gluon-quark-antiquark vertex, which should be also considered in the process of rigorous calculation of the coefficient β_0).

The Borel images calculated by this procedure for the GLS and Bjp sum rules coincide and have the following form ⁸⁾:

$$B[C_{\text{Bjp}}](\delta) = B[C_{\text{GLS}}](\delta) = -\frac{(3+\delta)\exp(5\delta/3)}{(1-\delta^2)(1-\delta^2/4)} . \quad (27)$$

They contain the IRR poles at $\delta = 1$ and $\delta = 2$ and the UVR poles at $\delta = -1$ and $\delta = -2$. Note that the $\delta = -1$ UVR poles in Eq. (27) are suppressed by a factor $(1/2)\exp(-10/3) = 0.018$, relative to the dominant IRR poles at $\delta = 1$ ⁹⁾. Therefore, in the asymptotic structure of the perturbative QCD effects in the expressions for $C_{\text{GLS}}(Q^2) \approx C_{\text{Bjp}}(Q^2)$ (where we neglect the small “light-by-light-type” effects, contributing to $C_{\text{GLS}}(Q^2)$) the sign-constant part in Eq. (5) dominates strongly with respect to the sign-alternating contribution, generated by $\delta = -1$ UVR.

Returning to the large- N_f expansion of the perturbative expressions

$$C_{\text{Bjp}}(Q^2) = C_{\text{GLS}}(Q^2) = 1 + \frac{C_F}{T_f N_f} \sum_{n=1}^{\infty} r_n (T_f N_f a_s)^n , \quad (28)$$

where $C_F = 4/3$, $T_f = 1/2$ and

$$r_n = \lim_{\delta \rightarrow 0} \left(-\frac{4}{3} \frac{d}{d\delta} \right)^{n-1} B[C_{\text{Bjp}}](\delta) , \quad (29)$$

we arrive at the following expansion in powers of $x = T_f N_f a_s$, namely

$$\sum_n r_n x^n = -3x + 8x^2 - \frac{920}{27}x^3 + \frac{38720}{243}x^4 + \dots , \quad (30)$$

which is known in the $\overline{\text{MS}}$ scheme up to $O(\alpha_s^9 N_f^9)$ terms ⁸⁾. Using now the traditional $\overline{\text{MS}}$ -scheme expansion in terms of the orders in $\alpha_s/\pi = 4a_s$, one can compare the results of explicit perturbative calculations of

$$C_{\text{Bjp}}(Q^2) = 1 + \sum_{n \geq 1} r_n \left(\frac{\alpha_s}{\pi} \right)^n \quad (31)$$

with the known numbers

$$r_1 = -1 \quad (32)$$

$$r_2 = -4.5833 + 0.33333N_f \quad (33)$$

$$r_3 = -41.440 + 7.6073N_f - 0.17747N_f^2 \quad (34)$$

obtained at $O(\alpha_s^2)$ in Ref. 12) and at $O(\alpha_s^3)$ in Ref. 13), with the results of the application of the NNA procedure 26) to the estimates of the perturbative QCD corrections from large- N_f expansion of Eq. (30) 2). Performing the shift $N_f \rightarrow N_f - 33/2$ in the second, third and fourth terms in Eq. (30), we arrive at the following estimates in the $\overline{\text{MS}}$ scheme 9):

$$r_2^{\text{NNA}} = -5.5 + 0.33333N_f \tag{35}$$

$$r_3^{\text{NNA}} = -48.316 + 5.8565N_f - 0.17747N_f^2 \tag{36}$$

$$r_4^{\text{NNA}} = -466.00 + 84.728N_f - 5.1350N_f^2 + 0.10374N_f^3 \quad . \tag{37}$$

Reasonable agreement can be observed between the sign structure and values of the NNA estimates and the results of explicit calculations (compare the estimates of Eqs. (35) and (36) with the numbers in Eqs. (33) and (34), respectively). As to the prediction for r_4^{NNA} , it may serve as a guide for understanding the rate of growth of the coefficients of the perturbative series generated by the single renormalon-chain approximation.

Consider now the Bjump sum rule, which is defined in Eq. (23). Within the large- N_f , expansion its perturbative coefficient function

$$C_{\text{Bjump}}(Q^2) = 1 + \sum_{n \geq 1} \tilde{r}_n \left(\frac{\alpha_s}{\pi} \right)^n \tag{38}$$

was calculated in the $\overline{\text{MS}}$ scheme and large- N_f expansion up to a $O(\alpha_s^9 N_f^9)$ -terms 9). Following the logic of our work, we present here the results for the first 4 terms only:

$$\sum_n \tilde{r}_n x^n = -2x + \frac{64}{9}8x^2 - \frac{2480}{81}x^3 + \frac{113920}{729}x^4 + \dots \tag{39}$$

As was already mentioned above, the explicit results of calculations of the perturbative contributions to the Bjump sum rule

$$C_{\text{Bjump}}(Q^2) = 1 + \sum_{n \geq 1} \tilde{r}_n \left(\frac{\alpha_s}{\pi} \right)^n \tag{40}$$

²It is worth noting that similar NNA analysis was performed previously, in Ref. 27), for the e^+e^- annihilation Adler D -function.

are known up to the order $O(\alpha_s^3)$ level. These results are:

$$\tilde{r}_1 = -2/3 \quad (41)$$

$$\tilde{r}_2 = -3.8333 + 0.29630N_f \quad (42)$$

$$\tilde{r}_3 = -36.155 + 6.3313N_f - 0.15947N_f^2 \quad (43)$$

where \tilde{r}_2 was calculated in Ref. ²⁴⁾ while \tilde{r}_3 was evaluated in Ref. ²⁵⁾. Applying now the NNA procedure to the series of Eq. (39), we find that, in the $\overline{\text{MS}}$ scheme, the estimated coefficients of the Bjunp sum rules have the following form ⁹⁾:

$$\tilde{r}_2^{\text{NNA}} = -4.8889 + 0.29630N_f \quad (44)$$

$$\tilde{r}_3^{\text{NNA}} = -43.414 + 5.2623N_f - 0.15947N_f^2 \quad (45)$$

$$\tilde{r}_4^{\text{NNA}} = -457.02 + 83.094N_f - 5.0360 N_f^2 + 0.10174N_f^3 \quad (46)$$

The estimate of Eq. (44) is in agreement with its exact partner of Eq. (42). The same situation holds for the $O(\alpha_s^3)$ corrections (compare Eq. (45) with Eq. (43)). It should be stressed, that the similarity of the next-to-next-to-leading-order $\overline{\text{MS}}$ -scheme perturbative QCD contributions to the Bjp and Bjunp sum rules was previously noticed in Ref. ²⁸⁾, although no explanation of this observation was given. Now, within the NNA procedure, it is possible to generalize this observation to higher-order level. Indeed, the NNA estimates of the $O(\alpha_s^4)$ corrections to the Bjp and Bjunp sum rules have a similar expressions as well. **These facts may indicate the close similarity in the full perturbative structure of the QCD corrections to the Bjunp sum rule, the Bjp sum rule and the GLS sum rule** (provided the “light-by-light-type” terms will not drastically modify the values of perturbative terms in the latter case in the one-renormalon chain approximation). Note that, generally speaking, from this order of perturbation theory the diagrams from the second renormalon chain are starting to contribute to the quantities under consideration. These diagrams may influence the asymptotic behaviour of the the series considered ²⁹⁾. In view of this it seems that it is more rigorous to use, in the phenomenological application, the order of α_s^4 -terms, estimated in Ref. ³⁰⁾ using the PMS approach ³¹⁾ and the effective-charges approach, developed in Ref. ³²⁾. However, since in this work we concentrated ourselves on the

structure of the QCD expressions, obtained in the one-renormalon chain approximation, we will avoid more detailed discussions of the possible influence of the multi-renormalon chain contributions to the results of our studies.

The observed in Ref. 28) similarity of the next-to-next-to-leading-order approximations for the B_{jp} and B_{junp} sum rules was attributed in Ref. 9) to the fact that the dominant $\delta = 1$ IRR contribution to the Borel images of these sum rules enters with identical residues. Indeed, the Borel images in the Borel integrals of Eq. (7) for the B_{junp} and B_{jp} sum rules turn out to be closely related 9), namely

$$B[C_{B_{\text{junp}}}] (\delta) = \left(\frac{2(1+\delta)}{3+\delta} \right) B[C_{B_{\text{jp}}}] (\delta) = - \frac{2 \exp(5\delta/3)}{(1-\delta)(1-\delta^2/4)} \quad . \quad (47)$$

Comparing Eq. (27) with Eq. (47) one can convince oneself that the residues of the poles at $\delta = 1$ in these two expressions are really the same and are equal to the factor $-(8/3)\exp(5/3)$.

Notice also the **absence** of $\delta = -1$ UVR pole and the **existence** in Eq. (47) of a $\delta = -2$ UVR pole together with the leading $\delta = 1$ IRR one. Thus we are observing one more interesting fact: the structure of the Borel image for the Borel sum, related to the B_{junp} sum rule, is **dual** to the structure of leading renormalon contributions to the Borel image of the Borel sum for the e^+e^- annihilation Adler D-function. Indeed, in the latter case the leading IRR is manifesting itself at $\delta = 2$, while the leading UVR pole is appearing at $\delta = -1$ (the general structure of renormalon singularities in the e^+e^- annihilation channel was analysed in Ref. 1), while the concrete $\overline{\text{MS}}$ -scheme calculations of the corresponding Borel image were done later on in Refs. 33) and 34).

The absence of $\delta = 1$ IRR in the Borel sum of the e^+e^- annihilation channel is related to the absence of $O(\Lambda^2/Q^2)$ non-perturbative power correction in the standard variant of the operator product expansion formalism, applied to the theoretical expression for the e^+e^- annihilation Adler D-function. Indeed, the existence of lowest dimension-4 quark and gluon condensates 35) in this channel can be associated in terms of renormalon language with the existence of the **leading** IRR pole, which in case of ‘‘Borelization’’ of the Adler D-function is appearing at $\delta = 2$. However, as was already discussed above, the dimension-2 non-perturbative corrections enter into the theoretical expressions for the three DIS sum rules we are interested in. In the IRR language, this

corresponds to the appearance of a $\delta = 1$ IRR pole²⁾, which manifests itself in the concrete results of Refs. 8), 9) (see Eqs. (27) and (47)). Thus, it should be stressed that the structure of singularities of the Borel sums (or images) is not universal and depends from the physical quantity under consideration.

3 IRR for DIS sum rules and the values of twist-4 corrections

In addition to controlling the sign-positive $n!$ growth of the asymptotic series the existence of $\delta = 1$ IRR gives an ambiguity in taking the Borel integral of Eq. (7) over this pole. In the case of large β_0 expansion and for the series we are interested in, this ambiguity was estimated in Ref. 4); and in our notation, it has the following expression:

$$\Delta C_{\text{sum rules}} \approx -\frac{32\exp(5/3)\Lambda_{\overline{\text{MS}}}^2}{9\beta_0 Q^2}. \quad (48)$$

This estimate may be coordinated with the definition of the twist-4 matrix element in the sum rules we are interested in. Therefore, we will make the assumption that the identical values and signs of the IRR ambiguities indicate that the values of twist-4 contributions to the expressions of GLS, Bjp and Bjump sum rules, normalized to unity, should have the same negative sign and a similar closed value¹⁰⁾.

Let us check this assumption, considering the following expressions for the sum rules we are interested in

$$\text{GLS}(Q^2) = 3 \left[1 - 4a_s - O(a_s^2) - \frac{A}{Q^2} \right], \quad (49)$$

$$\text{Bjp}(Q^2) = \frac{g_A}{6} \left[1 - 4a_s - O(a_s^2) - \frac{B}{Q^2} \right], \quad (50)$$

$$\text{Bjump}(Q^2) = \left[1 - \frac{8}{3}a_s - O(a_s^2) - \frac{C}{Q^2} \right], \quad (51)$$

where $A = \langle\langle O_1 \rangle\rangle/3$, $B = \langle\langle O_2 \rangle\rangle(6/g_A)$ and $C = \langle\langle O_3 \rangle\rangle$ and compare in Table 1 the results of different theoretical and phenomenologically based evaluations of the twist-4 parameters A, B and C.

In the case of the GLS and Bjump sum rules the results of the original application of the three-point function QCD sum rules method gave $\langle\langle O^S \rangle\rangle = 0.33 \text{ GeV}^2$ and $\langle\langle O^{\text{NS}} \rangle\rangle = 0.15 \text{ GeV}^2$, with over 50% error bars³⁶⁾, while

Table 1: *The results for twist-4 contributions to the GLS, B_{jp} and B_{jnp} sum-rule expressions of Eqs. (49)–(51).*

	A [GeV ²]	B [GeV ²]	C [GeV ²]
QCD sum rules (Ref. 36))	0.098 ± 0.049	—	0.133 ± 0.065
QCD sum rules (Ref. 19)	—	0.063 ± 0.031	—
QCD sum rules (Ref. 20)	0.158 ± 0.078	0.223 ± 0.118	0.16 ± 0.08
QCD sum rules (Ref. 21))	—	0.025 ± 0.012	—
Instanton model (Ref. 39))	0.078 ± 0.039	0.087 ± 0.043	—
Instanton model (Ref. 40))	—	—	0.16 ± 0.08
Experiment (Ref. 41))	—	0.098 ± 0.028	—
Experiment (Ref. 43))	0.04 ± 0.13	—	—

the three-point function estimates for the modified results of calculations of the twist-4 parameter of the B_{jp} sum rule resulted in the following value $M_N^2 f_2^{p-n} = -0.18 \pm 0.09 \text{ GeV}^2$ in the region where nucleon target mass corrections of $O(M_N^2/Q^2)$ may be neglected¹⁹⁾. As was already mentioned, these calculations were re-examined using three-point function QCD sum-rules approach in Refs. 20) and 21). In the first case the obtained result turned out to be larger than the original results from Ref. 19) and has the following value of $M_N^2 f_2^{p-n} = -0.634 \pm 0.317 \text{ GeV}^2$ ²⁰⁾, while in the latter case it was considerably smaller, namely $M_N^2 f_2^{p-n} = -0.07 \pm 0.035$ ²¹⁾, although within 50% theoretical uncertainty we adopt for all calculations within three-point function QCD sum-rules approach, this value does not disagree with the results obtained in Ref. 19).

In Table 1 we present the estimates of twist-4 corrections to different DIS sum rules, obtained with the help of the three-point function QCD sum-rules approach and compare them with the results of the application of different theoretical approach, based on the picture of the QCD vacuum as a “medium” of instantons³⁷⁾. This picture was further developed in the method in Ref. 38) and applied for estimating twist-4 contributions to the GLS sum rule and B_{jp} sum rule in Ref. 39), while the number for the twist-4 contribution to the B_{jnp} sum rule, which follows from this approach, was presented in Ref. 40). In the absence of estimates of theoretical uncertainties within this approach, we will

apply to them the careful 50% estimate. All these results support the original results of the three-point function QCD sum rules calculations of the twist-4 corrections to the GLS, Bjunp sum rules ³⁶⁾ and Bjp sum rule ¹⁹⁾, though the additional three-point function QCD sum rules cross-check of the results of Ref. ¹⁹⁾ may be rather useful.

The experimentally motivated value of the twist-4 contribution to the Bjorken sum rule $M_n^2 f_2^{p-n} = -0.28 \pm 0.08 \text{ GeV}^2$ ⁴¹⁾ was obtained by means of integrating in x the numerator of the dimensionless $h(x)/Q^2$ contributions, extracted from the fits of world average data for $g_1^p(x, Q^2)$ and $g_1^n(x, Q^2)$ performed in Ref. ⁴²⁾. From the results of Table 1 one can see that the agreement with the QCD sum-rules calculations of Ref. ¹⁹⁾ and instanton-based calculations of Ref. ³⁹⁾ is more than qualitative.

The experimentally inspired estimate for the twist-4 contribution to the GLS sum rule was obtained only recently ⁴³⁾ as a result of the integration of x -dependence of the twist-4 contribution $h(x)/Q^2$, extracted in the works of Ref. ⁴⁴⁾ devoted to the analysis of xF_3 data of CCFR collaboration. One can see that the central value of the contribution is negative (in fact it comes with the negative sign in the sum rule) but has rather large uncertainties. So, at the present level we cannot obtain from this estimate even qualitative information and additional work on its improvement is needed.

To conclude, we present the final results for the GLS, Bjp and Bjunp sum rules, where for definiteness the twist-4 matrix elements are estimated using the central values of the three-point function QCD sum-rules results from Refs. ³⁶⁾ and ¹⁹⁾:

$$\text{GLS}(Q^2) = 3 \left[1 - 4a_s - O(a_s^2) - \frac{0.098 \text{ GeV}^2}{Q^2} \right], \quad (52)$$

$$\text{Bjp}(Q^2) = \frac{g_A}{6} \left[1 - 4a_s - O(a_s^2) - \frac{0.063 \text{ GeV}^2}{Q^2} \right], \quad (53)$$

$$\text{Bjunp}(Q^2) = \left[1 - \frac{8}{3}a_s - O(a_s^2) - \frac{0.133 \text{ GeV}^2}{Q^2} \right]. \quad (54)$$

It should be stressed that they all have the same negative sign and within existing theoretical uncertainties are in agreement with each other. This fact was anticipated by the identical value of the ambiguity, generated by the $\delta = 1$ IRR pole of the Borel images of all these three sum rules (see Eq. (48)). More-

over, as follows from the results of application of the single-renormalon chain approximation in the perturbative sector presented in Sec.2, we may expect a similar asymptotic behaviour of the perturbative corrections to all these three sum rules (compare Eqs.(33)–(36) with Eqs.(42)–(45)). It is interesting that the similar property is manifesting itself in perturbative series under investigations at the $O(\alpha_s^3)$ level, studied within scheme-invariant approaches in Ref. 30).

These facts give us the idea that the sum rules we are interested in are closely related and that, in the region, where we can neglect target mass corrections and twist-3 contributions to the Bjp sum rule and quark-mass dependent corrections (say in the region $Q^2 \geq 2 \text{ GeV}^2$) we can write down the following basic relation 10):

$$\text{Bjp}(Q^2) \approx (g_A/18)\text{GLS}(Q^2) \approx (g_A/6)\text{Bjump}(Q^2) \quad . \quad (55)$$

In the next section we will present more detailed considerations of the experimental consequences of these relations than those, that are briefly outlined in Ref. 10).

4 IRR- inspired relations and experiment

In order to test whether our basic relation Eq. (55) is respected by experiment, we first present the results of the extraction of the GLS sum rule by combining CCFR neutrino DIS data with the data for other neutrino DIS experiments for $1 \text{ GeV}^2 < Q^2 < 15 \text{ GeV}^2$ 45). It is known that the weighted extraction of $\alpha_s(M_Z)$ from these data result in the rather rough value $\alpha_s(M_Z) = 0.115 \pm_{0.12}^{0.009}$, which, however, is in agreement with $\alpha_s(M_Z) = 0.115 \pm 0.001$ (*stat*) ± 0.005 (*syst*) ± 0.003 (*twist*) ± 0.0005 (*scheme*), extracted in Ref. 46) from the previous CCFR data for the GLS sum rule at $Q^2 = 3 \text{ GeV}^2$ 47). However, for our purposes we will not need to re-extract $\alpha_s(M_Z)$ values from the GLS sum rule results of Ref. 45), but will use these, which are presented in Table 2.

To estimate the values of the Bjp sum rule from the results of Table 2 we will use our main equation (55) and will compare them with available experimental data for the Bjp sum rule. The results of these studies are presented in Table 3.

One can see that though the central values of estimated numbers for the Bjp SR are higher than the results of the SLAC E143 collaboration 48), they

Table 2: *The results for the GLS sum rule from Ref. 45)*

Q^2 [GeV ²]	GLS sum rule
2.00	$2.49 \pm 0.08 \pm 0.14$
3.16	$2.55 \pm 0.08 \pm 0.10$
5.01	$2.78 \pm 0.06 \pm 0.19$
7.94	$2.82 \pm 0.07 \pm 0.19$
12.59	$2.80 \pm 0.13 \pm 0.18$

Table 3: *The comparison of the results of application of Eq. (55) with direct experimentally motivated numbers.*

Q^2 [GeV ²]	Bjp from Table 1	Bjp SR (exp)
2.00	$0.174 \pm 0.006 \pm 0.010$	0.169 ± 0.025 [Ref. 48)]
3.16	$0.178 \pm 0.004 \pm 0.007$	0.164 ± 0.023 [Ref. 48)]
5.01	$0.195 \pm 0.004 \pm 0.013$	0.181 ± 0.012 (stat) ± 0.018 (syst) [Ref. 49)]
7.94	$0.197 \pm 0.005 \pm 0.013$	—
12.5	$0.196 \pm 0.009 \pm 0.013$	0.195 ± 0.029 Ref. 50)

agree within error bars. It is also interesting to compare the result from Table 3 with the value of the Bjp sum rule extracted in Ref. 51) from the SLAC and SMC data $B_{jp}(3 \text{ GeV}^2) = 0.177 \pm 0.018$ and which, within error bars, do not contradict the value $B_{jp}(3 \text{ GeV}^2) = 0.164 \pm 0.011$ used in the work of Ref. 52). It is rather inspiring that within error bars these results agree with the GLS sum rule value at $Q^2 = 3.16 \text{ GeV}^2$. The same feature holds for the Bjp sum rules at $Q^2 = 5 \text{ GeV}^2$, namely for the SMC result of Ref. 49). Thus we think that within existing uncertainties our approximate IRR-inspired basic equation (55) is supported by existing experimental data.

5 Conclusions

We demonstrated that the existing phenomenological data do not contradict the basic relation of Eq. (55) and therefore **the reliability of the one-renormalon chain approximation of the theoretical quantities under consideration**. For its more detailed studies, we may rely on the appearance of Neutrino Factory data for all sum rules, which enter in Eq. (55). In fact it may

provide rather useful data not only for the GLS and Bjp sum rules, but for the Bjp sum rule as well (for a discussion of this possibility see Refs. 53), 54).

Another interesting option of the relation of Eq. (55) is to analyse the sources of its possible violation in the lower energy region of over $Q^2 \approx 1 \text{ GeV}^2$, where one may compare the CCFR data for the GLS sum rule at the energy point $Q^2 = 1.26 \text{ GeV}^2$ 45) and the JLAB data for the Bjp sum rule at $Q^2 = 1.10 \text{ GeV}^2$ 22).

To conclude this section, we would like to emphasize that the problems considered by us in this work are complementary to the considerations of Ref. 55). In the former analysis, the GLS and Bjp sum rules were determined in the high energy point of over $Q^2 = 12.33 \text{ GeV}^2$ from the generalized Crewther relation constructed in 8), 55), 56) using the extension of the BLM approach of Ref. 57) and the analysis of e^+e^- annihilation data from Ref. 58). Certainly, the renormalon-chain insertions are absorbed in this approach into the BLM scale. However, the considerations within this language of the high-twist effects is still missed. It may be of interest to think of the possibility of evaluating high-twist contributions to the Crewther relation, which relates, in the Euclidian region we are working massless QCD perturbative contributions to the Adler D-function of e^+e^- -annihilation with the perturbative corrections to the GLS and Bjp sum rules.

6 Acknowledgements

I am grateful to D.J. Broadhurst for a productive collaboration. It is a pleasure to express my personal thanks to S.I. Alekhin, G. Altarelli, Yu.L. Dokshitzer, J. Ellis, G. Grunberg, A.V. Sidorov and V.I. Zakharov for useful discussions at various stages of this work. This article grew up from my talk at the 19th Rencontre de Physique de la Vallée d'Aoste (27 February-5 March, 2005, La Thuile, Aosta Valley, Italy). I would like to thank its organizers, G. Bellettini and M. Greco for their invitation. This work is supported by RFBR Grants N03-02-17047, 03-02-17177 and is done within scientific project of RFBR Grant N 05-01-00992. It was completed during my visit to CERN. I have real pleasure in thanking the members of the CERN Theory Group for hospitality.

References

1. V. I. Zakharov, Nucl. Phys. B **385**, 452 (1992).
2. A. H. Mueller, Phys. Lett. B **308**, 355 (1993).
3. M. Beneke, Phys. Rep. **317**, 1 (1999) [arXiv:hep-ph/9807443].
4. M. Beneke and V. M. Braun, In the “Boris Ioffe Festschrift : At the Frontiers of Particle Physics/Handbook of QCD”, Ed. by M. Shifman (World Scientific, 2001), pp. 1719–1773 [arXiv:hep-ph/0010208].
5. G. Altarelli, CERN/TH-95-309, Proc. Int. School of Subnuclear Physics: 33rd Course “Vacuum and Vacua: The Physics of Nothing”, Ed. A. Zichichi, 1995, pp. 221–248.
6. R. B. Dingle, Asymptotic expansions: their derivation and interpretation, Ch. XXI (Academic Press, London and New York, 1973).
7. M. Beneke, V. M. Braun and N. Kivel, Phys. Lett. B **443**, 308 (1998) [arXiv:hep-ph/9809287].
8. D. J. Broadhurst and A. L. Kataev, Phys. Lett. B **315**, 179 (1993) [arXiv:hep-ph/9308274].
9. D. J. Broadhurst and A. L. Kataev, Phys. Lett. B **544**, 154 (2002) [arXiv:hep-ph/0207261].
10. A. L. Kataev, to appear in JETP. Lett. **81** (2005); arXiv:hep-ph/0505108.
11. D. J. Gross and C. H. Llewellyn Smith, Nucl. Phys. B **14**, 337 (1969).
12. S. G. Gorishny and S. A. Larin, Phys. Lett. B **172**, 109 (1986).
13. S. A. Larin and J. A. M. Vermaseren, Phys. Lett. B **259**, 345 (1991).
14. E. V. Shuryak and A. I. Vainshtein, Nucl. Phys. B **199**, 451 (1982).
15. J. D. Bjorken, Phys. Rev. **148**, 1467 (1966).
16. E. V. Shuryak and A. I. Vainshtein, Nucl. Phys. B **201**, 141 (1982).
17. X. D. Ji and P. Unrau, Phys. Lett. B **333**, 228 (1994) [arXiv:hep-ph/9308263].
18. I. Hinchliffe and A. Kwiatkowski, Annu. Rev. Nucl. Part. Sci. **46**, 609 (1996) [arXiv:hep-ph/9604210].
19. I. I. Balitsky, V. M. Braun and A. V. Kolesnichenko, Phys. Lett. B **242** 245 (1990) [Erratum-*ibid.* B **318**, 648 (1993)] [arXiv:hep-ph/9310316].
20. G. G. Ross and R. G. Roberts, Phys. Lett. B **322**, 425 (1994) [arXiv:hep-ph/9312237].

21. E. Stein, P. Gornicki, L. Mankiewicz, A. Schafer and W. Greiner, Phys. Lett. B **343**, 369 (1995) [arXiv:hep-ph/9409212].
22. A. Deur *et al.*, Phys. Rev. Lett. **93**, 212001 (2004) [arXiv:hep-ex/0407007].
23. J. D. Bjorken, Phys. Rev. **163**, 1767 (1967).
24. K. G. Chetyrkin, S. G. Gorishny, S. A. Larin and F. V. Tkachov, Phys. Lett. B **137**, 230 (1984).
25. S. A. Larin, F. V. Tkachov and J. A. M. Vermaseren, Phys. Rev. Lett. **66**, 862 (1991).
26. D. J. Broadhurst and A. G. Grozin, Phys. Rev. D **52**, 4082 (1995) [arXiv:hep-ph/9410240].
27. C. N. Lovett-Turner and C. J. Maxwell, Nucl. Phys. B **452**, 188 (1995) [arXiv:hep-ph/9505224].
28. E. Gardi and M. Karliner, Nucl. Phys. B **529**, 383 (1998) [arXiv:hep-ph/9802218].
29. A. I. Vainshtein and V. I. Zakharov, Phys. Rev. Lett. **73**, 1207 (1994) [Erratum-*ibid.* **75**, 3588 (1995)] [arXiv:hep-ph/9404248].
30. A. L. Kataev and V. V. Starshenko, Mod. Phys. Lett. A **10**, 235 (1995) [arXiv:hep-ph/9502348].
31. P. M. Stevenson, Phys. Rev. D **23**, 2916 (1981).
32. G. Grunberg, Phys. Rev. D **29**, 2315 (1984).
33. M. Beneke, Nucl. Phys. B **405**, 424 (1993).
34. D. J. Broadhurst, Z. Phys. C **58**, 339 (1993).
35. M. A. Shifman, A. I. Vainshtein and V. I. Zakharov, Nucl. Phys. B **147**, 385 (1979).
36. V. M. Braun and A. V. Kolesnichenko, Nucl. Phys. B **283**, 723 (1987).
37. E. V. Shuryak, Nucl. Phys. B **203**, 93 (1982).
38. D. Diakonov and V. Y. Petrov, Nucl. Phys. B **245**, 259 (1984).
39. J. Balla, M. V. Polyakov and C. Weiss, Nucl. Phys. B **510**, 327 (1998) [arXiv:hep-ph/9707515].
40. C. Weiss, J. Phys. G **29**, 1981 (2003) [arXiv:hep-ph/0210132].
41. A. V. Sidorov and C. Weiss, arXiv:hep-ph/0410253.

42. E. Leader, A. V. Sidorov and D. B. Stamenov, Phys. Rev. D **67**, 074017 (2003) [arXiv:hep-ph/0212085].
43. A. V. Sidorov, private communication.
44. A. L. Kataev, A. V. Kotikov, G. Parente and A. V. Sidorov, Phys. Lett. B **417**, 374 (1998) [arXiv:hep-ph/9706534];
A. L. Kataev, G. Parente and A. V. Sidorov, Nucl. Phys. B **573**, 405 (2000) [arXiv:hep-ph/9905310] ;
A. L. Kataev, G. Parente and A. V. Sidorov, Phys. Part. Nucl. **34**, 20 (2003) [Fiz. Elem. Chast. Atom. Yadra **34**, 43 (2003)] [arXiv:hep-ph/0106221].
45. J. H. Kim *et al.*, Phys. Rev. Lett. **81**, 3595 (1998) [arXiv:hep-ex/9808015].
46. J. Chyla and A. L. Kataev, Phys. Lett. B **297**, 385 (1992) [arXiv:hep-ph/9209213].
47. W. C. Leung *et al.*, Phys. Lett. B **317**, 655 (1993).
48. K. Abe *et al.* [E143 collaboration], Phys. Rev. D **58**, 112003 (1998) [arXiv:hep-ph/9802357].
49. B. Adeva *et al.* [Spin Muon Collaboration], Phys. Rev. D **58**, 112002 (1998).
50. B. Adeva *et al.* [Spin Muon Collaboration (SMC)], Phys. Lett. B **412**, 414 (1997).
51. G. Altarelli, R. D. Ball, S. Forte and G. Ridolfi, Nucl. Phys. B **496**, 337 (1997) [arXiv:hep-ph/9701289].
52. J. R. Ellis, E. Gardi, M. Karliner and M. A. Samuel, Phys. Lett. B **366**, 268 (1996) [arXiv:hep-ph/9509312].
53. M. L. Mangano *et al.*, arXiv:hep-ph/0105155.
54. S. I. Alekhin and A. L. Kataev, J. Phys. G **29**, 1993 (2003) [arXiv:hep-ph/0209165].
55. S. J. Brodsky, G. T. Gabadadze, A. L. Kataev and H. J. Lu, Phys. Lett. B **372**, 133 (1996) [arXiv:hep-ph/9512367].
56. R. J. Crewther, Phys. Rev. Lett. **28**, 1421 (1972) and Phys. Lett. B **397**, 137 (1997) [arXiv:hep-ph/9701321].
57. S. J. Brodsky, G. P. Lepage and P. B. Mackenzie, Phys. Rev. D **28**, 228 (1983).
58. A. C. Mattingly and P. M. Stevenson, Phys. Rev. D **49**, 437 (1994) [arXiv:hep-ph/9307266].

SESSION IV – HEAVY FLAVOUR PHYSICS

- *Mario Antonelli* $|V_{us}|$ and Rare K_S Decays at KLOE
- *Fabio Ambrosino* KLOE Results on the $f_0(980)$, $a_0(980)$ Scalars and η Decays
- *Gang Li* Recent Results on Charmonium Physics at BES
- *Ping Wang* Psi-Psi Phases and Impact on Measurements in Charmonium
- *Alex Smith* Recent Results from CLEO-c
- *Mike Hildreth* Production, Lifetimes, and Masses of B and C Hadrons
- *A. Kuzmin* Charm Physics at BELLE
- *Steven Robertson* Rare Decays and Exotic States at BaBar
- *Vittorio Lubicz* Determination of V_{us} : Recent Progresses from Theory
- *Victor Novikov* Binary Systems in QM and in QFT: CTP

$|V_{us}|$ & RARE K_S DECAYS FROM KLOE

the KLOE collaboration,

A. Aloisio, F. Ambrosino, A. Antonelli, M. Antonelli, C. Bacci,
G. Bencivenni, S. Bertolucci, C. Bini, C. Bloise, V. Bocci, F. Bossi,
P. Branchini, S. A. Bulychjov, R. Caloi, P. Campana, G. Capon,
T. Capussela, G. Carboni, F. Ceradini, F. Cervelli, F. Cevenini,
G. Chiefari, P. Ciambrone, S. Conetti, E. De Lucia, P. De Simone,
G. De Zorzi, S. Dell’Agnello, A. Denig, A. Di Domenico, C. Di Donato,
S. Di Falco, B. Di Micco, A. Doria, M. Dreucci, O. Erriquez,
A. Farilla, G. Felici, A. Ferrari, M. L. Ferrer, G. Finocchiaro,
C. Forti, P. Franzini, C. Gatti, P. Gauzzi, S. Giovannella,
E. Gorini, E. Graziani, M. Incagli, W. Kluge, V. Kulikov,
F. Lacava, G. Lanfranchi, J. Lee-Franzini, D. Leone, F. Lu, M. Martemianov,
M. Martini, M. Matsyuk, W. Mei, L. Merola, R. Messi,
S. Miscetti, M. Moulson, S. Müller, F. Murtas, M. Napolitano,
F. Nguyen, M. Palutan, E. Pasqualucci, L. Passalacqua, A. Passeri,
V. Patera, F. Perfetto, E. Petrolo, L. Pontecorvo, M. Primavera,
P. Santangelo, E. Santovetti, G. Saracino, R. D. Schamberger,
B. Sciascia, A. Sciubba, F. Scuri, I. Sfiligoi,
A. Sibidanov, T. Spadaro, E. Spiriti, M. Tabidze, M. Testa, L. Tortora,
P. Valente, B. Valeriani, G. Venanzoni, S. Veneziano, A. Ventura,
S. Ventura, R. Versaci, I. Villella, G. Xu

Abstract

From a sample of about 10^9 ϕ -mesons produced at DAΦNE, we select K_L and K_S tagged mesons. We present the results on the search for $K_S \rightarrow 3\pi^0$, the first observation of $K_S \rightarrow \pi\mu\nu$, and the measure the major K_L branching ratios, including the semileptonic decays relevant for the $|V_{us}|$ determination. A measurement of the K_L lifetime, using $K_L \rightarrow \pi^0\pi^0\pi^0$ decays, is also given.

The KLOE experiment ¹⁾ operates at DAΦNE ²⁾, an e^+e^- collider working at a center of mass energy $W \sim m_\phi \sim 1.02$ GeV. ϕ -mesons are produced with a visible cross section of $\sim 3.2\mu\text{b}$. Data for an integrated luminosity of 450 pb^{-1} at the ϕ peak have been collected during years 2001 and 2002, corresponding to $\sim 1.4 \times 10^9$ ϕ -mesons produced.

A ϕ meson decays $\sim 34\%$ of the times into $K^0\bar{K}^0$ pairs. Neutral kaons get a momentum of $\sim 110 \text{ MeV}/c$ ($\beta_K \sim 0.22$). At these momenta, K_S and K_L can be distinguished by their mean decay lengths: $\lambda_S \sim 0.6 \text{ cm}$ and $\lambda_L \sim 340 \text{ cm}$.

The KLOE detector ³⁾ consists essentially of a 4 m diameter drift chamber surrounded by a lead-scintillating fiber electromagnetic calorimeter. A superconducting coil surrounding the barrel provides a 0.52 T magnetic field. Momentum resolution for tracks at large polar angle is $\sigma_p/p \leq 0.4\%$. Calorimeter energy resolution is $\sigma_E/E \sim 5.7\%/\sqrt{E(\text{GeV})}$ and the intrinsic time of flight resolution is $\sigma_T = 54 \text{ ps}/\sqrt{E(\text{GeV})} \oplus 50 \text{ ps}$.

When a ϕ meson decays, C -parity invariance forces $K^0 - \bar{K}^0$ to be in a correlated K_S - K_L state. The observation of a K_S therefore, tags the K_L in the opposite hemisphere and vice-versa.

About half of the K_L -mesons reach the calorimeter, where most originate a nuclear interaction, “ K_L -crash”. A K_L -crash is identified as a local energy deposit with energy above 100 MeV and a time of flight consistent with $\beta \sim 0.22$. The coordinates of the energy deposit determine the K_L 's direction to $\sim 20 \text{ mrad}$. K_S tagging efficiency is $\sim 30\%$.

K_L events are identified by the presence of a $K_S \rightarrow \pi^+\pi^-$ decay. We require a vertex with two opposite curvature tracks close to the IP. The two-tracks invariant mass must be within 5 MeV of m_{K_S} . The magnitude of the total momentum of the two tracks must be within 10 MeV of the value expected from the value of \vec{p}_ϕ . Tagging efficiency is $\sim 65\%$.

The tagged K_S (K_L) momentum is obtained from the decay kinematics of $\phi \rightarrow K_S K_L$ using the reconstructed K_L (K_S) direction and the known value of \vec{p}_ϕ .

1 Search for $K_S \rightarrow \pi^0 \pi^0 \pi^0$

A K_L -crash tag and six neutral clusters coming from the IP are required in the search for $K_S \rightarrow \pi^0 \pi^0 \pi^0$. The major background is $K_S \rightarrow 2\pi^0 + 2$ fake photons from shower fragments, machine background clusters in overlap with the events or both.

To reduce the background a kinematic fit has been performed. The K_S mass, K_L 4-momentum conservation and $\beta = 1$ for each γ is imposed. We also define 2 pseudo- χ^2 , $\chi_{3\pi}^2$ and $\chi_{2\pi}^2$. The $\chi_{3\pi}^2$ is based on only the 3 best reconstructed pion masses, while the $\chi_{2\pi}^2$ selects 4 out of the 6 photons providing the best kinematic agreement with the $\pi^0 \pi^0$ decay.

The residual contamination due to fake K_L -crash tags from $K_S \rightarrow \pi^+\pi^-$, $K_L \rightarrow 3\pi^0$ events is reduced to a negligible amount by vetoing events with tracks coming from the IP. To enforce the selection we add a cut on the variable $\Delta E = M_\phi/2 - \sum E_i$, where the sum runs over the four γ 's chosen by the $\chi^2_{2\pi}$.

An optimisation of the cuts was performed to obtain the best average upper limit following the \bar{N}_{90} prescription⁴⁾. The final cuts have been set to: $\chi^2_{fit} < 40.4$, $\Delta E > 1.7$ MeV and we have defined the following signal box region ($12.1 < \chi^2_{2\pi} < 60$ and $\chi^2_{3\pi} < 4.6$).

The selection efficiency is $\varepsilon_{3\pi} = (24.4 \pm 0.6)\%$, and the expected background is $N_b = 3.13 \pm 0.9$. The systematic error on the background is evaluated by comparing data and MC expectations in control boxes around the signal in the $\chi^2_{3\pi}-\chi^2_{2\pi}$ plane.

Two events are found in the data in agreement with the background expectation. We obtain an upper limit on the number of $K_S \rightarrow 3\pi^0$ events of 3.45 at 90% C.L. In the same tagged sample, we get $3.8 \cdot 10^7$ $K_S \rightarrow \pi^0\pi^0$ events so using the $\text{BR}(K_S \rightarrow \pi^0\pi^0)$ we finally derive $\text{BR}(K_S \rightarrow 3\pi^0) \leq 1.2 \cdot 10^{-7}$ at 90% C.L.

2 First observation of $K_S \rightarrow \pi\mu\nu$

The K_L -crash tagged event sample is used for this measurement. Two tracks of opposite curvature forming a vertex close to the IP are required. The invariant mass $M_{\pi\pi}$ of the pair, calculated assuming both tracks are pions, must be smaller than 490 MeV. This rejects $\sim 95\%$ of the $\pi^+\pi^-$ decays.

Muons and pions are discriminated by time of flight (TOF). In order to avoid uncertainties due to the determination of t_0 (the time of the bunch crossing producing the event), we make cuts on the two-track time difference.

Residual background from $K_S \rightarrow \pi^+\pi^-(\gamma)$ is rejected with kinematic cuts and photon detection.

The number of signal events is obtained by fitting the $E_{\text{mis}} - |\vec{p}_{\text{mis}}|$ distribution from data to a linear combination of signal and background Monte Carlo distributions. Background is mostly due to $K_S \rightarrow \pi^+\pi^-$ decays. About 10^3 signal events have been found with a signal to background ratio of about 4.

3 K_L Branching Ratios and $\tau(K_L)$

The K_L absolute branching fractions can be determined on a tagged K_L events sample by counting the fraction of K_L decays in each channel, correcting for acceptances, reconstruction efficiencies and background. However, the tagging procedure is not perfect, because the tagging efficiency depends slightly on the

K_L evolution¹ mainly because of trigger requirements. Therefore care has been put to optimize the tagging algorithm to minimize the tag bias. The tag bias is defined as the ratio of the tagging efficiency of each channel and the overall tagging efficiency.

The hardware calorimeter trigger, which requires two local energy deposits above some threshold (50 MeV on the barrel and 150 MeV on the end caps), is used for the present analysis. The trigger efficiency is essentially 100% for $\pi^0\pi^0\pi^0$, between 95-85% for charged decays and lower for K_L interacting in the calorimeter or escaping. A tighter tag has been used so that the K_S alone satisfies at 99.8% the trigger. The overall efficiency of this tagging is about 10%. The average tag bias is 0.97, 0.98 and 1.00 for $\pi^\pm e^\mp\nu$ or $\pi^\pm\mu^\mp\nu$, $\pi^+\pi^-\pi^0$ and $\pi^0\pi^0\pi^0$ decays, respectively.

The FV used for the analysis is defined inside the drift chamber by $35 < \sqrt{x^2 + y^2} < 150$ cm and $|z| < 120$ cm, where (x, y, z) are the K_L decay vertex position coordinates. The FV acceptance depends on the K_L lifetime.

K_L charged decay modes

We require two good K_L decay tracks forming a vertex to improve the momentum resolution of the K_L decay products. The average tracking efficiency is 54% for K_{e3} 52% for $K_{\mu3}$ and 38% for $\pi^+\pi^-\pi^0$ as evaluated from Monte Carlo simulation and checked on data.

From Monte Carlo studies we found that the best discriminant amongst the K_L charged decay modes is the smallest of the two values of $\Delta_{\mu\pi} = |\vec{p}_{\text{mis}}| - E_{\text{mis}}$, where \vec{p}_{mis} is the missing momentum and E_{mis} is the missing energy evaluated assigning to the two particles the pion and muon masses. The number of signal events is obtained from a fit to the $|\vec{p}_{\text{mis}}| - E_{\text{mis}}$ distribution from data to a linear combination of Monte Carlo distributions for $K_L \rightarrow \pi^\pm e^\mp\nu$, $K_L \rightarrow \pi^\pm\mu^\mp\nu$ and $K_L \rightarrow \pi^+\pi^-\pi^0$.

Neutral K_L decays

The position of the K_L vertex for decays to neutrals, π^0 , is obtained from the photon time of arrival at the EMC. Each photon determines the K_L decay length L_K . The best value of L_K is the energy weighted average of each measurement. At least three photons with energy greater than 20 MeV originating from the K_L decay are required for the $K_L \rightarrow \pi^0\pi^0\pi^0$ event selection. A similar selection⁶⁾ has been used for the lifetime measurement. The selection efficiency is about 99% with a residual contamination of 1.3% mainly due to $\pi^+\pi^-\pi^0$.

¹We include events with the K_L interacting in the calorimeter, escaping the detector and all K_L decays

A total of about 13×10^6 tagged K_L events are used for the measurement of the branching fractions. Almost twice as many additional events provide calibration.

The results of the measurement of the absolute branching fractions obtained using for the lifetime the best PDG result, are:

$$\begin{aligned} \text{BR}(K_L \rightarrow \pi^\pm e^\mp \nu) &= \\ &0.4049 \pm 0.0006_{\text{stat}} \pm 0.0008_{\text{syst-stat}} \pm 0.0018_{\text{syst}} \pm 0.0025_{\text{corr-syst}}, \\ \text{BR}(K_L \rightarrow \pi^\pm \mu^\mp \nu) &= \\ &0.2726 \pm 0.0006_{\text{stat}} \pm 0.0006_{\text{syst-stat}} \pm 0.0014_{\text{syst}} \pm 0.0017_{\text{corr-syst}}, \\ \text{BR}(K_L \rightarrow \pi^0 \pi^0 \pi^0) &= \\ &0.2018 \pm 0.0003_{\text{stat}} \pm 0.0004_{\text{syst-stat}} \pm 0.0023_{\text{syst}} \pm 0.0012_{\text{corr-syst}}, \\ \text{BR}(K_L \rightarrow \pi^+ \pi^- \pi^0) &= \\ &0.1276 \pm 0.0004_{\text{stat}} \pm 0.0004_{\text{syst-stat}} \pm 0.0014_{\text{syst}} \pm 0.0008_{\text{corr-syst}}. \end{aligned}$$

Systematic errors due to the accuracy of corrections, data Monte Carlo consistency, signal extraction stability, and limited knowledge of the K_L lifetime have been studied. They amount to 0.9-1 % depending on the decay mode, and are dominated by the knowledge of the $\tau(K_L)$ value and by the uncertainties on the tag bias evaluation.

The sum of all measured BR's above, plus the PDG value for rare decays, 0.0036, is $1.0104 \pm 0.0018_{\text{stat}} \pm 0.0074_{\text{syst}}$, where the result, as remarked earlier depends on K_L lifetime. Turning the argument around, by renormalizing the sum to 1.0 we obtain an indirect measurement of the K_L lifetime:

$$\tau_{K_L} = 50.72 \pm 0.08_{\text{stat}} \pm 0.12_{\text{syst-stat}} \pm 0.33_{\text{syst}} \text{ ns}$$

The K_L proper time distribution obtained with $\sim 15 \times 10^6$ $K_L \rightarrow \pi^0 \pi^0 \pi^0$ decays. is fitted with an exponential inside the FV, with L_K ranging from 50 to 160 cm. In this interval the decay reconstruction efficiency is flat to ~ 0.3 %. Variations of the fit result vs the FV choice are well within the statistical accuracy of the fit itself. Our preliminary result is:

$$\tau(K_L) = 50.87 \pm 0.16_{\text{stat}} \pm 0.26_{\text{syst}} \text{ ns}$$

in agreement with the indirect measurement. The systematic error is dominated by the knowledge of the residual background contamination.

4 $|V_{us}|$ determination

The most precise check on the unitarity of the CKM mixing matrix is provided by measurements of $|V_{us}|$ and $|V_{ud}|$, the contribution of V_{ub} being at the level of

10^{-5} . $|V_{us}|$ is proportional to the square root of the kaon semileptonic partial width. Many factors are necessary for reaching the desired result ⁷⁾. In general we can write for $|V_{us}| \times f_+^{K^0}(0)$

$$\left[\frac{192 \pi^3 \Gamma}{G^2 M^2 S_{ew} I_i(\lambda'_+, \lambda''_+, \lambda_0)} \right]^{1/2} \frac{1}{1 + \delta_{em}^i + \Delta I_i/2}$$

where $f_+^{K^0}$ is the normalization of the form factors at zero momentum transfer and $I_i(\lambda'_+, \lambda''_+, \lambda_0)$ is the integral of the phase space density, factoring out $f_+^{K^0}$ and without radiative corrections. Short distance radiative corrections are in the universal term S_{ew} ⁸⁾. In addition long distance radiative corrections ^{9, 10)} for form factor and phase space density are included as δ_{em}^i and $\Delta I_i(\lambda)$. λ'_+ and λ''_+ are the slope and curvature of the vector form factor f_+ . λ_0 is the slope of the scalar form factor. Using the values $\lambda'_+ = 0.0221 \pm 0.0011$, $\lambda''_+ = 0.0023 \pm 0.0004$ and $\lambda_0 = 0.0154 \pm 0.0008$, from KTeV ¹¹⁾ and ISTRA+ ¹²⁾ we obtain:

$$\begin{aligned} f_+^{K^0} \times |V_{us}| &= 0.2164 \pm 0.0007 \text{ from } K_{Le3} \\ f_+^{K^0} \times |V_{us}| &= 0.2174 \pm 0.0009 \text{ from } K_{L\mu3} \\ f_+^{K^0} \times |V_{us}| &= 0.2169 \pm 0.0017 \text{ from } K_{Se3} \end{aligned}$$

A precise estimate $f_+^{K^0}(0) = 0.961 \pm 0.008$ was first given in 1984 ¹³⁾. Very recently lattice calculations ¹⁴⁾ have given $f_+^{K^0}(0) = 0.960 \pm 0.009$, in excellent agreement with ¹³⁾. Using $V_{ud} = 0.9740 \pm 0.0005$ from ¹⁵⁾ the unitarity band is:

$$f_+^{K^0} \pi^- (0) \times |V_{us}| = 0.2177 \pm 0.0028$$

The possible violation of unitarity in the first row of the CKM matrix which followed from the value for $\text{BR}(K_{e3})$ given in the PDG particle listings is clearly no longer present.

References

1. KLOE coll. **LNF-92/019** (IR) (1992)
2. A. Drago, *et al.* **LNF-03/012** (2003).
3. KLOE coll., M. Adinolfi, *et al.*, *NIM A* **488**, 51 (2002); KLOE coll., M. Adinolfi, *et al.*, *NIM A* **482**, 363 (2002).
4. J.F. Grivaz *et al.*, LAL **92-37**, (1992).

5. Eidelman, S. *et al.*, *Phys. Lett. B* **592**.
6. KLOE coll. , M. Adinolfi, *et al.*, *Phys. Lett. B* **566**, 61.
7. M. Battaglia *et al.*, hep-ph/0304132.
8. A. Sirlin, *Nucl. Phys.* **B196**, 83 (1982).
9. V. Cirigliano *et al.*, *Eur. Phys. J.* **C23**, 121 (2002).
10. V. Cirigliano, H. Neufeld, and H. Pichl, *Eur. Phys. J.* **C35**, 53 (2004).
11. KTeV coll., T. Alexopoulos *et al.*, *Phys. Rev.* D70 (2004).
12. Yushchenko, O. P. *et al.*, *Phys. Lett.* B589 (2004).
13. H. Leutwyler and M. Roos, *Zeit. Phys.* **C25**, 91 (1984).
14. D. Becirevic *et al.*, hep-ph/0403217.
15. Czarnecki, A. *et al.*, hep-ph/0406324.

KLOE RESULTS ON $f_0(980)$, $a_0(980)$ SCALARS AND η DECAYS

The KLOE Collaboration

presented by F. Ambrosino

Dipartimento di Scienze Fisiche

Università degli Studi di Napoli "Federico II" e Sezione INFN, Napoli

Abstract

The KLOE¹ experiment running at the ϕ -factory DAΦNE has collected $\sim 450 \text{ pb}^{-1}$ in the 2001–2002 data taking. We report preliminary results on light meson spectroscopy based on this data sample obtained studying ϕ radiative decays. The nature of $f_0(980)$ and $a_0(980)$ is investigated by studying the shape of the resulting mass spectra, which is sensitive to their structure. A detailed study of the $\eta \rightarrow \pi\pi\pi$ dynamics through a Dalitz plot analysis gives the possibility to confront with theory expectations in view of extracting information on the light quarks mass difference. Finally, the branching ratio for the $\eta \rightarrow \pi^0\gamma\gamma$ decay is compared with previous measurements and with the expectations from Chiral Perturbation Theory.

¹The KLOE Collaboration:

F. Ambrosino, A. Antonelli, M. Antonelli, C. Bacci, P. Beltrame, G. Bencivenni, S. Bertolucci, C. Bini, C. Bloise, V. Bocci, F. Bossi, D. Bowring, P. Branchini, R. Caloi, P. Campana, G. Capon, T. Capussela, F. Ceradini, S. Chi, G. Chiefari, P. Ciambrone, S. Conetti, E. De Lucia, A. De Santis, P. De Simone, G. De Zorzi, S. Dell’Agnello, A. Denig, A. Di Domenico, C. Di Donato, S. Di Falco, B. Di Micco, A. Doria, M. Dreucci, G. Felici, A. Ferrari, M. L. Ferrer, G. Finocchiaro, C. Forti, P. Franzini, C. Gatti, P. Gauzzi, S. Giovannella, E. Gorini, E. Graziani, M. Incagli, W. Kluge, V. Kulikov, F. Lacava, G. Lanfranchi, J. Lee-Franzini, D. Leone, M. Martini, P. Massarotti, W. Mei, S. Meola, S. Miscetti, M. Moulson, S. Müller, F. Murtas, M. Napolitano, F. Nguyen, M. Palutan, E. Pasqualucci, A. Passeri, V. Patera, F. Perfetto, L. Pontecorvo, M. Primavera, P. Santangelo, E. Santovetti, G. Saracino, B. Sciascia, A. Sciubba, F. Scuri, I. Sfiligoi, T. Spadaro, M. Testa, L. Tortora, P. Valente, B. Valeriani, G. Venanzoni, S. Veneziano, A. Ventura, R. Versaci, G. Xu

1 Introduction

The KLOE experiment ¹⁾ operates at DAΦNE, ²⁾ the Frascati e^+e^- collider, whose center of mass energy is equal to the ϕ mass. The detector consists of a large, He based fully stereo drift chamber, and a fine sampling hermetic lead/scintillating fibers calorimeter. A superconducting coil provides a 0.52 T field along the beam axis. Transverse momentum resolution for charged tracks is $\approx 0.4\%$ while energy and time resolution in the calorimeter are respectively $\sigma_E/E = 5.7\%/\sqrt{E(\text{GeV})}$ and $\sigma_t = 54\text{ps}/\sqrt{E(\text{GeV})} \oplus 50\text{ps}$. Data collected in 2001-2002, corresponding to $\sim 450 \text{ pb}^{-1}$, are used to study light scalar and pseudoscalar mesons produced through ϕ radiative decays.

2 Light Scalar Mesons: $f_0(980)$ and $a_0(980)$

The scalar mesons $f_0(980)$ (I=0) and $a_0(980)$ (I=1) appear as resonances in the spectrum of the radiative decays of the ϕ to the final states $\pi^+\pi^-\gamma$, $\pi^0\pi^0\gamma$ and $\eta\pi^0\gamma$ respectively.

The observed mass spectra are sensitive to the nature of the light scalars ³⁾ which is quite unclear ^{4, 5, 6)}: in fact hypotheses have been made about these mesons being four quark states or $K\bar{K}$ molecules rather than “standard” q-qbar mesons. We compare data with two different theoretical models. In the first one the scalar amplitude is described by the kaon-loop model ⁷⁾ while in the second one a point-like approach is followed, with no dynamical assumption. In both cases, the interference with the background with the same final state is taken into account in the fit procedure.

For the $\pi^+\pi^-\gamma$ final state there is a huge irreducible non resonant background $e^+e^- \rightarrow \pi^+\pi^-(\gamma)$ with the additional photon due to either initial state radiation (ISR) or final state radiation (FSR). The signal is enhanced with respect to this background by requiring two tracks and a photon at large angle inside the detector. A clean signal is detected in the $M_{\pi\pi}$ region above 850 MeV (see Fig. 1 left). Moreover, a forward-backward asymmetry

$$A = \frac{N^+(\theta > 90^\circ) - N^+(\theta < 90^\circ)}{N^+(\theta > 90^\circ) + N^+(\theta < 90^\circ)}$$

is expected due to the interference of FSR and ISR. ⁸⁾ In Fig. 1 (right) we show this asymmetry as a function of $M_{\pi\pi}$, both for data and for theoretical predictions with ISR and FSR only. We observe a clear deviation from pure ISR-FSR expectations in the f_0 mass region and in the mass range below 700 MeV, thus adding a further evidence on the observation of a scalar resonance in the $\pi^+\pi^-$ final state.

In the case of the $\pi^0\pi^0\gamma$ final state the $f_0 \rightarrow \pi^0\pi^0$ signal is observed together with a non-resonant background having the same signature, produced

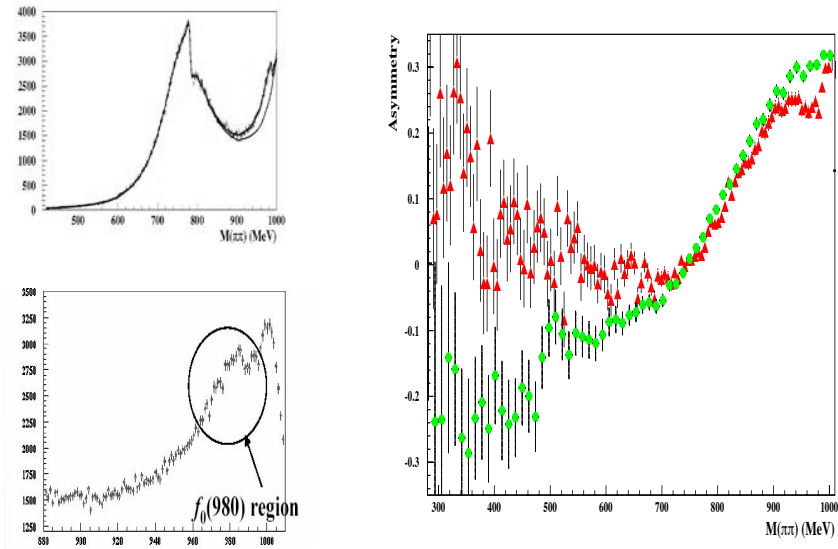


Figure 1: *Upper Left: two pion invariant mass for $\pi^+\pi^-\gamma$ events. The upper and lower curves are the result of the fit and the contribution due to FSR+ISR respectively. Lower Left: zoom of the f_0 region. Right: Forward-backward asymmetry as a function of $M_{\pi\pi}$. Experimental data are reported as dark triangles while light dots represent the Monte Carlo expectations for FSR and ISR only.*

through $\omega\pi^0/\rho\pi^0$ intermediate states. The intensity of this background is twice the signal. In order to account properly the effect of its possible interference with the scalar term we fit the Dalitz plot distribution considering all the amplitudes giving the same final state. A smaller background contamination dominated by $\phi \rightarrow \eta\gamma$, with $\eta \rightarrow \pi^0\pi^0\pi^0$ and two lost or merged photons, is estimated by Monte Carlo and subtracted from the Dalitz plot. When using the kaon-loop model we cannot describe data without introducing a scalar term due to a $\sigma(600)$ meson.

For the fully neutral search of $\phi \rightarrow a_0\gamma$, the background with the same $\eta\pi^0\gamma$ final state is small and simplifies the fit procedure. On the other hand, having a yield ten times smaller than the $f_0 \rightarrow \pi^0\pi^0$, it is contaminated by a large non-interfering background with a five photon signature. The a_0 decay chain with $\eta \rightarrow \pi^+\pi^-\pi^0$ has instead a rate three times smaller than the neutral channel, but it is completely background free. A combined fit of the two channels is in progress to extract the a_0 parameters.

3 Dynamics of $\eta \rightarrow \pi\pi\pi$

The $\eta \rightarrow \pi\pi\pi$ decay is due to the isospin breaking part of the strong Lagrangian and its amplitude is proportional to the d-u quark mass difference; a precise study of this decay can lead to a very accurate measurement of $Q^2 = (m_s^2 - \hat{m}^2)/(m_d^2 - m_u^2)$.

Using the 17 millions η mesons produced in 2001/2002, the dynamics of both $\pi^+\pi^-\pi^0$ and $\pi^0\pi^0\pi^0$ final states has been studied through a Dalitz plot analysis.

The η mesons are clearly tagged by detecting the monochromatic recoil photon of the $\phi \rightarrow \eta\gamma$ decay ($E_{\text{recoil}} = 363$ MeV); the background is at the level of few per mill. Efficiency is almost flat all over the kinematically allowed region (see Fig.2).

For the $\pi^+\pi^-\pi^0$ final state, we choose the conventional Dalitz variables $X \propto T_+ - T_-$ and $Y \propto T_0$, where T is the kinetic energy of the pion. The measured distribution is parametrized as: $|A(X, Y)|^2 = 1 + aY + bY^2 + cX + dX^2 + eXY + fY^3$. As expected from C parity conservation, the odd powers of X are consistent with zero (see Tab. 1) and can be removed from the fit without affecting the determination of the remaining parameters. We clearly observe a non zero quadratic slope in X , and we reach for the first time sensitivity to a cubic term of the expansion; all the cubic terms other than f turn out to be zero in our fit. Using our fitted parameters, the value of Q can be extracted. For example, in Ref. ⁹⁾ the value $Q = 22.8 \pm 0.4$ is obtained, the error being dominated by the $\eta \rightarrow \pi^+\pi^-\pi^0$ width. This value points to a significant violation of the Dashen theorem, and is in agreement with Chiral Perturbation Theory (χ_{PT}) predictions ¹⁰⁾ and with other evaluations based on η decays,

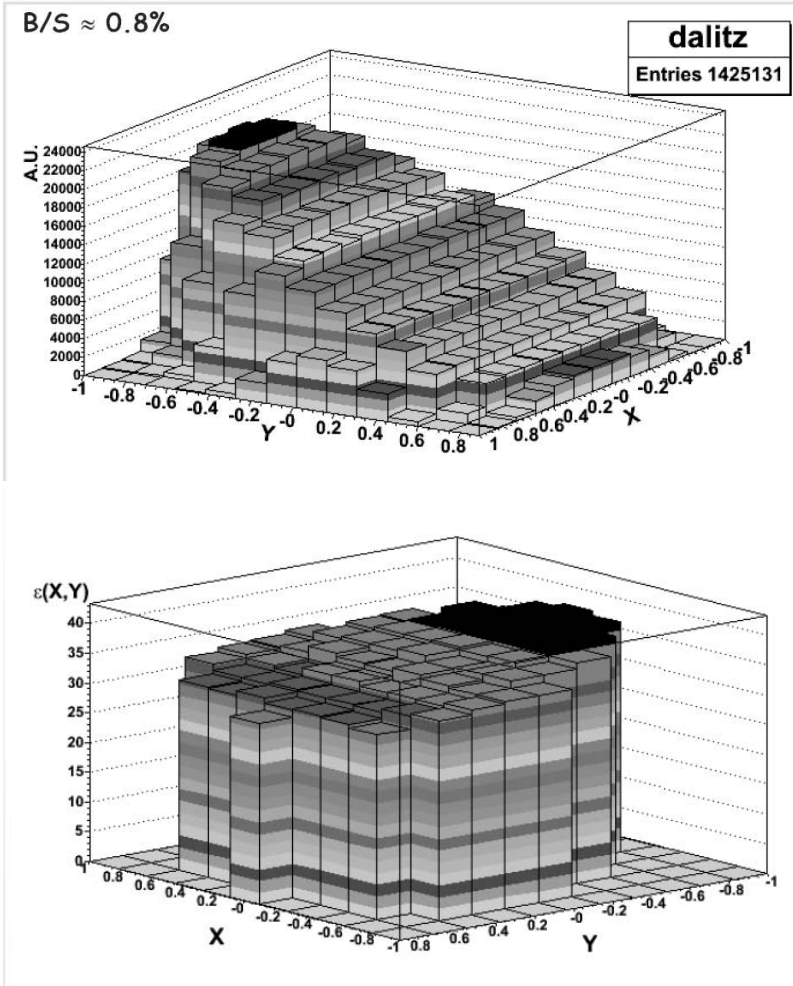


Figure 2: Upper: Dalitz plot of selected $\eta \rightarrow \pi^+ \pi^- \pi^0$ events. Lower: Efficiency of the selection over the kinematically allowed region

a	b	c
$-1.072 \pm 0.006^{+0.005}_{-0.007}$	$0.117 \pm 0.006^{+0.004}_{-0.006}$	$0.0001 \pm 0.0029^{+0.0003}_{-0.0021}$
d	e	f
$0.047 \pm 0.006^{+0.004}_{-0.005}$	$0.006 \pm 0.008^{+0.013}_{-0.000}$	$0.13 \pm 0.01^{+0.02}_{-0.01}$

Table 1: *Fitted parameters of the $\eta \rightarrow \pi^+\pi^-\pi^0$ Dalitz plot. The χ^2 probability is 60% for a 147 dof fit.*

11, 12) which have larger errors.

For the $\eta \rightarrow \pi^0\pi^0\pi^0$ decay the Dalitz plot density is described by a single parameter α : $|A|^2 \propto 1 + 2\alpha z$. Here $z = \rho^2/\rho_{max}^2$ is the square ratio of the distance of a point from the Dalitz plot center (ρ) to the maximum kinematically allowed distance (ρ_{max}). Being related to the square of the three pion energies in the η rest frame α is thus a quadratic slope. Photons are paired to π^0 's after kinematically constraining the total 4-momentum, thus improving the energy resolution; as a second step a fit constraining also the π^0 mass is performed in order to further improve the resolution. By fitting a sample with high purity on pairing (98.5%), corresponding to an analysis efficiency of 4.5%, we get:

$$\alpha = -0.013 \pm 0.005_{\text{stat}} \pm 0.004_{\text{syst}}. \quad (1)$$

4 The $\eta \rightarrow \pi^0\gamma\gamma$ Decay

The $\eta \rightarrow \pi^0\gamma\gamma$ decay is an important test of χ_{PT} because of its sensitivity to p^6 on both the branching ratio (BR) and the $M_{\gamma\gamma}$ spectrum. ^{13, 14)} The present experimental situation is not completely clear: the most accurate determination of the BR ¹⁵⁾ is far from theoretical predictions while a more recent measurement, ¹⁶⁾ with a larger relative error, gives a significantly lower value. Moreover, all previous searches were done at hadron machines, using mainly $\pi^-p \rightarrow \eta n$. The value of the BR has decreased by three orders of magnitude in the last 40 years, due to the improved separation of the $\eta \rightarrow \pi^0\pi^0\pi^0$ background.

KLOE searches for this decay in a much cleaner environment, with different background topologies and experimental systematics. The two orders of magnitude higher background with the same five photon final state ($e^+e^- \rightarrow \omega\pi^0 \rightarrow \pi^0\gamma\pi^0$, $\phi \rightarrow f_0\gamma \rightarrow \pi^0\pi^0\gamma$, $\phi \rightarrow a_0\gamma \rightarrow \eta\pi^0\gamma$ with $\eta \rightarrow \gamma\gamma$) is reduced by vetoing the additional $\omega/\pi^0/\eta$ particles in the event. The remaining background is $\eta \rightarrow \gamma\gamma$ with additional clusters from shower fragmentation or machine background and $\eta \rightarrow \pi^0\pi^0\pi^0$ with merged/lost photons. We reject

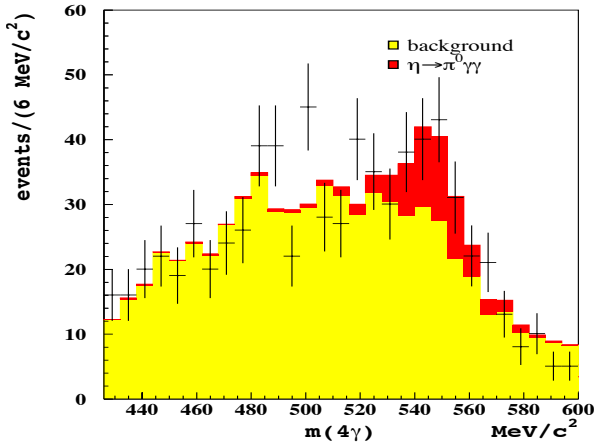


Figure 3: *Four photon invariant mass for $\eta \rightarrow \pi^0 \gamma \gamma$ events. Data (crosses) are fitted with the signal and background contributions evaluated from MC (solid histograms).*

them with energy momentum conservation and a likelihood technique to identify merged clusters. The preliminary results obtained fitting the η invariant mass spectrum (Fig. 3) gives a BR in agreement with $\mathcal{O}(p^6)$ χ_{PT} calculations, with a central value which is three times smaller than the previous measurement:

$$\text{BR}(\eta \rightarrow \pi^0 \gamma \gamma) = (8.4 \pm 2.7_{\text{stat}} \pm 1.4_{\text{syst}}) \times 10^{-5}. \quad (2)$$

References

1. The KLOE Collaboration (A. Aloisio et al.), LNF-92/019 (IR) (1992) and LNF-93/002 (IR) (1993).
2. S. Guiducci et al., Proc. of the 2001 Particle Accelerator Conference (Chicago, Illinois, USA), P. Lucas S. Webber Eds. 353 (2001).
3. N. N. Achasov and V. N. Ivanchenko, *Nucl. Phys. B* **315**, 465 (1989).
4. N. A. Törnqvist, *Phys. Rev. Lett.* **49**, 624 (1982).
5. R. L. Jaffe, *Phys. Rev. D* **15**, 267 (1997).
6. J. Weinstein and N. Isgur, *Phys. Rev. Lett.* **48**, 659 (1982).

7. N. N. Achasov and V. V. Gubin, *Phys. Rev. D* **56**, 4084 (1997).
8. S. Binner, J. H. Kuhn, K. Melnikov, *Phys. Lett. B* 459 (1999) 279
9. B. V. Martemyanov and V. S. Sopov, *Phys. Rev. D* **71**, 017501 (2005).
10. J. Donoghue and A. Perez, *Phys. Rev. D* **55**, 7075 (1997); J. Bijnens and J. Prades, *Nucl. Phys. B* **490**, 239 (1997).
11. J. Kambor, C. Wiesendanger and D. Whyler, *Nucl. Phys. B* **465**, 215 (1996).
12. A. V. Anisovich and H. Leutwyler, *Phys. Lett. B* **375**, 335 (1997).
13. J. Bijnens and J. Gasser, Proc. of Workshop on Production, Interaction and Decay of the η Meson (Uppsala, October 2001), J. Bijnens, G. Fäldt and B. M. K. Nefkens Eds., T99, 34 (Phys. Scripta, Stockholm, 2002)
14. E. Oset, J. R. Pelaez, L. Roca, *Phys. Rev. D* **67**, 073013 (2003).
15. Alde et al., *Z. Phys. C* **25**, 225 (1984).
16. N. Knecht et al., *Phys. Lett. B* **589**, 14 (2004).

RECENT RESULTS ON CHARMONIUM PHYSICS AT BES

Gang, LI *

*China Center for Advanced Science and Technology,
CAS, Beijing, 100049, China*

Abstract

With 58 million J/ψ events and 14 million $\psi(2S)$ events, Partial Wave Analyses have been performed to study scalar mesons κ and σ . There is evidence for the κ near the $K\pi$ threshold and its pole position is $(760 \sim 840) - i(310 \sim 420)\text{MeV}$. The low mass enhancement in $\pi^+\pi^-$ invariant mass spectrum is seen in $J/\psi \rightarrow \omega\pi^+\pi^-$ and its pole position has been determined to be $(541 \pm 39) - i(252 \pm 42)\text{MeV}$; in $\psi(2S) \rightarrow \pi^+\pi^- J/\psi$, the σ destructively interferes with the background term, which suppress the $\pi\pi$ amplitude near threshold to zero. The σ pole position determined in this channel is consistent with that of $J/\psi \rightarrow \omega\pi^+\pi^-$. Many two-body decay channels are studied, which include VP and PP modes. Based on systematical measurements for charmonium decay, 12% rule is tested.

*on behalf of BES Collaboration

1 Introduction

Charmonium decay continues to present itself as a challenge to our understanding of the strong interaction. Up to 2004, BES collaboration has collected 14 Million (M) $\psi(2S)$ events (corresponding integrated luminosity is 19.72 pb^{-1}), 58 M J/ψ events and 6.4 pb^{-1} data taken at 3.65 GeV for continuum study. With all these samples, studies have been made systematically for charmonium decay. Herein the results of $\psi(2S)$ and J/ψ decay include two parts: the scalar meson study on κ and σ and the test of the pQCD 12% rule. The scalar meson are one of the most controversial subjects in hadron physics, especially in case of κ and σ . κ and σ have been carefully studied by performing Partial Wave Analysis(PWA) on many channels of BES data. The results of $\psi(2S)$ and J/ψ decay contain the following topics: decays of $\psi(2S)$ to Vector Pseudoscalar (VP) and Pseudoscalar Pseudoscalar (PP) channels.

2 κ and σ study

2.1 κ in $J/\psi \rightarrow \pi^+\pi^-K^+K^-$ and $J/\psi \rightarrow k_0^*(892)k\pi$

Events over all of the 4-body phase space for $J/\psi \rightarrow \pi^+\pi^-K^+K^-$ have been fitted. We find evidence for the κ in the process $J/\psi \rightarrow K(890)\kappa, \kappa \rightarrow (K\pi)_S$. We select a $K^+\pi^-$ pair in the $K^-\pi^+$ invariant mass in the range $892 \pm 100 \text{ MeV}$ to fit.

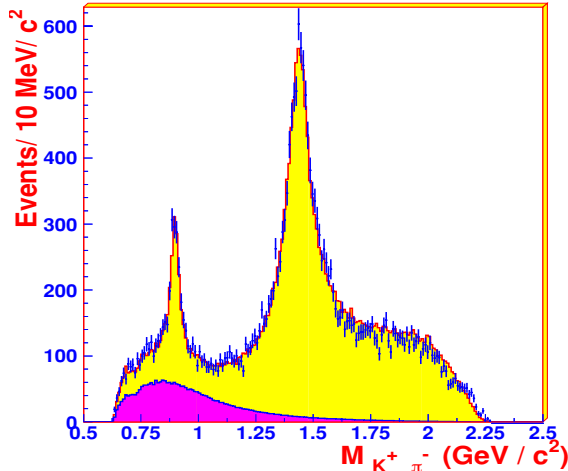


Figure 1: Fit results of $J/\psi \rightarrow K^*K^+\pi^-$. The figure shows the invariant mass distribution of accompanying $K^+\pi^-$ pairs (crosses). The heavy shaded(purple) region is the κ contribution.

The data are fitted with a form for the κ containing an Adler zero in the width. The pole position for κ is at $(760 \pm 20(sta) \pm 40(sys)) - i(420 \pm 45(sta) \pm 60(sys))\text{MeV}$.

For the $K^*(892)K^+\pi^-$ system in the $K^+K^-\pi^+\pi^-$ data, two independent analyses have been performed. Figure ?? shows the recoil $K^+\pi^-$ invariant mass spectrum against $\bar{K}^*(892)^0$, while the heavy shaded histogram is the κ contribution. Both analyses favor that the low mass enhancement in the $K^+\pi^-$ spectrum is a scalar resonance, which is considered to be the κ particle. Its pole position is determined to be $(841 \pm 30_{-73}^{+81}) - i(309 \pm 45_{-72}^{+48})\text{MeV}$.

2.2 σ in $J/\psi \rightarrow \omega\pi^+\pi^-$ and $\psi(2S) \rightarrow J/\psi\pi^+\pi^-$

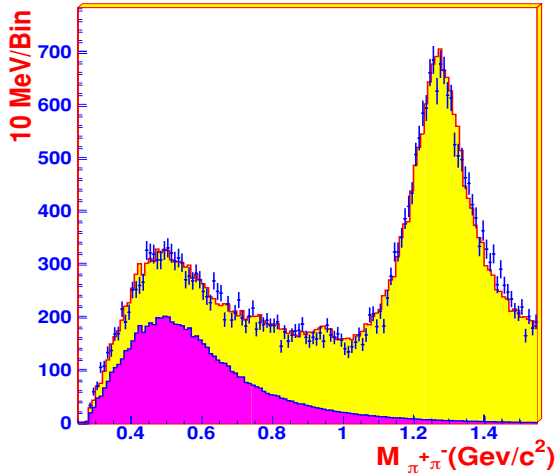


Figure 2: Data and fit results of $J/\psi \rightarrow \omega\pi^+\pi^-$. The figure shows the invariant mass distribution of $\pi^+\pi^-$ pair recoiling a reconstructed ω in an event. (crosses for data and histogram for Monte Carlo projection, the heavy shaded(purple) region is the σ contribution).

In $J/\psi \rightarrow \omega\pi^+\pi^-$, a low mass enhancement in the $\pi\pi$ mass spectrum is observed, which is proved to be not coming from background processes, phase space effect or threshold effect. Two independent partial wave analyses have been performed on this channel^{?)}. In one method, the recoil $\pi^+\pi^-$ mass spectrum in the whole mass region against the ω particle is analyzed. In this analysis the ω decay is considered, and the background is estimated by directly sideband subtraction. In another method, the ω is treated as stable particle. In order to avoid complicity in the higher mass region, only the $\pi\pi$ mass spectrum in the region $M_{\pi\pi} < 1.5\text{GeV}$ is analyzed, and the background is fitted by a

non-interference phase space term in the PWA. In this analysis, the low mass enhancement is proved to be a 0^{++} isoscalar resonance.

Figure ?? shows the $\pi\pi$ invariant mass distribution from $J/\psi \rightarrow \omega\pi^+\pi^-$. The full histogram in Figure ?? shows the maximum likelihood fit, the heavy shaded region shows the σ contribution. Four parametrizations for the σ amplitude are tried in the analyses, and the pole position of the σ particle by these parameterizations are consistent each other. The average pole position is determined to be $(541 \pm 39) - i(252 \pm 42)$ MeV.

Recently, an analysis on $\psi(2S) \rightarrow \pi^+\pi^- J/\psi$ channel has been performed to study the structure of $\pi^+\pi^-$ mass spectrum. The Covariant Helicity Amplitude Analysis is performed on the decay process $\psi(2S) \rightarrow \pi^+\pi^- J/\psi, J/\psi \rightarrow \mu^+\mu^-$.

The $\pi^+\pi^-$ mass spectrum is distinctly different from that of phase space, which suggests the σ production in this process.

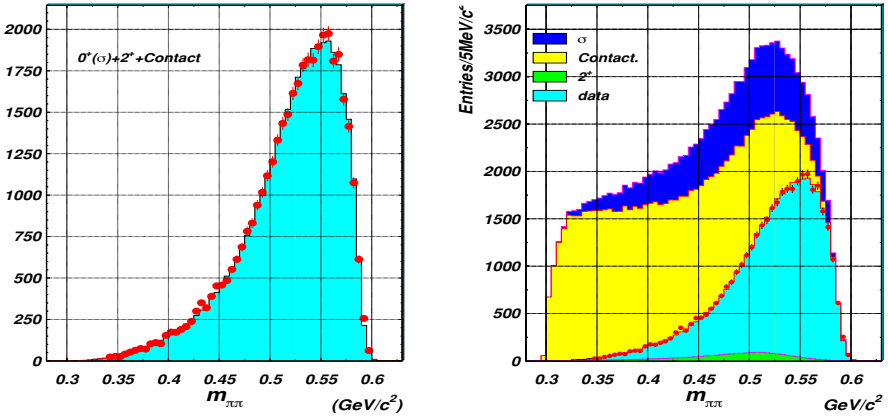


Figure 3: Fit results of $\psi(2S) \rightarrow \pi^+\pi^- J/\psi$. Dot with error bar stands for data and histogram for Monte Carlo. The left is $\pi^+\pi^-$ invariant mass, the right contributions from single components (σ , contact term, d-wave term and data, d-wave is enlarged by a factor of 20.)

Three types of Breit-Wigner parameterizations for the σ are tried in the fit to the data. With a large destructive interference, the $\pi\pi$ amplitude near the threshold is suppressed to almost zero, which is expected by the chiral theory. In addition, the d-wave only gives a very small contribution. Figure ?? shows the fit results. In the left figure the shaded histogram is the fit and the point with error bar is data, and the right shows the contributions from each component (σ , contact term and d-wave term). The σ pole position are

determined to be $(554 \pm 14 \pm 53) - i(242 \pm 5 \pm 24)\text{MeV}$, which is consistent with that of $J/\psi \rightarrow \omega\pi^+\pi^-$

3 Test of 12% rule with $\psi(2S)$ and J/ψ decay

As it is known, both J/ψ and $(2S)$ decays are expected to be dominated by annihilation into three gluons, with widths that are proportional to the square of the $c\bar{c}$ wave function at the origin^{?)}. This yields the pQCD expectation (so-called 12% rule) that

$$Q_h = \frac{B_{\psi(2S) \rightarrow X_h}}{J/\psi \rightarrow X_h} = \frac{B_{\psi(2S) \rightarrow e^+e^-}}{B_{J/\psi \rightarrow e^+e^-}} = (12.3 \pm 0.7)\% \quad (1)$$

The observation of deviation from 12% rule will provide some new clues concerning the dynamics of charmonium decay.

3.1 VP decay mode of $\psi(2S)$

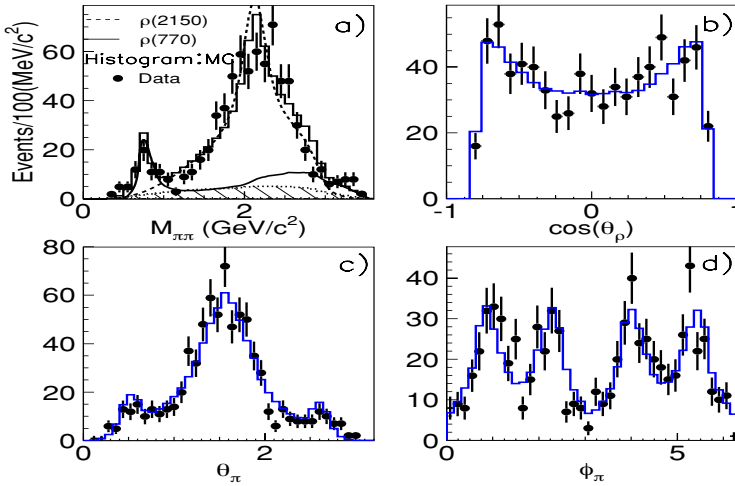


Figure 4: Comparison between data (dots with error bars) and the final fit (solid histograms) for (a) two pion invariant mass, with a solid line for the $\rho(770)\pi$, a dashed line for the $\rho(2150)\pi$, and a hatched histogram for background; (b) the ρ polar angle in the $\psi(2S)$ rest frame; and (c) and (d) for the polar and azimuthal angles of the designated π in ρ helicity frame.

The selected $\pi^+\pi^-\pi^0$ events are fitted in the helicity amplitude formalism with an unbinned maximum likelihood method based on MINUIT (?). The fit shown in Figure ?? describes the data reasonably well, and the $\rho(2150)$ serves as an effective description of the high mass enhancement near 2.15 GeV/ c^2 in $\pi\pi$ mass (?). The branching fractions of $\psi(2S) \rightarrow \pi^+\pi^-\pi^0$, $\rho(770)\pi$ and $\rho(2150)\pi \rightarrow \pi^+\pi^-\pi^0$ are $(18.1 \pm 1.8 \pm 1.9) \times 10^{-5}$, $(5.1 \pm 0.7 \pm 1.1) \times 10^{-5}$ and $(19.4 \pm 2.5^{+11.5}_{-3.4}) \times 10^{-5}$, respectively, where the first error is statistical and the second one is systematic.

Table 1: *The results of $\psi(2S)$ two-body decay.*

VP channels	$B(\psi(2S) \rightarrow) \times 10^{-5}$	$B(J/\psi \rightarrow) \times 10^{-4}$	Q_h (%)
$\rho\pi$	$5.1 \pm 0.7 \pm 1.1$	127 ± 9	0.40 ± 0.11
$K^*(892)^+K^- + c.c.$	$2.9^{+1.3}_{-1.7} \pm 0.4$	50 ± 4	$0.59^{+0.27}_{-0.36}$
$K^*(892)^0\bar{K}^0 + c.c.$	$13.3^{+2.4}_{-2.8} \pm 1.7$	42 ± 4	3.2 ± 0.8
$\omega\pi$	$1.87^{+0.68}_{-0.62} \pm 0.28$	4.2 ± 0.6	$4.4^{+1.8}_{-1.6}$
$\rho\eta$	$1.78^{+0.67}_{-0.62} \pm 0.17$	1.93 ± 0.23	$9.2^{+3.6}_{-3.3}$
$\rho\eta'$	$1.87^{+1.64}_{-1.11} \pm 0.33$	1.05 ± 0.18	$17.8^{+15.9}_{-11.1}$
$\phi\pi^0$	< 0.41	< 0.068	–
$\phi\eta$	$3.3 \pm 1.1 \pm 0.5$	6.5 ± 0.7	5.1 ± 1.9
$\phi\eta'$	$2.8 \pm 1.5 \pm 0.6$	3.3 ± 0.4	8.5 ± 5.0
$\omega\eta$	< 3.2	15.8 ± 1.6	< 2.0
$\omega\eta'$	$3.1^{+2.4}_{-2.0} \pm 0.7$	1.67 ± 0.25	19^{+15}_{-13}
PP channels	$B(\psi(2S) \rightarrow) \times 10^{-5}$	$B(J/\psi \rightarrow) \times 10^{-4}$	Q_h (%)
$K_S K_L$	$5.24 \pm 0.47 \pm 0.48$	$1.82 \pm 0.04 \pm 0.13$	28.8 ± 3.7

For the analysis of electromagnetic decays $\psi(2S) \rightarrow \omega\pi, \rho\eta$ and $\rho\eta'$, beside the $\psi(2S)$ data sample, we also analyze 6.42 pb $^{-1}$ of continuum data at $\sqrt{s} = 3.650$ GeV, and 17.3 pb $^{-1}$ at the $\psi(3770)$. Table ?? lists the cross sections of $e^+e^- \rightarrow \omega\pi, \rho\eta$ and $\rho\eta'$; the branching fractions of $\psi(2S) \rightarrow \omega\pi, \rho\eta$ and $\rho\eta'$ (?) are listed in Table ??.

For $\psi(2S) \rightarrow K^*(892)\bar{K}^- + c.c.$, we study its final state $K_s^0 K^\pm \pi^\mp \rightarrow \pi^+\pi^- K^\pm \pi^\mp$ (?). A large isospin-violation between the charge and neutral mode has been observed. The other decay modes are studied with ϕ decays to K^+K^- , ω to $\pi^+\pi^-\pi^0$, η' to $\eta\pi^+\pi^-$ or $\gamma\pi^+\pi^-$, and π^0 and η to 2γ (?). The results are also listed in Table ??.

3.2 PP decay mode of $\psi(2S)$

The decay $\psi(2S) \rightarrow K_S K_L$ is observed using 14 million $\psi(2S)$ events; the branching fraction is determined to be $B(\psi(2S) \rightarrow K_S K_L) = (5.24 \pm 0.47 \pm 0.48) \times 10^{-5}$ (?). Compared with $J/\psi \rightarrow K_S K_L$ (?), the $\psi(2S)$ branching fraction is enhanced by more than 4σ relative to the prediction of the perturbative QCD "12%" rule.

4 Summary

Partial wave analyses have been performed on BES data to study the scalar mesons. The κ near $K\pi$ threshold is needed and the pole position is $(760 \sim 840) - i(310 \sim 420)\text{MeV}$. The σ is seen clearly in $J/\psi \rightarrow \omega\pi^+\pi^-$ channel and gives an accurate pole position, $(541 \pm 39) - i(252 \pm 42)\text{MeV}$. In $\psi(2S) \rightarrow \pi^+\pi^- J/\psi$, we can fit the $\pi^+\pi^-$ invariant mass spectrum well through a strong destructive interference between σ and contact term, and the σ pole was determined to be $(554 \pm 14 \pm 53) - i(242 \pm 5 \pm 24)\text{MeV}$, which is consistent with that of $J/\psi \rightarrow \omega\pi^+\pi^-$.

The Q-values of 12% rule for two kinds of two-body decay, VP and PP, are listed in Table 1. The branching fractions in our measurement are consistent with those of CLEO (?). It shows clearly the Q-value is enhanced for some channels while suppressed for others. The experimental results show that 12% rule seems to be too simplistic.

I would like to thank Prof. Giorgio Chiarelli for the friendly hospitality. I also would like to thank my colleagues of BES collaboration who provide me so many good results which are reported here.

References

1. M. Ablikim *et al*, Phys. Lett. B**598**, 149 (2004).
2. M. Ablikim *et al*, hep-ex/0408047.
3. F. James, CERN Program Library Long Writeup D506
4. T. Appelquist *et al*, Phys. Rev. Lett. **34**, 43 (1975);
A. De Rújula *et al*, Phys. Rev. Lett. **34**, 46 (1975).
5. J.Z. Bai *et al*, Phys. Rev. D**70**70112007(2004).
6. M. Ablikim *et al*, hep-ex/0407037.
7. J.Z. Bai *et al*, Phys. Rev. D**70**70112003(2004).

8. J.Z. Bai *et al*, Phys. Rev. Lett. **92**, 052001 (2004)
9. J.Z. Bai *et al*, Phys.Rev.D**69**, 052001 (2004)
10. N. E. Adam *et al*, Phys. Rev. Lett. **94**012005(2005)

$\Psi - \Psi'$ PHASES AND IMPACT ON MEASUREMENTS
IN CHARMONIUM

Ping Wang
IHEP, Beijing, China

Written contribution not received

RECENT RESULTS FROM CLEO-c

Alex Smith

University of Minnesota

116 Church St. S.E.

Minneapolis, MN Minnesota 55455

Abstract

This paper describes recent preliminary results from the CLEO-c experiment using an initial $\sim 60 \text{ pb}^{-1}$ sample of data collected in e^+e^- collisions at a center of mass energy around the mass of the $\psi(3770)$. A first measurement of the branching fraction $\mathcal{B}(D^+ \rightarrow \mu^+\nu) = (3.5 \pm 1.4 \pm 0.6) \times 10^{-4}$ and the corresponding decay constant $f_D = (202 \pm 41 \pm 17) \text{ MeV}$ has been made. Several charged and neutral D meson absolute exclusive semileptonic branching fractions have been measured, including first measurements of the branching fractions $\mathcal{B}(D^0 \rightarrow \rho^- e^+\nu) = (0.19 \pm 0.04 \pm 0.02)\%$ and $\mathcal{B}(D^+ \rightarrow \omega e^+\nu) = (0.17 \pm 0.006 \pm 0.01)\%$. Estimated uncertainties for inclusive D semileptonic decay modes are also presented. Fits to single and double D tagged events are used to extract absolute branching fractions of several hadronic D decay modes and $D\bar{D}$ production cross sections. Most of these results from this small preliminary sample are already of greater sensitivity than previously published results.

1 Introduction

The CLEO-c physics program is focused on the study of charm decays in e^+e^- collisions in the CESR-c storage ring at energies near the $\psi(3770)$ and J/ψ resonances and above $D_s\overline{D}_s$ threshold. The results presented in this paper are based on approximately 60 pb^{-1} of data collected at the $\psi(3770)$, just above $D\overline{D}$ threshold.

For many electroweak quantities measured by the B factories at SLAC and KEK, in particular many that contribute to constraining the CKM unitarity triangle ¹⁾, the precision is limited by theoretical uncertainties rather than experimental precision. One of the primary goals of these measurements is the calibration and validation of lattice QCD. Lattice QCD will soon be able to predict many quantities such as the decay constants f_D and f_{D_S} of D and D_S mesons with few percent uncertainties. Measurement of f_D will lead to a determination of f_B , since lattice QCD can predict the ratio f_B/f_D better than the absolute decay constants. It is critical, however, that the uncertainties of the lattice calculations be verified by experimental measurements. CLEO-c measurements of absolute branching fractions and form factors for a full isospin set of semileptonic decays will provide a stringent test of form factor calculations and models.

In addition to verification of lattice QCD, CLEO-c will improve on the existing measurements of $|V_{cs}|$ and $|V_{cd}|$ and measure absolute branching fractions for many important hadronic normalization modes which contribute significant uncertainties to important measurements at higher energies.

2 Purely Leptonic D Meson Decay Absolute Branching Fraction and the Decay Constant f_D

The decay constant f_D is an important parameter which quantifies the annihilation probability of the valence quarks of the D meson. This parameter can be determined from the absolute branching fraction $\mathcal{B}(D^+ \rightarrow \mu^+\nu)$. A first measurement of the absolute branching fraction of the decay $D^+ \rightarrow \mu^+\nu$ was recently made by CLEO-c.

The analysis relies on fully reconstructing or “tagging” one D or \overline{D} meson in the $D\overline{D}$ pair produced in the $\psi(3770)$ decay. This technique works quite well at the $\psi(3770)$ resonance, since there is not enough energy in the event to produce hadrons other than the $D\overline{D}$ pair. Using the decay modes $D^- \rightarrow K^+\pi^-\pi^-$, $K^+\pi^-\pi^-\pi^0$, $\overline{K}_S^0\pi^-$, $\overline{K}_S^0\pi^-\pi^-\pi^+$, $\overline{K}_S^0\pi^-\pi^0$ for the tag side D , an efficiency of approximately 25% for the tag reconstruction is achieved.

A very pure sample of 28651 ± 207 tagged D mesons is selected. The tag D meson is combined with an additional charged track of the correct sign, presumed to be a muon. The distribution of “missing mass squared”, defined to

be $M_{\text{miss}}^2 \equiv (E_{\text{beam}} - E_{\mu^+})^2 - (\vec{p}_{D^-} - \vec{p}_{\mu^+})^2$, is shown in Fig. 1. A significant and well-defined peak of eight events at the neutrino mass around zero is observed. The peak at $0.25 \text{ GeV}^2/c^4$ corresponds to a background from decays to the $K_L^0 \pi^+$ final state, which is well separated from the signal region. The total contribution of backgrounds in the signal region is estimated in a maximum likelihood fit to be one event. This leads to a branching fraction of $\mathcal{B}(D^+ \rightarrow \mu^+ \nu) = (3.5 \pm 1.4 \pm 0.6) \times 10^{-4}$ and a D meson decay constant of $f_D = (202 \pm 41 \pm 17) \text{ MeV}$, where the first uncertainty is statistical and the second is systematic ²).

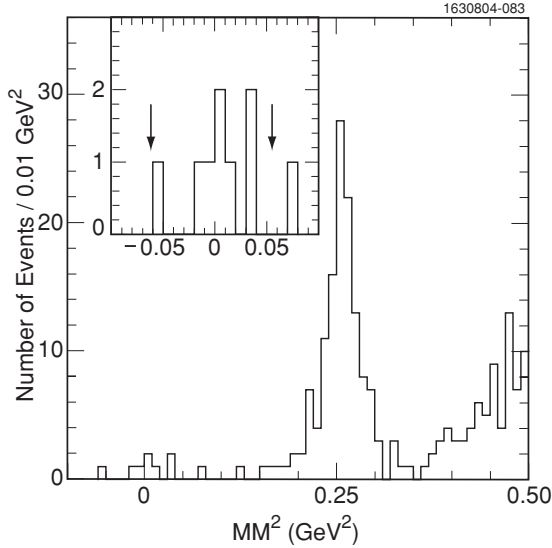


Figure 1: *Missing mass distribution of $D^+ \rightarrow \mu^+ \nu$ candidates. The signal peaks at zero missing mass.*

3 Absolute Branching Fractions of Exclusive Semileptonic D Meson Decays

The analysis of exclusive semileptonic decays also uses a tag of the other D meson in the event. These tag D mesons are selected using the beam-constrained mass of the candidate, defined as

$$M_{bc} \equiv \sqrt{E_{\text{beam}}^2 - \vec{p}_{\text{cand}}^2}, \quad (1)$$

Table 1: Absolute branching fraction measurements by CLEO-c (center column) compared with the present measurements tabulated in the particle data book ³⁾ (right). All results are preliminary.

Decay Mode	B (%) (CLEO-c)	B (%) (PDG '04)
$D^0 \rightarrow \pi^- e^+ \nu$	$0.25 \pm 0.03 \pm 0.02$	0.36 ± 0.06
$D^0 \rightarrow K^- e^+ \nu$	$3.52 \pm 0.10 \pm 0.25$	3.58 ± 0.18
$D^0 \rightarrow K^{*-}(K^- \pi^0) e^+ \nu$	$2.07 \pm 0.23 \pm 0.18$	2.15 ± 0.35
$D^0 \rightarrow \rho^- e^+ \nu$	$0.19 \pm 0.04 \pm 0.02$	–
$D^+ \rightarrow K^0 e^+ \nu$	$8.71 \pm 0.38 \pm 0.37$	6.7 ± 0.9
$D^+ \rightarrow K^{*0}(K^- \pi^+) e^+ \nu$	$5.70 \pm 0.28 \pm 0.25$	5.5 ± 0.7
$D^+ \rightarrow \pi^0 e^+ \nu$	$0.44 \pm 0.06 \pm 0.03$	0.31 ± 0.15
$D^+ \rightarrow \rho^0(\pi^+ \pi^-) e^+ \nu$	$0.21 \pm 0.04 \pm 0.02$	0.25 ± 0.10
$D^+ \rightarrow \omega(\pi^+ \pi^- \pi^0) e^+ \nu$	$0.17 \pm 0.06 \pm 0.01$	–

and the energy difference between the beam and the candidate, defined to be

$$\Delta E = E_{\text{beam}} - E_{\text{cand}}. \quad (2)$$

The remaining observable tracks are then reconstructed to form the daughter meson. The missing energy, E_{miss} , and missing momentum, $|\vec{p}_{\text{miss}}|$, in the event are used to form the kinematic variable $U \equiv E_{\text{miss}} - |\vec{p}_{\text{miss}}|$, which is fit to determine the signal and background contributions. These distributions and fits are shown in Fig. 2 and Fig. 3 for the neutral and charged D meson modes, respectively.

These raw numbers of events are corrected for efficiency and divided by the number of tag D mesons to produce absolute branching fractions. The efficiencies are determined using a combination of GEANT Monte Carlo and data. These measurements include first observations of the modes $D^0 \rightarrow \rho^- e^+ \nu$ and $D^+ \rightarrow \omega e^+ \nu$.

The absolute branching fraction measurements for these modes are summarized in Table 1. Even with only a small fraction of the final sample, the sensitivity is already an improvement over previous measurements ³⁾ for most modes.

4 Inclusive Decay Channels

The inclusive branching fractions $\mathcal{B}(D^0 \rightarrow e^+ X)$ and $\mathcal{B}(D^+ \rightarrow e^+ X)$ are being measured by the CLEO-c collaboration. At present, the branching fractions are not yet public, however, even with the preliminary $\sim 60 \text{ pb}^{-1}$ sample, the statistical uncertainties are $\sim 0.2\%$ and $\sim 0.3\%$ for the $D^0 \rightarrow e^+ X$ and $D^+ \rightarrow e^+ X$

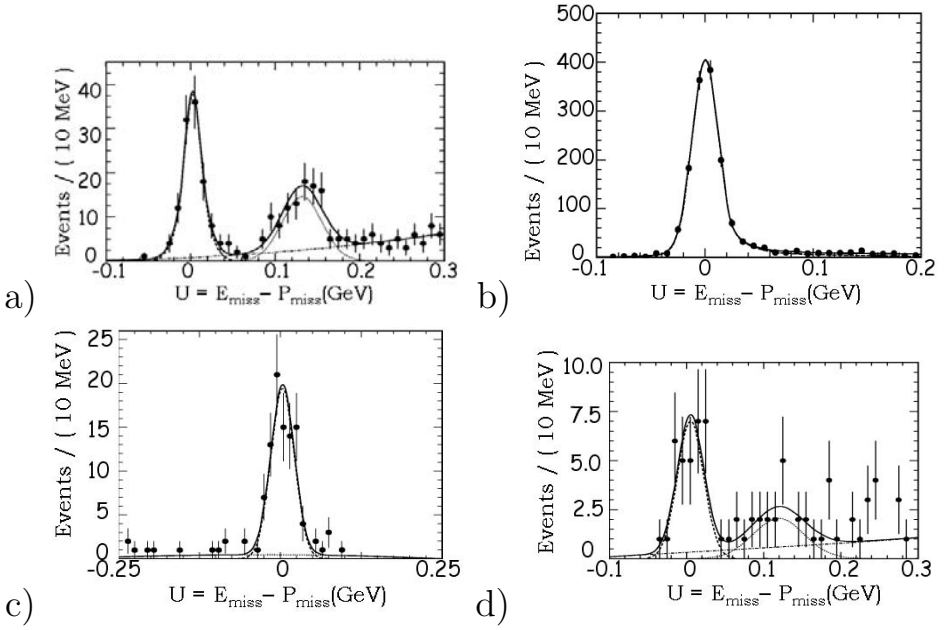


Figure 2: Distributions of the variable $U \equiv E_{\text{miss}} - P_{\text{miss}}$ for D^0 meson decays to a) $\pi^- e^+ \nu$, b) $K^- e^+ \nu$, c) $K^{*-} e^+ \nu$, ($K^{*-} \rightarrow K^- \pi^0$), d) $\rho^- e^+ \nu$.

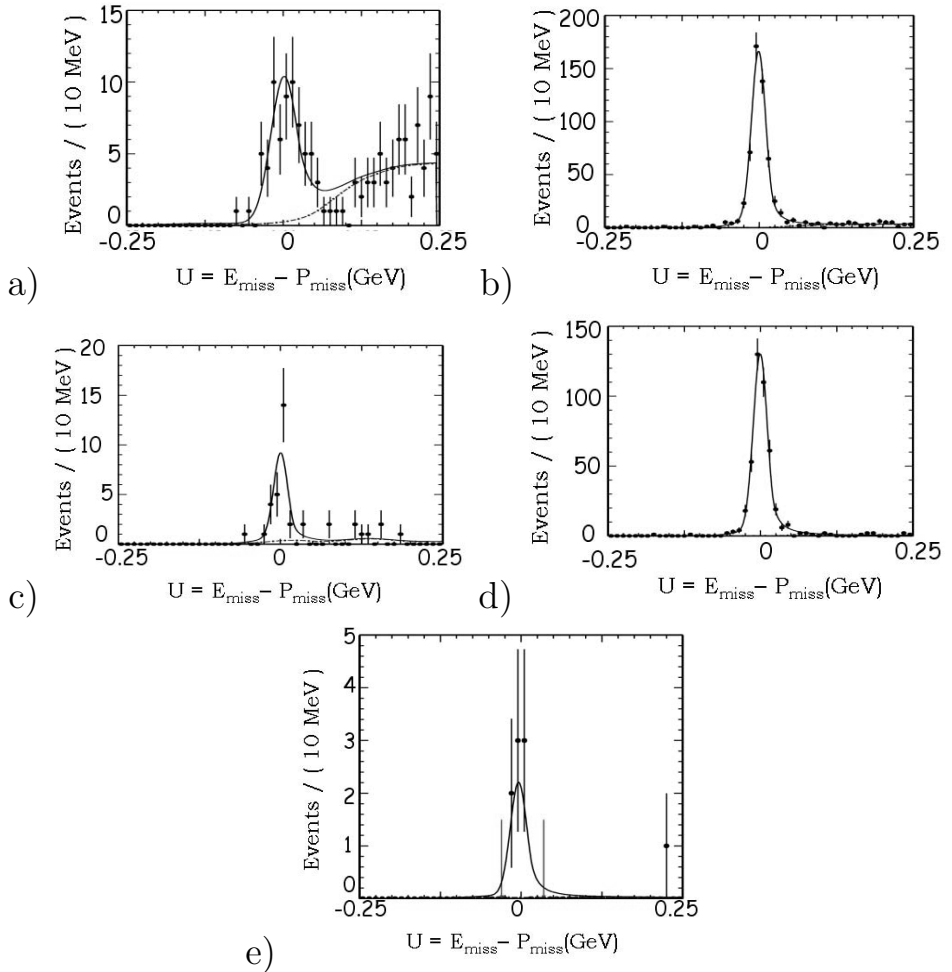


Figure 3: Distributions of the variable $U \equiv E_{\text{miss}} - P_{\text{miss}}$ for D^+ meson decays to a) $\pi^0 e^+ \nu$, b) $\bar{K}^0 e^+ \nu$, c) $\rho^0 e^+ \nu$, d) $K^{*0} e^+ \nu$ ($K^{*0} \rightarrow K^- \pi^+$), e) $\omega e^+ \nu$.

channels, respectively. The corresponding statistical \oplus systematic uncertainties for the present best measurements are $\sim 0.3\%$ and $\sim 1.9\%$ for these channels.

5 D Meson Absolute Hadronic Branching Fractions and $D\bar{D}$ Production Cross Sections

Using samples of single and double D tagged events, absolute branching fractions of several hadronic D decay modes are determined independent of the integrated luminosity, which would typically add a large uncertainty to the measurement. This technique is similar to that used by the Mark III collaboration ⁴⁾ ⁵⁾. The number of single D tagged events in a given decay mode i is given by

$$N_i = N_{D\bar{D}}\mathcal{B}_i\varepsilon_i \quad (3)$$

and the number of double tagged events with decays to modes i and j is given by

$$N_{ij} = N_{D\bar{D}}\mathcal{B}_i\mathcal{B}_j\varepsilon_{ij}. \quad (4)$$

Equations 3 and 4 can be combined to give the number of $D\bar{D}$ pairs produced and the branching fraction of each mode i :

$$N_{D\bar{D}} = \frac{N_i N_j}{N_{ij}} \frac{\varepsilon_{ij}}{\varepsilon_i \varepsilon_j} \quad (5)$$

and

$$\mathcal{B}_i = \frac{N_i}{N_j} \frac{\varepsilon_j}{\varepsilon_{ij}}. \quad (6)$$

In practice, a simultaneous fit to the neutral modes $D^0 \rightarrow K^-\pi^+$, $D^0 \rightarrow K^-\pi^+\pi^0$, and $D^0 \rightarrow K^-\pi^+\pi^+\pi^-$ and charged modes $D^+ \rightarrow K^-\pi^+\pi^+$ and $D^+ \rightarrow K_S^0\pi^+$ is performed to extract the branching fractions and number of $D\bar{D}$. All statistical and systematic correlations between modes are taken into account in the fit. The fit is of good quality with $\chi^2/N_{\text{d.o.f}} = 9.0/16$ and a confidence level of 91.4%.

The efficiencies are determined from a combination of data and Monte Carlo. The denominator of the efficiency calculation may be determined using missing mass to select events in data and Monte Carlo. The effects of final state radiation are included in this analysis.

The single and double D tagged yields are determined using the variables ΔE and M_{bc} , defined in Eqs. (2) and (1), respectively. Approximately 2500 double tagged neutral D mesons and 500 double tagged charged D mesons are reconstructed.

Table 2 sums up the branching fractions and cross sections determined from this preliminary analysis. The statistical uncertainties on the neutral modes are of order 2.0% and of order 4.5% for charged modes.

Table 2: Absolute branching fractions and ratios of branching fractions of hadronic decays and $D\bar{D}$ production cross sections. All results are preliminary.

Quantity	CLEO-c Measurement
$\sigma(e^+e^- \rightarrow D^0\bar{D}^0)$	$3.47 \pm 0.07 \pm 0.15$ nb
$\sigma(e^+e^- \rightarrow D^+D^-)$	$2.59 \pm 0.11 \pm 0.11$ nb
$\sigma(e^+e^- \rightarrow D\bar{D})$	$6.06 \pm 0.13 \pm 0.22$ nb
$N_{D^+D^-}/N_{D^0\bar{D}^0}$	$0.75 \pm 0.04 \pm 0.02$
$N_{D^0\bar{D}^0}$	$(1.98 \pm 0.04 \pm 0.03) \times 10^5$
$\mathcal{B}(D^0 \rightarrow K^-\pi^+)$	$0.0392 \pm 0.0008 \pm 0.0023$
$\mathcal{B}(D^0 \rightarrow K^-\pi^+\pi^0)$	$0.143 \pm 0.003 \pm 0.010$
$\mathcal{B}(D^0 \rightarrow K^-\pi^+\pi^+\pi^-)$	$0.081 \pm 0.002 \pm 0.009$
$N_{D^+D^-}$	$(1.48 \pm 0.06 \pm 0.04) \times 10^5$
$\mathcal{B}(D^+ \rightarrow K^-\pi^+\pi^+)$	$0.098 \pm 0.004 \pm 0.008$
$\mathcal{B}(D^+ \rightarrow K_S^0\pi^+)$	$0.0161 \pm 0.0008 \pm 0.0015$
$\mathcal{B}(D^0 \rightarrow K^-\pi^+\pi^0)/\mathcal{B}(D^0 \rightarrow K^-\pi^+)$	$3.64 \pm 0.05 \pm 0.17$
$\mathcal{B}(D^0 \rightarrow K^-\pi^+\pi^+\pi^-)/\mathcal{B}(D^0 \rightarrow K^-\pi^+)$	$2.05 \pm 0.03 \pm 0.14$
$\mathcal{B}(D^+ \rightarrow K_S^0\pi^+)/\mathcal{B}(D^+ \rightarrow K^-\pi^+\pi^+)$	$0.164 \pm 0.004 \pm 0.006$

The uncertainties in the charged track efficiencies used in this preliminary analysis will be reduced by about a factor of four in the final analysis of this preliminary data set. Improvements to the π^0 and K_S^0 efficiencies are also nearly complete. Four more charged D modes are presently being added and will improve the statistics in those modes by about a factor of three. These measurements will impact the determination of $|V_{cb}|$ by the B factories using $B \rightarrow D^*\ell\nu$.

6 Conclusions

CLEO-c is producing results that will have a large impact on electroweak physics. These measurements are essential for the B factories and the Tevatron experiments to realize their full potential on many measurements. Using only a small preliminary sample corresponding to an integrated luminosity of 60 pb^{-1} many of these measurements are already the most significant. A considerably larger sample is presently being collected at the $\psi(3770)$. The CLEO-c collaboration also plans to study D_s decays in collisions above $D_s\bar{D}_s$ threshold and study radiative J/ψ decays.

7 Acknowledgments

We gratefully acknowledge the effort of the CESR staff in providing us with excellent luminosity and running conditions. This work was supported by the National Science Foundation and the U.S. Department of Energy.

References

1. M. Kobayashi and T. Maskawa, *Prog. Theor. Phys.* **49**, 652 (1973).
2. CLEO Collaboration, G. Bonvicini *et al*, *Phys. Rev. D* **70**, 112004 (2004).
3. Particle Data Group, S. Eidelman *et al*, *Phys. Lett. B* **592**, 1 (2004).
4. Mark III Collaboration, R. M. Baltrusaitis *et al*, *Phys. Rev. Lett.* **56**, 2140, (1986).
5. Mark III Collaboration, J. Adler *et al*, *Phys. Rev. Lett.* **60**, 89, (1988).

PRODUCTION, LIFETIMES, AND MASSES OF B AND C HADRONS

Michael D. Hildreth

Université de Notre Dame du Lac, Notre Dame, IN 46556, USA
for the DØ Collaboration

Abstract

We present an overview of recent results from the Tevatron concerning the production, lifetimes, and masses of hadrons containing bottom and charm quarks. Many results are based on a substantial fraction of the total Run II integrated luminosity. Where appropriate, comparisons are presented with theoretical expectations.

1 Overview

The range of physics encompassed by heavy flavor production, masses, and lifetimes is quite broad. An understanding of heavy flavor production relies on detailed knowledge of higher-order QCD, including parton luminosities and fragmentation functions that describe the energy distributions of the produced heavy quarks. The spectrum of heavy hadron masses, lifetimes, and decay parameters are the realm of the Heavy Quark Expansion and Heavy Quark Effective Theory ¹⁾. Since the theoretical predictions of these quantities are expressed in terms of a small number of universal parameters, more precise measurements lead to a reduction in the theoretical uncertainties in other areas of the heavy quark sector, most importantly the parameters that govern heavy flavor mixing and CP violation. While these measurements may lead to the underpinnings of the discovery of New Physics through the interpretation of heavy-flavor mixing and the CKM matrix, the direct observation of any of several rare decay modes whose branching fractions can be significantly enhanced by physics beyond the Standard Model would be a sure sign of such a discovery. The Tevatron and the B-Factories provide complementary venues for exploring the vast parameter space of possibilities and measurements. At the time of La Thuile, total integrated luminosities for the two Tevatron experiments, DØ and CDF, had reached almost 0.6 fb^{-1} , with 1 fb^{-1} expected by the end of the calendar year.

2 Heavy Quark Production

Over the past decade, seemingly large discrepancies emerged between the observed and predicted rate of heavy flavor production in $p\bar{p}$ collisions at the Tevatron. Recent theoretical work and several experimental analyses have significantly improved the overall situation. An extensive exposition of this was presented at La Thuile 2004 ²⁾. The major improvements have been advances in the theory calculations of heavy quark production, which are now performed at NLO plus NLL corrections. Further clarifications of the relevance of higher order moments of fragmentation functions and their different roles at hadron and e^+e^- colliders has improved the understanding of the scope of experimental measurements. On the experimental side as well, an increased appreciation of the importance of a self-consistent treatment of calculations, Monte Carlo simulations, and hadronic corrections has led to better (larger) estimates of systematic errors. Figure 1 shows recent results on the total b hadron production cross section from Run II compared with the recent theoretical predictions. The total reported cross section is measured to be $29.4 \pm 0.6 \pm 6.2 \mu\text{b}$ for rapidities y where $|y| < 1$ ³⁾. The inclusive charm production cross section, measured earlier ⁴⁾, is approximately a factor of 50 higher. As an aside, these cross sec-

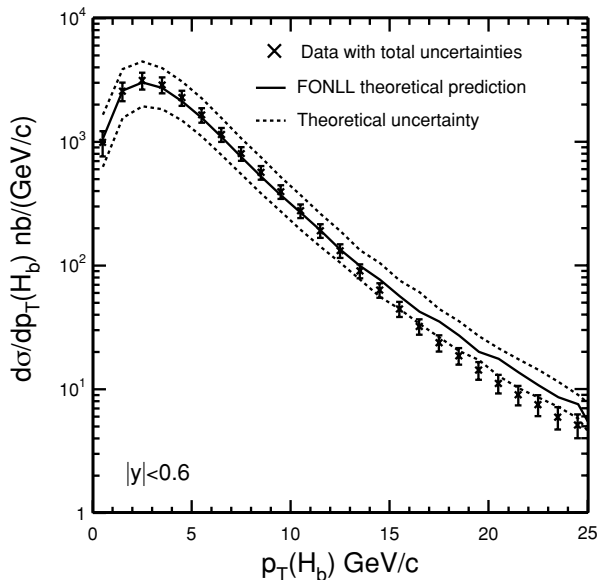


Figure 1: *The measured b -hadron production cross section as a function of b -hadron p_T , compared with recent NLO plus NLL calculations.*

tions and the “democratic” production of heavy flavor hadron species are what enable the Tevatron to make such a substantial contribution to heavy quark physics. The cross sections quoted in above correspond to 3 kHz of central b hadron production, with a factor of two more within the $D\bar{0}$ muon acceptance of $|\eta| < 2$. Charm hadrons are produced at 150 kHz into the central region of the detectors. Given the integrated luminosities, this implies that 2×10^{10} b hadrons and 1×10^{12} charm hadrons have already been “seen” by the two experiments! Triggering and bandwidth to tape become the only limitation in recording near-infinite statistics for heavy flavor studies. As an example of the lepton triggers used to select heavy flavor events at the trigger level, Figure 2 from CDF shows the di-muon mass distributions collected by their various dedicated heavy flavor triggers.

3 Quarkonia Production

Compared to inclusive heavy flavor production, the production of quarkonia is placed in a slightly different theoretical context. Bound states of heavy quarks

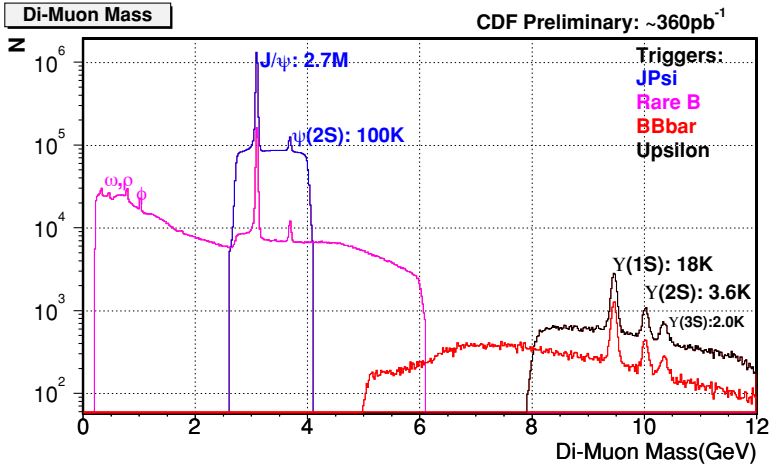


Figure 2: A plot from CDF showing the dimuon invariant mass spectrum of samples recorded by their various b -hadron triggers. The relative importance of each trigger is reflected by the number of events.

are best described by Non-relativistic QCD (NRQCD) ⁵⁾. Production rates are described by short distance cross sections convoluted with non-perturbative matrix elements for evolution to the quarkonium state. CDF demonstrated in Run I that a simple color singlet model was insufficient to reproduce the observed rates. Rather, color octet modes are required on top of color singlet to describe quarkonium production.

New Run II results from $D\bar{0}$ are consistent with this picture. Shown in Figure 3 is the $\Upsilon(1s)$ production cross section as a function of Υ transverse momentum for different rapidity regions, compared with a NRQCD color-octet model ⁶⁾.

4 B Hadron Masses

In the theoretical context of the Heavy Quark Expansion (cite), the mass splittings between the various hadrons are calculable corrections in powers of Λ_{QCD}^2/m_Q , where Λ_{QCD} is the fundamental QCD scale of the theory, and m_Q is the heavy quark mass. Evaluation of these terms, however, requires knowledge of the dynamics of the light degrees of freedom associated with the meson. An

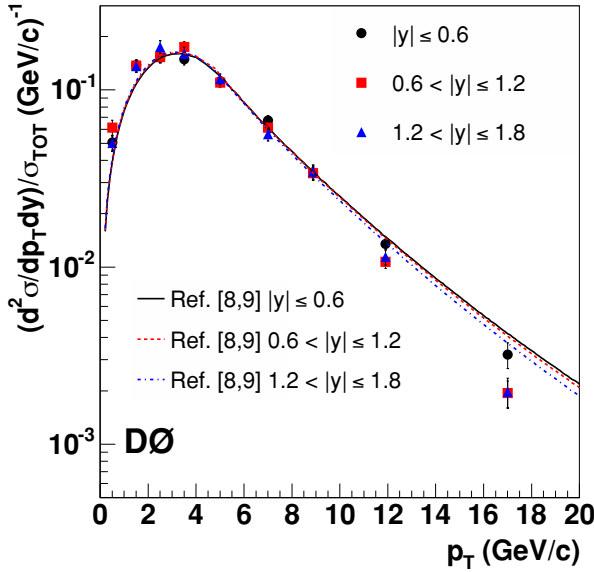


Figure 3: The cross section for Υ production measured by the $D\bar{O}$ Collaboration for different η regions.

example of the mass splitting calculation is given by

$$M_B = m_b + \bar{\Lambda} + \frac{\mu_\pi^2 - \mu_G^2}{2m_b} + \frac{\mu_3^2}{m_b^2}. \tag{1}$$

Here, $\bar{\Lambda}$ is something, and μ_π , μ_G and μ_3 represent bound state and hadronization effects expressed in terms of local Heavy Quark operators. These same operators are necessary ingredients to the understanding and extraction of the CKM parameters in the B system; measurements constraining them are of considerable importance.

CDF have produced preliminary mass measurements of the four “standard” b hadrons whose precision are either world-best or extremely competitive with previous results. They are as follows:

$$m_{B^\pm} = 5279.10 \pm 0.41(\text{stat}) \pm 0.36(\text{syst})\text{MeV} \tag{2}$$

$$m_{B^0} = 5279.63 \pm 0.53(\text{stat}) \pm 0.33(\text{syst})\text{MeV} \tag{3}$$

$$m_{B_s} = 5366.01 \pm 0.73(\text{stat}) \pm 0.33(\text{syst})\text{MeV} \tag{4}$$

$$m_{\Lambda_b} = 5619.7 \pm 1.2(\text{stat}) \pm 1.2(\text{syst})\text{MeV} \quad (5)$$

The exacting precision is achieved by using all-charged decay modes, such as $B^+ \rightarrow J/\psi K^+$. The branching fractions for these modes are small, but the overwhelming production rate and the presence of muons for trigger purposes allow them to be used.

The lowest lying $L = 1$ excited B meson states have now been observed by CDF and $D\bar{O}$. The B_1 and the B_2^* are $1P(\frac{3}{2})$ states that were predicted to be narrow. Both experiments used the combination of a fully-reconstructed B meson plus an additional pion from the $B^{**} \rightarrow B^{(*)}\pi$ transition. The three peaks seen in Figure 4 are from the $B_1 \rightarrow B^*\pi$, $B_2^* \rightarrow B^*\pi$ and $B_2^* \rightarrow B\pi$. The $B_2^* - B_1$ mass splitting is sufficiently small that the two decay peaks cannot be resolved and appear as a single larger peak. $D\bar{O}$ values for the mass splitting and masses for the excited states are $M(B_1) = 5724 \pm 4 \pm 7\text{MeV}/c^2$ and $\Delta M(B_2 - B_1) = 23.6 \pm 7.7 \pm 3.9\text{MeV}/c^2$.

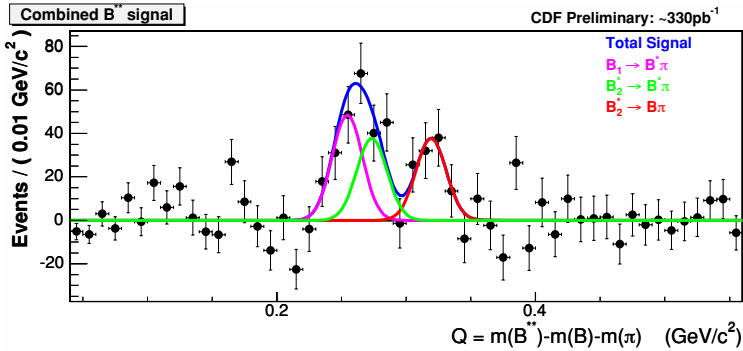


Figure 4: Signals for the excited B hadron states B_2 and B_1 as seen by the CDF Collaboration.

CDF have also prepared a preliminary measurement of the B_c mass using a novel “blind” technique to search for a significant mass peak over background using the all-charged final state $B_c \rightarrow J/\psi\pi^\pm \rightarrow \mu^+\mu^-\pi^\pm$, which has a total branching fraction of 7.8×10^{-5} . Monte Carlo studies and $B^+ \rightarrow J/\psi K^+$ events were used to optimize the selection criteria. Only one mass peak was found with a significance exceeding the selection criteria which had been pre-selected before the data were analyzed. This also represents the first use of the innermost Layer 00 component of the CDF silicon tracker; optimum lifetime resolution was required for background rejection. The result, $m_{B_c} = 6.2870 \pm 0.0048 \pm 0.0011\text{GeV}/c^2$, is about 100 times more precise than previous measurements using semi-leptonic decays.

5 B Hadron Lifetimes

A general feature of lifetime calculations in the HQE (and a general property of QCD due to the gauge structure) is that there are no corrections to the lifetime to $\mathcal{O}\left(\frac{1}{m_Q}\right)$. In HQE, for example, the lowest-order corrections to the b hadron lifetimes are

$$\delta\tau_{H_b} \sim \mathcal{O}\left(\frac{\Lambda_{\text{QCD}}^2}{m_b^2}\right) + \sim \mathcal{O}\left(\frac{\Lambda_{\text{QCD}}^3}{m_b^3}\right) + \dots \quad (6)$$

Precise lifetime measurements, then, allow direct access to the unknown coefficients of the Heavy Quark operator terms necessary for the determination of the CKM matrix elements without some of the uncertainties associated with the light quark dynamics. Correspondingly, precise predictions of ratios of lifetimes are possible. Examples include ⁷⁾

$$\frac{\tau(B_d^+)}{\tau(B_d^0)} = 1.06 \pm 0.02 \quad (7)$$

$$\left|1 - \frac{B_s}{B_d^0}\right| \leq 0.02 \quad (8)$$

$$\frac{\tau(\Lambda_b)}{\tau(B_d^0)} = 0.86 \pm 0.05 \quad (9)$$

Verification of these predictions tests the calculational validity of the HQE and, once understood, can provide direct input to the understanding of the Unitarity Triangle.

6 B_d Meson Lifetimes

While the Tevatron experiments cannot yet compete directly with the B Factories in terms of fully reconstructed B mesons, the high average boost of the B in Tevatron $p\bar{p}$ collisions leads to very high statistics at large proper times. Careful measurements thus can be made of the *ratio* of the B_d^+ and B_d^0 lifetimes. DØ has presented a very precise result using semi-leptonic B decays where $B \rightarrow \mu D^0 X$. In the case where no other charged particle can be associated to the D^0 to form a charged, orbitally-excited D^* , the B meson sample is almost exclusively B^\pm . Where a charged pion can be associated to the D^0 to form a D^* , the B meson sample is almost exclusively B^0 . By using the expected composition of each sample, and measuring the ratio of the lifetimes of the two samples, the ratio $\tau(B_d^+)/\tau(B_d^0)$ can be measured. The raw ratio plot showing the best fit to the ratio as a function of proper time can be seen in Figure 5. The result is ⁸⁾

$$\tau(B_d^+)/\tau(B_d^0) = 1.080 \pm 0.016 \pm 0.014 \quad (10)$$

Note that this agrees rather well with the theoretical predictions presented in the previous section.

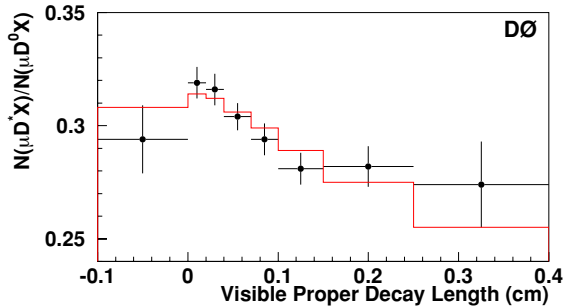


Figure 5: *The ratio of the number of $B \rightarrow \mu D^0 X (= B^+)$ events to the number of $B \rightarrow \mu D^* X (= B^0)$ events vs. the proper lifetime of the decay. This raw distribution clearly shows a difference in the lifetimes of the B^+ and B^0 hadrons.*

7 Other b Hadron Lifetime Measurements

We now turn to results that are only currently available from the Tevatron experiments. The B_s lifetime has been measured in semi-leptonic decays, which contain a mix of CP eigenstates, and in the exclusive decay $B_s \rightarrow J/\psi\phi$, which is a CP-even eigenstate. (Does this matter?) The current world-average results give

$$1 - \frac{B_s}{B_d^0} = 0.061 \pm 0.044 \quad (11)$$

also in good agreement with the predictions given above.

The Λ_b lifetime has been measured in Run II by both CDF and D0 in the $\Lambda_b \rightarrow J/\psi\Lambda$ mode⁹). At the moment, the statistical errors on these measurements are somewhat large, but the all-charged final state makes for particularly small systematic errors. These measurements will begin to dominate the world averages as more luminosity is included in the lifetime analyses. This can be seen in Figure 6, where the current equality in weight between the LEP and Tevatron measurements will gradually shift towards the Tevatron.

The B_c lifetime has been measured previously in semi-leptonic decays. A new D0 result uses the $J/\psi\mu X$ final state, which is very clean experimentally.

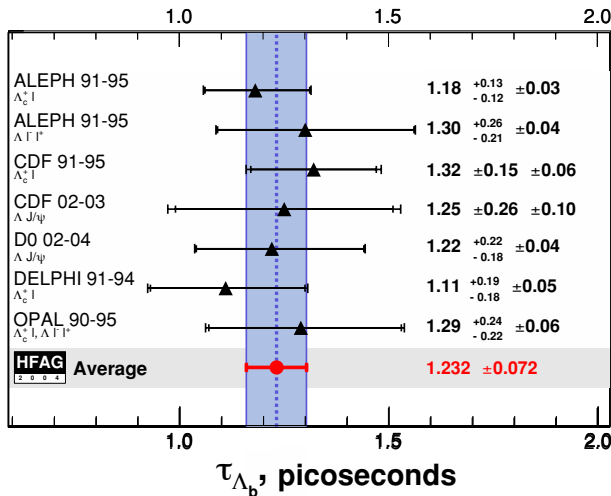


Figure 6: The Heavy Flavor Averaging Group results for the Λ_b lifetime.

The $J/\psi\mu$ invariant mass is used as a discriminant to statistically separate the B_c sample ¹⁰⁾. The combined Tevatron average for the B_c lifetime is 0.45 ± 0.12 ps. Thus, all of the b hadron lifetimes are in agreement with the HQE predictions within errors.

8 Rare B Decays

Exploiting potential enhancements to branching ratios from unknown higher-energy particles contributing to the decay amplitudes is a common technique to search for the effects of New Physics beyond the Standard Model. Because of the strength of constraint imposed by flavor-changing neutral currents, dilepton modes provide the greatest constraints of those decay modes easily visible at the Tevatron. Typically, coupling to new, weakly-interacting particles will be proportional to m_ℓ^2 , so muon modes are the most interesting. The classic Tevatron search mode is $B_s \rightarrow \mu\mu$, whose Standard Model branching ratio is expected to be around 4×10^{-9} ¹¹⁾. SUSY models, where this branching ratio is dependent on the charged higgs mass and $\tan^6 \beta$ can enhance this to $\sim 10^{-7}$ or even higher. Both CDF and DØ have attempted to observe this decay mode. The current limits are $Br(B_s \rightarrow \mu\mu) < 7.5 \times 10^{-7}$ at 95% confidence level (CDF) ¹²⁾ and $Br(B_s \rightarrow \mu\mu) < 5.0 \times 10^{-7}$ at 95% confidence

level ($D\bar{0}$)¹³⁾. Both improvements in analysis techniques and the addition of more data should push these limits to smaller values; this will begin to have consequences for some SUSY models in the near future.

Another realm under exploration is that of penguin contributions to various decay amplitudes. Since these are notoriously difficult to calculate, measurements of specific decay rates that are expected to be dominated by EW or QCD penguins should constrain the uncertainties associated with these effects. This, again, will allow a better understanding of crucial measurements that play a role in the study of CP violation and Unitarity Triangle. CDF has shown the first observation of the decay mode $B_s \rightarrow \phi\phi$, which is expected to proceed through QCD and EW penguins diagrams, but may be dominated by EW penguins. To calculate relative branching ratios and efficiencies, the $\phi\phi$ mode was normalized to $B_s \rightarrow J/\psi K^{*0}$, yielding¹⁴⁾

$$Br(B_s \rightarrow \phi\phi) = (1.4 \pm 0.6(\text{stat}) \pm 0.2(\text{syst}) \pm 0.5(\text{BR}'s)) \times 10^{-5} \quad (12)$$

This is obviously just the initial step in a long series of analyses that will examine accessible interesting rare decays using the huge Tevatron dataset.

9 Rare Charm Decays

Due to the massive production cross section for charm hadrons, a multitude of potentially-interesting rare charm decay modes are accessible to the Tevatron experiments. CDF published a result¹⁵⁾ on the decay $D^0 \rightarrow \mu\mu$, with a limit of $Br(D^0 \rightarrow \mu\mu) < 3.1 \times 10^{-6}$ at the 95% confidence level. $D\bar{0}$ have recently begun study of the decay $D^+ \rightarrow \pi^+\mu^+\mu^-$. Modes like these are particularly sensitive to enhancements from New Physics; theories such as R-parity-violating SUSY allow flavor-changing neutral currents at tree level in the decay $c \rightarrow u\mu\mu$ ¹⁶⁾. A full exploration of these modes requires more data, since it is the production cross section away from the ϕ and ω resonance substructure that is enhanced. (Figure?) However, as a first step, $D\bar{0}$ observes a 7-sigma signal for $D_s \rightarrow \pi\phi$ with an as-yet statistically insignificant peak at the D^+ . The mass plot is shown in Figure 7¹⁷⁾. Further luminosity should yield greatly enhanced results.

10 Conclusions

The Heavy Flavor program at the Tevatron benefits both from the massive production cross sections for heavy hadrons and the significantly-improved performance of the upgraded detectors. The sheer number of heavy flavor hadrons produced is staggering: since the beginning of Run II, each experiment has seen approximately 2×10^{10} b hadrons and 1×10^{12} charm hadrons in their fiducial

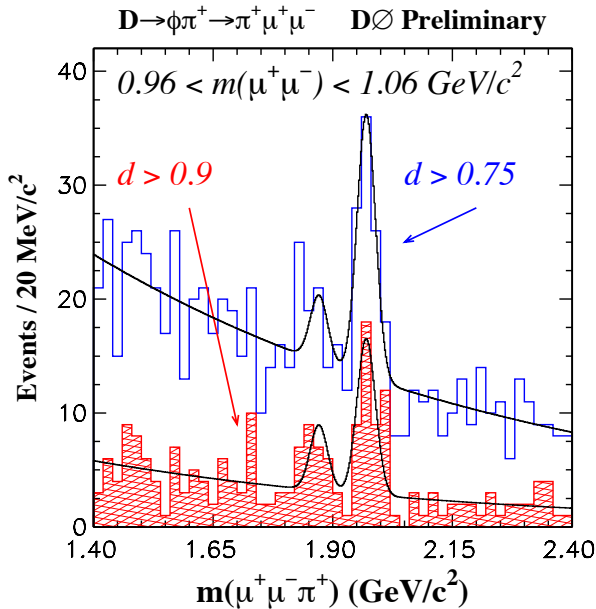


Figure 7: Reconstructed $\pi\phi$ invariant mass for two different cuts on d a multivariate likelihood designed to select D meson decays.

volumes. For reasons of trigger selection, semi-leptonic and multi-leptonic decay modes have dominated the results so far, but both detectors will now be able to exploit displaced vertex triggers to enhance their heavy-flavor samples.

The datasets and detector capabilities should allow the Tevatron experiments to dominate the world scene for several crucial measurements, especially the lifetime measurements of b hadrons. Searches for rare decay modes and spectroscopy results will form the other significant portion of the “Production, Masses, and Decays” program outside of the mixing and CP-violation measurements. Outside of the rare decays searches, the main contribution of these studies is to constrain the unknown parameters in the HQE theory so that more accurate predictions are possible for the CKM sector. We can only hope that, with the increased level of precision, deviations from the Standard Model will arise.

11 Acknowledgements

The author would like to thank the heavy-flavor groups from $D\bar{O}$ and CDF for their assistance and support in the preparation of this talk. Work supported by the Department of Energy, the National Science Foundation, and the Research Corporation.

References

1. *e.g.* I. Bigi, M. Shifman, N. Uraltsev, *Ann. Rev. Nucl. Part. Sci.* **47** 591 (1997).
2. *e.g.* M. Cacciari, S. Frixione, M.L. Mangano, P.Nason, G.Ridolfi, *JHEP* **0407** 033 (2004).
3. D. Acosta *et al.* (CDF Collab.) *Phys. Rev.* **D71** 032001 (2005).
4. D. Acosta *et al.* (CDF Collab.) *PRL* **91**, 241804 (2003).
5. G. P. Lepage *et al.*, *PRD* **46** 4052 (1992).
6. V.M. Abazov *et al.* ($D\bar{O}$ Collab.) *Phys. Rev. Lett.* **94** 232001 (2005).
7. These predictions can be found in *e.g.*, E. Franco, V. Lubicz, F. Mescia, C. Tarantino, *Nucl. Phys.* **B633** 212 (2002);
F. Gabbiani, A. Onishchenko, A. Petrov *Phys. Rev.* **D70** 094031 (2004).
8. V.M. Abazov *et al.* ($D\bar{O}$ Collab.) *Phys. Rev. Lett.* **94** 182001 (2005).
9. CDF Conference note 6393, 2003.
V.M. Abazov *et al.* ($D\bar{O}$ Collab.) *Phys. Rev. Lett.* **94** 102001 (2005).
10. $D\bar{O}$ Conference Note 4539-CONF, 2005.
11. $B_s \rightarrow \mu\mu$ SM prediction.
12. D. Acosta *et al.* (CDF Collab.) *Phys. Rev. Lett.* **93** 032001 (2004).
13. V.M. Abazov *et al.* ($D\bar{O}$ Collab.) *Phys. Rev. Lett.* **94** 071802 (2005).
14. CDF Conference Note 7525, 2005.
15. D. Acosta *et al.* (CDF Collab.) *Phys. Rev.* **D68** 091101 (2003).
16. G. Burdman, E. Golowich, J. Hewett, S. Pakvasa *Phys.Rev.* **D66** 014009 (2002).
17. $D\bar{O}$ Conference Note 4731-CONF, 2005.

CHARM PHYSICS AT BELLE

A. Kuzmin

Budker Institute of Nuclear Physics, Novosibirsk
for Belle collaboration

Abstract

The recent results on charm physics at Belle are presented. The presentation comprises $D^0 - \bar{D}^0$ mixing in $D^0 \rightarrow K^+\pi^-$ and $\bar{D}^0 \rightarrow K^+e^-\bar{\nu}_e$ final states, D^{**} study in B decays, $B \rightarrow D_{sJ}K/\pi$ results and observation of double charm production.

1 Introduction

Successful operation of B-factories during the last 5 years provides large data sample of the $e^+e^- \rightarrow$ hadrons events. Belle detector has already collected integrated luminosity of more than 300 fb^{-1} at $\Upsilon(4S)$. At this energy charm particles can be produced by direct annihilation of $e^+e^- \rightarrow c\bar{c}$ followed by the fragmentation of c -quarks as well as in B -meson decays to the charm hadrons. The cross section of each process is about 1 nb . In the case of the charm production in B decays the spin of initial state is fixed which allows to carry out the partial wave analysis.

In this report we present recent result of D^0 - \bar{D}^0 mixing, study of p-wave excitation of charm mesons and updated results on double charmonium production.

2 Experiment description

The Belle detector ¹⁾ operates at the KEKB asymmetric e^+e^- collider ²⁾. The detector consists of a three-layer silicon vertex detector (SVD), a 50-layer central drift chamber (CDC), an array of aerogel threshold Cherenkov counters (ACC), time-of-flight scintillation counters (TOF), and an electromagnetic calorimeter based on CsI(Tl) crystals. These detectors are located within a solenoid coil providing a 1.5 T magnetic field. An iron flux-return outside the coil is instrumented to identify muons and K_L^0 mesons.

3 Search for D^0 - \bar{D}^0 mixing.

The phenomenon of mixing among quark flavors has been observed in the K^0 - \bar{K}^0 and B^0 - \bar{B}^0 systems but not yet in the D^0 - \bar{D}^0 system. Neutral D mass eigenstates are $D^0 - \bar{D}^0$ combinations with masses m_1, m_2 . The parameters used to characterize mixing are $x \equiv \Delta m/\bar{\Gamma}$ and $y \equiv \Delta\Gamma/(2\bar{\Gamma})$, where Δm and $\Delta\Gamma$ are the differences in mass and decay width between the two D^0 - \bar{D}^0 mass eigenstates, and $\bar{\Gamma}$ is the mean decay width. The rate for D^0 - \bar{D}^0 mixing within the Standard Model (SM) is small, typically well below experimental upper limits ³⁾. Observation of mixing much larger than this expectation could indicate new physics. Such nonstandard processes may also give rise to CP -violating effects.

In this report we present $D^0 - \bar{D}^0$ mixing measurements in the time evolution of the wrong-sign two-body decay of the $D^0 \rightarrow K^+\pi^-$ and in the wrong-sign decay amplitude $D^0 \rightarrow K^+l^-\nu$.

3.1 Search for $D^0\text{-}\overline{D}^0$ mixing in $D^0 \rightarrow K^+\pi^-$ decays.

We search for mixing by reconstructing the “wrong-sign” (WS) decay $D^0 \rightarrow K^+\pi^-$, which would arise from a D^0 mixing to \overline{D}^0 and subsequently decaying via $\overline{D}^0 \rightarrow K^+\pi^-$ (4). The flavor of the D is identified by requiring that it originate from $D^{*+} \rightarrow D^0\pi^+$ or $D^{*-} \rightarrow \overline{D}^0\pi^-$ and noting the charge of the accompanying pion. In addition to arising via mixing, $D^0 \rightarrow K^+\pi^-$ can also occur via a doubly-Cabibbo-suppressed (DCS) amplitude. The two processes can be distinguished via the decay-time distribution. This method has been used by FNAL E791 (5), CLEO (6), and BaBar (7) to search for mixing and measure or constrain the DCS decay rate.

For $|x|, |y| \ll 1$ and negligible CPV , the decay time distribution for $D^0 \rightarrow K^+\pi^-$ can be expressed as

$$\frac{dN}{dt} \propto e^{-\overline{\Gamma}t} \left[R_D + \sqrt{R_D} y' (\overline{\Gamma}t) + \frac{x'^2 + y'^2}{4} (\overline{\Gamma}t)^2 \right], \quad (1)$$

where R_D is the ratio of DCS to Cabibbo-favorite (CF) decay rates, $x' = x \cos \delta + y \sin \delta$, $y' = y \cos \delta - x \sin \delta$, and δ is the strong phase difference between the DCS and CF amplitudes. The first term in brackets is due to the DCS amplitude, the last term is due to mixing, and the middle term is due to interference between the two processes. The time-integrated rate for $D^0 \rightarrow K^+\pi^-$ relative to that for $D^0 \rightarrow K^-\pi^+$ is $R_D + \sqrt{R_D} y' + (x'^2 + y'^2)/2$. To allow for CP violation, we apply Eq. (1) to D^0 and \overline{D}^0 decays separately. This results in six observables: $\{R_D^+, x'^{+2}, y'^+\}$ for D^0 and $\{R_D^-, x'^{-2}, y'^-\}$ for \overline{D}^0 . CP violation is parametrized by the asymmetries $A_D = (R_D^+ - R_D^-)/(R_D^+ + R_D^-)$ and $A_M = (R_M^+ - R_M^-)/(R_M^+ + R_M^-)$, where $R_M^\pm = (x'^{\pm 2} + y'^{\pm 2})/2$. The asymmetry A_D characterizes CPV in the DCS decay amplitude, and A_M characterizes CPV in $D^0\text{-}\overline{D}^0$ mixing.

The selection criteria for this process are described in detail in Ref. (8). The decay-time resolution is typically 0.2 ps.

We measure R_D , x'^2 , and y' of Eq. (1) using an unbinned maximum likelihood fit to the WS decay-time distribution. The likelihood function consists of probability density functions (pdf’s) for signal and several backgrounds. The pdf’s depend on the decay time, the mass $m_{K\pi}$, and the kinetic energy released $Q \equiv m_{K\pi\pi_{\text{slow}}} - m_{K\pi} - m_\pi$.

There are four backgrounds to the WS sample: (a) random π background, in which a random π^+ is paired with a $\overline{D}^0 \rightarrow K^+\pi^-$ decay (the pdf is peaked in $m_{K\pi}$ but broad in Q); (b) $D^{*+} \rightarrow D^0\pi^+$ followed by D^0 decaying to ≥ 3 -body final states (the pdf is broad in $m_{K\pi}$ and broad but enhanced in Q); (c) D^+/D_s^+ decays; and (d) combinatorial. We determine the level of each background by performing a two-dimensional fit to the $m_{K\pi}\text{-}Q$ distribution. The RS fit finds $227\,721 \pm 497$ $D^0 \rightarrow K^-\pi^+$ decays, and the WS fit finds 845 ± 40 $D^0 \rightarrow K^+\pi^-$

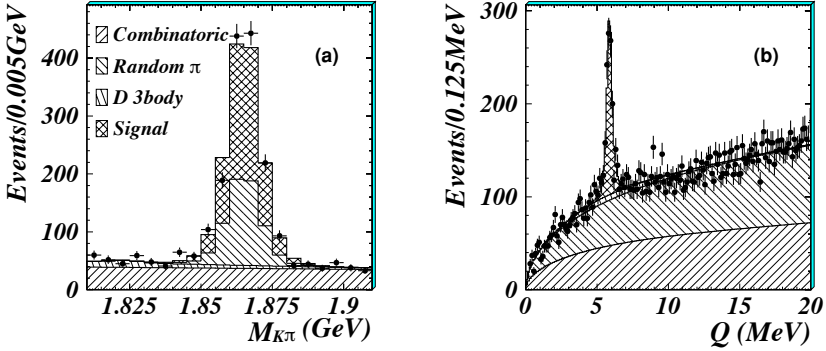


Figure 1: Distributions of (a) WS $m_{K\pi}$ with $|Q - 5.9 \text{ MeV}| < 0.6 \text{ MeV}$; and (b) WS Q with $|m_{K\pi} - m_{D^0}| < 20 \text{ MeV}/c^2$. Superimposed on the data (points with error bars) are projections of the $m_{K\pi}$ - Q fit.

decays. The ratio $R_{\text{WS}} \equiv \Gamma(D^0 \rightarrow K^+ \pi^-) / \Gamma(D^0 \rightarrow K^- \pi^+) = (0.371 \pm 0.018)\%$ (statistical errors only). The WS $m_{K\pi}$ and Q distributions are shown in Fig. 1 along with the fit projections. The ratio of WS signal to background is 0.9; the latter is mostly random π (59%) and combinatorial (36%).

To fit the decay-time distributions of RS and WS samples, we consider the 4σ region $|m_{K\pi} - m_{D^0}| < 22 \text{ MeV}/c^2$ and $|Q - 5.9 \text{ MeV}| < 1.5 \text{ MeV}/c^2$. The signal and background yields (which normalize the pdf's in the likelihood function) are determined from the $m_{K\pi}$ - Q fit described above.

Four fits are done, yielding the results listed in Table 1. For the first fit the CP assumed to be conserved. The projection of this fit superimposed on the data is shown in Fig. 2; the χ^2 of the projection is 71.9 for 60 bins. The central value for x'^2 is negative thus the most-likely value is zero, and we refit the data fixing $x'^2 = 0$. The χ^2 of this fit projection is 73.2 for 60 bins, which is satisfactory. For the third fit we allow for CPV and fit the $D^0 \rightarrow K^+ \pi^-$ and $\bar{D}^0 \rightarrow K^- \pi^+$ samples separately. Finally, for the last fit we assume no mixing or CPV and set $x'^2 = y' = 0$; the χ^2 of this fit projection is 75.6 for 60 bins, somewhat worse than for the case of mixing.

To obtain 95% CL limits on x'^2 and y' , we use a frequentist method with Feldman-Cousins ordering⁹⁾. The obtained contours are shown in Fig. 2(b).

Table 1: Summary of results from the separate likelihood fits. The 95% CL intervals are obtained from a frequentist method (see text) and include systematic errors.

Fit Case	Parameter	Fit Result ($\times 10^{-3}$)	95% CL interval ($\times 10^{-3}$)
No CPV	x'^2	$-1.53^{+0.80}_{-1.00}$	$x'^2 < 0.81$
	y'	$25.4^{+11.1}_{-10.2}$	$-8.2 < y' < 16$
	R_D	2.87 ± 0.37	$2.7 < R_D < 4.0$
	R_M	–	$R_M < 0.42$
No CPV $x' = 0$ (fixed)	y'	6.0 ± 3.3	–
	R_D	3.43 ± 0.26	–
CPV allowed	A_D	-80 ± 77	$-250 < A_D < 110$
	A_M	987^{+13}_{-380}	$-991 < A_M < 1000$
	x'^2	–	$x'^2 < 0.89$
	y'	–	$-30 < y' < 27$
	R_M	–	$R_M < 0.46$

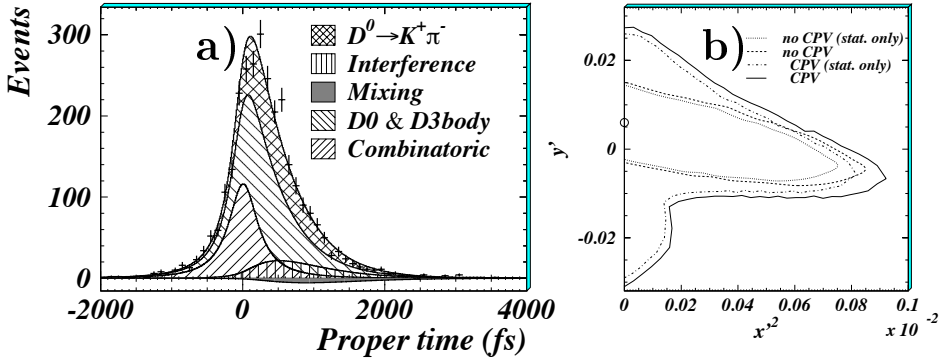


Figure 2: (a) The decay-time distribution for WS events satisfying $|m_{K\pi} - m_{D^0}| < 22 \text{ MeV}/c^2$ and $|Q - 5.9 \text{ MeV}| < 1.5 \text{ MeV}$. Superimposed on the data (points with error bars) are projections of the decay-time fit. (b) 95% CL regions for (x'^2, y') .

3.2 Search for $D^0 - \overline{D}^0$ mixing using semileptonic decays.

The semileptonic decay modes don't suffer from a background of doubly Cabibbo suppressed (DCS) decays but they are more difficult to reconstruct due to the presence of a neutrino in the final state.

For the present analysis, data collected by the Belle detector at the center-of-mass energy of the $\Upsilon(4S)$ resonance, corresponding to an integrated luminosity of 140 fb^{-1} were used. To search for the $D^0 - \overline{D}^0$ mixing in this case we used the $D^{*+} \rightarrow D^0 \pi_s^+$, $D^0 \rightarrow K^- e^+ \nu$ decay chain. The flavor of the produced D meson is tagged by the charge of the slow pion (π^\pm) emerging in the D^* decay. The charge of the electron determines the nature of the D meson at decay.

The events with slow pion momentum of less than $600 \text{ MeV}/c$, electron momentum $p > 600 \text{ MeV}/c$ and charged kaon candidates momentum above $800 \text{ MeV}/c$ were selected. Additional cuts on the $p^*(Ke) > 2 \text{ GeV}/c$, the second and zeroth Fox-Wolfram moments $R_2 > 0.2$ and $M(Ke) < 1.82 \text{ GeV}/c^2$ were applied. The detailed description of the selection criteria are presented in Ref. 10).

For the events satisfying the described criteria, the neutrino reconstruction was performed. A first approximation for the neutrino four-momentum P_ν

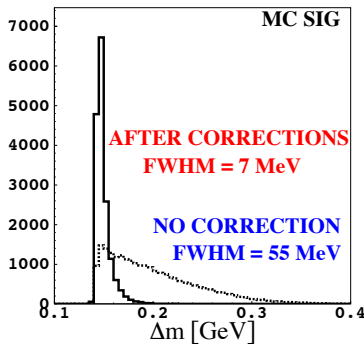


Figure 3: Δm distribution for simulated signal events using the missing momentum for neutrino reconstruction (dashed histogram) or the missing momentum together with the constraints on the missing mass and the mass of the D^{*+} (full histogram).

is obtained from the four-momentum conservation $P_\nu = P_{\text{cms}} - P_{\pi_s Ke} - P_{\text{rest}}$, where cms stands for the center-of-mass four-momentum of the e^+e^- system, and the index *rest* indicates the four-momentum of all detected particles except the slow pion, charged kaon and the electron candidate. P_{rest} is calculated using all the remaining charged tracks in the event with $|\delta r| < 1 \text{ cm}$ and $|\delta z| < 2 \text{ cm}$

and all photons with an energy above 100 MeV.

Two kinematic constraints were used to improve the resolution on the neutrino momentum. First, for events with $-4 \text{ GeV}/c^2 < M(\pi_s K e \nu)^2 < 36 \text{ GeV}/c^2$, the magnitude of P_{rest} was rescaled by a factor x requiring the invariant mass $M(\pi_s K e \nu)^2 = (P_{\text{cms}} - x \cdot P_{\text{rest}})^2$ should equal the mass of the $D^{*\pm}$ meson. Second, for events satisfying $-2 \text{ GeV}/c^2 < m_\nu^2 < 0.5 \text{ GeV}/c^2$, the square of the missing mass $m_\nu^2 = (E_{\text{cms}} - E_{\pi_s K e} - E_{\text{rest}})^2 - p_{\pi_s K e}^2 - p_{\text{rest}}^2 - 2p_{\pi_s K e} p_{\text{rest}} \cos \alpha$ was set to zero by correction of the angle α between the direction of \vec{p}_{rest} and the direction of the $\pi_s K e$ system. As it is shown in Fig. 3 the constraints allow to improve Δm resolution about 7 times. We use simple cut on $t > 1.5\tau_D$ to suppress D^0 mistag background.

The distribution on Δm for RS and WS events are shown in Fig. 4. The signal and background shapes are estimated from the data, with a small MC-derived corrections. The results of the number of events for RS and WS obtained from the fit are the following: $N_{RS} = 40198 \pm 329$ and $N_{WS} = 19 \pm 67$. Using the data we obtained the mixing value $r_D = \frac{D^0 \rightarrow e^- K^+ \bar{\nu}_e}{D^0 \rightarrow e^+ K^- \nu_e} = \frac{x^2 + y^2}{2} = (0.20 \pm 0.70 \pm 0.11) \times 10^{-3}$ which corresponds to the upper limit of $r_D < 1.4 \times 10^{-3}$ at 90% C.L. The detailed description of the analysis can be found in Ref. 10).

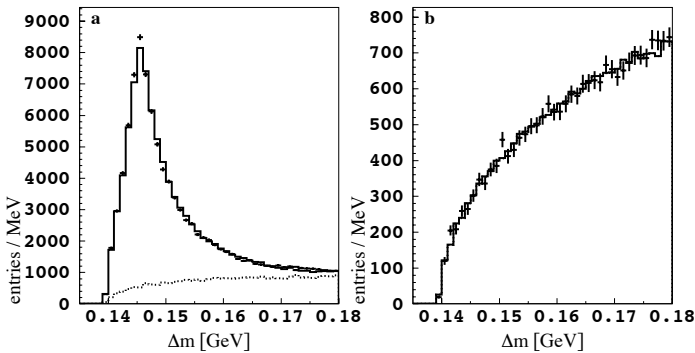


Figure 4: Distribution of Δm for RS events (a) and for WS events (b). Data is shown with error bars, the full histogram shows the fit. The background contribution is shown as the dashed histogram.

4 P-wave excitations of D mesons.

Study of the production of excited states of D -mesons, collectively referred to as D^{**} 's, provides tests of Heavy Quark Effective Theory (HQET) and QCD sum rules. Figure 5 shows the spectrum of D -meson excitations. In the heavy quark limit, the heavy quark spin \vec{s}_c decouples from the other degrees of freedom and the total angular momentum of the light quark $\vec{j}_q = \vec{L} + \vec{s}_q$ is a good quantum number. There are four P-wave states with the following spin-parity and light quark angular momenta: $0^+(j_q = 1/2)$, $1^+(j_q = 1/2)$, $1^+(j_q = 3/2)$ and $2^+(j_q = 3/2)$, which are usually labeled as D_0^* , D_1' , D_1 and D_2^* , respectively.

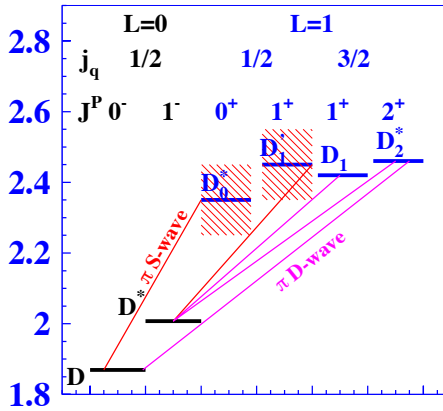


Figure 5: *Spectrum of D -meson excitations. Lines show possible one pion transitions.*

The $B \rightarrow D^{(*)}\pi\pi$ decay provides a possibility to study D^{**} production. The fixed spin of the initial state makes it possible to perform an angular analysis of the decay products and to separate final states with different quantum numbers. The list of possible waves for B and D^{**} decays is listed in Table 2.

We performed analysis of $B^- \rightarrow D^{(*)+}\pi^-\pi^-$ based on $65 \times 10^6 B\bar{B}$ events. The $D^{(*)}$ mesons were reconstructed in the following modes: $D^+ \rightarrow K^-\pi^+\pi^+$, $D^{*+} \rightarrow D^0\pi^+$, $D^0 \rightarrow K^-\pi^+$ and $D^0 \rightarrow K^-\pi^+\pi^-\pi^+$. Candidate events are identified by their center of mass (c.m.) energy difference, $\Delta E = (\sum_i E_i) - E_b$, and beam-constrained mass, $M_{bc} = \sqrt{E_b^2 - (\sum_i \vec{p}_i)^2}$, where $E_b = \sqrt{s}/2$ is the beam energy in the $\Upsilon(4S)$ c.m. frame, and \vec{p}_i and E_i are the c.m. three-momenta and energies of the B meson candidate decay products. We select events from the signal region $|\Delta E| < 25$ MeV and $|M_{bc} - M_B| < 5$ MeV/ c^2 . The description of the details can be found in Ref. [11]. The projection of the

Table 2: Possible waves in B and D^{**} decays

B -decay		D^{**} -decay	
$B \rightarrow D_2^* \pi$	D-wave	$D_2^* \rightarrow D\pi, D^* \pi$	D-wave
$B \rightarrow D_1 \pi$	P-wave	$D_1 \rightarrow D^* \pi$	D-wave
$B \rightarrow D_1' \pi$	P-wave	$D_1' \rightarrow D^* \pi$	S-wave
$B \rightarrow D_0^* \pi$	S-wave	$D_0^* \rightarrow D\pi$	S-wave

minimal $D^{(*)}\pi$ mass distribution for the signal events is shown in the Fig. 6 together with the background distribution estimated from ΔE sideband. Together with the narrow peaks corresponding to D_2^{*0} and D_1^0 resonances we observe additional broad structure. To extract the contributions of the differ-

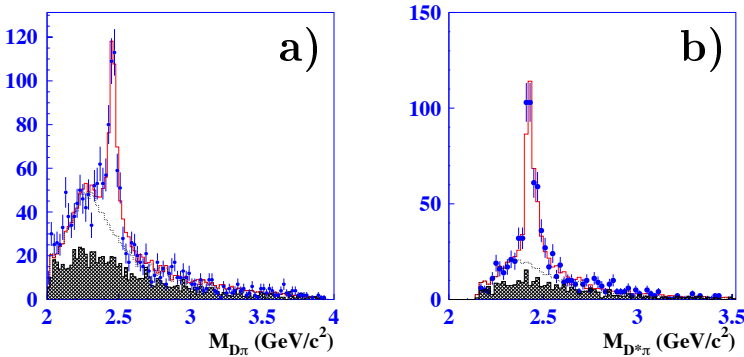


Figure 6: The minimal $D\pi$ (a) and $D^*\pi$ (b) mass distribution of $B^- \rightarrow D^+\pi^-\pi^-$ candidates. The points with error bars correspond to the signal box events, while the hatched histogram shows the background obtained from the sidebands. The open histogram is the result of the unbinned fit while the dashed one shows the fitting function in the case when the narrow resonance amplitude is set to zero.

ent D^{**} 's the unbinned likelihood fit of Dalitz plot for $D\pi\pi$ was performed. For the $D^*\pi$ final state we have a decaying vector D^* particle. There are two additional degrees of freedom and, in addition to the $D^*\pi$ and $\pi\pi$ invariant masses squared, two other variables are needed to specify the final state. In this case unbinned likelihood fit was performed in four-dimensional space. Contributions of all four neutral D^{**} 's have been observed. This was the first observation of

Table 3: *The branching fraction products for the different D^{**} production.*

	$B(B^- \rightarrow D^{**0}\pi^-) \times$ $B(D^{**0} \rightarrow D^+\pi^-)$ $\times 10^{-4}$	$B(B^- \rightarrow D^{**0}\pi^-) \times$ $B(D^{**0} \rightarrow D^{*+}\pi^-)$ $\times 10^{-4}$
D_2^{*0}	$3.4 \pm 0.3 \pm 0.6 \pm 0.4$	$1.8 \pm 0.3 \pm 0.3 \pm 0.2$
D_1^0		$6.8 \pm 0.7 \pm 1.3 \pm 0.2$
D_0^{*0}	$6.1 \pm 0.6 \pm 0.9 \pm 1.6$	
D_1^{*0}		$5.0 \pm 0.4 \pm 1.0 \pm 0.4$
	$B(\bar{B}^0 \rightarrow D^{**+}\pi^-) \times$ $B(D^{**+} \rightarrow D^0\pi^+)$ $\times 10^{-4}$	$B(\bar{B}^0 \rightarrow D^{**+}\pi^-) \times$ $B(D^{**+} \rightarrow D^{*0}\pi^+)$ $\times 10^{-4}$
D_2^{*+}	$3.08 \pm 0.33 \pm 0.09_{-0.02}^{+0.15}$	$2.45 \pm 0.42_{-0.45-0.17}^{+0.35+0.39}$
D_1^+		$3.68 \pm 0.60_{-0.40-0.30}^{+0.71+0.65}$
D_0^{*+}	< 1.2 at 90 % C.L.	
D_1^{*+}		< 0.7 at 90 % C.L.

the broad states D_0^{*0} and D_1^{*0} . The obtained branching fractions are listed in the Tab. 3.

Similar analysis has been performed for $\bar{B}^0 \rightarrow D^{(*)0}\pi^+\pi^-$ decay based on $152 \times 10^6 B\bar{B}$ events¹²⁾. In this case together with the $D^{(*)}\pi$ structure in the final state we have contribution of $\pi^+\pi^-$ structure which corresponds to production and decay of ρ^0 , f_0 , f_2 mesons. The amplitude for Dalitz plot description includes both $D^{(*)}\pi$ and $\pi^+\pi^-$ final states. The branching fractions obtained from the unbinned fit are shown in the Tab. 3, 4. $D^{(*)}\pi$ and $\pi\pi$ mass distributions are shown in th Fig. 7. In this case we observed the narrow resonances but the contribution of broad structures is smaller than in the case

Table 4: *Branching fractions of $\bar{B}^0 \rightarrow D^*X$, $X \rightarrow \pi\pi$*

decay	Branching fraction $\times 10^{-4}$
$B(\bar{B}^0 \rightarrow D^0\rho)$	$2.91 \pm 0.28 \pm 0.33_{-0.54}^{+0.08}$
$B(\bar{B}^0 \rightarrow D^0f_2)$	$1.95 \pm 0.34 \pm 0.38_{-0.02}^{+0.32}$
$B(\bar{B}^0 \rightarrow D^{*0}\rho)$	$3.73 \pm 0.87 \pm 0.46_{-0.08}^{+0.18}$
$B(\bar{B}^0 \rightarrow D^{*0}f_2)$	$1.86 \pm 0.65 \pm 0.60_{-0.52}^{+0.80}$

of charged B decay.

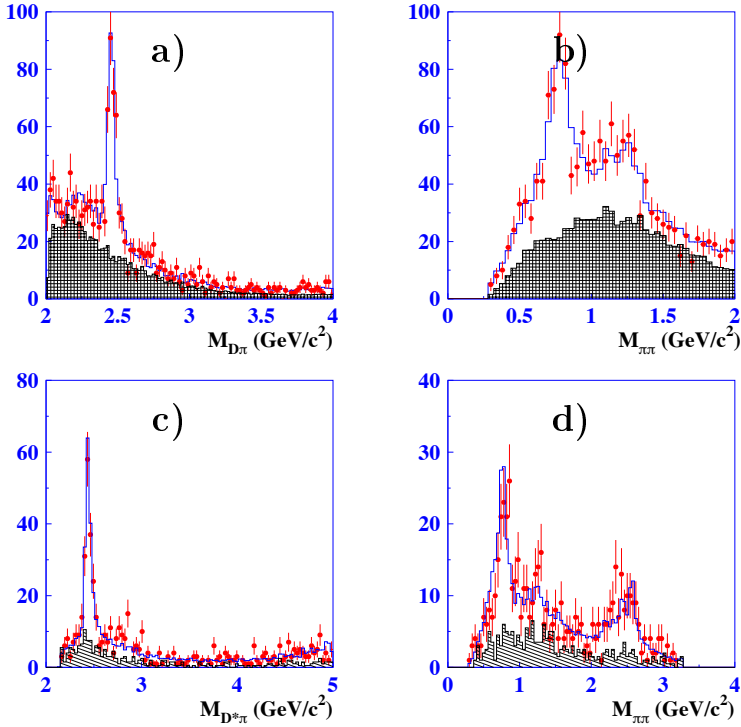


Figure 7: Mass distribution for decay $\bar{B}^0 \rightarrow D^0 \pi^+ \pi^-$: $D\pi$ - (a), $\pi\pi$ - (b) and for decay $\bar{B}^0 \rightarrow D^{*0} \pi^+ \pi^-$: $D^*\pi$ - (c), $\pi\pi$ - (d). The points with error bars correspond to the signal box events, the hatched histogram — to the background obtained from sidebands. The open histogram shows the fit function after efficiency correction.

The branching fraction products obtained for the narrow ($j = 3/2$) resonances are similar to those obtained in the case of charged B decays. The measured values of the branching fractions for the broad resonance D_0^{*+} and D_1^{*+} production in neutral B decay are, however, significantly lower than those for charged B decays. One possible explanation for this phenomenon is that for charged B decay to $D^{*+} \pi$, the amplitude receives contributions from both tree and the color suppressed diagrams as shown in Fig. 8.

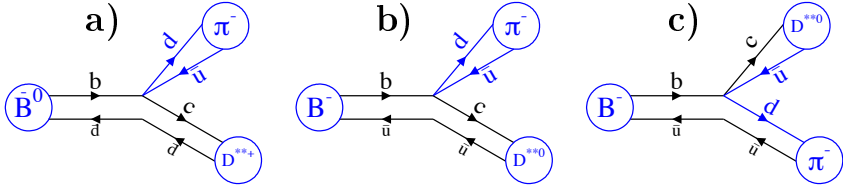


Figure 8: Feynman diagrams for charged (a), (b) and neutral (c) B decays.

5 Search for $\bar{B}^0 \rightarrow D_{sJ}^+ K^-$, $\bar{B}^0 \rightarrow D_{sJ}^- \pi^+$ decays.

Two narrow resonances denoted as $D_{sJ}^*(2317)^+$ and $D_{sJ}(2460)^+$ have been observed recently in e^+e^- continuum interactions [13, 14, 15, 16]. These resonances were initially seen in the $D_{sJ}^*(2317)^+ \rightarrow D_s^+ \pi^0$, $D_{sJ}(2460)^+ \rightarrow D_s^+ \gamma$ and $D_{sJ}(2460)^+ \rightarrow D_s^{*+} \pi^0$ decay modes and their quantum numbers were tentatively classified as $J^P = 0^+$ for $D_{sJ}^*(2317)^+$ and $J^P = 1^+$ for $D_{sJ}(2460)^+$. However the measured masses of these resonances are significantly smaller than predicted within the potential model for 0^+ and 1^+ states. The D_{sJ} mesons were also observed in $B \rightarrow \bar{D}^0 D_{sJ}$ decay modes with branching fractions an order of magnitude less than those for $B \rightarrow \bar{D}^0 D_s$ decay modes with a pseudoscalar D_s [17]. Angular analysis of $B \rightarrow \bar{D}^0 D_{sJ}(2460)^+$ favors a spin 1 assignment for $D_{sJ}(2460)^+$. There has been a significant effort to explain the surprising D_{sJ} masses [18], and some authors discussed an exotic four-quark content for the D_{sJ}^+ [19, 20, 21, 22, 23].

We report the results from a search for $\bar{B}^0 \rightarrow D_{sJ}^+ K^-$ and $\bar{B}^0 \rightarrow D_{sJ}^- \pi^+$ decays, where D_{sJ}^+ mesons are reconstructed in the modes $D_{sJ}^*(2317)^+ \rightarrow D_s^+ \pi^0$ and $D_{sJ}(2460)^+ \rightarrow D_s^+ \gamma$. The corresponding $\bar{B}^0 \rightarrow D_s^+ K^-$ and $\bar{B}^0 \rightarrow D_s^- \pi^+$ decays have been observed recently by Belle [24] and BaBar [25].

The decay mode $\bar{B}^0 \rightarrow D_{s(J)}^- \pi^+$ can be described by a tree diagram with the b to u transition and only a few $\bar{B}^0 \rightarrow D_{sJ}^- \pi^+$ events can be expected to be observed in the current Belle data.

The decays $\bar{B}^0 \rightarrow D_{s(J)}^+ K^-$ are of special interest because the quark content of the initial \bar{B}^0 meson ($b\bar{d}$) is completely different from that of the $D_{s(J)}^+ K^-$ final state ($cs\bar{s}\bar{u}$), indicating an unusual configuration with both initial quarks involved in the weak decay.

The analysis was performed using a 140 fb^{-1} data sample, containing $152 \times 10^6 B\bar{B}^0$ pairs. The detailed analysis description can be found in [26].

The signal yields were obtained from the fit of $\Delta M(D_{sJ}) \equiv M(D_{sJ}^+ \pi^0(\gamma)) -$

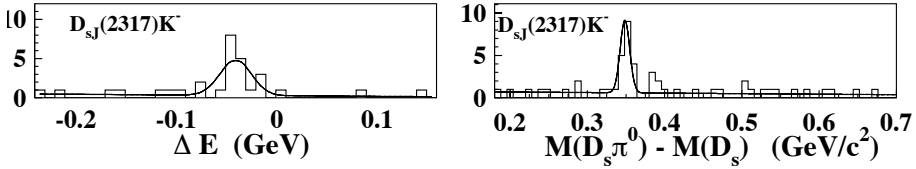


Figure 9: ΔE and ΔM distributions for $\bar{B}^0 \rightarrow D_{sJ}^*(2317)^+ K^-$ events.

Table 5: Signal yields, product branching fractions (or limits), and significances for the $\bar{B}^0 \rightarrow D_{sJ}^+ K^-$ and $D_{sJ}^- \pi^+$ decay modes.

Decay mode	Yield $\Delta M(D_{sJ})$	$\mathcal{B}(B^0 \rightarrow D_{sJ} h) \times$ $\mathcal{B}(D_{sJ} \rightarrow D_s \pi^0(\gamma))$ $\times 10^{-5}$	Signif. σ
$\bar{B}^0 \rightarrow D_{sJ}^*(2317)^+ K^-$	$16.6^{+4.6}_{-4.1}$	$5.3^{+1.5}_{-1.3} \pm 0.7 \pm 1.4$	6.8
$B^0 \rightarrow D_{sJ}^*(2317)^- \pi^+$	$2.9^{+3.3}_{-2.8}$	< 2.5 (90% C.L.)	
$\bar{B}^0 \rightarrow D_{sJ}(2460)^+ K^-$	$2.0^{+2.9}_{-2.2}$	< 0.94 (90% C.L.)	
$\bar{B}^0 \rightarrow D_{sJ}(2460)^- \pi^+$	$-1.9^{+3.1}_{-2.6}$	< 0.40 (90% C.L.)	

$M(D_s^+)$ distributions for events in the ΔE and M_{bc} signal region. They are described by signal Gaussians with widths fixed from MC and mass differences fixed to $348.6 \text{ MeV}/c^2$ or $487.9 \text{ MeV}/c^2$, and linear backgrounds. A clear $\bar{B}^0 \rightarrow D_{sJ}^*(2317)^+ K^-$ signal is observed; no significant signals are observed in the remaining modes (Fig. 9). The \bar{B}^0 yields, based on fits to histograms combining all three D_s^+ decay modes, are listed in Table 5.

The $\bar{B}^0 \rightarrow D_{sJ}^*(2317)^+ K^-$ mode was observed, with product branching fraction $\mathcal{B}(\bar{B}^0 \rightarrow D_{sJ}^*(2317)^+ K^-) \times \mathcal{B}(D_{sJ}^*(2317)^+ \rightarrow D_s^+ \pi^0) = (5.3^{+1.5}_{-1.3} \pm 0.7 \pm 1.4) \cdot 10^{-5}$. Recent measurements imply that the $D_{sJ}^*(2317)^+ \rightarrow D_s^+ \pi^0$ channel is dominant and the $D_{sJ}(2460)^+ \rightarrow D_s^+ \gamma$ fraction is around $\sim 30\%$. Taking into account these approximate values, we can conclude that $\mathcal{B}(\bar{B}^0 \rightarrow D_{sJ}^*(2317)^+ K^-)$ is of the same order of magnitude as $\mathcal{B}(\bar{B}^0 \rightarrow D_s^+ K^-)$, but at least a factor two larger than the $\bar{B}^0 \rightarrow D_{sJ}(2460)^+ K^-$ branching fraction, in contrast to the naïve expectation that decays with the same spin-doublet $D_{sJ}^*(2317)^+$ and $D_{sJ}(2460)^+$ mesons would have similar rates. In agreement with the expectation, no significant signals for $\bar{B}^0 \rightarrow D_{sJ}^- \pi^+$ decays were seen.

6 Double charmonium production

The large rate for processes of the type $e^+e^- \rightarrow J/\psi \eta_c$ and $J/\psi (c\bar{c})_{\text{non-res}}$ reported by Belle ²⁷⁾ remains unexplained. Following the publication of this result, the cross-section for $e^+e^- \rightarrow J/\psi \eta_c$ via e^+e^- annihilation into a single virtual photon was calculated using non-relativistic QCD (NRQCD) to be $\sim 2\text{fb}$ ²⁸⁾, which is at least an order of magnitude smaller than the measured value. Several hypotheses have been suggested in order to resolve this discrepancy. In particular, the authors of Ref. ²⁹⁾ have proposed that processes proceeding via two virtual photons may be important. Other authors ³⁰⁾ suggest that since the dominant mechanism for charmonium production in e^+e^- annihilation is expected to be the color-singlet process $e^+e^- \rightarrow c\bar{c}gg$, the final states observed by Belle contain a charmonium state and a $M \sim 3\text{GeV}/c^2$ glueball. The glueball states with this mass are predicted by lattice QCD.

In this presentation we report an extended analysis of the $e^+e^- \rightarrow J/\psi (c\bar{c})$ process to check the above hypotheses and provide extra information that might be useful to resolve the puzzle. This study is performed using a data sample of 140fb^{-1} collected at the $\Upsilon(4S)$ resonance and 15fb^{-1} at an energy 60MeV below the $\Upsilon(4S)$.

J/ψ are reconstructed from two oppositely charged muons or electrons with invariant mass within 30MeV of J/ψ nominal mass. A mass-constrained fit is then performed to improve the $p_{J/\psi}^*$ resolution and the recoil mass $M_{\text{recoil}} = \sqrt{(E_{\text{CM}} - E_{J/\psi}^*)^2 - p_{J/\psi}^{*2}}$ is calculated, where $E_{J/\psi}^*$ is the J/ψ CM energy after the mass constraint. $\psi(2S)$ is reconstructed via its decay to $J/\psi \pi^+\pi^-$ and the $\psi(2S)$ signal window is defined as $|M_{J/\psi \pi^+\pi^-} - M(\psi(2S))| < 10\text{MeV}/c^2$ ($\approx 3\sigma_M$) The analysis is described in detail in Ref. ³¹⁾.

The $M_{\text{recoil}}(J/\psi)$ spectrum for the data is presented in Fig. 10: clear peaks around the nominal η_c and χ_{c0} masses are evident; another significant

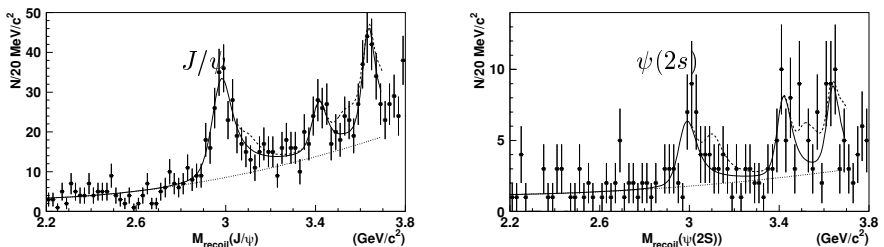


Figure 10: *The mass of the system recoiling against the reconstructed J/ψ in inclusive $e^+e^- \rightarrow J/\psi X$ events. The curves are described in the text.*

peak around $\sim 3.63 \text{ GeV}/c^2$ is identified as the $\eta_c(2S)$. The spectrum was fitted including all of the known narrow charmonium states. The fit results are listed in Table 6.

Table 6: *Summary of the signal yields (N), charmonium masses (M), significances, and cross-sections ($\sigma_{Born} \times \mathcal{B}_{>2}((c\bar{c})_{res})$) for $e^+e^- \rightarrow J/\psi (c\bar{c})_{res}$; $\mathcal{B}_{>2}$ denotes the branching fraction for final states with more than two charged tracks.*

$(c\bar{c})_{res}$	N	$M [\text{GeV}/c^2]$	Signif.	$\sigma_{Born} \times \mathcal{B}_{>2} [\text{fb}]$
η_c	235 ± 26	2.972 ± 0.007	10.7	$25.6 \pm 2.8 \pm 3.4$
J/ψ	-14 ± 20	fixed	—	< 9.1 at 90% CL
χ_{c0}	89 ± 24	3.407 ± 0.011	3.8	$6.4 \pm 1.7 \pm 1.0$
$\chi_{c1} + \chi_{c2}$	10 ± 27	fixed	—	< 5.3 at 90% CL
$\eta_c(2S)$	164 ± 30	3.630 ± 0.008	6.0	$16.5 \pm 3.0 \pm 2.4$
$\psi(2S)$	-26 ± 29	fixed	—	< 13.3 at 90% CL

We perform a similar study with reconstructed $\psi(2S) \rightarrow J/\psi \pi^+ \pi^-$ decays to search for $e^+e^- \rightarrow \psi(2S)(c\bar{c})_{res}$ processes. The recoil mass spectrum for the data is presented in Fig. 10: peaks corresponding to the η_c , χ_{c0} , and $\eta_c(2S)$ can be seen. Using a larger data set we confirm our published observation of

Table 7: *Summary of the signal yields (N), significances, and cross-sections ($\sigma_{Born} \times \mathcal{B}_{>0}((c\bar{c})_{res})$) for $e^+e^- \rightarrow \psi(2S)(c\bar{c})_{res}$; $\mathcal{B}_{>0}$ denotes the branching fraction for final states containing charged tracks.*

$(c\bar{c})_{res}$	N	Signif.	$\sigma_{Born} \times \mathcal{B}_{>0} [\text{fb}]$
η_c	36.7 ± 10.4	4.2	$16.3 \pm 4.6 \pm 3.9$
J/ψ	6.9 ± 8.9	—	< 16.9 at 90% CL
χ_{c0}	35.4 ± 10.7	3.5	$12.5 \pm 3.8 \pm 3.1$
$\chi_{c1} + \chi_{c2}$	6.6 ± 8.0	—	< 8.6 at 90% CL
$\eta_c(2S)$	36.0 ± 11.4	3.4	$16.0 \pm 5.1 \pm 3.8$
$\psi(2S)$	-8.3 ± 8.5	—	< 5.2 at 90% CL

$e^+e^- \rightarrow J/\psi \eta_c$, $J/\psi \chi_{c0}$ and $J/\psi \eta_c(2S)$ and find no evidence for the process $e^+e^- \rightarrow J/\psi J/\psi$. We have calculated the cross-sections for $e^+e^- \rightarrow J/\psi \eta_c$, $J/\psi \chi_{c0}$, and $J/\psi \eta_c(2S)$ with better statistical accuracy and reduced systematic errors and set an upper limit for $\sigma(e^+e^- \rightarrow J/\psi J/\psi) \times \mathcal{B}(J/\psi \rightarrow >$

2 charged) of 9.1fb at the 90% CL. Although this limit is not inconsistent with the prediction for the $J/\psi J/\psi$ rate given in Ref. 29), the suggestion that a large fraction of the inferred $J/\psi \eta_c$ signal consists of $J/\psi J/\psi$ events is ruled out. We have measured the production and helicity angle distributions for $e^+e^- \rightarrow J/\psi \eta_c$, $J/\psi \chi_{c0}$, and $J/\psi \eta_c(2S)$; the distributions are consistent with expectations for these states, and disfavor a spin-0 glueball contribution to the η_c peak. We observe $\psi(2S)(c\bar{c})_{\text{res}}$ production for the first time, and find that the production rates for these final states are of the same magnitude as the corresponding rates for $J/\psi(c\bar{c})_{\text{res}}$.

7 Summary

Successful operation of the KEKB and the Belle allows to obtain many interesting results in charm physics.

The measurement of $D^0 - \bar{D}^0$ mixing in $D \rightarrow K\pi$ mode provides the world's-most-restrictive-limit on y' and x'^2 -mixing values of the level 10^{-2} and 10^{-3} respectively.

The sensitivity to $D^0 - \bar{D}^0$ mixing in $D \rightarrow Kl\nu$ mode also reached a 10^{-3} level.

The branching fractions of $B^- \rightarrow D^{**0}\pi^-$ have been measured both for narrow and for broad states. Masses and widths of D^{**} have been measured. Significantly smaller branching fractions of $\bar{B}^0 \rightarrow D^{**+}\pi^-$ for the broad states has been observed.

$\bar{B}^0 \rightarrow D_{sJ}^{*+}K^-$ and $\bar{B}^0 \rightarrow D_{sJ}^-\pi^+$ decays were studied for the first time. The branching fraction of $\bar{B}^0 \rightarrow D_{sJ}^*(2317)^+K^-$ is of the same order as $\bar{B}^0 \rightarrow D_s^{*+}K^-$ and at least a factor of 2 larger than the $\bar{B}^0 \rightarrow D_{sJ}(2460)^+K^-$. No significant signal from $\bar{B}^0 \rightarrow D_{sJ}^-\pi^+$ were observed.

Double charmonia production has been confirmed and the measured cross section is at least one order of magnitude larger than theoretical calculations.

8 Acknowledgements

We thank the KEKB group for the excellent operation of the accelerator, the KEK Cryogenics group for the efficient operation of the solenoid, and the KEK computer group and the NII for valuable computing and Super-SINET network support. We acknowledge support from MEXT and JSPS (Japan); ARC and DEST (Australia); NSFC (contract No. 10175071, China); DST (India); the BK21 program of MOEHRD and the CHEP SRC program of KOSEF (Korea); KBN (contract No. 2P03B 01324, Poland); MIST (Russia); MESS (Slovenia); NSC and MOE (Taiwan); and DOE (USA).

References

1. A. Abashian *et al.* (Belle), Nucl. Instr. Meth. A **479**, 117 (2002).
2. S. Kurokawa and E. Kikutani, Nucl. Instr. Meth. A **499**, 1 (2003).
3. For a comprehensive review see S. Bianco, F. L. Fabbri, D. Benson, and I. Bigi, Riv. Nuovo Cim. **26N7-8**, 1 (2003). See also A. Falk *et al.*, Phys. Rev. D **69**, 114021 (2004).
4. Charge conjugate modes are implicitly included everywhere.
5. E. Aitala *et al.* (E791), Phys. Rev. D **57**, 13 (1998).
6. R. Godang *et al.* (CLEO), Phys. Rev. Lett. **84**, 5038 (2000).
7. B. Aubert *et al.* (BaBar), Phys. Rev. Lett. **91**, 171801 (2003).
8. J. Li, *et al.* (Belle Collaboration), Phys. Rev. Lett. **94**, 071801 (2005).
9. G. J. Feldman and R. D. Cousins, Phys. Rev. D **57**, 3873 (1998).
10. K. Abe *et al.* (the Belle Collaboration) Contributed to 32nd International Conference on High-Energy Physics (ICHEP 04), Beijing, China, 16-22 Aug 2004, e-Print Archive: hep-ex/0408112.
11. K. Abe *et al.* (Belle Collaboration), Phys. Rev. D **69**, 112002 (2004).
12. K. Abe *et al.* (Belle Collaboration), BELLE-CONF-0460, ICHEP-04-11-0710, Dec 2004. 24pp. Presented at 32nd International Conference on High-Energy Physics (ICHEP 04), Beijing, China, 16-22 Aug 2004. e-Print Archive: hep-ex/0412072
13. BaBar Collaboration, B. Aubert *et al.*, Phys. Rev. Lett. **90**, 242001 (2003).
14. CLEO Collaboration, D. Besson *et al.*, Phys. Rev. D **68**, 032002 (2003).
15. Belle Collaboration, Y. Mikami *et al.*, Phys. Rev. Lett. **92**, 012002 (2004).
16. BaBar Collaboration, B. Aubert *et al.*, Phys. Rev. D **69**, 031101 (2004).
17. Belle Collaboration, P. Krokovny *et al.*, Phys. Rev. Lett. **91**, 262002 (2003).
18. See P. Colangelo, F. De Fazio and R. Ferrandes, BARI-TH/04-486, hep-ph/0407137 and references therein.
19. T. Barnes, F.E. Close, H.J. Lipkin, Phys. Rev. D **68**, 054006 (2003).
20. H.-Y. Cheng, W.-S. Hou, Phys. Lett. B **566**, 193 (2003).

21. R. Terasaki, Phys. Rev. D **68**, 011501 (2003).
22. T. Browder, S. Pakvasa, A. Petrov, Phys. Lett. B **578**, 365 (2004).
23. C.-H. Chen, H.-n Li, Phys. Rev. D **69**, 054002 (2004).
24. Belle Collaboration, P. Krokovny *et al.*, Phys. Rev. Lett. **89**, 231804 (2002).
25. BaBar Collaboration, B. Aubert *et al.*, Phys. Rev. Lett. **90**, 181803 (2003).
26. A. Drutskoy *et al* (Belle Collaboration), Phys. Rev. Lett. **94**, 961802 (2005).
27. K. Abe *et al.* (Belle Collab.), Phys. Rev. Lett. **89**, 142001 (2002).
28. E. Braaten and J. Lee, Phys. Rev. **D67**, 054007 (2003); predictions for the angular distributions are listed in the appendix.
29. G.T. Bodwin, J. Lee and E. Braaten, Phys. Rev. Lett. **90**, 162001 (2003).
30. S.J. Brodsky, A.S. Goldhaber and J. Lee, Phys. Rev. Lett. **91**, 112001 (2003).
31. K. Abe *et al.* (Belle Collaboration), Phys. Rev. D **70**, 071102(R) (2004).

RARE DECAYS AND EXOTIC STATES WITH BABAR

Steven H. Robertson

Dept. of Physics, McGill University

3600 University St. Montreal, Quebec, Canada

for the *BABAR* collaboration

Abstract

Results from the *BABAR* experiment are presented for searches for several rare FCNC B and D meson decays, including the modes $B^0 \rightarrow \ell^+\ell^-$ and $D^0 \rightarrow \ell^+\ell^-$, $B \rightarrow (\rho, \omega)\gamma$ and $B^+ \rightarrow (K, \pi)^+\nu\bar{\nu}$. Limits on lepton flavour violation in neutrino-less τ decays are also discussed. Finally, results of *BABAR* searches for the strange pentaquark states $\Theta^+(1540)$, $\Xi^{--}(1860)$ and $\Xi^0(1860)$ are summarized.

1 Introduction

In addition to the CP-violation studies for which is better known, the large inclusive samples of $B\bar{B}$, continuum $e^+e^- \rightarrow q\bar{q}$ and $e^+e^- \rightarrow \tau^+\tau^-$ recorded by the *BABAR* experiment are providing unprecedented sensitivity to rare decays of heavy-flavour mesons and τ leptons as well as to exotic states such as the controversial $\Theta^+(1540)$ pentaquark. In these proceedings we present results of searches for a number of rare $b \rightarrow d, s$ and $c \rightarrow u$ flavour-changing neutral-current (FCNC) processes, the lepton-flavour violating (LFV) decay $\tau^+ \rightarrow \mu^+\gamma$ and the strange pentaquark states $\Theta^+(1540)$, $\Xi^{--}(1860)$ and $\Xi^0(1860)$.¹

The data used for analyses described in these proceedings were collected with the *BABAR* detector¹⁾ at the PEP-II asymmetric-energy e^+e^- storage ring at SLAC. Since 1999 the *BABAR* experiment has collected a data sample of approximately 245 million $B\bar{B}$ pairs, corresponding to an integrated luminosity of approximately 221 fb⁻¹ at the $\Upsilon(4S)$ resonance. An additional 23 fb⁻¹ sample was collected at a centre-of-mass (CM) energy approximately 40 MeV below $B\bar{B}$ threshold and is used to study continuum production of $e^+e^- \rightarrow q\bar{q}$ ($q = u, d, s, c$) and dilepton events. *BABAR* data taking was shut down during the summer of 2004 to permit upgrades to the PEP-II accelerator and *BABAR* detector. In particular, two sextants of an upgraded muon system based on limited-streamer tubes were installed during this period. The resumption of data-taking, anticipated to begin in October 2004, was delayed by several months due to an electrical accident at SLAC, but was imminent at the time of this conference. It is anticipated that the current run will continue essentially without interruption until the summer of 2006, at which time the remaining sextants of the muon system will be installed during a several-month shutdown. It is anticipated that *BABAR* will have integrated a total luminosity of 500 fb⁻¹ by the end of this run.

Charged particle tracking and dE/dx for particle identification (PID) are provided by a five-layer double-sided silicon vertex tracker and a 40-layer drift chamber contained within the magnetic field of a 1.5 T superconducting solenoid. A ring-imaging Cherenkov detector (DIRC) provides charged $K - \pi$ separation of greater than 3σ , over the relevant momentum range for analyses presented here. The energies of neutral particles are measured by an electromagnetic calorimeter (EMC) consisting of 6580 CsI(Tl) crystals, which provides an energy resolution of $\sigma_E/E = (2.3/E^{1/4} \oplus 1.9)\%$ (E is in GeV). The magnetic flux return of the solenoid is instrumented with resistive plate chambers in order to provide muon identification. A full *BABAR* detector Monte Carlo (MC) simulation based on GEANT4²⁾ is used to evaluate signal efficiencies and to identify and study background sources.

¹Charge conjugate modes are implied throughout this paper.

2 $B^0 \rightarrow \ell^+\ell^-$ and $D^0 \rightarrow \ell^+\ell^-$

The leptonic decays $B^0 \rightarrow \ell^+\ell^-$ and $D^0 \rightarrow \ell^+\ell^-$ FCNC processes proceed via one-loop electroweak penguin and box diagrams in the Standard Model (SM). These processes are cleanly calculable, since the only non-vanishing operator is the axial-current O_{10} and the hadronic matrix elements are just the meson decay constants $f_{B,D}$. For B^0 mesons the SM branching fractions are predicted to be $\sim 10^{-15}$, 10^{-10} and 10^{-8} for the e^+e^- , $\mu^+\mu^-$ and $\tau^+\tau^-$ modes respectively. New physics may contribute additional loop diagrams, may preferentially couple to heavier quark flavours and will not in general exhibit the helicity suppression of the SM decays. Consequently, various non-SM models predict enhancements to SM rates by two or more orders of magnitude. Experimentally, $B^0 \rightarrow \ell^+\ell^-$ ($\ell = e, \mu$) are also very clean in a B-factory environment ($B^0 \rightarrow \tau^+\tau^-$ unfortunately is extremely challenging due to the presence of neutrinos). Results of *BABAR* searches for $B^0 \rightarrow e^+e^-$, $\mu^+\mu^-$ and the lepton-flavour violating mode $e^+\mu^-$ based on 111 fb^{-1} of data have recently been submitted for publication³⁾. The experimental search proceeds by identifying two oppositely-charged high-momentum lepton candidates. The lepton four-vectors are combined to yield a B meson candidate which is expected to have invariant mass equal to the B mass and a centre-of-mass (CM) energy E_B equal to the CM beam energy E_{beam} (where the total CM energy is $2 \cdot E_{\text{beam}}$). These requirements are enforced via the kinematic variables $m_{ES} \equiv \sqrt{E_{\text{beam}}^2 - p_B^2}$ and $\Delta E \equiv E_B - E_{\text{beam}}$, which exploit the fact that the CM energy is very precisely determined in a B-factory environment. For $B^0 \rightarrow \ell^+\ell^-$ the m_{ES} and ΔE resolutions are estimated to be less than about $3 \text{ MeV}/c^2$ and 25 MeV respectively. Additional suppression of non- $B\bar{B}$ continuum backgrounds is achieved through cuts on event-shape variables, particularly $\cos\theta_T$, the cosine of the angle between the thrust axis defined by the reconstructed B candidate and the thrust axis defined by the combination of all other tracks and clusters in the event. Signal efficiencies are determined from simulation, while backgrounds are determined directly from data by extrapolating m_{ES} and ΔE sidebands into the expected signal region. Efficiency systematics arise predominantly due to knowledge of the shapes of the signal m_{ES} and ΔE distributions, and from tracking and PID uncertainties. The total estimated systematics range from 5.7% to 7.1% for the three signal modes. Unblinding of the data revealed a total of two signal candidate in the three modes, consistent with the background expectations. Branching fraction limits are derived using a modified frequentist approach and are listed in table 1.

A related *BABAR* analysis searches for the corresponding leptonic decays of D^0 mesons⁴⁾. This analysis complements the $B^0 \rightarrow \ell^+\ell^-$ search in that it is potentially sensitive to new physics couplings of up-type quarks rather than down-type quarks. D^0 candidates are reconstructed from combinations

Table 1: $B^0 \rightarrow \ell^+ \ell^-$ results.

Mode	Efficiency	Expected background	Events observed	Limit (90% C.L.)
$B(B^0 \rightarrow e^+ e^-)$	21.8 ± 1.2	0.71 ± 0.31	0	$< 6.1 \times 10^{-8}$
$B(B^0 \rightarrow \mu^+ \mu^-)$	15.9 ± 1.1	0.72 ± 0.26	0	$< 8.3 \times 10^{-8}$
$B(B^0 \rightarrow e^\pm \mu^\mp)$	18.1 ± 1.2	1.29 ± 0.44	2	$< 18 \times 10^{-8}$

of oppositely-charged electrons and muons as described above. Due to substantial combinatorial backgrounds arising from double-semileptonic decays of $B\bar{B}$ events, the resulting D^0 candidates are required to possess CM momentum $p_D > 2.4$ GeV/ c and are further required to combine with a charged pion to yield a $D^{*+} \rightarrow D^0 \pi^+$ candidate consistent with the expected D^{*+} mass. Since this analysis does not utilize $\Upsilon(4S)$ events for the signal channel, the offpeak data is also included, for a total dataset of 122 fb $^{-1}$. Remaining backgrounds arise either from purely combinatorial sources or from D^0 decays with kaons or pions misidentified as leptons. In the latter case, the reconstructed dilepton invariant mass is shifted slightly from the nominal D^0 mass, permitting estimation of this background source directly from data sidebands along with the purely combinatorial background component. Signal yields are obtained by a simultaneous fit of the signal and background shapes to the dilepton invariant mass distribution in data, yielding branching fraction limits of

$$\begin{aligned}
 B(D^0 \rightarrow e^+ e^-) &< 1.2 \times 10^{-6} \\
 B(D^0 \rightarrow \mu^+ \mu^-) &< 1.3 \times 10^{-6} \\
 B(D^0 \rightarrow e^\pm \mu^\mp) &< 0.81 \times 10^{-6}
 \end{aligned}$$

at the 90% confidence level.

3 $B \rightarrow \rho(770)\gamma$ and $B \rightarrow \omega(782)\gamma$

Penguin-mediated $b \rightarrow s\gamma$ FCNC decays have been relatively precisely measured in both inclusive and exclusive modes. In contrast, the CKM suppressed $b \rightarrow d\gamma$ modes have been more elusive. The decay rates for the exclusive decays $B \rightarrow \rho(770)\gamma$ and $B \rightarrow \omega(782)\gamma$ are related in spectator quark models, permitting the combined rate, $\bar{B}[B \rightarrow (\rho, \omega)\gamma]$, to be expressed as

$$\bar{B}[B \rightarrow (\rho, \omega)\gamma] \equiv \frac{1}{2} \{ B(B^+ \rightarrow \rho^+ \gamma) + \frac{\tau_{B^+}}{\tau_{B^0}} [B(B^0 \rightarrow \rho^0 \gamma) + B(B^0 \rightarrow \omega \gamma)] \} \quad . \quad (1)$$

The SM expectation is $\bar{B}[B \rightarrow (\rho, \omega)\gamma] \sim (0.9-1.8) \times 10^{-6}$ but, as is the case for other FCNC decays, enhancements to this rate are predicted in various new

physics models. *BABAR* has recently reported the results of a search for the exclusive decays $B^+ \rightarrow \rho^+\gamma$, $B^0 \rightarrow \rho^0\gamma$ and $B \rightarrow \omega(782)\gamma$ based on 191 fb^{-1} of data. $\rho^0 \rightarrow \pi^+\pi^-$, $\rho^+ \rightarrow \pi^+\pi^0$ and $\omega \rightarrow \pi^+\pi^-\pi^0$ candidates are reconstructed from combinations of charged and neutral pions which yield invariant masses $630 < m(\pi\pi) < 940 \text{ MeV}/c^2$ and $764 < m(\pi^+\pi^-\pi^0) < 795 \text{ MeV}/c^2$. These are combined with identified photons to obtain charged and neutral B meson candidates. Background arise primarily from $e^+e^- \rightarrow q\bar{q}$ events containing energetic photons from initial state radiation, π^0/η decays, or from other radiative B decays such as $B \rightarrow K^*\gamma$. Events are vetoed if the photon candidate can be combined with any other photon to yield $m(\gamma\gamma)$ consistent with a π^0 or η . Additional background rejection is obtained using a combination of a neural net based on activity in the detector which is not associated with the signal photon or ρ/ω candidate (i.e. the so-called “rest of event”), and using a Fisher discriminant based on the kinematics of the signal candidate (the helicity angle, flight direction of the reconstructed B candidate, etc.). The signal candidate yield is extracted from data using a four-dimensional extended maximum likelihood fit to the m_{ES} and ΔE distributions and the outputs of the neural net and Fisher as shown in figure 1. Branching fraction limits are obtained both for the individual modes as well as the $B \rightarrow (\rho, \omega)\gamma$ combination, yielding

$$\begin{aligned} B(B^+ \rightarrow \rho^+\gamma) &< 1.8 \times 10^{-6} \\ B(B^0 \rightarrow \rho^0\gamma) &< 0.4 \times 10^{-6} \\ B(B^0 \rightarrow \omega\gamma) &< 1.0 \times 10^{-6} \\ \bar{B}[B \rightarrow (\rho, \omega)\gamma] &< 1.2 \times 10^{-6} \end{aligned}$$

at 90% confidence level. These results are compared with theoretical predictions and current Belle experimental results in figure 2, from which is clear that current experimental sensitivity has reached the SM level.

Because SM $b \rightarrow s/d\gamma$ processes are dominated by penguin diagrams with a top quark in the loop, the branching fractions are sensitive to CKM elements V_{tx} ($x = d, s, b$). Although the absolute branching fractions possess relatively large theoretical uncertainties, many of these are expected to cancel in the ratio of $b \rightarrow d\gamma$ and $b \rightarrow s\gamma$ modes,

$$\frac{\bar{B}(B \rightarrow (\rho, \omega)\gamma)}{B(B \rightarrow K^*(892)\gamma)} = \left| \frac{V_{td}}{V_{ts}} \right|^2 \left(\frac{1 - m_\rho^2/M_B^2}{1 - m_{K^*}^2/M_B^2} \right)^3 \xi^2 [1 + \Delta R] \quad (2)$$

where m are the masses of the decay daughters, M_B is the B meson mass⁹⁾, and ξ and ΔR are correction factors relating to flavour SU(3) breaking and weak annihilation respectively with values $\xi^2 = 0.85 \pm 0.10$ and $\Delta R = 0.1 \pm 0.1$.⁷⁾ Using $\bar{B}[B \rightarrow (\rho, \omega)\gamma]$ from above and combining it with a previously published *BABAR* measurement¹⁰⁾ of $B(B \rightarrow K^*(892)\gamma)$ yields a limit on the

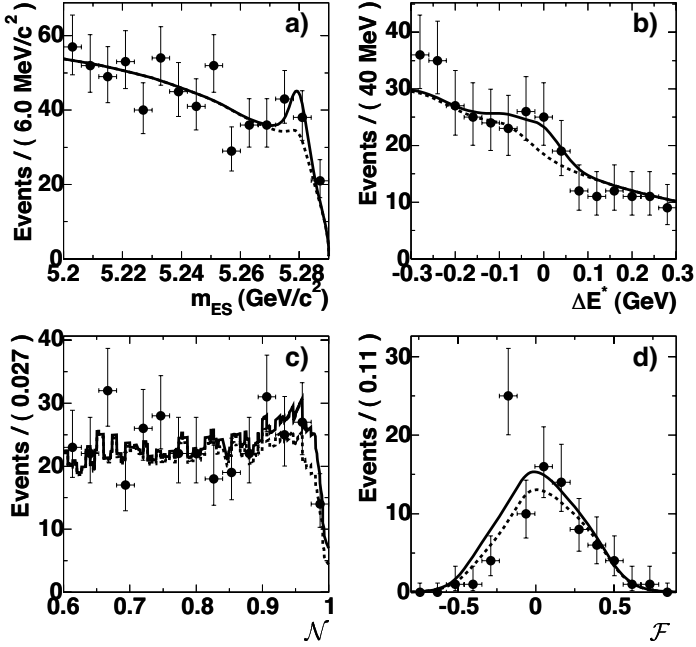


Figure 1: Projections of the combined $B \rightarrow (\rho, \omega)\gamma$ fit to BABAR data (points) in the four fitting variables (a) m_{ES} , (b) ΔE , (c) the neural net output \mathcal{N} and (d) the Fisher discriminant output \mathcal{F} . The dashed curves are the expected background, while the solid curves indicate the total signal plus background.

ratio $\bar{B}(B \rightarrow (\rho, \omega)\gamma)/B(B \rightarrow K^*(892)\gamma) < 0.029$ at 90% which, neglecting theoretical uncertainties, can be interpreted as a limit on the ratio $|V_{td}|/|V_{ts}| < 0.19$. It is worth noting that this limit is beginning to impose a significant constraint on the B meson unitarity triangle fits.

4 $B^+ \rightarrow K^+\nu\bar{\nu}$ and $B^+ \rightarrow \pi^+\nu\bar{\nu}$

The $b \rightarrow s\nu\bar{\nu}$ branching fraction is considered to be one of the most theoretically clean probes of new physics in the B sector. Unlike the charged lepton modes $b \rightarrow s\ell^+\ell^-$, the neutrino modes do not possess a photonic penguin diagram (only Z penguin and W box diagrams contribute) and hence are governed by only a single Wilson coefficient. $b \rightarrow s\nu\bar{\nu}$ is also free of long

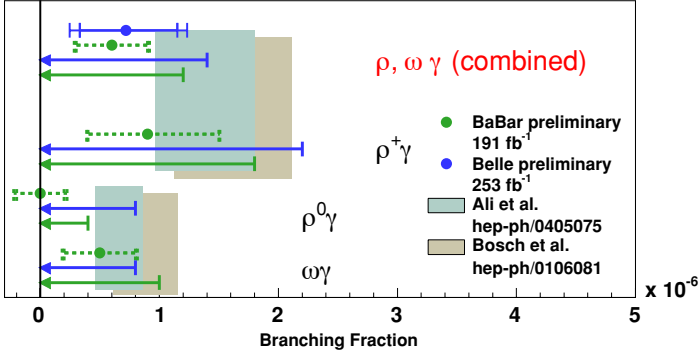


Figure 2: Comparison of $b \rightarrow d\gamma$ branching fractions experimental results from BABAR ⁵⁾ and Belle ⁶⁾ with theoretical predictions ^{7) 8)}.

distance contributions which additionally complicate the interpretation of the charged lepton modes. The situation for $b \rightarrow d\nu\bar{\nu}$ is similar, except that there is an additional suppression factor of $|V_{td}|^2/|V_{ts}|^2$ relative to the strange modes. Unfortunately, $b \rightarrow s\nu\bar{\nu}$ is experimentally very difficult due to the presence of the two undetected neutrinos. Consequently, it is necessary to search for the exclusive decay $B^+ \rightarrow K^+\nu\bar{\nu}$ rather than perform an inclusive search. The SM prediction for the $B^+ \rightarrow K^+\nu\bar{\nu}$ branching fraction is $\sim 4 \times 10^{-6}$, however substantial enhancement can occur in new physics models as a result of contributions of heavy non-SM particles in the loop. BABAR has recently reported the results of a search for $B^+ \rightarrow K^+\nu\bar{\nu}$ and $B^+ \rightarrow \pi^+\nu\bar{\nu}$ decays based on 82 fb⁻¹ of data ¹¹⁾. The signature for these modes is the presence of a single charged kaon or pion plus significant missing energy recoiling against a reconstructed charged B meson. The analysis proceeds by first exclusively reconstructing a charged B candidate in either an hadronic or semileptonic decay mode of the form $B^- \rightarrow D^{(*)0} X_{\text{had}}^-$ or $B^- \rightarrow D^{(*)0} \ell^- \bar{\nu}$, where X_{had}^- is a combination of up to five charged or neutral hadrons. Once a charged B candidate has been identified, all remaining particles in the event are considered to comprise the signal candidate. Events are retained if the signal candidate contains exactly one track with charge opposite the reconstructed B , with CM momentum $p_{K,\pi} > 1.25\text{GeV}/c$ and with PID consistent with either a kaon (for $B^+ \rightarrow K^+\nu\bar{\nu}$) or pion (for $B^+ \rightarrow \pi^+\nu\bar{\nu}$). True signal events may also contain a small number of low-energy calorimeter clusters resulting hadronic split-offs, beam backgrounds, bremsstrahlung photons etc., while background events typically contain significant additional calorimeter activity

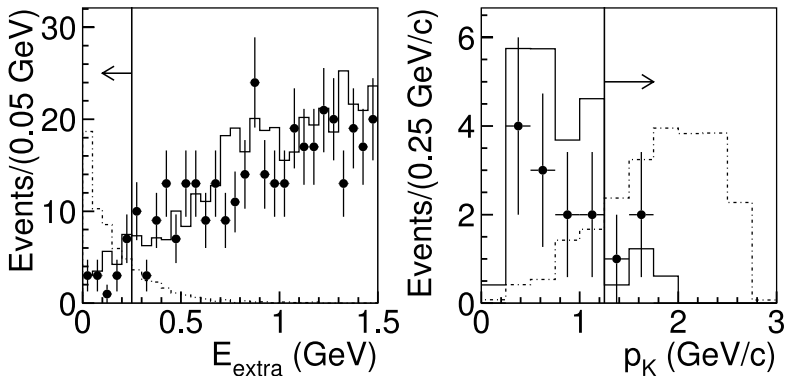


Figure 3: *Distribution (a) of the total energy, E_{extra} , of all calorimeter clusters in $B^+ \rightarrow K^+ \nu \bar{\nu}$ signal candidate events which are not used in the reconstruction of the accompanying B meson, and (b) distribution of the signal kaon CM momentum, p_K for events surviving the e_{extra} indicated in (a). Data are shown as solid points, while the MC predictions for the signal and background distributions are plotted as dashed and solid curves respectively. In both plots only events with an hadronic accompanying B are shown.*

due to the presence of neutral hadrons in the event (see figure 3a). The total extra calorimeter energy associated with the signal candidate is required to be less than 250MeV. For $B^+ \rightarrow K^+ \nu \bar{\nu}$, the overall B reconstruction plus signal selection efficiencies were estimated to be $(0.055 \pm 0.005)\%$ and $(0.115 \pm 0.009)\%$ respectively for the hadronic and semileptonic reconstruction samples, dominated in both cases by the low B reconstruction efficiencies. Unblinding of the data revealed three and six events respectively, consistent with background estimates. A combined branching ratio limit of $B(B^+ \rightarrow K^+ \nu \bar{\nu}) < 5.2 \times 10^{-5}$ is obtained using a modified frequentist approach. Comparable signal efficiencies were obtained for the $B^+ \rightarrow \pi^+ \nu \bar{\nu}$ search, however substantially larger backgrounds were expected and subsequently observed in data, resulting in a limit of $B(B^+ \rightarrow \pi^+ \nu \bar{\nu}) < 10 \times 10^{-5}$ at 90% confidence level.

5 Neutrino-less τ decays and lepton-flavour violation

In the SM with non-zero neutrino masses LFV can occur in one-loop penguin processes via neutrino mixing, but only at a level which is many orders of magnitude below current or expected future experimental sensitivity. Hence any observation of LFV would provide unambiguous evidence of new physics.

Various new physics scenarios predict enhancements in various LFV τ decays up to the current experimental limits. *BABAR* has recently reported the results of a search for the LFV mode $\tau^+ \rightarrow \mu^+\gamma$, based on a sample $2.07 \times 10^8 e^+e^- \rightarrow \tau^+\tau^-$ events, corresponding to an integrated luminosity of 232 fb^{-1} (on- plus off-peak data). Events are divided into two hemispheres along a plane perpendicular to the event thrust axis and events consisting of a 1-1 or 1-3 charged track topology are retained. The so-called “tag” hemisphere is labelled as e , μ , h or $3h$ according to the particle identification of the track(s). The opposing hemisphere is then required to contain only a single muon and a photon with energy $E_\gamma > 200 \text{ MeV}$. Background rejection is achieved using a five-input neural net utilizing the event missing mass and transverse momentum, the tag particle momenta and the signal candidate helicity angle. Signal candidates are selected within a region defined by a 2σ ellipse in the kinematic variables $\delta E = E_{\mu\gamma} - \sqrt{s}/2$ and m_{EC} , defined as the invariant mass resulting from a kinematic fit to the $\mu\gamma$ combination with $E_{\mu\gamma}$ constrained to $\sqrt{s}/2$. A total of four events are observed in the combination of all tag modes. Backgrounds are determined from extrapolation of m_{EC} and ΔE sideband regions into the signal region and are estimated to total 6.2 ± 0.5 events. A branching fraction limit is derived from a maximum likelihood fit to the m_{EC} distribution (see figure 4), yielding $B(\tau^+ \rightarrow \mu^+\gamma) < 6.8 \times 10^{-8}$ at the 90% confidence level.

6 $\Theta_5^+(1540)$ and $\Xi_5^-(1860)$ Pentaquark searches

A flurry of recent experimental searches for pentaquark states was triggered by a theoretical paper¹⁵⁾ based on a chiral soliton model using the $N^+(1710)$ as input and mass splittings of $\sim 180 \text{ MeV}/c^2$. Evidence was subsequently reported by several experimental groups for an exotic state, $\Theta_5^+(1540)$, which is presumed to have minimal quark content of $udud\bar{s}$. *BABAR* reported preliminary null results at ICHEP 2004¹⁶⁾ for the $\Theta_5^+(1540)$, $\Xi_5^-(1860)$, $\Xi_5^0(1860)$ as well as other members of the antidecuplet and corresponding octet. These searches have recently been refined and subsequently submitted for publication¹⁷⁾. Since the production mechanism at an e^+e^- collider is not known the *BABAR* searches utilize all events accepted by the trigger, estimated to be more than 99% efficient for $e^+e^- \rightarrow q\bar{q}$ events. Θ^+ candidates are reconstructed in the mode pK_s^0 ($K_s^0 \rightarrow \pi^+\pi^-$), with a resulting invariant mass resolution ranging from 2-8 MeV/c depending on the signal candidate momentum. The signal efficiency is estimated from Monte Carlo simulation and validated by comparing the data yield for $\Lambda_c^+ \rightarrow pK_s^0$ with the simulation predictions. A clear $\Lambda_c^+ \rightarrow pK_s^0$ peak containing approximately 98000 events is visible in data, however no evidence of the $\Theta_5^+(1540)$ is visible (see figure 5 left). Limits are obtained by fitting both the inclusive pK_s^0 spectrum and the differential

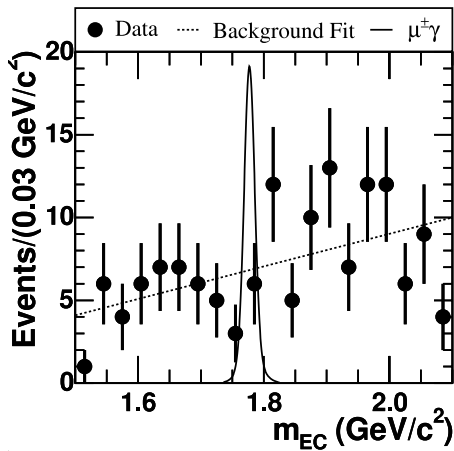


Figure 4: *The energy-constrained invariant mass m_{EC} for $\tau^+ \rightarrow \mu^+ \gamma$ signal candidate events. Data are shown as solid points, while the fitted background shape is shown as a dashed curve. The signal shape is shown for illustration as a solid curve.*

spectra obtained in bins of the CM pK_s^0 candidate momenta (figure 5 right and table 2) assuming both a width of $1 \text{ MeV}/c^2$ and a natural width of $8 \text{ MeV}/c^2$. Production rates are consistent with zero across the entire momentum range and for all width hypotheses.

Searches for the $\Xi_5^-(1860)$ and $\Xi_5^0(1860)$ pentaquarks proceed in a similar manner, via the channels $\Xi_5^-(1860) \rightarrow \Xi^- \pi^-$ and $\Xi_5^0(1860) \rightarrow \Xi^- \pi^+$, where $\Xi^- \rightarrow \Lambda^0 \pi^-$, $\Lambda^0 \rightarrow p \pi^-$. A total of 290000 Ξ^- candidates are obtained, with a signal to background ratio of 23:1 in the $\Lambda^0 \pi^-$ invariant mass. The overall reconstruction efficiency for $\Xi_5^-(1860)$ and $\Xi_5^0(1860)$ is estimated to range from 6.5% at low momentum to 12% at high momentum. The $\Xi_5^0(1860)$ efficiency is further validated by comparing the yield of conventional $\Xi^0(1530)$ and Ξ_c baryons in data and simulation. Signal yields are extracted both inclusively and in bins of momentum as was done in the Θ^+ search, for signal widths ranging from 1-18 MeV/c^2 . No evidence for either $\Xi_5^-(1860)$ or $\Xi_5^0(1860)$ was found. The resulting limits are reported in table 2.

7 Summary

We have reported the results of *BABAR* searches for several rare decays with potential sensitivity to beyond-SM physics. In several cases, such as $B \rightarrow (\rho, \omega) \gamma$

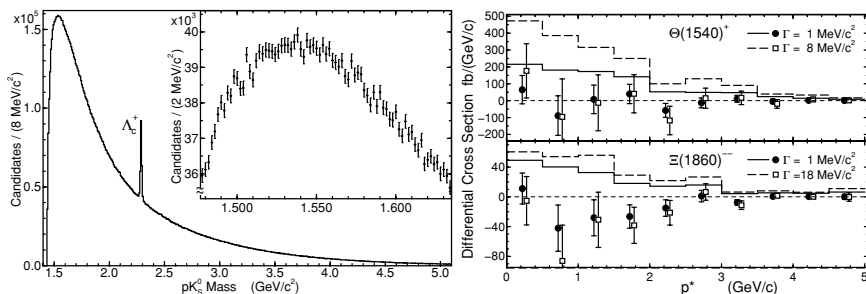


Figure 5: The pK_s^0 invariant mass distribution (left), with detail of the $\Theta_5^+(1540)$ signal region shown inset. Limits on the differential production cross section (right) for $\Theta_5^+(1540)$ and $\Xi_5^-(1860)$ in bins of the signal candidate CM momentum assuming two different possible decay widths (solid and dashed lines).

Table 2: Pentaquark search results integrated over the entire momentum range and quoted as both cross section upper limits and in terms of the rate per event. Numbers in brackets assume ($\Lambda = \text{natural width}$), while unbracketed numbers assume ($\Lambda = 1 \text{ MeV}/c^2$).

Pentaquark state	Cross section upper limit (fb)	$e^+e^- \rightarrow q\bar{q}$ yield upper limit ($\times 10^5/\text{event}$)
$\Theta_5^+ + \Theta_5^-$	171 (363)	5 (11)
$\Xi_5^{--} + \Xi_5^{++}$	25 (36)	0.74 (1.1)

and $B^+ \rightarrow K^+ \nu \bar{\nu}$, these limits are approaching SM predictions. In other cases, such as $B^0 \rightarrow \ell^+ \ell^-$ and $\tau^+ \rightarrow \mu^+ \gamma$, the current experimental limits are many orders of magnitude from the SM, but the limits are currently constraining new physics. In addition, we have described searches for the strange pentaquark states $\Theta_5^+(1540)$, $\Xi_5^-(1860)$ and $\Xi_5^0(1860)$. While large, cleanly reconstructed samples of similar conventional baryons are obtained with excellent invariant mass resolution, we see no evidence of these pentaquark states and conclude that if they exist, then production must be significantly suppressed in e^+e^- compared to conventional baryons.

References

1. B. Aubert *et al.*(*BABAR* Collaboration), Nucl. Instrum. Meth. **A479**, 1 (2002).
2. S. Agostinelli *et al.*, [GEANT4 Collaboration], Nucl. Inst. Meth. **A506**, 250 (2003).
3. B. Aubert *et al.*(*BABAR* Collaboration), hep-ex/0408096 (Aug 2004) 7p. (submitted to Phys. Rev. Lett.).
4. B. Aubert *et al.*(*BABAR* Collaboration), Phys. Rev. Lett. **93**, 191801 (2004).
5. B. Aubert *et al.*(*BABAR* Collaboration), Phys. Rev. Lett. **94**, 011801 (2005).
6. K. Abe *et al.*(Belle Collaboration), hep-ex/0408137 (Aug 2004) 10p..
7. A. Ali, E. Lunghi, A. Y. Parkhomenko, Phys. Lett. B **595**, 323, (2004); hep-ph/0405075.
8. S. Bosch and G. Buchalla, Nucl. Phys. **B621** 459-478 (2002); hep-ph/0106081.
9. Particle Data Group, S. Eidelman *et al.*, Phys. Lett. B **592**, 1 (2004).
10. B. Aubert *et al.*(*BABAR* Collaboration), Phys. Rev. D **70**, 112006 (2004).
11. B. Aubert *et al.*(*BABAR* Collaboration), Phys. Rev. Lett. **94**, 101801 (2005).
12. B. Aubert *et al.*(*BABAR* Collaboration), hep-ex/0502032 (Feb 2005) 7p. (submitted to Phys. Rev. Lett.).
13. B. Aubert *et al.*(*BABAR* Collaboration), Phys. Rev. Lett. **92**, 121801 (2004).
14. B. Aubert *et al.*(*BABAR* Collaboration), hep-ex/0409036 (Sep 2004) 17p.
15. D. Diakonok, V. Petrov and M. Polyakov, Z. Phys. **A 359**, 305 (1997).
16. B. Aubert *et al.*(*BABAR* Collaboration), hep-ex/0408064 (Aug 2004) 22p..
17. B. Aubert *et al.*(*BABAR* Collaboration), hep-ex/0502004 (Feb 2005) 7p. (submitted to Phys. Rev. Lett.).

**DETERMINATION OF V_{us} :
RECENT PROGRESSES FROM THEORY**

Vittorio Lubicz

*Dip. di Fisica, Università di Roma Tre and INFN, Sez. di Roma III,
Via della Vasca Navale 84, I-00146 Rome, Italy*

Abstract

Recent experimental and theoretical results on kaon semileptonic decays have significantly improved the determination of the CKM matrix element V_{us} . After briefly summarizing the impact of the new experimental determinations, I will concentrate in this talk on the theoretical progresses, coming in particular from lattice QCD calculations. These results lead to the estimate $|V_{us}| = 0.2250 \pm 0.0021$, in good agreement with the expectation based on the determination of $|V_{ud}|$ and the unitarity of the CKM matrix.

1 Introduction

The determination of the Cabibbo angle is of particular phenomenological and theoretical interest since it provides at present the most stringent unitarity test of the CKM matrix. This is expressed by the “first row” unitarity condition:

$$|V_{ud}|^2 + |V_{us}|^2 + |V_{ub}|^2 = 1. \quad (1)$$

Since $|V_{ub}| \sim 10^{-3}$, its contribution to Eq. (1) can be safely neglected.

The value of $|V_{ud}|$ is accurately determined from nuclear superallowed $0^+ \rightarrow 0^+$ beta decays. An analysis of the results, based on nine different nuclear transitions, leads to the very precise estimate ¹⁾

$$|V_{ud}| = 0.9740 \pm 0.0005. \quad (2)$$

This determination of $|V_{ud}|$ is more accurate, by approximately a factor three, than the one obtained from the analysis of neutron beta decay. In the neutron case, the error is dominated by the uncertainty on the contribution of the weak axial current, which is determined experimentally, $g_A/g_V = 1.2720 \pm 0.0022$ ³⁾. It is also worth to mention that a new measurement of the neutron lifetime has been recently presented ⁴⁾ whose new value, $\tau_n = (878.5 \pm 0.8)$ sec., differs by more than six standard deviations with respect to the previous average quoted by the PDG, $\tau_n = (885.7 \pm 0.8)$ sec. ⁵⁾. Combined together, the neutron beta decay results lead to the determination $|V_{ud}| = 0.9750 \pm 0.0017$, in agreement with Eq. (2) but with a much larger error. In the following, I will take the estimate in Eq. (2) as the final average of $|V_{ud}|$, and concentrate the discussion on the remaining entry of Eq. (1), the matrix element $|V_{us}|$.

The most accurate determination of $|V_{us}|$ is obtained from semileptonic kaon decays ($K_{\ell 3}$). The analysis of the experimental data gives access to the quantity $|V_{us}| \cdot f_+(0)$, where $f_+(0)$ is the vector form factor at zero four-momentum transfer square. In the SU(3) limit, vector current conservation implies $f_+(0) = 1$. The deviation of $f_+(0)$ from unity represents the main source of theoretical uncertainty. This deviation has been estimated many years ago by Leutwyler and Roos (LR) ⁶⁾, who combined a leading order analysis in chiral perturbation theory (ChPT) with a quark model calculation. They obtained $f_+^{K^0 \pi^-}(0) = 0.961 \pm 0.008$, and this value still represents the referential estimate ⁵⁾.

¹⁾After this talk, the estimate of $|V_{ud}|$ from nuclear superallowed decays has been updated by Marciano at the CKM 2005 Workshop on the Unitarity Triangle. The new estimate, whose uncertainty is further reduced, reads $|V_{ud}| = 0.9739 \pm 0.0003$ ²⁾.

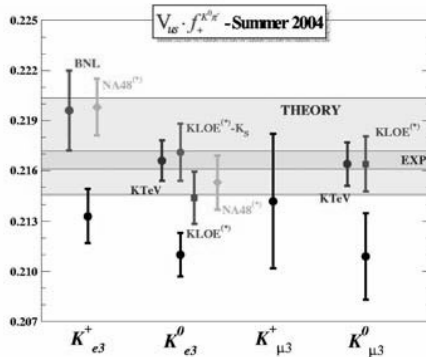


Figure 1: *Experimental results for $|V_{us}| \cdot f_+(0)$. The “EXP” and “THEORY” bands indicate respectively the average of the new experimental results and the unitarity prediction combined with the LR and lattice (see Sect. 4) determination of the vector form factor.*

By averaging old experimental results for K_{l3} decays with the recent measurement by E865 at BNL ⁷⁾, and using the LR determination of the vector form factor, the PDG quotes $|V_{us}| = 0.2200 \pm 0.0026$ ⁵⁾. This value, once combined with the determination of $|V_{ud}|$ given in Eq. (2), implies about 2σ deviation from the CKM unitarity condition, i.e. $|V_{us}|^{\text{unit.}} \simeq \sqrt{1 - |V_{ud}|^2} = 0.2265 \pm 0.0022$.

2 K_{l3} decays: the new experimental results

With respect to the PDG 2004 analysis, however, a significant novelty is represented by several new experimental results, for both charged and neutral K_{l3} decays, which have been recently presented by KTeV ⁸⁾, NA48 ⁹⁾ and KLOE ¹⁰⁾. Expressed in terms of $|V_{us}| \cdot f_+(0)$, these determinations are shown in Fig. 1, together with the BNL result and the averages of the old K_{l3} results quoted by the PDG. Remarkably, the average of the new results ¹¹⁾, represented by the darker band in the plot (“EXP”), is in very good agreement with the unitarity prediction, once the LR determination of the vector form factor is taken into account. The unitarity prediction is shown in Fig. 1 by the lighter band (“THEORY”).

3 $K\ell 3$ decays: theory status

An important theoretical progress in the determination of $|V_{us}|$ is represented by the first (quenched) lattice determination, with significant accuracy, of the vector form factor at zero momentum transfer $f_+(0)$ ¹²⁾. The lattice result turns out to be in very good agreement with the quark model estimate obtained by LR, thus putting the evaluation of this form factor on a firmer theoretical basis. Before outlining the strategy of the lattice calculation, I would like to summarize the theoretical status of the $f_+(0)$ evaluations.

A good theoretical control on $K\ell 3$ transitions is assured by the Ademollo-Gatto (AG) theorem¹³⁾, which states that $f_+(0)$ is renormalized only by terms of at least second order in the breaking of SU(3)-flavor symmetry. Nevertheless, the error on the shift of $f_+(0)$ from unity represents not only the main source of theoretical uncertainty but it also dominates the overall error in the determination of $|V_{us}|$.

The amount of SU(3) breaking due to light quark masses can be investigated within ChPT, by performing an expansion of the form $f_+(0) = 1 + f_2 + f_4 + \dots$, where $f_n = \mathcal{O}(p^n) = \mathcal{O}[M_{K,\pi}^n/(4\pi f_\pi)^n]$. Thanks to the AG theorem, the first non-trivial term in the chiral expansion, f_2 , does not receive contributions of local operators appearing in the effective theory and can be computed unambiguously in terms of M_K , M_π and f_π ($f_2 = -0.023$, in the $K^0 \rightarrow \pi^-$ case⁶⁾). The higher-order terms of the chiral expansion involve instead the coefficients of local chiral operators, that are difficult to estimate. The quark model calculation by LR provides an estimate of the next-to-leading correction f_4 , and it is based on a general parameterization of the SU(3) breaking structure of the pseudoscalar meson wave functions.

An important progress in this study is represented by the complete two-loop ChPT calculation of f_4 , performed in Refs.^{14, 15)}. In Ref. 15), the result has been written in the form

$$f_4 = \Delta(\mu) - \frac{8}{F_\pi^4} [C_{12}(\mu) + C_{34}(\mu)] (M_K^2 - M_\pi^2)^2, \quad (3)$$

where $\Delta(\mu)$ is expressed in terms of chiral logs and the $\mathcal{O}(p^4)$ low-energy constants, while the second term is the analytic one coming from the $\mathcal{O}(p^6)$ chiral Lagrangian. As can be seen from Eq. (3), this local contribution involves a single combination of two (unknown) chiral coefficients entering the effective Lagrangian at $\mathcal{O}(p^6)$. In addition, the separation between non-local and local contribution quantitatively depends on the choice of the renormalization scale μ , only the whole result for f_4 being scale independent. This dependence is found to be large¹⁶⁾; for instance, at three typical values of the scale one finds

$$\Delta(\mu) = \begin{cases} 0.031, & 0.015, & 0.004 \\ \mu = M_\eta & \mu = M_\rho & \mu = 1 \text{ GeV} \end{cases} \quad (4)$$

An important observation by Bijens and Talavera¹⁵⁾ is that the combination of low-energy constants entering f_4 could be in principle constrained by experimental data on the slope and curvature of the scalar form factor. The required level of experimental precision, however, is far from what is currently achieved. Thus, one is left with either the LR result or other model dependent estimates of the local term in Eq. (3). Recent attempts in this direction include the estimate by resonance saturation obtained in Ref. 17) and the dispersive analysis of Ref. 18). The model results, however, are in disagreement within each other. In addition, the large scale dependence of the $\mathcal{O}(p^6)$ loop calculation shown in Eq. (4) seems to indicate that the error ± 0.010 quoted in Refs. 15, 16, 18) might be underestimated.² For all these reasons, a first principle lattice determination of the vector form factor is of great phenomenological relevance.

4 Strategy of the lattice calculation

The first lattice calculation of the vector form factor at zero momentum transfer has been recently presented in Ref. 12). In order to reach the challenging goal of about 1% error on the lattice determination of $f_+(0)$, a new strategy has been proposed and applied in the quenched approximation. This strategy is based on three steps.

1) Precise evaluation of the scalar form factor $f_0(q^2)$ at $q^2 = q_{\text{max}}^2$

This evaluation follows a procedure originally proposed by the FNAL group to study heavy-light form factors¹⁹⁾. For $K_{\ell 3}$ decays, the scalar form factor $f_0(q^2)$ can be calculated very efficiently at $q^2 = q_{\text{max}}^2 = (M_K - M_\pi)^2$ by studying the following double ratio of matrix elements,

$$\frac{\langle \pi | \bar{s} \gamma_0 u | K \rangle \langle K | \bar{u} \gamma_0 s | \pi \rangle}{\langle K | \bar{s} \gamma_0 s | K \rangle \langle \pi | \bar{u} \gamma_0 u | \pi \rangle} = \frac{(M_K + M_\pi)^2}{4M_K M_\pi} [f_0(q_{\text{max}}^2)]^2, \quad (5)$$

where all the external particles are taken at rest. There are several crucial advantages in using the double ratio (5) which are described in details in Ref. 12). The most important point is that this ratio gives values of $f_0(q_{\text{max}}^2)$ with a statistical uncertainty smaller than 0.1%, as it is illustrated in Fig. 2 (left).

²A different factorization between local and non-local contributions has been considered in Ref. 17), which partly reduces the dependence on the factorization scale.

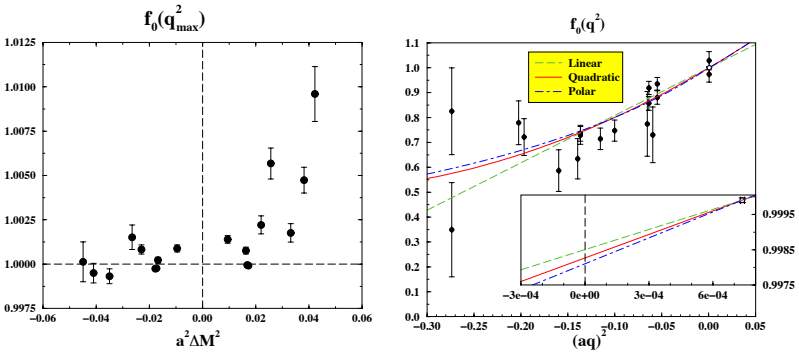


Figure 2: Left: Values of $f_0(q_{\max}^2)$ versus the $SU(3)$ -breaking parameter $a^2\Delta M^2 \equiv a^2(M_K^2 - M_\pi^2)$. Right: The form factor $f_0(q^2)$ as a function of q^2 for one of the quark mass combinations. The inset is an enlargement of the region around $q^2 = 0$.

2) Extrapolation of $f_0(q_{\max}^2)$ to $f_0(0) = f_+(0)$

This extrapolation is performed by studying the q^2 -dependence of $f_0(q^2)$. New suitable double ratios are also introduced in this step, that improve the statistical accuracy of $f_0(q^2)$. The quality of the extrapolation is shown in Fig. 2 (right). Three different functional forms in q^2 have been considered, namely a polar, a linear and a quadratic one. The lattice result for the slope λ_0 of the scalar form factor is in very good agreement with the recent accurate determination from KTeV ²⁰⁾. In the case of the polar fit, for instance, the lattice result is $\lambda_0 = 0.0122(22)$ (in units of $M_{\pi^+}^2$) to be compared with the experimental determination $\lambda_0 = 0.0141(1)$.

3) Extrapolation to the physical masses

The physical value of $f_+(0)$ is finally reached after extrapolating the lattice results to the physical kaon and pion masses. The problem of the chiral extrapolation is substantially simplified if the AG theorem (which holds also in the quenched approximation ²¹⁾) is taken into account and if the leading (quenched) chiral logs are subtracted. This is achieved by introducing the following ratio

$$R = \frac{\Delta f}{(M_K^2 - M_\pi^2)^2} = \frac{1 + f_2^q - f_+(0)}{(M_K^2 - M_\pi^2)^2}, \quad (6)$$

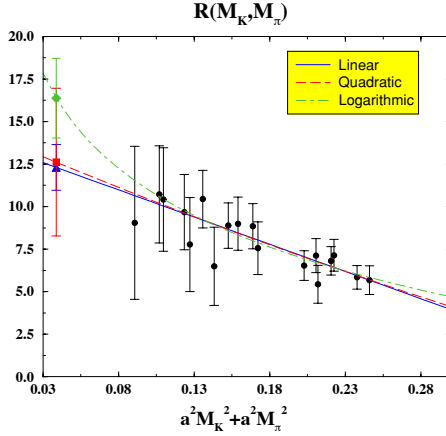


Figure 3: Comparison among linear, quadratic and logarithmic fits of the ratio $R(M_K, M_\pi)$ as a function of $[a^2 M_K^2 + a^2 M_\pi^2]$.

where f_2^q represents the leading chiral contribution calculated in quenched ChPT ¹²⁾ and the quadratic dependence on $(M_K^2 - M_\pi^2)$, driven by the AG theorem, is factorized out. It should be emphasized that the subtraction of f_2^q in Eq. (6) does not imply necessarily a good convergence of (quenched) ChPT at $\mathcal{O}(p^4)$ for the meson masses used in the lattice simulation. The aim of the subtraction is to access directly on the lattice the quantity Δf , defined in Eq. (6) in such a way that its chiral expansion starts at $\mathcal{O}(p^6)$ independently of the values of the meson masses. After the subtraction of f_2^q , the ratio R of Eq. (6) is smoothly extrapolated in the meson masses as illustrated in Fig. 3. In order to check the stability of the results, linear, quadratic and logarithmic fits have been considered. The chiral extrapolation leads to the final result

$$f_+^{K^0 \pi^-}(0) = 0.960 \pm 0.005_{\text{stat}} \pm 0.007_{\text{sys}}, \quad (7)$$

where the systematic error does not include quenching effects beyond $\mathcal{O}(p^4)$. Removing this error represents one of the major goal of future lattice studies of $K_{\ell 3}$ decays. Remarkably, two preliminary unquenched calculations have been already presented. The results read ^{22, 23)}

$$f_+^{K^0 \pi^-}(0) = 0.962 \pm 0.006 \pm 0.007 \quad (8)$$

$$f_+^{K^0 \pi^-}(0) = 0.954 \pm 0.009, \quad (9)$$

in very good agreement with the quenched estimate of Eq. (7).

The value (7) compares well with the LR result $f_+^{K^0\pi^-}(0) = 0.961 \pm 0.008$ quoted by the PDG ⁵⁾ and, once combined with the average of the more recent experimental results, implies

$$|V_{us}| = 0.2256 \pm 0.0022, \quad (10)$$

in good agreement with the unitarity prediction.

A strategy similar to the one discussed above has been also applied to study hyperon semileptonic decays on the lattice, and preliminary results have been presented in ²⁴⁾.

5 Conclusions

We have discussed the most recent experimental and theoretical progresses achieved in the determination of V_{us} from semileptonic kaon decays. On the theoretical side, the main novelty is represented by the first lattice QCD calculation of the $K_{\ell 3}$ vector form factor at zero-momentum transfer, $f_+(0)$. This calculation is the first one obtained by using a non-perturbative method based only on QCD, except for the quenched approximation. Once combined with the new measurements of kaon semileptonic decays, the lattice result leads to a determination of V_{us} in very good agreement with the expectation based on the determination of V_{ud} and the unitarity of the CKM matrix.

Acknowledgments

It is a pleasure to thank the organizers for their success in creating the stimulating and very much enjoyable atmosphere of the Rencontres.

References

1. A. Czarnecki, W. J. Marciano and A. Sirlin, *Phys. Rev. D* **70** (2004) 093006.
2. W. J. Marciano, presented at the CKM 2005 Workshop on the Unitarity Triangle, San Diego, California, 15-18 March 2005.
See <http://ckm2005.ucsd.edu/agenda/fri3/isidori.pdf>.
3. M. Battaglia *et al.*, based on the Workshop on CKM Unitarity Triangle (CERN 2002-2003), Geneva, Switzerland, 13-16 Feb 2002, to appear as CERN Yellow Report. hep-ph/0304132.
4. A. Serebrov *et al.*, *Phys. Lett. B* **605** (2005) 72.
5. PDG: S. Eidelmann *et al.*, *Phys. Lett.* **B592**, 1 (2004).
6. H. Leutwyler and M. Roos, *Z. Phys.* **C25**, 91 (1984).
7. A. Sher *et al.* [E865 Coll.], *Phys. Rev. Lett.* **91**, 261802 (2003); J. A. Thompson, D. E. Kraus and A. Sher [E865 Collaboration], eConf **C0304052** (2003) WG608.
8. T. Alexopoulos *et al.* [KTeV Collaboration], *Phys. Rev. Lett.* **93** (2004) 181802.
9. A. Lai *et al.* [NA48 Collaboration], *Phys. Lett. B* **602** (2004) 41; *Phys. Lett. B* **604** (2004) 1.
10. P. Franzini [Kloe Coll.], invited talk at PIC 2004, hep-ex/0408150. M. Antonelli [Kloe Coll.], talk given at ICHEP'04, <http://www.ihep.ac.cn/>.
11. F. Mescia, contributed to 32nd International Conference on High-Energy Physics (ICHEP 04), Beijing, China, 16-22 Aug 2004, hep-ph/0411097.
12. D. Becirevic *et al.*, *Nucl. Phys. B* **705** (2005) 339.
13. M. Ademollo and R. Gatto, *Phys. Rev. Lett.* **13**, 264 (1964).
14. P. Post and K. Schilcher, *Eur. Phys. J.* **C25**, 427 (2002).
15. J. Bijnens and P. Talavera, *Nucl. Phys.* **B669**, 341 (2003).
16. V. Cirigliano, H. Neufeld and H. Pichl, *Eur. Phys. J. C* **35** (2004) 53.
17. V. Cirigliano, G. Ecker, M. Eidemuller, R. Kaiser, A. Pich and J. Portoles, hep-ph/0503108.
18. M. Jamin, J. A. Oller and A. Pich, *JHEP* **0402** (2004) 047.

19. S. Hashimoto *et al.*, Phys. Rev. **D61**, 014502 (2000).
20. T. Alexopoulos *et al.* [KTeV Collaboration], Phys. Rev. D **70** (2004) 092007.
21. G. Colangelo and E. Pallante, Nucl. Phys. B **520** (1998) 433.
22. M. Okamoto, talk given at FPCP04 conference in Daegu (Korea), hep-lat/0412044.
23. S. Hashimoto, presented at “From Actions to Experiments”, The 2nd International Lattice Field Theory Network Workshop, Edinburgh, March 7-10 2005.
24. D. Guadagnoli, G. Martinelli, M. Papinutto and S. Simula, Nucl. Phys. Proc. Suppl. **140** (2005) 390; D. Becirevic *et al.*, Eur. Phys. J. A **24S1** (2005) 69.

BINARY SYSTEMS IN QM AND IN QFT: CPT

Victor Novikov
ITEP, Moscow, Russia

Abstract

Quasi-degenerate neutral systems like a (K, \bar{K}) type are investigated in Quantum Field Theory (QFT). A constant mass matrix as the one used in Quantum Mechanics (QM) can only be introduced as a linear approximation to QFT. We study the phenomenological consequences of the differences between the QFT and QM treatments. The role of “spurious” states with zero norm at the poles is emphasized. The $K_L - K_S$ mass splitting triggers a tiny difference between the CP violating parameters ϵ_L and ϵ_S , without any violation of TCP . Non-vanishing semi-leptonic asymmetry $\delta_S - \delta_L$ does not signal TCP violation (usual claims notwithstanding), while A_{TCP} keeps vanishing when TCP is good symmetry.

This talk is based on the paper written in collaboration with B. Machtet and M.Vysotsky ¹⁾.

1 Introduction

I would like to reconsider the theory of binary quasi-degenerate neutral systems such as (K, \bar{K}) , (D, \bar{D}) and (B, \bar{B}) . The result of this revision will be the well-known conventional theory plus tiny corrections. It seems unlikely that these corrections can be ever measured experimentally but conceptually they are rather interesting.

The (K, \bar{K}) meson system is among the most magnificent ones in particle physics. Fifty years ago Gell-Mann, Pais, and Pais and Piccioni ²⁾ discovered and described in great detail such beautiful phenomenon as K meson oscillations. Later CP symmetry violation ³⁾ was found in (K, \bar{K}) system. Nowadays the search for CP violation in (B, \bar{B}) system is a hot topic in experimental particle physics. Binary systems are also well suited to test CPT symmetry and Quantum Mechanics (QM) in general.

The main property of the binary systems is that the splitting between two states in binary systems is extremely small in comparison with other masses. Thus it is widely believed that with good accuracy one can separate the dynamics of quasi-degenerate states from the details of the dynamics of other states. In other words one can integrate over infinite number of degrees of freedom in Quantum Field Theory (QFT) and deal with the rest finite number of degrees of freedom, i.e. with effective Quantum Mechanics.

According to this philosophy in the case of binary systems one deals with effective QM with 2×2 non-hermitian Hamiltonian

$$H = M - \frac{i}{2}\Gamma, \quad (1)$$

where $M = M^\dagger$, $\Gamma = \Gamma^\dagger$. The details of QM treatment of binary systems can be found in text-books. A brief and a very transparent version of this conventional theory is presented in Review of Particle Physics ⁴⁾. As a rule the text-books do not go beyond (QM) level in treatment of (K, \bar{K}) system. Only recently the need of a treatment of these systems in the framework of Quantum Field Theory arose ⁵⁾, ⁶⁾. It was actually mainly motivated by the leptonic sector, i.e. by the attempts to treat neutrino oscillations in terms of QFT .

The formalism of a mass matrix seems never to be in doubt, though its existence, as we shall see, can only be assumed in a certain approximation. The growing need for precise criteria to test discrete symmetries made necessary an

exhaustive investigation of these systems in *QFT*. This was done in ¹⁾ and a short version of this study is presented here.

2 $K\bar{K}$ system in QM

First let me remind the conventional QM wisdom for (K, \bar{K}) system. In Wigner-Weisskopf approximation to describe decaying particles we use non-hermitian effective Hamiltonian

$$H = M - \frac{i}{2}\Gamma, \quad (2)$$

with mass matrix $M = M^\dagger$ and decay matrix $\Gamma = \Gamma^\dagger$. Thus

$$H = \begin{pmatrix} m_{11} - \frac{i}{2}\gamma_{11} & m_{12} - \frac{i}{2}\gamma_{12} \\ \overline{m_{12}} - \frac{i}{2}\overline{\gamma_{12}} & m_{22} - \frac{i}{2}\gamma_{22} \end{pmatrix}, \quad (3)$$

where $m_{11}, m_{22}, \gamma_{11}, \gamma_{22}$ are real numbers. Matrix elements of M and Γ can be considered as a set of phenomenological parameters that can be extracted from the experimental data. On the other hand the same matrix elements H_{ik} of the effective Hamiltonian can be connected with matrix elements of the fundamental weak Hamiltonian H_W . For example

$$M_{ik} = m\delta_{ik} + \langle i|H_W|k \rangle + \sum_{\beta} \langle i|H_W|\beta \rangle \langle \beta|H_W|k \rangle / (m - E_{\beta}), \quad (4)$$

where i, k numerate K^0, \bar{K}^0 mesons and β numerates all other states.

The eigenvectors that correspond to "stationary" non-mixing states are K_S and K_L states

$$|K_S \rangle = \sqrt{N_S}(|K_1^0 \rangle + \epsilon_S |K_2^0 \rangle), \quad |K_L \rangle = \sqrt{N_L}(|K_2^0 \rangle + \epsilon_L |K_1^0 \rangle), \quad (5)$$

where $|K_1^0 \rangle$ and $|K_2^0 \rangle$ are CP -even and CP -odd states. Mixing parameters $\epsilon_{S,L}$ can be calculated in terms of matrix elements H_{ik} of effective Hamiltonian.

There are few constraints on the elements H_{ik} that follows from the general symmetries of the system.

Thus from CPT symmetry one can derive that diagonal elements of effective hamiltonian are identical, i.e. $H_{11} = H_{22}$. From this equation one gets that mixing parameters $\epsilon_{S,L}$ are the same $\epsilon_S = \epsilon_L$.

For CP-symmetric interaction one derives additional constraint on the non-diagonal elements. Namely, one gets that $H_{12} = e^{i\alpha}H_{21}$. From this equation it follows that mixing parameter is zero $\epsilon = 0$, and that eigenvectors of

effective Hamiltonian are the states with definite CP-parity, i.e. $|K_1^0\rangle$ and $|K_2^0\rangle$.

One can calculate all *CP* and *CPT* violating asymmetries in terms of mixing parameters $\epsilon_{L,S}$.

Formalism of Mass Matrix for $K\bar{K}$ system seems never to be in doubt, though in the very early publications people mentioned possible corrections to Wigner- Weisskopf approximation. (Although see ref. ⁸⁾).

3 Normal and non-normal Quantum Mechanics

Quantum Mechanics with non-hermitian Hamiltonian eq. (2) is rather different from the conventional *QM*. The reason is that in general case the effective Hamiltonian eq.(2) is not a normal operator.

Let me recall a definition of a normal matrix:

$$M \text{ normal} \Leftrightarrow [M, M^\dagger] = 0. \quad (6)$$

Normality is a remarkable property of matrices:

- 1) any matrix that commutes with its hermitian conjugate can be diagonalized by a single unitary transformation;
- 2) its right and left eigenstates accordingly coincide;
- 3) it admits complex eigenvalues, which makes it specially suited to describe unstable particles.

When *CP* is conserved, we have shown that the propagator of neutral kaons and effective Hamiltonian H must be normal. This will provides us with the most general *CP* eigenstates in the (K^0, \bar{K}^0) basis.

It is very tempting to have a normal propagator and normal effective Quantum Mechanics, since in this case the right eigenstates and left eigenstates coincide. Unfortunately this is impossible. In general the mass matrix M does not commute with the decay matrix Γ ,

$$[M, \Gamma] \neq 0. \quad (7)$$

Thus Hamiltonian H does not commute with its hermitian conjugate H^\dagger

$$[H, H^\dagger] \neq 0, \quad (8)$$

and is non-normal operator.

In this case the left and right eigenstates

$$H |in\rangle = E_{in} |in\rangle, \quad \langle out| H = \langle out| E_{out} \quad (9)$$

are independent sets of vectors, i.e. they are not connected by complex conjugation

$$\langle out | \neq | in \rangle^\dagger . \tag{10}$$

As for the eigenvalues, one can prove that

$$E_{out} = E_{in} . \tag{11}$$

For K -meson system all these can be rewritten as

$$H |K_{L,S} \rangle = (m_{L,S} - \frac{i}{2}\gamma_{L,S}) |K_{L,S} \rangle , \tag{12}$$

$$\langle K_{L,S} | H = (m_{L,S} - \frac{i}{2}\gamma_{L,S}) \langle K_{L,S} | \tag{13}$$

Left eigenstates are orthogonal to the right eigenstates

$$\langle K_{L,S} | K_{S,L} \rangle = 0 \tag{14}$$

and there is no complex conjugation, i.e.

$$\langle K_L | \neq | K_L \rangle^\dagger . \tag{15}$$

All these mean that $\langle K_L |_{out}$ and $| K_L \rangle_{in}$ are different mixtures of K and \bar{K} state. This statement, being formally absolutely correct, is rather unconventional and encourages us to look for different description of binary systems.

4 Effective QFT approach

It seems natural to start from QFT and to derive effective QM as some approximation to QFT . Partly this line of reasoning was motivated by numerous attempts to develop theory of ν -oscillation in terms of Green functions.

We work within effective Field Theory where K -mesons, pions, etc are considered as elementary particles that are described by the corresponding field operators $\phi_K(x)$, $\phi_\pi(x)$, etc. The propagator of these particle are given by v.e.v. of T-product of the appropriate field operators. Say propagation of K^0 into K^0 is equal to

$$\langle K^0 | \Delta(x) | K^0 \rangle = \langle 0 | T \{ \phi_{K^0}(x), \phi_{K^0}^\dagger(0) \} | 0 \rangle . \tag{16}$$

For (K, \bar{K}) mesons quasi-degenerate system the propagator is described by 2×2 matrix

$$\Delta(z) = \begin{pmatrix} \langle K|\Delta|K \rangle & \langle K|\Delta|\bar{K} \rangle \\ \langle \bar{K}|\Delta|K \rangle & \langle \bar{K}|\Delta|\bar{K} \rangle \end{pmatrix} \quad (17)$$

where $z = q^2$ and q is momentum. For any momenta q one can diagonalize Δ and find corresponding eigenstates, i.e.

$$\Delta(z)|R_{\pm}(z)\rangle = \lambda_{\pm}(z)|R_{\pm}(z)\rangle, \langle L_{\pm}(z)|\Delta(z) = \langle L_{\pm}(z)|\lambda_{\pm}(z). \quad (18)$$

The eigenstates are “stationary” states (i.e. there is no oscillation between K_L and K_S). Eigenvalues of the propagator λ_{\pm} are the same for *in* and *out* states. There is no reason for $\Delta(z)$ to be normal. Thus complex conjugation does not transform left states into right states and visa verse, i.e.

$$\langle R_{\pm} | \equiv |R_{\pm}\rangle^{\dagger} \Leftrightarrow \langle R_{+}|R_{-}\rangle \neq 0. \quad (19)$$

This is in one-to-one correspondence with QM approach.

One can write Dyson-Schwinger equation for all 4 propagators. For inverse matrix $\Delta^{-1}(z)$ it looks like

$$\Delta^{-1} = \begin{pmatrix} q^2 - m^2 - \Pi_{KK}(q^2) & \Pi_{K\bar{K}}(q^2) \\ \Pi_{\bar{K}K}(q^2) & q^2 - m^2 - \Pi_{\bar{K}\bar{K}}(q^2) \end{pmatrix}, \quad (20)$$

where $(\Pi_{KK}(q^2), \Pi_{\bar{K}\bar{K}}(q^2))$ and $(\Pi_{K\bar{K}}(q^2), \Pi_{\bar{K}K}(q^2))$ are diagonal and non-diagonal self-energy functions. Dyson-Schwinger equations for these self-energy functions include vertex operators. There are infinite number of equations for vertex operators and QFT with its infinite number of degrees of freedom exhibits itself exactly at this level. But whenever self-energy functions are known one can describe (K^0, \bar{K}^0) system in terms of 2×2 propagators matrix. These functions are analog of matrix elements H_{ik} in QM approach.

Actually to construct a bridge between QFT and QM we need to know a little about these self-energy functions. To proceed it is useful to consider analytical properties of propagator.

4.1 Källén-Lehmann representation

Analyticity: It can be demonstrated, with very general hypothesis that propagator satisfies a Källén-Lehmann representation ⁷⁾, which is written, in Fourier space, as

$$\Delta(z) = \int_0^{\infty} dk^2 \frac{\rho(k^2)}{k^2 - z}, \quad (21)$$

where, eventually, z gets close to the cut on the real axis by staying in the physical upper half-plane $z \rightarrow (p^2 + i\varepsilon)$, $p^2 \in R$. A consequence is that the propagator $\Delta(z)$ is an holomorphic function in the complex z plane outside the cuts.

Positivity: The spectral function $\rho(k^2)$ is a positive hermitian matrix. A consequence is that the propagator $\Delta(z)$ in the complex z plane outside the cuts satisfies 7)

$$\Delta(z) = [\Delta(\bar{z})]^\dagger. \quad (22)$$

Indeed, one can write, using the hermiticity of ρ

$$\Delta(\bar{z}) = \int_0^\infty dk^2 \frac{\rho(k^2)}{k^2 - \bar{z}}, [\Delta(\bar{z})]^\dagger = \int_0^\infty dk^2 \left[\frac{\rho(k^2)}{k^2 - \bar{z}} \right]^\dagger = \int_0^\infty dk^2 \frac{\rho^\dagger(k^2)}{k^2 - z}. \quad (23)$$

This general property should be distinguished from the (Schwarz) reflection principle or its refined version called the “edge of the wedge” theorem 7); indeed, as soon as complex coupling constants can enter the game, in particular to account for CP violation, the discontinuity on the cut is no longer the sole origin for the imaginary part of the propagator; it can be non-vanishing outside the cut, which is likely to invalidate the principle of reflection.

In QFT , the physical masses are the poles of propagator $\Delta(z)$, i.e.

$$Mass \ states \Leftrightarrow Det(\Delta^{-1}(q^2)) = 0. \quad (24)$$

Thus for binary system of K -mesons we have two complex poles

$$z_1 = M_L^2, \quad z_2 = M_S^2. \quad (25)$$

4.2 Introducing a mass matrix: from QFT to QM

Here we demonstrate how the effective mass matrix that describes unstable particles can be derived from propagator. This matrix automatically respects the positivity and analyticity properties of the propagator.

In QFT , the physical masses are the poles of propagator $\Delta(z)$ or the zeroes of inverse propagator $\Delta^{-1}(z)$. Thus close to the poles, a linear approximation for Δ^{-1} should be suitable,

$$\Delta^{-1}(z) \approx Az + B, \quad (26)$$

where A and B are some constant matrices.

From the positivity of the propagator one can derive that $A = A^\dagger$ is a positive hermitian matrix. If the property of positivity is true everywhere then

$B = B^\dagger$. In this case, the mass matrix is hermitian, its eigenvalues are real and cannot describe unstable particles. However, if one only wants to preserve this property in the upper (physical) half plane $\Im(z) \geq 0$, it is enough to have $\Im(B) \geq 0$. If this is so, then, writing $B = B_1 + iB_2, B_2 \geq 0$, one has

$$\Delta^{-1}(z) \approx \sqrt{A} \left(z + \frac{1}{\sqrt{A}} (B_1 + iB_2) \frac{1}{\sqrt{A}} \right) \sqrt{A} = \sqrt{A} \left(z - \left(M^{(2)} \right) \right) \sqrt{A}. \quad (27)$$

To find the mass of the state we have to diagonalize matrix $M^{(2)}$. Thus matrix $M^{(2)}$ plays a role of a mass matrix. More accurately

$$M^{(2)} \equiv \left(M - \frac{i}{2} \Gamma \right)^2. \quad (28)$$

Thus mass matrix $M^{(2)}$ is defined in terms of propagator's matrices A and B

$$M^{(2)} \equiv m^{(2)} - i \frac{\Gamma^{(2)}}{2} = -\frac{1}{\sqrt{A}} (B_1 + iB_2) \frac{1}{\sqrt{A}}, \text{ with } \Gamma^{(2)} \geq 0, A = A^\dagger. \quad (29)$$

It is no longer hermitian and can describe unstable kaons. Since $\Gamma^{(2)} \geq 0$, the zeroes of the approximate inverse propagator (poles of the approximate propagator) are located in the lower (unphysical) half plane. The hermitian matrix A normalizes the states.

Near any given pole z_i of the propagator we get some new mass matrix M_i . In other words for any given state we construct a new Effective Hamiltonian. Thus according to *QFT* in the case of binary system like (K^0, \bar{K}^0) we have to introduce two different effective Hamiltonians - one for K_S and another for K_L .

4.3 (K^0, \bar{K}^0) in QFT.

Consider this construction in more details. For any momenta $z = q^2$ the propagator $\Delta(z)$ has two eigenvalues $\lambda_\pm(z)$ and four eigenvectors, i.e. two (in) states $|R_\pm(z)\rangle$ and two (out) states $\langle L_\pm(z)|$. The same is true for the momenta near the pole $z_1 = M_L^2$. It is clear that one of the eigenvalues of $\Delta^{-1}(z_1)$ has to be zero. Corresponding eigenvectors are the physical states that describe K_L meson on-mass shell:

$$|R_+(z_1)\rangle = |K_L\rangle_{in}, \quad \langle L_+(z_1)| = \langle K_L|_{out}. \quad (30)$$

Another eigenvalue of $\Delta^{-1}(z_1)$ is $2M_L^2$. Corresponding eigenvectors $|R_-(z_1)\rangle$ and $\langle L_-(z_1)|$ are non-physical spurious states, i.e they do not correspond to

propagation of any particle on-mass shell. One can check that these states have zero norm.

Similar situation takes place for the momenta near the pole $z_2 = M_S^2$. Thus we get four on-mass shell states vs four spurious states. One can not delete spurious states since they make the system of eigenvectors complete.

It is also clear that since we have different Hamiltonians for K_L and K_S the mixing parameters of eigenstates for two different Hamiltonians are also different. Thus CPT symmetry of fundamental QFT does not entail that CP parameter ϵ_L of K_L is identical to the one ϵ_S of K_S . That means that for CPT invariant theory

$$|K_S \rangle_{in} \sim (|K_1^0 \rangle + \epsilon_S^{in} |K_2^0 \rangle), \quad |K_L \rangle_{in} \sim (|K_2^0 \rangle + \epsilon_L^{in} |K_1^0 \rangle). \quad (31)$$

and

$$\epsilon_L^{in} \neq \epsilon_S^{in} \quad (32)$$

This conclusion is in a sharp contrast with QM treatment of K mesons where CPT symmetry and equality $\epsilon_L = \epsilon_S$ are just the same statement! In the next section we shall check whether this difference in formalism exhibits in physical observables.

5 "Applications"

The standard way to test CPT symmetry is to measure semi-leptonic asymmetries $\delta_{L,S}$ and A_{TCP} (see ⁴⁾):

$$\delta_{L,S} = \frac{|\langle \pi^- l^+ \nu | K_{L,S} \rangle|^2 - |\langle \pi^+ l^- \nu | K_{L,S} \rangle|^2}{|\langle \pi^- l^+ \nu | K_{L,S} \rangle|^2 + |\langle \pi^+ l^- \nu | K_{L,S} \rangle|^2}; \quad (33)$$

and

$$A_{TCP} = \frac{|\langle \pi^- l^+ \nu | \bar{K} \rangle|^2 - |\langle \pi^+ l^- \nu | K \rangle|^2}{|\langle \pi^- l^+ \nu | \bar{K} \rangle|^2 + |\langle \pi^+ l^- \nu | K \rangle|^2}. \quad (34)$$

In the Standard Model A_{TCP} can be also rewritten as

$$A_{TCP} = \frac{|\langle \bar{K}(t_f) | \bar{K}(t_i) \rangle|^2 - |\langle K(t_f) | K(t_i) \rangle|^2}{|\langle \bar{K}(t_f) | \bar{K}(t_i) \rangle|^2 + |\langle K(t_f) | K(t_i) \rangle|^2}. \quad (35)$$

According to PDG booklet ⁴⁾ these two asymmetries are related to the difference of mixing parameters $\epsilon_{S,L}$:

$$A_{TCP} = \delta_S - \delta_L \simeq 2\Re(\epsilon_S - \epsilon_L) \quad (36)$$

Explicit perturbative calculation within our formalism gives

$$\delta_S = 2\Re(\epsilon_S^{in}), \delta_L = 2\Re(\epsilon_L^{in}). \quad (37)$$

Thus

$$\delta_S - \delta_L = 2\Re(\epsilon_S - \epsilon_L) \neq 0 \quad (38)$$

for *CPT* symmetric theory!

The calculation of A_{TCP} is slightly more subtle exercise (see ¹⁾). We find that to construct correct perturbation theory for effective Hamiltonian one has to take into account spurious states. The contribution of these spurious states into A_{TCP} exactly cancel the contribution of physical states. As a result,

$$A_{TCP} = 0 \neq \delta_S - \delta_L \quad (39)$$

for *CPT* symmetric theories. Thus A_{TCP} is a good test of *CPT* violation.

6 Numerical estimates

In spite of conventional *QM* treatment of (K, \bar{K}) system mixing parameters for K_L and K_S states are different even for *CPT* symmetric theory. Now we perform order of magnitude estimate of this difference $\epsilon_S^{in} - \epsilon_L^{in}$.

To do that we need to know the dependence of (K, \bar{K}) self-energy functions on momenta. The main contribution comes from $K \leftrightarrow \bar{K}$ transition amplitude that takes place in the second order in weak interactions. To estimate the order of magnitude of the effect we calculate quark box diagram for $K \leftrightarrow \bar{K}$ transition. Inspecting this diagram we find ¹⁾

$$\epsilon_S^{in} - \epsilon_L^{in} \sim \epsilon \frac{\Delta m_{L,S}}{m_K} \sim 10^{-17}. \quad (40)$$

This effect is extremely small compared with the current experimental bounds on *CPT* violation (see ^{4, 9, 10}).

As for theoretical estimates of expected *CPT* violation effects they extend from the order of unity to zero. At this conference Dolgov presented arguments that spin-statistics relation is different for neutrino. That will immediately break *CPT* symmetry by order of unity. To observe such violation of *CPT* one can safely use conventional formalism from ⁴).

On the other hand if we believe in conventional field theory the only source of *CPT* violation comes from non-locality of *QFT* due to effects of gravity at small distances. This non-locality of *QFT* should be very small due to Plank mass in the denominator. At best they are of the order $\sim m_W/m_{Pl} \sim 10^{-17}$. If one dreams to measure such effect one needs our formalism with all tiny corrections in order to separate genuine *CPT* violation effects from the fake ones.

7 Conclusions

Let me summarize the results.

There is substantial difference between QM and QFT in treatment of binary systems. We find that correct formalism for (K, \bar{K}) system imitates the effects that can be considered as CPT violation in conventional formalism. Thus one has to remember that

1) QM is not appropriate framework for CPT violation if effects are small;

2) Asymmetry $\delta_L - \delta_S$ tests the difference $\epsilon_L - \epsilon_S$, not CPT violation;

3) Asymmetry A_{TCP} measures CPT violation.

8 Acknowledgments

I would like to thank the organizers of La Thuile conference, particular Mario Greco, for their warm hospitality and for excellent conference.

References

1. B. Machet, V. Novikov, and M. Vysotsky, hep-ph/0407268, to appear in Int. J. Mod. Phys. A
2. M.Gell-Mann, A.Pais, Phys.Rev. **97**, 1387(1955), A. Pais, O. Piccioni, Phys.Rev. **100**, 1487(1955).
3. J.H. Christensen, J.W. Cronin, V.L. Fitch and R. Turlay, Phys. Rev. Lett. **13**, 138 (1964).
4. D. Kirkby and Y. Nir, Review of Particle Physics. Physics Letters **B 592**, chapter 12 (2004).
5. M. Blasone, A. Capolupo, O.Romei and G.Vitiello, Phys. Rev. **D63**, 125015 (2001).
6. M. Beuthe, Phys. Rept. **375**, 105-218 (2003), and references therein
7. R.F.Streater & A.S.Wightman: "PCT, spin and statistics, and all that", Mathematical Physics Monograph Series, Benjamin/Cumming Publishing Company, Inc, Advanced Book Program, Reading, Massachusetts (London - Amsterdam - Don Mills, Ontario - Sydney - Tokyo) 1964.
8. Ya.I. Azimov, JETP Lett. **58**, 159-162 (1993); Phys. Atom. Nucl. **59**, 856-863 (1996).

9. CPLEAR Collaboration, Nucl. Phys. Proc. Suppl. **93**, 276-282 (2001).
10. KLOE coll. (presented by C. Gatti) “Kaon semileptonic decays at KLOE”; Proc. of DAFNE 2004: Physics at meson factories, 7-11 June 2004, Frascati (Aug. 2004).
KLOE coll. (presented by T. Spadaro): “Recent results from KLOE at DAFNE”; Proc. of “Les Rencontres de Physique”, La Thuile 29-2/6-3 2004 (Aug. 2004).

SESSION V – CP VIOLATION AND RARE DECAYS

- *Marco S. Sozzi* Search for Direct CP Violation in Charged K Decays
- *Sasha Glazov* Klong in e-e-gamma
- *Thomas E. Latham* Unitary Triangle Angle Measurement at Babar
- *Rolf Dubitzky* Measurement of $|V_{ub}|$ and $|V_{cb}|$ at BaBar
- *Alan Schwartz* Angles of the CKM Unitarity Triangle Measured at BELLE
- *Isamu Nakamura* Sides of the Unitarity Triangle from BELLE
- *Stephanie Menzemer* B_s Oscillations and Prospects for Δm_s at the Tevatron
- *Eugenij Shabalin* How Large are CP Effects Produced by Different Mechanisms of CP Violation in $K^\pm \rightarrow 3\pi$ Decays
- *Amarjit Soni* CP Violation Highlights: Circa 2005

SEARCH FOR DIRECT CP VIOLATION IN CHARGED K DECAYS

Marco S. Sozzi *

Scuola Normale Superiore, Pisa, Italy

Abstract

The NA48/2 experiment at the CERN SPS collected an unprecedented statistics of charged Kaon decays with a unique double-beam technique, which allows high control of systematics, with the main goal of looking for direct CP violation asymmetries. A preliminary result is presented on the CP-violating Dalitz plot linear slope asymmetry in $K^\pm \rightarrow \pi^\pm \pi^+ \pi^-$ decays, which corresponds to a ten-fold improvement in accuracy with respect to previous measurements.

1 Introduction

More than 40 years after its discovery ¹⁾, the phenomenon of CP violation still eludes a deep understanding, and holds a central role on the present and future agenda of high-energy physics experimental investigations. After a long hiatus during which this elusive effect seemed to be confined to a rather peculiar sector of particle physics, two recent breakthroughs were the experimental evidences for direct CP violation in neutral kaons (*i.e.* ϵ'/ϵ , ²⁾ ³⁾ ⁴⁾), and the evidence for CP violation effects in B meson decays ⁵⁾. Direct CP violation, manifesting itself as an asymmetry in two CP-conjugate decay amplitudes (which was recently detected also for B mesons ⁶⁾), is the most “straightforward” manifestation of CP violation, and while its importance cannot be overestimated, as a strong qualitative test of the way the Standard Model accommodates CP violation (*i.e.* the CKM paradigm), its quantitative exploitation to constrain fundamental parameters of the theory has been hampered so far by theoretical difficulties in providing accurate predictions in terms of the underlying fundamental parameters, due to the complexity of the hadronic environment. Still, an intense theoretical program is under way to devise new approaches to improve such predictions, to ultimately allow the experimental direct CP measurements to be used also as strong quantitative constraints to the Standard Model; lattice QCD appears to be the most promising candidate for this program.

After a successful program of investigations with neutral kaons, which culminated with the proof of direct CP violation ³⁾, and after an experiment (NA48/1) devoted to the study of rare K_S decays, the NA48 collaboration undertook a high-statistics investigation of charged K decays (NA48/2), with the main purpose ⁷⁾ of looking for further CP violation effects, which for charged particles can only be of the direct type.

The relatively low mass of the K^\pm in the hadron spectrum results in a limited number of decay modes with large branching fractions; the most common ones which are expected to possibly support CP violation are the 3π modes: $\pi^\pm\pi^+\pi^-$ and $\pi^\pm\pi^0\pi^0$, with branching fractions 5.6% and 1.7% respectively. The interest in these decay modes surged from the observation that they do not share some of the intrinsic *a priori* suppression factors which make direct CP violation effects small for neutral kaons (*i.e.* $|\epsilon'| \simeq 4 \cdot 10^{-6}$).

It turns out, however, that explicit predictions for CP violating asymmetries in the Standard Model, while being quite uncertain, are usually very small; while this fact likely precludes present experiments from detecting such effects, it opens up a large window of opportunity for challenging the Standard Model itself.

The usual phenomenological description of $K \rightarrow 3\pi$ decays is made in

terms of the bi-dimensional Dalitz plot parameters ⁸⁾ u and v , related to the energy sharing to the “odd” pion (*i.e.* the one having opposite charge with respect to the two other ones), and among the two “even” pions respectively:

$$u = \frac{s_3 - s_0}{m_\pi^2} = 2m_K \frac{m_K/3 - E_3^*}{m_\pi^2} \quad v = \frac{s_2 - s_1}{m_\pi^2} = 2m_K \frac{E_1^* - E_2^*}{m_\pi^2}$$

where $s_i = (p_K - p_i)^2$, p_K being the four-momentum of the decaying kaon and p_i ($i = 1, 2, 3$) those of the pions (with index $i = 3$ for the odd one), and $s_0 = (s_1 + s_2 + s_3)/3$. After transforming to the kaon centre of mass frame, the pion centre of mass energies E_i^* appear. The matrix element is naively expanded as

$$|M|^2 \propto 1 + gu + hu^2 + kv^2 + \dots$$

where ⁸⁾:

$$g(\pi^\pm \pi^+ \pi^-) = -0.2154 \pm 0.0035 \quad g(\pi^\pm \pi^0 \pi^0) = 0.652 \pm 0.031$$

and $|h|, |k| \ll |g|$ imply smaller quadratic terms. While other results from NA48/2 show that this simple parameterization around the centre of the Dalitz plot is not entirely adequate to describe the physics, it is the conventional one adopted so far.

Among the possible CP asymmetries between K^+ and K^- are those of partial decay widths (*i.e.* $|M|^2$): these are very highly suppressed in any model for symmetry reasons, and therefore not very promising for experimental detection. The experimental measurement of such rate asymmetries would require a precise knowledge of the relative kaon fluxes for both charge signs. On the other hand, the measurement of differences among the above parameters describing the decay distributions is independent on flux and can be performed just by comparing the Dalitz plot *shapes*. The main goal of the NA48/2 experiment is to measure the slope asymmetries

$$A_g = \frac{g_+ - g_-}{g_+ + g_-}$$

with a precision of $2.2 \cdot 10^{-4}$ for the $\pi^\pm \pi^+ \pi^-$ decay mode and $3.5 \cdot 10^{-4}$ for $\pi^\pm \pi^0 \pi^0$.

The above figures require collecting very large samples, and therefore intense beams, large acceptance and data acquisition bandwidths; these have to be matched with a careful control of systematics, which requires novel experimental approaches.

The available experimental information on A_g is summarized in table 1, and some experimental predictions within the Standard Model and other models are shown in table 2 (where as usual some care must be taken with the

Table 1: Summary of experimental measurements on direct CP violating slope asymmetries in K^\pm decays.

Asymmetry	Events	Experiment
$A_g(\pi^\pm\pi^+\pi^-) = (-70 \pm 53) \cdot 10^{-4}$	3.2M	BNL AGS (1970) ⁹⁾
$A_g(\pi^\pm\pi^0\pi^0) = (19 \pm 125) \cdot 10^{-4}$	115K	CERN PS (1975) ¹⁰⁾
$A_g(\pi^\pm\pi^+\pi^-) = (22 \pm 15 \pm 37) \cdot 10^{-4}$	54M	HyperCP (2000) ¹¹⁾ prelim.
$A_g(\pi^\pm\pi^0\pi^0) = (2 \pm 19) \cdot 10^{-4}$	620K	Protvino IHEP (2005) ¹²⁾

quoted “theoretical” errors, and central values could admittedly vary by up to an order of magnitude). One can see that NA48/2 has a great potential for closing the wide gap between experiments and theory, reaching the interesting region in which one could detect enhancements due to physics beyond the Standard Model, which were out of reach with lower experimental accuracy. Theoretical estimates are difficult and not far from being exhaustive, particularly for what concerns specific extensions of the Standard Model.

Table 2: Some theoretical predictions for direct CP violating slope asymmetries in K^\pm decays.

Asymmetry	Model	Reference
$ A_g(\pi^\pm\pi^+\pi^-) \simeq 14 \cdot 10^{-4}$	SM	Bel’kov <i>et al.</i> (1989) ¹³⁾
$ A_g(\pi^\pm\pi^0\pi^0) \simeq 14 \cdot 10^{-4}$	SM	Bel’kov <i>et al.</i> (1989) ¹³⁾
$ A_g(\pi^\pm\pi^+\pi^-) \simeq (3.7 \pm 1.4) \cdot 10^{-4}$	SM, NLO	Bel’kov <i>et al.</i> (1993) ¹⁴⁾
$ A_g(\pi^\pm\pi^0\pi^0) \simeq (3.1 \pm 1.4) \cdot 10^{-4}$	SM, NLO	Bel’kov <i>et al.</i> (1993) ¹⁴⁾
$ A_g(\pi^\pm\pi^+\pi^-) \lesssim 0.45 \cdot 10^{-4}$	SM, NLO	D’Ambrosio <i>et al.</i> (1991) ¹⁵⁾
$ A_g(\pi^\pm\pi^+\pi^-) \sim 2 \cdot 10^{-4}$	3HD	Shabalin (1998) ¹⁸⁾
$ A_g(\pi^\pm\pi^+\pi^-) \lesssim (0.5 \pm 0.2) \cdot 10^{-4}$	SM, NLO	Shabalin (1993) ¹⁹⁾
$ A_g(\pi^\pm\pi^+\pi^-) \simeq (0.023 \pm 0.006) \cdot 10^{-4}$	SM, NLO	Maiani <i>et al.</i> (1995) ¹⁶⁾
$ A_g(\pi^\pm\pi^0\pi^0) \simeq (0.013 \pm 0.004) \cdot 10^{-4}$	SM, NLO	Maiani <i>et al.</i> (1995) ¹⁶⁾
$ A_g(\pi^\pm\pi^+\pi^-) \sim 10^{-5} \div 10^{-4}$	SUSY	D’Ambrosio <i>et al.</i> (2000) ¹⁷⁾
$A_g(\pi^\pm\pi^+\pi^-) \simeq (-0.24 \pm 0.12) \cdot 10^{-4}$	SM, NLO	Gamiz <i>et al.</i> (2003) ²³⁾
$A_g(\pi^\pm\pi^+\pi^-) \simeq (-0.42 \pm 0.08) \cdot 10^{-4}$	SM, NLO	Shabalin (2004) ²⁰⁾
$A_g(\pi^\pm\pi^+\pi^-) \simeq (-0.2 \div -0.8) \cdot 10^{-4}$	SM, NLO	Shabalin (2004) ²¹⁾
$A_g(\pi^\pm\pi^+\pi^-) \simeq 0.3 \cdot 10^{-4}$	SM, NLO	Shabalin (2005) ²²⁾
$A_g(\pi^\pm\pi^0\pi^0) \simeq 0.02 \cdot 10^{-4}$	SM, NLO	Shabalin (2005) ²²⁾

2 The NA48/2 experiment

The NA48/2 experiment largely exploits the existing NA48 detector and infrastructure, with some additional element and a completely new beam line, providing for the first time simultaneous and collinear K^+ and K^- beams.

A hadron beam is produced by 400 GeV/c protons from the SPS impinging on a beryllium target rod 40 cm long and 2 mm in diameter at zero degrees. The proton beam intensity is about $7 \cdot 10^{11}$ per pulse of 4.8 s duration. A first achromatic momentum selection stage collects charged particles of (60 ± 3) GeV/c momentum and both charge signs for further transmission. After being recombined, the two hadron beams, containing about $6.4 \cdot 10^7$ particles per pulse (12 times more pions than kaons), with a kaon charge ratio $K^+/K^- \sim 1.8$, pass through magnetic focusing and muon sweeping stages, before being again split in the vertical plane by a second achromatic set of magnetic dipoles (see fig. 1). At this stage the vertical positions of individual beam particles are measured by MICROMEGA detectors (KABES), thus allowing a 1% momentum measurement of the incoming kaons.

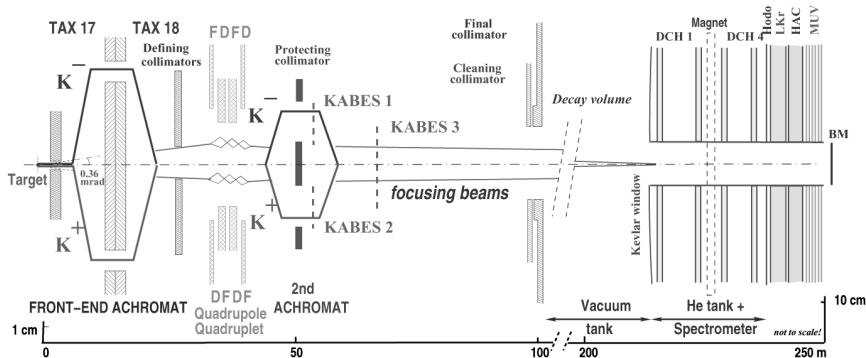


Figure 1: Sketch of the NA48/2 beam setup. Note that two beams are superimposed to within ~ 1 mm all along the decay region.

Both beams, whose transverse dimensions are about 5 mm RMS, are thereafter recombined along the experiment axis, and remain superimposed to within 1 mm while traveling through the ~ 114 m long vacuum decay region towards a focus point at the detector. The detector itself has a central hole for a vacuum pipe in which the undecayed charged particles of the beams keep traveling. Note that the decay products from charged pions in the beam, due to the limited transverse momentum available, are mostly confined to remain

within such pipe, without illuminating the detector itself.

The main part of the NA48 detector used for the measurement of the CP-violating asymmetry in $K^\pm \rightarrow \pi^\pm \pi^+ \pi^-$ decays is the magnetic spectrometer ²⁴⁾, composed of four large drift chambers and a dipole magnet (120 MeV/c horizontal magnetic kick) enclosed in a helium-filled tank. Each octagonal chamber has four double planes of sense wires with 1 cm spacing, aligned along four directions oriented at 45° with respect to each other. The momentum resolution is $\sigma(p)/p = 1.0\% \oplus 0.044\% p$ (p in GeV/c).

The trigger to select $K^\pm \rightarrow \pi^\pm \pi^+ \pi^-$ decays is a two-level one. At the first level a two-layer scintillator hodoscope provides a fast coincidence signal consistent with a minimum track multiplicity of two, and such signal starts a farm of fast processors ²⁵⁾ which performs track reconstruction based on three drift chambers' data. Events with at least two tracks consistent with being originated in the decay volume are kept, giving a rate of about 30K in 4.8 s. For part of the 2003 run and all of the 2004 run events which were not selected by the above condition were also kept if one track consistent with having originated in the decay volume was reconstructed and the missing mass (assuming it to be a charged pion originating from a 60 GeV/c nominal momentum kaon traveling along the beam axis) was incompatible with the kinematics of $K^\pm \rightarrow \pi^\pm \pi^0$ decay.

3 Principle of the measurement

The presence of the two oppositely charged beams, being spatially superimposed and present at the same time plays an important role in enforcing by design large cancellations of detector acceptance effects and response drifts on the measured asymmetries, therefore leading to robust cancellations of possible systematic errors.

The density of K^\pm events in the Dalitz plot is projected onto the u axis to obtain one-dimensional distributions $N^\pm(u)$. The ratio $R(u) = N^+(u)/N^-(u)$ of such distributions is to first order independent on the distortions induced by the variation of the detector acceptance over the Dalitz plot, and can be fit to a linear function $\bar{R}(1 + \Delta g u)$ to extract $\Delta g = g_+ - g_- = A_g 2g$ to sufficient accuracy.

Clearly, any instrumental effect has to be both charge-asymmetric and u -dependent, in order to potentially bias the measurement.

Charge-related beam and detector differences can induce spurious asymmetries, the most obvious one being that due to imperfect left-right detector symmetry when coupled with the lateral deflecting effect of the spectrometer dipole magnet. While the beam is carefully aligned along the detector axis, any unavoidable local imperfection of the spectrometer can introduce an acceptance asymmetry. This effect is canceled to first order by periodically reversing

(each day¹) the polarity of the spectrometer magnetic field, therefore effectively equalizing the time-averaged acceptance for K^+ and K^- .

The largest instrumental effect on the event density in the Dalitz plot occurs at large u values, where a steep drop in acceptance corresponds to the “odd” pion being lost into the central beam pipe hole for any spatial decay orientation. Similar cuts occurs at large $-(u \pm v)/2$ values, where one of the “even” pions is lost, but these are mapped onto wider u regions after projecting. The most critical region is therefore the high u edge, where any difference in the way the acceptance-defining central hole is seen by the two beams, due *e.g.* to an asymmetric relative mismatch between a beam axis, (which can drift by ~ 1 mm) and the detector axis, can directly induce a u asymmetry, which is moreover magnified by the large lever arm due to the distortion occurring at the edge of the distribution. For this reason software acceptance cuts are enforced, which are centered on the effective beam axis, independently for K^+ and K^- : the momentum-weighted average of the three tracks’ impact points at the first and last drift chambers are continuously monitored to high precision from the data, and all tracks are required to cross the first (last) drift chamber at a radial distance larger than 11.5 (13.5) cm from the average measured centre of the beam from which they originate. The larger cut at the last drift chamber accounts for the additional ~ 2 cm lateral displacement due to the magnetic deflection. On top of the tracking of the time-dependent variations of the beam axis’ positions, the coupling of such positions to the value of kaon momentum and their dependence on the spill extraction time, due to the residual chromaticity of the beam line, are also factored out. The above acceptance cuts are always larger than the physical dimensions of the beam pipe hole and properly symmetrize the acceptance without resorting to MonteCarlo simulation and correction. A conservative limit of $\delta(\Delta g) = 0.5 \cdot 10^{-4}$ on the residual systematic effects is set by studying the result sensitivity to different acceptance cuts.

The coupling of resolution effects to acceptance variations are minimized by using a definition of u in terms of the odd pion energy in the centre of mass frame, which has the best possible resolution in the critical region at large u .

The effects of small residual differences between the “upper” and “lower” beam paths in the achromats are canceled by periodically reversing (once per week) also all the magnetic fields along the beam lines, so that the paths of K^\pm are exchanged. Note that the rather large intensity difference for the positive and negative beams is irrelevant for the measurement; also, accidental rate effects affect both K^\pm events in the same way, since both beams are obtained simultaneously from the same target.

A complete independent data set (“supersample”) therefore corresponded usually to a two-week long data-taking period, comprises four K^+ and four K^-

¹During the 2004 data-taking period the period was reduced to a few hours.

samples with all combinations of beam-line and spectrometer magnet polarities. The actual ratio $R(u)$ to be fit is obtained as a quadruple ratio of K^+/K^- :

$$R(u) = R_{US}R_{UJ}R_{DS}R_{DJ} \simeq \bar{R}(1 + 4\Delta gu)$$

where the subscript $U(D)$ relates to the beam line magnets' polarities, denoting a sample in which K^+ travel along the upper (lower) beam path in the achromatic magnet sets, while the subscript $S(J)$ relates to the spectrometer magnet polarity, denoting a sample in which particles with the same charge as the beam from which they originate are deflected to the right (left) in the spectrometer (*i.e.* towards the Salève (Jura) mountains respectively).

The above ratio exploits several cancellations: beam line differences - by comparing K^+ and K^- traveling along the same paths, detector asymmetries - by comparing K^+ and K^- illuminating the detector in the same way, while global time-dependent effects are canceled by the simultaneous detection of K^+ and K^- events. The only residual effects which can induce a spurious asymmetry are therefore detector left-right asymmetries which vary in time on a time-scale shorter than that corresponding to a single magnet polarity configuration.

While the principle of the experiment is such that MonteCarlo simulation is not required nor used to correct the measurement, a detailed GEANT-based MonteCarlo program with full detector simulation, including time-varying local drift chamber inefficiency and alignment maps and beam line geometry variations, is used to check the sensitivity of the result to various systematic effects.

4 Data analysis

The experiment took data in 2003 (50 days) and 2004 (60 days), collecting the unprecedented sample of $\sim 4 \cdot 10^9$ $K^\pm \rightarrow \pi^\pm \pi^+ \pi^-$ decays, out of a total of about 200 TBytes of data written to tape.

Apart from the magnetic spectrometer and the scintillator hodoscope, no other sub-detector is involved in this analysis.

The spectrometer internal alignment was periodically calibrated by using data from special runs with no magnetic field, in which only beam halo muons are illuminating the detector Track reconstruction combines hit information from all four drift chambers, using the measured magnetic field maps scaled for the measured dipole magnet current, and correcting for the small magnetic fields due to the vacuum tank magnetization and the Earth's field, which were measured before the run.

The vertex-constrained track parameters are used to compute the three-pion invariant mass with a resolution of about $1.7 \text{ MeV}/c^2$. Small non-Gaussian invariant mass tails arise from kink tracks in which a charged pion decayed; in

order to avoid introducing potential instrumental asymmetries from other sub-detectors, no muon rejection is applied, which is possible because background is entirely negligible. The charge symmetry of the muon decay invariant mass tails has been tested with MonteCarlo to a level corresponding to $\delta(\Delta g) = 0.4 \cdot 10^{-4}$.

A fine control on the spectrometer internal alignment is obtained by continuously monitoring the difference in the reconstructed three-pion invariant masses for K^+ and K^- (equal by CPT), which can be induced by a residual horizontal misalignment between chambers before and after the spectrometer magnet, at the level of $\sim 1.5 \text{ keV}/\mu\text{m}$. Tiny relative drifts of the drift chambers' positions, as small as a few μm per day up to $200 \mu\text{m}$ were detected in this way, and the reconstructed momenta were corrected accordingly as $p \rightarrow p(1 + \beta qp)$, where p is the measured track momentum (in GeV/c), q its charge sign and β a parameter of order 10^{-5} GeV^{-1} related to the measured mass difference for positive and negative events.

While each spectrometer magnetic field reversal was preceded by a full degaussing procedure, the reproducibility of the absolute magnitude of the field integral, and its equality for both polarities, can be controlled online only to within $\sim 10^{-3}$. Effects induced by smaller magnitude differences are canceled by the fact that geometric acceptance cuts were defined with respect to the average beam positions (both before and after magnetic deflection) and by a continuous momentum recalibration procedure which constrains the reconstructed three-pion invariant masses to its nominal (PDG) value with $\sim 10^{-5}$ precision. This recalibration affects both K^\pm events which are collected at the same time.

The trigger as a potential source of bias due to charge-asymmetric inefficiencies is studied directly from the data, by using downscaled control samples collected with alternative trigger conditions uncorrelated to the elements under scrutiny. Only those parts of the inefficiencies which are correlated to spatial positions are potentially dangerous, since rate-dependent effects cancel due to the simultaneous beam scheme. The first level trigger inefficiency is measured to be small, $\sim 7 \cdot 10^{-4}$, charge-symmetric and flat in u to good accuracy and constant in time, leading to no correction and an uncertainty of $\delta(\Delta g) = 0.4 \cdot 10^{-4}$ reflecting the statistical size of the control sample. For the second level trigger (online track/vertex reconstruction) inefficiencies are larger (0.2 to 1.8%) and do change in time, being largely related to drift chambers' wire inefficiencies, to which the online reconstruction is more sensitive. While no statistically significant charge asymmetry or u dependence of the asymmetry was measured, the size of the collected control sample is not sufficient to exclude such effects to a high precision, so that a conservative approach is adopted by correcting each sample by the measured u -dependent trigger efficiencies, and therefore introducing a significant error due to the statistical power of the above sample. This turns out to be the largest systematic uncertainty at this stage of the analysis, although it could be reduced by further study.

Other possible sources of bias were studied, such as the dependence on the u computation or the fitting limits ($-1 \leq u \leq 1$ for this result), the effects due to the uncertainty on the knowledge of the stray magnetic fields, pile-up effects, inhomogeneities in the spectrometer misalignment, the accuracy of time-tracking of various changes in the beam geometry and those due to charge-asymmetric pion interactions. All contributions to the systematic uncertainty are summarized in table 3.

Table 3: Summary of systematic uncertainties on $\Delta g = A_g 2g$ in units of 10^{-4} .

Acceptance, beam geometry	0.5
Spectrometer alignment	0.1
Spectrometer magnet	0.1
Pion decay	0.4
u computation and fitting	0.5
Accidental activity	0.3
Total systematic uncertainty	0.9
Trigger efficiency: level 1	0.4
Trigger efficiency: level 2	0.8
Total trigger uncertainty	0.9
Total systematic error	1.3

5 Preliminary result

The final 2003 sample of $K^\pm \rightarrow \pi^\pm \pi^+ \pi^-$ after all cuts contains $1.6 \cdot 10^9$ events. The preliminary result is obtained as the average of three independent analysis, all of them giving consistent results. The results for each of the four super-samples of 2003 are averaged after trigger efficiency corrections; the results from all four super-samples are statistically consistent with each other ($\chi^2/\text{ndf} = 3.2/3$), as shown in figure 2.

The result stability was checked with respect to several variables, such as kaon energy and decay position, without finding any significant dependence (see fig. 3).

Null checks were performed by building ratios of events of the same charge, which are deflected in opposite directions in the spectrometer magnet or which are distinguished only by the upper or lower path of kaons along the beam line; any asymmetry in such ratios just reflects instrumental biases coupled to time variations. Such effects are seen to be at the 10^{-4} level and are fully

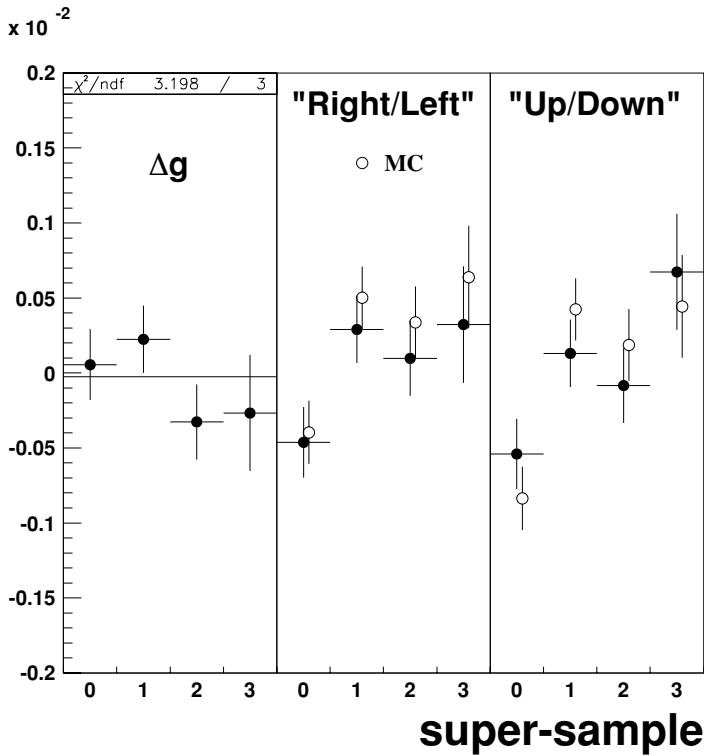


Figure 2: Stability of the preliminary result (in terms of Δg) and of null asymmetries as a function of supersample.

reproduced by the MonteCarlo simulation as due to the time variation of the detector inefficiencies and beam optics (see fig. 2).

The preliminary result from the 2003 data for the asymmetry $A_g = \Delta g 2g$ (using the average PDG ⁸⁾ value for the slope parameter g) is:

$$A_g = (0.5 \pm 2.4_{\text{stat}} \pm 2.1_{\text{stat(trig)}} \pm 2.1_{\text{syst}}) \cdot 10^{-4} = (0.5 \pm 3.8) \cdot 10^{-4}$$

This result is consistent with no CP violation, and its precision is one order of magnitude better than earlier measurements. The systematic uncertainty can be reduced with further studies and using more data.

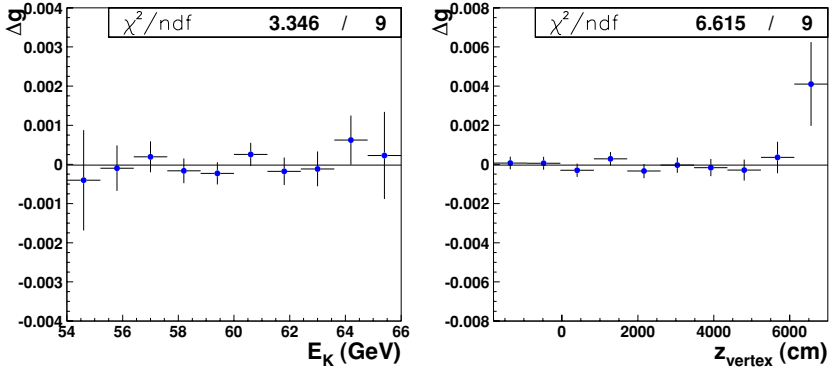


Figure 3: The linear slope difference Δg as a function of kaon energy (left) and of longitudinal decay vertex position (right).

6 Further prospects

The 2004 data, which is presently being analyzed, contains more data than the 2003 one, of higher quality, so that the control of some systematic uncertainties is expected to be better, and the proposal goal seems within reach.

Other interesting possibilities being investigated to enhance the quality of the result include the use of the beam spectrometer information as an additional tool for systematic checks, and possibly as a means of allowing the measurement of the slope asymmetry also for events in which one of the pions is outside the detector acceptance, by using the measured K momentum and direction to close kinematically the event: such sample, likely affected by different systematic effects, would be significantly larger and with a different u spectrum, therefore being interesting as an alternative measurement.

NA48/2 also collected a large sample of $K^\pm \rightarrow \pi^\pm \pi^0 \pi^0$ decays (about $2 \cdot 10^8$ in total), from which a measurement of the corresponding slope asymmetry will be extracted. Despite the lower branching ratio and acceptance for this mode, its larger Dalitz plot slope compensates, leading to a comparable statistical uncertainty on the slope asymmetry (*e.g.* $\sim 2.2 \cdot 10^{-4}$ for $28 \cdot 10^6$ events in a sub-sample of 2003 data). Systematic uncertainties will be different in this case, but it is interesting to notice that for this decay the asymmetry can be computed using practically only information from the electro-magnetic calorimeter, therefore leading to a rather complementary CP-violation mea-

surement.

The slope asymmetries for the two 3π decay modes are expected to be strongly correlated in any given model (albeit such correlation is also affected by theoretical uncertainties), and the measurement of both would allow to constrain better the underlying parameters.

References

1. J.H. Christenson *et al.*, Phys. Rev. Lett. **13** (1964) 138.
2. G. Barr *et al.* (NA31), Phys. Lett. B **317** (1993) 233.
3. V. Fanti *et al.* (NA48), Phys. Lett. B **465** (1999) 335.
A. Lai *et al.* (NA48), Eur. Phys. J. C **22** (2001) 231.
J.R. Batley *et al.* (NA48), Phys. Lett. B **544** (2002), 97.
4. A. Alavi-Harati *et al.* (KTeV), Phys. Rev. Lett. **83** (1999) 22.
A. Alavi-Harati *et al.* (KTeV), Phys. Rev. D **67** (2003) 012005.
Erratum: Phys. Rev. D **70** (2004) 079904.
5. B. Aubert *et al.* (BABAR), Phys. Rev. Lett. **87** (2001) 091801.
K. Abe *et al.* (BELLE), Phys. Rev. Lett. **87** (2001) 091802.
6. K. Abe *et al.* (BELLE), Phys. Rev. Lett. **93** (2004) 021601.
B. Aubert *et al.* (BABAR), Phys. Rev. Lett. **93** (2004) 131801.
7. R. Batley *et al.* (NA48/2), Addendum III to Proposal P253, CERN/SPSC 2000-003, CERN, January 2000.
8. S. Eidelman *et al.* (Particle Data Group), Phys. Lett. B **592** (2004) 1.
9. W.T. Ford *et al.*, Phys. Rev. Lett. **25** (1970) 1370.
10. K.M. Smith *et al.*, Nucl. Phys. B **91** (1975) 45.
11. W-S. Choong, Ph.D. thesis, Berkeley (2000) LBNL-47014.
12. G.A. Akopdzhanov *et al.*, Eur. Phys. J. C **40** (2005) 343.
13. A.A. Bel'kov *et al.*, Phys. Lett. B **232** (1989) 118.
A.A. Bel'kov *et al.*, Int. J. Mod. Phys. A **7** (1992) 4757.
14. A.A. Bel'kov *et al.*, Phys. Lett. B **300** (1993) 283.
15. G. D'Ambrosio *et al.*, Phys. Lett. B **273** (1991) 497.
16. L. Maiani *et al.*, The Second DAΦNE Physics Handbook, Vol. I (1995), 51.

17. G. D'Ambrosio *et al.*, Phys. Lett. B **480** (2000) 164.
18. E.P. Shabalin, ITEP preprint 8-98 (1998).
19. E.P. Shabalin, Nucl. Phys. B **409** (1993) 87.
20. E.P. Shabalin, Proc. Les Rencontres de Physique de la Vallee d'Aoste, La Thuile (Italy), 2003, p. 417; preprint [hep-ph/0305320](#).
21. E.P. Shabalin, Phys.Atom.Nucl. 68 (2005) 88.
22. E.P. Shabalin *et al.*, preprint [hep-ph/0503241](#), and these proceedings.
23. E. Gámiz *et al.*, JHEP **0310** (2003) 042.
24. D. Bédérède *et al.*, Nucl. Instr. Meth. A **367** (1995) 88.
25. S. Anvar *et al.*, Nucl. Instr. Meth. A **419** (1998) 686.

KLONG IN e-e-gamma

Sasha Glazov

University of Chicago / DESY

Written contribution not received

**UNITARITY TRIANGLE ANGLE MEASUREMENTS AT
*BABAR***

Thomas E. Latham
(representing the *BABAR* Collaboration)
*Department of Physics, University of Warwick,
Coventry, CV4 7AL, United Kingdom*

Abstract

We present recent results of measurements of the Unitarity Triangle angles α , β and γ made with the *BABAR* detector at the PEP-II asymmetric *B* Factory.

1 Introduction

The measurements of the angles α , β and γ of the Unitarity Triangle at the *BABAR* and Belle experiments are providing precision tests of the description of *CP* violation in the Standard Model (SM). This description is provided by the Cabibbo-Kobayashi-Maskawa (CKM) quark-mixing matrix ¹⁾, which relates the weak and flavour eigenstates of the quarks in the weak Lagrangian

$$\mathcal{L}_{CC} = -\frac{g}{\sqrt{2}} (\bar{u}_L, \bar{c}_L, \bar{t}_L) \gamma^\mu V_{\text{CKM}} \begin{pmatrix} d_L \\ s_L \\ b_L \end{pmatrix} W_\mu^\dagger + \text{h.c.} \quad (1)$$

where

$$\begin{aligned} V_{\text{CKM}} &\equiv \begin{pmatrix} V_{ud} & V_{us} & V_{ub} \\ V_{cd} & V_{cs} & V_{cb} \\ V_{td} & V_{ts} & V_{tb} \end{pmatrix} \\ &\approx \begin{pmatrix} 1 - \frac{\lambda^2}{2} & \lambda & A\lambda^3(\rho - i\eta) \\ -\lambda & 1 - \frac{\lambda^2}{2} & A\lambda^2 \\ A\lambda^3(1 - \rho - i\eta) & -A\lambda^2 & 1 \end{pmatrix} + \mathcal{O}(\lambda^4) \end{aligned} \quad (2)$$

is the 3×3 CKM matrix shown here in the Wolfenstein parameterisation ²⁾. The imaginary coefficient η is the source of *CP* violation.

The CKM matrix is a unitary matrix and using this condition one can write down several relationships of the following form

$$\sum_i V_{ij} V_{ik}^* = 0 \quad (j \neq k). \quad (3)$$

There are six such equations, each of which represents a triangle in the complex plane. One of these has sides of similar magnitude and also contains some of the least well constrained CKM matrix elements:

$$V_{ud}V_{ub}^* + V_{cd}V_{cb}^* + V_{td}V_{tb}^* = 0. \quad (4)$$

The triangle, rescaled by $\frac{1}{V_{cd}V_{cb}^*}$, is illustrated in fig. 1. The internal angles of the triangle are given by

$$\alpha \equiv \arg \left[-\frac{V_{td}V_{tb}^*}{V_{ud}V_{ub}^*} \right], \quad \beta \equiv \arg \left[-\frac{V_{cd}V_{cb}^*}{V_{td}V_{tb}^*} \right], \quad \gamma \equiv \arg \left[-\frac{V_{ud}V_{ub}^*}{V_{cd}V_{cb}^*} \right]. \quad (5)$$

This paper will review recent measurements of these CKM angles from the *BABAR* collaboration. The *BABAR* detector and the PEP-II accelerator are described in detail elsewhere ^{3, 4)}.

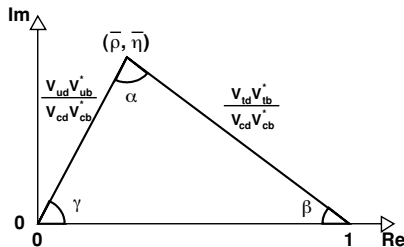


Figure 1: The Unitarity Triangle.

2 Measurements relating to β

The primary goal of the *BABAR* experiment was to measure $\sin 2\beta$ in the so called “golden modes” that proceed via the decay $b \rightarrow c\bar{c}s$, such as $B^0 \rightarrow J/\psi K_S^0$. These channels are considered golden since they are not too challenging experimentally and are theoretically clean due to the presence of only one weak phase. The latest *BABAR* measurement using a data sample of 227 million $B\bar{B}$ pairs is: $\sin 2\beta = 0.722 \pm 0.040 \pm 0.023$ ⁵⁾. Measuring $\sin 2\beta$ results in a four-fold ambiguity on β itself but one of the four solutions is in excellent agreement with the predictions of the Standard Model based on experimental knowledge of other parameters, as can be seen from fig. 2.

2.1 Measurement of the sign of $\cos 2\beta$

In order to properly test the Standard Model it is important to reduce the ambiguity on the measurement of β . The existing four-fold ambiguity can be reduced to two-fold by determining the sign of $\cos 2\beta$ ⁶⁾.

The decay $B \rightarrow J/\psi K^*$ has a dependence on $\cos 2\beta$ due to the interference of the one CP -odd and two CP -even components. This dependence appears in the time-dependent angular distributions in the observables:

$$\cos(\delta_{\parallel} - \delta_{\perp}) \cdot \cos 2\beta, \quad \cos(\delta_{\perp} - \delta_0) \cdot \cos 2\beta \quad (6)$$

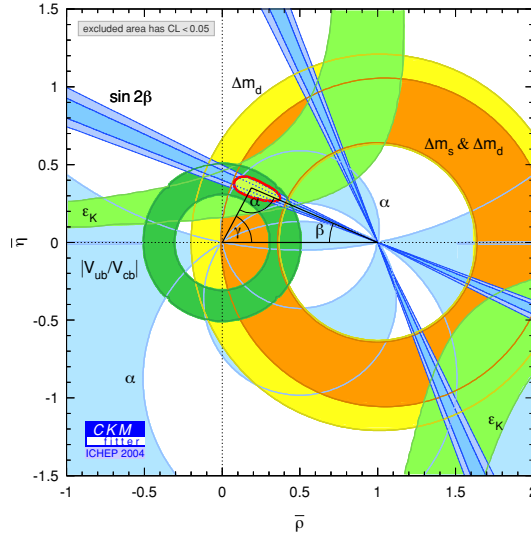


Figure 2: The $\bar{\rho} - \bar{\eta}$ plane showing the various constraints on the Unitarity Triangle.

where δ_i are the strong phases of the decay amplitudes:

$$A_i = |A_i|e^{i\delta_i}. \tag{7}$$

Using samples of both neutral and charged decays it is possible to measure these strong phases up to a two-fold ambiguity:

$$(\delta_{\parallel} - \delta_0, \delta_{\perp} - \delta_0) \Leftrightarrow (-(\delta_{\parallel} - \delta_0), \pi - (\delta_{\perp} - \delta_0)). \tag{8}$$

Under this transformation $\cos(\delta_{\parallel} - \delta_{\perp})$ and $\cos(\delta_{\perp} - \delta_0)$ change sign and so the two sets of parameters:

$$(\delta_{\parallel} - \delta_0, \delta_{\perp} - \delta_0, \cos 2\beta) \Leftrightarrow (-(\delta_{\parallel} - \delta_0), \pi - (\delta_{\perp} - \delta_0), -\cos 2\beta) \tag{9}$$

are equivalent, meaning that the sign of $\cos 2\beta$ is still ambiguous.

However, it is known from previous experiments that the $K^*(892)$ is not the only contribution in this region of $K\pi$ mass and that a broad S-wave is also present ⁷⁾. This additional contribution also has an associated strong

phase, δ_S , and so a new relative phase enters the problem: $\gamma = (\delta_S - \delta_0)$. The ambiguity of eq. (8) now becomes:

$$(\delta_{\parallel} - \delta_0, \delta_{\perp} - \delta_0, \gamma) \Leftrightarrow (-(\delta_{\parallel} - \delta_0), \pi - (\delta_{\perp} - \delta_0), -\gamma). \tag{10}$$

The ambiguity on γ can be broken however using Wigner’s causality principle ⁸⁾, which states that the phase of a resonance rotates anticlockwise with increasing mass. Since the phase of the S-wave is moving very slowly in the region of the $K^*(892)$ while the phase of the P-wave is moving very rapidly the relative phase γ must rotate clockwise. fig. 3 shows the behaviour of γ as a function of $K\pi$ mass for both solutions along with the data from the LASS experiment ⁷⁾, which shows remarkable agreement with the one solution that also obeys Wigner’s principle.

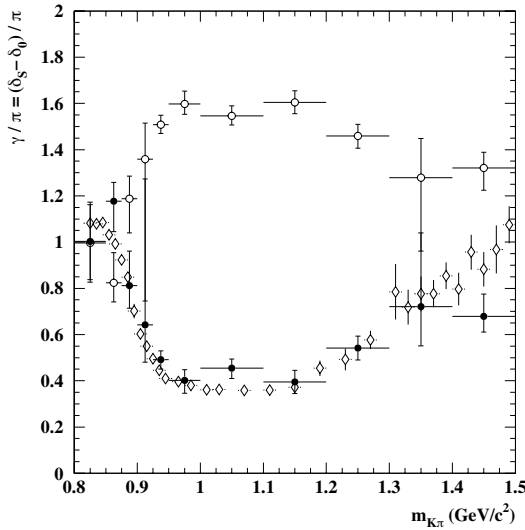


Figure 3: The relative phase γ as a function of $K\pi$ mass. The open circles are “Solution 1”, the filled circles are “Solution 2” and the open diamonds are the LASS data. A global offset of π has been added to the LASS data.

With the strong phase ambiguity broken a time-dependent fit can be performed to the $B^0 \rightarrow J/\psi K^{*0}(K_S^0\pi^0)$ data sample in order to extract $\cos 2\beta$

and $\sin 2\beta$. With $\sin 2\beta$ floating in the fit the results obtained are:

$$\begin{aligned}\cos 2\beta &= +3.32_{-0.96}^{+0.76} \pm 0.27 \\ \sin 2\beta &= -0.10 \pm 0.57 \pm 0.14.\end{aligned}\quad (11)$$

If $\sin 2\beta$ is fixed to the world average value of 0.731 we obtain:

$$\cos 2\beta = +2.72_{-0.79}^{+0.50} \pm 0.27. \quad (12)$$

If $\cos 2\beta$ and $\sin 2\beta$ are considered to be measuring the same angle β then $\cos 2\beta$ should be ± 0.68 . A toy Monte Carlo technique is used to determine which of these solutions is more likely. It is found that the positive solution is preferred at the 89% confidence level. The projection of the time dependent fit is shown in fig. 4. This analysis used a sample of 88 million $B\bar{B}$ pairs.

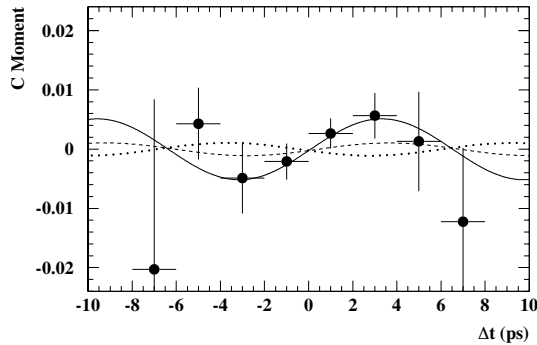


Figure 4: Moment of the function weighting the $\cos 2\beta$ contribution to the amplitude. The solid line is the result of the fit with both $\cos 2\beta$ and $\sin 2\beta$ floating. The dashed line corresponds to the preferred value $\cos 2\beta = +0.68$ and the dotted to $\cos 2\beta = -0.68$.

2.2 $\sin 2\beta$ from $b \rightarrow s\bar{s}s$ Penguin Modes

The time dependent CP asymmetry for a given B^0/\bar{B}^0 decay is given by:

$$\begin{aligned} A_{f_{CP}}(\Delta t) &= \frac{\Gamma(\bar{B}^0(\Delta t) \rightarrow f_{CP}) - \Gamma(B^0(\Delta t) \rightarrow f_{CP})}{\Gamma(\bar{B}^0(\Delta t) \rightarrow f_{CP}) + \Gamma(B^0(\Delta t) \rightarrow f_{CP})} \\ &= \eta_{f_{CP}} S_{f_{CP}} \sin(\Delta m_d \Delta t) - \eta_{f_{CP}} C_{f_{CP}} \cos(\Delta m_d \Delta t) \end{aligned} \quad (13)$$

where $\eta_{f_{CP}}$ is the CP eigenvalue of the final state f_{CP} , Δm_d is the mass difference between the two neutral B mass eigenstates and Δt is the time difference between the decays of the two B mesons. Measurements of the S coefficient of this CP asymmetry in decay channels dominated by $b \rightarrow s\bar{s}s$ ‘‘penguin diagrams’’ are expected to be equal to $\eta_{f_{CP}} \sin 2\beta$ where $\sin 2\beta$ is that measured in the $b \rightarrow c\bar{c}s$ decays. If the measured values are found to deviate then this could be an indication of new particles entering in the loop and contributing to the amplitude. However, care must be taken in the interpretation as small deviations are expected in some modes due to the presence of SM suppressed amplitudes with different weak and strong phases.

2.2.1 $B^0 \rightarrow \phi K_s^0$ and $B^0 \rightarrow \phi K_L^0$

This channel is the most theoretically clean of all the penguin modes in that it is expected to have no contribution from tree diagrams. This means that to very good approximation $C_{f_{CP}}$ should be zero and $S_{f_{CP}}$ should be $+\sin 2\beta$ for ϕK_s^0 and $-\sin 2\beta$ for ϕK_L^0 . From a data sample of 227 million $B\bar{B}$ pairs *BABAR* reconstructs $114 \pm 12 \phi K_s^0$ events and $98 \pm 18 \phi K_L^0$ events. Combining these samples in a time-dependent fit yields the following results ⁹⁾:

$$\begin{aligned} S_{\phi K^0} &= 0.50 \pm 0.25^{+0.07}_{-0.04} \\ C_{\phi K^0} &= 0.00 \pm 0.23 \pm 0.05 \end{aligned} \quad (14)$$

These results are in good agreement with the SM since C is zero and S is consistent with $\sin 2\beta$ within 1σ .

2.2.2 $B^0 \rightarrow K^+ K^- K_s^0$ excluding ϕK_s^0

The $B^0 \rightarrow K^+ K^- K_s^0$ Dalitz plot contains many more events than those simply due to ϕK_s^0 and so can reduce the statistical uncertainty on the measurement of $\sin 2\beta$ in these modes. However, there are possible contributions from other

amplitudes making it theoretically less clean. Additionally, the CP content of the final state is not known and must be determined. This is achieved using a moments analysis that takes advantage of the statistical technique known as $sPlot$ ¹⁰⁾. The S- and P-wave intensities are shown in fig. 5 along with the CP -even fraction, all as a function of K^+K^- mass. The average number obtained for the CP -even fraction was $0.89 \pm 0.08 \pm 0.06$ from the data sample of 227 million $B\bar{B}$ pairs. The time-dependent CP fit then yielded the following results⁹⁾:

$$\begin{aligned}
 S_{K^+K^-K_S^0} &= -0.42 \pm 0.17 \pm 0.03 \\
 C_{K^+K^-K_S^0} &= +0.10 \pm 0.14 \pm 0.04 \\
 \sin 2\beta_{\text{eff}} &= +0.55 \pm 0.22 \pm 0.04 \pm 0.11
 \end{aligned}
 \tag{15}$$

where the third error on $\sin 2\beta$ is due to the uncertainty in the CP -even content. As with the ϕK^0 results the central value of $\sin 2\beta$ is slightly lower than the SM value but agrees within errors. The C value is again zero within errors. The time-dependent asymmetries for this mode as well as ϕK_S^0 and ϕK_L^0 are shown in fig. 6.

2.2.3 $B^0 \rightarrow K_S^0 K_S^0 K_S^0$

This mode, like ϕK^0 , is very clean from a theoretical standpoint. It is also a pure CP -even state making the experimental determination simpler. An experimental complication is that there are no tracks originating from the primary vertex and as such the determination of the vertex separation (essential for a time-dependent analysis) was thought to be impossible. However, it was found in the *BABAR* analysis of $B^0 \rightarrow K_S^0 \pi^0$ that applying a beam-spot constraint allows successful vertexing with reasonable errors¹¹⁾. Firstly a branching fraction fit is performed that only uses kinematic and event topology variables and then a time-dependent CP fit is performed¹²⁾. The branching fraction fit yields 88 ± 10 signal events from a data sample of 227 million $B\bar{B}$ pairs, which gives the following branching fraction: $\mathcal{B}(B^0 \rightarrow K_S^0 K_S^0 K_S^0) = (6.9_{-0.8}^{+0.9} \pm 0.6) \times 10^{-6}$. The CP fit gives the following results:

$$\begin{aligned}
 S_{K_S^0 K_S^0 K_S^0} &= -0.71_{-0.32}^{+0.38} \pm 0.04 \\
 C_{K_S^0 K_S^0 K_S^0} &= -0.34_{-0.25}^{+0.28} \pm 0.05 \\
 \sin 2\beta_{\text{eff}} &= +0.79_{-0.36}^{+0.29} \pm 0.04
 \end{aligned}
 \tag{16}$$

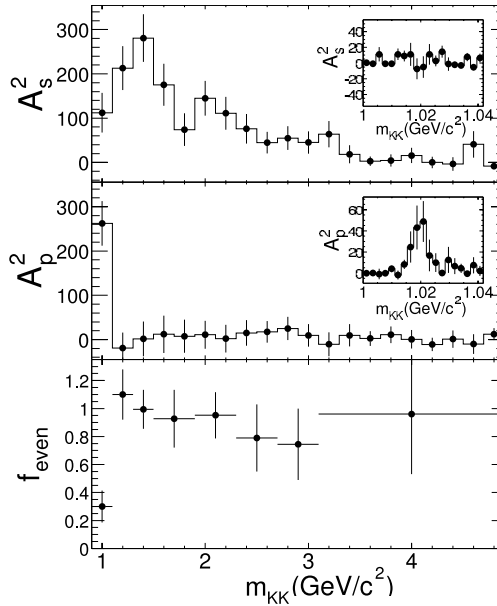


Figure 5: S- and P-wave intensities and CP -even fraction as a function of K^+K^- mass.

Again, these results are highly consistent with the SM value of $\sin 2\beta$. The distributions of Δt for B^0 and \bar{B}^0 tagged events are shown in fig. 7 along with the time-dependent asymmetry.

2.2.4 Summary of $\sin 2\beta$ from $b \rightarrow s\bar{s}$ Penguin Modes

The results presented above are all consistent with the value of $\sin 2\beta$ measured in the charmonium modes. However, there are measurements in the penguin modes that are not so consistent, shown in fig. 8, and the average of all the penguin modes differs from the average of the charmonium modes by 3.7σ . It must be emphasised, however, that the theoretical uncertainty on many of the modes is high, so large deviations may be possible within the Standard Model. More precise measurements of these modes, particularly the most clean modes such as ϕK^0 , are necessary before any conclusions can be drawn about the presence of New Physics.

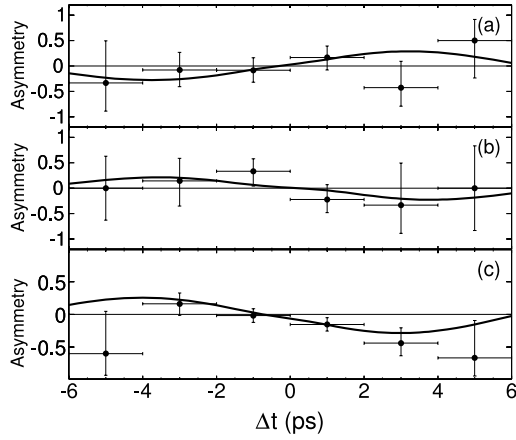


Figure 6: Time-dependent asymmetry distributions for (a) ϕK_S^0 , (b) ϕK_L^0 and (c) $K^+ K^- K_S^0$ excluding ϕK_S^0 . The signal to background ratio is enhanced by a cut on the likelihood ratio.

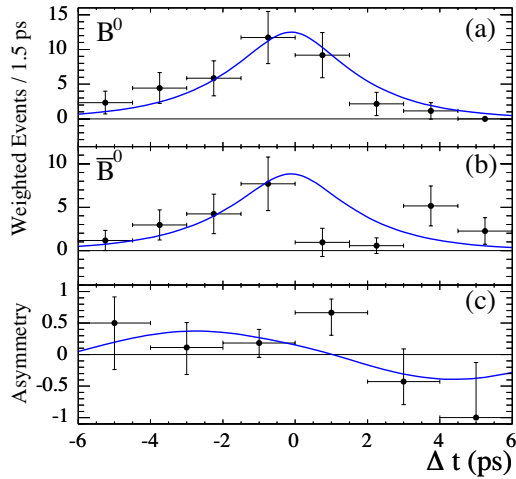


Figure 7: Time-dependent distributions for $B^0 \rightarrow K_S^0 K_S^0 K_S^0$.

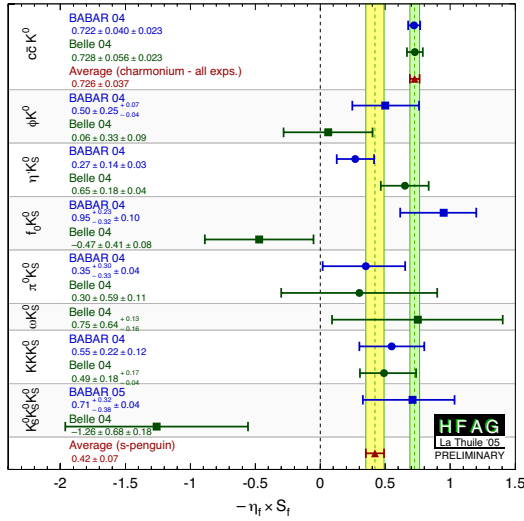


Figure 8: Comparison of $\sin 2\beta$ measured in charmonium and $b \rightarrow s\bar{s}s$ penguin modes

3 Measurements relating to α

The decays of neutral B mesons to the final states hh , where $h = \rho, \pi$, are sensitive to the CKM angle α in the interference between decay and mixing. The presence of penguin loop diagrams complicates the situation by introducing additional phases such that the measured parameter is $\alpha_{\text{eff}} = \alpha + \delta\alpha_{\text{penguin}}$. In terms of the time-dependent asymmetry defined in eq. (13) the coefficients are given by:

$$S_{hh} = \frac{2\text{Im}(\lambda_{hh})}{1 + |\lambda_{hh}|^2}, \quad C_{hh} = \frac{1 - |\lambda_{hh}|^2}{1 + |\lambda_{hh}|^2} \quad (17)$$

and λ_{hh} is given by:

$$\lambda_{hh} = \frac{q}{p} \frac{\bar{A}}{A} = e^{2i\alpha} \frac{1 - \frac{P}{T} e^{-i\alpha}}{1 - \frac{P}{T} e^{+i\alpha}} = |\lambda| e^{2i\alpha_{\text{eff}}} \quad (18)$$

where q and p are the B mixing coefficients and $\frac{P}{T}$ is the penguin to tree amplitude ratio, which can be different for $\pi\pi$, $\rho\pi$ and $\rho\rho$.

3.1 Isospin analysis in $B \rightarrow hh$

Taking the case of $B \rightarrow \pi\pi$ we can see how isospin symmetry can be employed to disentangle α from α_{eff} . The following relations can be formed relating the amplitudes for the decays of B^0 and \bar{B}^0 mesons to various $\pi\pi$ final states¹⁴):

$$\frac{1}{\sqrt{2}}A^{+-} = A^{+0} - A^{00}, \quad \frac{1}{\sqrt{2}}\bar{A}^{+-} = \bar{A}^{+0} - \bar{A}^{00} \quad (19)$$

By also noting that

$$|A^{+0}| = |\bar{A}^{+0}| \quad (20)$$

(in the absence of electroweak penguin diagrams) it can be seen that these decay amplitudes form two triangles with a common base in the complex plane as illustrated in fig. 9.

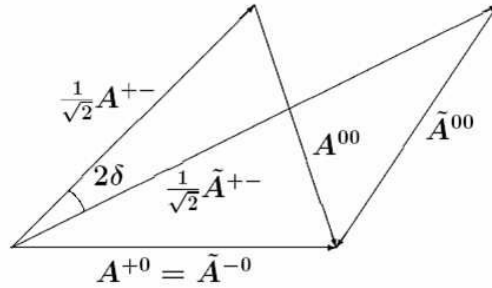


Figure 9: Illustration of the $B \rightarrow \pi\pi$ isospin triangles. $\delta = |\alpha - \alpha_{\text{eff}}|$.

For the modes $B \rightarrow \rho\rho$ there can be up to three such triangles depending on the angular structure of the decays and for $B \rightarrow \rho\pi$ a pentagon isospin analysis is required¹⁵) or a Dalitz plot analysis¹⁶).

3.2 $B \rightarrow \pi\pi$

As seen in the last section this is the simplest set of decay modes to study when attempting to measure α . The measurements of the various branching fractions and CP asymmetries are summarised in tab. 1, where S and C are the coefficients are defined in eq. (17) and \mathcal{A}_{CP} is the charge (tag) asymmetry in the case of a charged (neutral) B decay. All the measurements are sufficiently well

Table 1: Summary of BABAR measurements of $B \rightarrow \pi\pi$ decays.

Mode	$\mathcal{B} \times 10^{-6}$	S	C
$\pi^+\pi^-$	$4.7 \pm 0.6 \pm 0.2$	$-0.30 \pm 0.17 \pm 0.03$	$-0.09 \pm 0.15 \pm 0.04$
		\mathcal{A}_{CP}	
$\pi^\pm\pi^0$	$5.8 \pm 0.6 \pm 0.4$	$-0.01 \pm 0.10 \pm 0.02$	
$\pi^0\pi^0$	$1.17 \pm 0.32 \pm 0.10$	$-0.12 \pm 0.56 \pm 0.06$	

established to perform an isospin analysis. However, the value of $\mathcal{B}(B \rightarrow \pi^0\pi^0)$ is the limiting factor in this analysis. Its value is too large to allow a tight bound to be placed on $|\alpha - \alpha_{\text{eff}}|$ but it isn't sufficiently large to allow a precision measurement of this quantity with the current statistics. The limit that results from the current isospin analysis is: $|\alpha - \alpha_{\text{eff}}| < 35^\circ$ at 90% confidence level¹³⁾.

3.3 $B \rightarrow \rho\rho$

The analysis of $B \rightarrow \rho\rho$ is potentially highly complicated due to the fact that there are three possible helicity states for the decay. The helicity zero state, which corresponds to longitudinal polarisation of the decay, is CP -even but the helicity ± 1 states are not CP eigenstates. Fortunately this complication is avoided due to the experimental determination that the longitudinally polarised fraction f_L is dominant^{17, 18)}. This and other $\rho\rho$ measurements are summarised in tab. 2^{19, 20)}. The measurements of the branching fractions of $B \rightarrow \rho^\pm\rho^0$ and $B \rightarrow \rho^0\rho^0$ indicate that the penguin pollution is small in these modes compared with $B \rightarrow \pi\pi$. As such it is possible to perform an isospin analysis on the longitudinal part of the decay and to place a much tighter bound on $|\alpha - \alpha_{\text{eff}}|$, at the same time as using the results of the CP fit to constrain α . From this analysis BABAR obtains the confidence level plot shown in fig. 10 and the measurement²⁰⁾:

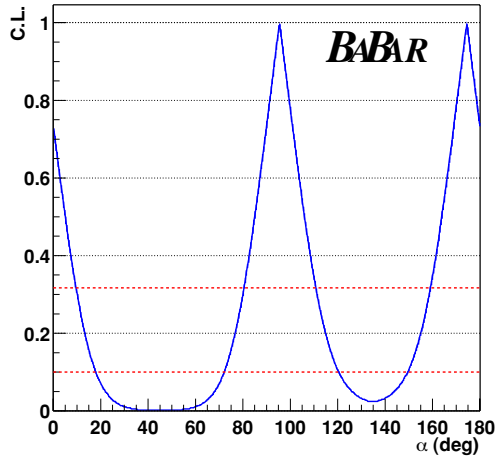
$$\alpha = (96 \pm 10 \pm 5 \pm 11)^\circ \tag{21}$$

3.4 $B \rightarrow \rho\pi$

Previous measurements of this mode have been made using a ‘‘quasi-two-body’’ approach²¹⁾, i.e. cutting out the interference regions of the Dalitz plot (DP) and analysing the regions containing the ρ resonances. This approach has the

Table 2: Summary of BABAR measurements of $B \rightarrow \rho\rho$ decays.

Mode	$\mathcal{B} \times 10^{-6}$	f_L	S	C
$\rho^+\rho^-$	$30 \pm 4 \pm 5$	$0.99 \pm 0.03 \pm 0.04$	$-0.19 \pm 0.33 \pm 0.11$	$-0.23 \pm 0.24 \pm 0.14$
			\mathcal{A}_{CP}	
$\rho^\pm\rho^0$	$22.5^{+5.7}_{-5.4} \pm 5.8$	$0.97^{+0.03}_{-0.07} \pm 0.04$	$-0.19 \pm 0.23 \pm 0.03$	
$\rho^0\rho^0$	< 1.1 90% C.L.	—	—	

Figure 10: Plot of the confidence level of the CKM angle α from the BABAR isospin analysis of $B \rightarrow \rho\rho$.

advantage that it avoids the need to understand the interference effects but by cutting out those regions of the DP statistical power is lost. Additionally, the statistics available to the B factories are not sufficient to perform the pentagon isospin analysis that is necessary in these modes. The measurements reported here are the results of the first attempt by either of the B factories to perform a time-dependent Dalitz plot analysis of a B decay mode²²⁾. This Dalitz analysis models the interference between the intersecting ρ resonance bands and so determines the strong phase differences from the Dalitz plot structure. The Dalitz amplitudes and time-dependence are all contained in various complex parameters within the likelihood fit. The values obtained for these parameters

are then converted back into the quasi-two-body CP observables, which are more intuitive in their interpretation and are defined in ²¹⁾:

$$\begin{aligned}
 S &= -0.10 \pm 0.14 \pm 0.04 \\
 C &= 0.34 \pm 0.11 \pm 0.05 \\
 \mathcal{A}_{CP} &= -0.088 \pm 0.049 \pm 0.013
 \end{aligned}
 \tag{22}$$

Using isospin with these results the confidence level plot shown in fig. 11 is obtained and the following constraint is placed on α :

$$\alpha = (113^{+27}_{-17} \pm 6)^\circ.
 \tag{23}$$

This result is of particular value because there is a unique solution between 0 and 180° , which helps to break the ambiguity on the $\rho\rho$ result, which is in itself more precise. The direct CP violation parameters C and \mathcal{A}_{CP} can be combined into more intuitive variables $A_{\rho\pi}^{+-}$ and $A_{\rho\pi}^{-+}$, which give the charge asymmetry in the modes where the ρ and the π respectively is emitted by the W boson. The contour plot for these observables can be found in fig. 12, which shows that there is a hint of direct CP violation at the 2.9σ level.

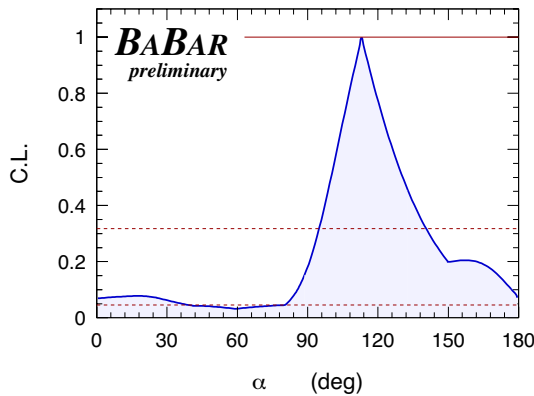


Figure 11: Plot of the confidence level of the CKM angle α from the *BABAR* isospin analysis of $B \rightarrow \rho\pi$.

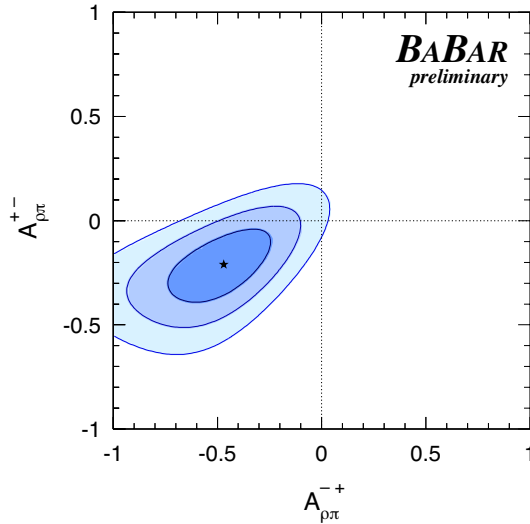


Figure 12: Plot of the confidence level contours for the direct CP violation observables $A_{\rho\pi}^{+-}$ and $A_{\rho\pi}^{-+}$.

3.5 Combined results for α

Combining all the *BABAR* results on α presented above gives the measurement:

$$\alpha = (103_{-10}^{+11})^\circ. \quad (24)$$

The confidence level plot of each individual measurement and the combined result is shown in fig. 13. Also included in the plot is the result for α from the global CKM fit not including the direct constraints from these results. The agreement is excellent.

4 Measurements relating to γ

Sensitivity to the CKM angle γ occurs in decay modes that have contributions from diagrams containing $b \rightarrow c$ and $b \rightarrow u$ transitions that interfere with one another. The size of the interference, and hence the sensitivity to γ , is determined by the relative magnitudes of the two processes. The two diagrams being considered here are those of $B^+ \rightarrow \bar{D}^0 K^+$ and $B^+ \rightarrow D^0 K^+$, which are

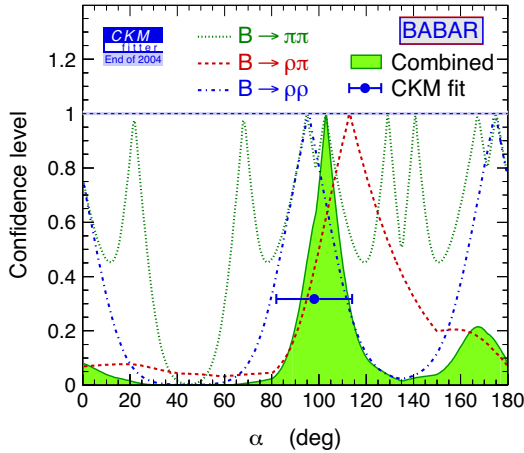


Figure 13: Plot of the confidence level contours for the CKM angle α using all *BABAR* measurements as an input. The blue point with error bar is the result of the full CKM fit without the direct constraints on α .

illustrated in fig. 14. In order for these two processes to interfere it is required that the final state be the same. Here we examine the decay of the D^0 and \bar{D}^0 to $K_S^0\pi^+\pi^-$.

In this decay mode, there are four unknowns

- γ ,
- $r_B = \frac{|A(B^+ \rightarrow D^0 K^+)|}{|A(B^+ \rightarrow \bar{D}^0 K^+)|}$
- δ_B - the strong phase of the B decay and
- δ_D - the strong phase of the D decay.

This last parameter is eliminated by using the Dalitz plot structure of the $D^0 \rightarrow K_S^0\pi^+\pi^-$ decay in the likelihood fit. This is determined by performing a full Dalitz plot analysis of this D decay mode using a very high statistics sample of D^{*+} decays. The resulting amplitude model is then fixed and used as the f terms in the following expressions:

$$M_+(m_-^2, m_+^2) = |A(B^+ \rightarrow \bar{D}^0 K^+)| [f(m_+^2, m_-^2) + r_B e^{i\delta_B} e^{i\gamma} f(m_-^2, m_+^2)]$$

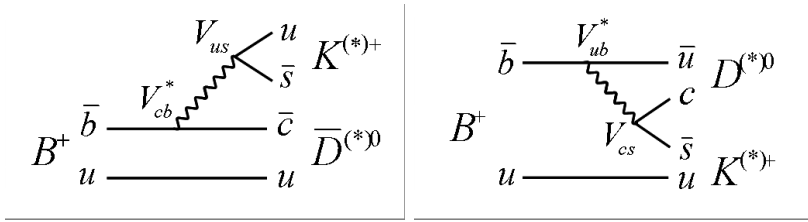


Figure 14: Diagrams for the decays $B^+ \rightarrow \bar{D}^0 K^+$ and $B^+ \rightarrow D^0 K^+$, which are sensitive to the angle γ in their interference if the D^0 and \bar{D}^0 decay to the same final state.

$$M_-(m_-^2, m_+^2) = |A(B^- \rightarrow D^0 K^-)| [f(m_-^2, m_+^2) + r_B e^{i\delta_B} e^{i\gamma} f(m_+^2, m_-^2)] \quad (25)$$

The fit to the D^* sample can be seen in fig. 15.

A simultaneous fit is then performed to both the B^+ and B^- data samples in order to determine γ , δ_B and r_B . In addition to the Dalitz plot information, kinematic and event topology information is used to separate the signal and background events. The number of signal events was found to be 261 ± 19 for the $D^0 K^+$ mode, 83 ± 11 for the $D^{*0}(D^0 \pi^0) K^+$ mode and 40 ± 8 for $D^{*0}(D^0 \gamma) K^+$. The results determined are ²³⁾:

$$\begin{aligned} r_B < 0.19 \text{ (90\%CL)}, \quad r_B^* = 0.155_{-0.077}^{+0.070} \pm 0.040 \pm 0.020 \\ \delta_B = (114 \pm 41 \pm 8 \pm 10)^\circ, \quad \delta_B^* = (303 \pm 34 \pm 14 \pm 10)^\circ \\ \gamma = (70 \pm 26 \pm 10 \pm 10)^\circ. \end{aligned} \quad (26)$$

5 Summary

In the last few years the measurements of the angles of the CKM Unitarity Triangle from the *BABAR* experiment have become increasingly sophisticated and precise. New techniques are allowing ambiguities to be resolved and measurements to be performed in modes that were not thought possible when the B factories were first conceived. The measurements are mostly in excellent agreement with the Standard Model predictions but there are possible hints of New Physics in the measurements of $\sin 2\beta$ in $b \rightarrow s$ penguin modes. *BABAR*

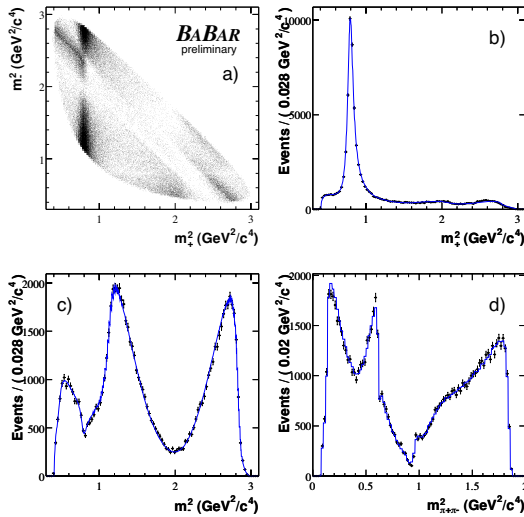


Figure 15: (a) The $D^0 \rightarrow K_S^0 \pi^+ \pi^-$ Dalitz distribution from D^* decays. Also shown are the projections onto the Dalitz variables (b) $m_+^2 = m_{K_S^0 \pi^+}^2$, (c) $m_-^2 = m_{K_S^0 \pi^-}^2$ and (d) $m_{\pi^+ \pi^-}^2$. The fit result is overlaid on the projections as a solid line.

intends to double its dataset by Summer 2006 and again by 2008 so we can look forward to further improvement in the measurements of these parameters.

6 Acknowledgements

Many thanks to Adrian Bevan, Paul Harrison and Andreas Hoecker for their advice and assistance in the preparation of this presentation and manuscript.

References

1. M. Kobayashi and T. Maskawa, Prog. Theor. Phys. **49**, 652 (1973).
2. L. Wolfenstein, Phys. Rev. Lett. **51**, 1945 (1983).
3. B. Aubert *et al.* [BABAR Collaboration], Nucl. Instrum. Meth. A **479**, 1 (2002).

4. W. Kozanecki, Nucl. Instrum. Meth. A **446**, 59 (2000).
5. B. Aubert *et al.* [*BABAR* Collaboration], Phys. Rev. Lett. **94**, 161803 (2005).
6. B. Aubert *et al.* [*BABAR* Collaboration], Phys. Rev. D **71**, 032005 (2005).
7. D. Aston *et al.*, Nucl. Phys. B **296**, 493 (1988).
8. E. P. Wigner, Phys. Rev. **98**, 145-147 (1955).
9. B. Aubert *et al.* [*BABAR* Collaboration], arXiv:hep-ex/0502019.
10. M. Pivk and F. R. Le Diberder, arXiv:physics/0402083.
11. B. Aubert *et al.* [*BABAR* Collaboration], Phys. Rev. Lett. **93**, 131805 (2004).
12. B. Aubert *et al.* [*BABAR* Collaboration], arXiv:hep-ex/0502013.
13. B. Aubert *et al.* [*BABAR* Collaboration], arXiv:hep-ex/0412037.
14. M. Gronau and D. London, Phys. Rev. Lett. **65**, 3381 (1990).
15. H. J. Lipkin, Y. Nir, H. R. Quinn and A. Snyder, Phys. Rev. D **44**, 1454 (1991).
16. A. E. Snyder and H. R. Quinn, Phys. Rev. D **48**, 2139 (1993).
17. B. Aubert *et al.* [*BABAR* Collaboration], Phys. Rev. Lett. **93**, 231801 (2004).
18. B. Aubert *et al.* [*BABAR* Collaboration], Phys. Rev. Lett. **91**, 171802 (2003).
19. L. Roos [*BABAR* Collaboration], arXiv:hep-ex/0407051.
20. B. Aubert *et al.* [*BABAR* Collaboration], arXiv:hep-ex/0408061.
21. B. Aubert *et al.* [*BABAR* Collaboration], Phys. Rev. Lett. **91**, 201802 (2003).
22. B. Aubert *et al.* [*BABAR* Collaboration], arXiv:hep-ex/0408099.
23. B. Aubert *et al.* [*BABAR* Collaboration], arXiv:hep-ex/0408088.

MEASUREMENTS OF $|V_{ub}|$ AND $|V_{cb}|$ AT BaBar

Rolf Dubitzky

Ruprecht-Karls-University, Heidelberg

Written contribution not received

ANGLES OF THE CKM UNITARITY TRIANGLE MEASURED AT BELLE

A. J. Schwartz

*Physics Department, University of Cincinnati
P.O. Box 210011, Cincinnati, Ohio 45221 USA*

Abstract

The Belle experiment has used several methods to measure or constrain the angles ϕ_1 , ϕ_2 , and ϕ_3 (or β , α , and γ) of the CKM unitarity triangle. The results are $\sin 2\phi_1 = 0.728 \pm 0.056$ (stat) ± 0.023 (syst) or $\phi_1 = (23.4^{+2.7}_{-2.4})^\circ$ from $B^0 \rightarrow J/\psi K^0$ decays (140 fb^{-1}); $\phi_2 = (0-19)^\circ$ or $(71-180)^\circ$ at 95.4% CL from $B^0 \rightarrow \pi^+\pi^-$ decays (253 fb^{-1}); and $\phi_3 = [68^{+14}_{-15}$ (stat) ± 13 (syst) ± 11 (model)] $^\circ$ from $B^\pm \rightarrow (D^0, \bar{D}^0)K^\pm$, $(D^0, \bar{D}^0) \rightarrow K_S^0 \pi^+\pi^-$ decays (253 fb^{-1}). These values satisfy the triangle relation $\phi_1 + \phi_2 + \phi_3 = 180^\circ$ within their uncertainties. The angle ϕ_1 is also determined from several $b \rightarrow s\bar{q}q$ penguin-dominated decay modes; the value obtained by taking a weighted average of the individual results differs from the $B^0 \rightarrow J/\psi K^0$ result by more than two standard deviations. The angle ϕ_2 is constrained by measuring a CP asymmetry in the decay time distribution; the asymmetry observed is large, and the difference in the yields of $B^0, \bar{B}^0 \rightarrow \pi^+\pi^-$ decays constitutes the first evidence for direct CP violation in the B system.

1 Introduction

The Standard Model predicts CP violation to occur in B^0 meson decays owing to a complex phase in the 3×3 Cabibbo-Kobayashi-Maskawa (CKM) mixing matrix ¹⁾. This phase is illustrated by plotting the unitarity condition $V_{ub}^*V_{ud} + V_{cb}^*V_{cd} + V_{tb}^*V_{td} = 0$ as vectors in the complex plane: the phase results in a triangle of nonzero height. Various measurements in the B system are sensitive to the internal angles ϕ_1 , ϕ_2 , and ϕ_3 (also known as β , α , and γ , respectively); these measurements allow us to determine the angles and check whether the triangle closes. Non-closure would indicate physics beyond the Standard Model. Here we present measurements of ϕ_1 and ϕ_2 obtained by measuring time-dependent CP asymmetries, and a measurement of ϕ_3 obtained by measuring an asymmetry in the Dalitz plot distribution of three-body decays. The results presented are from the Belle experiment ²⁾, which runs at the KEKB asymmetric-energy e^+e^- collider ³⁾ operating at the $\Upsilon(4S)$ resonance.

In Belle, pion and kaon tracks are identified using information from time-of-flight counters, aerogel Čerenkov counters, and dE/dx information from the central tracker ⁴⁾. B decays are identified using the “beam-constrained” mass $M_{bc} \equiv \sqrt{E_{\text{beam}}^2 - p_B^2}$ and the energy difference $\Delta E \equiv E_B - E_{\text{beam}}$, where p_B is the reconstructed B momentum, E_B is the reconstructed B energy, and E_{beam} is the beam energy, all evaluated in the e^+e^- center-of-mass (CM) frame. A tagging algorithm ⁵⁾ is used to identify the flavor at production of the decaying B , i.e., whether it is B^0 or \bar{B}^0 . This algorithm examines tracks not associated with the signal decay to identify the flavor of the non-signal B . The signal-side tracks are fit for a decay vertex, and the tag-side tracks are fit for a separate decay vertex; the distance Δz between vertices is to a very good approximation proportional to the time difference Δt between the B decays: $\Delta z \approx (\beta\gamma c)\Delta t$, where $\beta\gamma$ is the Lorentz boost of the CM system.

The dominant background is typically $e^+e^- \rightarrow q\bar{q}$ continuum events, where $q = u, d, s, c$. In the CM frame such events tend to be jet-like, whereas $B\bar{B}$ events tend to be spherical. The sphericity of an event is usually quantified via Fox-Wolfram moments ⁶⁾ of the form $h_\ell = \sum_{i,j} p_i p_j P_\ell(\cos\theta_{ij})$, where i runs over all tracks on the tagging side and j runs over all tracks on either the tagging side or the signal side ⁷⁾. The function P_ℓ is the ℓ th Legendre polynomial and θ_{ij} is the angle between momenta \vec{p}_i and \vec{p}_j in the CM frame. These moments are combined into a Fisher discriminant, and this is combined with the probability density function (PDF) for $\cos\theta_B$, where θ_B is the polar angle in the CM frame between the B direction and the z axis (nearly along the e^- beam direction). $B\bar{B}$ events are produced with a $1 - \cos^2\theta_B$ distribution while $q\bar{q}$ events are produced uniformly in $\cos\theta_B$. The PDFs for signal and $q\bar{q}$ background are obtained using MC simulation and M_{bc} - ΔE sidebands in data,

respectively. We use the products of the PDFs to calculate a signal likelihood \mathcal{L}_s and a continuum likelihood $\mathcal{L}_{q\bar{q}}$ and require that $\mathcal{L}_s/(\mathcal{L}_s + \mathcal{L}_{q\bar{q}})$ be above a threshold.

The angles ϕ_1 and ϕ_2 are determined by measuring the time dependence of decays to CP -eigenstates. This distribution is given by

$$\frac{dN}{d\Delta t} \propto e^{-\Delta t/\tau} \left[1 - q\Delta\omega + q(1 - 2\omega) [\mathcal{A} \cos(\Delta m \Delta t) + \mathcal{S} \sin(\Delta m \Delta t)] \right], \quad (1)$$

where $q = +1$ (-1) corresponds to B^0 (\bar{B}^0) tags, ω is the mistag probability, $\Delta\omega$ is a possible difference in ω between B^0 and \bar{B}^0 tags, and Δm is the B^0 - \bar{B}^0 mass difference. The CP -violating coefficients \mathcal{A} and \mathcal{S} are functions of the parameter λ : $\mathcal{A} = (|\lambda|^2 - 1)/(|\lambda|^2 + 1)$ and $\mathcal{S} = 2 \text{Im}(\lambda)/(|\lambda|^2 + 1)$, where

$$\lambda = \frac{q}{p} \frac{A(\bar{B}^0 \rightarrow f)}{A(B^0 \rightarrow f)} \approx \sqrt{\frac{M_{12}^*}{M_{12}}} \frac{A(\bar{B}^0 \rightarrow f)}{A(B^0 \rightarrow f)} = \left(\frac{V_{td} V_{tb}^*}{V_{td}^* V_{tb}} \right) \frac{A(\bar{B}^0 \rightarrow f)}{A(B^0 \rightarrow f)}. \quad (2)$$

In this expression, q and p are the complex coefficients relating the flavor eigenstates B^0 and \bar{B}^0 to the mass eigenstates, M_{12} is the off-diagonal element of the B^0 - \bar{B}^0 mass matrix, and we assume that the off-diagonal element of the decay matrix is much smaller: $\Gamma_{12} \ll M_{12}$. If only one weak phase enters the decay amplitude $A(\bar{B}^0 \rightarrow f)$, then $|A(\bar{B}^0 \rightarrow f)/A(B^0 \rightarrow f)| = 1$ and $\lambda = \eta_f e^{i2\theta}$, where $\eta_f = \pm 1$ is the CP of the final state f . For the final states discussed here, $|\theta| = \phi_1$ or ϕ_2 .

2 The angle ϕ_1

This angle is most accurately measured using $B^0 \rightarrow J/\psi K^0$ decays¹. The decay is dominated by a $b \rightarrow c\bar{c}s$ tree amplitude and a $b \rightarrow s\bar{c}c$ penguin amplitude. The latter can be divided into two pieces: a piece with c and t in the loop that has the same weak phase as the tree amplitude, and a piece with u and t in the loop that has a different weak phase but is suppressed by $\sin^2 \theta_C$ relative to the first piece. Due to this suppression, $A(\bar{B}^0 \rightarrow f)$ is governed by a single weak phase: $\text{Arg}(V_{cb} V_{cs}^*)$. The ratio $A(\bar{B}^0 \rightarrow J/\psi K_S^0)/A(B^0 \rightarrow J/\psi K_S^0)$ includes an extra factor $(p/q)_K = V_{cd}^* V_{cs}/(V_{cd} V_{cs}^*)$ to account for the \bar{K}^0 oscillating to a K_S^0 , and thus $\lambda = -[V_{td} V_{tb}^*/(V_{td}^* V_{tb})][V_{cb} V_{cs}^*/(V_{cb}^* V_{cs})][V_{cd}^* V_{cs}/(V_{cd} V_{cs}^*)] = -e^{-i2\phi_1}$. The CP asymmetry parameters are therefore $\mathcal{S} = \sin 2\phi_1$, $\mathcal{A} = 0$. To determine ϕ_1 , we fit the Δt distribution for \mathcal{S} ; the result is $\sin 2\phi_1 = 0.728 \pm 0.056$ (stat) \pm

¹This measurement includes $B^0 \rightarrow J/\psi K_S^0$, $J/\psi K_L^0$, $\psi(2S)K_S^0$, $\chi_{c1}K_S^0$, $\eta_c K_S^0$, and $J/\psi K^{*0}$ ($K^{*0} \rightarrow K_S^0 \pi^0$); we use “ $B^0 \rightarrow J/\psi K^0$ ” to denote all six modes.

Table 1: *Decay modes used to measure $\sin 2\phi_1$, the number of candidate events, the value of $\sin 2\phi_1$ obtained, and the parameter \mathcal{A} obtained [see Eq. (1)]. The $B^0 \rightarrow J/\psi K^0$ result corresponds to 140 fb^{-1} of data; the other results correspond to 253 fb^{-1} of data.*

(CP) Mode	Candidates	$\sin 2\phi_1$	\mathcal{A}
(-) $J/\psi K_S^0$	2285	$0.728 \pm 0.056 \pm 0.023$	-
(+) $J/\psi K_L^0$	2332		
(-) ϕK_S^0	139 ± 14	$0.08 \pm 0.33 \pm 0.09$	$0.08 \pm 0.22 \pm 0.09$
(+) ϕK_L^0	36 ± 15		
(\pm) $K^+ K^- K_S^0$ (+ = 83%)	398 ± 28	$0.74 \pm 0.27^{+0.39}_{-0.19}$	$-0.09 \pm 0.12 \pm 0.07$
(+) $f_0(980) K_S^0$	94 ± 14	$-0.47 \pm 0.41 \pm 0.08$	$-0.39 \pm 0.27 \pm 0.09$
(+) $K_S^0 K_S^0 K_S^0$	88 ± 13	$-1.26 \pm 0.68 \pm 0.20$	$0.54 \pm 0.34 \pm 0.09$
(-) $\eta' K_S^0$	512 ± 27	$0.65 \pm 0.18 \pm 0.04$	$-0.19 \pm 0.11 \pm 0.05$
(-) $\pi^0 K_S^0$	247 ± 25	$0.32 \pm 0.61 \pm 0.13$	$-0.11 \pm 0.20 \pm 0.09$
(-) ωK_S^0	31 ± 7	$0.76 \pm 0.65^{+0.13}_{-0.16}$	$0.27 \pm 0.48 \pm 0.15$

0.023 (syst), or $\phi_1 = (23.4^{+2.7}_{-2.4})^\circ$ (the smaller of the two solutions for ϕ_1). The fit result for \mathcal{A} yields $|\lambda| = 1.007 \pm 0.041$ (stat) ± 0.033 (syst), in agreement with the theoretical expectation. These results correspond to 140 fb^{-1} of data ⁸⁾.

There are several decay modes that proceed exclusively via penguin amplitudes (e.g., $\overline{B}^0 \rightarrow \phi \overline{K}^0$ proceeding via $b \rightarrow s\bar{s}s$) or else are dominated by penguin amplitudes (e.g., $\overline{B}^0 \rightarrow (\eta'/\omega/\pi^0)\overline{K}^0$ proceeding via $b \rightarrow s\bar{d}d$) but have the same weak phase as the $b \rightarrow c\bar{c}s$ tree amplitude. This is because the penguin loop factorizes into a c, t loop with the same weak phase and a u, t loop with a different weak phase; the latter, however, is suppressed by $\sin^2 \theta_C$ relative to the former and plays a negligible role. We thus expect these decays to also have $\mathcal{S} = \sin 2\phi_1$, $\mathcal{A} = 0$. There are small mode-dependent corrections ($|\Delta\mathcal{S}| \leq 0.10$) to this prediction due to final-state rescattering ⁹⁾. Table 1 lists these modes and the corresponding values ¹⁰⁾ of $\sin 2\phi_1$ obtained from fitting the Δt distributions; Fig. 1 shows these results in graphical form. Neglecting the small rescattering corrections and simply averaging the penguin-dominated values gives $\sin 2\phi_1 = 0.40 \pm 0.13$. This value differs from the $B^0 \rightarrow J/\psi K^0$ world average value by 2.4 standard deviations, which may be a statistical fluctuation or may indicate new physics.

3 The angle ϕ_2

This angle is measured by fitting the Δt distribution of $B^0 \rightarrow \pi^+ \pi^-$ decays. The rate is dominated by a $b \rightarrow u\bar{u}d$ tree amplitude with a weak phase $\text{Arg}(V_{ub} V_{ud}^*)$.

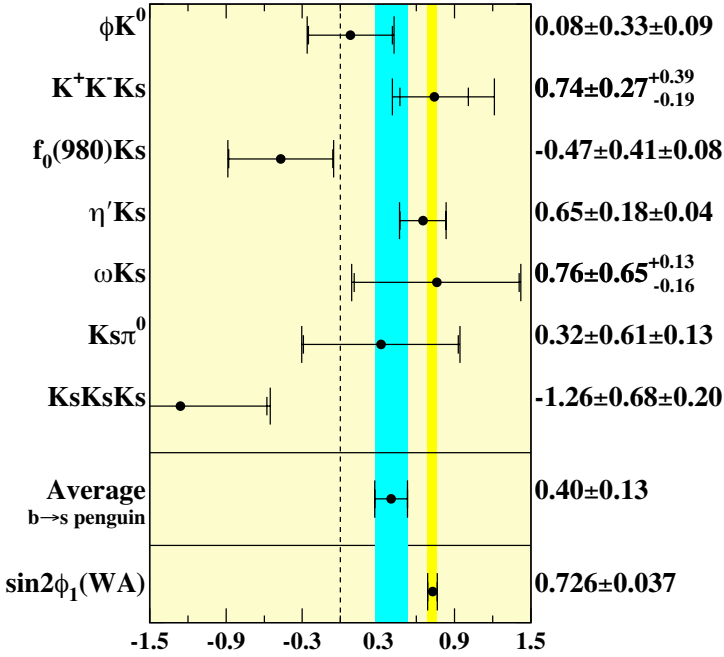


Figure 1: Values of $\sin 2\phi_1$ measured in decay modes dominated by $b \rightarrow s \bar{q}q$ penguin amplitudes, for 253 fb^{-1} of data. The average value differs from the world average (WA) value measured in $B^0 \rightarrow J/\psi K^0$ decays.

If only this phase were present, then $\lambda = [V_{td} V_{tb}^* / (V_{td}^* V_{tb})] [V_{ub} V_{ud}^* / (V_{ub}^* V_{ud})] = e^{i2\phi_2}$, and $\mathcal{S} = \sin 2\phi_2$, $\mathcal{A} = 0$. However, a $b \rightarrow d \bar{u}u$ penguin amplitude also contributes, and, unlike the penguin in $B^0 \rightarrow J/\psi K_S^0$ decays, the piece with a different weak phase is not CKM-suppressed relative to the piece with the same weak phase. The CP asymmetry parameters are therefore more complicated ¹¹⁾:

$$\mathcal{A}_{\pi\pi} = -\frac{1}{R} \cdot \left(2 \left| \frac{P}{T} \right| \sin(\phi_1 + \phi_2) \sin \delta \right) \quad (3)$$

$$\mathcal{S}_{\pi\pi} = \frac{1}{R} \cdot \left(2 \left| \frac{P}{T} \right| \sin(\phi_1 - \phi_2) \cos \delta + \sin 2\phi_2 - \left| \frac{P}{T} \right|^2 \sin 2\phi_1 \right) \quad (4)$$

$$R = 1 - 2 \left| \frac{P}{T} \right| \cos(\phi_1 + \phi_2) \cos \delta + \left| \frac{P}{T} \right|^2, \quad (5)$$

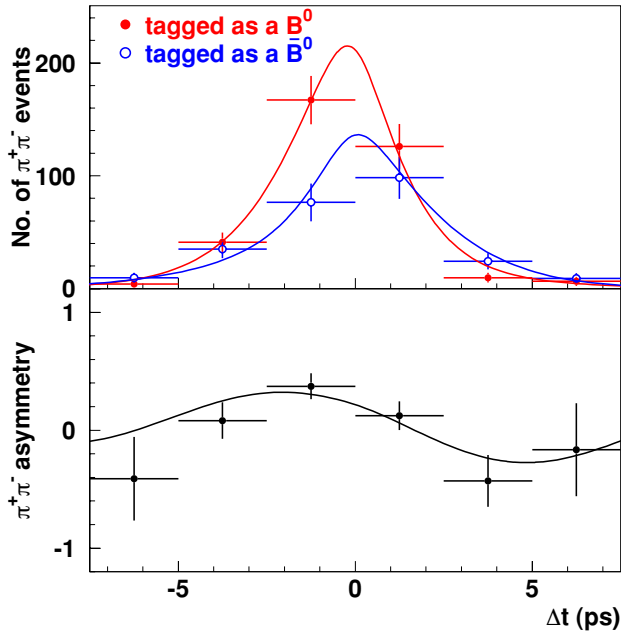


Figure 2: The Δt distribution of background-subtracted $B^0, \bar{B}^0 \rightarrow \pi^+ \pi^-$ candidates (top), and the resulting CP asymmetry $[N(\bar{B}^0) - N(B^0)] / [N(\bar{B}^0) + N(B^0)]$ (bottom). The smooth curves are projections of the unbinned ML fit.

where $|P/T|$ is the magnitude of the penguin amplitude relative to that of the tree amplitude, δ is the strong phase difference between the two amplitudes, and ϕ_1 is known from $B^0 \rightarrow J/\psi K^0$ decays. Since Eqs. (3) and (4) have three unknown parameters, measuring $\mathcal{A}_{\pi\pi}$ and $\mathcal{S}_{\pi\pi}$ determines a volume in δ - $|P/T|$ - ϕ_2 space.

The most recent Belle measurement¹²⁾ uses 253 fb^{-1} of data; the event sample consists of 666 ± 43 $B^0 \rightarrow \pi^+ \pi^-$ candidates after background subtraction. These events are subjected to an unbinned maximum likelihood (ML) fit for Δt ; the results are $\mathcal{A}_{\pi\pi} = 0.56 \pm 0.12$ (stat) ± 0.06 (syst) and $\mathcal{S}_{\pi\pi} = -0.67 \pm 0.16$ (stat) ± 0.06 (syst), which together indicate large CP violation. The nonzero value for $\mathcal{A}_{\pi\pi}$ indicates *direct* CP violation. Fig. 2 shows the Δt distributions for $q = \pm 1$ tagged events along with projections of the ML fit; a clear difference is seen between the fit results.

The values of $\mathcal{A}_{\pi\pi}$ and $\mathcal{S}_{\pi\pi}$ determine a 95.4% CL (2σ) volume in δ - $|P/T|$ - ϕ_2 space. Projecting this volume onto the δ - $|P/T|$ axes gives the region shown

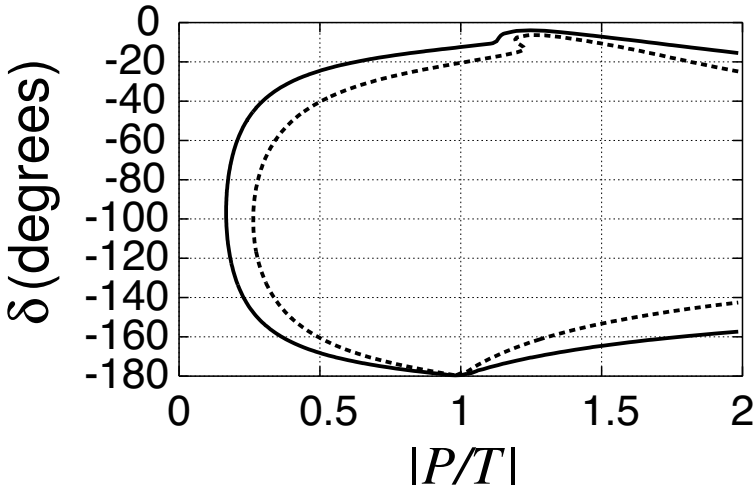


Figure 3: Projection of the 68.3% CL (dashed) and 95.4% CL (solid) volumes in δ - $|P/T|$ - ϕ_2 space onto the δ - $|P/T|$ axes. From the solid contour we obtain the constraints $|P/T| > 0.17$ and $-180^\circ < \delta < -4^\circ$ (95.4% CL).

in Fig. 3; from this region we obtain the constraints $|P/T| > 0.17$ for any value of δ , and $-180^\circ < \delta < -4^\circ$ for any value of $|P/T|$.

The dependence upon δ and $|P/T|$ can be removed by performing an isospin analysis¹³⁾ of $B \rightarrow \pi\pi$ decays. This method uses the measured branching fractions for $B \rightarrow \pi^+\pi^-$, $\pi^\pm\pi^0$, $\pi^0\pi^0$ and the CP asymmetry parameters $\mathcal{A}_{\pi^+\pi^-}$, $\mathcal{S}_{\pi^+\pi^-}$, and $\mathcal{A}_{\pi^0\pi^0}$. We scan values of ϕ_2 from 0° – 180° and for each value construct a χ^2 based on the difference between the predicted values for the six observables and the measured values. We convert this χ^2 into a confidence level (CL) by subtracting off the minimum χ^2 value and inserting the result into the cumulative distribution function for the χ^2 distribution for one degree of freedom. The resulting function $1 - \text{CL}$ is plotted in Fig. 4. From this plot we read off a 95.4% CL interval $\phi_2 = (0 - 19)^\circ$ or $(71 - 180)^\circ$, i.e., we exclude the range $20^\circ - 70^\circ$.

4 The angle ϕ_3

The angle ϕ_3 is challenging to measure by fitting the Δt distribution, as the two requisite interfering amplitudes have very different magnitudes, and the small ratio of magnitudes multiplies the ϕ_3 -dependent term $[\sin(2\phi_1 + \phi_3 \pm \delta)]$ ¹⁴⁾. As an alternative, one can probe ϕ_3 via interference in the Dalitz plot distribution

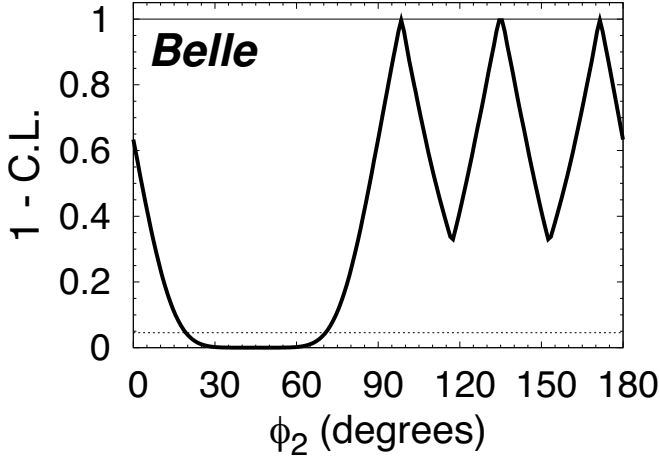


Figure 4: The result of fitting the branching fractions for $B \rightarrow \pi^+\pi^-, \pi^\pm\pi^0, \pi^0\pi^0$ and the CP asymmetry parameters $\mathcal{A}_{\pi^+\pi^-}, \mathcal{S}_{\pi^+\pi^-}$, and $\mathcal{A}_{\pi^0\pi^0}$, as a function of ϕ_2 (see text). The vertical axis is one minus the confidence level. The horizontal line at $1-\text{CL} = 0.046$ corresponds to a 95.4% CL interval for ϕ_2 .

of $B^\pm \rightarrow (D^0, \bar{D}^0)K^\pm$ decays: the additional phase ϕ_3 causes a difference between the interference pattern for B^+ decays and that for B^- decays¹⁵).

We study this asymmetry by reconstructing $B^\pm \rightarrow (D^0, \bar{D}^0)K^\pm$ decays in which the D^0 or \bar{D}^0 decays to the common final state $K_S^0\pi^+\pi^-$. Denoting $m(K_S^0, \pi^+) \equiv m_+, m(K_S^0, \pi^-) \equiv m_-, A(D^0 \rightarrow K_S^0\pi^+\pi^-) \equiv A(m^+, m^-)$, and $A(\bar{D}^0 \rightarrow K_S^0\pi^+\pi^-) \equiv \bar{A}(m^+, m^-) = A(m^-, m^+)$ (i.e., assuming CP conservation in D^0 decays), we have

$$A(B^+ \rightarrow \tilde{D}^0 K^+, \tilde{D}^0 \rightarrow K_S^0 \pi^+ \pi^-) = A(m_+^2, m_-^2) + r e^{i(\delta + \phi_3)} A(m_-^2, m_+^2) \quad (6)$$

$$A(B^- \rightarrow \tilde{D}^0 K^-, \tilde{D}^0 \rightarrow K_S^0 \pi^+ \pi^-) = A(m_-^2, m_+^2) + r e^{i(\delta - \phi_3)} A(m_+^2, m_-^2), \quad (7)$$

where \tilde{D}^0 denotes $(D^0 + \bar{D}^0)$, r is the ratio of magnitudes of the two amplitudes $|A(B^+ \rightarrow D^0 K^+)/A(B^+ \rightarrow \bar{D}^0 K^+)|$, and δ is the strong phase difference between the amplitudes. The decay rates are given by

$$\left| A(B^+ \rightarrow \tilde{D}^0 K^+ \rightarrow (K_S^0 \pi^+ \pi^-) K^+) \right|^2 = |A(m_+^2, m_-^2)|^2 + r^2 |A(m_-^2, m_+^2)|^2 +$$

$$2r|A(m_+^2, m_-^2)||A(m_-^2, m_+^2)| \cos(\delta + \phi_3 + \theta) \quad (8)$$

$$\left| A(B^- \rightarrow \tilde{D}^0 K^- \rightarrow (K_S^0 \pi^+ \pi^-) K^-) \right|^2 = r^2 |A(m_+^2, m_-^2)|^2 + |A(m_-^2, m_+^2)|^2 + 2r|A(m_+^2, m_-^2)||A(m_-^2, m_+^2)| \cos(\delta - \phi_3 + \theta), \quad (9)$$

where θ is the phase difference between $A(m_+^2, m_-^2)$ and $A(m_-^2, m_+^2)$ and varies over the Dalitz plot. Thus, given a $D^0 \rightarrow K_S^0 \pi^+ \pi^-$ decay model $A(m_+^2, m_-^2)$, one can fit the B^\pm Dalitz plots to Eqs. (8) and (9) to determine the parameters r , δ , and ϕ_3 . The decay model is determined from data, i.e., $D^0 \rightarrow K_S^0 \pi^+ \pi^-$ decays produced via $e^+ e^- \rightarrow c\bar{c}$.

The data sample used consists of 253 fb^{-1} ; there are $209 \pm 16 B^\pm \rightarrow \tilde{D}^0 K^\pm$ candidates with 75% purity, and an additional $58 \pm 8 B^\pm \rightarrow \tilde{D}^{0*} K^\pm$ ($\tilde{D}^{0*} \rightarrow \tilde{D}^0 \pi^0$) candidates with 87% purity¹⁶⁾. The background is dominated by $q\bar{q}$ continuum events in which a real D^0 is combined with a random kaon, and random combinations of tracks in continuum events. The Dalitz plots for the final samples are shown in Fig. 5.

The events are subjected to an unbinned ML fit for r , δ , and ϕ_3 . The decay model is a coherent sum of two-body amplitudes and a constant term for the nonresonant contribution:

$$A(m_+^2, m_-^2) = \sum_{j=1}^N a_j e^{i\alpha_j} \mathcal{A}_j(m_+^2, m_-^2) + a_{\text{nonres}} e^{i\alpha_{\text{nonres}}}, \quad (10)$$

where a_j , α_j , and \mathcal{A}_j are the magnitude, phase, and matrix element, respectively, of resonance j ; and $N=18$ resonances are considered. The parameters a_j and α_j are determined by fitting a large sample of continuum $D^0 \rightarrow K_S^0 \pi^+ \pi^-$ decays. The dominant intermediate modes¹⁶⁾ as determined from the fraction $\int |a_j \mathcal{A}_j|^2 dm_+^2 dm_-^2 / \int |A(m_+^2, m_-^2)|^2 dm_+^2 dm_-^2$ are $K^*(892)^+ \pi^-$ (61.2%), $K_S^0 \rho^0$ (21.6%), nonresonant $K_S^0 \pi^+ \pi^-$ (9.7%), and $K_0^*(1430)^+ \pi^-$ (7.4%).

The central values obtained by the fit are $r=0.25$, $\delta=157^\circ$, and $\phi_3=64^\circ$ for $B^+ \rightarrow \tilde{D}^0 K^+$; and $r=0.25$, $\delta=321^\circ$, and $\phi_3=75^\circ$ for $B^+ \rightarrow \tilde{D}^{*0} K^+$. The errors obtained by the fit correspond to Gaussian-shaped likelihood distributions, and for this analysis the distributions are non-Gaussian. We therefore use a frequentist MC method to evaluate the statistical errors. We first obtain a PDF for the fitted parameters r , δ , ϕ_3 as a function of the true parameters \bar{r} , $\bar{\delta}$, $\bar{\phi}_3$. We do this by generating several hundred experiments for a given set of \bar{r} , $\bar{\delta}$, $\bar{\phi}_3$ values, with each experiment having the same number of events as the data, and fitting these experiments as done for the data. The resulting distributions for $\alpha_\pm = r \cos(\delta \pm \phi_3)$ and $\beta_\pm = r \sin(\delta \pm \phi_3)$ are modeled as Gaussians (G) with mean values $\bar{\alpha}_\pm$ and $\bar{\beta}_\pm$ and common standard deviation σ , and

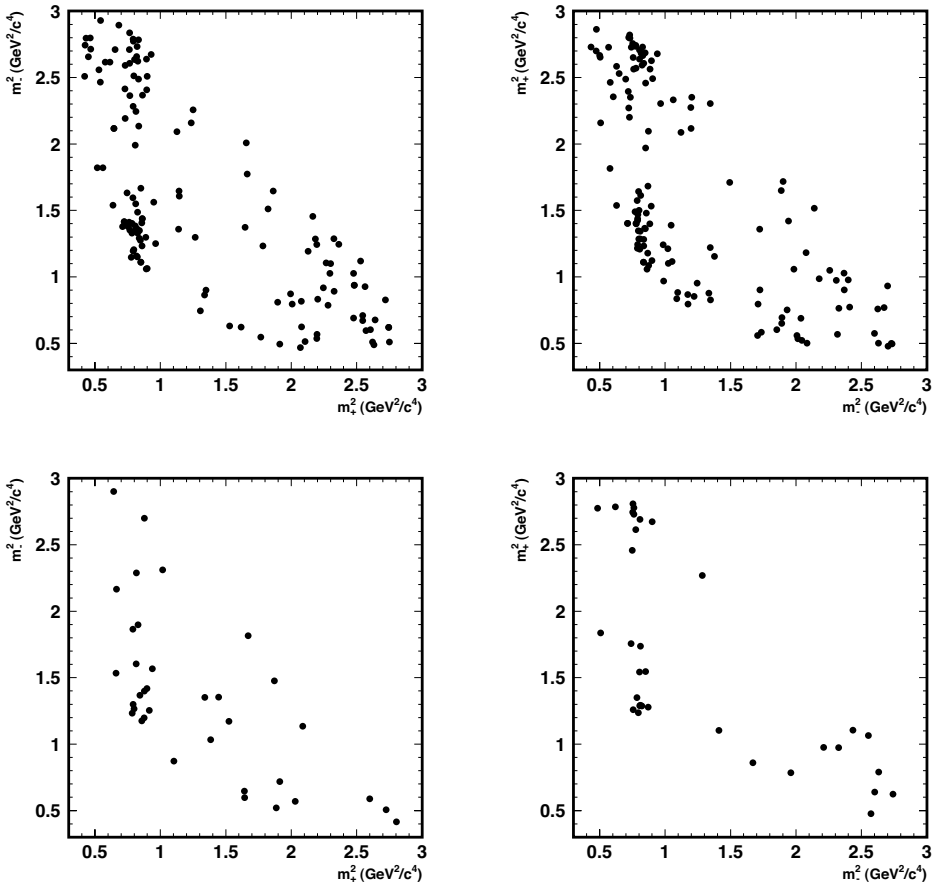


Figure 5: Dalitz plots of $\tilde{D}^0 \rightarrow K_S^0 \pi^+ \pi^-$ decays obtained from samples of $B^+ \rightarrow \tilde{D}^0 K^+$ (top left), $B^- \rightarrow \tilde{D}^0 K^-$ (top right), $B^+ \rightarrow \tilde{D}^{*0} K^+$ (bottom left), and $B^- \rightarrow \tilde{D}^{*0} K^-$ (bottom right).

Table 2: Results of the Dalitz plot analysis for r , δ , and ϕ_3 . The first error listed is statistical and is obtained from a frequentist MC method (see text); the second error listed is systematic but does not include uncertainty from the $\tilde{D}^0 \rightarrow K_S^0 \pi^+ \pi^-$ decay model; the third error listed is due to the decay model.

Parameter	$B^+ \rightarrow \tilde{D}^0 K^+$	$B^+ \rightarrow \tilde{D}^{*0} K^+$
r	$0.21 \pm 0.08 \pm 0.03 \pm 0.04$	$0.12_{-0.11}^{+0.16} \pm 0.02 \pm 0.04$
δ	$157^\circ \pm 19^\circ \pm 11^\circ \pm 21^\circ$	$321^\circ \pm 57^\circ \pm 11^\circ \pm 21^\circ$
ϕ_3	$64^\circ \pm 19^\circ \pm 13^\circ \pm 11^\circ$	$75^\circ \pm 57^\circ \pm 11^\circ \pm 11^\circ$

the product $G(\alpha_+ - \bar{\alpha}_+) \cdot G(\alpha_- - \bar{\alpha}_-) \cdot G(\beta_+ - \bar{\beta}_+) \cdot G(\beta_- - \bar{\beta}_-)$ is used to obtain the PDF $\mathcal{P}(r, \delta, \phi_3 | \bar{r}, \bar{\delta}, \bar{\phi}_3)$. With this PDF we calculate the confidence level for $\{\bar{r}, \bar{\delta}, \bar{\phi}_3\}$ given the fit values $\{0.25, 157^\circ, 64^\circ\}$ for $B^+ \rightarrow \tilde{D}^0 K^+$ and $\{0.25, 321^\circ, 75^\circ\}$ for $B^+ \rightarrow \tilde{D}^{*0} K^+$. The resulting confidence regions for pairs of parameters are shown in Fig. 6. The plots show 20%, 74%, and 97% CL regions, which correspond to one, two, and three standard deviations, respectively, for a three-dimensional Gaussian distribution. The 20% CL regions are taken as the statistical errors; the values that maximize the PDF are taken as the central values. Of the two possible solutions (δ, ϕ_3) or $(\delta + \pi, \phi_3 + \pi)$, we choose the one that satisfies $0^\circ < \phi_3 < 180^\circ$.

All results are listed in Table 2. The second error listed is systematic and results mostly from uncertainty in the background Dalitz plot density, variations in efficiency, the $m_{\pi\pi}^2$ resolution, and possible fitting bias. The third error listed results from uncertainty in the $D^0 \rightarrow K_S^0 \pi^+ \pi^-$ decay model, e.g., from the choice of form factors used for the intermediate resonances and the q^2 dependence of the resonance widths.

We combine the $B^+ \rightarrow \tilde{D}^0 K^+$ and $B^+ \rightarrow \tilde{D}^{*0} K^+$ results by multiplying together their respective PDF's, taking the parameter $\bar{\phi}_3$ to be common between them. This gives a PDF for the six measured parameters $r_1, \delta_1, \phi_{3(1)}, r_2, \delta_2, \phi_{3(2)}$ in terms of the five true parameters $\bar{r}_1, \bar{\delta}_1, \bar{r}_2, \bar{\delta}_2, \bar{\phi}_3$. The value of $\bar{\phi}_3$ that maximizes the PDF is taken as the central value, and the 3.7% CL interval prescribed by the PDF (corresponding to 1σ for a five-dimensional Gaussian distribution) is taken as the statistical error. The systematic error is taken from the $B^+ \rightarrow \tilde{D}^0 K^+$ measurement, as this sample dominates the combined measurement. The overall result is

$$\phi_3 = [68_{-15}^{+14} (\text{stat}) \pm 13 (\text{syst}) \pm 11 (\text{decay model})]^\circ.$$

The 2σ confidence interval including the systematic error and decay model error is $22^\circ < \phi_3 < 113^\circ$.

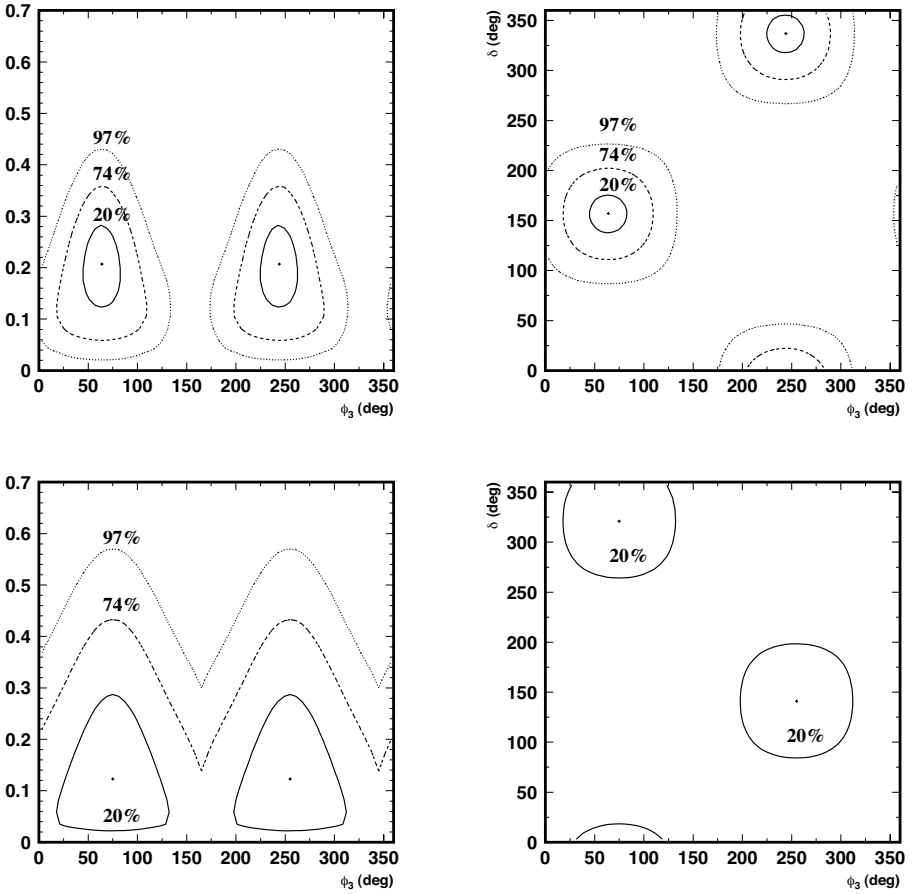


Figure 6: Confidence regions for pairs of parameters: the left-most plots correspond to r - ϕ_3 and the right-most plots to δ - ϕ_3 . The top row corresponds to $B^\pm \rightarrow \bar{D}^0 K^\pm$ decays and the bottom row to $B^\pm \rightarrow \bar{D}^{*0} K^\pm$ decays.

In summary, the Belle experiment has measured or constrained the angles ϕ_1 , ϕ_2 , and ϕ_3 of the CKM unitarity triangle. We obtain $\sin 2\phi_1 = 0.728 \pm 0.056$ (stat) ± 0.023 (syst) or $\phi_1 = (23.4^{+2.7}_{-2.4})^\circ$ with 140 fb^{-1} of data; $\phi_2 = (0 - 19)^\circ$ or $(71 - 180)^\circ$ at 95.4% CL with 253 fb^{-1} of data; and $\phi_3 = [68^{+14}_{-15}$ (stat) ± 13 (syst) ± 11 (decay model)] $^\circ$ with 253 fb^{-1} of data. Within their uncertainties, these values satisfy the triangle relation $\phi_1 + \phi_2 + \phi_3 = 180^\circ$. The angle ϕ_1 is measured from $B^0 \rightarrow J/\psi K^0$ decays and also from several $b \rightarrow s\bar{q}q$ penguin-dominated decay modes; the value obtained from the penguin modes differs from the $B^0 \rightarrow J/\psi K^0$ result by 2.4σ . The ϕ_2 constraint results from measuring the CP asymmetry coefficients $\mathcal{A}_{\pi\pi}$ and $\mathcal{S}_{\pi\pi}$ in $B^0 \rightarrow \pi^+\pi^-$ decays; the results are $\mathcal{A}_{\pi\pi} = 0.56 \pm 0.12$ (stat) ± 0.06 (syst) and $\mathcal{S}_{\pi\pi} = -0.67 \pm 0.16$ (stat) ± 0.06 (syst), which together indicate large CP violation. The nonzero value for $\mathcal{A}_{\pi\pi}$ indicates direct CP violation; the statistical significance (including systematic uncertainty) is 4.0σ . These values also imply that the magnitude of the penguin amplitude relative to that of the tree amplitude ($|P/T|$) is greater than 0.17 at 95.4% CL, and that the strong phase difference (δ) lies in the range $(-180^\circ, -4^\circ)$ at 95.4% CL. The ϕ_3 measurement is obtained from a Dalitz plot analysis of $B^\pm \rightarrow \tilde{D}^{(*)0} K^\pm$, $\tilde{D}^0 \rightarrow K_S^0 \pi^+\pi^-$ decays; the statistical significance of the observed (direct) CP violation is 98%.

5 Acknowledgments

The author thanks his Belle colleagues for many fruitful discussions, and the organizers of *Les Rencontres de Physique de la Vallée d'Aoste* for a well-organized and stimulating conference.

References

1. M. Kobayashi and T. Maskawa, *Prog. Theor. Phys.* **49**, 652 (1973).
2. <http://belle.kek.jp>
3. S. Kurokawa and E. Kikutani, *Nucl. Instr. Meth.* **A499**, 1 (2003), and other papers published in this volume.
4. A. Abashian *et al.* (Belle Collaboration), *Nucl. Instr. Meth.* **A479**, 117 (2002).
5. H. Kakuno *et al.*, *Nucl. Instr. Meth.* **A533**, 516 (2004).
6. G. C. Fox and S. Wolfram, *Phys. Rev. Lett.* **41**, 1581 (1978).
7. S. H. Lee *et al.* (Belle Collaboration), *Phys. Rev. Lett.* **91**, 261801 (2003).

8. K. Abe *et al.* (Belle Collaboration), Phys. Rev. **D71**, 072003 (2005).
9. H.-Y. Cheng, Ch.-K. Chua, and A. Soni, Phys. Rev. **D72**, 014006 (2005).
10. K.-F. Chen *et al.* (Belle Collaboration), Phys. Rev. **D72**, 012004 (2005).
K. Sumisawa *et al.* (Belle Collaboration), hep-ex/0503023, to appear in Phys. Rev. Lett.
11. M. Gronau and J. L. Rosner, Phys. Rev. **D65**, 093012 (2002).
12. H. Ishino *et al.* (Belle Collaboration), hep-ex/0502035, to appear in Phys. Rev. Lett.
13. M. Gronau and D. London, Phys. Rev. Lett. **65**, 3381 (1990).
14. I. Dunietz, Phys. Lett. **B427**, 179 (1998).
R. Fleischer, Nucl Phys. **B671**, 459 (2003).
15. A. Giri, Y. Grossman, A. Soffer, and J. Zupan, Phys. Rev. **D68**, 054018 (2003).
A. Bondar, "Improved Gronau-Wyler method for ϕ_3 extraction," in: Proceedings of the BINP Special Analysis Meeting on Dalitz Analysis (Novosibirsk, Russian Federation, September 2002), unpublished.
16. K. Abe *et al.* (Belle Collaboration), BELLE-CONF-0476, hep-ex/0411049.

Sides of the Unitarity Triangle at BELLE

中村 勇 (NAKAMURA Isamu)

High Energy Accelerator Reserch Organization, KEK, Tsukuba Ibaraki 305 Japan.

Abstract

Measurements of the sides of the unitarity triangle performed using the data collected by the Belle detector located on the KEKB collider are reported. One of the CKM matrix elements $|V_{ub}|$ is measured in two different methods. One is inclusive measurement of $\mathcal{B}(B \rightarrow X_u \ell \nu)$ using the full reconstruction technique. The other utilizes the branching fractions of exclusive decays, $B \rightarrow \pi \ell \nu$ and $B \rightarrow \rho \ell \nu$. Also reported is the search for the decay $b \rightarrow d \gamma$, whose branching fraction is related to the CKM matrix element $|V_{td}|$.

1 Introduction

Measurements of the sides of the unitarity triangle performed using the data collected by the Belle detector located on the KEKB collider are reported. One of the CKM matrix elements $|V_{ub}|$ is measured in two different methods. One is inclusive measurement of $\mathcal{B}(B \rightarrow X_u \ell \nu)$ using the full reconstruction technique. The other utilizes the branching fractions of exclusive decays, $B \rightarrow \pi \ell \nu$ and $B \rightarrow \rho \ell \nu$. Also reported is the search for the decay $b \rightarrow d \gamma$, whose branching fraction is related to the CKM matrix element $|V_{td}|$.

2 V_{ub} measurement with semileptonic decays

Measurement of the Cabbibo-Kobayashi-Masukawa matrix element $|V_{ub}|$ is crucial to test the Standard Model. Two measurements are performed with data corresponding to an integrated luminosity of 140 fb^{-1} . One is the inclusive measurement of the branching fraction $\mathcal{B}(B \rightarrow X_u \ell \nu)$ with full reconstruction tag and the other is the exclusive measurement of $\mathcal{B}(B \rightarrow \pi \ell \nu)$ or $\mathcal{B}(B \rightarrow \rho \ell \nu)$ with semileptonic tag.

2.1 Inclusive measurement with Full Reconstruction 1)

In this measurement, one of the B mesons is fully reconstructed to tag the flavour and to reconstruct the momentum of the B meson. This allows a precise determination of kinematic properties of semileptonic B decay which contains a neutrino, such as the invariant mass of hadronic system, m_X or the invariant mass squared of leptonic system, q^2 . To discriminate $B \rightarrow X_u \ell \nu$ events from $B \rightarrow X_c \ell \nu$ decays while maintaining the uncertainty from the theory small, kinematic requirements are applied simultaneously to both m_X and q^2 .

In the full reconstruction tag, total of about 180 decay modes are tested to reconstruct full decay chain of the B meson. It covers about 18% of all the decay channels of B meson. The tagging efficiency is about 0.3% with purity of 50%. An event is required to have only one electron or muon with momentum in the center-of-mass (CM) frame greater than 0.6 GeV or 0.8 GeV, respectively and should satisfy $-0.2 \text{ GeV} < \Delta E < 0.05 \text{ GeV}$, where the ΔE is the difference between beam energy and the reconstructed B energy in CM frame. By fitting the beam constrained mass, m_{bc} distribution, the number of semileptonic event is extracted as $(5.07 \pm 0.04) \times 10^4$. The m_{bc} distribution of selected semileptonic events together with fitted Monte Carlo distributions are shown in Figure 1.

After applying additional selections to suppress $B \rightarrow X_c \ell \nu$ events, such as kaon vetoes or requirement on the missing mass, events are required to have q^2 greater than 8 GeV^2 . To get m_X distribution without background, m_{bc}

distributions are fitted in each m_X bins. The distribution is then fitted with two template distributions obtained from $B \rightarrow X_u \ell \nu$ and $B \rightarrow X_c \ell \nu$ Monte Carlo events to extract number of $B \rightarrow X_u \ell \nu$ events. Figure 1 shows the background subtracted m_X distributions with fitted Monte Carlo distributions. The number of $B \rightarrow X_u \ell \nu$ events in the kinematic region of $q^2 > 8 \text{ GeV}^2$ and $m_X < 1.7 \text{ GeV}$ is extracted as 171 ± 26 events after correcting the detector resolution.

The partial branching fraction, where the kinematic selection is applied, is then derived by a formula,

$$\Delta \mathcal{B}(B \rightarrow X_u \ell \nu) = \frac{N_{b \rightarrow u}}{N_{sl}} \cdot \frac{1}{\epsilon_{\text{sel}}^{b \rightarrow u}} \cdot R_{\text{sel}} \cdot \mathcal{B}(B \rightarrow X \ell \nu), \quad (1)$$

where $N_{b \rightarrow u}$ and N_{sl} are the measured numbers of $B \rightarrow X_u \ell \nu$ and semileptonic events, $\epsilon_{\text{sel}}^{b \rightarrow u}$ is the efficiency of the additional selection described above, R_{sel} is the ratio of efficiencies to select fully reconstructed semileptonic events between $B \rightarrow X_u \ell \nu$ and semileptonic decays, and $\mathcal{B}(B \rightarrow X \ell \nu)$ is the nominal semileptonic decay branching fractions²⁾. The measured partial branching fraction is then extrapolated to the total branching fraction with the relation,

$$\mathcal{B}(B \rightarrow X_u \ell \nu) = \Delta \mathcal{B}(B \rightarrow X_u \ell \nu) / f_u. \quad (2)$$

The factor f_u is obtained using the method based on the shape function scheme³⁾. The b quark shape function parameters are determined by fitting the photon energy distribution measured in the Belle $B \rightarrow X_s \gamma$ analysis,⁴⁾. The f_u is estimated to be 0.294 ± 0.044 . That yields

$$\mathcal{B}(B \rightarrow X_u \ell \nu) = (3.37 \pm 0.50 \text{ (stat.)} \pm 0.60 \text{ (syst.)} \pm 0.14 \text{ (b} \rightarrow \text{u)}) \quad (3)$$

$$\pm 0.24 \text{ (b} \rightarrow \text{c)} \pm 0.50 (f_u) \times 10^{-3}, \quad (4)$$

where the first two errors are from statistical and experimental systematics, the next two accounts for the uncertainties in the modeling of b decays, and the last error comes from the uncertainty in the calculation of the f_u .

Finally, $|V_{ub}|$ is obtained using the PDG formula²⁾,

$$|V_{ub}| = 0.00424 \left(\frac{\mathcal{B}(B \rightarrow X_u \ell \nu)}{0.002} \frac{1.61 \text{ ps}}{\tau_B} \right)^{\frac{1}{2}} \quad (5)$$

as,

$$|V_{ub}| = (5.54 \pm 0.42 \text{ (stat.)} \pm 0.50 \text{ (syst.)} \pm 0.12 \text{ (b} \rightarrow \text{u)}) \quad (6)$$

$$\pm 0.19 \text{ (b} \rightarrow \text{c)} \pm 0.42 (f_u) \pm 0.27 (\mathcal{B} \rightarrow |V_{ub}|) \times 10^{-3}, \quad (7)$$

where the last error is due to the uncertainty of the relation between \mathcal{B} and V_{ub} in equation (5).

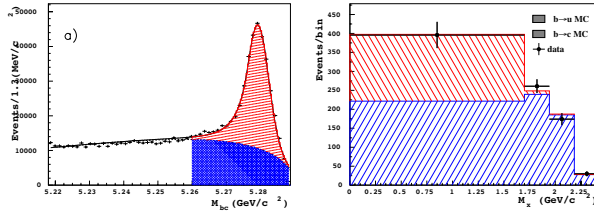


Figure 1: Left: Beam-constrained mass distribution for semioptonic decays with fully reconstructed tagging side. Right: m_X distribution for selected events with $q^2 > 8\text{GeV}^2$, Data and fitted Monte Carlo distributions.

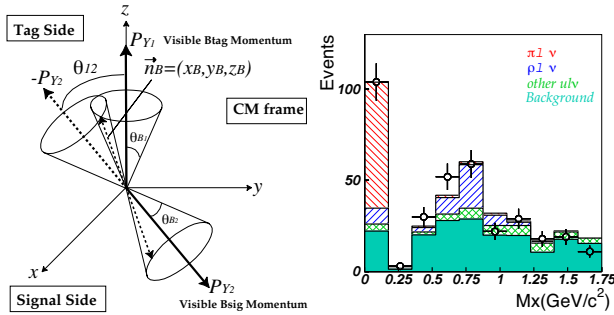


Figure 2: Left: Schematics of event kinematics of the double semileptonic decay events. Right: m_X distributions for Data and Fitted MC components.

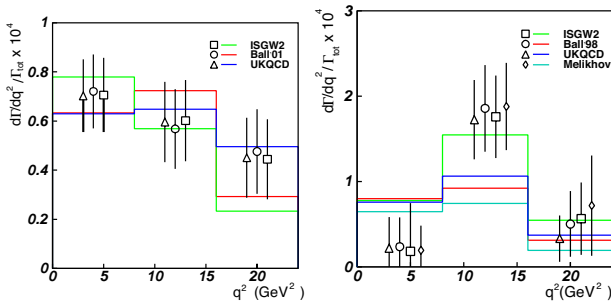


Figure 3: q^2 distribution extracted by this analysis. Left: $B \rightarrow \pi l \nu$ Right: $B \rightarrow \rho l \nu$.

2.2 Exclusive measurement using $D^{(*)}\ell\nu$ tag ⁵⁾

In this analysis the signal side is either $B \rightarrow \pi\ell\nu$ or $B \rightarrow \rho\ell\nu$. To improve the purity while maintaining the efficiency, the tag side is required to be $D^{(*)}\ell\nu$. Then a kinematic constraint of the double semileptonic decay in the CM frame is applied as in reference ⁵⁾. If an event is consistent with the double semileptonic decay, the variable defined as

$$x_B^2 \equiv 1 - \frac{1}{\sin\theta_{12}} \left(\cos^2\theta_{B_1} + \cos^2\theta_{B_2} - 2\cos\theta_{B_1}\cos\theta_{B_2}\cos\theta_{12} \right) \quad (8)$$

must range from 0 to 1 (see Figure 2). This x_B^2 is used in the fit procedure. The q^2 is calculated by neglecting the p_i of the B mesons.

The numbers of $B^0 \rightarrow \pi^-\ell^+\nu$ and $B^0 \rightarrow \rho^-\ell^+\nu$ signals are extracted simultaneously by fitting the two-dimensional x_B^2 - m_X distribution. The fit uses four components namely $B^0 \rightarrow \pi^-\ell^+\nu$, $B^0 \rightarrow \rho^-\ell^+\nu$, the other $B \rightarrow X_q\ell\nu$ events and the other B decays. Figure 2 shows the projected m_X distribution obtained by the fit.

Figure 3 shows the q^2 distributions extracted from the fit for different form factor (FF) models. Averaging the result of the fit for different FF models, the branching fractions are determined as

$$\mathcal{B}(B^0 \rightarrow \pi^-\ell^+\nu) = (1.76 \pm 0.28 \pm 0.20 \pm 0.03) \times 10^{-4} \quad \text{and} \quad (9)$$

$$\mathcal{B}(B^0 \rightarrow \rho^-\ell^+\nu) = (2.54 \pm 0.78 \pm 0.85 \pm 0.30) \times 10^{-4}, \quad (10)$$

where the errors are statistical, experimental systematic and error due to FF uncertainties, respectively. Then the $|V_{ub}|$ is derived using the relation,

$$|V_{ub}| = \sqrt{\frac{\mathcal{B}(B^0 \rightarrow \pi^-\ell^+\nu, q^2 > 16\text{GeV}^2)}{\Gamma_{\text{theo}}\tau_{B^0}}}, \quad (11)$$

where Γ_{theo} is the FF normalization predicted by Lattice QCD(LQCD) and the τ_{B^0} is the B^0 lifetime. Since the Γ_{theo} is only available for limited decay mode and for kinematic phase space, only the result for the $\pi\ell\nu$ mode with $q^2 > 16 \text{ GeV}^2$ is used to extract $|V_{ub}|$. Recently two independent results using unquenched LQCD calculations become available from two groups, FNAL04 and HPQCD. From these calculations, the $|V_{ub}|$ is calculated as,

$$|V_{ub}| = (3.87 \pm 0.70 \pm 0.22_{-0.51}^{+0.85}) \times 10^{-3} \text{ (FNAL04)}, \quad (12)$$

$$|V_{ub}| = (4.73 \pm 0.85 \pm 0.27_{-0.50}^{+0.74}) \times 10^{-3} \text{ (HPQCD)} \quad (13)$$

3 Search for $b \rightarrow d\gamma$ ⁶⁾

The $b \rightarrow d\gamma$ process is a flavour changing neutral current transition via loop diagrams in the Standard Model. It is suppressed with respect to similar $b \rightarrow s\gamma$ process by the CKM factor $|V_{td}/V_{ts}|^2 \sim 0.04$ with a large uncertainty from the poor precision of $|V_{td}|$. Here the searches for the exclusive decays $B \rightarrow \rho\gamma$ and $B \rightarrow \omega\gamma$ have been performed. These decays are also suppressed with respect to the corresponding $B \rightarrow K^*\gamma$ decay by $|V_{td}/V_{ts}|^2$. The analysis uses the data sample of 273 million B meson pairs corresponding to an integrated luminosity of 253 fb^{-1} .

After the event selection, signal yield is extracted by the unbinned maximum likelihood fit to the data in the $m_{bc}-\Delta E$ plane, simultaneously for three signal and the $B \rightarrow K^*\gamma$ modes. The results of the fit is shown in Figure 4. Since there is no significant excess in the fitted results, 90% CL upper limit is calculated as,

$$\mathcal{B}(B \rightarrow (\rho, \omega)\gamma) < 1.4 \times 10^{-6} \quad (14)$$

The significances and limits for individual decay modes are summarized in Table 1.

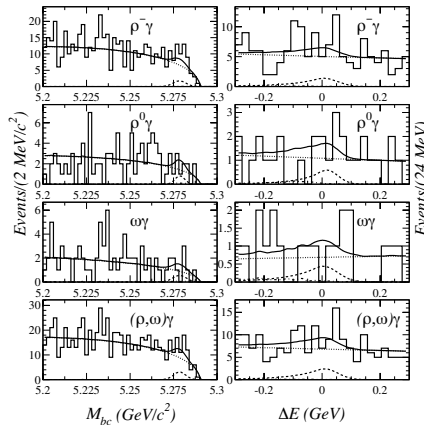


Figure 4: Projections of the simultaneous fit results to m_{bc} and ΔE .

A similar fit is performed by using the ratio of branching fractions $\mathcal{B}(B \rightarrow (\rho, \omega)\gamma)/\mathcal{B}(B \rightarrow K^*\gamma)$ so that some of the systematic errors cancel out. From the fit a limit of

$$\mathcal{B}(B \rightarrow (\rho, \omega)\gamma)/\mathcal{B}(B \rightarrow K^*\gamma) < 0.035 \text{ at } 90\% \text{ CL} \quad (15)$$

Table 1: Significance and the upper limit for branching fraction.

Mode	significance	90%CL upper limit
$B \rightarrow (\rho, \omega)\gamma$ combined	1.9	1.4×10^{-6}
$B^- \rightarrow \rho^- \gamma$	2.1	2.2×10^{-6}
$\bar{B}^0 \rightarrow \rho^0 \gamma$	0.6	0.8×10^{-6}
$\bar{B}^0 \rightarrow \omega \gamma$	0.2	0.8×10^{-6}

is obtained. from this result one can constrain $|V_{td}/V_{ts}|$ using the relation

$$\frac{\mathcal{B}(B \rightarrow (\rho, \omega)\gamma)}{\mathcal{B}(B \rightarrow K^* \gamma)} = \left| \frac{V_{td}}{V_{ts}} \right|^2 \frac{\left(1 - m_{(\rho, \omega)}^2/m_B^2\right)^3}{\left(1 - m_{K^*}^2/m_B^2\right)^3} \zeta^2 (1 + \Delta R), \quad (16)$$

where $\zeta = 0.85 \pm 0.10$ is the FF ratio and the correction factor $\Delta R = 0.1 \pm 0.1$ accounts for the $SU(3)$ breaking effect ⁷⁾. Finally the limit,

$$\left| \frac{V_{td}}{V_{ts}} \right| < 0.21 \quad (90\% \text{ CL}) \quad (17)$$

is obtained. This limit is consistent with other measurements of $|V_{td}/V_{ts}|$.

References

1. K. Abe *et al.* Belle Collaboration, "Measurement of the inclusive charmless semileptonic branching fraction of B meson using the full reconstruction tag," hep-ex/0408115.
2. K. Hagiwara *et al.*, Phys. Rev. **D66**, 010001 (2002).
3. F. De Fazio and M. Neubert, J. High Energy Phys. **9906**, 017 (1999).
4. A. Limozani and T. Nozaki (Belle Collaboration), hep-ex/0407052.
5. K. Abe *et al.* BELLE Collaboration, "Measurement of exclusive $B \rightarrow X_{ii} \ell \nu$ decays with $D^{(*)} \ell \nu$ decay tagging," hep-ex/0408145.
6. K. Abe *et al.* BELLE Collaboration, "Search for the $b \rightarrow d$ gamma process," hep-ex/0408137.
7. A. Ali, E. Lunghi, A. Parkhomenko, Phys. Lett. **B595**, 323 (2004).

**B_s OSCILLATION AND PROSPECTS
FOR Δm_s AT THE TEVATRON**

Stephanie Menzemer
Massachusetts Institute of Technology
for the CDF and D0 Collaboration

Abstract

Till the start of the LHC, the Tevatron is the only running accelerator which produces enough B_s mesons to perform Δm_s measurements. The status - as it was at the time of the conference - of two different Δm_s analysis performed both by the CDF and D0 collaboration will be presented.

1 Introduction

The Tevatron collider (Fermilab, Batavia, USA) has a huge b production rate which is 3 orders of magnitudes higher than the production rate at e^+e^- colliders running on the $\Upsilon(4S)$ resonance. Among the produced B particles there are as well heavy and excited states which are currently uniquely accessible at the Tevatron, such as for example B_s , B_c , Λ_b , θ_b , B^{**} or B_s^{**} . Dedicated triggers are able to pick 1 B event out of 1000 QCD events by selecting leptons and or events with displaced vertices already on hardware level.

The aim of the B physics program of the Tevatron experiments CDF and D0 is to provide constraint to the CKM matrix which takes advantage of the unique features of a hadron collider.

One of the flagship analysis for the Tevatron experiments is to exploit the B_s system in order to measure the mass difference (Δm_s) of the heavy and the light B_s mass eigenstate. Two different analysis were performed to access Δm_s : fitting for the B_s oscillation and measuring the lifetime difference of the heavy and light B_s mass eigenstate. The status of those will be discussed in the following.

2 Detectors and Triggers

After a 5 year shutdown with major detector and accelerator upgrade, CDF and D0 restarted data taking in March 2001.

Both the CDF and the D0 detector are symmetric multi-purpose detectors having both silicon vertex detectors, high resolution tracking in a magnetic field and lepton identification.

CDF is for the first time in an hadronic environment able to trigger already on hardware level on large track impact parameters which indicates displaced vertices (Figure 1, 2). Thus it is very powerfull in fully hadronic B modes. A Time-of-Flight system and the energy-loss measurements in the drift chamber provide particle identification. The CDF detector has a large extension of the tracking system in radial direction which provides a good mass resolution.

D0 has an excellent muon coverage and very good forward tracking which makes it very strong in J/Ψ and semileptonic modes. Additionally the good muon identification contributes significantly to the performance of the opposite side muon tagger. D0 is currently commissioning a displaced vertex trigger in order to get better access to fully reconstructed modes, too.

3 Motivation

Figure 3 shows the current status of a common fit of the CKM triangle from all measurements performed so far. The side of the unitarity triangle opposite

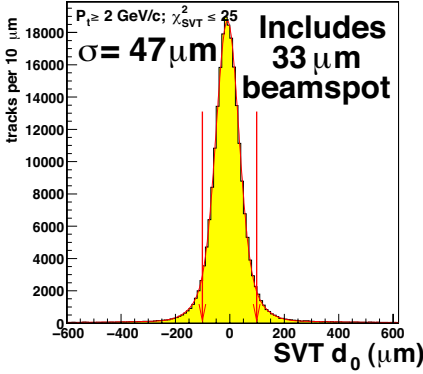


Figure 1: *Impact parameter resolution of the secondary vertex trigger (CDF).*

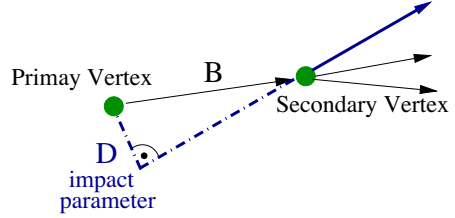


Figure 2: *Sketch of the impact parameter of tracks from secondary vertex.*

to the angle γ is determined by the measurement of the mass difference of the B_d system, Δm_d , and the lower limits on Δm_s . The length of this side is proportional to the CKM matrix-elements $|V_{td}V_{tb}^*|$. The angle γ and $|V_{td}V_{tb}^*|$ are the less well determined quantities of the triangle, thus measuring them is crucial to test its unitarity. While the determination of $|V_{td}V_{tb}^*|$ from Δm_d suffers from large theoretical uncertainties a lot of them cancel in studying $\Delta m_d/\Delta m_s$. A measurement of this ratio would determine the related CKM elements with 5 % uncertainty only (e.g. see the hatched area in Figure 3).

The range for Δm_s predicted by the Standard Model is $\Delta m_s \leq 24 \text{ ps}^{-1}$ while all Standard Model extensions predict a larger value of at least 30 ps^{-1} . Thus the measurement of Δm_s provides a handle to either confirm the Standard Model or to find evidence for New Physics beyond the Standard Model.

Two different analysis measuring/constraining Δm_s are uniquely able to be performed at the Tevatron. The first one is the B_s mixing analysis ($\mathcal{A}(t) \sim \mathcal{D} \times \cos(\Delta m_s t)$) which is especially sensitive to lower Δm_s values. The second one is the measurement of the B_s decay width difference $\Delta \Gamma_s$, which is related to Δm_s (in the Standard Model) via the theoretical very clean relation:

$$\frac{\Delta m_s}{\Delta \Gamma_s} \approx \frac{2}{3\pi} \frac{m_t^2}{m_b^2} \left(1 - \frac{8}{3} \frac{m_c^2}{m_b^2}\right)^{-1} h\left(\frac{m_t^2}{M_W^2}\right) \quad (1)$$

This measurement is at the Tevatron sensitive to high values of Δm_s .

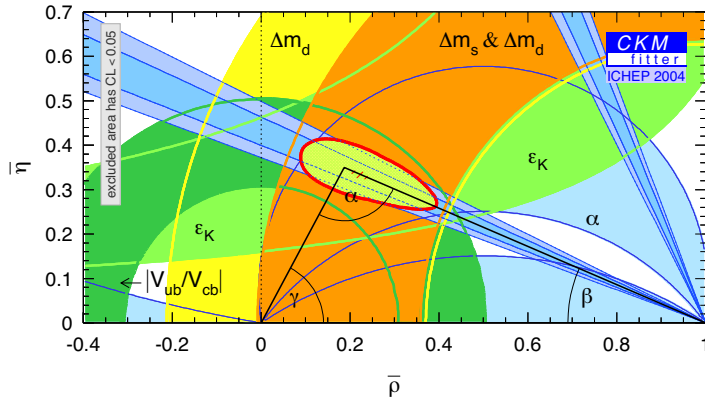


Figure 3: Status of the fit for the CKM triangle at the time of the XIX Rencontres de Physics.

4 $\Delta\Gamma$ Measurement in $B_s \rightarrow J/\Psi\phi$

In order to measure the decay width difference $\Delta\Gamma_s$ we need to disentangle the heavy and light B_s mass eigenstates and measure their lifetimes separately. In the B_s system CP violation is supposed to be small ($\delta\phi_s \approx 0$). Thus the heavy and light B_s mass eigenstates directly correspond to the CP even and CP odd eigenstates. So the separation of the B_s mass eigenstates can be done by identifying the CP even and CP odd contributions.

Generally final states are mixtures of CP even and odd states, but for pseudoscalar particles such as the B_s decaying into two vector particles such as the J/Ψ and the ϕ it is possible to disentangle the CP even and CP odd eigenstates by an angular analysis. The decay amplitude decomposes into 3 linear polarization states with the amplitudes A_0 , $A_{||}$ and A_{\perp} with

$$|A_0|^2 + |A_{||}|^2 + |A_{\perp}|^2 = 1. \quad (2)$$

A_0 and $A_{||}$ correspond to the S and D wave and are therefore the CP even contribution, while A_{\perp} corresponds to the P wave and thus to the CP odd component.

Fitting at the same time for the angular distributions and for the lifetimes it is possible to measure the lifetimes of the heavy and light B_s mass eigenstate.

A similar angular analysis has been already performed by the BABAR and BELLE collaboration in the $B_d \rightarrow J/\Psi K^{*0}$ mode. This mode has as well been studied at the Tevatron as a cross check for the $B_s \rightarrow J/\Psi\phi$ analysis (Figure 4).

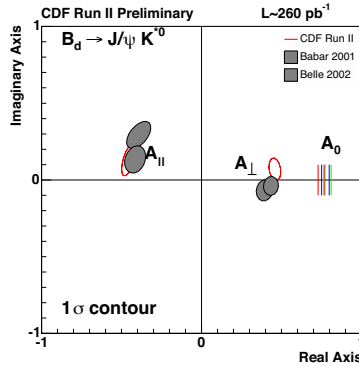


Figure 4: Angular analysis of the $B_d \rightarrow J/\Psi K^{*0}$ mode. BABAR, BELLE and CDF results are in good agreement.

In order to perform this analysis first of all a $B_s \rightarrow J/\Psi\phi$ signal has to be established. Both experiments have measured the B_s mass and lifetime (Figure 5, 6) and obtain the following results, where the lifetime τ_s is measured with respect to τ_d from the topological similar decay $B_d \rightarrow J/\Psi K^{*0}$:

$$M(B_s) = 5360 \pm 5 \text{ MeV}/c^2 \text{ (D0)} \tag{3}$$

$$M(B_s) = 5366.01 \pm 0.73(\text{stat}) \pm 0.033(\text{syst}) \text{ MeV}/c^2 \text{ (CDF)} \tag{4}$$

$$\tau_s/\tau_d = 0.980^{+0.075}_{-0.070}(\text{stat}) \pm 0.0003(\text{syst}) \text{ (D0)} \tag{5}$$

$$\tau_s/\tau_d = 0.980 \pm 0.072(\text{tot}) \text{ (CDF)} \tag{6}$$

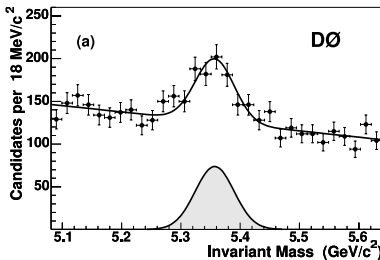


Figure 5: Mass of $B_s \rightarrow J/\Psi\phi$ candidates from D0.

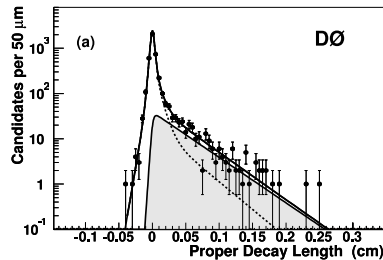


Figure 6: Average lifetime of $B_s \rightarrow J/\Psi\phi$ candidates from D0.

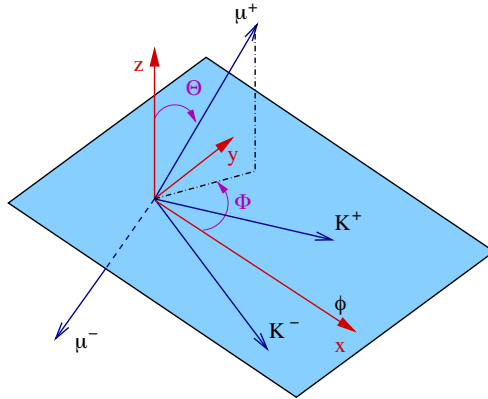


Figure 7: Definition of the transversity frame and the transversity angles.

The angular analysis has been performed in the transversity basis in the J/Ψ rest-frame which is introduced in Figure 7. The both kaons of the ϕ decay define the x-y plane, the flight direction of the ϕ defines the positive x-axis and the positively charged kaon the positive y-axis. The flight direction of the positively charged muon of the J/Ψ decay defines the positive z-axis. The angles used in this analysis are θ and Φ , the polar and azimuthal angle of the μ^+ and Ψ the helicity angle of the ϕ .

The fit projections of the common fit of the both lifetimes and the angular distributions for the CDF and for the D0 analysis are shown in Figure 8.

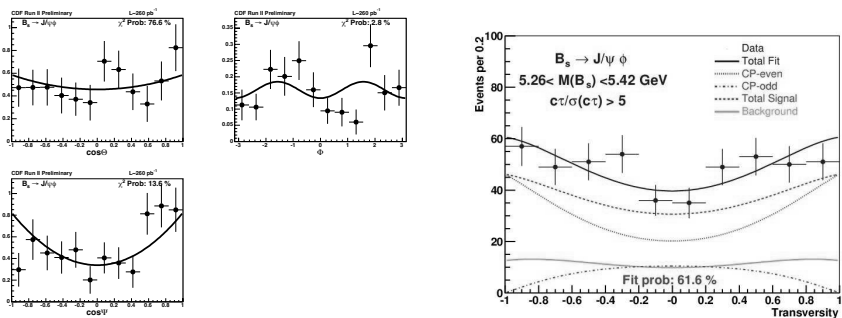


Figure 8: Fit projections of the common fit of the angular distribution in the transversity frame and the two different B_s lifetimes, CDF (left), D0 (right).

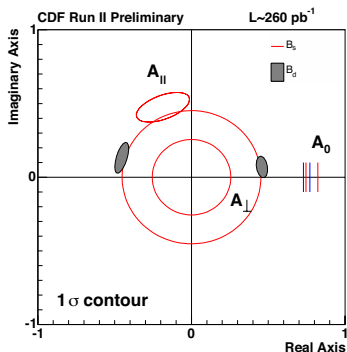


Figure 9: *Fit result of the angular amplitudes of the $B_s \rightarrow J/\Psi\phi$ and $B_d \rightarrow J/\Psi K^{*0}$ decays (CDF).*

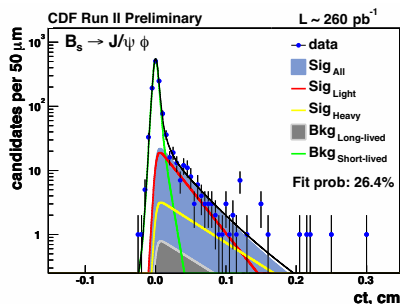


Figure 10: *Fit projections of the common fit of the lifetime and angular distribution in the transversity frame (CDF).*

The following results are obtained by the CDF analysis ¹⁾ (Figure 9, 10):

$$|A_{\perp}| = 0.354 \pm 0.098 \pm 0.003 \quad (7)$$

$$A_0 = 0.784 \pm 0.039 \pm 0.007 \quad (8)$$

$$\tau_L = 1.05^{+0.16}_{-0.13} \pm 0.02 ps \quad (9)$$

$$\tau_H = 2.07^{+0.58}_{-0.40} \pm 0.03 ps \quad (10)$$

$$\Delta\Gamma/\Gamma = 0.65^{+0.25}_{-0.33} \pm 0.01 \quad (11)$$

$$\Delta\Gamma = 0.47^{+0.19}_{-0.24} \pm 0.01 ps^{-1} \quad (12)$$

With about 200 signal events CDF finds a large value for the lifetime difference which is about 2.5σ way from being zero and about 2σ away from the Standard Model predictions of $\Delta\Gamma_s/\Gamma_s = 0.12$. The CDF results favors high values of Δm_s but is currently statistically limited. The systematic uncertainties are very small thus this is a beautiful measurement ones more data is available. The D0 result of this analysis was on the way but not yet available at the time of this conference. It can be found in ²⁾.

5 B Mixing

The dominant Feynman diagrams describing the mixing processes are shown in Figure 11. The probability that a B meson decays at proper time t and has

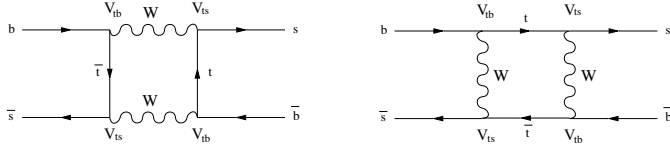


Figure 11: *Feynman diagrams for dominant B_s mixing processes.*

or has not already mixed to the \bar{B} state is given by:

$$P_{unmix}(t) \approx \frac{1}{2}(1 + \cos \Delta mt), \quad (13)$$

$$P_{mix}(t) \approx \frac{1}{2}(1 - \cos \Delta mt). \quad (14)$$

The canonical B mixing analysis, in which oscillations are observed and the mixing frequency, Δm , is measured, proceeds as follows. The B meson flavor at the time of its decay is determined by exclusive reconstruction of the final state. The proper time, $t = m_B L / pc$, at which the decay occurred is determined by measuring the decay length, L , and the B momentum, p . Finally the production flavor must be tagged in order to classify the decay as being mixed or unmixed at the time of its decay.

Oscillation manifests itself in a time dependence of, for example, the mixed asymmetry:

$$\mathcal{A}_{mix}(t) = \frac{N_{mixed}(t) - N_{unmixed}(t)}{N_{mixed}(t) + N_{unmixed}(t)} = -\cos \Delta mt \quad (15)$$

In practice, the production flavor will be correctly tagged with a probability P_{tag} which is significantly smaller than one but larger than one half (which corresponds to a random tag). The measured mixing asymmetry in terms of dilution, \mathcal{D} , is

$$\mathcal{A}_{mix}^{meas}(t) = \mathcal{D} \mathcal{A}_{mix} = -\mathcal{D} \cos \Delta mt \quad (16)$$

where $\mathcal{D} = 2P_{tag} - 1$.

Figure 12 illustrates the mixed asymmetry for $\Delta m_d = 0.5 \text{ ps}^{-1}$ and for a fictive Δm_s value of 20 ps^{-1} , which is within the Standard Model expectations. This clearly demonstrates the need for good proper decay time resolution in order to resolve such a high Δm_s mixing frequency.

The second important ingredient for a mixing analysis is the flavor tagging. As the examined decays are flavor specific modes the decay flavor can be determined via the decay products. But for the production flavor additional

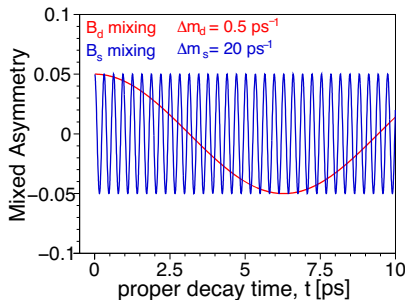


Figure 12: *Example of mixed asymmetry for a B_d like and a fictive B_s like mixing frequency with a dilution $\mathcal{D} = 5\%$.*

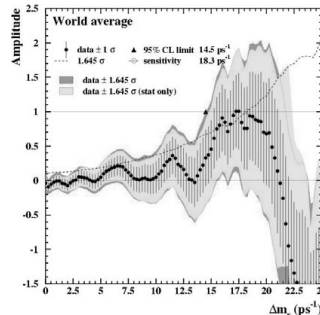


Figure 13: *World average of the current B_s mixing analysis.*

information from the event has to be evaluated in order to tag the event. A good and well measured tagging performance is needed to set a limit on Δm_s . The last component are the B_s candidates. Sufficient statistic is needed to be sensitive to high mixing frequencies.

Figure 13 shows the current status of the B_s mixing measurement. The world average for the mass difference Δm_s is 14.5 ps^{-1} @ 95% CL which is a combination of 13 measurements from LEP, SLD and CDF I.

5.1 Flavor Tagging

There are two different kinds of flavor tagging algorithms, opposite side tagging (OST) and same side tagging (SST), which are illustrated in Figure 14. OST algorithms use the fact that b quarks are mostly produced in $b\bar{b}$ pairs, therefore the flavor of the second (opposite side) b can be used to determine the flavor of the b quark on the signal side.

5.1.1 Jet-Charge Tagging

The average charge of an opposite side b -jet is weakly correlated to the charge of the opposite b quark and can thus be used to determine the opposite side b flavor. The main challenge of this tagger is to select the b -jet. Information of a displaced vertex or displaced tracks in the jet help to identify b -jets. This tagging algorithm has a very high tagging efficiency but the dilution is relatively

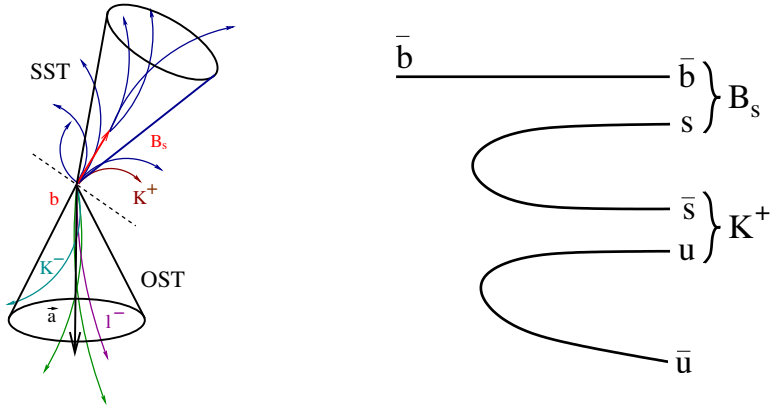


Figure 14: *Left: Sketch of different tagging algorithms; Right: Same-side kaon tagging.*

low. By separating sets of tagged events of different qualities e.g. how b like the jet is, it is possible to increase the overall tagging performance.

5.1.2 Soft-Lepton-Tagging

In 20 % of cases the opposite b decays semileptonically either into an electron or a muon ($b \rightarrow l^- X$). The charge of the lepton is correlated to the charge of the decaying B meson. Depending on the type of the B meson there is a certain probability of oscillation between production and decay (0 % for B^\pm , 17.5 % for B_d and 50 % for B_s). Therefore this tagging algorithm already contains an intrinsic dilution. Another potential source of miss-tag is the transition of the b quark into a c quark which then forms a D meson and subsequently decays semileptonically ($\bar{b} \rightarrow \bar{c} \rightarrow l^- X$). Due to the different decay length and momentum distribution of B and D meson decays this source of miss-tag can mostly be eliminated.

5.1.3 Kaon-Tagging

Due to the transition chain $b \rightarrow c \rightarrow s$ it is more likely that a \bar{B} meson contains a K^- than a K^+ in the final state. Therefore a K^- on the opposite side is a hint, that there was a \bar{b} quark on the signal side. This tagging algorithm heavily relies on the kaon identification power and the capability of separating kaons from the fragmentation by kaons from the opposite B decay by a good vertex resolution. At the moment non of the both Tevatron experiments use an opposite side kaon tagger.

ϵD^2 (%)	CDF semileptonic channels	D0
SST(B_d)	$1.04 \pm 0.35 \pm 0.06$	1.00 ± 0.36
Soft μ	0.56 ± 0.05	1.00 ± 0.38
Soft e	0.29 ± 0.03	-
Jet-Q	0.57 ± 0.06	~ 1 (measured combined with SST)

Table 1: *Tagger performance of the CDF and D0 experiments as measured on semileptonic B_d and B_u samples.*

5.1.4 Same-Side-Tagging

During fragmentation and the formation of the $B_{s/d}$ meson there is a left over \bar{s}/\bar{d} quark which is likely to form a K^+/π^+ (Figure 14). So if there is a nearby charged particle, which is additionally identified as a kaon/pion, it is quite likely that it is the leading fragmentation track and its charge is then correlated to the flavor of the $B_{s/d}$ meson. While the performance of the opposite side tagger does not depend on the flavor of the B on the signal side the SST performance heavily depends on the signal fragmentation processes. Therefore the opposite side performance can be measured in B_d mixing and can then be used for setting a limit on the B_s mixing frequency. But for using the SST for a limit on Δm_s we have to heavily rely on Monte Carlo simulation. The SST potentially has the best tagger performance, but before using it for a limit, fragmentation processes have to be carefully understood.

5.2 Δm_d Measurement and Calibration of Taggers

For setting a limit on Δm_s the knowledge of the tagger performance is crucial. Therefore it has to be measured in kinematically similar B_d and B^+ samples.

The Δm_s and Δm_d analysis is a complex fit with up to 500 parameters which combine several B flavor and several decay modes, various different taggers and deals with complex templates for mass and lifetime fits for various sources of background. Therefore the measurement of Δm_d is beside the calibration of the opposite side taggers very important to test and trust the fitter framework although the actual Δm_d result at the Tevatron is not competitive with the B factories.

D0 measured Δm_d applying combined opposite and same side taggers in semileptonic decay channels with 250 pb^{-1} of data and obtained ³⁾

$$\Delta m_d = 0.456 \pm 0.034 \text{ (stat)} \pm 0.025 \text{ (syst)} \text{ ps}^{-1} \quad (17)$$

CDF performed two measurements using opposite side taggers only based on

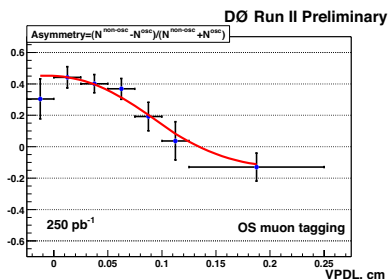
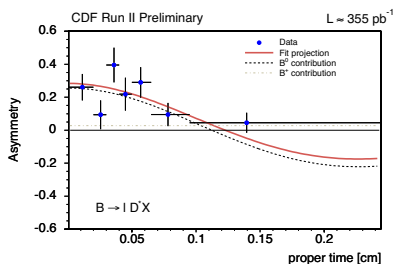


Figure 15: *Asymmetry fit projection for Δm_d using opposite side muon tagger in semileptonic decays (CDF).* Figure 16: *Asymmetry fit projection for Δm_d using opposite side muon tagger in semileptonic decays (D0).*

semileptonic ⁴⁾ and hadronic channels ⁵⁾ respectively using 355 pb^{-1} of data:

$$\Delta m_d = 0.497 \pm 0.028 \text{ (stat)} \pm 0.015 \text{ (sys)} \text{ ps}^{-1} \text{ (semileptonic)} \quad (18)$$

$$\Delta m_d = 0.503 \pm 0.063 \text{ (stat)} \pm 0.015 \text{ (sys)} \text{ ps}^{-1} \text{ (hadronic)} \quad (19)$$

An example of the fitted asymmetry using the opposite side muon tagger on the semileptonic decay modes is displayed in Figures 15, 16. The measured tagging performances are listed in Table 1.

5.3 Amplitude Scan

An alternative method for studying neutral B meson oscillations is the so called “amplitude scan”, which is explained in detail in Reference ⁶⁾. The likelihood term describing the tagged proper decay time of a neutral B meson is modified by including an additional parameter multiplying the cosine; the so-called amplitude A .

The signal oscillation term in the likelihood of the Δm thus becomes

$$\mathcal{L} \propto \frac{1 \pm AD \cos(\Delta mt)}{2} \quad (20)$$

The parameter A is left free in the fit while \mathcal{D} is supposed to be known and fixed in the scan. The method involves performing one such A -fit for each value of the parameter Δm , which is fixed at each step; in the case of infinite statistics, optimal resolution and perfect tagger parameterization and calibration, one would expect A to be unit for the true oscillation frequency and zero for the remaining of the probed spectrum. In practice, the output

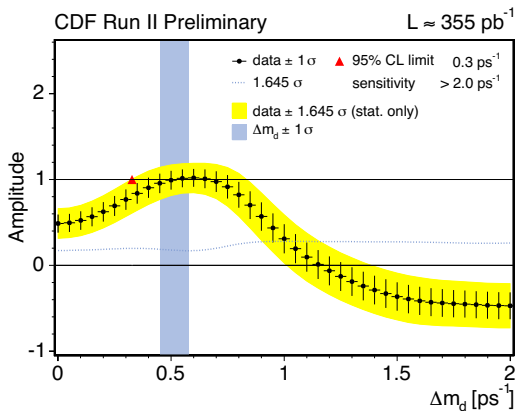


Figure 17: Amplitude scan for Δm_d in hadronic decay modes (CDF). The scan is compatible with 1 around the result of the actual Δm_d fit.

of the procedure is accordingly a list of fitted values (A , σ_A) for each Δm hypothesis. Such a Δm hypothesis is excluded to a 95% confidence level in case the following relation is observed,

$$A + 1.645 \cdot \sigma_A < 1$$

The sensitivity of a mixing measurement is defined as the lowest Δm value for which $1.645 \cdot \sigma_A = 1$.

The amplitude method will be employed in the ensuing B_s mixing analysis. One of its main advantages is the fact that it allows easy combination among different measurements and experiments.

The plot shown in Figure 17 is obtained when the method is applied to the hadronic B_d samples of the CDF experiment, using the exclusively combined opposite side tagging algorithms. The expected compatibility of the measured amplitude with unit in the vicinity of the true frequency, $\Delta m_d = 0.5 \text{ ps}^{-1}$, is confirmed.

However, we observe the expected increase in the amplitude uncertainty for higher oscillation frequency hypotheses. This is equivalent to saying that the significance is reduced with increasing frequency.

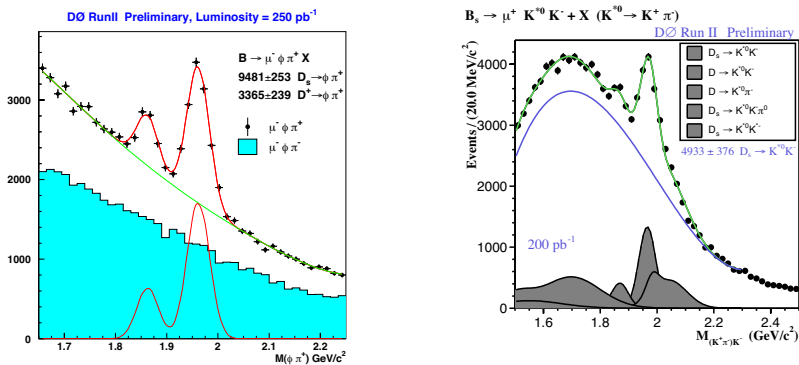


Figure 18: Reconstructed semileptonic B_s decays for Δm_s analysis ($D0$).

5.4 Reconstructed B_s Decays

$D0$ exploits the high statistics muon trigger to study semileptonic B_s decays. About 10,000 B_s candidates have been reconstructed in the $B_s \rightarrow \mu X D_s$, ($D_s \rightarrow \phi \pi$) mode in 250 pb^{-1} of data. Additionally 5,000 B_s candidates were reconstructed when $D_s \rightarrow K^{*0} K$, ($K^{*0} \rightarrow K \pi$) decays were added (Figure 18).

Due to the missing neutrino the B_s momentum in semileptonic decays is not fully reconstructed. Thus a correction factor obtained from Monte Carlo simulation (K factor) has to be introduced in order to extract the proper decay time of the B_s meson.

$$c\tau = \frac{L_{xy} * M(B)}{p_T(B)} = \frac{L_{xy} * M(B)}{p_T(\ell D)} * K \quad (21)$$

This introduced an additional uncertainty on the proper decay time. The maximal reach of sensitivity of the B_s mixing for semileptonic modes is limited by the proper decay time resolution.

$D0$ is currently working on reconstructing fully hadronic B_s decays on the non trigger side in this sample and profiting from the trigger muon as opposite side muon tag.

CDF performs the B_s mixing analysis using both fully reconstructed B_s decays ($B_s \rightarrow D_s \pi$) obtained by the two track trigger and semileptonic decays ($B_s \rightarrow \ell X D_s$) collected in the lepton+displaced track trigger (Figure 19). In both cases the D_s is reconstructed in the $D_s \rightarrow \phi \pi$, $D_s \rightarrow K^{*0} K$ and $D_s \rightarrow \pi \pi \pi$ modes. Altogether those are about 700 hadronic and 8000 semileptonic B_s candidates in 355 pb^{-1} of data. The proper modelling of the background

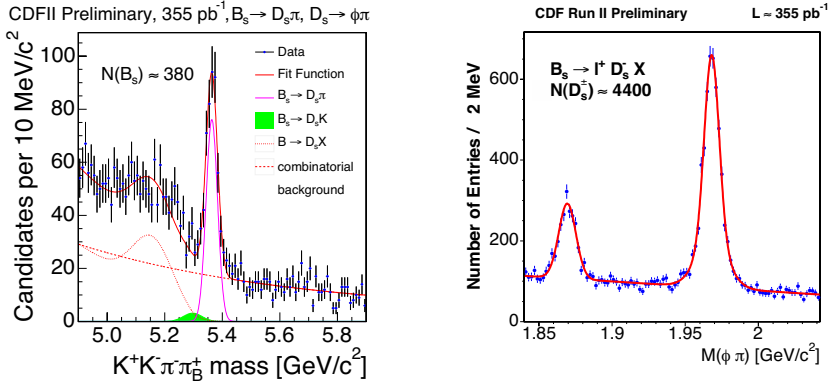


Figure 19: Reconstructed B_s decays for Δm_s analysis (CDF) in the $D_s \rightarrow \phi\pi$ mode.

especially in the hadronic modes from reflections and partial reconstructed B candidates is one of the challenges on the way to the B_s mixing analysis. For the semileptonic decays the background including a real D_s meson is hard to reject and to measure and thus is the largest source of systematic uncertainties, although the mixing analysis is by far dominated by the statistic uncertainties.

The results of the B_s mixing analysis from both experiments, CDF and D0, using those decays were not ready in time for this conference, but they have been presented a few days later and can be found in 8), 7).

For the first time in RUN II CDF and D0 have performed a Δm_s mixing analysis, which is a very complex measurement. We have proven to be able to do it and further improvements are expected, e.g. by adding additional decay modes and by using same side tagging.

6 Conclusion

Two different analysis to measure Δm_s have been presented, which are performed both by the CDF and D0 collaboration. The measurement of the decay width difference $\Delta\Gamma_s$ of the heavy and light B_s mass eigenstate is especially sensitive to high Δm_s values. The B_s mixing analysis is sensitive to lower values. Together they have the potential to cover the whole range of possible Δm_s values in the Standard Model and as well beyond. Those analysis currently suffer from lack of statistics, but their principle feasibility has been demonstrated, thus we expect soon to get further constraints on Δm_s from the Tevatron experiments.

7 Acknowledgments

I would like to thank the organizers Giorgio Bellettini, Giorgio Chiarelli and Mario Greco for a very enjoyable conference.

References

1. The CDF Collaboration, Phys. Rev. Lett. **94** (2005) 101803, hep-ex/0412057
2. The D0 Collaboration, <http://www-d0.fnal.gov/Run2Physics/WWW/results/prelim/B/B17>
3. The D0 Collaboration, <http://www-d0.fnal.gov/Run2Physics/WWW/results/prelim/B/B15>
4. The CDF Collaboration, <http://www-cdf.fnal.gov/physics/new/bottom/050224blessed-mix-bld>
5. The CDF Collaboration, <http://www-cdf.fnal.gov/physics/new/bottom/050224.blessed-hadr-ost>
6. H.G. Moser, A.Roussrie, *Mathematical methods for $B^0\bar{B}^0$ oscillation analysed*, NIM A384 (1997), 491-505
7. The CDF Collaboration, <http://www-cdf.fnal.gov/physics/new/bottom/050310.bsmix-combined>
8. The D0 Collaboration, <http://www-d0.fnal.gov/Run2Physics/WWW/results/prelim/B20>

HOW LARGE ARE CP EFFECTS PRODUCED BY DIFFERENT MECHANISMS OF CP VIOLATION IN $K^\pm \rightarrow 3\pi$ DECAYS

E. Shabalin

*Institute for Theoretical and Experimental Physics,
B. Chermushkinskaya 25, Moscow, Russia*

Abstract

The CP-odd difference of the slope parameters $\Delta g = (g^+ - g^-)/(g^+ + g^-)$ characterising the energy distributions of "odd" pions in $K^\pm \rightarrow 3\pi$ decays is studied. For $K^\pm \rightarrow \pi^0\pi^0\pi^\pm$ decays, Δg is expressed through the known experimental characteristics of $K \rightarrow 2\pi$ decays and is fixed around $2 \cdot 10^{-6}$. But for $K^\pm \rightarrow \pi^\pm\pi^\pm\pi^\mp$ decays, where the electroweak penguin contributions increase the QCD penguin contribution, Δg could be one order larger.

1 Introduction

The Collaboration NA48/2 at CERN looks now for CP-odd difference in energy distributions of "odd" pions in decays

$$\begin{aligned} K^\pm &\rightarrow \pi^\pm \pi^\pm \pi^\mp && (\tau\text{-decay}) \\ K^\pm &\rightarrow \pi^0 \pi^0 \pi^\pm && (\tau'\text{-decay}) \end{aligned} \quad (1)$$

This difference is characterised by the parameters g_τ^\pm , $g_{\tau'}^\pm$ defined by the relations

$$|M(K^\pm(k) \rightarrow \pi^\pm(p_1)\pi^\pm(p_2)\pi^\mp(p_3))|^2 \sim 1 + g_\tau^\pm Y + \dots \quad (2)$$

$$|M(K^\pm(k) \rightarrow \pi^0(p_1)\pi^0(p_2)\pi^\pm(p_3))|^2 \sim 1 + g_{\tau'}^\pm Y + \dots \quad (3)$$

where

$$Y = (s_3 - s_0)/m_\pi^2, \quad s_3 = (k - p_3)^2, \quad s_0 = \frac{1}{3}m_K^2 + m_\pi^2. \quad (4)$$

The difference is generated in Standard Model (SM) by the complex coupling constants figurating in so-called QCD penguin (QCDP) diagrams and electroweak penguin (EWP) diagrams. For some observables, in particular, for ε' in $K^0 \rightarrow 2\pi$ decays, the QCDP and EWP contributions are of opposite signs that leads to considerable decrease of this parameter [1]. There were many attempts to calculate QCDP and EWP contributions, but they gave ε' with an uncertainty of order ten

$$few \cdot 10^{-4} \leq \varepsilon'/\varepsilon \leq few \cdot 10^{-3} \quad (5)$$

Now, when ε' is measured and known with 15% accuracy

$$\varepsilon'/\varepsilon = (1.67 \pm 0.26)10^{-3} \quad (6)$$

it becomes to be possible to clear up the individual role of QCDP and EWP in *direct* CP violation. It may be done measuring the quantities

$$\Delta g_\tau = \frac{g_\tau^+ - g_\tau^-}{g_\tau^+ + g_\tau^-}, \quad \Delta g_{\tau'} = \frac{g_{\tau'}^+ - g_{\tau'}^-}{g_{\tau'}^+ + g_{\tau'}^-} \quad (7)$$

in $K^\pm \rightarrow 3\pi$ decays.

It will be shown that EWP increases Δg_τ and decreases $\Delta g_{\tau'}$, and what's more, $\Delta g_{\tau'}$ turns out to be proportional practically to the same combination of QCDP and EWP contributions as for ε' ! Then, $\Delta g_{\tau'}$ becomes fixed and the separate contributions of QCDP and EWP may be evaluated from $\Delta g_\tau/\Delta g_{\tau'}$.

Our analysis is based on employment of the effective $\Delta S = 1$ non-leptonic lagrangian in the form proposed in [2]:

$$L(\Delta S = 1) = \sqrt{2}G_F \sin \theta_C \cos \theta_C \sum c_i O_i \tag{8}$$

where O_{1-6} are the 4-quark operators represented in [2] and

$$O_7 = \frac{3}{2} \bar{s} \gamma_\mu (1 + \gamma_5) d \left(\sum_{q=u,d,s} e_q \bar{q} \gamma_\mu (1 - \gamma_5) q \right) \tag{9}$$

$$O_8 = -12 \sum_{q=u,d,s} e_q (\bar{s}_L q_R) (\bar{q}_R d_L), \quad e_q = \left(\frac{2}{3}, -\frac{1}{3}, -\frac{1}{3} \right) \tag{10}$$

The bosonization may be carried out using the relations [3]:

$$\bar{q}_j (1 + \gamma_5) q_k = -\frac{F_\pi r}{\sqrt{2}} \left[U - \frac{1}{\Lambda^2} \partial^2 U \right]_{kj} \tag{11}$$

$$\bar{q}_j \gamma_\mu (1 + \gamma_5) q_k = i [\partial_\mu U \cdot U^\dagger - U \cdot \partial_\mu U^\dagger - \frac{F_\pi r}{\sqrt{2}} (m \partial_\mu U^\dagger - \partial_\mu U m)]_{kj} \tag{12}$$

where

$$r = \frac{2m_\pi^2}{(m_u + m_d)}, \quad \Lambda \approx 1 \text{ GeV}, \quad F_\pi = 93 \text{ MeV}, \quad m = \text{diag}\{m_u, m_d, m_s\}$$

$$U = \frac{F_\pi}{\sqrt{2}} \exp(i\sqrt{2}\hat{\pi}/F_\pi) \tag{13}$$

where $\hat{\pi}$ is 3×3 matrix of pseudoscalar fields.

Using this technics and representing the matrix elements $M(K \rightarrow 2\pi)$ in the form

$$\begin{aligned} M(K_1^0 \rightarrow \pi^+ \pi^-) &= A_0 e^{i\delta_0} - A_2 e^{i\delta_2} \\ M(K_1^0 \rightarrow \pi^0 \pi^0) &= A_0 e^{i\delta_0} + 2A_2 e^{i\delta_2} \\ m(K^+ \rightarrow \pi^+ \pi^0) &= -\frac{3}{2} A_2 e^{i\delta_2} \end{aligned} \tag{14}$$

we obtain

$$A_0 = \kappa \left[c_1 - c_2 - c_3 + \frac{32}{9} \beta (\Re \tilde{c}_5 + i \Im \tilde{c}_5) \right] \tag{15}$$

$$A_2 = \kappa \left[c_4 + i \frac{2}{3} \beta \Lambda^2 \Im \tilde{c}_7 (m_K^2 - m_\pi^2)^{-1} \right] \tag{16}$$

where

$$\kappa = G_F F_\pi \sin \theta_C \cos \theta_C \frac{m_K^2 - m_\pi^2}{\sqrt{2}}, \quad \beta = \frac{2m_\pi^4}{\Lambda^2 (m_u + m_d)^2},$$

$$\tilde{c}_5 = c_5 + \frac{3}{16}c_6, \quad \tilde{c}_7 = c_7 + 3c_8.$$

As $\tilde{c}_7/\tilde{c}_5 \sim \alpha_{em}$, we have neglected EWP contribution to A_0 .

From data on $K \rightarrow 2\pi$ rates one obtains [4]:

$$c_4 = 0.328, \quad c_1 - c_2 - c_3 + \frac{32}{9}\beta\Re\tilde{c}_5 = -10.13.$$

At $c_1 - c_2 - c_3 = -2.89$ [2],[5]

$$\frac{32}{9}\beta\Re\tilde{c}_5 = -7.24.$$

Using the general relation

$$\varepsilon' = ie^{i(\delta_2 - \delta_0)} \left[-\frac{\Im A_0}{\Re A_0} + \frac{\Im A_2}{\Re A_2} \right] \cdot \left| \frac{A_2}{A_0} \right| \quad (17)$$

and the experimental value of ε' , we obtain [6]:

$$\beta\Im\tilde{c}_5 \left(1 + \frac{24.36}{1 - \Omega} \frac{\Im\tilde{c}_7}{\Im\tilde{c}_5} \right) = \frac{3.32(1 \pm 0.15)10^{-4}}{1 - \Omega}, \quad (18)$$

where Ω takes into account $K \rightarrow \pi^0\eta(\eta') \rightarrow \pi^0\pi^0$ transitions. A magnitude of the above quantity will allow to fix $\Delta g_{\tau'}$.

2 $K^\pm \rightarrow 3\pi$ decays

Applying the same technics and taking into account an appearance of CP-even imaginary parts due to the strong $\pi\pi$ rescattering, we find in leading p^2 approximation:

$$M(K^\pm(k) \rightarrow \pi^\pm(p_1)\pi^\pm(p_2)\pi^\mp(p_3)) = \tilde{\kappa}[1+ia + \frac{1}{2}g_\tau Y(1+ib^\tau \pm i(b_{KM}^\tau - a_{KM}^\tau) + \dots)] \quad (19)$$

$$M(K^\pm(k) \rightarrow \pi^0(p_1)\pi^0(p_2)\pi^\pm(p_3)) = \frac{\tilde{\kappa}}{2}[1+ia + \frac{1}{2}g_{\tau'} Y(1+ib^{\tau'} \pm i(b_{KM}^{\tau'} - a_{KM}^{\tau'}) + \dots)] \quad (20)$$

where a , b^τ , $b^{\tau'}$ are the CP-even imaginary parts having the same sign for K^+ and K^- mesons. $a_{KM}^{\tau, \tau'}$, $b_{KM}^{\tau, \tau'}$ are the CP-odd imaginary parts produced by Kobayashi-Maskawa phase and having the opposite signs for K^+ and K^- mesons.

For $K^\pm \rightarrow \pi^\pm\pi^\pm\pi^\mp$ [6].

$$\begin{aligned} a_{KM}^\tau &= \left[\frac{32}{9}\beta\Im\tilde{c}_5 + 4\beta\Im\tilde{c}_7 \left(\frac{3\Lambda^2}{2m_K^2} + 2 \right) \right] / c_0, \\ b_{KM}^\tau &= \left[\frac{32}{9}\beta\Im\tilde{c}_5 + 8\beta\Im\tilde{c}_7 \right] / (c_0 + 9c_4), \\ a &= 0.12, \quad b^\tau = 0.71, \quad g_\tau = -\frac{3m_\pi^2}{m_K^2} \left(1 + \frac{9c_4}{c_0} \right), \\ c_0 &= c_1 - c_2 - c_3 - c_4 + \frac{32}{9}\beta\Re\tilde{c}_5 = -10.46. \end{aligned} \quad (21)$$

For $K^\pm \rightarrow \pi^0 \pi^0 \pi^\pm$ [7].

$$\begin{aligned} a_{KM}^{\tau'} &= \left[\frac{32}{9} \beta \Im \tilde{c}_5 + \frac{6\beta \Lambda^2 \Im \tilde{c}_7}{m_K^2} \right] / c_0, \\ b_{KM}^{\tau'} &= \left[\frac{32}{9} \beta \Im \tilde{c}_5 + \frac{3\beta \Lambda^2 \Im \tilde{c}_7}{m_K^2 - m_\pi^2} \right] / (c_0 - \frac{9c_4}{2}), \\ b^{\tau'} &= 0.49, \quad g_{\tau'} = \frac{6m_\pi^2}{m_K^2} (1 - \frac{9c_4}{2c_0}). \end{aligned} \tag{22}$$

It follows from our formulae that

$$\Delta g_{\tau'} = (g_{\tau'}^+ - g_{\tau'}^-) / (g_{\tau'}^+ + g_{\tau'}^-) = a(b_{KM}^{\tau'} - a_{KM}^{\tau'}) / (1 + ab^{\tau'}). \tag{23}$$

Replacing τ' by τ , one obtains Δg_τ .

$$b_{KM}^{\tau'} - a_{KM}^{\tau'} = \frac{16c_4}{c_0(c_0 - 9c_4/2)} \{ \beta \Im \tilde{c}_5 (1 + 27.8 \Im \tilde{c}_7 / \Im \tilde{c}_5) \} \tag{24}$$

The combination inside the figure brackets is very similar to the combination (18) defining ε' . At $\Omega = 0.124$ these combinations coincide. Then

$$\Delta g_{\tau'} = 1.8(1 \pm 0.15) 10^{-6} \tag{25}$$

At $\Omega = 0.25$

$$\Delta g_{\tau'} = 2.1 \cdot 10^{-6} \left(1 - \frac{4.7 \Im \tilde{c}_7 / \Im \tilde{c}_5}{1 + 32.48 \Im \tilde{c}_7 / \Im \tilde{c}_5} \right) \approx 2.4(1 \pm 0.15) 10^{-6} \tag{26}$$

Both values of Ω do not contradict to the estimates figurating in the literature (see, for example, [8]).

For $K^\pm \rightarrow \pi^\pm \pi^\pm \pi^\mp$

$$b_{KM}^\tau - a_{KM}^\tau = -2 \frac{16c_4}{c_0(c_0 + 9c_4)} (1 - 14.34 \Im \tilde{c}_7 / \Im \tilde{c}_5) \tag{27}$$

Then

$$\frac{-\Delta g_\tau}{\Delta g_{\tau'}} = 2 \frac{c_0 - 9c_4/2}{c_0 + 9c_4} \cdot \frac{1 + ab^{\tau'}}{1 + ab^\tau} \cdot \frac{1 - 14.34 \Im \tilde{c}_7 / \Im \tilde{c}_5}{1 + 27.8 \Im \tilde{c}_7 / \Im \tilde{c}_5} \tag{28}$$

Therefore:

1) If EWP do not play any significant role in direct CP violation, then

$$-\Delta g_\tau / \Delta g_{\tau'} = 3.1 \quad \text{or} \quad -\Delta g_\tau > 0.56 \cdot 10^{-5}.$$

2) If EWP cancel half of QCDD contribution, then

$$-\Delta g_\tau = 7.8 \Delta g_{\tau'} > 1.4 \cdot 10^{-5}.$$

3) If EWP cancel 3/4 of QCDD contribution, then

$$-\Delta g_\tau = 17.2 \Delta g_{\tau'} > 3.1 \cdot 10^{-5}.$$

3 The role of p^4 corrections

The role of p^4 corrections for Δg_τ was studied in [6]. They increase Δg_τ by 23%.

As for $\Delta g_{\tau'}$, such examination is not fulfilled so far. But one effect is seen immediately. Because $\Delta g_{\tau,\tau'} \sim a$ and $(a)_{p^2+p^4} = 1.3(a)_{p^2}$ [6], it is expected, that

$$(\Delta g_{\tau'})_{corr} \approx 2.4 \cdot 10^{-6}.$$

4 Conclusion

- 1) $\Delta g_{\tau'}$ is fixed to be around $2.4 \cdot 10^{-6}$.
- 2) Δg_τ could be one order larger.
- 3) The parallel measurement of Δg_τ and $\Delta g_{\tau'}$ will allow to clear up the relative significance of QCDP and EWP mechanisms in direct CP violation.

5 References

1. J.M. Flynn and L. Randall, Phys.Lett. **224**, 221 (1989);
G. Buchalla et al., Nucl.Phys. **B 337**, 313 (1990); E.A. Paschos and Y.L. Wu, Mod.Phys.Lett., **A 6**, 93 (1991).
2. M.A. Shifman, A.I. Vainshtein and V.I. Zakharov, Zh.Eksp.i Teor. Fiz. (JETP), **72**, 1277 (1977).
3. M.A. Bardeen, A.J. Buras and J.-M. Gerard, Nucl. Phys. **B 293**, 787 (1987).
4. E.P. Shabalin, Nucl.Phys. **B 409**, 87 (1993).
5. L.B. Okun, *Leptons and Quarks* (North-Holland, Amsterdam 1982) pp.315,323.
6. E.P. Shabalin, Phys. Atom. Nucl. **68**, 88 (2005); hep-ph/0405229.
7. G. Fäldt and E. Shabalin, hep-ph/0503241
8. V. Cirigliano et al., Eur.Phys.J. **C 33**, 369 (2004);
S. Bertolini, M. Fabbrichesi and J.O. Eeg, hep-ph/9802405 v.2.

CP VIOLATION HIGHLIGHTS: CIRCA 2005

Amarjit Soni

*High Energy Theory, Department of Physics,
Brookhaven National Laboratory, Upton, NY 11973-5000*

Abstract

Recent highlights in CP violation phenomena are reviewed. B-factory results imply that CP-violation phase in the CKM matrix is the dominant contributor to the observed CP violation in K and B-physics. Deviations from the predictions of the CKM-paradigm due to beyond the Standard Model CP-odd phase are likely to be a small perturbation. Therefore, large data sample of clean B's will be needed. Precise determination of the unitarity triangle, along with time dependent CP in penguin dominated hadronic and radiative modes are discussed. *Null tests* in B, K and top-physics and separate determination of the K-unitarity triangle are also emphasized.

1 B-factories help attain an important milestone: Good and bad news

The two asymmetric B-factories at SLAC and KEK have provided a striking confirmation of the CKM paradigm ¹⁾. Existing experimental information from the indirect CP violation parameter, ϵ for the $K_L \rightarrow \pi\pi$, semileptonic $b \rightarrow ue\nu$ and $B^0 - \bar{B}^0$ mixing along with lattice calculations predict that in the SM, $(\sin 2\beta) \simeq .70 \pm .10$ ^{2, 3, 4)}. This is in very good agreement with the BELLE and BABAR result ⁵⁾:

$$\mathcal{A}_{CP}(B^0 \rightarrow \psi K^0) = \sin 2\beta = .726 \pm .037 \quad (1)$$

This leads to the conclusion that the CKM phase of the Standard Model (SM) is the dominant contributor to \mathcal{A}_{CP} . That, of course, also means that CP-odd phase(s) due to beyond the Standard Model (BSM) sources may well cause only small deviations from the SM in B-physics.

Actually, there are several reasons to think that BSM phase(s) may cause only small deviations in B-physics. In this regard, SM itself teaches a very important lesson.

2 Important lesson from the CKM-paradigm

We know now that the CKM phase is $0(1)$ (actually, the CP violation parameter η is $0(.3)$ ^{2, 3, 4)}. The CP effects that it causes on different observables though is quite different. In K-decays, the CP asymmetries are $\leq 10^{-3}$. In charm physics, also there are good reasons to expect small observable effects. In top physics, the CKM phase causes completely negligible effects ^{6, 7)}. Thus only in B-decays, the large asymmetries (often $0(1)$) are caused by the CKM phase. So even if the BSM phase(s) are $0(1)$ it is unlikely that again in B-physics they will cause large effects just as the SM does.

3 Remember the m_ν

Situation with regard to BSM CP-odd phase(s) (χ_{BSM}) is somewhat reminiscent of the neutrino mass (m_ν) ⁸⁾. There was no good reason for m_ν to be zero; similarly, there are none for χ_{BSM} to be zero either. In the case of ν 's, there were the solar ν results that were suggestive for a very long time; similarly, in the case of χ_{BSM} , the fact that in the SM, baryogenesis is difficult to accommodate serves as the beacon.

It took decades to show m_ν is not zero: Δm^2 had to be lowered from \sim

$O(1 - 10)eV^2$ around 1983 down to $O(10^{-4}eV^2)$ before $m_\nu \neq 0$ was established via neutrino oscillations. We can hope for better luck with χ_{BSM} but there is no good reason to be too optimistic; therefore, we should not rely on luck but rather we should seriously prepare for this possibility.

To recapitulate, just as the SM-CKM phase is $0(1)$, but it caused only $0(10^{-3})$ CP symmetries in K- decays, an $0(1)$ BSM-CP-odd phase may well cause only very small asymmetries in B-physics. To search for such small effects:

- 1) We need lots and lots of clean B's (*i.e.* $0(10^{10})$ or more)
- 2) Intensive study of B_s mesons (in addition to B's) becomes very important as comparison between the two types of B-mesons will teach us how to improve quantitative estimates of flavor symmetry breaking effects.
- 3) We also need clean predictions from theory (wherein item 2 should help).

4 Improved searches for BSM phase

Improved searches for BSM-CP-odd phase(s) can be subdivided into the following main categories:

- a) Indirect searches with theory input
- b) Indirect searches without theory input
- c) Direct searches.

4.1 Indirect searches with theory input

Among the four parameters of the CKM matrix, λ, A, ρ and η , $\lambda = 0.2200 \pm 0.0026$, $A \approx 0.850 \pm 0.035$ ⁹⁾ are known quite precisely; ρ and η still need to be determined accurately. Efforts have been underway for many years to determine these parameters. The angles α, β, γ , of the unitarity triangle (UT) can be determined once one knows the 4-CKM parameters.

A well studied strategy for determining these from experimental data requires knowledge of hadronic matrix elements. Efforts to calculate several of the relevant matrix elements on the lattice, with increasing accuracy, have been underway for past many years. A central role is played by the following four inputs ^{2, 3, 4)}:

- B_K from the lattice with ϵ from experiment
- $f_B\sqrt{B_B}$ from the lattice with Δm_d from experiment
- ξ from the lattice with $\frac{\Delta m_s}{\Delta m_d}$ from experiment

- $\frac{b \rightarrow ul\nu}{b \rightarrow cl\nu}$ from experiment, along with input from phenomenology especially heavy quark symmetry as well as the lattice.

As mentioned above, for the past few years, these inputs have led to the important constraint: $\sin 2\beta_{SM} \approx 0.70 \pm 0.10$ which is found to be in very good agreement with direct experimental determination, Eq. 1.

Despite severe limitations (e.g. the so-called quenched approximation) these lattice inputs provided valuable help so that with B-Factory measurements one arrives at the very important conclusion that in $B \rightarrow J/\psi K^0$ the CKM-phase is the dominant contributor; any new physics (NP) contribution is unlikely to be greater than about 15%.

What sort of progress can we expect from the lattice in the next several years in these (indirect) determination of the UT? To answer this it is useful to look back and compare where we were to where we are now. Perhaps this gives us an indication of the pace of progress of the past several years. Lattice calculations of matrix elements around 1995¹⁰⁾ yielded (amongst other things) $\sin 2\beta \approx 0.59 \pm 0.20$, whereas the corresponding error decreased to around ± 0.10 around 2001²⁾. In addition to β , such calculations also now constrain $\gamma (\approx 60^\circ)$ with an error of around 10° ²⁾.

There are three important developments that should help lattice calculations in the near future:

1. Exact chiral symmetry can be maintained on the lattice. This is especially important for light quark physics.
2. Relatively inexpensive methods for simulations with dynamical quarks (esp. using improved staggered fermions¹¹⁾) have become available. This should help overcome limitations of the quenched approximation.
3. About a factor of 20 increase in computing power is now being used compared to a few years ago.

As a specific example one can see that the error on B_K with the 1st use of dynamical domain wall fermions¹²⁾ now seems to be reduced by about a factor of two¹³⁾. In the next few years or so errors on lattice determination of CKM parameters should decrease appreciably, perhaps by a factor of 3. So the error in $\sin 2\beta_{SM} \pm 0.10 \rightarrow \pm 0.03$; $\gamma \pm 10^\circ \rightarrow 4^\circ$ etc. While this increase in accuracy is very welcome, and will be very useful, there are good reasons to believe, experiment will move ahead of theory in direct determinations of unitarity angles in the next 5 years. (At present, experiment is already ahead of theory for $\sin 2\beta$).

4.2 Indirect searches without theory input: Elements of a superclean UT

One of the most exciting developments of recent years in B-physics is that methods have been developed so that all three angles of the UT can be determined cleanly with very small theory errors. This is very important as it can open up several ways to test the SM-CKM paradigm of CP violation; in particular, the possibility of searching for small deviations. Let us very briefly recapitulate the methods in question:

- Time dependent CP asymmetry (TDCPA) measurements in $B^0, \bar{B}^0 \rightarrow \psi K^0$ type of final states should give the angle β very precisely with an estimated irreducible theory error (ITE) of $\leq O(0.1\%)$ ¹⁴).
- Direct CP (DIRCP) studies in $B^\pm \rightarrow "K^\pm" D^0, \bar{D}^0$ gives γ very cleanly ^{15, 16}).
- TDCPA measurements in $B^0, \bar{B}^0 \rightarrow "K^0" D^0, \bar{D}^0$ gives $(2\beta + \gamma)$ and also β very cleanly ^{17, 18}).
- In addition, TDCPA measurements in $B_s \rightarrow KD_s$ type modes also gives γ very cleanly ¹⁹).
- Determination of the rate for the CP violating decay $K_L \rightarrow \pi^0 \nu \bar{\nu}$ is a very clean way to measure the Wolfenstein parameter η , which is indeed the CP-odd phase in the CKM matrix ²⁰).

It is important to note that the ITE for each of these methods is expected to be $\leq 1\%$, in fact perhaps even $\leq 0.1\%$.

- Finally let us briefly mention that, TDCPA studies of $B^0, \bar{B}^0 \rightarrow \pi\pi$ or $\rho\pi$ or $\rho\rho$ gives α ^{21, 22, 23}). However, in this case, isospin conservation needs be used and that requires, *assuming* that electro-weak penguins (EWP) make negligible contribution. This introduces some model dependence and may cause an error of order a few degrees, *i.e.* for α extraction the ITE may well end up being O(a few %). However, given that there are three types of final states each of which allows a determination of α , it is quite likely that further studies of these methods will lead to a reduction of the common source of error originating from isospin violation due to the EWP.

It is extremely important that we make use of these opportunities afforded to us by as many of these very clean redundant measurements as possible. In order to exploit these methods to their fullest potential and

get the angles with errors of order ITE will, for sure, require a SUPER-B Factory(SBF) 8, 30, 31, 32).

This in itself constitutes a strong enough reason for a SBF, as it represents a great opportunity to precisely nail down the important parameters of the CKM paradigm.

4.2.1 Prospects for precision determination of γ

Below we briefly discuss why the precision extraction of γ seems so promising.

For definiteness, let us recall the basic features of the ADS method ²⁴⁾. In this interference is sought between two amplitudes of roughly similar size *i.e.* $B^- \rightarrow K^- D^0$ and $B^- \rightarrow K^- \bar{D}^0$ where the D^0 and \bar{D}^0 decay to common final states such as the simple two body ones like $K^+\pi^-$, $K^+\rho^-$, $K^+a_1^-$, $K^{+*}\pi^-$ or they may also be multibody modes e.g. the Dalitz decay $K^+\pi^-\pi^0$, $K^+\pi^-\pi^+\pi^-$ etc. It is easy to see that the interference is between a colored allowed B decay followed by doubly Cabibbo suppressed D decay and a color-suppressed B decay followed by Cabibbo allowed D decay and consequently then interference tends to be maximal and should lead to large asymmetries.

For a given (common) final state of D^0 and \bar{D}^0 the amplitude involves three unknowns: the color suppressed $\text{Br}(B^- \rightarrow K^- \bar{D}^0)$, which is not directly accessible to experiment ²⁴⁾, the strong phase $\xi_{f_i}^K$ and the weak phase γ . Corresponding to each such final state (FS) there are two observables: the rate for B^- decay and for the B^+ decay.

Thus, if you stick to just one common FS of D^0 , \bar{D}^0 , you do not have enough information to solve for γ . If you next consider two common FS of D^0 and \bar{D}^0 then you have one additional unknown (a strong phase) making a total of 4-unknowns with also 4-observables. So with two final states the system becomes solvable, *i.e.* we can then use the experimental data to solve not only the value of γ but also the strong phases and the suppressed Br for $B^- \rightarrow K^- \bar{D}^0$. With N common FS of D^0 and \bar{D}^0 , you will have $2N$ observables and $N + 2$ unknowns. We need $2N \geq (N + 2)$ *i.e.* $N \geq 2$. The crucial point, though, is that there are a very large number of possible common modes of D^0 and \bar{D}^0 which can all be used to improve the determination of γ .

Let us briefly mention some of the relevant common modes of D^0 and \bar{D}^0 :

- The CP-eigenstate modes, originally discussed by GLW ²¹⁾: $K_S [\pi^0, \eta, \eta', \rho^0, \omega]; \pi^+\pi^-, \dots$
- CP-non-eigenstates (CPNES), discussed by GLS ²⁶⁾: $K^{*+}K^-, \rho^+\pi^- \dots$ These are singly Cabibbo suppressed modes.
- CPNES modes originally discussed by ADS ^{24, 25)}: $K^{+(*)}[\pi^-, \rho^-, a_1^- \dots]$

- There are also many multibody modes, such as the Dalitz D^0 decays: $K_S\pi^+\pi^-$ (27) or $K^+\pi^-\pi^0$ (25) etc; and also modes such as $K^-\pi^+\pi^-\pi^+$, $K^-\pi^+\pi^-\pi^+\pi^0$, or indeed $K^-\pi^+ + n\pi$ (17, 28, 29). Furthermore, multibody modes such as $B^+ \rightarrow K_i^+ D^0 \rightarrow (K\pi)^+ D^0$ or $(Kn\pi)^+ D^0$ (28, 33) can also be used.

Fig. 1 and Fig. 2 show how combining different strategies helps a great deal. In the fig. we show χ^2 versus γ . As indicated above when you consider an individual final state of D^0 and \bar{D}^0 then of course there are 3 unknowns (the strong phase, the weak phase (γ) and the “unmeasureable” Br) and only two observables (the rate for B^- and the rate for B^+). So in the figure, for a fixed value of γ , we search for the minimum of the χ^2 by letting the strong phase and the “unmeasureable” Br take any value they want.

Fig. 1 and Fig. 2 show situation with regard to under determined and over determined cases respectively. The upper horizontal line corresponds roughly to the low luminosity i.e. comparable to the current B-factories (30, 32) whereas the lower horizontal curve is relevant for a super B-factory. In Fig. 1 in blue is shown the case when only the input from (GLW) CPES modes of D^0 is used; note all the CPES modes are included here. You see that the resolution on γ then is very poor. In particular, this method is rather ineffective in giving a lower bound; its upper bound is better.

In contrast, a single ADS mode ($K^+\pi^-$) is very effective in so far as lower bound is concerned, but it does not yield an effective upper bound (red).

Note that in these two cases one has only two observables and 3 unknowns. In purple is shown the situation when these two methods are combined. Then at least at high luminosity there is significant improvement in attaining a tight upper bound; lower bound obtained by ADS alone seems largely unaffected.

Shown in green is another under determined case consisting of the use of a single ADS mode, though it includes K^{*-} as well D^{*0} ; this again dramatically improves the lower bound. From an examination of these curves it is easy to see that combining information from different methods and modes improves the determination significantly (28).

Next we briefly discuss some over determined cases (Fig. 2). In purple all the CPES modes of D^0 are combined with just one doubly Cabibbo-suppressed (CPNES) mode. Here there are 4 observables for the 4 unknowns and one gets a reasonable solution at least especially for the high luminosity case.

The black curve is different from the purple one in only one respect; the black one also includes the D^{0*} from $B^- \rightarrow K^- D^{0*}$ where subsequently the D^{0*} gives rise to a D^0 . Comparison of the black one with the purple shows considerable improvement by including the D^{0*} . In this case the number of observables (8) exceeds the number of unknowns (6).

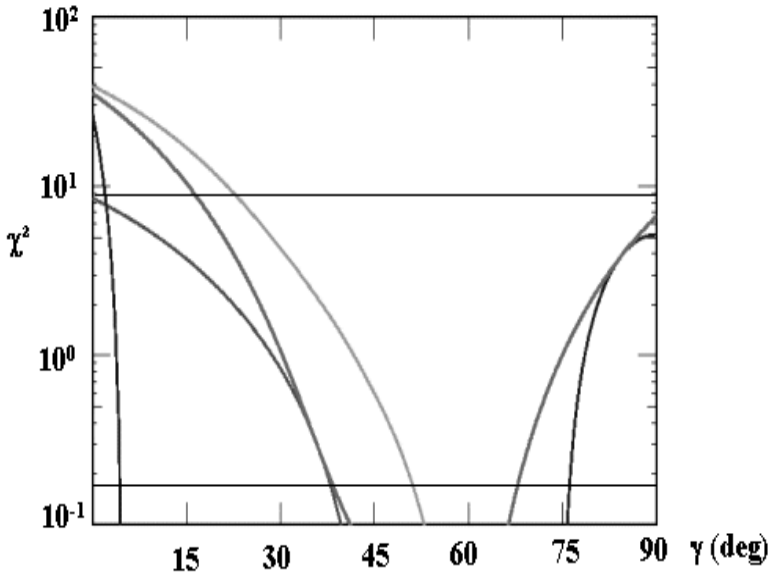


Figure 1: γ determination with incomplete input (*i.e.* cases when the number of observables is less than the number of unknown parameters). The upper horizontal line corresponds to low-luminosity *i.e.* around current B-factories whereas the lower horizontal curve is relevant for a SBF. Blue uses all CPES modes of D^0 , red is with only $K^+\pi^-$ and purple uses combination of the two. Green curve again uses on D^0 , $\bar{D}^0 \rightarrow K^+\pi^-$ but now includes K^{*-} and D^{*0} ; see text for details.

Actually, the D^{0*} can decay to D^0 via two modes: $D^{0*} \rightarrow D^0 + \pi$ or $D^0 + \gamma$. Bondar and Gershon³⁴⁾ have made a very nice observation that the strong phase for the γ emission is opposite to that of the π emission. Inclusion (blue curves) of both types of emission increases the number of observables to 12 with no increase in number of unknowns. So this improves the resolving power for γ even more.

The orange curves show the outcome when a lot more input is included; not only K^- , K^{*-} , D^0 , D^{0*} but also Dalitz and multibody decays of D^0 are included. But the gains now are very modest; thus once the number of observables exceeds the number of unknowns by a few (say $O(3)$) further increase in input only has a minimal impact.

Let us briefly recall that another important way to get these angles is by studying time-dependent CP (TDCP) (or mixing-induced CP (MIXCP))

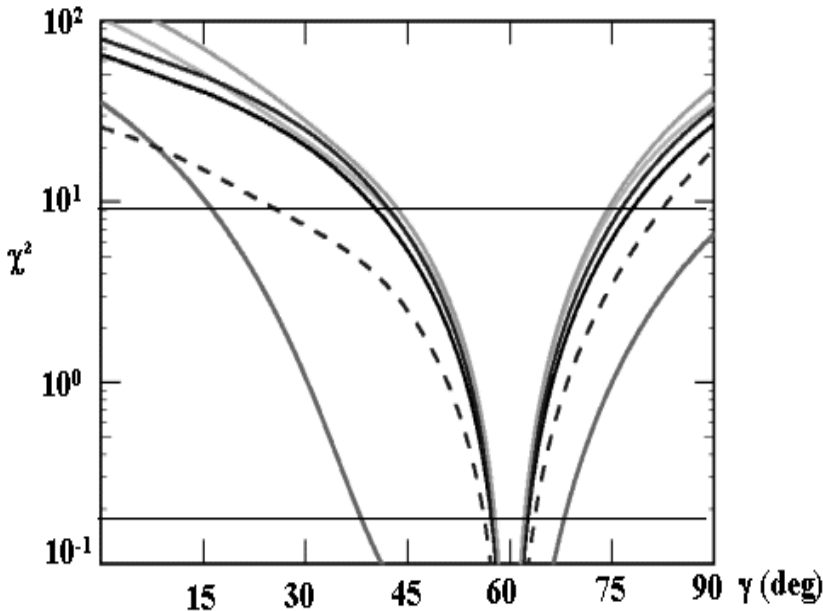


Figure 2: γ extraction with over-determined cases. Purple curve shows the effect of combining GLW (all CPES modes) with one ADS ($K^+\pi^-$) mode; black curve differs from purple only in that it also includes D^0 from D^{*0} ; blue curves show the effect of properly including the correlated strong phase between $D^{0*} \rightarrow D^0 + \pi$ and $D^{0*} \rightarrow D^0 + \gamma$. Orange curve includes lot more input including Dalitz and multibody modes. see text for details (See also Fig 1). Adopted from ²⁸).

violation via $B^0 \rightarrow D^{0(*)}K^0$. Once again, all the common decay modes of D^0 and \bar{D}^0 can be used just as in the case of direct CP studies involving B^\pm decays. Therefore, needless to say input from charm factory ^{29, 35, 36}) also becomes desirable for MIXCP studies of $B^0 \rightarrow D^{0(*)}K^0$ as it is for direct CP using B^\pm . It is important to stress that this method gives not only the combinations of the angles ($2\beta + \gamma \equiv \alpha - \beta + \pi$) but also in addition this is another way to get β cleanly ^{17, 18}). In fact whether one uses B^\pm with DIRCP or $B^0 - \bar{B}^0$ with TDCP these methods are very clean with (as indicated above) the ITE of $\approx 0.1\%$. However, the TDCP studies for getting γ (with the use of β as determined from ψK_s) is less efficient than with the use of DIRCP involving B^\pm . Once we go to luminosities $\geq 1ab^{-1}$, though, the two methods for γ should become competitive. Note that this method for getting

Table 1: *Projections for direct determination of UT.*

	Now(0.2/ab)	2/ab	10/ab	ITE
$\sin 2\phi_1$	0.037	0.015	0.015(?)	0.001
$\alpha(\phi_2)$	13°	4°(?)	2°(?)	1°(?)
$\gamma(\phi_3)$	$\pm 20^\circ \pm 10^\circ \pm 10^\circ$	5° to 2°	< 1°(?)	0.05°

β is significantly less efficient than from the ψK_s studies¹⁷⁾.

Table 1 summarizes the current status and expectations for the near future for the UT angles. With the current O(0.4/ab) luminosity between the two B-factories, $\gamma \approx (69 \pm 30)$ degrees. Most of the progress on γ determination so far is based on the use of the Dalitz mode, $D^0 \rightarrow K_s \pi^+ \pi^-$ ²⁷⁾. However, for now, this method has a disadvantage as it entails a modelling of the resonances involved; though model independent methods of analysis, at least in principle, exist^{17, 27, 28)}. The simpler modes (*e.g.* $K^+ \pi^-$) require more statistics but they would not involve such modelling error as in the Dalitz method. Also the higher CP asymmetries in those modes should have greater resolving power for determination of γ . The table shows the statistical, systematic and the resonance-model dependent errors on γ separately. Note that for now i do not think the model dependent error (around 10 degrees) ought to be added in quadrature. That is why the combined error of ± 30 degrees is somewhat inflated to reflect that. The important point to note is that as more B's are accumulated, more and more decay modes can be included in determination of γ ; thus for the next several years the accuracy on γ is expected to improve faster than $1/\sqrt{N_B}$, N_B being the number of B's.

4.3 Direct searches: Two important illustrations

B-decays offers a wide variety of methods for searching for NP or for BSM-CP-odd phase(s). First we will elaborate a bit on the following two methods.

- Penguin dominated hadronic final states in $b \rightarrow s$ transitions.
- Radiative B-decays.

Then we will provide a brief summary of the multitude of possibilities that a SBF offers, in particular, for numerous important approximate null tests (ANTs).

4.4 Penguin dominated hadronic final states in $b \rightarrow s$ transitions

For the past couple of years, experiments at the two B-factories have been showing some indications of a tantalizing possibility *i.e.* a BSM-CP-odd phase

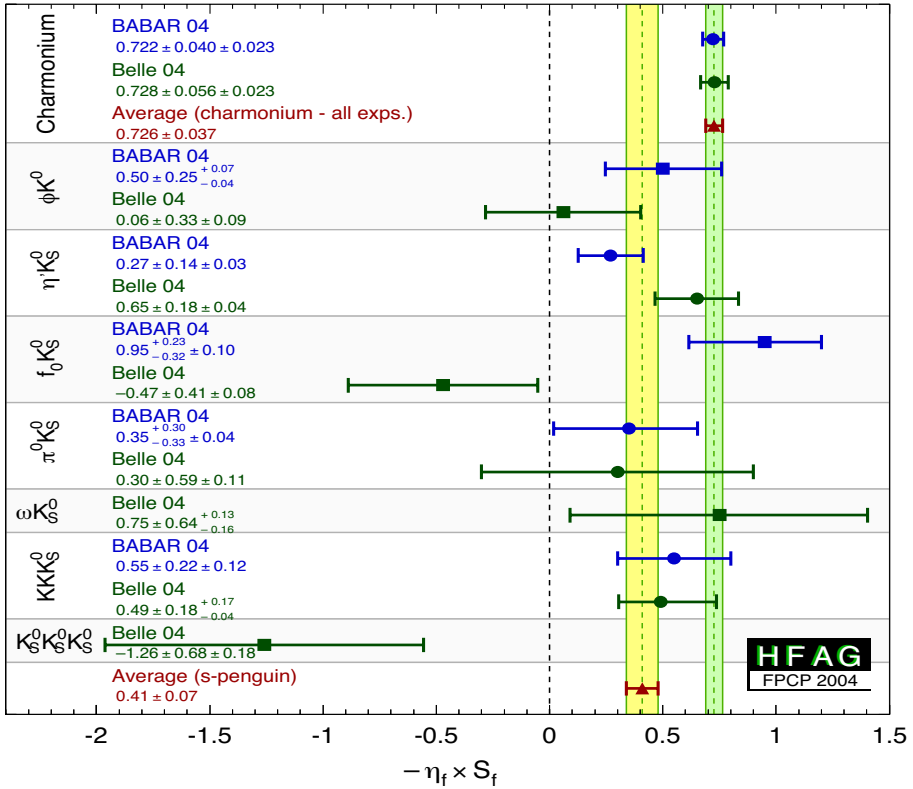


Figure 3: Experimental status of $\sin 2\beta$ from penguin-dominated modes; taken from 5).

in penguin dominated $b \rightarrow s$ transitions. Let us briefly recapitulate the basic idea.

Fig. 3 show the experimental status 5). With about 250×10^6 B-pairs in each of the B-factories, there are two related possible indications. In particular, BABAR finds about a 3σ deviation in $B \rightarrow \eta' K_s$. Averaging over the two experiments, this is reduced to about 2.3σ . Secondly adding all such penguin dominated modes seems to indicate a 3.5σ effect.

Since $B \rightarrow \eta' K_s$ seems to be so prominently responsible for the indications of deviations in the current data sample, let us briefly discuss this particular FS. That the mixing induced CP in $\eta' K_s$ can be used to test the SM was 1st proposed in 37). This was triggered in large part by the discovery of the unexpectedly large Br for $B \rightarrow \eta' K_s$. Indeed ref. 37) emphasized that the large Br may be very useful in determining $\sin 2\beta$ with $B \rightarrow \eta' K_s$ and comparing it with the value obtained from $B \rightarrow \psi K_s$. In fact it is precisely the large Br of $B \rightarrow \eta' K_s$ that is making the error of the TDCP measurement the

smallest amongst all the penguin dominated modes presently studied. Note also that there is a corresponding proposal to use the large Br of the inclusive $\eta' X_s$ for searching for NP with the use of direct CP (38, 39).

Ref. (37) actually suggested use of TDCP studies not just in $\eta' K_s$ but in fact also $[\eta, \pi^0, \omega, \rho, \phi \dots] K_s$ to test the SM. These are, indeed most of the modes currently being used by BABAR & BELLE.

Simple analysis in (37) suggested that in all such penguin dominated ($b \rightarrow s$) modes Tree/Penguin is small, < 0.04 . In view of the theoretical difficulties in reliably estimating these effects, Ref (37) emphasized that it would be very difficult in the SM to accomodate $\Delta S > 0.10$, as a cautious bound.

4.4.1 Final state interaction effects

The original papers (40, 37) predicting,

$$\Delta S_f = S_f - S_{\psi K} \approx 0 \quad (2)$$

used naive factorization; in particular, FSI were completely ignored. A remarkable discovery of the past year is that in several charmless 2-body B-decays direct CP asymmetry is rather large. This means that FSI (CP-conserving) phase(s) in exclusive B-decays need not be small (41). Since these are non-perturbative (42), model dependence becomes unavoidable. Indeed characteristically these FSI phase(s) arise formally from $O(1/m_B)$ corrections:

- In pQCD (43) a phenomenological parameter k_T , corresponding to the transverse momentum of partons, is introduced in order to regulate the end point divergences encountered in power corrections. This in turn gives rise to sizable strong phase difference from penguin induced annihilation.
- In QCDF (44), in its nominal version, the direct CP asymmetry in many channels (e.g $B^0 \rightarrow K^+ \pi^-, \rho^- \pi^+, \pi^+ \pi^- \dots$) has the opposite sign compared to the experimental findings. Just like in the pQCD approach where the annihilation topology play an important role in giving rise to large strong phases, and for explaining the penguin-dominated VP modes, it has been suggested in (45) that in a specific scenario (S4), for QCDF to agree with the Br of penguin-dominated PV modes as well as with the measured sign of the direct asymmetry in the prominent channel $B^0 \rightarrow K^+ \pi^-$, a large annihilation contribution be allowed by choosing $\rho_A = 1$, $\phi_A = -55^\circ$ for PP, $\phi_A = -20^\circ$ for PV and $\phi_A = -70^\circ$ for VP modes.

- In our approach ⁴¹⁾, QCDF is used for short-distance (SD) physics; however, to avoid double-counting, we set the above two parameters [ρ_A , ϕ_A] as well as two additional parameters [ρ_H , ϕ_H] that they have ⁴⁵⁾ to zero. Instead we try to include long-distance ($1/m_B$) corrections by using on-shell rescattering of 2-body modes to give rise to the needed FS phases.

So, for example, color-suppressed modes such as $B^0 \rightarrow K^0 \pi^0$ gets important contributions from color allowed processes: $B^0 \rightarrow K^{-(*)} \pi^+ (\rho^+)$, $D_S^{-(*)} D^{+(*)}$. The coupling strengths at the three vertices of such a triangular graph are chosen to give the known rates of corresponding physical processes such as $B^0 \rightarrow D_S^- D^{+(*)}$, $D^* \rightarrow D + \pi$ etc. Furthermore, since these vertices are not elementary and the exchanged particles are off-shell, form-factors have to be introduced so that loop integrals become convergent. Of course, there is no way to determine these reliably. We vary these as well as other parameters so that Br's are in rough agreement with experiment, then we calculate the CP-asymmetries.

Recall the standard form for the asymmetries:

$$\frac{\Gamma(\overline{B}(t) \rightarrow f) - \Gamma(B(t) \rightarrow f)}{\Gamma(\overline{B}(t) \rightarrow f) + \Gamma(B(t) \rightarrow f)} = \mathcal{S}_f \sin(\Delta mt) + \mathcal{A}_f \cos(\Delta mt) \quad (3)$$

The TDCP asymmetry (S_f) and direct CP asymmetry [$A_f \equiv -C_f$ (BaBar notation)] both depend on the strong phase. Thus measurements of direct CP asymmetry A_f (in addition to S_f) allows tests of model calculations, though in practice its real use may be limited to those cases where the direct CP asymmetry is not small. This is the case, for example, for $\rho^0 K_S$ and ωK_S ⁴⁶⁾.

It is also important to realize that not only there is a correlation between S_f and A_f for FS in B^0 decays, but also that the model entails specific predictions for direct CP in the charged counterparts. So, for example, in our model for FSI, large direct CP asymmetry is also expected in the charged counterparts of the above two modes.

In addition to two body modes there are also very interesting 3-body modes such as $B^0 \rightarrow K^+ K^- K_S(K_L)$, $K_S K_S K_S(K_L)$. These may also be useful to search for NP as they are also penguin dominated. We use resonance-dominance of the relevant two body channels to extend our calculation of LD rescattering phases in these decays ⁴⁷⁾.

Tables 2 and 3 summarize our results for ΔS and A for two body and 3-body modes. We find that ^{46, 47)} $B^0 \rightarrow \eta' K_S$, ϕK_S and $3K_S$ are cleanest ⁴⁸⁾, i.e. central values of ΔS as well as the errors are rather small, O(a few%). Indeed we find that even after including the effect of FSI, ΔS in

Table 2: Direct CP asymmetry parameter \mathcal{A}_f and the mixing-induced CP parameter ΔS_f^{SD+LD} for various modes. The first and second theoretical errors correspond to the SD and LD ones, respectively (see ⁴⁶) for details). The $f_0 K_S$ channel is not included as we cannot make reliable estimate of FSI effects on this decay; table adopted from ⁴⁶).

Final State	ΔS_f		$\mathcal{A}_f(\%)$	
	SD+LD	Expt	SD+LD	Expt
ϕK_S	$0.03^{+0.01+0.01}_{-0.04-0.01}$	-0.38 ± 0.20	$-2.6^{+0.8+0.0}_{-1.0-0.4}$	4 ± 17
ωK_S	$0.01^{+0.02+0.02}_{-0.04-0.01}$	$-0.17^{+0.30}_{-0.32}$	$-13.2^{+3.9+1.4}_{-2.8-1.4}$	48 ± 25
$\rho^0 K_S$	$0.04^{+0.09+0.08}_{-0.10-0.11}$	–	$46.6^{+12.9+3.9}_{-13.7-2.6}$	–
$\eta' K_S$	$0.00^{+0.00+0.00}_{-0.04-0.00}$	-0.30 ± 0.11	$2.1^{+0.5+0.1}_{-0.2-0.1}$	4 ± 8
ηK_S	$0.07^{+0.02+0.00}_{-0.05-0.00}$	–	$-3.7^{+4.4+1.4}_{-1.8-2.4}$	–
$\pi^0 K_S$	$0.04^{+0.02+0.01}_{-0.03-0.01}$	$-0.39^{+0.27}_{-0.29}$	$3.7^{+3.1+1.0}_{-1.7-0.4}$	-8 ± 14

most of these penguin-dominated modes, it is very difficult to get $\Delta S > 0.10$ in the SM. Thus we can reiterate (as in ³⁷) that $\Delta S > 0.10$ would be a strong evidence for NP.

Having said that, it is still important to stress that genuine NP in these penguin dominated modes must show up in many other channels as well. Indeed, on completely model independent grounds ⁸), the underlying NP has to be either in the 4-fermi vertex ($bss\bar{s}$) or (bsg , $g = gluon$). In either case, it has to materialize into a host of other reactions and phenomena and it is not possible that it only effects time dependent CP in say $B \rightarrow \eta' K_s$ and/or ϕK_s and/or $3K_s$. For example, for the 4-fermi case, we should also expect non-standard effects in $B_d \rightarrow \phi(\eta')K^*$, $B^+ - > \phi(\eta')K^{+(*)}$, $B_s \rightarrow \phi\phi(\eta')$...In the second case not only there should be non-standard effects in these reactions but also in $B_{d(u)} \rightarrow X_s\gamma$, $K^*\gamma$, $B_s \rightarrow \phi\gamma$ and also in the corresponding l^+l^- modes. Unless corroborative evidence is seen in many such processes, the case for NP due to the non-vanishing of ΔS is unlikely to be compelling, especially if (say) $\Delta S \lesssim 0.15$.

4.4.2 Averaging issue

As already emphasized in ³⁷), to the extent that penguin contributions dominate in these many modes and *tree/penguin* is only a few percent testing the SM by adding $\Sigma\Delta S_f$, where $f = K_S + \eta'(\phi, \pi, \omega, \rho, \eta, K_S K_S \dots)$, is sensible at least from a theoretical standpoint. At the same time it is important to emphasize that a convincing case for NP requires unambiguous demonstration of significant effects (i.e. $\Delta S > 0.10$) in several individual channels.

Table 3: Mixing-induced and direct CP asymmetries $\sin 2\beta_{\text{eff}}$ (top) and \mathcal{A}_f (bottom), respectively, in $B^0 \rightarrow K^+K^-K_S$ and $K_S K_S K_S$ decays. Results for $(K^+K^-K_L)_{CP\pm}$ are identical to those for $(K^+K^-K_S)_{CP\mp}$; table taken from 47)

Final State	$\sin 2\beta_{\text{eff}}$	Expt.
$(K^+K^-K_S)_{\phi K_S}$ excluded	$0.749^{+0.080+0.024+0.004}_{-0.013-0.011-0.015}$	$0.57^{+0.18}_{-0.17}$
$(K^+K^-K_S)_{CP+}$	$0.770^{+0.113+0.040+0.002}_{-0.031-0.023-0.013}$	
$(K^+K^-K_L)_{\phi K_L}$ excluded	$0.749^{+0.080+0.024+0.004}_{-0.013-0.011-0.015}$	0.09 ± 0.34
$K_S K_S K_S$	$0.748^{+0.000+0.000+0.007}_{-0.000-0.000-0.018}$	0.65 ± 0.25
$K_S K_S K_L$	$0.748^{+0.001+0.000+0.007}_{-0.001-0.000-0.018}$	
	$\mathcal{A}_f(\%)$	Expt.
$(K^+K^-K_S)_{\phi K_S}$ excluded	$0.16^{+0.95+0.29+0.01}_{-0.11-0.32-0.02}$	-8 ± 10
$(K^+K^-K_S)_{CP+}$	$-0.09^{+0.73+0.16+0.01}_{-0.00-0.27-0.01}$	
$(K^+K^-K_L)_{\phi K_L}$ excluded	$0.16^{+0.95+0.29+0.01}_{-0.11-0.32-0.02}$	-54 ± 24
$K_S K_S K_S$	$0.74^{+0.02+0.00+0.05}_{-0.06-0.01-0.06}$	31 ± 17
$K_S K_S K_L$	$0.77^{+0.12+0.08+0.06}_{-0.28-0.11-0.07}$	

4.4.3 Sign of ΔS

For these penguin-dominated modes, ΔS_f is primarily proportional to the hadronic matrix element $\langle f | \bar{u}\Gamma b \bar{s}\Gamma' u | B^0 \rangle$. Therefore, in the SM for several of the final states (f), ΔS_f could have the same sign. So a systematic trend of ΔS_f being positive or negative (*and small of $O(a \text{ few } \%)$*) does not necessarily mean NP.

The situation wrt to $\eta' K_S$ is especially interesting. As has been known for the past many years this mode has a very large Br, almost a factor of 7 larger than the similar two body $K \pi$ mode. This large Br is of course also the reason why the statistical error is the smallest, about a factor of two less than any other mode being used in the test. For this reason, it is gratifying that $\eta' K_S$ also happens to be theoretically very clean in several of the model calculations. This has the important repercussion that confirmation of a significant deviation from the SM, may well come 1st by using the $\eta' K_S$ mode, perhaps well ahead of the other modes (49).

4.4.4 Concluding remarks on penguin-dominated modes

Concluding this section we want to add that while at present there is no clear or compelling deviation from the SM the fact still remains that this is a very important approximate null test (ANT). It is exceedingly important to follow this test with the highest luminosity possible to firmly establish that as ex-

pected in the SM, ΔS_f is really $\lesssim 0.05$ and is not significantly different from this expectation. To establish this firmly, for several of the modes of interest, may well require a SBF.

5 Time dependent CP in exclusive radiative B-decays

Br ($B \rightarrow \gamma X_{s(d)}$) and direct CP asymmetry $a_{cp}(B \rightarrow \gamma X_{s(d)})$ are well known tests of the SM [50, 51, 52, 53]. Both of these use the inclusive reaction where the theoretical prediction for the SM are rather clean; the corresponding exclusive cases are theoretically problematic though experimentally more accessible. In 1997 another important test [54] of the SM was proposed which used mixing induced CP (MICP) or time-dependent CP (TDCP) in exclusive modes such as $B^0 \rightarrow K^* \gamma, \rho \gamma, \dots$. This is based on the simple observation that in the SM, photons produced in reactions such as $B \rightarrow K^* \gamma, K_2^* \gamma, \rho \gamma, \dots$ are predominantly right-handed whereas those in \bar{B}^0 decays are predominantly left-handed. To the extent that FS of B^0 and \bar{B}^0 are different MICP would be suppressed in the SM. Recall, the LO H_{eff} can be written as

$$H_{\text{eff}} = -\sqrt{8}G_F \frac{em_b}{16\pi^2} F_{\mu\nu} \left[F_L^q \bar{q}\sigma^{\mu\nu} \frac{1+\gamma_5}{2} b + F_R^q \bar{q}\sigma^{\mu\nu} \frac{1-\gamma_5}{2} b \right] + h.c. \quad (4)$$

Here F_L^q (F_R^q) corresponds to the amplitude for the emission of left (right) handed photons in the $b_R \rightarrow q_L \gamma_L$ ($b_L \rightarrow q_R \gamma_R$) decay, *i.e.* in the $\bar{B} \rightarrow \bar{F} \gamma_L$ ($\bar{B} \rightarrow \bar{F} \gamma_R$) decay.

5.1 Application to $B^0, B_s \rightarrow$ vector meson + photon

Thus, based on the SM, LO H_{eff} , in b-quark decay (*i.e.* \bar{B} decays), the amplitude for producing wrong helicity (RH) photons $\propto m_q/m_b$ where $m_q = m_s$ or m_d for $b \rightarrow s \gamma$ or $b \rightarrow d \gamma$ respectively. Consequently the TDCP asymmetry is given by,

$$\begin{aligned} B^0 \rightarrow K^{*0} \gamma & : A(t) \approx (2m_s/m_b) \sin(2\beta) \sin(\Delta mt) , \\ B^0 \rightarrow \rho^0 \gamma & : A(t) \approx 0 , \\ B_s \rightarrow \phi \gamma & : A(t) \approx 0 , \\ B_s \rightarrow K^{*0} \gamma & : A(t) \approx -(2m_d/m_b) \sin(2\beta) \sin(\Delta mt) , \end{aligned} \quad (5)$$

where K^{*0} is observed through $K^{*0} \rightarrow K_S \pi^0$.

Interestingly not only emission of wrong-helicity photons from B decays is highly suppressed, in many extensions of the SM, *e.g.* Left-Right Symmetric models (LRSM) or SUSY [55, 56, 57] or Randall-Sundrum (warped extra

Process	SM	LRSM
$A(B \rightarrow K^* \gamma)$	$2 \frac{m_s}{m_b} \sin 2\beta \sin(\Delta m_t)$	$\sin 2\omega \cos 2\beta \sin(\Delta m_t)$
$A(B \rightarrow \rho \gamma)$	≈ 0	$\sin 2\omega \sin(\Delta m_t)$

Table 4: Mixing-induced CP asymmetries in radiative exclusive B-decays in the SM and in the LRSM. Note $|\sin 2\omega| \lesssim 0.67$ is allowed ^{54, 8)}

dimension ⁵⁸⁾) models, in fact they can be enhanced by the ratio m_{heavy}/m_b where m_{heavy} is the mass of the virtual fermion in the penguin-loop. In LRSM as well as some other extensions this enhancement can be around m_t/m_b . So while in the SM the asymmetries are expected to be very small, they can be sizeable in LRSM ⁵⁴⁾ (see Table 4) as well as in many other models.

5.2 Generalization to $B^0, B_s \rightarrow$ two pseudoscalars + photon

An important generalization was made in Ref ⁵⁹⁾. It was shown that the basic validity of this test of the SM does not require the final state to consist of a spin one meson (a resonance such as K^* or ρ) in addition to a photon. In fact the hadronic final states can equally well be two mesons; *e.g.* $K_S(\pi^0, \eta', \eta, \phi...)$ or $\pi^+\pi^-$. Inclusion of these non-resonant final states, in addition to the resonances clearly enhances the sensitivity of the test considerably. For the case when the two mesons are antiparticle of each other *e.g.* $\pi^+\pi^-$, then there is the additional advantage that both the magnitude and the weak phase of any new physics contribution may be determined from a study of the angular distribution ⁵⁹⁾.

5.3 Theoretical subtleties

In principle, photon emission from the initial light-quark is a non-perturbative, long-distance, contamination to the interesting signal of the short-distance dipole emission from H_{eff} ^{60, 61)}. Fortunately, it can be shown ⁵⁹⁾ that predominantly these LD photons have the same helicity as those from H_{eff} .

Another important source of SM contamination was recently emphasized in Ref. ⁶²⁾ from processes such as $b \rightarrow s\gamma$ + gluon which are from non-dipole operators. Such processes do not fix the helicity of the photon and so can make a non-vanishing SM contribution to mixing induced CP.

It was emphasized in Ref ⁵⁹⁾ that the presence of such non-dipole contributions can be separated from the dipole contributions, though, it may require larger amount of data, the resolution to this problem is data driven.

To briefly recapitulate, the different operator structure in H_{eff} would mean, that in contrast to the pure dipole case, the time dependent CP asymmetry (S) would be a function of the Dalitz variables, the invariant mass (s) of the meson pair, and the photon angle of emission (z). A difference in the values of S for two resonances of identical J^{PC} would also mean presence of non-dipole contributions. Schematically, we may write:

$$dS^i/(dsdz) = [A_\sigma + A_0^i] + B^i s + C^i z \quad (6)$$

where A_σ is the “universal” contribution that one gets from the dipole operator of the H_{eff} no matter if it is a resonance, or a non-resonance mode. It is distinct from the contribution of the 4-quark operators as not only it is independent of energy (s) or angle (z) Dalitz variables but also it is independent of the specific nature of the hadronic FS (*i.e.* resonant or non-resonant). The remaining contributions are all originating from 4-quark operators; not only they dependent on energy and angle but also the coefficients are expected to vary from one FS to another. In particular the 4-quark operators may give a FS dependent (energy and angle independent) constant A_0^i . It is easy to convince oneself that with sufficient data the important term A_σ , at least in principle, can be separated. Once that is done its size should be indicative of whether it is consistent with expectations from SM or requires new physics to account for it.

5.4 Approximate null tests aglore!

If the effects of a BSM CP-odd phase on B-physics are small, then searching for these via **null tests** becomes especially important. Since CP is not an exact symmetry of the SM, it is very difficult if not impossible to find exact null tests. Fortunately clean environment at a SBF should allow many interesting approximate null tests (ANTs); see Table 5⁸⁾.

Clearly there is a plethora of powerful tests for a new CP-odd phase and /or new physics that a SBF should allow us to do. Perhaps especially noteworthy (in addition to penguin-dominated hadronic and radiative B decays) are the numerous very interesting tests pertaining to $B \rightarrow X(K, K^*)l^+l^-$ 50, 51).

Furthermore search for the transverse polarization^{63, 64)} of the τ in $B \rightarrow X(D, D^*)\tau\nu_\tau$ due to their unique cleanliness are extremely interesting especially in light of the discovery of neutrino mass and the potential richness of neutrinos with the possible presence of Majorana neutrinos in simple ground-up extensions of the SM as well as in many other approaches^{65, 66)}.

Sensitivity of each of these to NP as well as theoretical cleanliness (*i.e.* how reliable SM predictions are) for each is also indicated. It should be clear

Table 5: Final states and observables in B - decays useful in searching for effects of New Physics. Reliability of SM predictions (*i.e.* how clean) and sensitivity to new physics are each indicated by stars (5 = *best*); table adopted from ⁸⁾

Final State	Observable	how clean	how sensitive
$\gamma[K_s^*, \rho, \omega]$	TDCP	5*	5*
$K_s[\phi, \pi^0, \omega, \eta', \eta, \rho^0]$	TDCP	4.5*	5*
$K^*[\phi, \rho, \omega]$	TCA	4.5*	5*
$[\gamma, l^+l^-][X_s, X_d]$	DIRCP	4.5*	5*
same	Rates	3.5*	5*
$J/\psi K$	TDCP, DIRCP	4*	4*
$J/\psi K^*$	TCA	5*	4*
$D(*)\tau\nu_\tau$	TCA (p_t^r)	5*	4*
same	Rate	4*	4*

that for most of these tests $> 5 \times 10^9$ B-pairs are essential, that is a SBF.

6 K-Unitarity Triangle

For the past many years, effort has been directed towards constraining the UT especially the parameters ρ and η by a combination of information from K and B-physics, as mentioned briefly in Section 1. With the advent of B-factories and significant advance that has been already made (and a lot more is expected to come) it has become possible to construct the UT purely from B-physics ^{3, 4)}. In fact it may also be very interesting and important to construct a separate UT from K-decays. This could become particularly useful in search for small deviations. Reactions that are relevant for a K-UT are ⁶⁷⁾:

- Indirect CP-violation parameter, ϵ_K with the hadronic matrix elements (parameter B_K) from the lattice. With the dawning of the era of dynamical simulations using discretizations that preserve chiral-flavor symmetries of the continuum ¹²⁾, lattice should be able to significantly reduce the errors on B_K ¹³⁾.
- Accurate measurements of the BR of $K^+ \rightarrow \pi^+\nu\bar{\nu}$ can give a clean determination of $|V_{td}|$ ²⁰⁾. Important progress has been recently made in the 1st step towards an accurate determination of this Br ⁶⁸⁾. Charm quark contribution in the penguin graph is difficult to reliably estimate but this is expected to be subdominant ⁶⁹⁾.

- Measurement of the BR of $K_L \rightarrow \pi^0 \nu \bar{\nu}$ can give an extremely clean value of η , *i.e.* ImV_{td} . This is clearly very challenging experimentally; however, it is unique in its cleanliness, perhaps on the same footing as γ from BKD processes discussed above.
- After enormous effort, the experimentalists have determined the direct CP violation parameter ϵ'/ϵ with considerable accuracy (70, 71). For theory a reliable calculation remains a very important outstanding challenge. Recently it has become clear that not only chiral symmetry on the lattice is essential for this calculation but also the quenched approximation suffers here from very serious pathology (72, 73). As mentioned above, since the past 2-3 years considerable effort is being expended in generation of dynamical configurations with domain wall quarks which possess excellent chiral properties. In the near future we should expect to see the application of these new generation of lattices for study of ϵ'/ϵ . It remains to be seen as to how accurately the current generation of computers can allow this important calculation to be done.

7 Neutron electric dipole moment: a classic ANT of the SM

In the SM, neutron electric dipole moment (nedm) cannot arise at least to two EW loops; thus is expected to be exceedingly small, *i.e.* $\lesssim 10^{-31} \text{ecm}$. Long series of experiments over the past several decades now place a 90 %CL bound of $\lesssim 6.3 \times 10^{-26} \text{ecm}$ (74). So the expectation from the SM is many orders of magnitude below the current experimental bound. In numerous extensions of the SM, including SUSY, warped extra dimensions etc. nedm close to or even somewhat bigger than the current experimental bound occurs (75, 58). Thus continual experimental improvements of this bound remains a very promising way to discover new BSM CP-odd phase(s).

8 Top quark electric dipole moment: another clean null test of the SM

The top quark is so heavy compared to the other quarks that the GIM-mechanism is extremely effective. Thus in the decays of the top-quark, in the SM, all FCNC are extremely suppressed. Once again, top quark edm cannot arise in the SM to two EW loops and is therefore expected to be extremely small. In many BSM scenarios with extra Higgs doublets (77, 78), LRSM, SUSY (7), the top quark can acquire edm at one loop and consequently can be considerably bigger (See Table 6). Therefore searches for the top dipole moment at the International Linear Collider will be an important goal (7, 76). Indeed if sufficient high

Table 6: Expectations for top edm form-factor in SM and beyond; adopted from 7)

type of moment ($e - cm$) \downarrow	\sqrt{s} (GeV) \downarrow	Standard Model	Neutral Higgs $m_h = 100 - 300$	Supersymmetry $m_{\tilde{g}} = 200 - 500$
$ \Im m(d_t^\gamma) $	500	$< 10^{-30}$	$(4.1 - 2.0) \times 10^{-19}$	$(3.3 - 0.9) \times 10^{-19}$
	1000		$(0.9 - 0.8) \times 10^{-19}$	$(1.2 - 0.8) \times 10^{-19}$
$ \Re e(d_t^\gamma) $	500	$< 10^{-30}$	$(0.3 - 0.8) \times 10^{-19}$	$(0.3 - 0.9) \times 10^{-19}$
	1000		$(0.7 - 0.2) \times 10^{-19}$	$(1.1 - 0.3) \times 10^{-19}$
$ \Im m(d_t^Z) $	500	$< 10^{-30}$	$(1.1 - 0.2) \times 10^{-19}$	$(1.1 - 0.3) \times 10^{-19}$
	1000		$(0.2 - 0.2) \times 10^{-19}$	$(0.4 - 0.3) \times 10^{-19}$
$ \Re e(d_t^Z) $	500	$< 10^{-30}$	$(1.6 - 0.2) \times 10^{-19}$	$(0.1 - 0.3) \times 10^{-19}$
	1000		$(0.2 - 1.4) \times 10^{-19}$	$(0.4 - 0.1) \times 10^{-19}$

luminosity could be attained top quark edm of around 10^{-19} ecm may well be detectable (See Table 7).

9 Summary

The new millennium marks the spectacular success of B-factories leading to a milestone in our understanding of CP-violation; in particular, for the first time CKM paradigm of CP violation is quantitatively confirmed.

Direct measurement of $\sin 2\beta$ by the B-factories agrees remarkably well with the theoretical expectation from the SM to about 10%. Furthermore, first relatively crude *direct* determination of the other two angles (α & γ) also are consistent with theoretical expectations. While these findings are good news for the SM, at the same ime, they imply that most likely the effect of BSM CP-odd phase on B-physics is likely to be a small perturbation. Thus discovery of new BSM-CP-odd source(s) of CP violation in B-physics is likely to require very large, clean, data samples and extremely clean predictions from theory.

For the search of such small deviations approximate null tests of the SM gain new prominence.

Also important for this purpose is the drive to directly determine all three angles of the UT with highest precision possible, *i.e.* with errors roughly around the errors allowed by theory. It should be clear that to accomplish this important goal would require a Super-B Factory.

Specifically regarding penguin-dominated hadronic FS, that have been

Table 7: Attainable $1\text{-}\sigma$ sensitivities to the CP-violating dipole moment form factors in units of 10^{-18} e-cm, with ($P_e = \pm 1$) and without ($P_e = 0$) beam polarization. $m_t = 180$ GeV. Table taken from [7, 79].

	$20 \text{ fb}^{-1}, \sqrt{s} = 500 \text{ GeV}$			$50 \text{ fb}^{-1}, \sqrt{s} = 800 \text{ GeV}$		
	$P_e = 0$	$P_e = +1$	$P_e = -1$	$P_e = 0$	$P_e = +1$	$P_e = -1$
$\delta(\Re d_t^V)$	4.6	0.86	0.55	1.7	0.35	0.23
$\delta(\Re d_t^Z)$	1.6	1.6	1.0	0.91	0.85	0.55
$\delta(\Im d_t^V)$	1.3	1.0	0.65	0.57	0.49	0.32
$\delta(\Im d_t^Z)$	7.3	2.0	1.3	4.0	0.89	0.58

much in the recent news, the current data does not show any convincing signal for deviation from the SM; however, it is a very important and sensitive test for new physics and its of vital importance to reduce the experimental errors to $O(5\%)$; for this purpose too a SBF may well be needed.

Outside of B-Physics, K-unitarity triangle, neutron electric dipole moment and top quark dipole moment are also very important *approximate null tests* of the SM that should be pursued vigorously.

10 Acknowledgements

I want to thank the organizers (and, in particular, Mario Greco) for their kind invitation. Useful discussions with David Atwood, Tom Browder, Chun-Khiang Chua, Tim Gershon, Masashi Hazumi, Jim Smith and especially Hai-Yang Cheng are gratefully acknowledged. This research was supported in part by DOE contract No. DE-FG02-04ER41291.

References

1. N. Cabibbo, Phys. Rev. Lett. **10**, 531 (1963); M. Kobayashi and T. Maskawa, Prog. Th. Phys. **49**, 652 (1973).
2. See, *e.g.*, D. Atwood and A. Soni, hep-ph/0103197
3. CKMfitter Group, J. Charles *et al*; hep-ph/0406184.
4. UTfit Collab. M. Bona *et al* hep-ph/0501119.
5. Heavy Flavor Averaging Group, hep-ph-ex/0412073.
6. G. Eilam, J. L. Hewett and A. Soni, Phys. Rev. Lett. **67**, 1979 (1991).

7. D. Atwood *et al*, Physics Reports, 347, 1-222(01).
8. T. Browder and A. Soni, hep-ph/0410192.
9. S. Eidelman *et al.*, Phys. Lett. **B592** 1, (2004).
10. See A. Soni, Proceeding of Lattice'95, hep-lat/9510036 (esp. p14).
11. C. T. H. Davies *et. al*, hep-lat/0304004.
12. Y. Aoki *et. al*, hep-lat/0411006.
13. Y. Aoki *et al*, hep-lat/0508011.
14. H. Boos, T. Mannel and J. Reuter, hep-ph/0403085.
15. D. Atwood and A. Soni, hep-ph/0212071
16. Y. Grossman, A. Soffer and J. Zupan, hep-ph/0505270
17. D. Atwood and A. Soni, hep-ph/0206045.
18. A. Bondar, T. Gershon, P. Krokovny, hep-ph/0503174.
19. See *e. g.* P. Ball *et. al*, hep-ph/0003238; R. Fleischer, hep-ph/0304027.
20. See *e.g.* A. J. Buras, hep-ph/0101336.
21. M. Gronau and D. London, Phys. Rev. Lett. **65**, 3381(90); M. Gronau and D. Wyler, Phys. Lett. **B265**, 172(91)
22. H. Lipkin *et. al* Phys. Rev. **D44**, 1454(91).
23. A. Falk *et. al* hep-ph/0310242.
24. D. Atwood, I. Dunietz and A. Soni, Phys. Rev. Lett. **78**, 3257(97)
25. D. Atwood, I. Dunietz and A. Soni, hep-ph/0008090
26. Y. Grossman, Z. Ligeti and A. Soffer, hep-ph/0210433.
27. A. Giri, Y. Grossman, A. Soffer and J. Zupan, hep-ph/0303187
28. D. Atwood and A. Soni, hep-ph/0312100
29. D. Atwood and A. Soni, hep-ph/0304085.
30. S. Hashimoto *et al*, KEK-REPORT-2004-4.
31. M. Neubert, hep-ph/0405105.

32. J. Hewett *et al*, hep-ph/0503261.
33. D. Atwood *et al*, Phys. Lett. **B341**, 372(1995).
34. A. Bondar and T. Gershon, hep-ph/0409281.
35. M. Gronau, Y. Grossman, J. Rosner, hep-ph/0103110.
36. J. L. Rosner, hep-ph/0508024.
37. D. London and A. Soni, hep-ph/9704277.
38. D. Atwood and A. Soni, Phys. Rev. Lett. **79**, 5206(97).
39. W-S Hou, B. Tseng, Phys. Rev. Lett. **80**, 434(97).
40. Y. Grossman and M. Worah, Phys. Lett. **B395**, 241(97).
41. H.-Y. Cheng, C.-K Chua and A. Soni, Phys. Rev. **D71**, 014030(2005).
42. The purely perturbative phases, for example from M. Bander, D. Silverman and A. Soni, Phys. Rev. Lett. **43**, 242(79), tend to be small.
43. Y. Y. Keum, H. N. Li and A. I. Sanda, Phys. Rev. **D63**, 054008(2001).
44. M. Beneke *et. al*, Nucl. Phys. **B606**, 245(2001) and references therein.
45. M. Beneke and M. Neubert, Nucl. Phys. **B675**, 333 (2003).
46. H.-Y. Cheng, C.-K Chua and A. Soni, Phys. Rev. **D72**, 014006 (2005).
47. H.-Y. Cheng, C.-K Chua and A. Soni, hep-ph/0508007.
48. See also, M. Beneke, Phys. Lett. **B620**, 143 (2005).
49. This point has been emphasized by Jim Smith (private communication).
50. T. Hurth, Rev. Mod. Phys. **75**, 1175(03).
51. G. Hiller, hep-ph/0308180.
52. A. Kagan and M. Neubert, Phys. Rev. **D58**, 094012(98).
53. K. Kiers, A. Soni and G.-H Wu, Phys. Rev. **D62**,116004(00).
54. D. Atwood, M. Gronau and A. Soni, Phys. Rev. Lett. **79**, 185(97).
55. C.-K. Chua, W.-S. Hou and M. Nagashima, hep-ph/0308298;
56. T. Goto *et. al*, hep-ph/0306093.

57. E. J. Chun, K. Hwang and J. S. Lee, hep-ph/0005013.
58. K. Agashe, G. Perez and A. Soni, hep-ph/0406101; hep-ph/0408134.
59. D. Atwood *et al*, hep-ph/0410036
60. D. Atwood, B. Blok and A. Soni, hep-ph/9408373.
61. B. Grinstein and D. Pirjol, Phys. Rev. **D62**, 093002(00).
62. B. Grinstein *et. al*, hep-ph/0412019.
63. D. Atwood, G. Eilam and A. Soni, Phys. Rev. Lett. **71**, 495(93).
64. Y. Grossman and Z. Ligeti, Phys. Lett. **9409418**.
65. See, *e.g.* D. Atwood, S. Bar-Shalom and A. Soni, hep-ph/0502234.
66. See also, *e. g.* R. N. Mohapatra *et al*, hep-ph/0412099.
67. See *e.g.* A. Soni, hep-ph/0307107.
68. S. Adler *et al* [E787 Collab], Phys. Rev. Lett. **88**,041802(02).
69. A. Falk, A. Lewandowski and A. Petrov, hep-ph/0012099.
70. A. Lai *et. al* [NA48 Collab.] hep-ex/0210053.
71. A. Alavi-Harati [KTeV Collab.] *et. al*, hep-ex/0208007.
72. M. Golterman and E. Pallante, hep-lat/0110183; hep-lat/0208069.
73. J. Laiho *et. al* in preparation and private communications.
74. P. G. Harris *et al*, Phys. Rev. Lett. **82**, 904 (99).
75. See, *e. g.* M. Brhlik, G. Good and G. Kane, hep-ph/9810457.
76. See articles in *Linear Collider Physics in the New Millennium*, Eds. K. Fujii, D. J. Miller and A. Soni, in press (World Scientific, Singapore).
77. A. Soni and R. M. Xu, Phys. Rev. Lett. **69**, 33(92).
78. W. Bernreuther, T. Schroder and T. N. Pham, Phys. Lett. **B279**, 389, 1992.
79. W. Bernreuther, A. Brandenburg, P. Overman, hep-ph/9602273.

SESSION VI – EW AND TOP PHYSICS

- *Giovanni Abbiendi* Running of the QED Coupling in Small-Angle Bhabha Scattering at LEP
- *Luca Trentadue* Measuring α_{QED} in e^+e^- : An Alternative Approach
- *Chris Parkes* W Boson Properties at LEP
- *Oliver Stelzer-Chilton* W Boson Production and Mass at the Tevatron
- *George Velez* Top Mass Measurements at the Tevatron RUN II
- *Frank Fiedler* Top Quark Production and Properties at the Tevatron
- *V. Daniel Elvira* Di-Boson Production and SM/SUSY Higgs Searches at the Tevatron

RUNNING OF THE QED COUPLING IN SMALL-ANGLE BHABHA SCATTERING AT LEP

G. Abbiendi

*INFN and Dipartimento di Fisica dell' Università di Bologna,
Viale C. Berti-Pichat 6/2, 40127 Bologna, Italy*

Abstract

Using the OPAL detector at LEP, the running of the effective QED coupling $\alpha(t)$ is measured for space-like momentum transfer, $2 \leq -t \leq 6 \text{ GeV}^2$, from the angular distribution of small-angle Bhabha scattering. This is currently the most significant direct observation of the running of the QED coupling in a single experiment and the first clear evidence of the hadronic contribution to the running in the space-like region. Our result is in good agreement with standard evaluations of $\alpha(t)$, based on data in the time-like region.

1 Introduction

The effective QED coupling $\alpha(t)$ is an essential ingredient for many precision physics predictions. It contributes one of the dominant uncertainties in the electroweak fits constraining the Higgs mass. The effective QED coupling is generally expressed as:

$$\alpha(t) = \frac{\alpha_0}{1 - \Delta\alpha(t)} \quad (1)$$

where $\alpha_0 = \alpha(t = 0) \simeq 1/137$ is the fine structure constant, t is the momentum transfer squared of the exchanged photon and $\Delta\alpha$ is the vacuum polarization contribution. Whereas the leptonic contributions to $\Delta\alpha$ are calculable to very high accuracy, the hadronic ones have to be evaluated by using a dispersion integral over the measured cross section of $e^+e^- \rightarrow \text{hadrons}$ at low energies, plus perturbative QCD ^{1, 2}). There are also many evaluations which are more theory-driven, extending the application of perturbative QCD down to ~ 2 GeV, see for example the reference ³). An alternative approach ⁴) uses perturbative QCD in the negative t (*space-like*) region.

There have been only a few direct observations of the running of the QED coupling ^{5, 6, 7, 8}). Here we present a new result from the OPAL collaboration. A full description can be found in the OPAL paper ⁹). The running of α is measured in the space-like region, by studying the angular dependence of small-angle Bhabha scattering, $e^+e^- \rightarrow e^+e^-$, at LEP. Small-angle Bhabha scattering appears to be an ideal process for a direct measurement of the running of $\alpha(t)$ in a single experiment, as it is an almost pure QED process, strongly dominated by t -channel photon exchange. Moreover the data sample has large statistics and excellent purity. The Bhabha differential cross section can be written in the following form for small scattering angle:

$$\frac{d\sigma}{dt} = \frac{d\sigma^{(0)}}{dt} \left(\frac{\alpha(t)}{\alpha_0} \right)^2 (1 + \epsilon) (1 + \delta_\gamma) + \delta_Z \quad (2)$$

where $d\sigma^{(0)}/dt = 4\pi\alpha_0^2/t^2$ is the Born term for the t -channel diagram, ϵ represents the radiative corrections to the Born cross section, while δ_γ and δ_Z are the interference contributions with s -channel photon and Z exchange respectively. δ_γ and δ_Z are much smaller than ϵ and the vacuum polarization. Therefore, with a precise knowledge of the radiative corrections (ϵ term) one can determine the effective coupling $\alpha(t)$ by measuring the differential cross section. This method has also been advocated in a recent paper ¹⁰).

2 Detector and event selection

We use OPAL data collected in 1993-95 at energies close to the Z resonance peak. In particular this analysis is based on the OPAL SiW luminometer ¹¹⁾. The SiW consisted of two cylindrical calorimeters encircling the beam pipe at a distance $z \simeq \pm 2.5$ m from the interaction point. Each calorimeter was a stack of 19 silicon layers interleaved with 18 tungsten plates, with a sensitive depth of 14 cm, representing 22 radiation lengths (X_0). The sensitive area fully covered radii between 6.2 and 14.2 cm from the beam axis, corresponding to scattering angles between 25 and 58 mrad. Each detector layer was segmented with R - ϕ geometry in a 32×32 pad array. The pad size was 2.5 mm radially and 11.25 degrees in azimuth. In total the whole luminometer had 38,912 readout channels corresponding to the individual silicon pads. Particles coming from the interaction point had to traverse the material constituting the beam pipe and its support structures as well as detector cables before reaching the face of the SiW calorimeters. This preshowering material was minimum near the inner angular limit, about $0.25 X_0$, while in the middle of the acceptance it increased to about $2 X_0$. When LEP 2 data-taking started in 1996 the detector configuration changed, with the installation of tungsten shields designed to protect the inner tracking detectors from synchrotron radiation. This reduced the useful acceptance of the detector at the lower angular limit. Therefore we limited this analysis to the LEP 1 data.

The event selection is similar to the one used for luminosity measurements ¹¹⁾. The selected sample is strongly dominated by two-cluster configurations, with almost full energy back-to-back e^+ and e^- incident on the two calorimeters. At leading order the momentum transfer squared t is simply related to the scattering angle θ , which is measured from the radial position R of the scattered e^+ and e^- at reference planes located within the SiW luminometers:

$$t = -s \frac{1 - \cos \theta}{2} \approx -\frac{s \theta^2}{4}; \quad \tan \theta = R/z. \quad (3)$$

At the center-of-mass energy $\sqrt{s} \approx 91$ GeV our angular acceptance corresponds to $2 \leq -t \leq 6$ GeV².

The radial distributions are shown in Fig. 1 for the complete data statistics, compared to the Monte Carlo distributions normalized to the same number of events. Due to the back-to-back nature of Bhabha events, the two sides do not contribute independent statistical information. After the studies mentioned in section 4, we decided to use the Right side distribution for the final fits, to keep at minimum possible unassessed systematic errors. Consistent results are obtained with the use of the Left side distribution.

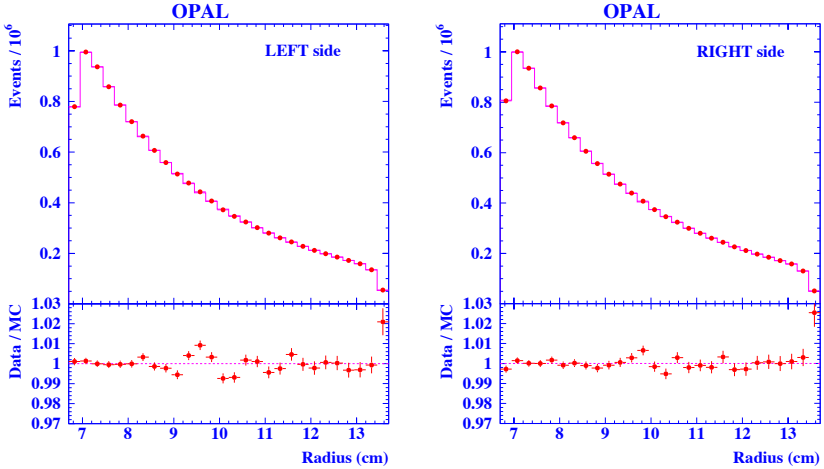


Figure 1: Radial distributions for the complete data statistics. The points show the data and the histogram the Monte Carlo prediction, assuming the expected running of α , normalized to the same number of events. The lower plots show the ratio between data and Monte Carlo.

3 Fit method

The counting rate of Bhabha events in the SiW is used to determine the integrated luminosity, so that we cannot make an absolute measurement of $\alpha(t)$ without an independent determination of the luminosity.

We compare the radial distribution of the data (and hence the t -spectrum) with the predictions of the BHLUMI Monte Carlo ¹²⁾. This is a multiphoton exponentiated generator accurate up to the leading logarithmic $\mathcal{O}(\alpha^2 L^2)$ terms ¹. Higher order photonic contributions are partially included by virtue of the exponentiation. It has been used to determine the luminosity at LEP and has been widely cross-checked with many alternative calculations. If the Monte Carlo is modified by setting the coupling to the constant value $\alpha(t) \equiv \alpha_0$, the ratio f of the number of data to Monte Carlo events in a given radial bin is:

$$f(t) = \frac{N_{\text{data}}(t)}{N_{\text{MC}}^0(t)} \propto \left(\frac{1}{1 - \Delta\alpha(t)} \right)^2. \quad (4)$$

The dominant dependence of $\Delta\alpha(t)$ expected from theory is logarithmic. We

¹ $L = \ln(|t|/m_e^2) - 1$ is the large logarithm.

therefore fitted the ratio $f(t)$ as:

$$f(t) = a + b \ln \left(\frac{t}{t_0} \right) \quad (5)$$

where $t_0 = -3.3 \text{ GeV}^2$ is the mean value of t in the data sample. The parameter a , about unity, is not relevant since the Monte Carlo is normalized to the data. The slope b represents the full observable effect of the running of $\alpha(t)$, both the leptonic and hadronic components. It is related to the variation of the coupling by:

$$\Delta\alpha(t_2) - \Delta\alpha(t_1) \simeq \frac{b}{2} \ln \left(\frac{t_2}{t_1} \right) \quad (6)$$

where $t_1 = -1.81 \text{ GeV}^2$ and $t_2 = -6.07 \text{ GeV}^2$ correspond to the acceptance limits.

4 Main systematic effects

It is important to realize which systematic effects could mimic the expected running or disturb the measurement. The most potentially harmful effects are biases in the reconstructed radial coordinate. Most simply one could think of dividing the detector acceptance into two and determining the slope using only two bins. In such a model the running is equivalent to a bias in the central division of $70 \mu\text{m}$. Biases on the inner or outer radial cut have a little less importance and could mimic the full running for 90 or $210 \mu\text{m}$ systematic offsets respectively. Concerning radial metrology, a uniform bias of 0.5 mm on all radii would give the same observable slope as the expected running. Knowledge of the beam parameters, particularly the transverse offset and the beam divergence, is also quite important. Thus, limitation of systematic error in the reconstructed radial coordinate is key to the current measurement.

Details of how the coordinates are formed from the recorded pad information are found in ¹¹⁾. The fine radial and longitudinal granularity of the detector are exploited to produce precise radial coordinates. The reconstruction determines the radial coordinate of the highest energy cluster, in each of the Right and Left calorimeters. Each coordinate uses a large number of pads throughout the detector, from many silicon layers, and is projected onto a reference layer, close to the average longitudinal shower maximum. The residual bias, or *anchor*, of this radial coordinate is then estimated at each pad boundary in a given layer of the detector. Here we rely on the fact that, on average, the pad with the maximum signal in any particular layer will contain the shower axis. Then from the anchors we obtain bin-by-bin acceptance corrections which are applied to the radial distribution. This procedure, named *anchoring*, is the

Table 1: Fit result for each dataset and average. For each value of b the first error is statistical and the second the full experimental systematic.

Dataset	\sqrt{s} (GeV)	Number of events	slope b ($\times 10^{-5}$)
93 -2	89.4510	879549	$662 \pm 326 \pm 89$
93 pk	91.2228	894206	$670 \pm 324 \pm 92$
93 +2	93.0362	852106	$640 \pm 332 \pm 89$
94 a	91.2354	885606	$559 \pm 326 \pm 86$
94 b	91.2170	4069876	$936 \pm 152 \pm 71$
94 c	91.2436	288813	$62 \pm 570 \pm 122$
95 -2	89.4416	890248	$839 \pm 325 \pm 124$
95 pk	91.2860	581111	$727 \pm 402 \pm 126$
95 +2	92.9720	885837	$156 \pm 325 \pm 128$
Average	91.2208	10227352	$726 \pm 96 \pm 70$
$\chi^2/\text{d.o.f. (stat.)}$			6.9/8
$\chi^2/\text{d.o.f. (stat.+syst.)}$			6.5/8

most delicate part of the analysis, and was carefully studied⁹⁾. The challenging aspect is controlling the residual bias on the radial coordinate to a level below $\approx 10 \mu\text{m}$ uniformly throughout the acceptance.

5 Results

The ratio of data to Monte Carlo is fitted to Eq. 5 and the results are given in Table 1. The nine datasets give consistent results, with $\chi^2/\text{d.o.f} = 6.9/8$ for the average b considering only statistical errors. The most important systematic errors come from the anchoring procedure and the preshowering material, both affecting the radial coordinate. The fit results are then combined, by considering the full error correlation matrix, obtaining:

$$b = (726 \pm 96 \pm 70 \pm 50) \times 10^{-5}$$

where here, and also in the results quoted below, the first error is statistical, the second is the experimental systematic and the third is the theoretical uncertainty. The total significance of the measurement is 5.6σ .

The theoretical uncertainty is dominated by the photonic corrections to the leading t -channel diagram, in particular by missing $\mathcal{O}(\alpha^2 L)$ terms, and the technical precision of the calculation. We estimated these uncertainties by

comparing BHLUMI with alternative Monte Carlo calculations. Other uncertainties, from Z interference and the contribution of light e^+e^- pairs, were also estimated and added in quadrature.

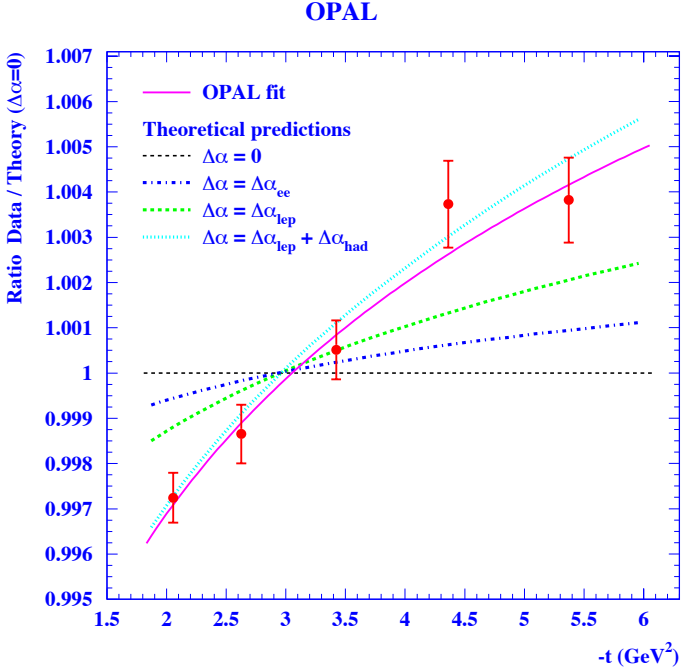


Figure 2: $|t|$ spectrum normalized to the BHLUMI theoretical prediction for a fixed coupling ($\Delta\alpha = 0$). The points show the combined OPAL data with statistical error bars. The solid line is our fit. The horizontal line (Ratio=1) is the prediction if α were fixed. The dot-dashed curve is the prediction of running α determined by vacuum polarization with only virtual e^+e^- pairs, the dashed curve includes all charged lepton pairs and the dotted curve the full Standard Model prediction, with both lepton and quark pairs.

The result for the combined data sample is illustrated in Fig. 2. The logarithmic fit to Eq. 5 describes the data very well, $\chi^2/\text{d.o.f} = 1.9/3$, although a simple linear fit would also be adequate, giving $\chi^2/\text{d.o.f} = 2.7/3$. The data are clearly incompatible with the hypothesis of a fixed coupling. The fitted logarithmic dependence agrees well with the full Standard Model prediction

including both leptonic and hadronic contributions, with the hadronic part obtained by the Burkhardt-Pietrzyk parameterization ²⁾.

The effective slope gives a measurement of the variation of the coupling $\alpha(t)$ from Eq. 6:

$$\Delta\alpha(-6.07 \text{ GeV}^2) - \Delta\alpha(-1.81 \text{ GeV}^2) = (440 \pm 58 \pm 43 \pm 30) \times 10^{-5}.$$

This is in good agreement with the Standard Model prediction, which gives $\delta(\Delta\alpha) = (460 \pm 16) \times 10^{-5}$ for the same t interval, where the error originates from the uncertainty of the hadronic component. The evaluation ²⁾ of $\Delta\alpha_{had}$ has a relative precision ranging from 2.5% at $t = -1.81 \text{ GeV}^2$ to 2.7% at $t = -6.07 \text{ GeV}^2$ ¹³⁾.

The absolute value of $\Delta\alpha$ in our range of t is expected to be dominated by e^+e^- pairs, with the relevant fermion species contributing in the approximate proportions: $e : \mu : \text{hadron} \simeq 4 : 1 : 2$. Our measurement is sensitive, however, not to the absolute value of $\Delta\alpha$, but only to its slope within our t range. Contributions to the slope b in this range are predicted to be in the proportion: $e : \mu : \text{hadron} \simeq 1 : 1 : 2.5$. Fig. 2 shows these expectations graphically. We can discard the hypothesis of running due only to virtual e^+e^- pairs with a significance of 4.4σ .

The data are also incompatible with the hypothesis of running due only to leptons. If we subtract the precisely calculable theoretical prediction for all leptonic contributions, $\delta(\Delta\alpha_{lep}) = 202 \times 10^{-5}$, from the measured result, we can determine the hadronic contribution as:

$$\Delta\alpha_{had}(-6.07 \text{ GeV}^2) - \Delta\alpha_{had}(-1.81 \text{ GeV}^2) = (237 \pm 58 \pm 43 \pm 30) \times 10^{-5}.$$

This has a significance of 3.0σ , considering all the errors.

Our result can be easily compared to the previous one by L3 ⁸⁾. If the latter is expressed as a slope according to Eq. 6, it becomes: $b^{(L3)} = (1044 \pm 348) \times 10^{-5}$. The two measurements are shown in Fig. 3. The L3 result has a larger error dominated by experimental systematics but is consistent with ours. The average gives: $b^{(ave)} = (759 \pm 113 \pm 50) \times 10^{-5}$, where the first error is obtained from the experimental errors and the second is the theoretical uncertainty that we estimated for our measurement, which will likely be common. The average is in good agreement with the prediction using the Burkhardt-Pietrzyk parameterization.

6 Conclusions

We have measured the scale dependence of the effective QED coupling from the angular distribution of small-angle Bhabha scattering at LEP, using the precise OPAL Silicon-Tungsten luminometer. We obtain the strongest direct evidence

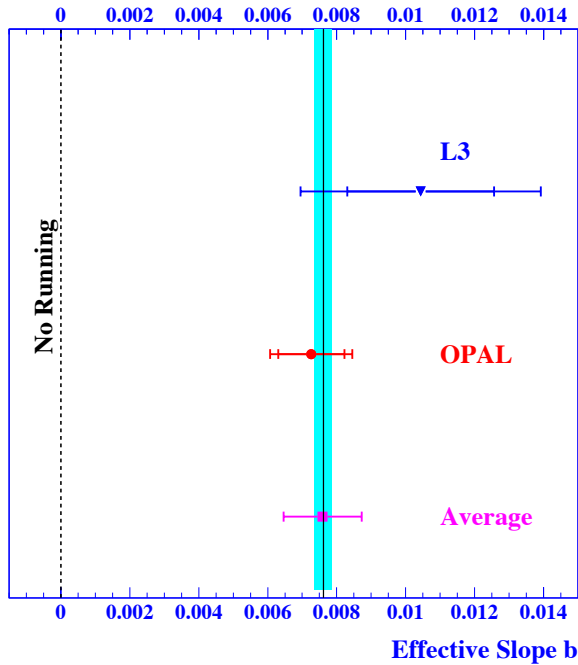


Figure 3: Effective slope $b = 2 \langle d\Delta\alpha/d\ln t \rangle$. The OPAL and L3 measurements are shown together with their average. The solid line is the SM prediction, with the band showing its uncertainty. The dashed line at $b = 0$ represents the case of no running.

for the running of the QED coupling ever achieved in a single experiment, with a significance above 5σ . Moreover we report the first clear experimental evidence for the hadronic contribution to the running in the space-like region, with a significance of 3σ . This measurement is one of only a very few experimental tests of the running of $\alpha(t)$ in the space-like region, where $\Delta\alpha$ has a smooth behaviour. Our result is in good agreement with standard evaluations of $\alpha(t)$, based on data in the time-like region.

References

1. S. Eidelman and F. Jegerlehner, *Z. Phys. C* **67**, 585 (1995).

2. H. Burkhardt and B. Pietrzyk, Phys. Lett. B **513**, 46 (2001).
3. J. F. de Troconiz and F. J. Yndurain, Phys. Rev. D **71**, 073008 (2005).
4. S. Eidelman, *et al.*, Phys. Lett. B **454**, 369 (1999); F. Jegerlehner, hep-ph/0308117.
5. TOPAZ Collaboration, I. Levine *et al.*, Phys. Rev. Lett. **78**, 424 (1997).
6. OPAL Collaboration, G. Abbiendi *et al.*, Eur. Phys. J. C **33**, 173 (2004).
7. VENUS Collaboration, S. Odaka *et al.*, Phys. Rev. Lett. **81**, 2428 (1998).
8. L3 Collaboration, M. Acciarri *et al.*, Phys. Lett. B **476**, 40 (2000).
9. OPAL Collaboration, G. Abbiendi *et al.*, submitted to Eur. Phys. J. C, <http://opalinfo.cern.ch/opal/doc/paper/info/pr407.html>.
10. A. B. Arbuzov *et al.*, Eur. Phys. J. C **34**, 267 (2004).
11. OPAL Collaboration, G. Abbiendi *et al.*, Eur. Phys. J. C **14**, 373 (2000).
12. S. Jadach *et al.*, Comput. Phys. Commun. **102**, 229 (1997).
13. H. Burkhardt and B. Pietrzyk, private communication.

MEASURING α_{QED} IN e^+e^- : AN ALTERNATIVE APPROACH*

Luca Trentadue

Dipartimento di Fisica, Università di Parma

and

INFN, Gruppo Collegato di Parma, I-43100 Parma, Italy

Abstract

We propose a method to determine the running of α_{QED} from a measurement of small angle Bhabha scattering. The method is suited to high statistics experiments at e^+e^- colliders equipped with luminometers in the appropriate angular region. A new simulation code predicting small angle Bhabha scattering is also presented.

*Work done in collaboration with A.B. Arbuzov, D. Haidt, C. Matteuzzi and M. Paganoni

1 Introduction

The electroweak Standard Model $SU(2) \otimes U(1)$ contains as a constitutive part Quantum Electrodynamics (QED). The running of the electromagnetic coupling α is determined by the theory

$$\alpha(q^2) = \frac{\alpha(0)}{1 - \Delta\alpha(q^2)} \quad (1)$$

where $\alpha(0) = \alpha_0$ is the Sommerfeld fine structure constant, which has been measured to a precision of $3.7 \cdot 10^{-9}$ ¹⁾. $\Delta\alpha(q^2)$ positive, arises from loop contributions to the photon propagator. The numerical prediction of electroweak observables involves the knowledge of $\alpha(q^2)$, usually for $q^2 \neq 0$. For instance, the knowledge of $\alpha(m_Z^2)$ is relevant for the evaluation of quantities measured by the LEP experiments. This is achieved by evolving α from $q^2=0$ up to the Z mass scale $q^2 = m_Z^2$. The evolution expressed by the quantity $\Delta\alpha$ receives contributions from leptons, hadrons and the gauge bosons. The hadronic contribution to the vacuum polarisation, which cannot be calculated from first principles, is estimated with the help of a dispersion integral and evaluated ²⁾ by using total cross section measurements of $e^+e^- \rightarrow hadrons$ at low energies. Therefore, any evolved value $\alpha(q^2)$, particularly for $|q^2| > 4m_\pi^2$, is affected by uncertainties originating from hadronic contributions. The uncertainty on $\alpha(m_Z^2)^{-1}$ induced by these data is as small as ± 0.09 ²⁾, nevertheless it turned out ³⁾ that it limits the accurate prediction of electroweak quantities within the Standard Model, particularly for the prediction of the Higgs mass. While waiting for improved measurements from BEPC, VEPP-4M and DAFNE as input to the dispersion integral, intense efforts are made to improve on estimating the hadronic shift $\Delta\alpha_{had}$, as for instance ^{4, 5, 6, 7)}, and to find alternative ways of measuring α itself. Attempts have been made to measure $\alpha(q^2)$ directly using e^+e^- -data at various energies, such as measuring the ratio of $e^+e^- \rightarrow \gamma/e^+e^-$ ⁸⁾ or more directly the angular distribution of *Bhabha* scattering ⁹⁾. We propose ¹⁰⁾ the running of α by using small angle *Bhabha* scattering. This process provides unique information on the QED coupling constant α at low *spacelike* momentum transfer $t = -|q^2|$, where $t = -\frac{1}{2} s (1 - \cos\theta)$ is related to the total invariant energy \sqrt{s} and the scattering angle θ of the final state electron. The small angle region has the virtue of giving access to values of $\alpha(q^2)$ without being affected by weak contributions. The cross section can be theoretically calculated with precision at the per mille level. It is dominated by the photonic t -channel exchange and the non-QED contributions have been computed ¹¹⁾ and are on the order of 10^{-4} , in particular contributions from boxes with two weak bosons are safely negligible. In general, the *Bhabha*-cross section is computed from the entire set of gauge invariant amplitudes in the s - and t -channel.

The s -channel contribution gives only a negligible contribution¹⁰⁾. Thus, the measurement of the angular distribution allows indeed to verify directly the running of the coupling $\alpha(t)$. Such a measurement constitutes a genuine test of QED alone. In fact, QED - as part of the electroweak theory - is valid as a consistent theory by itself, since for the applications considered here the conditions $|q^2| \ll m_W^2, m_Z^2$ are fulfilled. Furthermore, for the actual calculations $\theta \gg m_e/E_{beam}$ and $E_{beam} \gg m_e$ must be satisfied. Obviously, in order to manifest the running, the experimental precision must be adequate. This idea can be realized by high statistics experiments at e^+e^- -colliders equipped with finely segmented luminometers, in particular by the LEP experiments given their large event samples, by SLC and future Linear Colliders. The relevant luminometers cover the t -range from a few GeV^2 to order 100 GeV^2 . The t -dependence of the quantity $\Delta\alpha(t)$ at small values of t may be obtained using the program *alphaQED* by Jegerlehner²⁾. At low energies is dominated by the contribution from the leptons, while with increasing energy also the contribution from loops due to hadrons gets relevant. The region where hadronic corrections are critical is contained in the considered t -range.

2 The Method

The experimental determination of the angular distribution of the *Bhabha* cross section requires the precise definition of a *Bhabha* event in the detector. The analysis follows closely the procedure adopted in the luminosity measurement which is described in detail, for instance in ref.¹⁴⁾(YR), and elaborates on the additional aspect related to the measurement of a differential quantity. To this aim the luminosity detector must have a sufficiently large angular acceptance and adequate fine segmentation. The variable t is reconstructed on an event-by-event basis.

The method to measure the running of α exploits the fact that the cross section for the process $e^+e^- \rightarrow e^+e^-$ can be conveniently decomposed into three factors :

$$\frac{d\sigma}{dt} = \frac{d\sigma^0}{dt} \left(\frac{\alpha(t)}{\alpha(0)} \right)^2 (1 + \Delta r(t)). \quad (2)$$

All three factors are predicted to a precision of 0.1 % or better. The first factor on the right hand side refers to the *Bhabha* Born cross section including soft and virtual photons according to ref.¹¹⁾, which is precisely known, and accounts for the strongest dependence on t . The vacuum polarization effect in the leading photon t -channel exchange is incorporated in the running of α and gives rise to the squared factor in eq.2. The third factor $\Delta r(t)$ collects all the remaining real (in particular collinear) and virtual radiative effects not incorporated in the running of α ^{11, 12)}. The experimental data after correction

for detector effects is to be compared with eq.2. This goal is achieved by using a newly developed program based on the already existing semianalytical code NLLBHA ^{11, 15}) called SAMBHA ¹⁰). The two-point functions $\Pi(t) = \Delta\alpha(t)$ and $\Pi(s) = \Delta\alpha(s)$ are responsible for the running of α in the space-like and time-like regions. In the language of Feynman diagrams the effect arises from fermion loop insertions into the virtual photon lines. Anticipating the application of the proposed method to measure the t -dependence of $\alpha(t)$ to the data of a real experiment, a Monte Carlo simulation is carried out ¹⁰). Electrons, positrons and photons are observed as clusters. Their reconstruction is based on a cluster algorithm. By applying the selection criteria the event sample is divided in clusters which are attributed to various rings in the luminometer ¹⁰). The hadronic contribution may be deduced by subtracting the leptonic contribution which is theoretically precisely known ¹⁰). The extraction of the hadronic contribution is only limited by the experimental precision (see the talk of G. Abbiendi at this conference ¹⁸). To conclude a novel experimental approach to access directly the running of α in the t -channel is proposed. It consists in analysing small angle *Bhabha* scattering. Depending on the particular angular detector coverage and on the energy of the beams, it allows to cover a sizeable range of the t -variable. The information obtained in the t -channel can be compared with the existing results of the s -channel measurements. This represents a complementary approach which is direct, transparent and based only on QED interactions and furthermore free of some of the drawbacks inherent in the s channel methods. The method outlined can be readily applied to the experiments at LEP ¹⁸) and SLC. It can also be exploited by future e^+e^- colliders as well as by existing lower energy machines. An exceedingly precise measurement of the QED running coupling $\Delta\alpha(t)$ for small values of t may be possibly envisaged with a dedicated luminometer even at low machine energies.

Acknowledgement

I would like to thank the organizers of this conference for making this presentation possible.

References

1. D.E. Groom et.al.: Eur. Phys. J. **C15** (2000) 1
2. S. Eidelman and F. Jegerlehner: Z. Phys. **C67** (1995) 602
3. K. Hagiwara, D. Haidt, S. Matsumoto and C.S. Kim : Z.Phys. **C64** (1994) 559; Z.Phys. **C68** (1995) 353;

- K. Hagiwara, D. Haidt and S. Matsumoto : Eur. Phys. J. **C2** (1998) 95
4. F. Jegerlehner: hep-ph/0308117
 5. M. Davier and A. Höcker : Phys. Lett. **B435** (1998) 427;
M. Davier, S. Eidelman, A. Höcker, Z. Zhang, Eur. Phys. J. **C27**(2003) 497-521
 6. D.Karlen and H.Burkhardt, Eur. Phys. J. **C22** (2001) 39; hep-ex/0105065 (2001)
 7. A.A. Pankov, N. Paver, Eur. Phys. J. **C29**(2003) 313-323
 8. TOPAZ Collaboration, I. Levine et al.: Phys. Rev. Lett. **78** (1997) 424
 9. L3 Collaboration : M. Acciarri *et al*, Phys. Lett. **B476** (2000) 48
 10. A.B.Arbutov, D.Haidt, C.Matteuzzi, M.Paganoni and L. Trentadue, European Physics Journal C35, 267 (2004) . hep-ph/0402211.
 11. A.B. Arbuzov, V.S. Fadin, E.A. Kuraev, L.N. Lipatov, N.P. Merenkov and L. Trentadue, Nucl. Phys. **B485** (1997) 457.
 12. E.A. Kuraev and V.S. Fadin, Sov. J. Nucl. Phys. **41** (1985) 466. O. Nicosini and L. Trentadue, Phys.Lett. **B196** (1987) 551; Z. Phys. **C39** (1988) 479.
 13. S.J. Brodsky, G.P. Lepage and P.B.Mackenzie, Phys. Rev. **D28** (1983) 228
 14. LEP Working Group, Yellow Report CERN 96-01, Event Generators for Bhabha scattering, Convenors : S.Jadach and O.Nicosini, p.229
 15. Yellow Report CERN 96-01 : *description of NLLBHA*
 16. S. Eidelman and F. Jegerlehner, Z. Phys. **C67** (1995) 585; hep-ph/9502298.
 17. A. Arbuzov *et al.*, Phys. Lett. **B383** (1996) 238; hep-ph/9605239.
 18. OPAL collaboration preprint 2005

W BOSON PROPERTIES AT LEP

Chris Parkes

*Department of Physics and Astronomy, Kelvin Building, University Avenue,
Glasgow, G12 8QQ, UK*

Abstract

The determination of the properties of the W boson provide a key precision test of the Standard Model. This article reviews the significant measurements made by the four LEP experiments using approximately 40,000 W-pair events collected at e^+e^- centre-of-mass energies from 161 to 209 GeV. These results include the measurement of the W^+W^- cross-section with a 1% accuracy, the determination of gauge boson self-couplings and the measurement of the W Mass with a 42 MeV/c² precision.

1 Introduction

The primary aim of the LEP2 measurement programme was the study of the properties of the W boson, including the estimation of the W mass to a precision of better than $50 \text{ MeV}/c^2$ and the observation and study of triple gauge boson vertices. The LEP experiments achieved these aims using the data sample of approximately 700 pb^{-1} per experiment delivered during five years of operation (1996-2000) of the LEP2 accelerator at centre-of-mass energies from 161 to 209 GeV.

This article presents the principal W physics measurements made at LEP. Section 2 starts by describing the production processes for W bosons at LEP. The following sections then provide results on the cross-section for W-pair and single W production, the W hadronic branching ratio and the interpretation of this in terms of the CKM matrix element $|V_{cs}|$. The W Mass and width measurements are discussed in section 3. The electroweak systematics discussed in section 3.2.2 are relevant to the cross-section, mass and couplings. Cross-talk effects between the two Ws in an event are discussed in section 3.2.3. Measurements of triple and quartic gauge couplings and the fraction of longitudinally polarised Ws are discussed in section 4. Some of the results presented here are preliminary, further details are available in ¹⁾.

2 W production and Cross-sections

2.1 W Boson Production

W bosons were primarily produced at LEP through the process $e^+e^- \rightarrow W^+W^-$. The leading order Feynman diagrams relevant to W^+W^- production at LEP2 are given in Figure 1. Close to the W-pair production threshold, where the initial LEP2 data samples were recorded, the production cross-section is dominated by the t-channel neutrino exchange diagram. At higher energies the s-channel diagrams, containing a triple gauge boson vertex, play a more significant role. The s and t channel interference terms contribute negatively to the total cross-section and the well-behaved nature of the W^+W^- cross-section at higher energies is a consequence of these cancellations, and thus of the specific forms of the gauge boson couplings in the Standard Model (SM).

In addition, single W boson production is also possible at LEP and occurs through t-channel diagrams with an electron and neutrino in the final state.

2.2 Cross-section Measurements

The W boson sample can be divided into Ws decaying leptonically and hadronically. Hence, the W-pair sample is divided into three distinct experimentally observed topologies. Fully hadronic $W^+W^- \rightarrow q\bar{q}'\bar{q}q'$ events constitute 46%

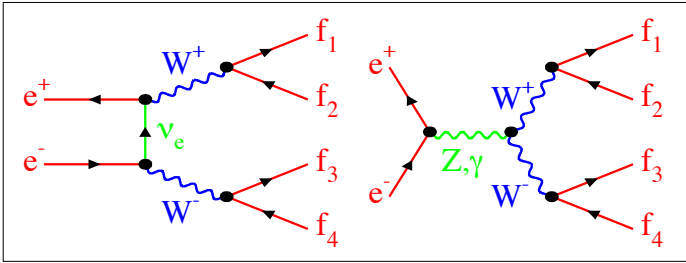


Figure 1: The leading order Feynman diagrams relevant to W^+W^- production at LEP2

of the total W^+W^- cross-section and have an experimental signature of four (or more) high energy jets resulting from the primary quarks (and additional hard gluon radiation). Semi-leptonic $W^+W^- \rightarrow \ell \bar{\nu}_\ell q \bar{q}'$ have a similar (44%) branching ratio and are characterised by two (or more) jets, a high momentum electron, muon or decay products of a tau and missing momentum due to the unobserved neutrino. The fully-leptonic events $W^+W^- \rightarrow \ell \bar{\nu}_\ell \bar{\ell} \nu_\ell$ have a smaller (10%) branching ratio and contain two charged leptons and at least two unobserved neutrinos. The event selections are based on these characteristics and commonly use neural network and discriminant techniques to obtain the best efficiencies and purities. The principal backgrounds are from $Z(\gamma)$ decays, with ZZ events also becoming significant at the higher LEP energies.

The measurement of the W^+W^- cross-section and theoretical predictions are shown in Figure 2. The measurements have been corrected for interference from other processes that can produce the same final state (e.g. $e^+e^- \rightarrow ZZ \rightarrow u\bar{u}d\bar{d}$) and represent the cross-section for the graphs shown in Figure 1. The average of the ratio of the observed cross-sections at all LEP2 energies to the predictions from the YFSWW Monte-Carlo routine ²⁾, known as the R_{WW} value, is 0.994 ± 0.009 . The YFSWW Monte-Carlo calculation includes the effect of $\mathcal{O}(\alpha)$ corrections which are discussed in section 3.2.2.

At LEP2 energies the single W production cross-section is more than an order of magnitude smaller than that for W-pair production. However, the rate is still measurable at LEP2 to better than 10%, the $R_{W e \nu_e}$ value for the combined LEP2 results to the expectation from WPHACT ³⁾ is 1.002 ± 0.075 .

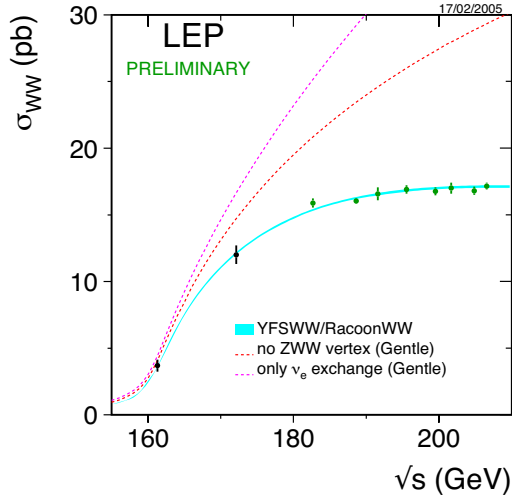


Figure 2: The data points and error bars show the combined measurements from the LEP experiments of the WW cross-section shown as a function of the centre-of-mass energy. Excellent agreement is obtained with the full theoretical prediction curves.

2.3 Branching Ratio and $|V_{cs}|$

2.3.1 W Branching Ratio

As described above the W^+W^- event selection proceeds through the separate identification of semi-leptonic, fully-leptonic and fully-hadronic events (with further splittings by charged lepton species). Hence, the branching ratio of the W boson may be extracted. Assuming lepton universality, the hadronic branching ratio of the W boson is measured to be $67.48 \pm 0.28 \%$ to compare with the Standard Model value of 67.51% . However, there is a 3.0 sigma discrepancy in the branching ratios (BR) of the tau lepton species:

$$2 \times BR(W \rightarrow \tau \bar{\nu}_\tau) / (BR(W \rightarrow e \bar{\nu}_e) + BR(W \rightarrow \mu \bar{\nu}_\mu)) = 1.077 \pm 0.026 \quad (1)$$

2.3.2 $|V_{cs}|$

The CKM matrix elements express the strength of the W coupling to the quark species. Hence, the hadronic branching ratio of the W can be interpreted as a measurement of the sum of the squares of the magnitudes of the six CKM matrix elements that do not involve the heavy top quark. The least well known of these elements is V_{cs} . Combining the LEP hadronic W branching ratio measurement with the existing measurements of the other elements provides the best determination of the magnitude of this element.

$$|V_{cs}| = 0.976 \pm 0.014 \quad (2)$$

where unitarity constraints have not been applied.

3 W Mass and Width

3.1 Method

The W boson invariant mass is reconstructed from fully hadronic and semi-leptonic W -pair events using the observed jet and lepton four-momenta and their estimated errors. Fully leptonic final states have a relatively low mass sensitivity as a result of the presence of at least two neutrinos in the event.

In the $q\bar{q}'\bar{q}q'$ final state the reconstructed jets must be appropriately paired to correspond to their parent W s. The more sophisticated analyses make use of all possible pairings, weighting them when performing the final M_W fit.

The mass resolution due to detector reconstruction effects is larger than the intrinsic width of the W boson. This experimental mass resolution is improved by imposing energy and momentum constraints upon the event in a constrained fit. Two highly correlated masses may be extracted for each event, or more commonly the additional constraint of equal masses is imposed.

The W mass and width are then evaluated by performing a maximum likelihood fit to the data using either reweighted simulation events or a semi-analytic function calibrated by simulation.

3.2 Systematics

The LEP2 determination of the W Mass is dominated by the systematic error. Three contributions to the systematic error of particular interest are discussed in this section.

3.2.1 Beam Energy Determination

The LEP beam energy is applied as a constraint in the kinematic fits used in the mass reconstruction. Hence, the fractional error on the beam energy

translates directly as a fractional error on the M_W determination.

At beam energies of up to 60 GeV polarised electron and positron beams could be produced and the beam energy determined extremely accurately (≈ 200 KeV) through the study of the e^+ or e^- spin precession frequency; this method is used to calibrate the methods used at higher energies. These methods include: measurements of the magnetic field in the LEP dipole magnets; measurement of the LEP beam bend angle in a specially constructed steel dipole of accurately known magnetic field; and measurements of the accelerator's synchrotron tune variation with RF voltage.

The LEP energy working group has recently published the final energy determination ⁴⁾, once this is incorporated in the final analyses the eventual error on the W mass resulting from the beam energy uncertainty will be approximately 10 MeV/c².

3.2.2 Electroweak Corrections

During the LEP2 programme $\mathcal{O}(\alpha)$ corrections to the four-fermion W^+W^- process have become available in event generators. These calculations include the effect of real ($4f + \gamma$) corrections and both factorisable and non-factorisable (e.g. γ exchange between decay products of different Ws) virtual corrections. All LEP collaborations are now using these corrections.

The LEP2 W^+W^- cross-section measurements, discussed above, provide evidence for the importance of these corrections. The ratio of the measurements to the GENTLE calculation ⁵⁾, that neglects these corrections gives 0.969 ± 0.009 , a 3.4 sigma deviation from unity.

The effect of electroweak corrections on differential distributions has also been studied. The effect of neglecting these corrections on the estimation of triple gauge boson vertices is significant ¹⁾. The effect on the W Mass is less important and the systematic error for analyses using these corrections has recently been investigated and shown to be less than 10MeV/c² ⁶⁾.

3.2.3 Final State Interactions

The statistical sensitivity of the fully-hadronic and semi-leptonic events is comparable, yet the fully-hadronic events have a weight of only 10% in the combined LEP W Mass average. This is due to the additional systematics applied in the fully-hadronic channel to account for final state interactions.

The decay distance of the W bosons produced at LEP2 (≈ 0.1 fm) is significantly less than the typical hadronisation scale (≈ 1 fm). Thus, cross-talk can occur between the final state particles from the two W bosons. Two effects are considered, Bose-Einstein Correlations and Colour Reconnection.

Bose-Einstein Correlations (BEC) give rise to the enhanced production of identical bosons (pions) close in momentum space. While BEC inside individual bosons are well established, the effect between the two different W s is not. By comparing fully-hadronic and semi-leptonic events all LEP experiments have reported results compatible with inter- W BEC significantly reduced from the preferred LUBOEI model implemented in JETSET⁷⁾. DELPHI do however report 2.4 sigma evidence for the existence of BEC between W s⁸⁾. The systematic error on the W Mass (and that on other measurements) is assessed using LUBOEI and hence is highly conservative.

Several phenomenological models of the potentially significant non-perturbative phase reconnection effects exist. The JETSET SK-I, ARIADNE-II and HERWIG models are the most widely studied by the LEP collaborations. The LEP experiments have conservatively chosen the SK-I model, that predicts some of the largest shifts, to assign the M_W systematic. Measurements of the effect have also been made by the LEP collaborations¹⁾ by studying particle production in the inter-jet regions inside a W and between W s. Removing the particles in the inter-jet regions and studying the W mass variation provides another technique of measuring the effect or reducing its effect on the W Mass analysis. However, the statistical sensitivity is limited and work is continuing in this area.

3.3 Results

The preliminary LEP2 average value of the W Mass is

$$M_W = 80.412 \pm 0.29(\text{stat.}) \pm 0.031(\text{syst.}) \text{ GeV}/c^2,$$

when combined with the measurements made at the TeVatron a value of

$$M_W = 80.425 \pm 0.034 \text{ GeV}/c^2$$

is obtained. The preliminary LEP2 average direct W Width measurement is

$$\Gamma_W = 2.150 \pm 0.068(\text{stat.}) \pm 0.060(\text{syst.}) \text{ GeV}/c^2.$$

4 Angular distributions, Couplings and Spin-States

The existence of the SM triple gauge coupling (TGC) γWW and $ZWWW$ vertices is confirmed by the W^+W^- cross-section results presented above. The dashed lines in Figure 2 show the result that would be obtained in the absence of these vertices, as discussed in section 2.2.

In addition to the cross-section, TGCs affect the differential cross-sections as a function of the five W production and decay angles. A combined measurement has been made of the variation of the differential W^+W^- cross-section

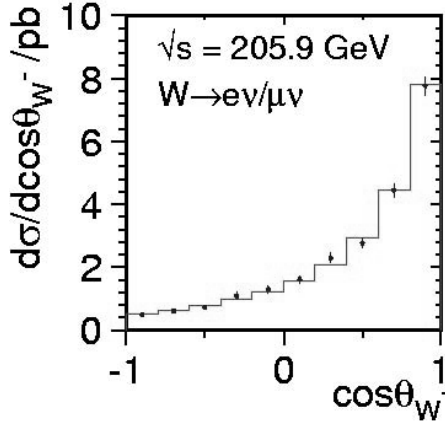


Figure 3: The W -pair differential cross-section as a function of the W - polar production angle for data collected at centre of mass energies above 204 GeV.

with the most important angle, the W - polar production angle with respect to the e - beam direction, for the $e\bar{\nu}_e q\bar{q}'$, $\mu\bar{\nu}_\mu q\bar{q}'$ decay channels. The charged lepton is required to be more than 20 degrees from the beam axis. This distribution, using measurements made by the ALEPH, DELPHI and L3 collaborations, is shown in Figure 3 for the data collected at the highest centre-of-mass energies in the year 2000.

The three coupling parameters which describe the TGC vertices and conserve C and P and SU(2) symmetry are denoted κ_γ , λ_γ and g_1^Z . Measurements of these parameters have been made by all LEP collaborations utilising cross-section and angular decay information. Single W production also carries TGC information, particularly on κ_γ , and hence is also included in the analyses of some experiments. Single parameter and two parameter fits have been performed and the results are compatible with the SM, with g_1^Z being determined to 2% accuracy.

Quartic Gauge couplings are also predicted by the SM but are below the sensitivity of the LEP experiments. However, limits have been placed on the existence of large anomalous QGCs and the cross-section for W^+W^- and a hard photon determined.

The existence of longitudinal polarised W s is generated in the SM through the electroweak symmetry breaking process. By exploiting the angular distribution of the W decay products or by using the Spin Density Method the fractions of longitudinal and transverse W s have been determined by the DEL-

PHI, L3 and OPAL collaborations. An experimental result of $23.6 \pm 1.6\%$ of longitudinal W s is obtained at the average centre-of-mass energy in agreement with the SM prediction of 24.0%.

5 Summary

The principal W boson measurements of the LEP collaborations have been presented: including the determination of the WW cross-section to 1% accuracy, the W Mass to $42 \text{ MeV}/c^2$ and the observation and determination of triple gauge couplings. The mass of the W boson makes a particularly important contribution to tests of the standard model, particularly when combined with the top quark mass measurements from the TeVatron. The combined fit to electroweak data inside the standard model prefers a relatively light SM Higgs and yields a preferred Higgs mass of $126_{-48}^{+73} \text{ GeV}/c^2$ (1).

6 Acknowledgements

I would like to thank the ALEPH, DELPHI, L3 and OPAL experiments and the LEP Electroweak and WW Working groups for their assistance in the preparation of this paper.

References

1. LEP Electroweak Working Group, hep-ex/0412015 (2004) and Winter 2004/2005 update, <http://www.cern.ch/LEPEWWG>
2. S. Jadach, W. Placzek, M. Skrzypek, B.F.L. Ward and Z. Was, *Comp. Phys. Comm.* **140** 475 (2001).
3. E. Accomando, A. Ballestrero and E. Maina, *Comp. Phys. Comm.* **150** 166 (2003).
4. R. Assmann *et al.*, *Eur. Phys. J.* **C39**, 253 (2005).
5. D. Bardin, J. Biebel, D. Lehner, A. Leike, A. Olchevski and T. Riemann, *Comp. Phys. Comm.* **104** 161 (1997).
6. F. Cossutti, *Electroweak correction uncertainties on the W mass measurement* CERN-EP-PH 2005-349, To be submitted to *Eur. Phys. J.*
7. L. Lönnblad and T. Sjöstrand, *Eur. Phys. J.* **C2**, 165 (1998).
8. J. Abdallah *et al.*, DELPHI Collab., *Bose-Einstein Correlations in W^+W^- events at LEP2* CERN-EP-PH 2004-072, Submitted to *Eur. Phys. J.*

W BOSON PRODUCTION AND MASS AT THE TEVATRON

Oliver Stelzer-Chilton

(on behalf of the CDF and DØ Collaborations)

University of Toronto, 60 St. George St.,

Toronto, Ontario, M5S 1A7, Canada

Email: oliversc@fnal.gov

Abstract

The CDF and DØ collaborations have analyzed up to $\sim 200 \text{ pb}^{-1}$ of Run 2 physics data to measure W production properties such as the W cross section, the W width, lepton universality and the W charge asymmetry. From the cross section measurements, CDF obtains a lepton universality of $\frac{g_\mu}{g_e} = 0.998 \pm 0.012$ and $\frac{g_\tau}{g_e} = 0.99 \pm 0.04$ and an indirect W width of $\Gamma_W = 2079 \pm 41 \text{ MeV}$. DØ measured the W width directly and finds $\Gamma_W = 2011 \pm 142 \text{ MeV}$. CDF has estimated the uncertainties on the W boson mass measurements in the electron and muon decay channels and obtains an overall uncertainty of 76 MeV.

1 Introduction

The properties of the Z boson have been measured to very high precision at LEP¹⁾. Naturally one wants to match this precision for the charged carriers of the electroweak interaction. Over the next few years the Tevatron is the only accelerator which can produce W bosons. Measuring the properties of the W boson to a very high precision is an important test of the Standard Model. From the measured W cross section, one can infer an indirect measurement of the W width and lepton universality. Since at the Tevatron the W bosons are produced through quark anti-quark annihilation, a significant uncertainty for all direct electroweak measurements comes from the knowledge of the parton distributions inside the proton. The probability of finding a parton carrying a momentum fraction x within the incoming proton is expressed in the parton distribution function (PDF). The measurement of the W charge asymmetry provides important input on the ratio of the u and d quark components of the PDF and will help to further constrain parton distribution functions. The W boson mass serves as a test of the Standard Model, but through radiative corrections is also sensitive to hypothetical new particles. Together with a precise measurement of the top quark mass²⁾, the W boson mass constrains the mass of the Higgs boson, which has not yet been observed experimentally.

Both CDF and DØ are multi-purpose detectors. They consist of tracking systems surrounded by calorimeter and muon identification systems. CDF's tracking system consists of a wire drift chamber (the Central Outer Tracker) and a 7-layer silicon microstrip vertex detector (SVXII) immersed in a 1.4 T magnetic field. A lead (iron) scintillator sampling calorimeter is used for measuring electromagnetic (hadronic) showers. DØ employs a silicon microstrip tracker (SMT) and a central fiber tracker (CFT), both located in a 2 T magnetic field. The sampling calorimeter consists of liquid argon and uranium.

Since the hadronic decay of the W boson has an extremely large background originating from strongly interacting processes, CDF and DØ use the clean leptonic decays to study the W boson. The signature is a high energy lepton with large missing transverse momentum originating from the neutrino, which does not interact with the detector. The momentum balance in the direction of the beam is unconstrained and as a result, the W events are studied in the plane transverse to the beam. A typically used quantity is the transverse mass:

$$M_T = \sqrt{2p_T^l p_T^\nu (1 - \cos(\Delta\phi))}, \quad (1)$$

which is similar to the invariant mass, just in the two transverse dimensions. If not otherwise stated, we restrict the lepton identification to the well instrumented central region of $|\eta| < 1$.

Z boson events are identified by two high energy leptons. These events have very low background.

2 Inclusive $p\bar{p} \rightarrow W/Z + X$ Cross Section Measurements

W and Z bosons are identified by their leptonic decays to electrons, muons and taus, from which the total rates $\sigma \times \text{Br}(W \rightarrow l\nu)$ and $\sigma \times \text{Br}(Z \rightarrow ll)$ are obtained. The cross section times branching ratio is calculated as follows:

$$\sigma \times \text{Br}(p\bar{p} \rightarrow W/Z \rightarrow ll) = \frac{N_{\text{cand}} - N_{\text{bkg}}}{A\epsilon L}. \quad (2)$$

The W and Z boson cross sections have been measured by CDF ³⁾ with different datasets in different sub-detectors. Figure 1 shows a summary of the CDF and DØ cross section measurements in all leptonic decay modes. All measure-

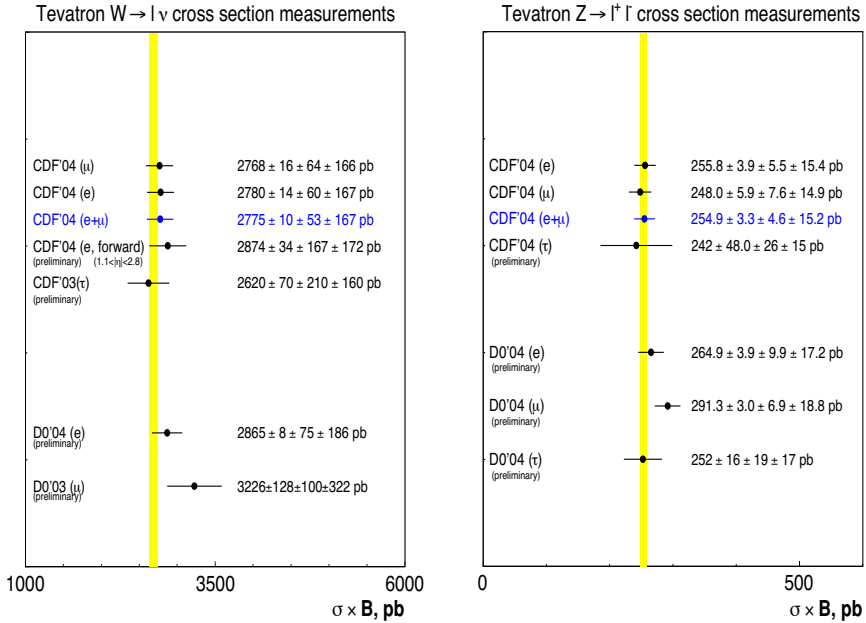


Figure 1: Summary of various CDF and DØ W and Z cross section measurements in all three leptonic decay channels, using different datasets and sub-detectors. The uncertainties are listed in the following order: statistical, systematic, and luminosity.

ments show good agreement with NNLO calculations ⁴⁾, represented by the vertical band.

2.1 Lepton Universality in W Decays

Lepton universality in W decays can be tested by extracting the ratio of the electroweak couplings g_μ/g_e and g_τ/g_e from the measured ratio of $W \rightarrow l\nu$ cross sections. The $W \rightarrow l\nu$ couplings are related to the measured production cross section ratio U as follows:

$$U = \frac{\sigma \times Br(W \rightarrow l\nu)}{\sigma \times Br(W \rightarrow e\nu)} = \frac{\Gamma(W \rightarrow l\nu)}{\Gamma(W \rightarrow e\nu)} = \frac{g_l^2}{g_e^2} \quad (3)$$

In this ratio, important systematic uncertainties cancel. The results obtained are ³⁾:

$$\frac{g_\mu}{g_e} = 0.998 \pm 0.012 \quad (4)$$

$$\frac{g_\tau}{g_e} = 0.99 \pm 0.04 \quad (5)$$

where the largest systematic uncertainty comes from event selection efficiencies. Since these efficiencies are measured using the $Z \rightarrow ll$ sample, the uncertainty will decrease as more Z bosons are collected.

2.2 Indirect W Width Determination

The ratio R of the cross section measurements for W and Z bosons can be used to extract the total width of the W boson. R can be expressed as:

$$R = \frac{\sigma(p\bar{p} \rightarrow W) \Gamma(W \rightarrow l\nu) \Gamma(Z)}{\sigma(p\bar{p} \rightarrow Z) \Gamma(Z \rightarrow ll) \Gamma(W)}. \quad (6)$$

Using the very precise measurement of $\Gamma(Z \rightarrow ll)/\Gamma(Z)$ from LEP and NNLO calculations of $\sigma(p\bar{p} \rightarrow W)/\sigma(p\bar{p} \rightarrow Z)$, together with the Standard Model prediction of $\Gamma(W \rightarrow l\nu)$ one can extract $\Gamma(W)$ from equation 6. Table 1 shows

Table 1: *Summary of indirect W width measurements.*

Channel	$\Gamma(W)(MeV)$	L (pb^{-1})
$W \rightarrow e\nu + W \rightarrow \mu\nu$	2079 ± 41	72
$W \rightarrow \mu\nu$	2056 ± 44	194
World average	2124 ± 41	

the values from CDF for two different datasets, together with the current world average (not including these measurements). The indirect width measurements show good agreement and have competitive uncertainties.

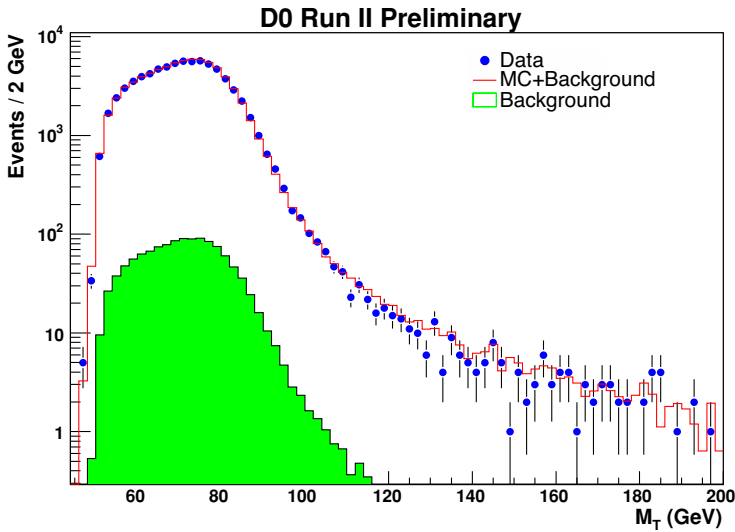


Figure 2: W width extraction from high transverse mass tail.

3 Direct W Width Measurement

DØ has measured the W boson width directly in the electron decay channel ⁵⁾. The measurement uses an integrated luminosity of 177 pb^{-1} . The width is determined by normalizing the predicted signal and background transverse mass distribution in the region of $50 \text{ GeV} < M_T < 100 \text{ GeV}$ and then fitting the predicted shape to the candidate events in the tail region $100 \text{ GeV} < M_T < 200 \text{ GeV}$, which is most sensitive to the width. Figure 2 shows the transverse mass distribution. The measurement yields $\Gamma_W = 2011 \pm 93(\text{stat}) \pm 107(\text{syst}) \text{ MeV}$, which is in good agreement with the world average, an improvement over the DØ Run 1 measurement ⁶⁾, and competitive to the CDF Run 1 measurements in the muon and electron decay channels ⁷⁾.

4 W Charge Asymmetry

The W bosons at the Tevatron are produced predominantly through annihilation of valence u (d) and anti- d (anti- u) quarks inside the proton and anti-protons for W^+ (W^-) production. Since u quarks carry, on average, a higher fraction of the proton momentum than d quarks, a W^+ tends to be boosted in the proton direction, while a W^- is boosted in the anti-proton direction. This

results in a non-zero forward-backward charge asymmetry, defined as:

$$A(y_W) = \frac{d\sigma(W^+)/dy_W - d\sigma(W^-)/dy_W}{d\sigma(W^+)/dy_W + d\sigma(W^-)/dy_W}, \quad (7)$$

where y_W is the rapidity of the W bosons and $d\sigma(W^\pm)/dy_W$ is the differential cross section for W^+ or W^- boson production. However, because the p_Z of the neutrino is unmeasured, y_W cannot be directly determined, and we instead measure:

$$A(\eta_e) = \frac{d\sigma(e^+)/d\eta_e - d\sigma(e^-)/d\eta_e}{d\sigma(e^+)/d\eta_e + d\sigma(e^-)/d\eta_e}, \quad (8)$$

where η_e is the electron pseudorapidity. Therefore, the observed asymmetry is a convolution of the aforementioned charge asymmetry and the Standard Model $V - A$ couplings describing the $W \rightarrow e\nu$ decays. A measurement of

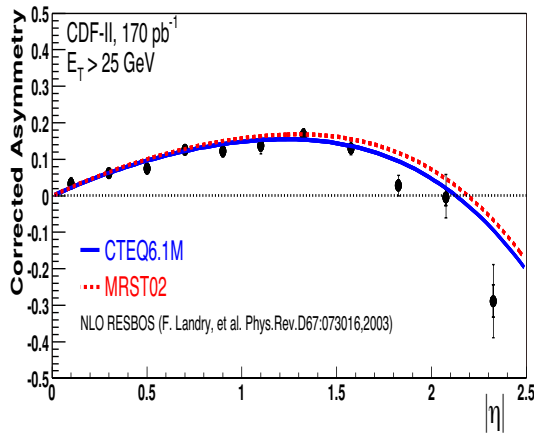


Figure 3: *Measured asymmetry corrected for the effects of charge misidentification and background contributions.*

the forward-backward charge asymmetry is sensitive to the ratio of the u and d quark components of parton distribution functions. CDF has measured this asymmetry in the electron channel up to a pseudorapidity of $|\eta| < 2.5$ using 170 pb^{-1} ⁸). Figure 3 shows the measured asymmetry corrected for the effects of charge misidentification and background contributions. The predictions using the latest CTEQ and MRST PDFs are overlaid. This measurement will provide important input for the next generation of PDFs.

5 W Mass

Since its discovery in 1983⁹⁾ 10), the W boson mass has been measured with increasing precision. From an initial uncertainty of 5 GeV, the uncertainty of the W mass has been reduced to 42 MeV from the LEP experiments¹¹⁾ and to 59 MeV from the Tevatron experiments⁷⁾. CDF has analyzed the first 200 pb⁻¹ of Run 2 data and estimated the corresponding W boson mass uncertainty in the electron and muon decay channels. The uncertainty includes contributions from statistics, production and decay modeling, lepton energy scale and resolution, hadronic recoil and resolution, and backgrounds.

There are two important aspects to a precision W mass measurement: Calibration of the detector to the highest possible precision, and simulation of the transverse mass spectrum, which cannot be predicted analytically. The simulation includes the production modeling and detector effects and produces transverse mass templates for a range of W boson masses. Since backgrounds contaminate the signal, they are included in the templates. The W mass is extracted from a maximum likelihood fit to the transverse mass spectrum.

5.1 Production Model

The uncertainty in the modeling of the W boson production and decay results from parton distribution functions, QED radiative corrections, the transverse momentum of the W boson and the W boson width.

The parton distribution functions affect the W mass through the limited acceptance of the detector for the W decay lepton. The uncertainty has been determined using the set of 40 CTEQ6 PDFs¹²⁾, which explore the uncertainty on the 20 orthogonal eigenvector directions in parameter space. Each eigenvector direction corresponds to some linear combination of PDF parameters. The resulting uncertainty is $\Delta M_W(e, \mu) = \pm 15$ MeV. A cross check using the latest MRST¹³⁾ PDF falls within this estimate.

The dominant higher-order QED effect on the W boson mass is photon radiation off the final-state charged lepton. Additional QED uncertainties arise from multi-photon radiation, initial state radiation and radiation from interference terms, none of which are included in the simulation used to extract the W boson mass. The uncertainty from QED corrections is $\Delta M_W(\mu) = \pm 20$ MeV in the muon channel and $\Delta M_W(e) = \pm 15$ MeV in the electron channel.

The initial-state QCD radiation in vector boson production is constrained by a phenomenological parametrization of the Z boson p_T measurement from the previous collider run. The parameters are used for the modeling of the W p_T distribution and their uncertainties result in $\Delta M_W(e, \mu) = \pm 13$ MeV.

The uncertainty on the W boson width affects the falling Jacobian edge and leads to $\Delta M_W(e, \mu) = \pm 12$ MeV.

5.2 Lepton Momentum/Energy Scale and Resolution

The lepton momentum measurement is based fundamentally on the calibration of the tracking wire chamber (COT). After the calibration of the track momentum and resolution using the muon decays of precisely known resonances, the energy scale of the electromagnetic calorimeter is calibrated using the ratio of calorimeter energy to track momentum (E/p) of electrons.

The quarkonium resonance decays $J/\Psi \rightarrow \mu\mu$ and $\Upsilon(1S) \rightarrow \mu\mu$ are used to set the momentum scale (Figure 4). The passive material in the simulation

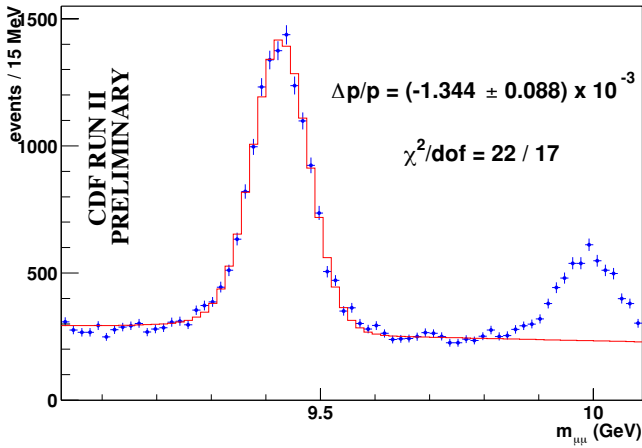


Figure 4: *The reconstructed invariant mass of muon candidate pairs in the $\Upsilon(1S)$ region. The fractional difference between the measured and PDG mass is shown.*

is tuned such that the reconstructed J/Ψ mass is constant as a function of mean track curvature. The measured momentum scale is the mean of the individual J/Ψ and $\Upsilon(1S)$ scales. The systematic uncertainty is taken as half the difference between the extracted scales which results in $\Delta M_W(e, \mu) = \pm 15$ MeV.

The track resolution is parametrized in the simulation by the individual hit resolution and by the hit multiplicity on the track. Muons from decays of Z bosons are used to determine the resolution. The resulting uncertainty corresponds to $\Delta M_W(e, \mu) = \pm 12$ MeV. An additional uncertainty of $\Delta M_W(e, \mu) = \pm 20$ MeV is assigned for tracking chamber misalignments.

The E/p distribution of electrons from W boson decays is used to calibrate the electromagnetic energy scale of the calorimeter (Figure 5). The

statistical uncertainty and the uncertainty from the momentum scale results in $\Delta M_W(e) = \pm 35$ MeV. Additional energy scale uncertainties arise from the cal-

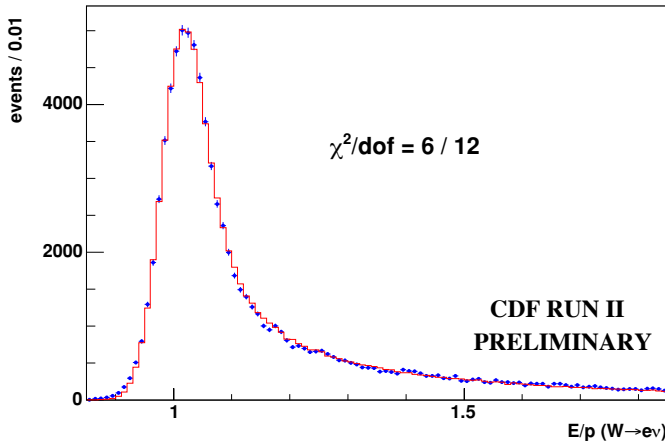


Figure 5: The E/p distribution of electrons from W boson decays. The region between 0.95 and 1.1 is used for the calibration of the electromagnetic energy scale.

ibration of the detector passive material and from the calorimeter non-linearity. The passive material was measured during detector construction and is tuned using electrons from photon conversions. A final tuning uses the tail of the E/p distribution which is sensitive to the amount of material modeled in the simulation. The uncertainty on the passive material results in $\Delta M_W(e) = \pm 55$ MeV. The calorimeter non-linearity is determined from the E_T dependence of the energy scale. After applying a correction, the uncertainty on the slope results in $\Delta M_W(e) = \pm 25$ MeV.

The calorimeter resolution is parametrized as $\sigma E_T/E_T = 13.5\%/\sqrt{E_T} \oplus \kappa$, where κ is determined from the width of the E/p signal. The uncertainty on κ results in $\Delta M_W(e) = \pm 7$ MeV.

The Z boson masses are used as cross checks for the momentum and energy scales.

5.3 Recoil Scale and Resolution

The hadronic recoil is measured by summing over the energy in all calorimeter towers, excluding the lepton towers. The simulation removes an equivalent set of towers by subtracting the mean underlying event energy as measured from

adjacent towers. The uncertainty on the measurement of this underlying event energy results in $\Delta M_W(e) = \pm 15$ MeV and $\Delta M_W(\mu) = \pm 10$ MeV uncertainties on the W mass.

The hadronic recoil scale is the ratio of measured to true recoil. It is parametrized as a function of the true recoil and tuned using Z events where both decay leptons are reconstructed and the Z boson p_T can be reconstructed precisely from the lepton momentum measurements. The uncertainty on the parametrization results in $\Delta M_W(e, \mu) = \pm 20$ MeV.

The recoil resolution model incorporates terms from the underlying event, which are modeled with generic inelastic collisions, and from hadronic jet resolution. The resolution uncertainty results in $\Delta M_W(e, \mu) = \pm 42$ MeV.

5.4 Backgrounds

The backgrounds in the W boson data sample include $W \rightarrow \tau\nu$, $Z \rightarrow ll$ where one lepton is outside the detector acceptance and not reconstructed, hadronic jets, where one jet mimics a lepton, cosmic rays, where one leg of the cosmic track is not reconstructed, and kaon decays, where the kaon track is misreconstructed, resulting in large apparent muon momentum. The background measurement uncertainties result in $\Delta M_W(e, \mu) = \pm 20$ MeV.

5.5 Mass Fits and Total Uncertainty

After including all measurement components, CDF obtains transverse mass (Figure 6) and transverse energy distributions which are well modeled. Table 2 summarizes the uncertainties for the M_T fits in the electron and muon decay channels. For comparison the uncertainties from the previous collider run ¹⁴⁾

Table 2: *The uncertainty on the W boson mass measurement using ~ 200 pb⁻¹ of Run 2 CDF data. The CDF Run 1b uncertainties are shown for comparison.*

Uncertainty	Electrons (Run 1b)	Muons (Run 1b)
Production and Decay Model	30 (30)	30 (30)
Lepton Energy Scale and Resolution	70 (80)	30 (87)
Recoil Scale and Resolution	50 (37)	50 (35)
Backgrounds	20 (5)	20 (25)
Statistics	45 (65)	50 (100)
Total	105 (110)	85 (140)

(Run 1b) are also included. The overall uncertainty is 76 MeV. The W boson mass fit results are currently blinded with a constant offset. The offset will be removed when further cross checks have been completed.

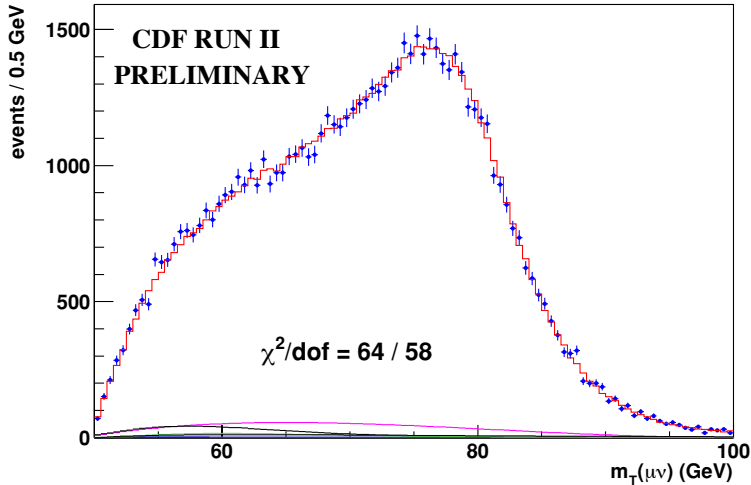


Figure 6: The M_T distribution in W boson decays to muons. The points represent the data, the histogram the simulation with backgrounds added. The region between 60-90 GeV is used to fit the W boson mass.

6 Summary

The W boson physics program at the Tevatron is very successful. CDF and DØ have measured the inclusive W and Z cross sections in all three leptonic decay channels, which show good agreement with NNLO calculations. From the cross section measurements, CDF has extracted competitive measurements on lepton universality and an indirect measurement of the W boson width. DØ has measured the W boson width directly in the electron channel with an uncertainty smaller than the Run 1 value. The new CDF W charge asymmetry will help to further constrain the uncertainties of parton distribution functions, which affect all the aforementioned measurements. With the addition of 600 pb^{-1} of data on tape, these measurements will further constrain the Standard Model.

CDF has determined the uncertainty on the W boson mass with the first $\sim 200 \text{ pb}^{-1}$ of Run 2 data to be 76 MeV, which is lower than its Run 1 uncertainty of 79 MeV. With the additional data to come, Run 2 promises the world's highest precision measurement of the W boson mass, with an anticipated uncertainty of 30 MeV for 2 fb^{-1} .

7 Acknowledgments

I would like to thank my colleagues from the CDF and DØ electroweak groups for their hard work and input to this talk.

References

1. Particle Data Group, Phys. Lett. B **592**, 343 (2004).
2. George Velev, these proceedings.
3. D. Acosta *et al.*, Phys. Rev. Lett. **94**, 091803 (2005).
4. C. Anastasiou *et al.*, Phys. Rev. D. **69**, 094008 (2004).
5. The DØ Collaboration, DØ note 4563-CONF (2004).
<http://www-d0.fnal.gov/Run2Physics/WWW/results/prelim/EW/E08/E08.pdf>
6. V. M. Abazov *et al.*, Phys. Rev. D. **66**, 032008 (2002).
7. The CDF Collaboration and the DØ Collaboration, Phys. Rev. D. **70**, 092008 (2004).
8. D. Acosta *et al.*, Phys. Rev. D. **71**, 051104 (2005).
9. G. Arnison *et al.*, Phys. Lett. B. **122**, 103 (1983).
10. M. Banner *et al.*, Phys. Lett. B. **122**, 476 (1983).
11. The LEP Electroweak Working Group, 2003-01 (2003)
http://lepewwg.web.cern.ch/LEPEWWG/lepww/mw/Winter03/mwgg_w03.ps.gz
12. J. Pumplin *et al.*, JHEP **07**, 012 (2002).
13. A. D. Martin *et al.*, hep-ph/0307262 (2003).
14. T. Affolder *et al.*, Phys. Rev. D. **64**, 052001 (2001).

TOP MASS MEASUREMENTS AT THE TEVATRON RUN II

Gueorgui V. Velev

e-mail: velev@fnal.gov

Fermi National Accelerator Laboratory, Batavia, IL 60510

for

the CDF and DØ collaborations

Abstract

The latest top quark mass measurements by the CDF and DØ experiments are presented here. The mass has been determined in the dilepton ($t\bar{t} \rightarrow e\mu, ee, \mu\mu$ + jets + \cancel{E}_T) and lepton plus jets ($t\bar{t} \rightarrow e$ or μ + jets + \cancel{E}_T) final states. The most accurate single result from lepton plus jets channel is $173.5^{+3.7}_{-3.6}$ (stat. + Jet Energy Scale Systematic) ± 1.3 (syst.) GeV/ c^2 , which is better than the combined CDF and DØ Run I average. A preliminary and unofficial average of the best experimental Run II results gives $M_{top} = 172.7 \pm 3.5$ GeV/ c^2 .

1 Introduction

Since the first evidence in 1994 ¹⁾ and the discovery of the top quark in 1995 ^{2) 3)}, the CDF and DØ Collaborations invested a lot of work to determine its properties, specially the value of its mass, which is a fundamental parameter of the Standard Model (SM). The ongoing Run II, with the upgraded Fermilab Tevatron collider and CDF and DØ detectors, gives new possibilities for a precise measurement of the top mass. Due to its large mass, corresponding to a Yukawa coupling of order unity, one may suspect that the top quark may have a special role in the electroweak symmetry breaking. In addition, due to its significant contribution to high order radiative corrections of a number of electroweak observables, a precise measurement of the top quark mass provides a tighter constrain on the Higgs mass ⁴⁾.

This paper reports on the latest CDF and DØ top quark mass results which are based on about 318 pb^{-1} (CDF) and 219 pb^{-1} (DØ) of data from the first two years of the Tevatron Run II (2002 to 2004). Another paper, presented on this conference ⁵⁾, summarized the top quark kinematics properties including its recently measured production cross section at the center of mass energy of $\sqrt{s}=1.96 \text{ TeV}$,

At this Tevatron energy, top quarks are produced generally in pairs from the processes $q\bar{q} \rightarrow t\bar{t}$ (in $\sim 85\%$ of the cases) and $gg \rightarrow t\bar{t}$ (in $\sim 15\%$ of the cases). Top can be produced as a single quark by electroweak interactions, by W-gluon fusion or virtual W^* production in the s-channel ⁶⁾, but with a smaller cross section. At this time, no signal has been observed from single top processes and they are not expected to be utilized for a precise mass measurement.

In the Standard Model the branching ratio of the decay $t \rightarrow bW$ is nearly 100%. When a $t\bar{t}$ pair is produced, each of the W-bosons can decay into either a charged lepton and a neutrino (branching ratio of 1/9 for each lepton family) or into a $q\bar{q}$ quark pair (branching ratio of 2/3). This allows us to classify the final states as:

- Dilepton final state, when both W's from the $t\bar{t}$ pair decay leptonically. This state is characterized by two high P_T charged leptons, two jets from $b\bar{b}$ quarks ¹ and significant missing transverse energy (E_T) from the neutrinos.
- Lepton plus jets final state, when one W boson decays leptonically and the other one hadronically. This state contains one high P_T charged

¹Errors in jet reconstruction and gluon radiation in the event may make the observed number of jets smaller or larger. This statement is valid for all final states.

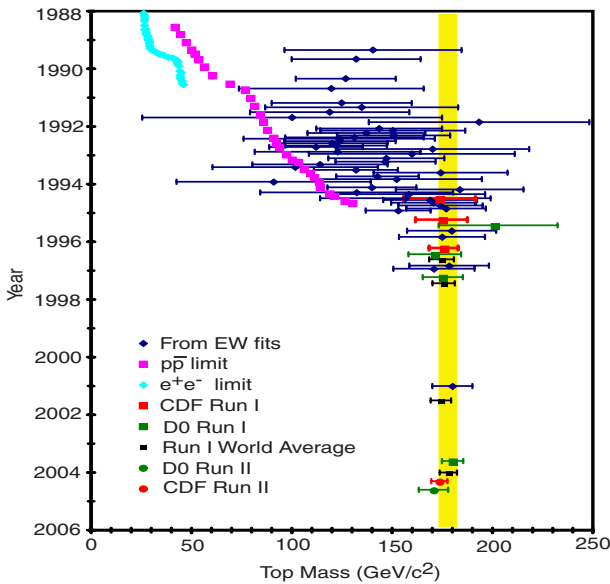


Figure 1: The summary of the top mass “evaluations” and direct measurements versus time. See the text for explanation of the points.

lepton, four jets and significant \cancel{E}_T .

- All hadronic final state, when both W’s decay hadronically. This state is characterized by 8 jets, two of which are from b -quarks.

In Run I, CDF and DØ used all of these signatures for the top mass measurements. At this time, the Run II top mass analyses from the all-hadronic channel are still in progress and will not be reported in this paper.

Figure 1 shows how our knowledge on the top quark mass improved with time. The diamonds represent the indirect determinations from fits to the electroweak observables ⁷⁾. The curves in the upper left corner of the figure represent the limits from direct searches in e^+e^- and $p\bar{p}$ machines. The Run I CDF and DØ results are presented with squares. The filled circles are the new Tevatron Run II results. The band represents the average Run I top mass results. One observes that the recent Tevatron results have equal or better accuracy than the Run I world average.

2 Top kinematics and mass reconstruction methods

The kinematics of the events in the lepton plus jets final state is over-constrained. In this channel, the number of measured quantities and the number of applicable energy-conservation equations, from five production and decay vertices, are larger than the number of non-measured kinematical event parameters. This feature allows for a complete reconstruction of the four-momenta of the final state particles in the event, for example using the two constrain kinematical fit (2CF), and for a reconstruction of the top mass event-by-event. In this type of analysis there is an ambiguity in how to assign the four leading jets to the two b quarks and two light quarks coming from the $t\bar{t}$ system. If none of these jets is tagged by b taggers ², there are 12 different ways of assigning jets to the 4 partons. Combining with the ambiguity from solving of a quadratic equation on P_z^ν , there are 24 different values of m_{top} returned by the fit. The combinations are reduced to 12 or to 4 if one or two of the jets are selected from b -taggers.

The variety of the CDF and $D\emptyset$ analyses in the lepton plus jet sample is relatively large. However, all analyses can be separated in three major categories:

1. Template type analyses, where the reconstructed mass distribution from the data is compared with expected distributions from Monte Carlo generated signal (mass-dependent) and background. In these types of analyses, all events are weighted equally. By doing so one neglects the additional information coming from a different mass resolution in single events. In addition no use is made of possible information from the dynamic of the process which can be assumed to be known. Typical examples for this type of analysis are the CDF and $D\emptyset$ Run I ¹⁰⁾ ¹¹⁾ and the latest, most accurate CDF Run II lepton plus jets analysis, described in Section 3.1.
2. Matrix Element type analyses, originally proposed by Dalitz and Goldstein ¹²⁾ and independently by Kondo ¹³⁾. These methods calculate the posterior probability, given the known production cross section, for every event with measured kinematic properties, to originate from a $p\bar{p} \rightarrow t\bar{t}$ process. A typical example is the $D\emptyset$ Matrix Element analysis which is the base of the best Run I top mass measurement ¹⁴⁾. In Run II CDF uses a method, proposed by K.Kondo ¹³⁾, called Dynamic Likelihood Analysis, which differs in the way that the normalization of the differential cross section is performed.

²CDF and $D\emptyset$ use taggers based on either displaced vertices (Secondary Vertex Tagging, SVX, for example see ⁸⁾) or on low P_T electrons or muons from the b -quark semileptonic decays (Soft Lepton Tagging, SLT ⁹⁾)

3. A mixture between methods 1) and 2). For example the $t\bar{t}$ event is reconstructed using the kinematic algorithms similar to the template analyses but an event-by-event probability of each kinematic reconstruction is exploited as a weight (for example $\exp(-\frac{\chi^2}{2})$). A typical example of this category is the DØ Ideogram Analysis ¹⁵⁾.

3 Lepton plus jet channel

3.1 CDF result

For the time being the most accurate top quark mass measurement comes from the lepton plus jets channel. This channel combines the benefits of good signal to background ratio, the possibility to reconstruct the top quark mass event by event with a relatively small combinatorial effect, and a large branching fraction. In brief, we discuss below the main selection criteria for this channel.

Lepton plus jets events have the signature $p\bar{p} \rightarrow t\bar{t}X \rightarrow \ell\nu b q\bar{q}'\bar{b}X$. The characteristics of this final state begins with the identification of one isolated central high energy lepton (e with $E_T > 20$ GeV or μ with $P_T > 20$ GeV) and $|\eta| < 1$ ³⁾.

Assuming that the lepton is coming from W boson decay, a companion neutrino should exist. This would spoil the balance of the observed momentum in the transverse plane. The missing transverse energy (\cancel{E}_T) is constructed by adding the calorimeter energy vectors in the plane transverse to the beam. The calorimeter clusters identified as jets are corrected for detector response and for multiple $p\bar{p}$ interactions. In muon events the \cancel{E}_T is computed using the muon momentum measured by the track instead of the muon calorimeter signal.

In order to fully reconstruct the $t\bar{t}$ system, at least four central jets $|\eta| \leq 2$ are required in the system. The SVX tagging algorithm is run over the leading jets ($E_T > 15$ GeV): some of them may be identified as b-jets. To obtain maximum statistical benefit from the event sample it is helpful to decompose it into several classes of events which are expected to have different signal-to-background ratios and top mass resolutions. The Monte Carlo studies showed that an optimal partitioning is obtained splitting the sample into four statistically independent categories: events with double SVX tags (2SVX), events with single SVX tag and tight fourth jet cut (four jets with $E_T > 15$ GeV, 1SXVT), events with single SVX tag and loose fourth jet cut ($15 > E_T > 8$ GeV for the 4th jet, 1SXVL) and finally events without tags (0-tag). Since the last sample has a high background contamination compared to SVX tagged ones, an additional

³⁾A complete description of the lepton selection, including all cuts used, can be found elsewhere ¹⁶⁾

Table 1: In the first four columns from left to right: lepton plus jets subsamples used in the top quark mass analysis, number of events in each sample, S/B ratio, and a summary of the jet energy cut selection are presented. A total of 165 $t\bar{t}$ candidates were selected. The last column summarizes the background fractions in % from $W + \text{light quark}$, $Wb\bar{b} + Wc\bar{c} + Wc$ and QCD multijet events (left to right).

Data Subsample	Number of events	S/B	Jet E_T cuts (GeV) jets 1-3 (4^{th} jet)	Bckg. type and fraction in %
2SVX	25	10.6/1	$E_T > 15$ ($E_T > 15$)	21/59/10
1SVXT	63	3.7/1	$E_T > 15$ ($E_T > 15$)	17/38/22
1SVXL	33	1.1/1	$E_T > 15$ ($15 > E_T > 8$)	29/48/14
0-tag	44	0.9/1	$E_T > 21$ ($E_T > 21$)	75/3/20

optimization of the jet E_T cuts ($E_T > 21$ GeV) was performed. A total of 165 $t\bar{t}$ candidates were selected from 318 pb^{-1} of data.

The dominant backgrounds in all samples are direct W plus multijet production, including heavy flavour production, and QCD multijet events where one jet is misidentified as a lepton. Additional small backgrounds are due to WW/WZ and single top production. The amount and composition of the background depends on the sample. In the case of the 2SVX sample, the $Wb\bar{b} + Wc\bar{c} + Wc$ background dominates ($\sim 60\%$) while in the case of the 0-tag sample, the W plus light quark production is responsible for $\sim 75\%$ of background. The information for these four subsamples, including the dominant type and background fraction, is summarized in Table 1.

Each event, either from data or MC samples, is fitted to the hypothesis $t\bar{t}X \rightarrow \ell\nu b q \bar{q}' \bar{b}X$. We use four kinematic constraints, as a consequence of the assumed lepton plus jets event structure ($M_{\ell\nu} = M_{jj} = M_W$ and $M_{\ell\nu b} = M_{jjb} = M_{top}$). The fitting procedure runs over all possible 24 combinations of assigning the four leading jets to the b, \bar{b} and $W \rightarrow q\bar{q}'$ partons (the order of the pair assigned to the W is irrelevant). If one or two of the four leading jets are tagged as a b -jets, they are assigned to the b -partons and the number of explored combinations is correspondingly smaller. All solutions with $\chi^2 < 9$ (cut optimized on the MC studies) are accepted. The top mass value corresponding to the combination with the minimum χ^2 is picked as the mass value indicated by the event.

The events from the MC samples are used to produce probability density distributions or so-called templates. In case of the signal MC, these distributions are parameterized as a function of reconstructed and input top masses. On the other hand, the background probability density distributions are parameterized only as a function of the reconstructed mass. The likelihood of

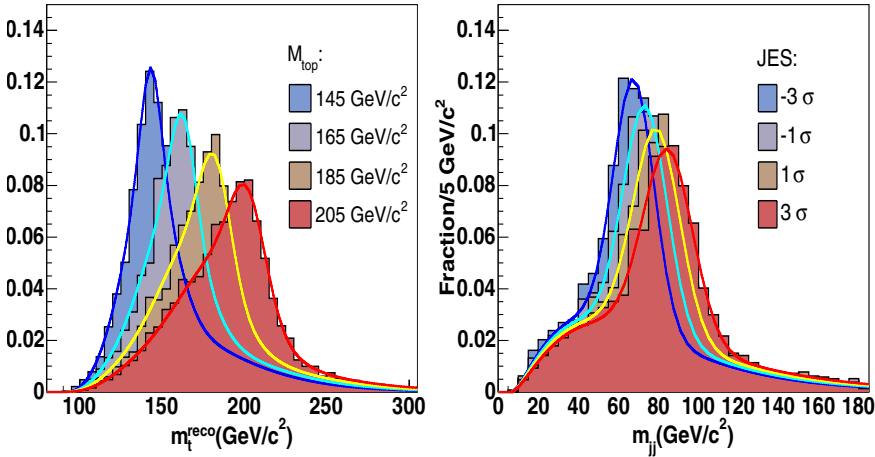


Figure 2: *Left: reconstructed top mass p.d.fs for input top masses from 145 to 205 GeV/c^2 and $\text{JES} = 0$. Right: reconstructed mass p.d.fs of the dijet system attributed to the W for different JES values in the range of $-3\sigma - +3\sigma$ and input top mass of 180 GeV/c^2 .*

each subsample uses the parameterized signal and background probability density functions (p.d.f) to evaluate the dependence of the likelihood on the input top mass.

To reduce the dominant systematic error coming from jet energy scale (JES) ¹⁰⁾ the latest CDF template analysis exploits the fact that the global JES scale can be determined from the decay $W \rightarrow q\bar{q}'$. MC studies have shown that this technique provides a 22% reduction in the JES uncertainty. Similar template distributions as for the kinematically reconstructed top mass are built for the dijet mass, with the exceptions of removing the $\chi^2 < 9$ requirement, exploiting all the possible jet-to-parton assignments in the event. Examples of top and dijet reconstructed masses p.d.fs are shown on Figure 2 left and right respectively.

The reconstructed top and W dijet mass values for every data event are simultaneously compared to the p.d.fs from signal and background sources

Table 2: *The systematic uncertainties in the CDF lepton plus jets top quark mass measurement.*

Source	ΔM_{top} (GeV/c ²)
b-jets modeling	0.6
Method	0.5
Initial state radiation	0.4
Final state radiation	0.6
Shape of background spectrum	0.8
<i>b</i> -tag bias	0.1
Parton distribution functions	0.3
Monte Carlo generators	0.2
MC statistics	0.3
Total	1.5

performing an unbinned likelihood fit. The fit finds a maximum likelihood value according to: the expected numbers of signal and background events in each subsample, the JES and the true top quark mass (M_{top}). Only M_{top} is a free parameter in the likelihood fit, the other are constrained within their uncertainties. For each subsample, the likelihood has the following form:

$$\mathcal{L} = \mathcal{L}_{shape}^{M_{top}} \cdot \mathcal{L}_{shape}^{m_{jj}} \cdot \mathcal{L}_{counting} \cdot \mathcal{L}_{bg}. \quad (1)$$

In (1), the main information on the top quark mass is hidden in the term $\mathcal{L}_{shape}^{M_{top}}$. It gives the probability for an event with reconstructed top mass m_{top}^{rec} to come from true top mass M_{top} . All other terms constrain the JES ($\mathcal{L}_{shape}^{m_{jj}}$), the number of observed events ($\mathcal{L}_{counting}$) and number of expected backgrounds in the subsample (\mathcal{L}_{bg}) and help to reduce the statistical and systematical uncertainties returned by the fit.

The systematic uncertainties are summarized in Table 2. For each systematic source, the relevant parameters are varied by $\pm 1\sigma$ in the $t\bar{t}$ MC sample with $M_{top}=178$ GeV/c² and sets of fake events are generated. These fake events are reconstructed in the same way as normal events. This procedure is called ‘‘pseudoexperiments’’ (PE). It propagates the $\pm 1\sigma$ effects to a shift in the top mass relative to the result from the nominal sample.

The reconstructed top masses in the four subsamples with overlaid best fit for the signal and background MC expectation are shown in Figure 3. The combined fit for all lepton plus jets events returned $M_{top} = 173.5_{-3.6}^{+3.7}$ (stat.+JES) ± 1.3 (syst.) GeV/c² and JES = $-0.10_{-0.91}^{+0.89}$ (stat.+syst.). This is the most precise single measurement available to date, better than the average Run I result.

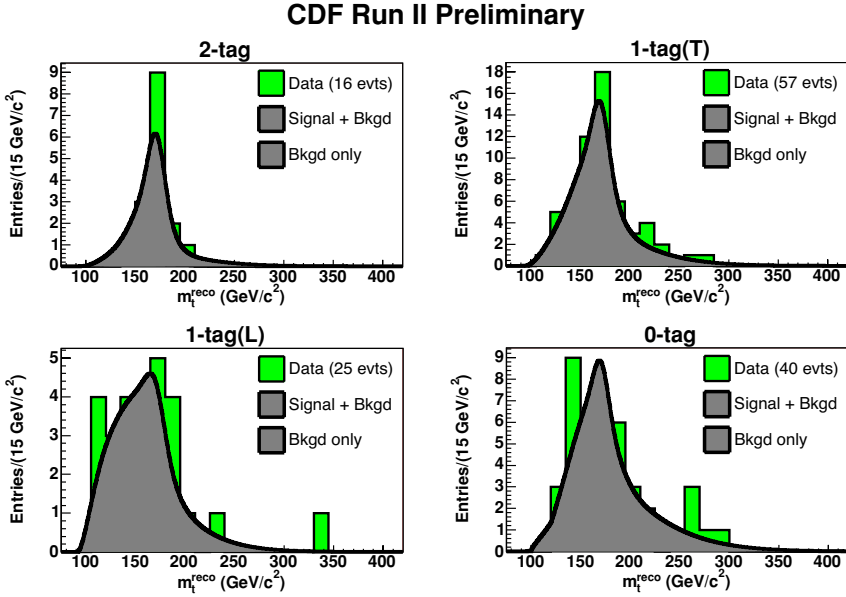


Figure 3: *The reconstructed mass distribution (histogram) for each lepton plus jets CDF subsamples is overlaid with the result of the likelihood fit (signal+background, hatched area). The cross hatched area represents only the background.*

3.2 $D\bar{O}$ Result

$D\bar{O}$ has measured the top quark mass in the lepton plus jets channel as well. The utilized data set corresponds to an integrated luminosity of approximately 229 pb^{-1} collected between April 2002 and March 2004.

The event selection criteria are similar to those used in CDF. As a first selection step, an identification of the a high P_T isolated electron or muon accompanied by substantial large $\cancel{E}_T > 20 \text{ GeV}$ is required. The isolated electron (muon) candidate should have $P_T > 20 \text{ GeV}$, satisfy a pseudo-rapidity cut of $|\eta| < 1.1$ ($|\eta| < 2.0$) and tight quality conditions. These initial selections provide the data sample.

Two separated analyses, b-tagged and topological, are performed on this sample. In the b-tagged analysis, to reconstruct the top mass the events are additionally selected to have at least 4 jets with $P_T > 15 \text{ GeV}$ and $|\eta| < 2.5$. A

further requirement of identification of one or more jets as b -jets is made. A jet is b -tagged based on the reconstruction of the secondary vertices using the charged particle tracks associated with it. 49 (29) e +jets (μ + jets) b -tagged events survive all cuts and are kinematically fitted to the $t\bar{t}$ hypothesis. In 42 (27) electron (muon) events the kinematic fit converged in a configuration where the lowest χ^2 solution is consistent with b -tagged jet permutation.

In the second analysis the information of the b -tagger is not exploited. To increase the signal to background ratio several modifications of the selection cuts are applied. For example the transverse momenta of the first four jets are increased to 20 GeV. There are 87 e +jets and 80 μ +jets events left after this requirement. Next, using the specific kinematics of the $t\bar{t}$ events, a discriminant (D) was constructed. It is designed to use variables which are uncorrelated or minimally correlated with the top quark mass ¹¹). Four topological variables are considered:

- \cancel{E}_T - missing transverse energy which comes from the neutrino of the W leptonic decay.
- \mathcal{A} - aplanarity of the event. It exploits the fact that the decay products from a massive particle have large aplanarity.
- H'_{T2} - the ratio of the scalar sum of the P_T of the jets, excluding the leading jet, and the scalar sum of $|p_z|$ of the jets, the lepton and of the reconstructed neutrino.
- $K'_{T^{min}}$ - a measure of the jet separation folded with the E_T of the reconstructed leptonic W boson.

Figure 4 shows the simulated discriminant distribution for signal and background. A cut of $D > 0.4$ is imposed to select the signal rich region. After the kinematical fit at least one jet permutation is required to have $\chi^2 < 10$.

Similar to the CDF lepton plus jets analysis, two dominant sources of background are accounted for: W plus multijet production, including heavy flavour, and QCD multijet events where one of the jets is misidentified as a lepton and there is significant \cancel{E}_T imbalance in the event due to detector resolution.

The systematic uncertainties of both analyses are summarized in Table 3. The main contributions are due to JES, gluon radiation (initial state-ISR and final state-FSR), and the MC $t\bar{t}$ signal modeling.

As expected, the dominant systematic uncertainty originates from the JES. The impact of JES on the reconstructed top mass was evaluated by scaling the jet energies by $\pm 1\sigma$ for both signal and background in the MC simulation. The uncertainty on the JES was conservatively assumed to be 5% for the $E_T^{jet} >$

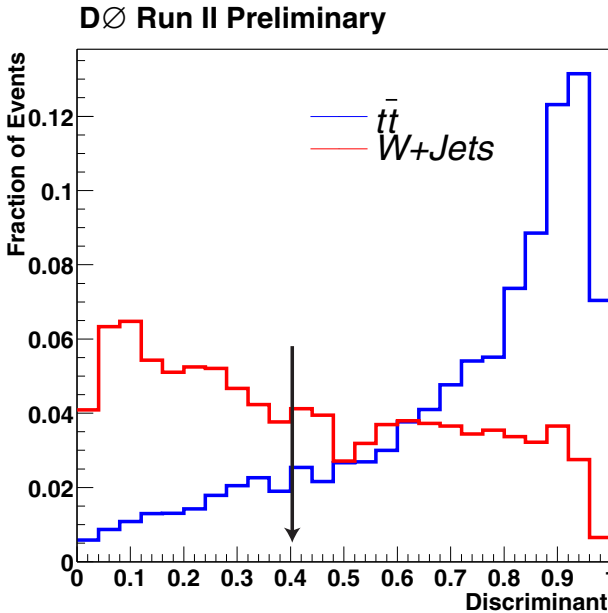


Figure 4: *Discriminant D for $t\bar{t}$ (solid dark line) and background (solid light line) events from MC simulation.*

30 GeV. For jets with $E_T^{jet} < 30$ GeV, the JES uncertainty decreases linearly as $\sigma = 30\% - 25\% \times (E_T^{jet}/30)$ GeV.

Next in importance to the JES is the systematic uncertainty coming from gluon radiation. Regardless of which jet permutation is used, the fitted mass will not be correct if the a radiated gluon is one in the four leading jets in the event. To understand how this affects the $t\bar{t}$ reconstruction, MC events with only four partons hadronizing and forming four jets were compared to events where one of the leading 4 jets comes from gluon radiation. A small deviation of ~ 0.2 GeV/ c^2 from the nominal top mass is observed when the events without gluon radiation are reconstructed. The difference becomes ~ 2.4 GeV/ c^2 when one of the leading jets is a radiated gluon.

In this analyses the model of the kinematic properties of the events is taken directly from MC simulation. Therefore some deficiencies in the MC model may lead to a substantial bias in the mass reconstruction. In order to perform a conservative estimate of this possible effect, in addition to the nominal sample for $t\bar{t}$ signal a complementary sample was generated where an

Table 3: Systematic uncertainties in the $D\bar{0}$ lepton plus jets top quark mass measurement. The uncertainty on JES, Gluon Radiation and Signal Model are the dominant sources of error on the mass.

Source	ΔM_{top} (GeV/c ²)	
	b-tagged analysis	Topological Analysis
JES	+4.7/-5.3	+6.86.5
Jet Resolution	± 0.9	± 0.9
Gluon Radiation	± 2.4	± 2.6
Signal Model	+2.3	+2.3
Background Model	± 0.8	± 0.7
<i>b</i> -tagging	± 0.7	N/A
Calibration	± 0.5	± 0.5
Trigger bias	± 0.5	± 0.5
MC statistics	± 0.5	± 0.5
Total	± 6.0	+7.8-7.1

additional parton is produced in association with the $t\bar{t}$ pair. The cross section for this process is approximately two times smaller than the cross section for the $t\bar{t}$ production. By analyzing this sample, an uncertainty of $+2.3$ GeV/c² due to the uncertainty on signal modeling is assigned to the analyses. All other possible systematic effects turned out to be relatively small, at the level of $0.5\sim 0.7$ GeV/c².

The distributions of the fitted masses and $-\ln(\mathcal{L})$ curves are shown in Figure 5. The top two figures show the result from the *b*-tagged analysis while the bottom two represent the topological one. Taking into account the output from the binned likelihood fit and the systematic uncertainties the final result for the analyses is $M_{top} = 170.6 \pm 4.2(\text{stat.}) \pm 6.0(\text{syst.})$ GeV/c² (*b*-tagged analysis) and $M_{top} = 169.9 \pm 5.8(\text{stat.}) \pm 7.1(\text{syst.})$ GeV/c² for the topological one.

4 Dilepton Channel

4.1 CDF result

CDF has several independent dilepton analyses which are found to return consistent values for the top mass. Since this sample has good signal to background ratio ($\sim 4/1$) one is stimulated to invent ingenious ways to reconstruct the events and extract M_{top} .

The event selection criteria are similar as in the lepton plus jets channel.

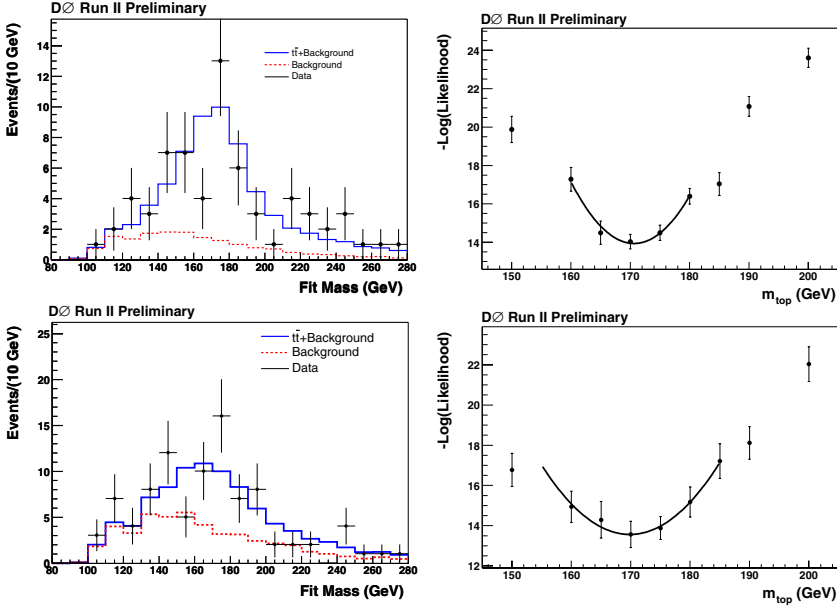


Figure 5: The result from the binned likelihood fit for the b -tagged (topological) analysis is presented on the upper (lower) left plot. The dots represent the data, the solid line is the fitted $t\bar{t}$ plus background and the dashed line is background only, normalized to the fraction returned by the fit. The right plots show the $-\ln(\mathcal{L})$ curves.

Two or more central jets with $E_T > 15$ GeV are required. A loose criterion is applied to the second lepton - it must have opposite charge but isolation is not mandatory. For the missing transverse energy the cut is increased to $\cancel{E}_T > 25$ GeV since two neutrinos are supposed to be presented in the event. If $\cancel{E}_T < 50$ GeV, a requirement for the angle between \cancel{E}_T and the nearest lepton or jet to be $\Delta\phi > 20^\circ$ is imposed. Also the transverse energy sum, H_T , has to be more than 200 GeV. Events due to cosmic rays, conversions or Z bosons are rejected.

Four major backgrounds are taken into account: di-boson plus jet production, W plus jets where one of the jet is faking a lepton, and Drell-Yan production, specially $Z/\gamma \rightarrow \tau\tau$. 33 events passed all cuts with an expected background of 11.6 ± 2.1 events.

In contrast to the lepton plus jets mode, in the dilepton case due to the presence of two neutrinos the kinematics is not constrained. The number

of non-measured kinematical variables is larger by one than the number of kinematic constraints ($-1CF$). Obviously, it is impossible to single out only one solution per event. We may take some event parameter (\vec{R}) as known in order to constrain the kinematics and then vary \vec{R} to determine a set of solutions. In order to determine a preferred mass, every solution should have a weight attached to it.

The minimal requirement in the case of $-1CF$ kinematics is to use a two dimensional vector as \vec{R} . We chose the azimuthal angles of the two neutrino momenta $\vec{R} = (\phi_{\nu 1}, \phi_{\nu 2})$ and create a net of solutions in the $(\phi_{\nu 1}, \phi_{\nu 2})$ plane.

For every point of the $(\phi_{\nu 1}, \phi_{\nu 2})$ plane we have 8 solutions. Two of them are generated by the two possibilities of associating the two charged leptons to the two leading jets which are assumed to originate from the $b\bar{b}$ partons. The four other solutions are generated from the four ways of associating each neutrino to two p_z momenta, satisfying the W decay kinematics. We select the minimal χ^2 solution for every point of the net for further use in our analysis.

Using the χ^2 value from a minimization we weight the selected solutions by $e(-\frac{\chi^2}{2})$. This is done in order to suppress the solutions which have worse compliance with the fit hypothesis.

The final extraction of the top quark mass from a sample of dilepton candidates is provided by the unbinned likelihood fit. The expected signal and background p.d.fs are obtained using Monte Carlo samples with detector simulation. The background-constrained fit ($N_b=11.6\pm 2.1$) returns: $M_{top} = 169.8 \pm_{9.3}^{9.2}$ GeV/ c^2 , with $23.4 \pm_{5.7}^{6.3}$ signal events. The left plot in Fig. 6 shows the fitted mass distribution. The insert shows the mass dependence of the negative log-likelihood function. The right plot represents the error distribution for Monte-Carlo simulated experiments, where the arrows indicate the data result.

We also performed a fit without constraining the number of background events. This fit returns $M_{top} = 169.2 \pm_{6.5}^{6.4}$ GeV/ c^2 , with $33.0 \pm_{5.8}^{6.0}$ signal events and $0.0 \pm_{0.0}^{4.2}$ background events.

4.2 $D\bar{O}$ result

To reconstruct the top quark mass in the dilepton channel, $D\bar{O}$ follows the ideas proposed by Dalitz and Goldstein in ¹⁷⁾. The analysis uses about 230 pb^{-1} of data. The initial selection includes:

- two leptons, electron or muon, with $p_{T} > 15$ GeV in the pseudorapidity regions $|\eta(e)| < 1.1$ or $1.5 < |\eta(e)| < 2.5$ for the electron and $|\eta(\mu)| < 2.0$ for the muon. In $e\text{-}\mu$ events a separation cut of $\sqrt{\Delta\phi^2 + \Delta\eta^2} > 0.25$ is applied;
- two or more jets with $p_{T} > 20$ GeV in the pseudorapidity region $|\eta^{jet}| < 2.5$;

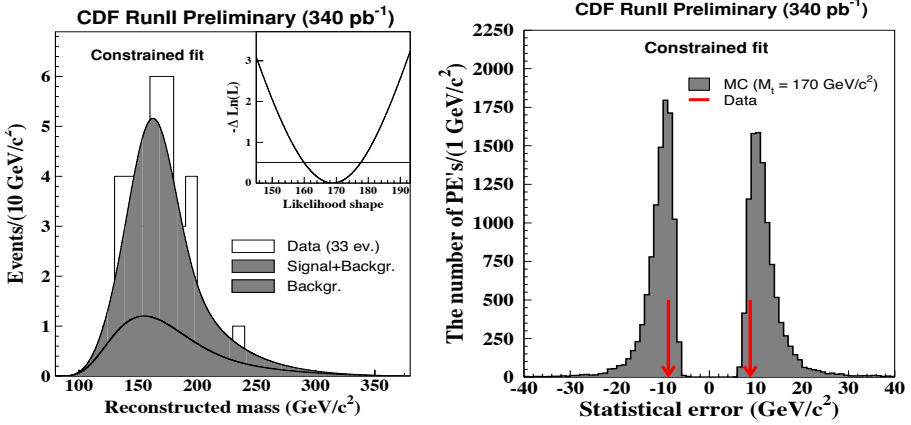


Figure 6: *Left: two-component constrained fit to the dilepton sample. The cross hatched area corresponds to the background returned by the fit and the line-shaded area is the sum of background and signal. The insert shows the mass-dependent negative log-likelihood used in the fit. Right: positive and negative error distributions returned by the fit in pseudo experiments. The arrows indicate the errors from the data fit.*

- large missing $\cancel{E}_T > 25$ GeV. However the \cancel{E}_T cut is varied for di-electron or di-muon events depending on the ee or $\mu\mu$ invariant mass;
- veto on the $Z \rightarrow ee, \mu\mu$ events;
- a cut $\Delta\phi(\mu, \cancel{E}_T) > 0.25$ rejects the events where the \cancel{E}_T and μ vectors are close to each other in the transverse plane;
- $H_T > 140$ GeV, where H_T is the scalar transverse momentum sum of the larger of the two lepton $p_{T\text{'s}}$ and of all jets over 15 GeV.
- for ee events a additional sphericity > 0.15 cut is applied.

8 $e\mu$, 5 ee and 0 $\mu\mu$ events satisfy all requirements, when 6.2 ± 0.6 , 2.8 ± 0.3 and 2.9 ± 0.6 events are correspondingly expected.

The $D\bar{O}$ analysis method can be summarized as follows. The momenta of the two highest p_T jets in the event are assigned to the $b\bar{b}$ from the decay of $t\bar{t}$ quarks. Then a likelihood to hypothesized values of the top mass in the region of 80~280 GeV is determined. For each event a solution is found when the pairs of $t\bar{t}$ momenta are consistent with the observed lepton and jet momenta and \cancel{E}_T . A weight to each solution is assigned as

$$\mathcal{W} = f(x)f(\bar{x})p(E_\ell^*|M_{top})p(E_{\bar{\ell}}^*|M_{top}), \quad (2)$$

where $f(x)$ ($f(\bar{x})$) is the parton distribution function for the proton (anti-proton) and the initial quark (anti-quark) is carrying a momentum fraction x (\bar{x}). $p(E_\ell^*|M_{top})$ denotes the probability for the top (anti-top) quark with a mass M_t to generate a lepton ℓ ($\bar{\ell}$) with the observed energy in the top quark rest frame.

There are two ways to assign the two jets to the b and \bar{b} quarks. In addition, for each jet-to-parton assignment, there might be up to four solutions for each hypothesized value of the mass, coming from the fact that every neutrino may have up to two real solutions for its p_z , satisfying the kinematics. Then the likelihood for each value of the top quark mass M_{top} is given by the sum of the weights $w_{i,j}$ over all possible solutions:

$$\mathcal{W}(M_t) = \sum_{p_z^* \text{ solutions}} \sum_{jet \text{ assignment}} w_{i,j}. \quad (3)$$

Up to now there was an implicit assumption that all momenta are measured perfectly. Therefore the weight in (3) is zero if no exact solutions are found. To account for detector resolution the weight calculations are repeated with input values for the particle momenta drawn from Gaussian distributions with means equal of the measured values and widths corresponding to the detector resolution. In addition the \cancel{E}_T value is recalculated from generated particle momenta and a random noise from a normal distribution with mean 0 GeV and rms 8 GeV is added. Figure 7 up (down) shows the weight curves for $e\mu$ (ee) events before (solid line) and after (shadow area) resolution smearing. For each event the value of the top quark mass at which the weight curve reaches its maximum is used as the estimator of the mass. After that, to extract the most probable top mass value from the data sample, a standard template method which exploits a binned maximum likelihood fit is applied. The likelihood fit returns $M_{top} = 155.{}^{+14}_{-13}(\text{stat.}) \pm 7.(\text{syst.})$ GeV/ c^2 . The JES uncertainty (5.6 GeV/ c^2) dominates the systematic error.

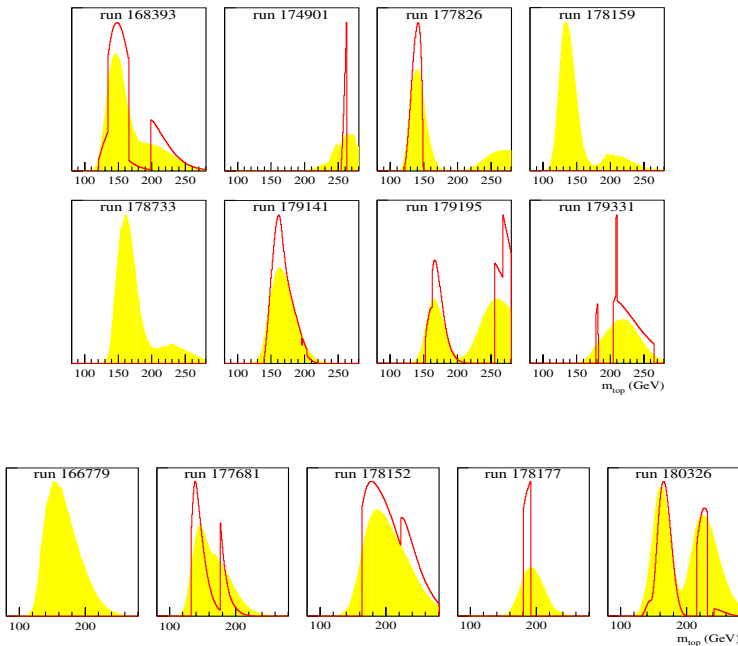


Figure 7: *Weight curves from 8 $e\mu$ events (top) and 5 ee events (bottom). The shadow histograms show the weight curves with resolution smearing while the open histograms represent the weight curves without resolution smearing.*

5 Summary of the Top Quark Mass Measurements and Run II Prospects

Combining the presently available most accurate Run II CDF and $D\bar{O}$ measurements in the dilepton and lepton plus jets decay topologies, one finds $172.7 \pm 3.5 \text{ GeV}/c^2$. This result is unofficial. The average is made by the author assuming simple correlations (0 or 1) between the systematic uncertainties in the CDF and $D\bar{O}$ measurements.

The expected CDF uncertainty for JES systematics as a function of integrated luminosity is shown in Figure 8, left. The right plots shows the total mass error versus integrated luminosity for the CDF lepton plus jet analysis. One may conclude that with a Run II integrated luminosity of 8 fb^{-1} the top quark mass could be measured by CDF with a precision of $\sim 2.0 \text{ GeV}/c^2$. This optimistic forecast is based on the present understanding that both the statisti-

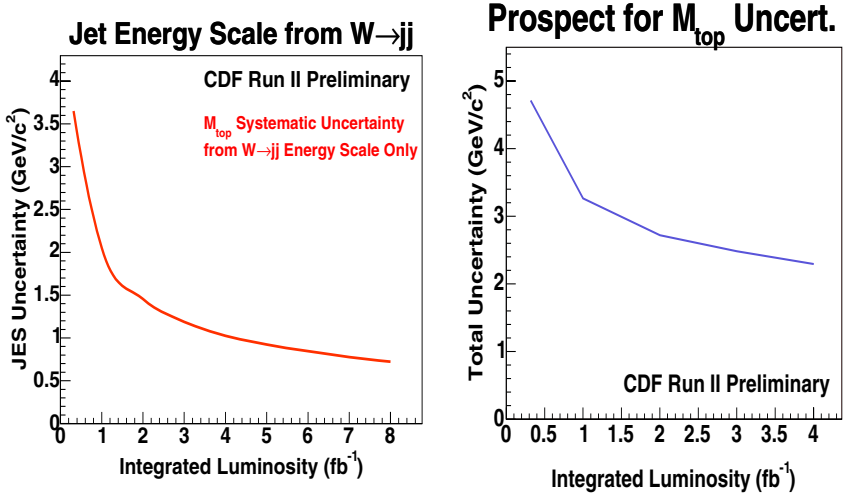


Figure 8: The expected JES uncertainty from $W \rightarrow jj$ as a function of integrated luminosity is shown on the left plot. On the right, the total expected top mass uncertainty, from CDF lepton plus jets events as a function of integrated luminosity, is shown.

cal and JES systematic uncertainties will decrease as expected with increasing integrated luminosity.

6 Conclusion

The top quark CDF results from the Tevatron 2002-2004 Run II, with an integrated luminosity of 318 and 230 pb^{-1} for CDF and $D\bar{O}$ are presented. The best, up to date, measurement of the top quark mass from the CDF lepton plus jets analysis is $173.5^{+3.9}_{-3.8}$ GeV/c^2 . Combining the CDF and $D\bar{O}$ dilepton and lepton plus jets Run II results, the author's average of the top quark mass is 172.7 ± 3.5 GeV/c^2 .

7 Acknowledgments

I would like to thank the organizers for their invitation and hospitality. This work is supported by the U.S. department of Energy and CDF and D O collaborating institutions and their funding agencies.

References

1. F. Abe *et al.*, Phys. Rev. D **50**, 2966 (1994) and Phys. Rev. Lett. **73**, 225 (1994).
2. F. Abe *et al.*, Phys. Rev. Lett. **74**, 2626 (1995).
3. S. Abachi *et al.*, Phys. Rev. Lett **74**, 2632 (1995).
4. C. Parkes, "W Boson Properties at LEP", these proceedings.
5. F. Fielder, "Top Properties and Cross Section", these proceedings.
6. B. W. Harris, E. Laenen, L. Phaf, Z. Sullivan, S. Weinzierl Phys. Rev. D **66**, 054024 (2002).
7. C. Quigg, **FERMILAB-Pub-97/091-T**.
8. D. Acosta *et al.*, hep-ex/0410041, (2004).
9. D. Kestenbaum, Ph.D. Thesis (unpublished), Harvard University (1996).
10. T. Affolder *et al.*, Phys. Rev. D **63**, 03203 (2001).
11. B. Abbott *et al.*, Phys. Rev. Lett **58**, 052001 (1998).
12. R. H. Dlaitz and G. R. Goldstein, Proc. R. Soc. London A **445**, 2803 (1999).
13. K. Kondo, J. Phys. Soc. **57**, 4126 (1998).
14. V. M. Abazov *et al.*, Nature **429**, 638 (2004).
15. DØ Public note *et al.*,
<http://www-d0.fnal.gov/Run2Physics/WWW/results/top.htm>.
16. D. Acosta *et al.*, Phys. Rev. Lett. **94**, 091803 (2005).
17. R. H. Dlaitz and G. R. Goldstein, Phys. Rev. D **45**, 1531 (1992).

TOP QUARK PRODUCTION AND PROPERTIES AT THE TEVATRON

Frank Fiedler

Munich University (LMU), Germany

on behalf of the CDF and DØ Collaborations

Abstract

The precise measurement of top quark production and properties is one of the primary goals of the Tevatron during Run II. The total $t\bar{t}$ production cross-section has been measured in a large variety of decay channels and using different selection criteria. Results from differential cross-section measurements and searches for new physics in $t\bar{t}$ production and top quark decays are available. Electroweak production of single top quarks has been searched for. The results from all these analyses, using typically 200 pb^{-1} of data, are presented.

1 Introduction

The top quark is special among the fermions of the Standard Model because of its large mass. Currently, the top quark can only be studied at the two Tevatron experiments CDF and DØ, where measurements of top quark production and properties are one of the key physics goals of Run II.

The top quark mass is discussed in a separate article ¹⁾. This article focuses on measurements of the total $t\bar{t}$ production cross-section, searches for new physics in $t\bar{t}$ production and top quark decay, and on the search for electroweak (single) top quark production. While the CDF and DØ experiments have both collected more than 500 pb^{-1} of data so far during Tevatron Run II, surpassing the Run I integrated luminosity by a factor ≥ 5 , the measurements summarized in this article typically use about 200 pb^{-1} .

In section 2, general aspects of top production and event topologies at the Tevatron are briefly discussed. Section 3 discusses the measurements of the total $t\bar{t}$ production cross-section, while further measurements in $t\bar{t}$ events are presented in section 4. The search for single top quark production is presented in section 5.

2 Top Quark Production at the Tevatron

In the Standard Model, the production of top quarks at a hadron collider can in principle proceed via two mechanisms: $t\bar{t}$ pair production via the strong interaction, and single top (or antitop) production via the electroweak interaction. The leading order Feynman diagrams are shown in figure 1 together with the Standard Model cross-sections in $p\bar{p}$ collisions at a centre-of-mass energy of 1.96 TeV (corresponding to the Tevatron collider at Run II) ^{2, 3)}.

In the following, the main characteristics of $t\bar{t}$ and single top events at the Tevatron are discussed.

2.1 Classification of $t\bar{t}$ Event Topologies

In the Standard Model, the branching fraction of top quark decays to a b quark and an on-shell W boson is close to 100%, other decay modes not being observable with Tevatron luminosities. The subsequent W decays determine the event topology seen in the detector, and $t\bar{t}$ events are classified as follows:

- **Dilepton events**, where both W bosons decay into an $e\nu$ or $\mu\nu$ final state, are characterized by two energetic, isolated leptons of opposite charge, two energetic b jets, and missing transverse energy. While the product branching ratio is only about 5%, pure event samples can be obtained requiring the two leptons in the event to be reconstructed.

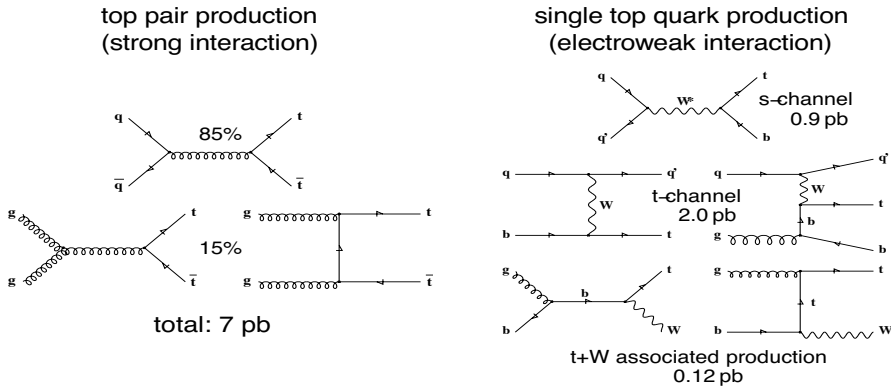


Figure 1: Leading order Feynman diagrams for top quark production at hadron colliders together with the Standard Model cross-sections at the Tevatron.

- In **lepton+jets events**, one W boson decays hadronically and the other into an $e\nu$ or $\mu\nu$ final state. This topology is characterized by an energetic, isolated electron or muon, four energetic jets (two b jets and two light-quark jets from the W decay), and missing transverse energy. The product branching ratio of $\approx 30\%$ is larger than for dilepton events, and the main background is from W +jets events.
- In **hadronic events**, one expects 6 energetic jets (of which two are b jets) and no significant missing transverse energy. Because of large backgrounds from QCD jet production, identifying $t\bar{t}$ events in the hadronic channel is challenging, despite the large product branching ratio of $\approx 44\%$.
- In about 21% of the $t\bar{t}$ events, at least one W boson decays into a $\tau\nu$ final state. Depending on its decay, the τ lepton can be identified as a narrow jet, an isolated track, or an electron or muon. Two energetic b jets, missing transverse energy, and the decay products from the second W boson complete the event topology.

In general, the reconstruction and selection of $t\bar{t}$ event candidates is based on reconstructing the directions and energies/momenta of isolated electrons or muons and jets, and on reconstructing the missing transverse energy \cancel{E}_T from the transverse momentum balance in the event. The purity of the event samples can be enhanced by identifying jets that originated from a b quark (b tagging), since in the Standard Model, every $t\bar{t}$ event contains two b jets. Both CDF and DØ use

- secondary vertex algorithms, based on explicit reconstruction of the decay vertex of the b hadron within the jet;
- impact parameter based algorithms that classify tracks inside a jet ac-

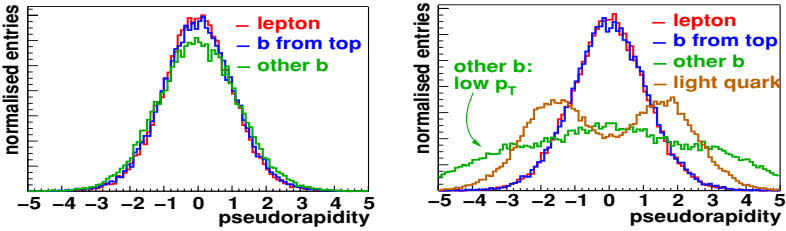


Figure 2: *Expected pseudorapidity distributions of the charged lepton and jets in single top events (left: s-channel, right: t-channel) ⁴⁾.*

ording to their distance of closest approach to the primary event vertex; and

- soft leptons from semileptonic bottom or charm hadron decay (only muons are used so far)

to identify b jets. The requirements on the jet multiplicity, the minimum jet transverse energies, b identification of the jets, and event kinematic information can be balanced to minimize the measurement error; depending on the selection, not all jets need to be explicitly reconstructed.

2.2 Single Top Quark Production

The total cross-section for single top quark production is only a factor ~ 2 smaller than that for $t\bar{t}$ production; however, the relevant backgrounds are substantially larger ($W+2$ jet instead of $W+4$ jet events). To reduce the background, the selection of single top event candidates focuses on top decays with leptonic W decays and on the identification of the b jet(s) in the event. Figure 2 shows the expected pseudorapidity distributions of the charged lepton and jets in single top events. For s-channel events, two b jets are expected in the center of the detector. In general only one b jet can be reconstructed in case of the t-channel, but here an additional light quark jet can be observed.

3 Measurements of the Total $t\bar{t}$ Production Cross-Section

The goal is to measure the $t\bar{t}$ cross-section in as many different modes as possible to check the predictions of the Standard Model. The measurements in the different channels are described in the following sub-sections.

3.1 Lepton+Jets Channel, Topological Analyses

Both CDF and DØ have measured the $t\bar{t}$ cross-section in the lepton+jets channel without relying on b jet identification. In the CDF analysis ⁵⁾, events with

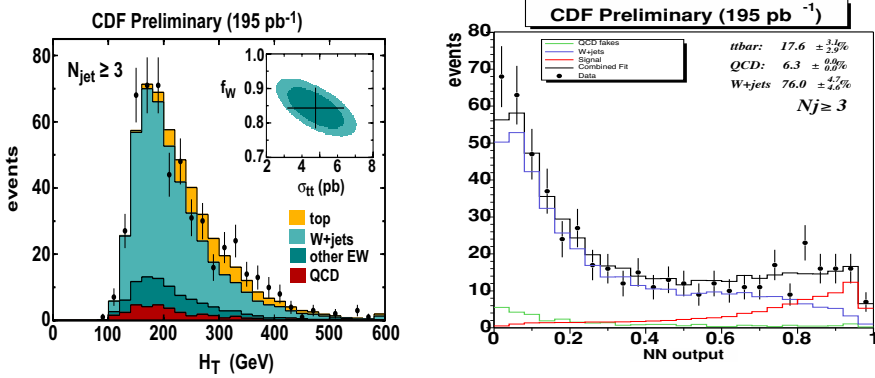


Figure 3: CDF $t\bar{t}$ cross-section measurement in the lepton+jets channel using topological information. Left: H_T distribution. Right: NN output.

one isolated electron with $E_T > 20$ GeV or muon with $p_T > 20$ GeV, missing transverse energy $\cancel{E}_T > 20$ GeV, and at least 3 jets with $E_T > 15$ GeV within the pseudorapidity range $|\eta| < 2.0$ are selected. For $\cancel{E}_T < 30$ GeV, there is an additional cut requiring the angle $\Delta\phi$ between the missing transverse energy and the highest E_T jet in the transverse plane to satisfy $0.5 < \Delta\phi < 2.5$. After this selection, the $t\bar{t}$ signal can be seen in the H_T distribution (H_T is the scalar sum of transverse energies of the lepton, jets, and the missing transverse energy) as shown in figure 3, and the $t\bar{t}$ cross-section is measured to be

$$\sigma(t\bar{t}) = (4.7 \pm 1.6(\text{stat.}) \pm 1.8(\text{syst.})) \text{ pb} \quad (1)$$

using a 195 pb^{-1} data sample. To optimise the measurement, 7 quantities have been chosen for training a neural network (NN) to separate the $t\bar{t}$ signal from the background. The NN output distribution is also shown in figure 3. From a fit to this distribution a result of

$$\sigma(t\bar{t}) = (6.7 \pm 1.1(\text{stat.}) \pm 1.6(\text{syst.})) \text{ pb} \quad (2)$$

is obtained from the same dataset. In both analyses, the main systematic error is from the uncertainty in the jet energy scale; it is however reduced from 30% in the H_T based measurement to 16% in the optimised analysis.

In the $D\mathcal{O}$ topological analysis ⁶⁾, events with one isolated electron or muon with $p_T > 20$ GeV, missing transverse energy ($\cancel{E}_T > 20$ GeV in the e+jets case and $\cancel{E}_T > 17$ GeV for μ +jets events), and at least four jets with $E_T > 15$ GeV within $|\eta| < 2.5$ are selected. So in contrast to CDF, four jets are required to be reconstructed, but a larger pseudorapidity region is allowed. To

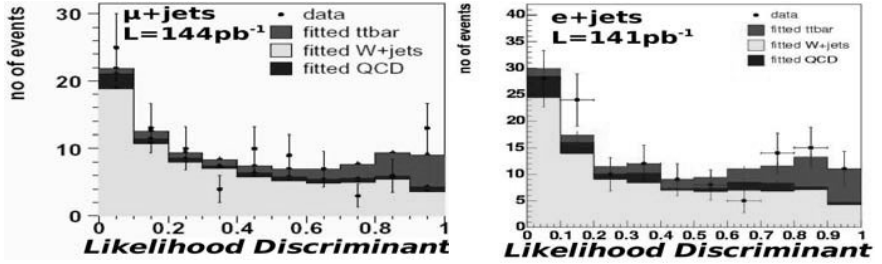


Figure 4: $D\bar{O} \, t\bar{t}$ cross-section measurement in the lepton+jets channel using topological information. The likelihood discriminant distributions are shown for e +jets (left) and μ +jets (right) events together with the fitted $t\bar{t}$ and background contributions.

further separate $t\bar{t}$ events from background, a likelihood is constructed using angular variables and ratios of energy dependent variables, to avoid direct dependence on the jet energy scale. The resulting distributions are given in figure 4. The combined fit to the e +jets and μ +jets distributions from 141 – 144 pb^{-1} of data yields

$$\sigma(t\bar{t}) = (7.2^{+2.6}_{-2.4}(\text{stat.})^{+1.6}_{-1.7}(\text{sys.}) \pm 0.5(\text{lumi.})) \text{ pb} . \quad (3)$$

3.2 Lepton+Jets Channel, b Tagging Analyses

For the $D\bar{O}$ measurements that make use of lifetime b tagging information ⁷⁾, events are selected with the same criteria as above. The $t\bar{t}$ cross-section is then determined from a combined fit to the jet multiplicity distributions for events with exactly one b tagged jet and events with at least two b tagged jets. Using a data sample of 158 – 169 pb^{-1} , $D\bar{O}$ obtains

$$\sigma(t\bar{t}) = (8.2 \pm 1.3(\text{stat.})^{+1.9}_{-1.6}(\text{sys.}) \pm 0.5(\text{lumi.})) \text{ pb} \quad (4)$$

using secondary vertex b tagging and

$$\sigma(t\bar{t}) = (7.2^{+1.3}_{-1.2}(\text{stat.})^{+1.9}_{-1.4}(\text{sys.}) \pm 0.5(\text{lumi.})) \text{ pb} \quad (5)$$

with a track impact parameter based algorithm. The jet multiplicity distributions obtained with secondary vertex b tagging are shown in figure 5. In a separate analysis, $D\bar{O}$ analyzes events with a semimuonic bottom or charm decay, resulting in ⁸⁾

$$\sigma(t\bar{t}) = (11.2 \pm 4.0(\text{stat.}) \pm 1.3(\text{sys.}) \pm 1.1(\text{lumi.})) \text{ pb} \quad (6)$$

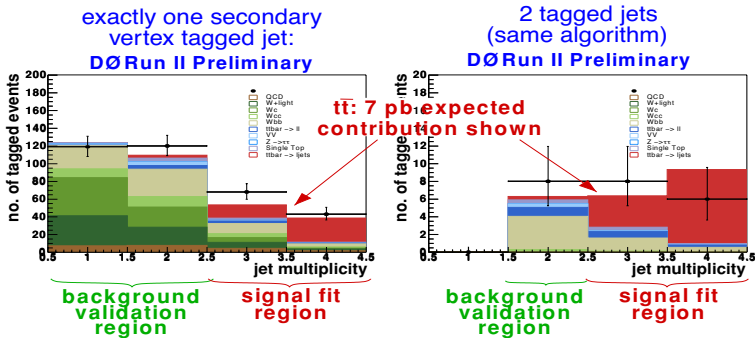


Figure 5: $D0$ $t\bar{t}$ cross-section measurement in the lepton+jets channel using b tagging information. The jet multiplicity distributions for single and double secondary vertex tagged events are shown together with the expected Standard Model signal and background.

based on 93 pb^{-1} .

Several CDF analyses make use of b tagging information. The preselection of events requires one lepton, missing transverse energy, and three jets as in section 3.1. When at least one jet is required to be secondary vertex tagged⁹⁾, a measurement of

$$\sigma(t\bar{t}) = (5.6_{-1.1}^{+1.2}(\text{stat.})_{-0.6}^{+0.9}(\text{syst.})) \text{ pb} \quad (7)$$

is obtained from the jet multiplicity distribution (where a value of $H_T > 200 \text{ GeV}$ is required for events with three or more jets) in 162 pb^{-1} shown in figure 6. Alternatively, the fraction of $t\bar{t}$ events in events with at least 3 jets is obtained from a fit to the E_T distribution of the leading jet, which is also shown in figure 6, yielding¹⁰⁾

$$\sigma(t\bar{t}) = (6.0 \pm 1.6(\text{stat.}) \pm 1.2(\text{syst.})) \text{ pb} . \quad (8)$$

For the CDF multiple tag analysis, a special version of the b tagging algorithm has been developed with looser criteria to increase the statistics. From the jet multiplicity distributions obtained with the regular and the loose b tag, measurements of^{9, 11)}

$$\sigma(t\bar{t}) = (5.0_{-1.9}^{+2.4}(\text{stat.})_{-0.8}^{+1.1}(\text{syst.})) \text{ pb} \quad (\text{regular } b \text{ tag}) \text{ and} \quad (9)$$

$$\sigma(t\bar{t}) = (8.2_{-2.1}^{+2.4}(\text{stat.})_{-1.0}^{+1.8}(\text{syst.})) \text{ pb} \quad (\text{loose } b \text{ tag}) \quad (10)$$

are obtained. Finally, CDF also uses events with b jets identified by an impact parameter based algorithm, yielding¹²⁾

$$\sigma(t\bar{t}) = (5.8_{-1.2}^{+1.3}(\text{stat.}) \pm 1.3(\text{syst.})) \text{ pb} \quad (11)$$

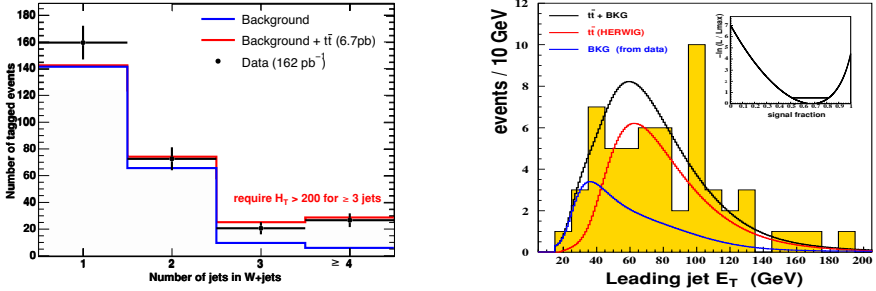


Figure 6: CDF $t\bar{t}$ cross-section measurement in the lepton+jets channel using b tagging information. Left: the jet multiplicity distribution for events with at least one b tagged jet. Right: the leading jet E_T distribution for events with at least 3 jets.

in 162 pb^{-1} , as well as events with a semimuonic bottom or charm hadron decay, resulting in ¹³⁾

$$\sigma(t\bar{t}) = (5.2_{-1.9}^{+2.9}(\text{stat.})_{-1.0}^{+1.3}(\text{syst.})) \text{ pb} \quad (12)$$

using 200 pb^{-1} .

3.3 Dilepton Channel

The CDF selection of $t\bar{t}$ events in the dilepton channel requires two isolated tracks ($p_T > 20\text{ GeV}$) and missing transverse energy ($\cancel{E}_T > 25\text{ GeV}$). The $t\bar{t}$ production cross-section is determined from the jet multiplicity distribution of events where both tracks are identified as leptons, or events where only one identified lepton is required. The combined result is ¹⁴⁾

$$\sigma(t\bar{t}) = (7.0_{-2.1}^{+2.4}(\text{stat.})_{-1.1}^{+1.6}(\text{syst.}) \pm 0.4(\text{lumi.})) \text{ pb} \quad (13)$$

using 200 pb^{-1} . The jet multiplicity distribution for the analysis with at least one identified lepton is shown in figure 7. One of the main backgrounds to $t\bar{t}$ production in the dilepton channel is diboson (mostly WW) production. In a separate analysis, CDF fits the two-dimensional jet multiplicity vs. \cancel{E}_T distribution to measure the $t\bar{t}$, WW , and $Z \rightarrow \tau\tau$ cross-sections simultaneously. This analysis yields ¹⁵⁾

$$\sigma(t\bar{t}) = (8.6_{-2.4}^{+2.5}(\text{stat.}) \pm 1.1(\text{syst.})) \text{ pb} \quad (14)$$

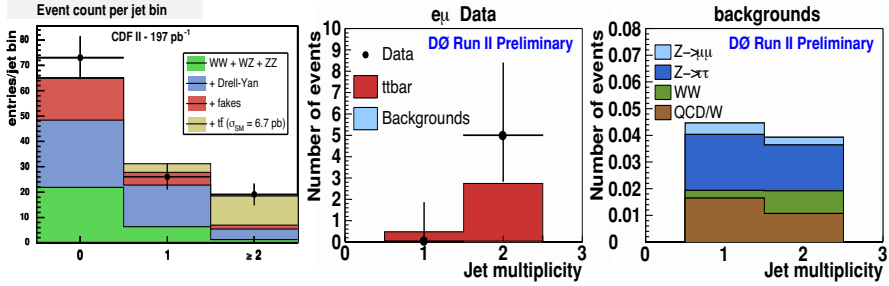


Figure 7: CDF and $D\bar{O}$ $t\bar{t}$ cross-section measurements in the dilepton channel. Left: jet multiplicity distribution in the CDF “lepton+track” analysis. Middle and right: jet multiplicity distributions for data (middle) and expected background (right) in the $D\bar{O}$ dilepton measurement with at least one secondary vertex b tagged jet.

For the $D\bar{O}$ dilepton analysis, events with two isolated leptons with $p_T > 15$ GeV ($p_T > 20$ GeV in the dielectron channel), two jets with $E_T > 20$ GeV, missing transverse energy $\cancel{E}_T > 35$ GeV ($\cancel{E}_T > 25$ GeV in the $e\mu$ channel), and $H_T^{\text{lead. } \ell} > 120(140)$ GeV in the $\mu\mu$ ($e\mu$) channel are selected, where $H_T^{\text{lead. } \ell}$ includes all jets and the leading lepton. Additional cuts reject events consistent with a $Z \rightarrow \ell\ell$ hypothesis. With no b tagging criteria applied, the analysis yields ¹⁶⁾

$$\sigma(t\bar{t}) = (14.3_{-4.3}^{+5.1}(\text{stat.})_{-1.9}^{+2.6}(\text{syst.}) \pm 0.9(\text{lumi.})) \text{ pb} \quad (15)$$

using $140 - 156 \text{ pb}^{-1}$. When requiring at least one jet to be secondary vertex b tagged, the $e\mu$ channel alone yields ¹⁷⁾

$$\sigma(t\bar{t}) = (11.1_{-4.3}^{+5.8}(\text{stat.}) \pm 1.4(\text{syst.}) \pm 0.7(\text{lumi.})) \text{ pb} \quad (16)$$

with a very high purity sample, see figure 7.

3.4 Hadronic Channel

To separate $t\bar{t}$ events in the hadronic channel from the large multijet background, both tight kinematic cuts and b tagging information are applied. CDF selects events with 6 to 8 jets and no isolated leptons and applies kinematic cuts. In the distribution of the number of b tagged jets as a function of jet multiplicity (see figure 8) the $t\bar{t}$ cross-section is then measured to be ¹⁸⁾

$$\sigma(t\bar{t}) = (7.8 \pm 2.5(\text{stat.})_{-2.3}^{+4.7}(\text{syst.})) \text{ pb} \quad (17)$$

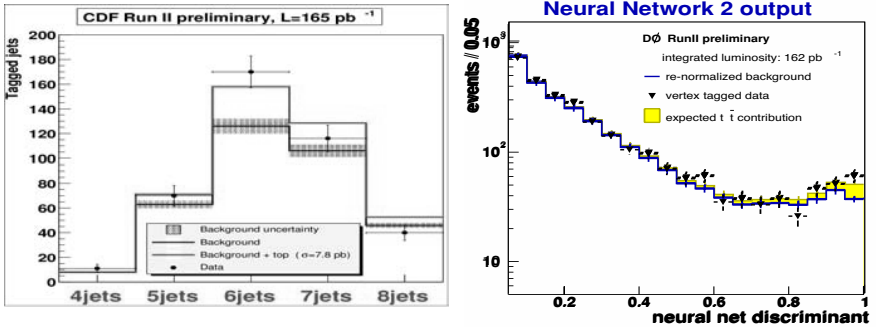


Figure 8: CDF and $DØ$ $t\bar{t}$ cross-section measurements in the hadronic channel. Left: number of b tagged jets in the CDF event sample as a function of jet multiplicity. Right: output of the final NN in the $DØ$ analysis.

in 165 pb^{-1} .

$DØ$ selects events with 6 or more jets, of which exactly one is required to be b tagged. A chain of NNs feeding into each other is used, and the $t\bar{t}$ cross-section is determined from the excess of events after a cut on the last NN output over background. A data sample of 162 pb^{-1} yields ¹⁹⁾

$$\sigma(t\bar{t}) = (7.7^{+3.4}_{-3.3}(\text{stat.})^{+4.7}_{-3.8}(\text{syst.}) \pm 0.5(\text{lumi.})) \text{ pb} . \quad (18)$$

3.5 Events with $W \rightarrow \tau\nu$ Decays

CDF searches for $t\bar{t}$ events where one W decays electronically or muonically, while the other decays into a $\tau\nu$ final state with a subsequent τ decay into hadron(s) and a neutrino ²⁰⁾. Events with an electron or muon with $E_T > 20 \text{ GeV}$, a tau lepton with $E > 15 \text{ GeV}$ and opposite charge, missing transverse energy $\cancel{E}_T > 20 \text{ GeV}$, at least two jets ($E_T(1) > 25 \text{ GeV}$, $E_T(2) > 15 \text{ GeV}$), and $H_T > 205 \text{ GeV}$ are selected. The two events observed in 193.5 pb^{-1} are consistent with the Standard Model expectation, and a limit of

$$Br(t \rightarrow b\tau\nu) < 5.0 \cdot Br_{\text{SM}}(t \rightarrow b\tau\nu) \quad (19)$$

is derived at 95% confidence level.

3.6 Summary of $t\bar{t}$ Cross-Section Measurements

The $t\bar{t}$ cross-section measurements at Tevatron Run II are summarized in figure 9. The measurements in all decay channels and by both CDF and $DØ$ are

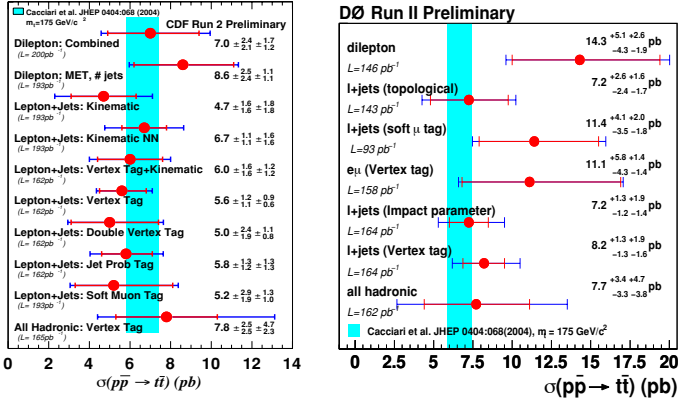


Figure 9: A summary of all Tevatron Run II $t\bar{t}$ cross-section measurements by CDF (left) and D0 (right).

mutually consistent and consistent with the prediction of the Standard Model.

4 Further $t\bar{t}$ Measurements

It is conceivable that physics beyond the Standard Model does not change the total $t\bar{t}$ cross-section, but either only affects differential cross-sections or top quark decays.

4.1 Searches for New Physics in $t\bar{t}$ Production

In a model independent analysis, CDF have searched for anomalous kinematic properties in their dilepton $t\bar{t}$ sample ²¹⁾. Four kinematic distributions where new physics signatures are expected to be likely to be seen were chosen a priori. While one of them, the leading lepton p_T spectrum shown in figure 10, shows an excess at low transverse momenta in 193 pb^{-1} , the other distributions agree with the expectation. The overall compatibility with the Standard Model prediction has been computed to be in the 1.0 – 4.5% range.

CDF searches explicitly for production of fourth generation quarks ²²⁾. If these t' quarks are heavier than the top quark, an excess of events at large H_T is expected. From a fit to the measured H_T distribution, which is consistent with the Standard Model expectation, upper limits on the cross-section of $t'\bar{t}'$ events can be placed, see figure 11.

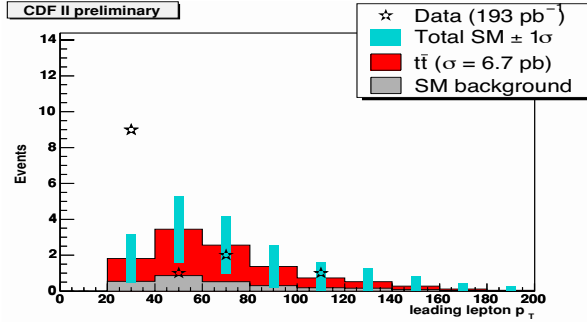


Figure 10: *CDF search for anomalous dilepton event properties. The p_T spectrum of the leading charged lepton in dilepton $t\bar{t}$ events at CDF.*

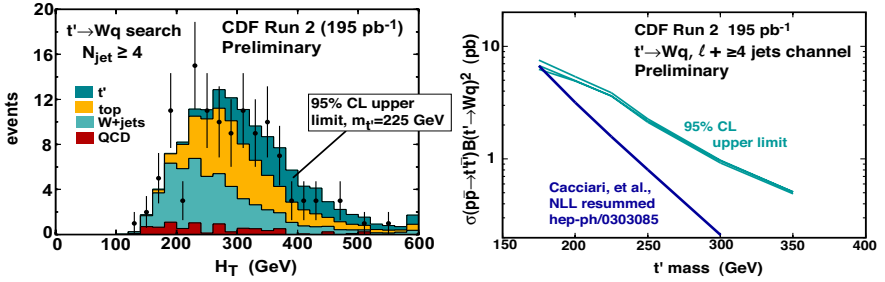


Figure 11: *CDF t' search. The H_T distribution in $W+4$ jets events at CDF with a topological selection is shown with a fit that includes a component from hypothetical t' quark production (left). The resulting t' cross-section limits as a function of assumed t' mass are also shown (right).*

4.2 Searches for New Physics in Top Quark Decays

The Standard Model predicts the fractions of longitudinal and left-handed W bosons from top decay to be $F_0 = 1/(1 + 2m_W^2/m_{top}^2) \approx 0.7$ and $F_- = 1 - F_0$, while the fraction F_+ of right-handed W bosons is essentially zero because the bottom quarks from top quark decay are left-handed due to the large mass difference between top and bottom quarks. The predicted distribution of the decay angle θ^* in the W rest frame is shown in figure 12. From measurements of this distribution (or quantities that depend on $\cos\theta^*$), one can either search for non-zero contributions from right-handed W bosons ($F_+ > 0$) or, assuming $F_+ = 0$, for deviations from the predicted ratio F_0/F_- .

CDF have measured the fraction F_0 from the charged lepton p_T spectrum

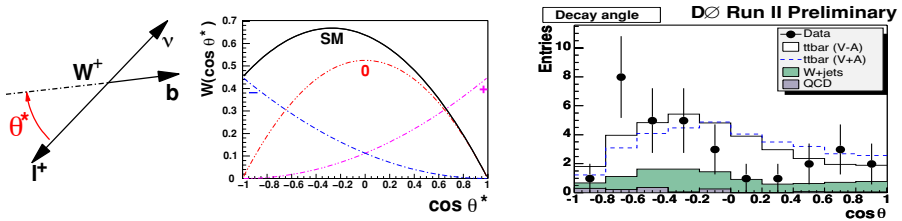


Figure 12: W helicity measurements. The definition of the angle θ^* in the W rest frame (left) and the expected $\cos \theta^*$ distribution (middle), compared with the measured $\cos \theta^*$ distribution in b tagged lepton+jets events from $159 - 169 \text{ pb}^{-1}$ at $D\bar{O}$ (right).

(using 200 pb^{-1}) to be ²³⁾

$$F_0 = 0.27_{-0.24}^{+0.35}, \quad (20)$$

and from explicit reconstruction of the value of $\cos \theta^*$ (using 162 pb^{-1}) ²⁴⁾ to be

$$F_0 = 0.89_{-0.34}^{+0.30}(\text{stat.}) \pm 0.17(\text{syst.}), \quad (21)$$

respectively – to be compared with the $D\bar{O}$ Run I value of ²⁵⁾ $F_0 = 0.56 \pm 0.31$. All of these values are consistent with the Standard Model expectation.

The two $D\bar{O}$ measurements both use explicit $\cos \theta^*$ reconstruction in an event sample obtained with a topological ²⁶⁾ selection or using b tagging ²⁷⁾ in $159 - 169 \text{ pb}^{-1}$. The $\cos \theta^*$ distribution from the b tagging analysis is shown in figure 12. Both analyses each yield a limit of

$$F_+ < 0.24 \text{ at } 90\% \text{ confidence level}, \quad (22)$$

to be compared with the CDF Run I exclusion limit of $F_+ < 0.18$ at 95% confidence level ²⁸⁾.

In supersymmetric models with $m_{H^\pm} < m_{top}$, the top quark may decay into a charged Higgs and a bottom quark. Depending on the values of $\tan \beta$ and m_{H^\pm} , one expects the following changes in the observed $t\bar{t}$ event topologies ²⁹⁾:

- an excess of τ decays due to $H^+ \rightarrow \tau^+ \nu$ decays for large $\tan \beta$,
- an excess of hadronic top decays due to $H^+ \rightarrow c\bar{s}$ decays for small $\tan \beta$ and small m_{H^\pm} , or
- $t\bar{t}$ events with two extra b jets from $H^+ \rightarrow W^+ b\bar{b}$ decays for small $\tan \beta$ and large m_{H^\pm} .

The CDF collaboration has therefore taken their measurements of the $t\bar{t}$ cross-section in the dilepton and lepton+jets channels as well as their limit on $t\bar{t} \rightarrow$

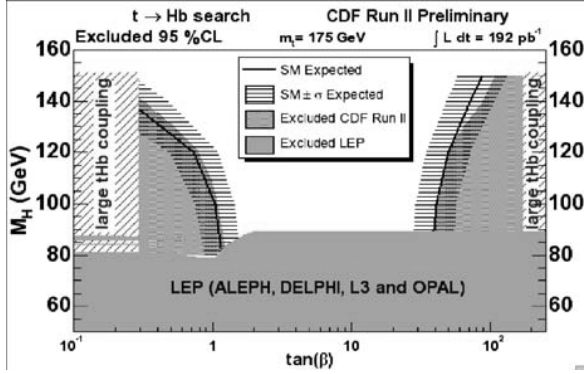


Figure 13: *CDF charged Higgs search. Charged Higgs limits in the m_{H^\pm} vs. $\tan\beta$ plane. The pink regions have been excluded, and the black lines with error bars indicate the expected limit.*

$\ell + \tau$ events³⁰⁾ to place limits on $t \rightarrow H^\pm b$ decays in the m_{H^\pm} vs. $\tan\beta$ plane, as shown in figure 13.

Both CDF and $D\bar{O}$ have compared their $t\bar{t}$ cross-section measurements obtained with different numbers of b tagged jets to determine the branching ratio $Br(t \rightarrow Wb)/Br(t \rightarrow Wq)$, where q denotes any down-type quark. The results are³¹⁾

$$\begin{array}{ll}
 1.11^{+0.21}_{-0.19} & \text{CDF, } 162 \text{ pb}^{-1}, \\
 0.65^{+0.34}_{-0.30}(\text{stat.})^{+0.17}_{-0.12}(\text{syst.}) & \text{D}\bar{O}, 158 - 169 \text{ pb}^{-1}, \text{ and} \\
 0.70^{+0.27}_{-0.24}(\text{stat.})^{+0.11}_{-0.10}(\text{syst.}) & \text{D}\bar{O}, 158 - 169 \text{ pb}^{-1},
 \end{array} \quad (23)$$

where the first $D\bar{O}$ result has been obtained with impact parameter b tagging and the second with secondary vertex b tagging. They show no sign of a deviation from the Standard Model expectation close to 1. It should be noted that this quantity does not constrain the value of $|V_{tb}|^2$ in models where top quark decays into quarks from more than three quark generations are allowed.

In summary, from measurements of $t\bar{t}$ production, there is currently no sign of physics beyond the Standard Model.

5 Search for Single Top Quark Production

The production cross-section for single top quarks is proportional to $|V_{tb}|^2$. Also, any differences to the Standard Model prediction could provide hints for new physics.

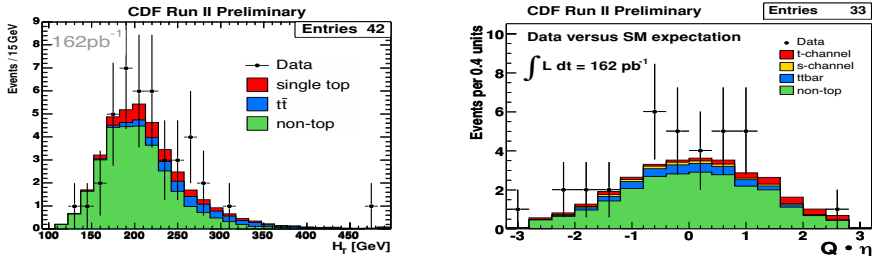


Figure 14: *CDF single top search: The H_T distribution for single top quark candidate events at CDF (left) and the lepton charge signed η distribution of the b jet (right) together with the Standard Model expectations for non-top and $t\bar{t}$ backgrounds and single top signal (the contributions from s -channel and t -channel events are shown separately in the right plot).*

In their searches for single top quark production, the Tevatron experiments concentrate on s -channel and t -channel production with expected cross-sections of 0.9 pb and 2.0 pb, respectively, see figure 1.

Both CDF and $D\bar{O}$ select events with an energetic isolated charged lepton, missing transverse energy, and exactly 2 (CDF) or 2–4 ($D\bar{O}$) jets out of which at least one must be b tagged. CDF then selects events with a reconstructed top quark mass between 140 GeV and 210 GeV, while $D\bar{O}$ requires $H_T > 150$ GeV. As shown in figure 14, single top events can be found at intermediate values of H_T , and s -channel and t -channel events can be disentangled using the lepton charge signed distribution of the pseudorapidity of the identified b jet. With the current data sets, sensitivity for Standard Model single top quark production has not yet been reached. No significant excess of events has been observed, and the following 95% confidence level limits have been placed on the single top quark cross-section³²⁾:

experiment	s – channel	t – channel	$s+t$ – channel	
CDF	13.6 pb	10.1 pb	17.8 pb	(24)
$D\bar{O}$	19 pb	25 pb	23 pb	

With more data being taken and analysed and refined methods being developed, sensitivity for Standard Model single top quark production is within reach for Tevatron Run II.

6 Conclusions

The current status of top quark measurements at the Tevatron experiments CDF and $D\bar{O}$ has been summarized, with the exception of the results for the

top quark mass which are covered in a separate article ¹⁾.

A wealth of measurements of the total $t\bar{t}$ production cross-section are available from Tevatron Run II. Measurements have been performed for dilepton, lepton+jets, all-hadronic events, and events with top quark decays involving τ leptons. They all yield results that are both mutually consistent and in agreement with the Standard Model prediction.

The event samples have been further interpreted by looking for non-Standard Model $t\bar{t}$ production mechanisms and top quark decays. No signs for physics beyond the Standard Model have been found so far, supporting the interpretation of the signal as $t\bar{t}$ production via QCD and top quark decay to Wb final states.

In the search for single (electroweak) production of top quarks, the sensitivity of the experiments has been improved over Run I. Even for Standard Model single top quark production, a significant cross-section measurement at the Tevatron is within reach in the near future.

7 Acknowledgements

The author would like to thank the organizers for a very interesting and enjoyable conference.

References

1. G. Velev, Top Mass Measurement at Tevatron Run II, these proceedings.
2. N. Kidonakis and R. Vogt, Phys. Rev. **D68**, 114014 (2004),
N. Kidonakis and R. Vogt, Eur. Phys. J. **C**, S466 (2004).
3. Z. Sullivan, Phys. Ref. **D70**, 114012 (2004).
4. DØ Collaboration, DØ note **4510**.
5. CDF Collaboration, CDF note **7154**. Updated values can be found at <http://www-cdf.fnal.gov/physics/new/top/top.html> .
6. DØ Collaboration, DØ notes **4422/4423**. Updated values can be found at <http://www-d0.fnal.gov/Run2Physics/top/> .
7. DØ Collaboration, DØ note **4625**. Updated values can be found at <http://www-d0.fnal.gov/Run2Physics/top/> .
8. DØ Collaboration, DØ note **4206**.
9. CDF Collaboration, Phys. Rev. **D71**, 052003 (2005). Updated values can be found at <http://www-cdf.fnal.gov/physics/new/top/top.html> .
10. CDF Collaboration, Phys. Rev. **D71**, 072003 (2005).
11. CDF Collaboration,
<http://www-cdf.fnal.gov/physics/new/top/public/ljets/LooseTagger/> .
12. CDF Collaboration, CDF note **7236**.
13. CDF Collaboration, CDF note **7174**.
14. CDF Collaboration, Phys. Rev. Lett. **93**, 142001 (2004).
15. CDF Collaboration, CDF note **7192**.
16. DØ Collaboration, DØ note **4623**.
17. DØ Collaboration, DØ note **4528**.
18. CDF Collaboration, CDF note **7075**.
19. DØ Collaboration, DØ note **4428**.
20. CDF Collaboration, CDF note **7179**.
21. CDF Collaboration, FERMILAB-PUB-04-396-E, hep-ex/0412042.

-
22. CDF Collaboration, CDF note **7113**.
 23. CDF Collaboration, CDF note **7058**.
 24. CDF Collaboration, CDF note **7173**.
 25. DØ Collaboration, FERMILAB-PUB-**04-057-E**, hep-ex/0404040.
 26. DØ Collaboration, DØ note **4549**.
 27. DØ Collaboration, DØ note **4545**.
 28. CDF Collaboration, Phys. Rev. **D71**, 031101 (2005).
 29. M. Beneke *et al*, CERN-TH-**2000-100**, hep-ph/0003033.
 30. CDF Collaboration, CDF note **7250**.
 31. CDF Collaboration, CDF note **7172**,
DØ Collaboration, DØ note **4586**.
 32. CDF Collaboration, Phys. Rev. **D71**, 012005 (2005),
DØ Collaboration, DØ note **4510**.
An updated DØ analysis is available in DØ Collaboration, DØ note **4722**.

DI-BOSON PRODUCTION AND SM/SUSY HIGGS SEARCHES AT THE TEVATRON

V. Daniel Elvira for the DØ and CDF Collaborations.

Fermi National Accelerator Laboratory, P.O. Box 500, Batavia, IL 60510, USA.

Abstract

The discovery of the Higgs boson would be a major success for the Standard Model (SM) and would provide further insights into the electroweak symmetry breaking mechanism. This report contains the latest results from the DØ and CDF Tevatron experiments on searches for the SM Higgs produced from gluon fusion with $H \rightarrow WW$, and in association with a W boson. It also includes searches for a supersymmetric Higgs in the $b\bar{b}$ and $\tau^+\tau^-$ decay channels. The study of di-boson production at the Tevatron is important to understand backgrounds in high mass Higgs searches. It also provides a test of the SM through the measurement of the production cross section and the gauge boson self couplings. This paper includes measurements of the WW , $W\gamma$, and WZ production cross sections, as well as limits on the anomalous couplings associated with the $WW\gamma$ and WWZ interactions. The results are based on sets of up to 320 pb^{-1} of data collected by the DØ and CDF experiments at the $\bar{p}p$ Tevatron collider, running at a center-of-mass energy of 1.96 TeV.

1 Physics Motivation

The Higgs boson is the only scalar elementary particle expected in the standard model (SM). Its discovery would be a major success for the SM and would provide further insights into the electroweak symmetry breaking mechanism. The constraints from precision measurements favor a Higgs boson sufficiently light to be accessible at the Fermilab Tevatron Collider. The Electroweak Working Group (EWWG) has updated, in the Winter of 2005, the constraints on the SM Higgs mass, based on measurements by the LEP, SLD, CDF, and DØ experiments ¹⁾. The preferred mass value, corresponding to the minimum of the solid curve in fig. 1, is at 126 GeV, with an experimental uncertainty of +73 and -48 GeV. Direct measurements at LEP have excluded the SM Higgs boson below 114.4 GeV at the 95% C.L. At the Tevatron, indirect searches involve precision measurements of the top quark and the W mass, while direct searches require high luminosity samples for discovery or exclusion in the low mass range. Although the expected luminosity necessary for its discovery at the Tevatron is higher than obtained thus far, the special role of the Higgs boson in the SM justifies extensive searches for a Higgs-like particle independent of expected sensitivity. The chances for discovery in a small sample improve according to supersymmetric extensions to the standard model ²⁾, which predict an enhancement of the Higgs cross-section relative to that of the SM.

At this stage of the Tevatron experiments, the effort is focused on the understanding of the physics objects, the backgrounds, missing transverse energy (\cancel{E}_T), as well b-tagging and calibration techniques. Di-boson production is, therefore, an important topic of study, not only as a background to high mass Higgs searches, but also as a test of the SM through the measurement of the production cross sections, and the gauge boson self couplings. The DØ ³⁾ and CDF ⁴⁾ detectors are described elsewhere.

2 Searches for SM/SUSY Higgs Production at the Tevatron

The two most promising mechanisms for Higgs production at the Tevatron $p\bar{p}$ collider, given the center-of-mass energy of $\sqrt{s}=1.96$ TeV, are gluon fusion and associated production with a W or a Z : $gg \rightarrow H$, $q\bar{q} \rightarrow W/Z + H$. Although the gg process would have the largest cross section, ~ 1 pb at $M_H^{SM}=115$ GeV, it is only an option in the search for a high mass Higgs boson ($M_H \gtrsim 140$ GeV) decaying to WW , since the $H \rightarrow b\bar{b}$ decay channel would be overwhelmed with background. For a low mass search, the Tevatron experiments explore WH and ZH associated production, which would give a clear signal with leptons, neutrinos, and b-jets: $q\bar{q} \rightarrow W/Z + H \rightarrow l\nu/l^+l^-/\nu\bar{\nu} + b\bar{b}$. In the first half of 2003, the DØ and CDF Collaborations performed a joint study on the sensitivity of the Tevatron experiments to either observe or rule out a low mass

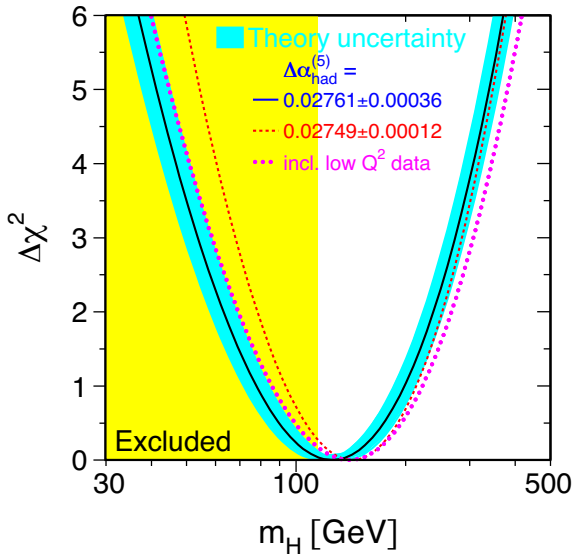


Figure 1: Constraints to the Higgs boson mass from the Electroweak Working Group.

SM Higgs⁵⁾. The results of the study are summarized in fig. 2. Given that systematic uncertainties were not taken into consideration in the sensitivity results, the amount of integrated luminosity per experiment for low mass Higgs discovery at 115 GeV would be in the 8-12 fb⁻¹ range. Evidence might be found with $\gtrsim 3\text{fb}^{-1}$, while Higgs masses less than ~ 130 GeV could be excluded with $\gtrsim 4\text{fb}^{-1}$.

In two-Higgs-doublet models of electroweak symmetry breaking, such as the minimal supersymmetric extension of the standard model (MSSM)²⁾, there are five physical Higgs bosons resulting from symmetry breaking: two neutral CP-even scalars, h and H, with H being the heavier state; a CP-odd, A; and two charged states, H[±]. The ratio of vacuum expectation values of the two Higgs fields is defined as $\tan \beta = v_2/v_1$ where v₂ and v₁ refer to the fields which couple to the up- and the down-type quarks. At tree level, the couplings of the neutral Higgs bosons to the down-type quarks, such as the bottom quark, are enhanced by a factor of $\tan \beta$ relative to the SM predictions,

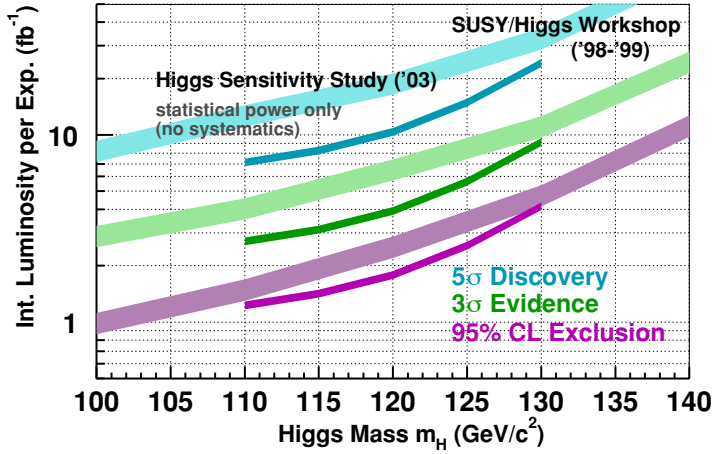


Figure 2: *Results from the Tevatron Higgs sensitivity study.*

thus production cross sections are enhanced by $\tan^2\beta$ 6). DØ and CDF search for SUSY Higgs production in two channels: $b\bar{b}h/bh \rightarrow b\bar{b}b\bar{b}/bb\bar{b}$, and inclusive Higgs production with $H \rightarrow \tau^+\tau^-$.

The Tevatron accelerator performed very well during 2004, providing more than 0.5 fb^{-1} per experiment since the beginning of Run II. The high instantaneous luminosity values recently achieved at the Tevatron raises the expectations of making strong statements about the Higgs sector by the end of Run II.

3 Di-boson Production and Anomalous Couplings

The study of di-bosons at the Tevatron is not only critical to understand backgrounds in high mass Higgs searches, but also provides a test of the SM through the measurement of the production cross section and the gauge boson self couplings. These couplings are a measure of the strength of the interaction of the W , Z and γ bosons with each other. The model independent way of describing new physics with anomalous couplings is through effective Lagrangians which

depend on a number of parameters. The effective Lagrangian for the WWZ and $WW\gamma$ interactions

$$\frac{L_{WWV}}{g_{WWV}} = g_V(W_{\mu\nu}^\dagger W^\mu V^\nu - W_\mu^\dagger V_\nu W^{\mu\nu}) + \kappa_V W_\mu^\dagger W_\nu V^{\mu\nu} + \frac{\lambda_V}{M_W^2} W_{\lambda\mu}^\dagger W_\nu^\mu V^{\nu\lambda} \quad (1)$$

depends on three anomalous coupling parameters: g_V , κ_V , and λ_V . The most general Lorenz and gauge invariant $ZV\gamma$ coupling, where V stands for either Z or γ , is described by eight coupling parameters h_i^V ($i=1,\dots,4$) [7]. Non-zero values of the CP violating h_1^V , h_2^V , or the CP conserving h_3^V , h_4^V would result in an increase of the $Z\gamma$ cross section, especially for large photon transverse energies. Partial wave unitarity restricts the $ZV\gamma$ couplings to vanish at high energies. The couplings are therefore parameterized as form-factors:

$$h_i^V = \frac{h_{i0}^V}{(1 + \hat{s}/\Lambda^2)^n} \quad (2)$$

where \hat{s} is the square of the $Z\gamma$ invariant mass, Λ is the form-factor scale, and h_{i0}^V are values of couplings at low energy.

Measurements at LEP and at the Tevatron results are complementary. The Tevatron experiments test values of \hat{s} higher than LEP, and the $W\gamma/Z\gamma$ processes independently. While $D\bar{O}$ measured the most restrictive limits on h_2^V and h_4^V , LEP obtained the best limits on h_1^V and h_3^V . $D\bar{O}$ limits on $WW\gamma/WWZ$ anomalous couplings are the tightest from hadron colliders.

4 Results

4.1 Measurement of WW Production Cross Section

Both $D\bar{O}$ and CDF measure the WW production cross section in the three channels: $2e2\nu/2\mu2\nu/e\mu2\nu$. CDF uses a 184 pb^{-1} sample collected from single lepton triggers, and $D\bar{O}$ 252, 224, 235 pb^{-1} samples from single or di-lepton triggers [8, 9].

$D\bar{O}$ requires two oppositely charged leptons with $p_T > 15 \text{ GeV}$, and at least one with $p_T > 20 \text{ GeV}$. ZZ and WZ backgrounds are eliminated by removing events in the Z mass window, and requiring a $\cancel{E}_T > 30, 40, 20 \text{ GeV}$ in the ee , $\mu\mu$ and $e\mu$ channels, respectively. Cuts on di-lepton transverse mass, and jet- \cancel{E}_T angular separation, help to eliminate the $Z\gamma$ and QCD backgrounds. The plots in fig. 3 show, for each channel, that the measured \cancel{E}_T distributions agree well with the Next-to-Leading Order (NLO) predictions for the signal plus the background contributions, estimated from Monte Carlo generators or extracted

from data, in the case of the QCD background⁸⁾. CDF performs a similar analysis and also observes good agreement between the measurement and the predictions for lepton p_T , \cancel{E}_T , and di-lepton invariant mass, as illustrated in fig. 4.

In the final sample, $D\mathcal{O}$ observes 25 events compared with $8 \pm 0.6(\text{stat}) \pm 0.6(\text{syst}) \pm 0.5(\text{lum})$ background events, and CDF 17 against $5 \pm 2.2/0.8$. As the probability of a background fluctuation is very small, the observation of the WW signal is well established by the two experiments. The cross sections measured by $D\mathcal{O}$ and CDF are $13.8 \pm 4.3/3.8(\text{stat}) \pm 1.2/0.9(\text{syst}) \pm 0.9(\text{lumin})$ pb and $14.6 \pm 5.8/5.1(\text{stat}) \pm 1.8/3.0(\text{syst}) \pm 0.9(\text{lumin})$ pb, respectively.

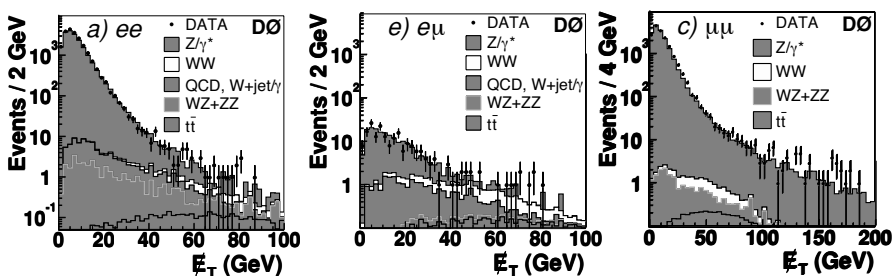


Figure 3: $D\mathcal{O}$ \cancel{E}_T distributions for WW events in the three decay channels.

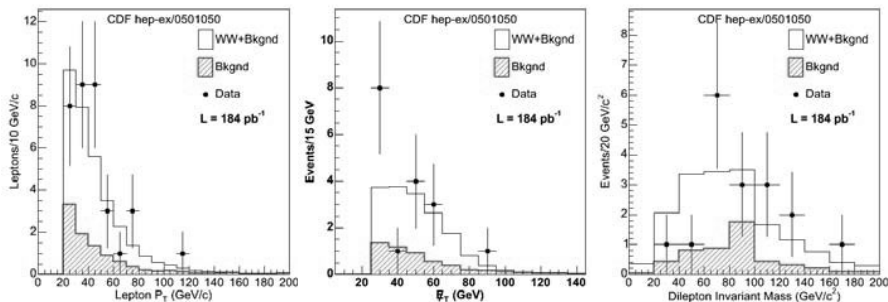


Figure 4: CDF measurements of lepton p_T , \cancel{E}_T , and di-lepton invariant mass in WW events.

4.2 Search for the SM Higgs boson $H \rightarrow WW^* \rightarrow l^+ \nu l'^- \bar{\nu}$

The search for the SM Higgs decaying into WW at $D\mathcal{O}$ is based on the same three leptonic channels used in the WW cross section measurement, corre-

sponding to an integrated luminosity of 177, 158, and 147 pb⁻¹. The sample selection includes cuts on the di-lepton invariant mass and event \cancel{E}_T , to remove the Z background, as well as on the sum of the event \cancel{E}_T and the p_T of the two leptons, to reject Drell-Yan and W +jets events. A $\Delta\phi_{ll} < 1.5$ -2 cut between the two leptons was used as a discriminant since the leptons are not back-to-back in Higgs decay due to spin correlations of the W bosons. Two events are observed in the $e\mu$ channel, as illustrated in fig. 5, and 9 in the combined sample, compared with a predicted signal ¹⁰⁾ of 0.272 ± 0.004 events at $M_H=160$ GeV, and an expected background ^{11, 12)} of 11.1 ± 3.2 events. The uppermost (blue) line in fig. 5 shows the $D\mathcal{O}$ 95% C.L. limit on the SM Higgs production, $H \rightarrow WW$, for masses between 100 and 200 GeV. For $M_H=160$ GeV, the limit is 5.7 pb. CDF does a similar search on a 184 pb⁻¹ sample. The plot on the left of fig. 6 shows the $\Delta\phi_{ll}$ distribution for the combined sample, which consists of 8 observed events, compared with a predicted signal sample of 0.17 ± 0.02 events, and a background sample of 8.9 ± 1 . For $M_H=160$ GeV, the CDF limit is 5.6 pb, as shown in fig. 6. The Tevatron limits are still over an order of magnitude above the SM prediction, due to low statistics.

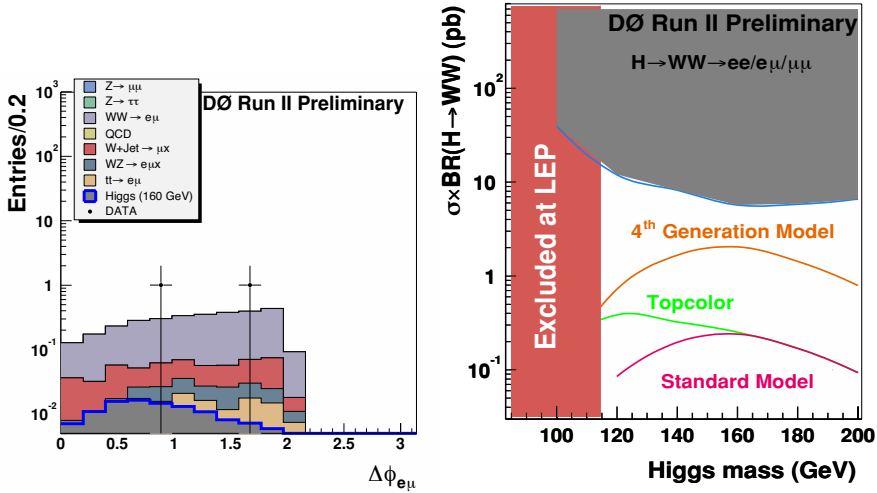


Figure 5: $D\mathcal{O}$ $\Delta\phi_{e\mu}$ distribution in $H \rightarrow WW^* \rightarrow l^+\nu l'^-\bar{\nu}$ events (left). SM Higgs production cross section limit for $H \rightarrow WW$ (right).

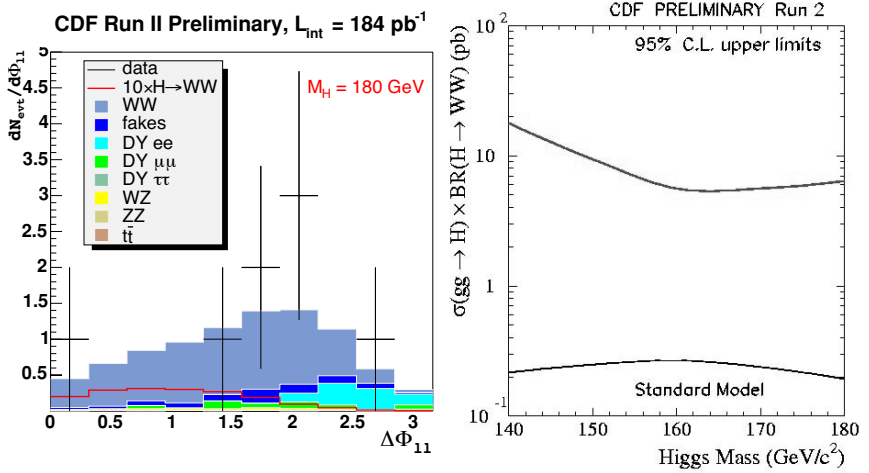


Figure 6: CDF $\Delta\phi_{11}$ distribution in $H \rightarrow WW^* \rightarrow l^+\nu l'^-\bar{\nu}$ events (left). SM Higgs production cross section limit for $H \rightarrow WW$.

4.3 Search for $Wb\bar{b}$ and SM Higgs Production in association with a W boson

The $D\bar{O}$ search for $W + b\bar{b}$ production in the $W \rightarrow e\nu$ channel is based on a 174 pb^{-1} sample containing one isolated electron with $p_T > 20 \text{ GeV}$ and $\cancel{E}_T > 25 \text{ GeV}$ (13). $W + b\bar{b}$ events are the main background for Higgs production associated with a W boson.

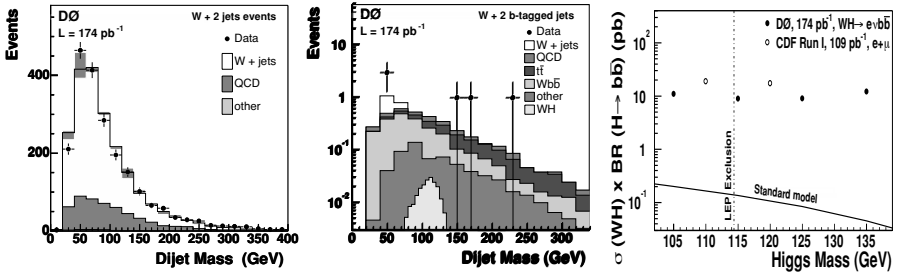


Figure 7: $D\bar{O}$ dijet mass distribution in $W + 2$ jets and $W + 2$ b-tagged jets samples (left). Limit on SM WH production (right).

The analysis also requires two b-tagged jets with p_T greater than 20 GeV. As illustrated in fig. 7, the measured dijet mass distribution is well described by the prediction for $W + b\bar{b}$ events, added to the estimated background, which

includes W + jets, QCD, and $t\bar{t}$ events. The number of observed events decreases from 2540 in the W +2 jets sample before b-tagging, to 76 in the sample with one or more b-tagged jet. In the 2 b-tagged jets sample, 6 events survive, compared with 4.4 ± 1.17 expected background events. Based on this result, shown in fig. 7, a 95% C.L. limit of 6.6 pb is measured on $Wb\bar{b}$ production for $p_T^b > 20$ GeV and an angular separation between b-jets greater than $\Delta R_{b\bar{b}} > 0.75$. By restricting the selection to a ± 25 GeV window around the Higgs mass, DØ establishes a 95% C.L. limit on the SM WH production cross section of 9-12.2 pb for Higgs masses in the range of 105-135 GeV. CDF does a similar search based on a 162 pb^{-1} sample with one electron or muon and \cancel{E}_T . The number of observed events decreases from more than 2072 in the W +2 jets sample to 62, when requiring one or more b-tagged jets. Figure 8 shows the CDF upper limit on the SM WH production cross section.

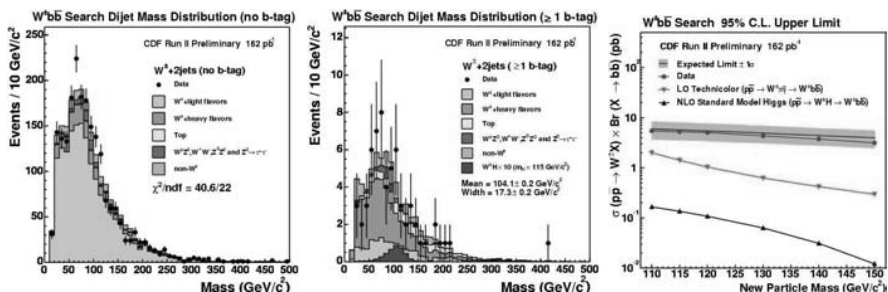


Figure 8: *CDF dijet mass distribution in W +2 jets and W +1 or more b-tagged jets samples (left). Limit on WH production (right).*

4.4 Search for Neutral SUSY Higgs Bosons in Multi-jet Events

Supersymmetry models predict the $hb\bar{b}$ cross section to scale with $\tan^2\beta$ at tree level, making the search for an MSSM Higgs in this channel well worth to pursue even on a small sample. DØ uses a 260 pb^{-1} sample of triple b-tagged multijet events¹⁴⁾. The main backgrounds are QCD heavy flavor and light jet events, Z + jets, and smaller contributions from other physics processes. The plot on the left in fig. 9 shows the dijet mass distribution of two leading jets in events with at least three b-tagged jets. The measurement agrees very well with the estimated background, shown as a solid line. The predicted signal for a Higgs mass of 120 GeV is shown separately as a dotted line. Since no excess of events is observed, limits on signal production cross section are extracted from this result. For a Higgs mass between 90 and 150 GeV, the limit on

the production cross section is 70-20 pb, as shown in the plot at the center of fig. 9. Figure 9 also shows the measured limits on the SUSY parameter $\tan \beta$ versus the mass of the neutral Higgs, m_A . DØ excludes a significant range of $\tan \beta$, depending on m_A , and the selected MSSM parameter set or scenario. For example, $\tan \beta$ is less than 55 at a 95% C.L. in the case of the maximum mixing scenario. There are other scenarios where the limit on $\tan \beta$ could be even more stringent ¹⁴⁾.

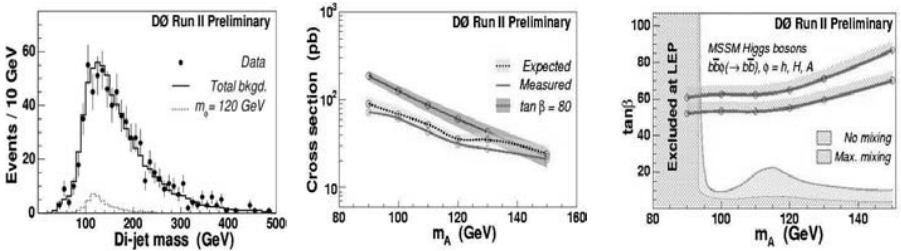


Figure 9: *Dijet mass distribution associated with events with at least three b -tagged jets (left). Limits on the $hb\bar{b}$ production cross section (center). Exclusion limits on $\tan \beta$ (right).*

CDF uses a 195 pb^{-1} sample from τ triggers to search for a MSSM Higgs. One τ decays into hadrons+ ν and the other to $e/\mu + 2\nu$. Cuts on the p_T of the leptons, the Z mass window, and the $\hat{H}_T = |p_T(\tau^+)| + |p_T(\tau^-)| + \cancel{E}_T$ variable are applied to remove the light quark background. The number of observed events in the final sample is 230 compared with the 263.6 ± 30.1 expected from signal (PYTHIA ¹¹⁾ and Tauola ¹⁵⁾) plus background ($Z \rightarrow \tau^+\tau^-$, $\text{jet} \rightarrow \tau$, $t\bar{t}$, di-bosons). Figure 10 shows the measured limit of $19\text{-}3 \text{ pb}$, in the mass range $115\text{-}200 \text{ GeV}$, on the Higgs production cross section, with $h \rightarrow \tau^+\tau^-$. This limit is extracted from the mass-like discriminating variable $m_{vis}(l, \tau, \cancel{E}_T)$.

4.5 Measurement of $W/Z + \gamma$ Cross Sections and Limits on Anomalous Couplings

DØ measures the $W\gamma$ production cross section in the e and μ channels, using samples of 162 and 134 pb^{-1} , respectively. Cuts on the e and γ transverse mass, angular separation, and event \cancel{E}_T are applied to remove the backgrounds, dominated by W + jets, and photons as final state radiation from the lepton. The photon p_T distribution shown in fig. 11 for the combined channels in the final sample is in good agreement with the theoretical prediction ¹⁶⁾ plus background estimates. The cross section, $14.8 \pm 1.6(\text{stat}) \pm 1.0(\text{syst}) \pm 1.0(\text{lum}) \text{ pb}$, agrees well with the SM prediction, $16.0 \pm 0.4 \text{ pb}$, for $E_{T\gamma} > 8 \text{ GeV}$ and

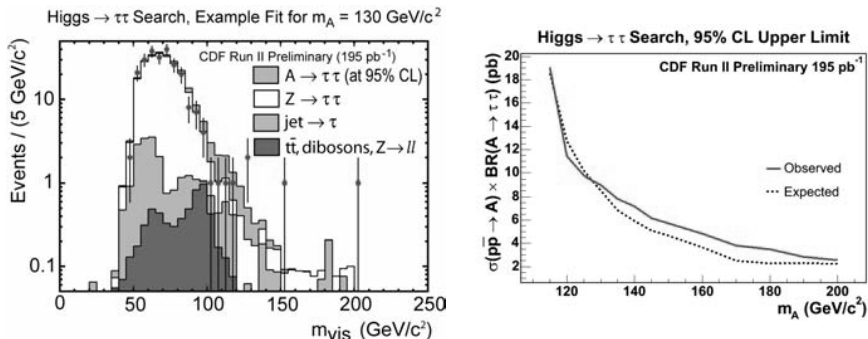


Figure 10: *Mass-like discriminating distribution, $m_{vis}(l, \tau, \cancel{E}_T)$ (left). Limit on the Higgs production cross section with $h \rightarrow \tau^+ \tau^-$ (right).*

$\Delta R_{l\gamma} > 0.7$. Limits on the anomalous couplings $\Delta\kappa_\gamma$ and λ_γ are extracted from the photon p_T spectrum, and are consistent with the zero value expectation from the SM. The point and bars in the λ versus $\Delta\kappa$ plot in fig. 11 indicate the 95% C.L. one dimensional (1D) intervals for each parameter with the other set to zero: $-0.93 < \Delta\kappa_\gamma < 0.97$, $-0.22 < \lambda_\gamma < 0.22$. The ellipse represents the 95% C.L. two dimensional (2D) exclusion limit. These results are the most stringent model independent constraints on $\Delta\kappa_\gamma$ and λ_γ from hadron colliders, and represent an improvement with respect to the Tevatron Run I measurements^{17, 18}. While the LEP experiments constrain the $WW\gamma$ and WWZ couplings simultaneously using WW events, single W , or single γ final states in e^+e^- collisions¹⁹, the Tevatron experiments study the $W\gamma$ process directly.

The CDF experiment has measured the $W\gamma$ production cross section²⁰ in a 200 pb^{-1} sample using the same decay channels as $D\phi$. Figure 12 shows the photon transverse energy spectrum and the transverse mass of the lepton-photon- \cancel{E}_T system for $W\gamma$ candidates. A total of 195 and 128 events are observed in the e and μ samples, respectively, in agreement with the 194.1 ± 19.1 and 142.4 ± 9.5 events expected from signal plus background. The CDF measured $W\gamma$ cross section of $18.1 \pm 3.1 \text{ pb}$ is in good agreement with the SM prediction of $19.3 \pm 1.4 \text{ pb}$, for $E_{T\gamma} > 7 \text{ GeV}$ and $\Delta R_{l\gamma} > 0.7$.

$D\phi$ also measures the $Z\gamma$ production cross section in the e^+e^- and $\mu^+\mu^-$ channels. The measured cross section of $4.2 \pm 0.4(\text{stat} + \text{syst}) \pm 0.3(\text{lum}) \text{ pb}$ is in good agreement with the NLO prediction¹⁶) of $3.9 \pm 0.1/0.2$ within the errors. Contrary to the $W\gamma$ case, the SM prohibits the $ZZ\gamma$ interactions at tree level, which means that any deviation of the h_i^V trilinear couplings from zero would signal the presence of new physics. $D\phi$ has measured the tightest

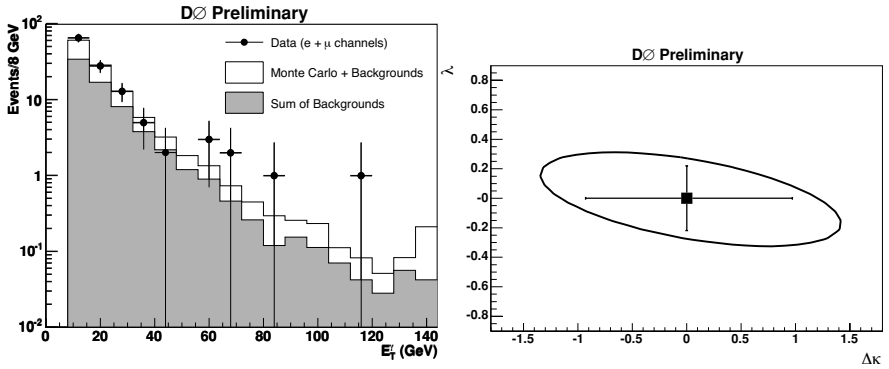


Figure 11: $D\bar{D}$ photon p_T distribution (left). One and two dimensional limits on $WW\gamma$ anomalous couplings (right).

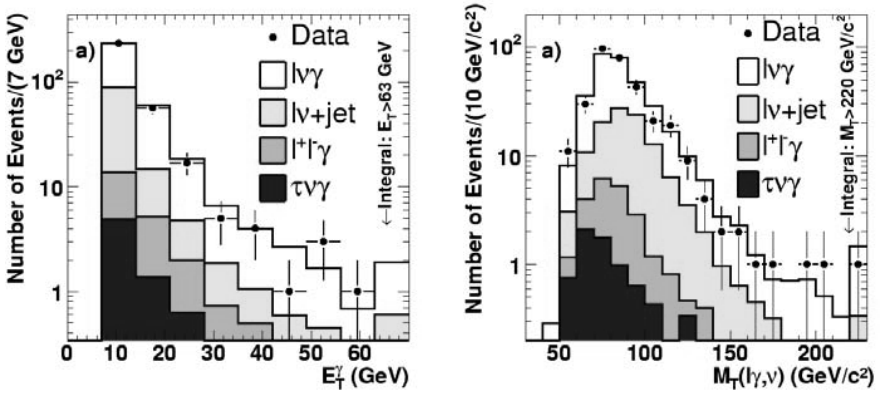


Figure 12: CDF photon transverse energy spectrum and the transverse mass of the lepton-photon- \cancel{E}_T system for $W\gamma$ candidates.

1D and 2D upper limits on the trilinear couplings from hadron colliders, which also represent an improvement of a factor of 2-3 with respect to the Run I measurements (17, 18). No deviation from the zero value SM prediction is observed: $|h_{30}^\gamma| < 0.22$, $|h_{40}^\gamma| < 0.019$, $|h_{30}^Z| < 0.21$, $|h_{40}^Z| < 0.019$.

The CDF $Z\gamma$ cross section measurement is based on the same initial sample used in the CDF $W\gamma$ analysis (20). The number of observed events in the e and μ channels is 36 and 35, respectively, in agreement with the signal plus background SM expectation. The measured cross section of 4.6 ± 0.6 pb is well in agreement with the 4.5 ± 0.3 pb obtained from NLO calculations for $E_{T\gamma} > 7$ GeV and $\Delta R_{l+\gamma} > 0.7$.

4.6 Search for WZ/ZZ Di-boson Events and Measurement of Limits on Trilinear Couplings

The two Tevatron experiments conducted a search for $W(l\nu)Z(l^+l^-)$ events, in the case of D0, and $WZ(l\nu l^+l^-) + ZZ(l^+l^-l^+l^-/l^+l^-\nu\nu)$ events, in the case of CDF. D0 reports evidence of WZ production, based on the observation of 3 events in 285 and 320 pb^{-1} samples, compared with an expected background of 0.71 ± 0.08 . The measured WZ inclusive production cross section by D0 is $4.5 \pm 3.5/2.6$ pb, in agreement with the SM prediction of 3.7 ± 0.1 pb (21). CDF uses a smaller sample, 194 pb^{-1} , to establish a limit of 15.2 pb to the $WZ + ZZ$ production cross section, based on the observation of 3 events compared with a signal plus background expectation of 3.3 ± 0.43 . Figure 13 shows the D0 1D and 2D limits on Δg_Z , λ_Z , and $\Delta \kappa_Z$, which are also summarized in tab. 1. These results are the most stringent from direct, model independent measurements to date, and about a factor of 2 to 3 better than the D0 Run I results (22). LEP has measured the $WW\gamma$ and WWZ couplings simultaneously using WW events (19).

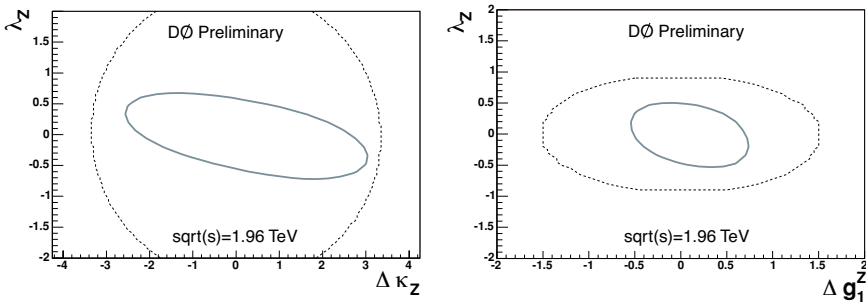


Figure 13: D0 1D and 2D limits on Δg_Z , λ_Z , and $\Delta \kappa_Z$.

Table 1: $D\bar{O}$ preliminary one dimensional 95% C.L. limits on WWZ trilinear couplings.

$\Lambda=1.0$ TeV	$\Lambda=1.5$ TeV
$-0.53 < \lambda_Z < 0.56$	$-0.48 < \lambda_Z < 0.48$
$-0.57 < \Delta g_Z < 0.76$	$-0.49 < \Delta g_Z < 0.66$
$-2.0 < \Delta \kappa_Z < 2.4$	

5 Conclusions

The hunt for the SM and SUSY Higgs bosons has started at the Tevatron. Di-boson production cross sections have been measured more accurately than before, and the tightest limits on anomalous couplings from hadron colliders have been measured by the $D\bar{O}$ experiment. A significant amount of new data will be necessary to exclude the Higgs boson in the low mass range, and even more for discovery. The Tevatron has performed very well during 2004, collecting more than 0.5 fb^{-1} since the beginning of Run II. It is now necessary to improve the particle identification, calibration, and analysis techniques to meet the challenges of the high luminosity environment.

References

1. S. Eidelman *et al.*, Phys. Lett. B **592**, 1 (2004); LEP Electroweak Working Group, <http://lepewwg.web.cern.ch/LEPEWWG/>
2. H. Nilles, Phys. Rept. **110**, 1 (1984); H. Haber and G. Kane, Phys. Rept. **117**, 75 (1985).
3. V. Abazov *et al.*, in preparation for submission to Nucl. Instrum. Methods Phys. Res. A; S. Abachi *et al.*, Nucl. Instrum. Methods Phys. Res. A **338**, 185 (1994).
4. The CDF Collaboration, FERMILAB-PUB-96-390-E.
5. CDF and $D\bar{O}$ Collaborations, FERMILAB-PUB-03/320-E.
6. J. Gunion *et al.*, "The Higgs Hunter's Guide", SCIPP-89/13 (1989).
7. U. Baur and E. Berger, Phys. Rev. D **47**, 4889 (1993).
8. V. M. Abazov *et al.*, Phys. Rev. Lett. **94**, 151801 (1995), hep-ex/0410066, and references therein.

9. D. Acosta *et al.*, submitted to Phys. Rev. Lett. , hep-ex/0501050, and references therein.
10. A. Djouadi *et al.*, Comp. Phys. Commun. 108, 56 (1997), hep-ph/9704448; M. Spira, Report DESY T-95-05 (1995), hep-ph/9510347.
11. T. Sjostrand *et al.*, Comp. Phys. Comm. **135**, 238 (2001).
12. M. Mangano *et al.*, JHEP 0307:001 (2003), hep-ph/0206293.
13. V. Abazov *et al.*, Phys. Rev. Lett. **94**, 091802 (2005), hep-ex/0410062, and references therein.
14. V. Abazov *et al.*, submitted to Phys. Rev. Lett. , hep-ex/0504018, and references therein.
15. S. Jadach *et al.*, Comp. Phys. Commun. **64** (1991).
16. U. Baur and E. Berger, Phys. Rev. D **41**, 1476 (1990).
17. S. Abachi *et al.*, Phys. Rev. Lett. **78**, 3634 (1997).
18. D. Acosta *et al.*, Phys. Rev. Lett. **75**, 1017 (1995).
19. LEP Electroweak Working Group (EWWG), hep-ex/0412015.
20. D. Acosta *et al.*, Phys. Rev. Lett. **94**, 041803 (2005), hep-ex/0410008, and references therein.
21. J. Campbell *et al.*, Phys. Rev. D **60**, 113006 (1999).
22. B. Abbott *et al.*, Phys. Rev. D **60**, 072002 (1999).

SESSION VII – SEARCH FOR PHYSICS BEYOND THE SM

- *Isabel Trigger* Search for Physics Beyond the Standard Model at LEP
- *Judith Katzy* EWK and New Physics at HERA
- *Arnaud Duperrin* Searches for SuperSymmetry at the Tevatron
- *Kaori Maeshima* Non SUSY Searches at the Tevatron
- *Andrea Romanino* Ignoring the Hierarchy Problem

SEARCH FOR PHYSICS BEYOND THE STANDARD MODEL AT LEP

Isabel TRIGGER
CERN, Geneva, Switzerland

Abstract

The ALEPH, DELPHI, L3 and OPAL collaborations searched for evidence of physics beyond the Standard Model in the data taken by the four detectors at the LEP collider from 1989 to 2000. None of these searches has shown significant evidence for a signal. Limits have been set on the cross-sections for many processes. These cross-section limits have been interpreted in the context of many popular models, and used to exclude regions of the models' parameter space and set lower limits on the masses of additional particles they predict.

1 Introduction

Since LEP stopped taking data in 2000, the four detector collaborations have already published the results of most of their searches for evidence of physics beyond the Standard Model. This talk summarized only results published or made public in the year preceding the Rencontres de La Vallée d'Aoste conference. For that reason, the searches described fall into three main categories: “new” ideas, generally interpretations of older analyses in the context of models which arose only recently; final results of very complicated searches; and combinations of final results from several collaborations.

2 New Ideas for Old Data

While most of the results presented in this talk are the final results of searches which have been ongoing since at least the beginning of LEP 2, there have been a few fresh initiatives in the last two or three years.

2.1 Pentaquarks

All four LEP experiments investigated their sensitivity to pentaquarks in the LEP 1 dataset, following the controversial publication of evidence for their existence. No evidence was found for a signal. The ALEPH collaboration published ¹⁾ the null results of their searches for resonances consistent with the decays of pentaquarks (see Table 1).

Table 1: *Upper limits on production rates of exotic states per hadronic Z^0 decay, from ¹⁾.*

Pentaquark State	Decay	Number per Z-decay
$\Theta(1535)^+$	pK_S^0	$< 6.2 \times 10^{-4}$
$\Xi(1862)^{--}$	$\Xi^- \pi^-$	$< 4.5 \times 10^{-4}$
$\Xi(1862)^0$	$\Xi^- \pi^+$	$< 8.9 \times 10^{-4}$
$\Theta_C(3100)^0$	pD^{*-}	$< 6.3 \times 10^{-4}$
$\Theta_C(3100)^0$	pD^-	$< 31 \times 10^{-4}$

2.2 Radions and Branons

Models of gravity propagating in additional dimensions may imply the existence of scalars which could be detected at LEP energies or could affect the

detection of the Standard Model Higgs at LEP. The OPAL collaboration re-evaluated ²⁾ the limits on the Standard Model Higgs boson and the Higgs limits from flavour-independent searches in the context of the Randall-Sundrum model ³⁾ of gravity propagating in an additional dimension with a special warped geometry which is introduced to solve the “hierarchy problem” associated with the large difference between the electro-weak and gravitational energy scales. This model predicts the existence of a new scalar, the radion, associated with fluctuations in the separation between branes. The radion could be light enough to be produced at LEP, even if all other scalars in the model, including the graviton, are too massive. The radion has the same quantum numbers as the Higgs boson, allowing the two scalars to mix; however, unlike the Higgs, the radion couples directly to gluon pairs. This means that its decays are quite different from those of the Standard Model Higgs. If the Higgs mixed with a radion, it might not have been detected in searches for the expected Standard Model fermionic final states. As a result, the limit on the mass eigenstate which in the absence of mixing would be the Standard Model Higgs decreases to only 58 GeV in the worst case.

The alternative Arkani-Hamed–Dimopoulos–Dvali models ⁴⁾ of gravity in large extra dimensions predict the existence of another scalar, the branon, associated with the brane tension f . Branons may be produced at lower energies than gravitons if f is much less than the extra dimension scale M_F . They would not interact in the detector, and would be observed as missing energy in the processes:

$$e^+e^- \rightarrow \tilde{\pi}\tilde{\pi}Z^0 \rightarrow \tilde{\pi}\tilde{\pi}q\bar{q} \quad (1)$$

$$e^+e^- \rightarrow \tilde{\pi}\tilde{\pi}\gamma \quad (2)$$

The L3 collaboration has reinterpreted ⁵⁾ their searches for photons and missing energy in the context of this model. No excess of these events is observed with respect to Standard Model predictions, so limits are set on the cross-section as a function of f and M_F . The 95% confidence level lower limits constrain the branon mass to be greater than 103 GeV in the extreme case of small brane tension ($f = 0$), and the branon tension to be greater than 180 GeV in the extreme case of light branons ($M_F = 0$).

2.3 Anomalous Higgs Couplings

If the couplings of the Higgs boson to fermions or gauge bosons are larger than the Standard Model or MSSM predictions, its production cross-section could be anomalously large at LEP energies. L3 derived limits ⁶⁾ on the couplings d , d_B , Δg_1^Z , $\Delta\kappa_\gamma$ and ξ^2 , and on the $H \rightarrow \gamma\gamma$ and $H \rightarrow \gamma Z$ decay rates. All were consistent with Standard Model predictions.

3 Final Results from Long-term Efforts

3.1 Photons with Missing Energy

The results of a topological search by the OPAL collaboration ⁷⁾ for final states containing only photons with missing transverse momentum are interpreted as electron-positron annihilation into pairs of weakly interacting neutral particles (“ $e^+e^- \rightarrow XX$ ”) with prompt radiative decays into other weakly interacting neutrals (“ $X \rightarrow \gamma Y$ ”) which escape undetected. In the more general case where both X and Y are massive (*e.g.* $e^+e^- \rightarrow \tilde{\chi}_2^0 \tilde{\chi}_2^0$, $\tilde{\chi}_2^0 \rightarrow \tilde{\chi}_1^0 \gamma$) the 95% cross-section limits on this process are set between 10 and 60 fb as long as $M_X - M_Y > 5$ GeV. In the special case of nearly massless Y (*e.g.* GMSB models where $X = \tilde{\chi}_1^0$ and $Y = \tilde{G}$ or composite models where X is an excited neutrino), the limits are between 20 and 40 fb.

3.2 Excited Leptons

The DELPHI collaboration has performed dedicated searches ⁸⁾ for charged and neutral excited leptons decaying to ordinary leptons and gauge bosons. If it is assumed that the weight factors f and f' , associated with the SU(2) and U(1) gauge groups respectively, are either equal (no photon decays for the excited neutrino) or equal and opposite (no photon decays for the excited charged lepton), then the results of all of these searches can be interpreted very simply as limits in the f/Λ versus m_l^* plane, where Λ is the compositeness scale.

3.3 Exotic Higgs Searches

The three following searches were made in the context of rather general two Higgs doublet models (2HDM). Most of the papers summarized here provide many plots showing regions of parameter space excluded at specific benchmark points; however, the most important and durable results from these searches are model-independent cross-section limits. These stand as the final results of LEP, and can be re-interpreted in the context of new models, as we saw in Section 2.

3.3.1 Fermiophobic Higgs

If the lightest neutral Higgs boson had a much larger branching ratio for decays to photon pairs than it does in the MSSM, anomalously large cross-sections would be observed for final states containing two photons and two jets, two photons and a lepton pair, or two photons and missing energy from neutrinos. The DELPHI collaboration searched for these final states ⁹⁾ and interpreted

them either as $h^0 Z^0$, in which case the invariant mass of the jet or lepton pair or the missing momentum was required to correspond to the Z^0 mass, or as $h^0 A^0$, in which case only the $b\bar{b}\gamma\gamma$ topology was considered, as the A^0 would still decay to fermions. The numbers of events selected in both analyses matched the Standard Model background predictions very closely.

3.3.2 Invisible Higgs

The L3 collaboration performed a search ¹⁰⁾ for $e^+e^- \rightarrow HZ^0$ in the case where the Z^0 decays to jets, electrons or muons and the Higgs to weakly interacting neutral particles (LSP, fourth generation neutrinos, scalars associated with extra dimensions, majorons, ...). The results were interpreted as a limit on the ratio of the cross-section for $h^0 Z^0$ with invisibly decaying Higgs to the Standard Model HZ^0 cross-section, as a function of the Higgs mass. For masses up to just over 112 GeV, this ratio is less than unity, meaning that the Standard Model cross-section is excluded.

3.3.3 Neutral Higgs Searches in Two-Higgs-Doublet Models

The OPAL collaboration combined many searches for neutral Higgs bosons and interpreted them very generally ¹¹⁾ in the context of 2HDM. Limits were given at many benchmark points, including ones where the usual assumption of CP-conservation in the Higgs sector was dropped, and the CP-even and CP-odd eigenstates were allowed to mix. In such a general scenario, LEP data can by no means exclude the whole of the kinematically allowed region. In addition to the benchmark scenario limits, there were model-independent cross-section limits on the ratio of the excluded cross-section for a given final state to σ_{HZ^0} in the Standard Model or $\sigma_{h^0 Z^0}$ in the MSSM with $\cos^2(\beta - \alpha) = 1$.

4 Final LEP Combinations

4.1 Lightest Supersymmetric Particle Mass Limit in the MSSM

The combination of MSSM LSP limits performed by the ALEPH collaboration ¹²⁾ was updated with the combined results of the four LEP collaborations for scalar lepton and Higgs searches ¹³⁾. The lower mass limits on the LSP depend slightly on the top mass limit, but are generally around 42 GeV if stau mixing is allowed, and about 5 GeV higher if it is assumed that there is no mixing in the stau sector. In the special case of minimal SUGRA, the limit is set at lower values of $\tan\beta$ at around 50 GeV, and depends rather more strongly on the top mass limit.

4.2 Neutral Higgs Searches in the MSSM

The results of the four LEP collaborations' searches for neutral Higgs bosons were combined¹⁴⁾, as discussed in the OPAL search of Section 3.3.3. Many of the CP-conserving MSSM benchmark scenarios considered are excluded over most of their parameter space.

4.3 Large Extra Dimensions

A sufficiently light graviton would be produced directly in the process $e^+e^- \rightarrow G\gamma$. Events from the four LEP experiments containing a single photon and nothing else were analyzed together¹⁵⁾. LEP can exclude a fundamental gravity scale M_D of up to about 1.6 TeV for two extra dimensions and about 650 GeV for six.

5 Conclusions and Summary

Most of the final LEP 2 search results have now been finalized and are either published or in the last stages of approval by the collaborations. As we can see from the pentaquark searches, new initiatives are still possible; however, big surprises seem unlikely at this stage.

The results of searches for physics beyond the Standard Model at LEP can be summarized briefly by the words "no significant excess found". While this may be disappointing, the LEP results have also excluded many of the original LHC benchmark scenarios, and are helping to point the way to where the new physics will be found in the near future.

References

1. S. Schael *et al.* (ALEPH Collaboration), "Search for Pentaquark States in Z Decays". Phys.Lett.B599 (2004) 1.
2. G. Abbiendi *et al.* (OPAL Collaboration), "Search for Radions at LEP2". Phys.Lett.B 609 (2005) 20.
3. L. Randall and R. Sundrum, "An Alternative to Compactification". Phys.Rev.Lett. 83 (4690) 1999.
4. N. Arkani-Hamed, S. Dimopoulos and G.R. Dvali, "The Hierarchy Problem and New Dimensions at a Millimetre". Phys.Lett.B429 (263) 1998.
5. P. Achard *et al.* (L3 Collaboration), "Search for Branons at LEP". Phys.Lett.B 597 (2004) 145.

6. P. Achard *et al.* (L3 Collaboration), “Search for Anomalous Couplings in the Higgs Sector at LEP”. Phys.Lett.B 589 (2004) 89.
7. G. Abbiendi *et al.* (OPAL Collaboration), “Multi-photon Events with Large Missing Energy in e^+e^- Collisions at $\sqrt{s} = 192 \text{ GeV} - 209 \text{ GeV}$ ” Phys.Lett.B602 (2004) 167.
8. W. Adam *et al.* (DELPHI Collaboration), “Search for excited leptons in $e+e^-$ collisions at $\text{sqrt}=189-208 \text{ GeV}$ ”. DELPHI–2004–024–CONF 699.
9. J. Abdallah *et al.* (DELPHI Collaboration), “Search for Fermiophobic Higgs Bosons in Final States with Photons at LEP 2”. Euro.Phys.J C35 (2004) 313.
10. P. Achard *et al.* (L3 Collaboration), “Search for an Invisibly Decaying Higgs Boson”. Phys.Lett.B 609 (2005) 35.
11. G. Abbiendi *et al.* (OPAL Collaboration), “Flavour Independent H^0A^0 Search and Two Higgs Doublet Model Interpretation of Neutral Higgs Boson Searches at LEP”. Hep-ex/0408097 (submitted to Euro.Phys.J C).
12. A. Heister *et al.* (ALEPH Collaboration), “Absolute Mass Lower Limit for the Lightest Neutralino of the MSSM from e^+e^- data up to $\sqrt{s} = 209 \text{ GeV}$ ”. Phys.Lett.B583 (2004) 247.
13. L. Pape *et al.* (LEP SUSY Working Group), <http://lepsusy.web.cern.ch/lepsusy/>.
14. P. Igo-Kemenes *et al.* (LEP Higgs Working Group), “Search for Neutral MSSM Higgs Boson at LEP”. LEP Higgs WG 2004–01.
15. W. Adam *et al.* (LEP Exotica Working Group), “Combination of LEP Results on Direct Searches for Large Extra Dimensions”. LEP Exotica WG 2004–03.

ELECTROWEAK PHYSICS AND SEARCHES FOR NEW PHYSICS AT HERA

J.Katzy

DESY Hamburg, Notkestr. 85, D-22607 Hamburg
on behalf of the H1 and ZEUS collaborations

Abstract

The charged and neutral current cross sections of deep inelastic ep scattering at HERA are presented. For the first time, these cross sections are also measured with longitudinally polarised electron (positron) beams. The cross sections are compared to the standard model expectations. No deviations are found. Recent results on further searches for physics beyond the standard model in the full HERA data set are reported. The data have been analysed searching for contact interactions, leptoquarks, squarks and light gravitinos in R -parity violating sypersymmetric models. A dedicated search for events with isolated leptons and missing transverse momentum is also reported.

1 Introduction

At the HERA collider electrons (positrons) and protons collide at a center-of-mass energy of about $\sqrt{s} = 320$ GeV (300 GeV before 1998). From 1994-2000 (HERA I), integrated luminosities of about 100 pb^{-1} of e^+p and 15 pb^{-1} of e^-p scattering data were collected by each of the two experiments H1 and ZEUS.

After an upgrade to run with high luminosity and with polarised leptons 60 pb^{-1} of e^+p data and 100 pb^{-1} of e^-p data with an average polarisation of 40% and helicity ± 1 have been collected since 2003 (HERA II).

The data were used to measure the charged and neutral cross sections with and without polarisation and to search for new physics beyond the Standard Model (SM).

2 Electroweak measurements

At HERA both neutral current (NC) interactions $ep \rightarrow ep$ via γ or Z^0 -exchange, or charged current (CC) interaction $ep \rightarrow e\nu$ via W^\pm exchange are observed. The cross sections are described in terms of Q^2 , the four momentum transfer squared, Bjorken x and the inelasticity y . These variables are related through $Q^2 = sxy$.

Fig. 1 shows the Q^2 dependence of the NC and CC cross sections for e^+p and e^-p data measured in HERA I. ¹ The data are well described by the SM as shown here with the CTEQ6D parametrisation for the parton densities in the proton. At low Q^2 the NC cross section exceeds the CC cross section by more than two orders of magnitude due to the dominating photon exchange with the propagator term $\sim 1/Q^4$. In contrast the CC cross section which is proportional to $M_W^2/(Q^2 + M_W^2)$ approaches a constant at low Q^2 . The CC and NC cross sections are of comparable size at $Q^2 \sim 10^4 \text{ GeV}^2$, where the photon and the Z^0 exchange contributions to the NC cross sections are of similar size to those of the W^\pm exchange. These measurements thus illustrate unification of the electromagnetic and the weak interactions in deep inelastic scattering.

Small differences between e^+ and e^- scattering can be observed in both cross sections. The difference between the e^+ and e^- scattering in the NC cross section is due to γZ interference. The difference of the CC cross sections arises from the difference between the up and down quark distributions and the less favourable helicity factor $(1-y)^2$ in the e^+p cross section:

$$\bar{\sigma}_{CC}^+ \sim x\bar{u} + (1-y)^2 x d \quad (1)$$

$$\bar{\sigma}_{CC}^- \sim xu + (1-y)^2 x\bar{d} \quad (2)$$

¹The e^+p data have been combined after scaling the 94-97 data to $\sqrt{s} = 319$ GeV.

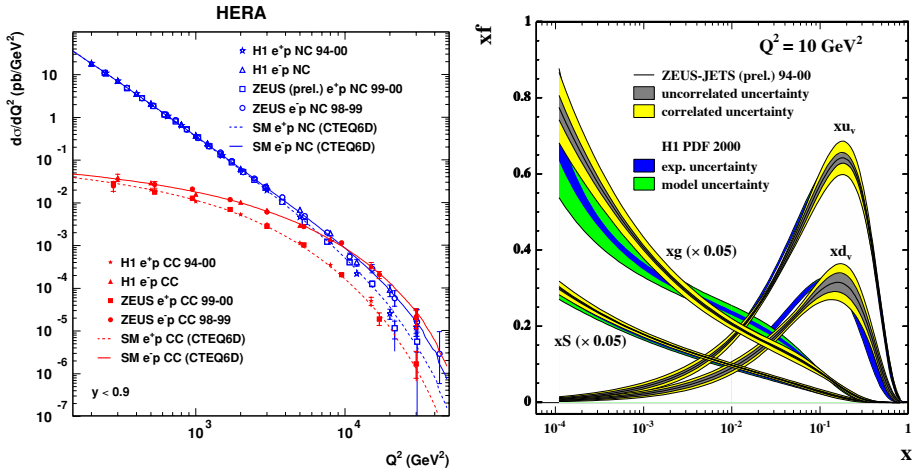


Figure 1: *left: NC and CC $e^\pm p$ scattering cross sections as a function of Q^2 right: parton density functions*

The high precision and the wide kinematic range covered by the HERA DIS data, over four orders of magnitude in x and Q^2 , allows the determination of the parton density functions (PDFs) in an NLO QCD fit using the DGLAP evolution equations as shown in Fig.1. The ZEUS fit uses in addition e^+p deep inelastic inclusive jet cross sections and direct photoproduction dijet cross sections to further constrain the gluon density ¹⁾. The PDFs extracted by both experiments agree and are in agreement with global fits. In a complementary measurement to the fits, the H1 collaboration extracted the u and d quark distributions in x and Q^2 bins where they contribute at least 70% to the cross section ²⁾. The results are in good agreement with the fits.

The longitudinally polarised leptons available in HERA II are used to measure the polarisation dependence of the total charged current cross section. Due to the non-existence of right handed currents in the SM a linear dependence of the CC cross section on the polarisation is expected:

$$\sigma_{CC}^\pm = (1 \pm P)\sigma_{CC}^{(P=0)} \tag{3}$$

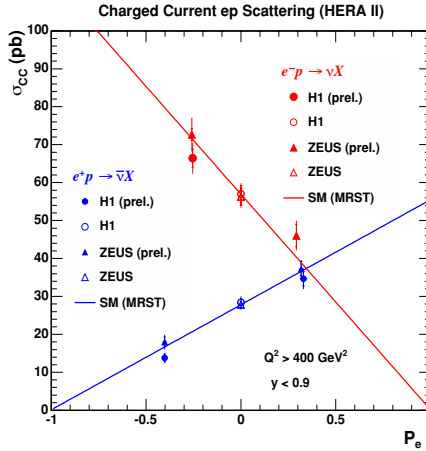


Figure 2: *CC cross sections as a function of polarisation.*

Fig.2 shows the total charged current cross section as a function of the polarisation for e^+p and e^-p scattering. The data agree well with the expectations from the SM and with a linear fit. Hence no sign for a right handed weak current is observed.

3 Physics beyond the SM

The precise CC and NC cross section measurements and the high statistics available allow to look for new particles or processes that would lead to deviations of the cross sections from the standard model predictions. The ep collider HERA is ideally suited to search for new particles coupling to electron-quark (positron-quark) pairs.

3.1 Contact interactions

To search for new particles associated to a large scale ($M_X \gg \sqrt{s}$) the possible interference of a new particle with the γ or Z field of the $e^\pm p$ NC scattering pro-

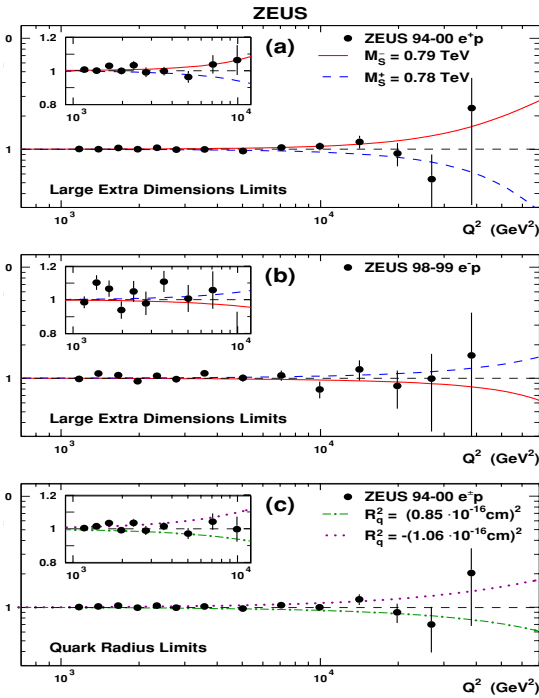


Figure 3: *ZEUS* $e^\pm p$ (a),(b) data compared with 95% C.L. exclusion limits for the effective Planck mass scale in models with large extra dimensions. (c) Exclusion limits for the effective mean-square radius of the electroweak charge of the quark. Results are normalized to the SM expectations calculated using the CTEQ5D parton distributions.

cess is parametrized and the effect on the NC cross section has been calculated, see Fig.3.

Since no deviations of the NC cross section from the SM are found various limits were derived: the effective mass scale in $eeqq$ contact interactions Λ is above 1.6 to 5.5 TeV (depending on the parametrisation); the ratio of leptoquark mass to the Yukawa coupling M_{LQ}/λ_{LQ} for heavy leptoquark models is above 0.3-1.4 TeV and mass scale parameters in models with large extra dimensions below 0.79 TeV are excluded ³⁾, ⁴⁾. The limit on the quark charge radius, in the classical form factor approximation, is $0.85 \cdot 10^{-18}$ cm.

3.2 Leptoquarks

Leptoquarks (LQ) are bosons that carry both lepton (L) and baryon (B) numbers and have lepton-quark couplings. Their fermion number ($F = 3B + L$) can be $F = 0$ or $|F| = 2$. Such bosons arise naturally in unified theories that arrange quarks and leptons in common multiplets such as GUT like theories, technicolor, compositeness.

HERA provides a unique facility for resonant production of first generation leptoquarks with $M_{LQ} = \sqrt{s_{ep}x}$ decaying into a lepton and a jet, with the lepton being either an electron or a neutrino. In the Buchmüller-Rückl-Wyler model ⁷⁾ the resonance-decay branching ratios β_e, β_ν are fixed to 0, 0.5 or 1, in generic models β is a free parameter.

Searches for narrow width resonances have been performed by both experiments ^{5), 6)}. No evidence for a resonance were found in either the eq or the νq topology. Limits were derived that depend only very weakly on β . The excluded mass regions depend on the leptoquark type and the coupling. For a coupling constant of electromagnetic strength ($\lambda \simeq \sqrt{4\pi\alpha_{em}}$) mass limits ranging from 275 to 325 GeV were set. These limits extend beyond the mass domain covered at the Tevatron, where however coupling independent bounds can be set.

The recent observations of neutrino oscillations have shown that lepton-flavor violation (LFV) does occur in the neutrino sector. The LFV induced in the charged-lepton sector by neutrino oscillations cannot be measured at existing colliders due to the low expected rate. However, there are many extensions of the SM such as GUT, SUSY and compositeness that predict possible $e \rightarrow \mu$ or $e \rightarrow \tau$ transitions mediated by leptoquarks at detectable rates. The presence of such processes, which can be detected almost without background, would clearly be a signal of physics beyond the SM.

A search for LFV interactions $ep \rightarrow \mu X$ and $ep \rightarrow \tau X$ has been performed by both experiments using the entire HERA I data sample ^{8), 9)}. No evidence for LFV was found and limits on M_{LQ} and the couplings $\lambda_{\mu q}, \lambda_{\tau q}$ were set. For $M_{LQ} = 250$ GeV, upper limits on $\lambda_{eq1} \sqrt{\beta_{\mu q}}$ ($\lambda_{eq1} \sqrt{\beta_{\tau q}}$) in the range 0.010-0.12 (0.013-0.15) were set.

3.3 Supersymmetry

Supersymmetry (SUSY) ¹⁰⁾ is an attractive concept which remedies some shortcomings of the SM. It introduces fermion-boson symmetry by associating a bosonic (fermionic) supersymmetric partner to each fermionic (bosonic) SM particle, differing in its spin by half a unit. Particles carry the number $R_p = (-1)^{L+3B+2S}$ where B denotes the baryon number, L the lepton number and S the spin of a particle. The masses of the new particles are related to

the symmetry breaking mechanism. Various models exist that differ in the description of the SUSY breaking mechanism and on whether R_p is conserved or violated. If R_p might be violated SUSY particles can be singly produced and the lightest supersymmetric particle (LSP) is not stable.

If R_p is violated squarks can be resonantly produced in lepton quark fusion at HERA via a Yukawa coupling λ' . H1 searched for such processes taking into account direct and indirect R-parity violating decay modes ¹¹⁾. No evidence for squark production is found in the multi-lepton and multi-jet final state topologies investigated. Mass dependent limits on the R_p violating couplings λ'_{ijk} are derived within a phenomenological version of the Minimal Supersymmetric Standard Model (MSSM). The existence of \tilde{u}_L -type and \tilde{d}_R -type squarks of all three generations with masses up to 275 GeV and 280 GeV respectively is excluded at the 95% CL for a Yukawa coupling of electromagnetic strength ($\lambda \sim \sqrt{4\pi\alpha_{em}}$) in a large part of the MSSM parameter space. These mass limits extend considerably beyond the reach of other collider experiments. Recently a squark search has been carried out by ZEUS restricted to the case of the stop and to a few decay modes ¹²⁾. Similar limits were observed.

Exclusion limits of 285 (275) GeV for \tilde{d}_R -type (\tilde{u}_L -type) squarks for $\lambda \sim \sqrt{4\pi\alpha_{em}}$ were also derived in the more restricted minimal Supergravity Model (mSUGRA) for which the limits obtained are partly competitive with and complementary to those derived at the LEP and Tevatron colliders.

In Gauge Mediated Supersymmetry Breaking (GMSB) models, new “messenger” fields are introduced which couple to the source of supersymmetry breaking. The breaking is then transmitted to the SM fields and their superpartners by gauge interactions. The gravitino, \tilde{G} , is the lightest supersymmetric particle and can be as light as 10^{-3} eV. At HERA, single neutralinos could be resonantly produced via t-channel selectron exchange. Both collaboration searched for R_p violating SUSY in a GMSB scenario at HERA ¹³⁾, ¹⁴⁾. For the case that the $\tilde{\chi}_1^0$ is the next-to-lightest supersymmetric particle and that the decay $\tilde{\chi}_1^0 \rightarrow \gamma\tilde{G}$ into a stable gravitino occurs with an unobservably small lifetime. The resulting experimental signature is a photon, a jet originating from the scattered quark and missing transverse momentum due to the escaping gravitino. No deviations from the SM were found and constraints on GMSB models are derived for different values of the R_p violating coupling. For small mass differences between the neutralino $\tilde{\chi}_1^0$ and the supersymmetric partner of the left-handed electron \tilde{e}_L , neutralinos with masses up to 112 GeV are ruled out at the 95% confidence level for R -parity-violating couplings λ' equal to 1. Similarly, for large mass differences, massed of \tilde{e}_L up to 164 GeV are excluded.

3.4 Isolated leptons

A search for events with a high energy isolated electron or muon and missing transverse momentum has been performed by both experiments for the HERA I and HERA II data sets. In the transverse plane, it is required that the hadronic final state and the lepton are not back-to-back, which reduces genuine background from deep inelastic scattering and ensures that the missing transverse momentum is due to an invisible particle (ν). For the remaining hadronic final state the transverse momentum (p_T^X) is measured.

Within the SM such events are expected to be mainly due to W boson production with subsequent leptonic decay. Searches have been performed by both experiments in the decay channels into electrons, muons and taus (15), (17), (16).

In the HERA I analyses an overall good agreement between data and the SM expectation was found at both experiments, see Tab.1. However, requiring $p_T^X > 25$ GeV, 5 electron and 6 muon events were observed by the H1 experiment compared to an expectation of 1.76 ± 0.30 and 1.68 ± 0.30 respectively. This excess is not confirmed by ZEUS (16)

To enhance the limited statistics isolated lepton events were investigated in the recent HERA II data set by both collaborations (18), (19). ZEUS modified his search to be more closely comparable to the H1 analysis than previous ZEUS searches. Fig. 4 shows the transverse momentum spectrum of events with isolated leptons (electron and muon channels combined) in the H1 HERA I+II data set. H1 found 11 events in the high p_T^X region ($p_T^X > 25$ GeV) compared to an expectation of 3.2 ± 0.6 with an isolated electron and 6 compared to an expectation of 3.2 ± 0.5 with an isolated muon, see Tab.1. ZEUS found 1 event in the electron channel compared to 1.50 ± 0.18 expected which is consistent with the SM.

3.5 Anomalous single top production

A search for single-top production $ep \rightarrow etX$ has been made by both experiments. Since the centre of mass energy in the ep collision at HERA is well above the top production threshold, single top production is kinematically possible. However, in the SM the dominant process for single top production is the charged current reaction $e^+p \rightarrow \bar{\nu}t\bar{b}X$ ($e^-p \rightarrow \bar{t}bX$). This process has a tiny cross section of less than 1 fb. However, in several extensions of the SM, the top quark is predicted to undergo flavour changing neutral current (FCNC) interactions, which could lead to a sizeable top production cross section. FCNC interactions are for example present in models which contain an extended Higgs sector (22) or SUSY (23). An observation of top quarks at HERA would thus be a clear indication of physics beyond the SM.

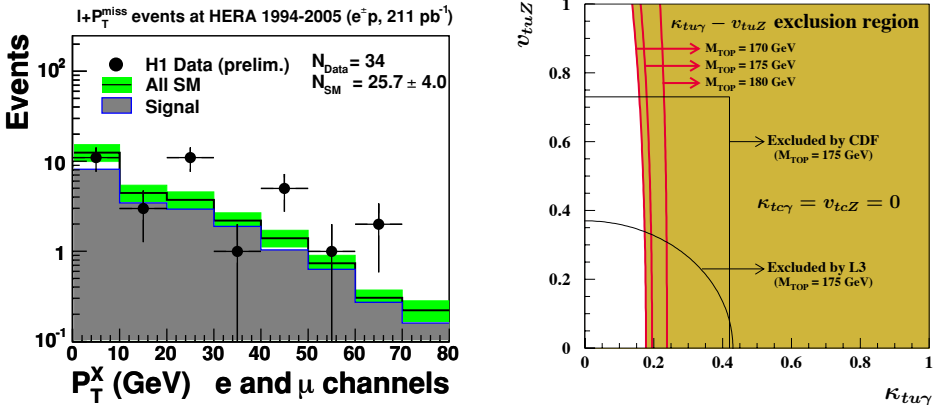


Figure 4: **left:** Transverse momentum distribution in the electron and muon channels combined of events with isolated leptons is compared to SM expectation (open histogram). The signal component of the SM expectation, dominated by real W production, is given by the hatched histogram. The total error on the SM expectation is given by the shaded band. **right:** FCNC exclusion region at 95% C.L. in the $\kappa_{tu\gamma} - \nu_{tuZ}$ plane for three values of M_{top} (170, 175 and 180 GeV) assuming $\kappa_{tc\gamma} = \nu_{tcZ} = 0$. The CDF and L3 exclusion limits are also shown.

Table 1: *HERA event yields in the search for isolated leptons with missing transverse momentum. The numbers are given for the electron and muon channel for different cuts p_T^X .*

data set	Electron obs./exp.	Muon obs./exp.	Combined
H1 94-00 $L(e^\pm) = 118 \text{ pb}^{-1}$			
Full sample	11 / 11.54 ± 1.50	8 / 2.94 ± 0.50	19 / 14.48 ± 2.0
$P_T^X > 25 \text{ GeV}$	5 / 1.76 ± 0.30	6 / 1.68 ± 0.30	11 / 3.44 ± 0.6
H1 94-05 $L(e^\pm) = 211 \text{ pb}^{-1}$			
all data	25 / 20.4 ± 2.9	9 / 4.5 ± 1.1	34 / 25.7 ± 4.0
$P_T^X > 25 \text{ GeV}$	11 / 3.2 ± 0.6	6 / 3.2 ± 0.5	17 / 6.4 ± 1.1
ZEUS (prel.) 99-04 $L(e^+) = 106 \text{ pb}^{-1}$			
$P_T^X > 25 \text{ GeV}$	1 / 1.50 ± 0.18		

Both experiments searched for decays of top quarks into a b quark and a W boson in the leptonic and hadronic decay channels of the W. ZEUS observed no event in the leptonic channel and no excess over the SM in the hadronic channels therefore limits were set on FCNC interactions of the type tqV . The contribution of the charm quark, which has only a small density in the proton at high Bjorken x, was ignored by setting $\kappa_{tc\gamma} = \nu_{tcZ} = 0$. Only the anomalous couplings involving a u quark $\kappa_{tu\gamma}$ and ν_{tuZ} were considered. By combining the results from both the leptonic and hadronic channels, an upper limit of $\kappa_{tu\gamma}$ derived see Fig.4, corresponding to a limit on the cross section for single-top production of $\sigma(ep \rightarrow etX) < 0.225 \text{ pb}$ at 95% C.L..

H1 observed 5 events in the leptonic channel while 1.31 ± 0.22 events are expected, in the hadronic channel no excess above the expectation for SM processes is found. Assuming that the observed events are due to a statistical fluctuation, an upper limit of 0.55 pb on the single top cross section is set.

4 Conclusions

Results on the electroweak measurements and searches for physics beyond the Standard Model (BSM) at HERA have been presented. Exploring the full HERA I data set no signal of BSM physics has been observed, but some interesting deviations were found to be followed up in the future.

First results from HERA II have been presented confirming the HERA I observations. The HERA II start-up is promising. With the new incoming

data (700 pb^{-1} until 2007) the sensitivity to new physics will increase.

References

1. ZEUS Collab., S.Chekanov *et al.*, DESY-05-050, submitted to Eur. Phys.J. C.
2. H1 Collab., C.Adloff *et al.*, DESY-03-038, Eur.Phys.J **C30** (2003)1-32.
3. ZEUS Collab., S.Chekanov *et al.*, Phys.Lett.**B592** (2004) 23-41.
4. H1 Collab., C. Adloff *et al.*, Phys.Lett.**B568** (2003) 35-47.
5. ZEUS Collab., S.Chekanov *et al.*, Phys.Rev.**D68**,052004 (2003).
6. H1 Collab., A.Aktas *et al.*, hep-ex/050644, accepted by Phys.Lett.B,06/05.
7. W.Buchmüller, R.Rückl and D.Wyler, Phys.Lett.B **191**, 442 (1987) [Erratum-ibid.B **448**, 320 (1999)].
8. ZEUS Collab., contributed paper, Abstract 498, International Europhysics Conference on High Energy Physics, (2003) Aachen.
9. H1 Collab., contributed paper, abstract 12-0766, ICHEP04 Beijing.
10. H.P.Nilles, Phys.Rept.**110** (1984) 1;
H.E.Haber and G.L.Kane, Phys.Rept. **117**(1985)75.
11. H1 Collab., A. Aktas *et al.*, Eur. Phys. J. **C36** (2004) 425-440.
12. ZEUS Collab., contributed paper abstract 258, XXII International Symposium on Lepton-Photon Interactions at High Energy, Upsala (2005).
13. H1 Collab., A. Aktas *et al.*, Phys. Lett. **B616** (2005) 31-42.
14. ZEUS Collab., contributed paper abstract 260, XXII International Symposium on Lepton-Photon Interactions at High Energy, Upsala (2005).
15. H1 Collab., V.Andreev *et al.*, Phys. Lett. **B561**, 241 (2003); H1 Collab., contributed paper, abstract 637, EPS2005, Lisbon.
16. ZEUS Collab., S.Chekanov *et al.*, Phys.Lett.B **583**, 41 (2004).
17. H1 Collab., contributed paper, abstract 12-0188, ICHEP04, Beijing.
18. H1 Collab., contributed paper, abstract 12-0765, ICHEP04, Beijing.
19. ZEUS Collab., contributed paper, abstract 257, Lepton-Photon 2005, Upsala.

20. ZEUS Collab., S. Chekanov *et al.*, Phys. Lett. B **559** (2003). Addendum: “Search for single top production in *ep* collisions at HERA”, DESY-03-188 (2003).
21. H1 Collab., A.Aktas *et al.* Eur. Phys.J C**33** (2004) 9 [hep-ex/0310032].
22. D.Atwood, L.Reina and A.Soni, Phys.Rev.D **53** (1996) 1199 [hep-ph/9506243].
23. G.M.de Divitiis, R.Ptronzio and L.Silvestrini, Nucl.Phys.**B504** (1997) 45 [hep-ph.9704244].

SEARCHES FOR SUPERSYMMETRY AT THE TEVATRON

Arnaud Duperrin

(duperrin@cppm.in2p3.fr)

for CDF and DØ collaboration

CPPM, IN2P3-CNRS, Université de la Méditerranée,

F-13288 Marseille, France

Abstract

With almost 0.4 fb^{-1} of $p\bar{p}$ collisions collected and analyzed at the Fermilab Tevatron at a center-of-mass energy of 1.96 TeV, by both the CDF and DØ experiments, searches for signs of Supersymmetry in the present Run II data sample are reviewed. The new results obtained by the upgraded detectors are summarized.

1 Introduction

Supersymmetry (SUSY) postulates a symmetry between bosonic and fermionic degrees of freedom and predicts the existence of a supersymmetric partner for each Standard Model particle. Most of these new particles could be light enough to be discovered at the Tevatron. For most analyses, minimal Supergravity (mSUGRA) is used as a reference model, but alternative scenarios have been considered as well, like gauge-mediated SUSY breaking and R-parity violation, leading to different final state topologies. The results shown are based on data collected in 2002-2004 and correspond to an integrated luminosity of up to 390 pb^{-1} , sample three times larger than the Run I data set. The accelerator and the two experiments were upgraded for Run II. The CDF and $D\bar{O}$ detectors are described in detail in Ref. ¹⁾ ²⁾. Since March 2001 the Tevatron is operating at a center-of-mass energy of 1.96 TeV, with a bunch spacing of 396 ns. Peak luminosities and monthly integrated luminosity of up to $1.23 \times 10^{32} \text{ cm}^{-2} \text{ s}^{-1}$ and 68.3 pb^{-1} , respectively, have been achieved. CDF and $D\bar{O}$ data taking efficiency is close to 90%. All the results reported here can be found in Ref. ³⁾ ⁴⁾.

2 Charginos and Neutralinos

In R-parity-conserving minimal supersymmetric extensions of the Standard Model (MSSM), the charged and the neutral partners of gauge and Higgs bosons (charginos and neutralinos) are produced in pairs at $p\bar{p}$ colliders and decay into fermions and the Lightest Supersymmetric Particle (LSP). As a guideline, the results are interpreted in this model with chargino and neutralino masses mainly following the relation $m_{\chi_1^\pm} \simeq m_{\chi_2^0} \simeq 2m_{\chi_1^0}$. Most of the points in the parameter space considered are characterized by low slepton masses, which lead to an enhanced leptonic branching fraction. The final state consist of three leptons and large missing transverse energy. The new result from $D\bar{O}$ combines six analyses, including final states where the second lepton is a tau decaying hadronically. The total integrated luminosity corresponds to $\mathcal{L} \approx 325 \text{ pb}^{-1}$. Table 1 shows no evidence for SUSY. The results are combined to extract limits on the total cross section using the likelihood ratio method. Systematic and statistical errors are taken into account in the combination including their correlations. The resulting cross-section limit is shown in fig.1 (left) as a function of the chargino mass in a scenario with comparable neutralino and slepton masses. The combination excludes chargino masses below 117.7 GeV. The inclusion of the τ analysis improves the limit by about 2 GeV. These results reach for the first time beyond the Run I and LEP2 limits in mSUGRA.

Table 1: Number of candidate events observed and background events expected (with stat. and syst. uncertainties) in the charginos and neutralinos $D\bar{O}$ searches.

Analysis	Data	Total Background
$e + e + l$	0	$0.21 \pm 0.11 \pm 0.05$
$e + \mu + l$	0	$0.31 \pm 0.13 \pm 0.03$
$\mu + \mu + l$	2	$1.75 \pm 0.37 \pm 0.44$
$\mu^\pm + \mu^\pm + l$	1	$0.64 \pm 0.36 \pm 0.13$
$e + \tau + l$	0	$0.58 \pm 0.11 \pm 0.09$
$\mu + \tau + l$	1	$0.36 \pm 0.12 \pm 0.06$
Total	4	$3.85 \pm 0.57 \pm 0.49$

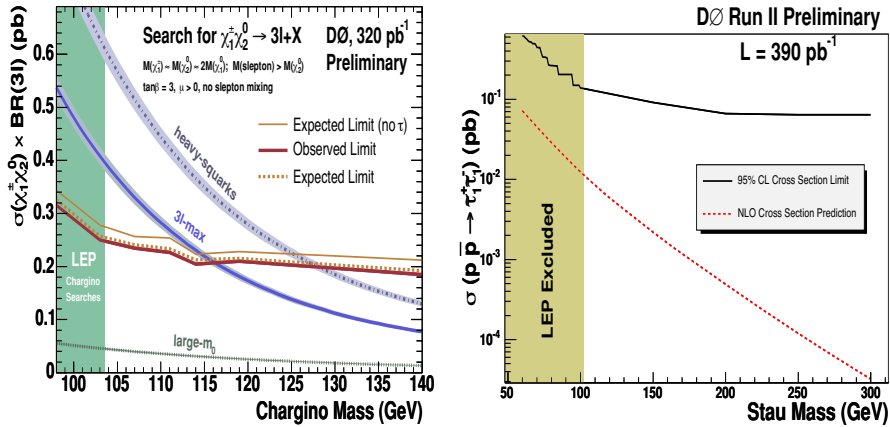


Figure 1: (Left) 95% CL Limits on the total cross section for associated chargino and neutralino production with leptonic final states. The expected limit corresponds to the dashed line. Lines corresponding to 3 models are also plotted as a reference. (Right) cross-section limit (solid line) and NLO production cross section (dashed line) versus stau mass for pair-produced staus.

3 Charge Massive Stable Particles

DØ has searched for the pair production of charged massive stable particles (CMSP) based on $\mathcal{L} \approx 390 \text{ pb}^{-1}$ of data. Their signature is the one of slow moving high p_T muons. The timing of the muon scintillators is used to calculate the speed of the two particles in the event. No excess of events is observed and 95% CL limits are set. One theoretical model explored is in the case where the next-to-lightest supersymmetric particle (NLSP) is the lightest scalar tau lepton (stau). In this case, the limits on the production cross-section vary from 0.06 pb to 0.62 pb, depending on the stau mass as shown in fig.1 (right), and are the most stringent limits to date from Tevatron. In another possible model a stable lightest chargino is present. This situation can occur in Anomaly-Mediated Supersymmetry Breaking (AMSB) or in models which do not have gaugino mass unification. The two general cases correspond to a chargino mostly higgsino or mostly gaugino. The upper limits are respectively 140 GeV and 174 GeV. These are currently the best limits to date on stable charginos. CDF also considered scenarios with a light stop in various decays and models. One of this model assumes that it is a long lived particle that decays outside the detector. It can also be experimentally characterized as a heavily ionizing and slow moving charged particle. Using standard muon triggers and the time of flight detector CDF derives a limit on the stop mass at 108 GeV.

4 R-parity violation

The gauge symmetry of the MSSM allows terms to be included in the superpotential which violate R-parity (RPV). The R-parity was introduced to impose conservation of the leptonic and baryonic numbers. The two experimental signatures considered here are RPV decay of the neutralino and resonant sparticle production. The experimental consequences are SUSY signatures with usually less missing transverse energy and more leptons and jets in the final state. DØ has searched for multilepton final states arising from SUSY particle pair production with RPV decays of the two neutralino LSP's. The couplings considered are λ_{121} and λ_{122} corresponding to six final states involving four charged leptons and two neutrinos. The neutralino mass is expected to be relatively small, the leptons are consequently rather soft and thus difficult to detect. No excess is observed. In the case of λ_{121} (λ_{122}), with $m_0 = 250 \text{ GeV}$, $\tan\beta = 5$, $A_0 = 0$, $\mu > 0$ a chargino limit is set at 181 GeV (165 GeV) using an integrated luminosity of $\mathcal{L} \approx 238 \text{ pb}^{-1}$ (160 pb^{-1}), improving results previously obtained with Run I data in this context. A new search has been performed by DØ with $\mathcal{L} \approx 199 \text{ pb}^{-1}$ where the neutralino decays into a tau, a neutrino and either an electron or a second tau. The τ is searched in his hadronic decay modes characterized by a narrow jet with low track multiplicity. The transverse momentum of the tau candidates after cuts on the neural networks used

to find them is displayed in fig.2 (left). The data are consistent with the SM, which suggest no evidence of λ_{133} coupling. This preliminary result allows to exclude at 95% CL the region : $m(\chi_1^\pm) < 118$ GeV, $m(\chi_1^0) < 66$ GeV for $\mu > 0$, $\tan\beta = 10$, $m_0 = 80$ GeV. $D\bar{O}$ has also searched in the resonant channel via a $\tilde{\mu}$ or a $\tilde{\nu}_\mu$. Masse reconstruction of the slepton and the neutralino are possible since all decay products are reconstructed. The data sample corresponds to $\mathcal{L} \approx 154$ pb $^{-1}$. No excess above the Standard Model expectation is observed, and limits on the λ'_{211} coupling have been set, as show in fig.2 (right) as a function of $m(\tilde{\mu})$.

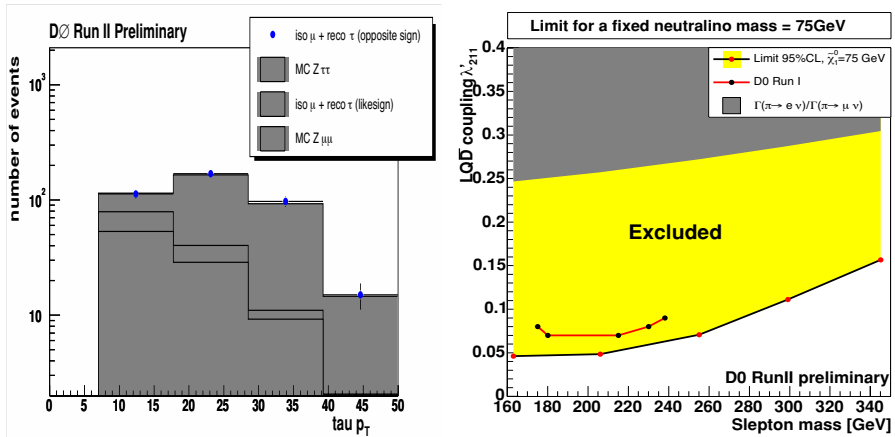


Figure 2: (left) Transverse momentum of the tau candidates after cuts on the neural networks in the $D\bar{O}$ search for RPV in two electrons + taus final state. (right) $D\bar{O}$ 95% CL on the LQD coupling λ'_{211} for fixed neutralino masses 75 GeV.

5 Search for $B_s^0 \rightarrow \mu^+ \mu^-$

The purely leptonic decay of $B_s^0 \rightarrow \mu^+ \mu^-$ is a flavor changing neutral current process, which is forbidden at the tree level and proceed only at very low rate through higher order diagrams. In SUSY, this decay amplitude can be enhanced. B_s mesons are produced at a very large rate at Tevatron, and possible decay into two muons can be identified with high efficiency. Both experiments have set limits on the branching fraction which start to probe the region of interest since the SM prediction on the branching ratio is 3.4×10^{-9} . The selection identified two muons from a displaced vertex and the search is performed using sideband and same side data to optimize cuts and check

background estimates. The combination at 90% CL of CDF ($\mathcal{L} \approx 171 \text{ pb}^{-1}$) and $D\emptyset$ ($\mathcal{L} \approx 240 \text{ pb}^{-1}$) analyses set a lower limit on the branching ratio at $BR(B_s^0 \rightarrow \mu^+ \mu^-) < 2.7 \times 10^{-7}$. CDF determined $BR(B_d^0 \rightarrow \mu^+ \mu^-) < 1.5 \times 10^{-7}$.

6 Gauge Mediated SUSY Breaking

Final states with two photons and \cancel{E}_T can be interpreted in Gauge Mediated SUSY breaking model (GMSB). In these analyses performed both by CDF and $D\emptyset$, the NLSP is assumed to be the lightest neutralino which decays into a photon and an undetected gravitino. Using inclusive single electromagnetic (EM) and di-EM triggers, $D\emptyset$ observed no excess of such events for a data set corresponding to $\mathcal{L} \approx 263 \text{ pb}^{-1}$ collected between April 2002 and March 2004. At 95% CL limits, the masses of the lightest chargino and neutralino are found to be larger than 195 and 108 GeV, respectively. These are the most restrictive limits to date. Similarly, CDF sets limits at 168 and 93 GeV using $\mathcal{L} \approx 202 \text{ pb}^{-1}$. As represented in fig.3 (left), CDF and $D\emptyset$ also combined their analysis for a representative point in the parameter space obtaining an improved limit at 95% CL of 209 GeV for the chargino mass.

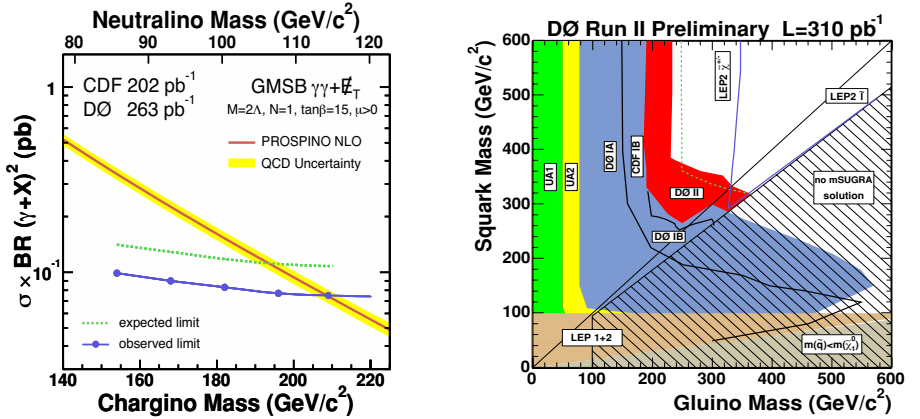


Figure 3: (left) The next-to-leading-order cross section and combined experimental (CDF- $D\emptyset$) limits as a function of the chargino and neutralino mass. (right) Excluded region at 95% CL confidence level in the $mSUGRA$ framework for $\tan\beta = 3$, $A_0 = 0$, $\mu < 0$ for the $D\emptyset$ search for squarks and gluinos. The expected limit is the dashed line. Limits inferred from the LEP2 chargino and slepton searches are also indicated.

7 Squark and Gluinos

Multijet final states with missing transverse energy (\cancel{E}_T) are characterized by large production cross sections at Tevatron but these searches suffer from a large experimental background. Generic squark and gluinos final states contain two or more jets and large \cancel{E}_T . DØ has searched in three different scenarios. The first one is for pair production of squarks, each decaying into a quark and a neutralino, leading to a two jets+ \cancel{E}_T final state. This decay channel is dominant if the gluino is heavier than the squark. The second case is when the squark is heavier than the gluino leading to a final state with 4 jets and \cancel{E}_T . The third case is for intermediate m_0 values, with a final state with three or more jets. Using dedicated multijet triggers, and requiring a tight cut on \cancel{E}_T and the scalar p_T sum, cross section upper limits at 95% CL have been obtained for the sets of mSUGRA parameters considered ($\tan\beta = 3$, $A_0 = 0$, $\mu < 0$). The observed and expected limits for $\mathcal{L} \approx 310 \text{ pb}^{-1}$ are shown in fig.3 (right) as functions of the squark and gluino masses, improving on previous limits.

For the third generation, mass unification is broken in many SUSY models due to potentially large mixing effects. This can result in sbottom or stop much lighter than the other squarks and gluinos. CDF has searched for sbottom in gluino decay leading to a 4 b-flavor jets + \cancel{E}_T final state. Using a secondary vertex algorithm to tag the “b-jet”, with $\cancel{E}_T > 80 \text{ GeV}$ and vetoing the presence of leptons, for a dataset corresponding to $\mathcal{L} \approx 156 \text{ pb}^{-1}$, no evidence for gluino pair production with sequential decay into a sbottom-pair is observed. Requiring inclusive double b-tag or exclusive single b-tag, 95% CL exclusion limits are set on the masses of the gluino and the sbottom of up to 280 GeV and 240 GeV respectively, as shown in fig.4 (left).

CDF also considered models with a light stop. The first case assumes that stops are long lived particles and is presented in section 3. The two other searches for direct production of stop have been performed, one in the RPV conserved scenario where the stop decays with a branching ratio of 100% into a charm and a neutralino, the second in the RPV framework where the stop decays into a “b-jet” and a τ . In the case of the stop decaying into a τ lepton and a “b-jet”, the final state is a leptonically decaying tau into either an electron or a muon, as well as a hadronically decaying tau lepton, and two or more jets. The good agreement between the data and the SM prediction obtained with $\mathcal{L} \approx 200 \text{ pb}^{-1}$, allows to derive a 95% CL on the stop mass, the result is shown in fig.4 (right). Including theoretical uncertainties in the cross-section calculation due to the renormalization scales and PDF’s, a conservative limit of $m(\tilde{t}) > 129 \text{ GeV}$ is obtained. These limits are also fully applicable to the case of the third generation scalar leptoquark (LQ_3) assuming a 100% branching ratio for the $LQ_3 \rightarrow \tau b$ decay mode. In the case of the stop decaying into charm, neutralino, where the neutralino is the LSP, the final state is characterized by two acoplanar “b-jets”+ \cancel{E}_T . The background is mostly dominated

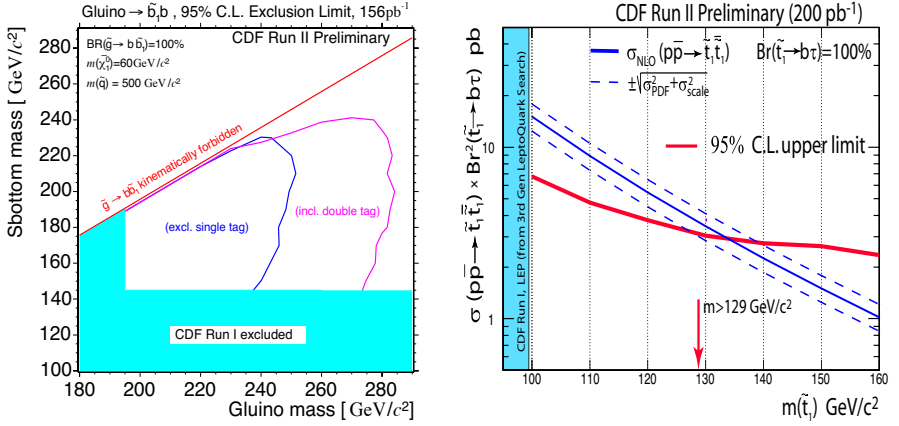


Figure 4: (left) CDF 95% CL exclusion contours in the gluino and sbottom mass plane. (right) CDF 95% CL limit curve for $t\bar{t}$ production in the final state of a lepton, a τ_h and two jets using 200pb^{-1} of data collected by CDF in the PRV framework.

by QCD multi-jet production, W and Z boson production in association with one or more jets, and top quark single and pair production. The CDF silicon vertex detector is used to tag heavy-flavor jets and reduce significantly the SM background. A jet probability is built based on the probability that all the tracks in the jet come from the primary vertex. This probability peaks at zero for bottom and charm jets. The distribution of the minimum jet probability of the taggable jets is shown in fig.5 (left). By tagging the two leading jets, 92% of the background is rejected while its efficiency for the signal is about 30%. CDF computes a 95% confidence level limit for the stop pair cross-section as a function of the stop mass. The result is shown in fig.5 (right) for a neutralino mass of 40 GeV, and compared with the theoretical cross-section. The data set corresponds to $\mathcal{L} \approx 163 \text{pb}^{-1}$. This analysis does not yet reach the sensitivity of the Run I result. Some reasons for this are a higher \cancel{E}_T trigger threshold and larger systematic uncertainties in the jet energy scale (6% to 33%) and in the heavy flavor tagging (13%) at Run II, as compared to Run I.

8 Conclusion

The Tevatron collider, and the CDF and DØ experiments are running well. The analysis described here are based on up to 390pb^{-1} . Only half of the SUSY particles have been found so far (W , Z , top ...), but there are already

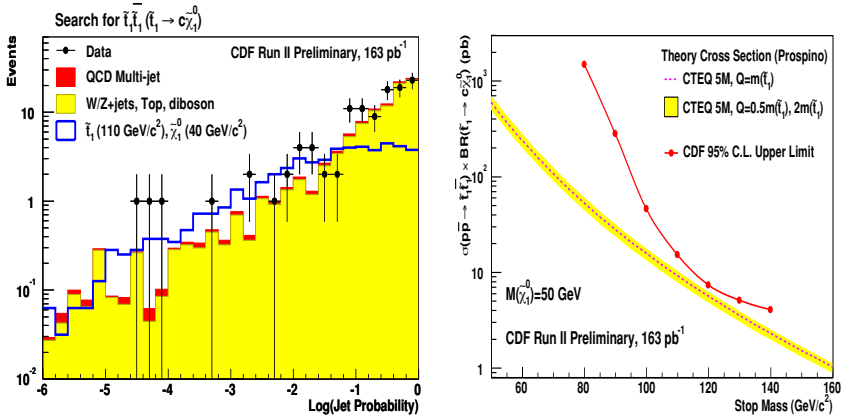


Figure 5: (left) Distribution of the minimum jet probability of the taggable jets in the CDF search for scalar top quark decaying into neutralino and a charm jet using 163 pb⁻¹. (right) The CDF 95% CL upper limit on the production cross-section $t\bar{t}$. The limit curve is shown for $m(\chi^0) = 50 \text{ GeV}$.

many new results which improve on existing limits and many more fb⁻¹ will be analyzed at Run II. Therefore, there are still many years to expand the frontiers of discoveries of New Phenomena for CDF and DØ experiments.

9 Acknowledgments

I would like to thank my colleagues at CDF and DØ. Especially those who construct, maintain, and calibrate the detectors, essential for any physics analysis reported here. I wish also to thank all the colleagues for providing the material for this presentation as well as the organizers of LaThuile 2005 conference, Giorgio Bellettini, Giorgio Chiarelli and Mario Greco, for this very well-organized, successful and enjoyable event.

References

1. CDF Collaboration, The CDF II Detector Technical Design Report, FERMILAB-Pub-96/390-E
2. DØ Collaboration, The Upgraded DØ Detector, to be submitted to Nucl. Instrum. Methods A; T. LeCompte and H.T. Diehl, Ann. Rev. Nucl. Part. Sci. 50,71 (2000).
3. CDF Collaboration, <http://www-cdf.fnal.gov/physics/exotic/exotic.html>
4. DØ Collaboration, <http://www-d0.fnal.gov/Run2Physics/WWW/results/np.html>

NON SUSY SEARCHES AT THE TEVATRON

Kaori Maeshima

Stanford Linear Accelerator Center, Stanford CA - 94309 (California) USA

Written contribution not received

IGNORING THE HIERARCHY PROBLEM

Andrea Romanino

SISSA/ISAS and INFN, I-34013 Trieste, Italy

Abstract

I discuss the possibility that the hierarchy problem has not direct implications for the physics beyond the electroweak scale. I show that an approach based on data (gauge coupling unification and the evidence for the existence of dark matter) identifies a supersymmetric model with a “split” spectrum as a natural candidate for the physics above the electroweak scale. I illustrate the phenomenology of the model and I discuss the possibility of accounting for the characteristic spectrum from the model building point of view.

1 Introduction and motivations

There is no doubt that the Standard Model (SM) is not the ultimate renormalizable theory of everything. One incontrovertible reason (among the many others) is that it does not incorporate gravitational interactions. The SM is instead an effective theory valid below a cutoff Q_{SM} . The hierarchy problem arises if $Q_{\text{SM}} \gg 1 \text{ TeV}$ because of the quadratic radiative corrections to the squared Higgs mass induced by its gauge, Yukawa, and self interactions, $\delta m_H^2 \sim (200 \text{ GeV})^2 (Q_{\text{SM}}/\text{TeV})^2$.¹ For $Q_{\text{SM}} \gg 1 \text{ TeV}$, in fact, the radiative corrections are much larger than the Higgs mass itself, and a delicate cancellation (fine-tuning) is required in order to keep the value of the Higgs mass within the experimental and theoretical bounds.

The hierarchy problem has been around for a couple of decades by now, and several solutions have been proposed. However, it is fair to say that none of those solution is *fully* satisfactory. One reason is that some of the solutions cannot reproduce gauge coupling unification (unless enough parameters are available to “fit” it), one of the most solid and precise hints available on physics beyond the electroweak (EW) scale. I’ll elaborate on this point later on. Another reason is associated with one of the most important legacies of LEP, the electroweak precision tests (EWPTs). The EWPTs set a lower limit on Q_{SM} and therefore a lower limit on the fine-tuning required to reproduce the Higgs mass. This limit is model-dependent. It is strongest for strongly interacting theories like technicolor or its extra-dimensional dual. In this case, the lower limit on Q_{SM} forces the radiative correction to the squared Higgs mass to be 3-4 orders of magnitude larger than the Higgs mass itself. It is milder, but still serious, for Little-Higgs theories and in other set-ups with extra-dimensions. In this case, the natural value of the squared Higgs mass is almost two orders of magnitude too large. From this point of view, the MSSM would be the perfect candidate for the physics at the TeV scale. Being a weakly interacting theory, the lower limit on Q_{SM} from EWPT is fully compatible with a natural determination of the Higgs mass at Q_{SM} . In fact, Q_{SM} is essentially the stop mass, $m_{\tilde{t}}$, and the radiative corrections proportional to Q_{SM}^2 are harmless if the stop mass is say below 1 TeV. On top of that, the SM gauge couplings precisely unify within the MSSM. On the other hand, the MSSM suffers from a new fine-tuning problem. A problem associated to one of the virtues of the MSSM, namely its potential to bridge the electroweak scale and the Planck scale M_{Pl} . It is because of this virtue that we can test gauge unification with high accuracy. On the other hand, the running of the Higgs mass from the EW scale to the grand unification (GUT) scale M_{GUT} induces additional radiative corrections to the Higgs mass. The latter are logarithmic in the MSSM cutoff

¹Strictly speaking, here Q_{SM} is the mass of the degrees of freedom cutting off the quadratic radiative corrections to the Higgs mass.

(the GUT or the Planck scale) and are enhanced by a large $\log(M_{\text{GUT}}^2/m_{\tilde{t}}^2)$ factor relative to the harmless correction discussed above. This in turn reintroduces a fine-tuning problem that can be quantified to have a likelihood of a few %.

It is of course possible that one of the known solutions of the hierarchy problem be the correct one and the evidence for gauge coupling unification or the fact that we find ourselves in a corner of the parameter space be just unfortunate accidents. It is also possible that a full solution of the hierarchy problem compatible with gauge coupling unification just requires a small departure from one of the classic solutions (the NMSSM is one example in this direction). Here, I would like to consider the possibility that the hierarchy problem has a different, unexpected, still unknown solution. I will namely abandon the hierarchy problem as a guideline on the physics beyond the SM and accept an arbitrary fine-tuning in the determination of the Higgs mass. We will see that a generalized version of the MSSM still emerges as a minimal and most appealing option. In this generalization, the new fermions (gaugino and Higgsinos), together with the SM Higgs doublet, are still bound to be close to the EW scale, but the new scalars (squarks, sleptons and a second Higgs doublet) are associated to a scale \tilde{m} that could be as low as in the MSSM or as high as the Planck scale (actually probably below $\sim 10^{13}$ GeV, as we will see later on). In the former case, we recover the MSSM. If \tilde{m} is instead larger than $(10 \div 100)$ TeV, we enter the “Split Supersymmetry” (SpS) regime ^{1, 2}).

In the SpS regime, the squared Higgs mass receives radiative corrections that are $\sim (\tilde{m}/\text{TeV})^2$ larger than the squared Higgs mass itself. The amount of fine-tuning necessary to reproduce $m_H \lesssim 250$ GeV is however still negligible compared to the fine-tuning required to account for a value of the cosmological constant of order 10^{-3} eV. The latter fine-tuning is in fact of order $(\tilde{m}/(10^{-3} \text{ eV}))^4/(16\pi^2)$, thus posing an even more serious hierarchy problem. In the case of the cosmological constant, there is no doubt that either the naturalness criterion fails and the radiative corrections are much larger than the cosmological constant itself; or, if some unknown mechanism regulates those corrections, that mechanism does not affect the physics we accurately probed at scales within orders of magnitude of the value of the cosmological constant. It is therefore appropriate to wonder whether the hierarchy problem for the Higgs mass could follow the same fate.

Needless to say, that has not to be necessarily the case. While from a field theory point of view the hierarchy problem for the Higgs mass and for the cosmological constant are completely analogous, the cosmological constant is not even an observable quantity in field theory — its observation requires gravity. It is therefore very plausible that the solution of the cosmological constant problem be related to the mysteries of gravity and not to the Higgs mass problem. Still, lacking a convincing solution of the cosmological constant problem,

and waiting for the LHC to provide us with an answer, it is at least prudent to consider the possibility that the Higgs mass problem has an unexpected solution.

It should be also mentioned that it is not unconceivable that the cosmological constant and the Higgs mass problem be related. For example, both problems could be solved by anthropic considerations ³⁾.

2 Alternative guidelines on new physics

Having abandoned the hierarchy problem as a (theoretical) guideline on the physics beyond the SM, we can turn to the evidence for dark matter and for gauge coupling unification as alternative (empirical) guidelines.

It is well known that a particle with weak cross-section and mass of the order of the EW scale is a natural candidate for dark matter, although not the only one. Let us take this observation seriously. We can then constrain the SM quantum numbers of the new (dark) matter at the EW scale by requiring that the gauge couplings unify.

Note that in this approach the evidence for unification comes first of all by the structure of the gauge quantum numbers of the SM fields. The 15 discrete and continuous SM gauge quantum numbers (actually 14, since the overall normalization of the hypercharge is arbitrary) can in fact be elegantly understood in the context of an SU(5) or SO(10) unified gauge group in terms of 2 or 1 unified gauge quantum numbers. The fact that within the SM the gauge couplings are not so far from unifying at a high energy scale also goes in the right direction. The fact that they do not actually unify is not surprising either, since we already know that something is missing in the analysis (the fields accounting for dark matter).

It is possible to perform a general one-loop analysis of the constraints that gauge coupling unification sets on the quantum numbers of the dark matter fields ²⁾. Sticking to the EW scale interpretation of the dark matter evidence and to minimality, we consider “one-step” unification. In other words, the SM running of the gauge coupling is modified (at one loop) at one scale only, near the EW scale. To avoid problems with the EWPT, we assume that the new fermions come in vector SM representations. We also make use of a “minimal fine-tuning” principle, according to which the doublet accounting for the EW symmetry breaking is the only light scalar.² The constraints we use are i) perturbativity of the unified gauge coupling, ii) $M_{\text{GUT}} > 10^{15}$ GeV to avoid problems with proton decay and $M_{\text{GUT}} < 10^{19}$ GeV in order to avoid the transplanckian regime, and iii) $\alpha_s(M_Z) = 0.119 \pm 2 \cdot 0.003$. These constraints

²This requirement can also be easily motivated with anthropic considerations.

identify a relatively small region in the parameter space of the possible quantum numbers of dark matter. In particular, they identify only two classes of allowed quantum numbers. The first one leads to a proton decay rate barely compatible with the experimental bounds. The minimal possibility in the second class of solutions turns out to correspond to the quantum numbers of the MSSM new fermions: gauginos and Higgsinos.

Note that although both a dark matter candidate and gauge coupling unification can be obtained in alternative frameworks (e.g. an axion could account for the dark matter and an intermediate scale could lead to a two-step coupling unification), in our case the same matter content (gauginos and Higgsinos) accounts at the same time for both of them in a minimal, predictive, and precise way.

What above shows how the fermion content of the MSSM emerges in a natural way and is bound (by the dark matter constraint) to be near the EW scale, independently of naturalness considerations. As for the squarks and the sleptons, they do not affect the one loop analysis sketched above, since they come in complete $SU(5)$ multiplets. As a consequence, they are allowed to live at an arbitrary scale. The MSSM also includes an additional Higgs doublet, which is not a complete $SU(5)$ multiplet, but affects the running of the gauge coupling only in a mild way (which goes in the right direction). Having abandoned the hierarchy problem, one wonders however if there is any need to introduce the MSSM scalars, and if there is any need for supersymmetry at all. From a fundamental point of view, supersymmetry is a crucial ingredient of string theory, but it could well not show up in our effective field theory below the Planck scale. However, from the phenomenological point of view, there are a number of hints for supersymmetry in this framework. First of all, the fermion spectrum “selected” by dark matter and unification turns out to be precisely the one predicted by supersymmetry (up to the Bino, which does not affect unification). In other words, the quantum numbers of the fermion spectrum can be understood in terms of supersymmetry. Supersymmetry also helps understanding the splitting of $SU(5)$ multiplets. The doublet-triplet splitting problem associated to the SM Higgs doublet is an example of the typical problems one encounters when some components of an otherwise heavy unified gauge multiplet lie near the EW scale. As we saw, gauge coupling unification requires four additional incomplete multiplets at low energy (two Higgsinos and two gauginos). Supersymmetry explains the splitting of the gauginos in terms of the splitting of the SM gauge bosons, namely in terms of the unified group breaking itself, and explains the splitting of the Higgsinos in terms of the usual doublet-triplet problem (moreover, it forces the Bino to be part of the game). Supersymmetry also provides a symmetry, the R -symmetry, able to account for the split structure of the spectrum, for the stability of dark matter and for lepton and baryon number conservation below the GUT scale. Last but not least, the new scalars associated to supersymmetry provide a decay channel for

the gluino. This is welcome, since a finite lifetime for the gluino, shorter than the age of the universe, allows to evade the strong experimental limits on the gluino abundance (see below). In turn, in the low energy effective description, gluino decay requires a dimension 6 operator whose most obvious origin is the mediation by bosons with the quantum numbers of the squarks.

3 Structure and phenomenology of the model

As mentioned, the SpS regime exacerbates the fine-tuning problem of the MSSM. This could be hard to accept, or not, depending on the interpretation of the fine-tuning problem. For sure, raising \tilde{m} provides a number of advantages.

3.1 Cleaning up the MSSM

The MSSM has a number of annoying features and is plagued by a number of little problems. First of all, the number of parameters in the MSSM is larger than 100, mainly due to the complex structure of the scalar sector. The number of parameters is significantly reduced in the “constrained” version of the MSSM (which is well motivated as a benchmark model, although perhaps less as a realistic model). Moreover, flavour changing neutral current (FCNC) and CP-violating quantities, in particular the electric dipole moments (EDMs), are typically one or two orders of magnitudes above the experimental limits in most of the wide MSSM parameter space. FCNC processes can be suppressed by invoking flavour symmetries or in specific scenarios for the supersymmetry breaking and its communication to the observable sector, for example gauge mediation or anomaly mediation (note that the suppression of the EDMs may require additional hypotheses). In the context of a grand unified theory, the proton decay rate associated to sfermion-mediated dimension 5 operators can also pose a problem. In fact, the minimal version of the supersymmetric SU(5) model is already ruled out by the Superkamiokande limit. However, non-minimal (and perhaps more realistic) models are still allowed. In the supergravity context, another potential problem comes from the gravitino decay, whose rate is slow enough to interfere with primordial nucleosynthesis. This problem can be solved for low enough values of the reheating temperature.

As we saw, none of the problems of the MSSM is deadly. On the contrary, standard solutions are available for each of those problems. Still, since all those problems are associated to the MSSM scalars, SpS neatly solves all of them at once. At the same time, two important successes of the MSSM, gauge coupling unification and the possibility to account for the observed amount of dark matter (associated to the MSSM fermions) are preserved.

3.2 A predictive theory with only 4 – 1 new parameters

The EW scale structure and lagrangian of SpS can be summarized in a few lines and only involve 4 parameters in addition to the SM ones. One parameter is the mass scale \tilde{m} of the sfermions.³ Above \tilde{m} we have the MSSM. At scales smaller than \tilde{m} , the field content only involves the two Higgsinos, \tilde{H}_u and \tilde{H}_d , and the three gauginos, \tilde{g} , \tilde{W} , and \tilde{B} , in addition to the SM fields. The relevant lagrangian is

$$\mathcal{L} = \mathcal{L}_{\text{SM}} + \sqrt{2}H^\dagger(g_u\tilde{W} + g'_u\tilde{B})\tilde{H}_u + \sqrt{2}H^T(g_d\tilde{W} + g'_d\tilde{B})\tilde{H}_d + \left(\frac{M_3}{2}\tilde{g}\tilde{g} + \frac{M_2}{2}\tilde{W}\tilde{W} + \frac{M_1}{2}\tilde{B}\tilde{B} + \mu\tilde{H}_u\tilde{H}_d + \text{h.c.}\right), \quad (1)$$

where the U(1), SU(2) and SU(3) generators and the contraction of the corresponding indexes have been understood. The four new Yukawa couplings g_u , g'_u , g_d , g'_d are determined through the matching at the scale \tilde{m} in terms of the SM gauge couplings and $\tan\beta$, the parameter that determines the linear combination of the two MSSM Higgs doublets that survives below \tilde{m} .

Assuming an unified boundary condition for the gaugino masses, the EW scale lagrangian is therefore determined in terms of only 4 new parameters: the Wino mass M_2 , the Higgsino mass μ , the matching scale \tilde{m} , and $\tan\beta$. On top of that, as in the MSSM, the Higgs quartic coupling λ_H is predicted through the matching at \tilde{m} in terms of the gauge couplings, $\lambda_H = (g^2 + g'^2) \cos^2(2\beta)/4$. Note that the values of the 4 new Yukawas and the Higgs mass are predicted in terms of 2 unknowns, \tilde{m} and $\tan\beta$. We therefore have 3 predictions. In terms of the two additional parameters M_2 and μ , the 4 neutralino and the two chargino masses are also predicted.

3.3 A rich phenomenology and new experimental signatures

Despite the small number of new parameters, the phenomenology of the model is rich, interesting, and different (from the MSSM one) in many respects.

With the model fully specified up to the GUT scale, the unification of gauge couplings can be reexamined in detail, taking into account thresholds and higher loop corrections^{2, 4)}. In all the allowed range of \tilde{m} , gauge coupling unification is at least as successful as in the MSSM. Increasing the mass of the scalars \tilde{m} (up to $\sim 10^9$ GeV) actually improves the convergence of the couplings, but this is not very significant, also given the expected size of GUT thresholds. The running of the top coupling λ_t is slower in the SpS regime. As

³The mass of the single sfermions will not be strictly equal of course. However, the detailed structure of the sfermion spectrum is not expected to affect in a significant way the results I will present.

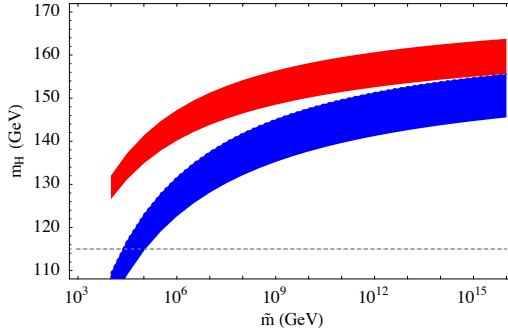


Figure 1: *The value of the Higgs mass as a function of \tilde{m} . The bands include 1σ errors on m_t and $\alpha_s(M_Z)$. The upper band corresponds to $\tan\beta = 50$ and the lower one to $\tan\beta = 1.5$.*

a consequence, the Landau pole is met later, and the lower limit on $\tan\beta$ from the perturbativity of λ_t up to the GUT scale is relaxed (2, 5). The bottom and tau mass unify for values of $\tan\beta$ close to its lower limit, where the larger top Yukawa enhances the bottom mass.

The tree level prediction for the Higgs mass, as in the MSSM, is corrected by radiative effects proportional to the logarithm of the stop mass. Since in SpS the stop is allowed to be heavy, larger values of the Higgs mass are allowed. Fig. 1 shows that values up to about 160 GeV are allowed. The Figure has been produced using the latest determination $m_t = (174.3 \pm 3.4)$ GeV. Note that, unlike in the MSSM, the experimental limit on the Higgs mass does not give rise to a lower limit on $\tan\beta$. That limit, in fact, crucially depends on the conventional choice of the stop mass used in the analysis and gets weaker for an heavier stop.

Since we have abandoned the naturalness criterion, the need to account for the observed amount of dark matter is the only handle which allows to keep the gauginos and the Higgsinos light. A precise analysis of the dark matter constraint is therefore important to assess the capability of collider experiments to probe the SpS parameter space. Let us first consider the case in which all

the observed dark matter is due to thermally produced neutralinos ^{2, 6}). Assuming gaugino mass unification, there are two allowed regions in the SpS parameter space. In the first one, the LSP is mostly Bino but it has a sizeable Higgsino component. The chargino and neutralino masses are correlated and vary from the EW scale to $\mathcal{O}(\text{TeV})$. The gluino is typically within the reach of the LHC. In the second region, the LSP is pure Higgsino and its mass is bound to be $\mu \simeq (1 \div 1.2) \text{ TeV}$, while the Wino mass is larger and not determined (but expected to be within one order of magnitude of the Higgsino mass ²). In this region, there is no guarantee that the gluino will be within the reach of the LHC, but a high energy linear collider such as CLIC would be able to probe the model. If the gaugino mass ratios are those predicted by anomaly mediation, the LSP is a pure Wino and its mass is bound to be $M_2 \simeq (2.0 \div 2.5) \text{ TeV}$. For arbitrary values of the gaugino mass ratios, the same upper bound holds ⁷). That bound also holds in the case of non-thermal neutralino production or in the presence of additional sources of dark matter. The prospects for direct detection in the next generation of experiments are quite good in the region of parameter space in which the gaugino-Higgsino mixing is sizeable (which is also the region relevant to LHC) ^{2, 7}). Indirect detection may be relevant in the presence of non-thermal sources, but requires very light Higgsinos or gauginos ^{8, 7}).

The gluino phenomenology is particularly relevant for SpS. First of all, the limits on the present gluino abundance from the searches for heavy isotopes ⁹) require the gluino to decay with a lifetime shorter than the age of the universe (or to be heavier than $\sim 10 \text{ TeV}$). In turn, this sets an upper limit on the mass of the squarks mediating the gluino decay ¹): $\tilde{m} \lesssim 10^{13} \text{ GeV}$ for a gluino mass of 1 TeV . In our approach, this is the main constraint on \tilde{m} . Moreover, in the SpS regime the gluino is stable on detector time-scales. The gluino therefore hadronizes and crosses the detector without decaying. The “ R -hadron” interacts through its cloud of light constituents. As a consequence, the effective interaction energy and the cross section are smaller. The behaviour of the R -hadron in the detector therefore crucially depends on its charge. A charged R -hadron would give rise to a slow, highly ionizing track, a clear signal. A neutral R -hadron would give rise to a missing energy signal. Once the event has been triggered (e.g. because of an associated gluon emission), a mild hadronic activity along the R -hadron trajectory could help telling the origin of the missing energy signal. In practice, both neutral and charged R -hadrons will be produced, and will have a few energy, charge, and Baryon-number exchanges before escaping from the detector. The sensitivities to gluino detection go from the $(200 \div 400) \text{ GeV}$ of Tevatron run II to the $(1.5 \div 2) \text{ TeV}$ of LHC ^{10, 11, 12}).

Chargino and neutralino searches at the LHC are harder in SpS than in the MSSM because neutralinos would only be produced through gauge inter-

actions and because the trilepton signal is suppressed by the smaller leptonic branching ratio ²⁾. On the other hand, a linear collider would be able not only to detect those particles but also to measure their couplings at the % level, thus probing the predictions of SpS ¹²⁾.

Particularly interesting is the analysis of fermion EDMs in SpS ^{4, 13, 14)}. As mentioned above, SpS easily solves the supersymmetric CP problem. The one-loop contributions to the SM fermion EDMs are in fact mediated by squarks or sleptons and are therefore suppressed in SpS. However, not all the new sources of CP-violation decouple when the sfermions become heavy. In fact, one phase (two if M_1/M_2 is not real) survive below the sfermion scale: $\phi \equiv \arg(g_u^* g_d^* M_2 \mu)$. Unless very small, this phase gives rise to EDMs that are safely below the experimental limits, but sizeable enough to be well within the sensitivity of the next generation of experiments. Such contributions only arise at the two loop level, since the new phases appear in the gaugino-Higgsino sector, which is not directly coupled to the SM fermions. The prediction for the electron EDM d_e is maximal for $|\sin \phi| = 1$ and $\tan \beta = 1$, in which case it ranges from the experimental limit $d_e < 1.7 \times 10^{-27} e$ ¹⁵⁾ down to $10^{-(28 \div 29)} e \text{ cm}$ depending on the value of the chargino masses in the (100 GeV \div 2) TeV range. EDM experiments are therefore at the frontier of testing Split Supersymmetry. They may reveal hints of new physics even before the start of the LHC. Ongoing and next generation experiments plan in fact to improve the EDM sensitivity by several orders of magnitude within a few years. For example, DeMille and his Yale group ¹⁶⁾ will reach $10^{-29} e \text{ cm}$ within three years, and possibly to $10^{-31} e \text{ cm}$ within five years. An improvement of the present limit by 8 orders of magnitude seems also feasible ¹⁷⁾.

Electroweak precision tests ¹⁸⁾, neutrinos model building ¹⁹⁾, baryogenesis ²⁰⁾ are also among the interesting phenomenological issues discussed in the context of the phenomenological analysis of SpS.

3.4 New model building options

Split Supersymmetry gives rise to a whole new class of model-building options. From the model building point of view one wonders how natural is reproducing the spectrum of split supersymmetry, characterized by a pronounced hierarchy between fermion and scalar supersymmetry breaking terms. A first simple answer is that an approximate R -symmetry, which forbids gaugino and Higgsino mass terms, can explain that hierarchy. Nevertheless, Split Supersymmetry can emerge from the high-energy theory not necessarily as a consequence of an imposed R -symmetry, but simply as a result of the pattern of supersymmetry breaking. In most models, supersymmetry is broken by the F -term of a chiral field (" F -breaking"). In principle, the D -term of a vector field (or equivalently,

$\langle X \rangle = F\theta^2$, where X is a chiral field forced to appear in the effective superpotential in the combination $X^\dagger X$ can equally well be the origin of the soft term (“ D -breaking”). Using the property that R -symmetric soft terms correspond to dimension-2 operators and R -breaking soft terms to dimension-3 operators, one can show ⁴⁾ that supersymmetry D -breaking leads to Split Supersymmetry, while F -breaking leads to the usual mass spectrum with no hierarchies among sparticles. In the case of D -breaking, the underlying R -symmetry protecting Higgsino and gaugino masses emerges as an accidental symmetry, much alike the approximate lepton-number conservation that protects neutrino masses in the Standard Model.

4 Conclusions

The hierarchy problem of the Higgs mass is likely to be a relevant guideline on the physics beyond the EW scale, and many appealing solutions of that problem are available (although some of them are plagued by a residual fine-tuning problem). However, lacking a convincing solution of the cosmological constant hierarchy problem, and waiting for the LHC to provide us with firm answers, it is at least prudent to consider the possibility that the Higgs mass problem has an unexpected, still unknown solution, and the Higgs mass, as the cosmological constant, appears to be fine-tuned.

This possibility is interesting also in the light of the rich phenomenology and the new experimental signatures associated with it. The LHC will be able to test a relevant portion of the parameter space of the model, and a high energy linear collider such as CLIC would be able to probe the whole parameter space. This should be compared with the case in which the naturalness criterion is used to constrain the scale of the MSSM particles — in this case, strictly speaking, no machine is capable of covering the whole parameter space. Moreover, the next generation of experiment on the electron EDM could be able to see a signal before the LHC and will also be able to probe most of the parameter space.

References

1. N. Arkani-Hamed and S. Dimopoulos, (2004), hep-th/0405159.
2. G.F. Giudice and A. Romanino, Nucl. Phys. B699 (2004) 65, hep-ph/0406088.
3. A.D. Linde, Phys. Lett. B129 (1983) 177; S. Weinberg, Phys. Rev. Lett. 59 (1987) 2607; V. Agrawal et al., Phys. Rev. D57 (1998) 5480, hep-ph/9707380; R. Bousso and J. Polchinski, JHEP 06 (2000) 006, hep-

- th/0004134; N. Arkani-Hamed, S. Dimopoulos and S. Kachru, (2005), hep-th/0501082.
4. N. Arkani-Hamed et al., Nucl. Phys. B709 (2005) 3, hep-ph/0409232.
 5. K. Huitu et al., (2005), hep-ph/0502052.
 6. A. Pierce, Phys. Rev. D70 (2004) 075006, hep-ph/0406144.
 7. A. Masiero, S. Profumo and P. Ullio, Nucl. Phys. B712 (2005) 86, hep-ph/0412058.
 8. A. Arvanitaki and P.W. Graham, (2004), hep-ph/0411376.
 9. P.F. Smith et al., Nucl. Phys. B206 (1982) 333; P. F. Smith, Contemp. Phys. **29** (1988) 159.
 10. H. Baer, K.m. Cheung and J.F. Gunion, Phys. Rev. D59 (1999) 075002, hep-ph/9806361; S. Raby and K. Tobe, Nucl. Phys. B539 (1999) 3, hep-ph/9807281; A. Mafi and S. Raby, Phys. Rev. D62 (2000) 035003, hep-ph/9912436.
 11. A.C. Kraan, Eur. Phys. J. C37 (2004) 91, hep-ex/0404001; J.L. Hewett et al., JHEP ; A.C. Kraan, (2005), hep-ex/0506009.
 12. W. Kilian et al., Eur. Phys. J. C39 (2005) 229, hep-ph/0408088;
 13. D. Chang, W.F. Chang and W.Y. Keung, Phys. Rev. D71 (2005) 076006, hep-ph/0503055; N.G. Deshpande and J. Jiang, Phys. Lett. B615 (2005) 111, hep-ph/0503116.
 14. G.F. Giudice and A. Romanino, in preparation.
 15. B. C. Regan, E. D. Commins, C. J. Schmidt and D. DeMille, Phys. Rev. Lett. **88** (2002) 071805.
 16. D. Kawall, F. Bay, S. Bickman, Y. Jiang and D. DeMille, electron in AIP Conf. Proc. **698** (2004) 192.
 17. S. K. Lamoreaux, arXiv:nucl-ex/0109014.
 18. S.P. Martin, K. Tobe and J.D. Wells, Phys. Rev. D71 (2005) 073014, hep-ph/0412424; G. Marandella, C. Schappacher and A. Strumia, Nucl. Phys. B715 (2005) 173, hep-ph/0502095.
 19. B. Bajc and G. Senjanovic, Phys. Lett. B610 (2005) 80, hep-ph/0411193.
 20. M. Carena et al., Nucl. Phys. B716 (2005) 319, hep-ph/0410352; S. Kasuya and F. Takahashi, Phys. Rev. D71 (2005) 121303, hep-ph/0501240.

SESSION VIII – FUTURE SCENARIOS

- *Tamas Budavari* Findings and Prospects for the Sloan Digital Sky Survey Search
- *Carlo Pagani* The OnGoing Effort Towards a Global Linear Collider
- *Jerome Faure* Laser Wakefield Acceleration of High Energy Quasi-Monoenergetic Electron Beams
- *Fabiola Gianotti* Preparing for Physics at the LHC

FINDINGS AND PROSPECTS FOR THE SLOAN DIGITAL SKY SURVEY

Tamás Budavári
The Johns Hopkins University

Erin Sheldon
University of Chicago

Daniel Eisenstein
University of Arizona

Adrian Pope
The Johns Hopkins University

for the SDSS Collaboration

Abstract

We present recent findings of the Sloan Digital Sky Survey that aim to put observational constraints on the properties of the dark matter and dark energy and help unravel their nature. We discuss results from weak lensing measurements that map the distribution of dark matter in halos by estimating the cluster-mass correlation function and integrating for the mass profile. Another recent significant result is the detection of the baryon feature in the galaxy correlation function. The measurement of the location of this bump allows us to calibrate the angular diameter distance redshift relation and constrain cosmological parameters to high precisions. We also discuss our current efforts to measure these parameters from the much larger photometric sample.

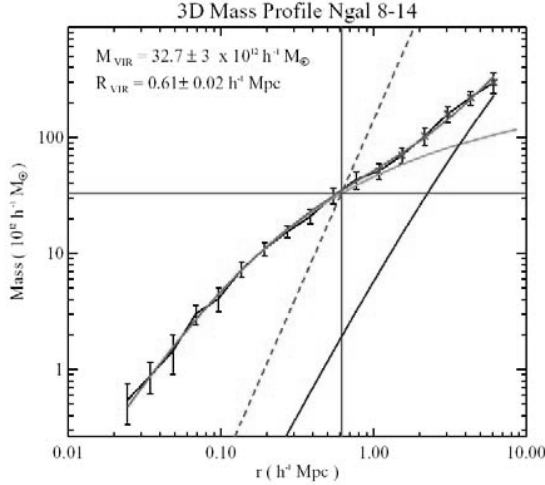


Figure 1: The mean dark matter distribution of halos with between 8 and 14 luminous red galaxies in the SDSS is reconstructed from the tangential shear measurements of SDSS galaxies.

1 The Cosmic Genome Project

The Sloan Digital Sky Survey (SDSS; York *et al.* 2000) is the most ambitious astronomical survey project ever undertaken. In fact, it is two surveys in one: the photometric survey will map one quarter of the entire sky, creating the ultimate census of 200 million objects, and the spectroscopic survey will measure the distances to a million galaxies and quasars. The observatory, a dedicated 2.5 m telescope located at Apache Point, NM, is equipped with a huge mosaic of 30 imaging CCDs. The unique multifiber spectrographs collect 640 spectra simultaneously and yield distances to thousands of celestial objects every night. The Collaboration has published close to 300 papers to date that address fundamental questions about the universe. In the following sections, we discuss two recent results that provide the the best constraints on dark matter and dark energy up to date using state-of-the art statistical analyses.

2 Weak Gravitational Lensing

One of the great successes of Einstein's General Relativity had been the prediction of bending of light by gravity. We know that massive objects act as lenses and the photons from background objects carry information about the universe between the source and us. In the weak lensing limit the observable parameters are essentially the magnification and the shear, background ob-

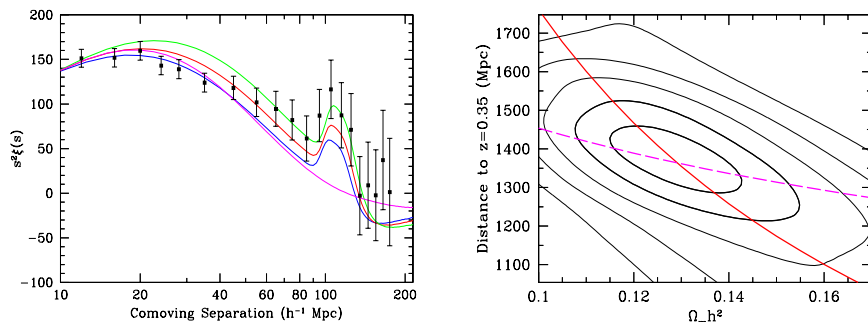


Figure 2: Our 3.4σ detection of the baryon bump in the correlation function of luminous red galaxies (left) not only confirms the role of gravity in structure formation but provides proof for dark matter at $z \sim 1000$. The scale of this feature in turn can be used to constrain cosmological models (right; see text).

jects appear brighter and their shape slightly distorted. This tangential shear (γ_T) is directly related to the projected surface mass density of the lens (Σ), $\gamma_T \Sigma_{\text{crit}} = \bar{\Sigma}(< R) - \bar{\Sigma}(R)$, where R is the apparent distance on the sky and the proportionality depends on the distances to the source (D_S) and the lens (D_L), $\Sigma_{\text{crit}}^{-1} = \frac{4\pi G D_L S D_L}{c^2 D_S}$. Sheldon *et al.* (2004) measured the shape characterized by adaptive moments of millions of background galaxies, whose distances are estimated from the colors of the objects, behind spectroscopically observed galaxies and inferred the projected surface mass density of the average cluster halo, $\Delta \Sigma(R)$. The galaxy-mass correlation function is then computed exploiting the spherical symmetry, which is valid assumption for the geometry of the averaged halo. The stacking of clusters also cancels the mass bias along the line-of-sight and yields a superb signal to ratio. Figure 1 shows the model independent mass profile of the mean halo around clusters with between 8 and 14 luminous elliptical galaxies from a similar analysis as calculated from the cluster-mass correlation function.

3 Cosmology from the Baryon Bump

Eisenstein *et al.* (2005) recently measured the large-scale correlation function from a spectroscopic sample of 46,748 luminous red galaxies from the Sloan Digital Sky Survey. The survey region covers $0.72 h^{-3} \text{Gpc}^3$ over 3816 square

degrees and $0.16 < z < 0.47$, making it the best sample yet for the study of large-scale structure. We find a well-detected peak in the correlation function at $100 h^{-1}\text{Mpc}$ separation that is an excellent match to the predicted shape and location of the imprint of the recombination-epoch acoustic oscillations on the low-redshift clustering of matter. This detection demonstrates the linear growth of structure by gravitational instability between $z = 1000$ and the present and confirms a firm prediction of the standard cosmological theory. The acoustic peak provides a standard ruler by which we can measure the ratio of the distances to $z = 0.35$ and $z = 1089$ to 4% fractional accuracy and the absolute distance to $z = 0.35$ to 5% accuracy. From the overall shape of the correlation function, we measure the matter density $\Omega_m h^2$ to 8% and find agreement with the value from cosmic microwave background (CMB) anisotropies. Independent of the constraints provided by the CMB acoustic scale, we find $\Omega_m = 0.273 \pm 0.025 + 0.123(1+w_0) + 0.137\Omega_K$. Including the CMB acoustic scale, we find that the spatial curvature is $\Omega_K = -0.010 \pm 0.009$ if the dark energy is a cosmological constant. More generally, our results provide a measurement of cosmological distance, and hence an argument for dark energy, based on a geometric method with the same simple physics as the microwave background anisotropies. The standard cosmological model convincingly passes these new and robust tests of its fundamental properties.

4 Angular Clustering of Red Galaxies

The much larger photometric sample can be also used to study the baryon wiggles in the galaxy power spectrum. Instead of measuring the 3D redshift space correlation function, one can use color based redshift estimates to select galaxies in narrow redshift shells and measure the angular power spectrum of these subsamples. For the luminous red galaxies that probe the largest cosmological volume, we can derive photometric redshift with the highest accuracy and derive the radial selection function of objects in the photometric redshift shells. This enables us to compare a measured angular power spectrum to theoretical predictions by projecting the 3D power spectrum of various parameters with the same redshift distribution. Our Fisher matrix simulations show that with existing SDSS observations, one can pin down cosmological parameters to even higher accuracy. Measurements are along their way.

References

1. D.G. York *et al.*, *Astronomical Journal* **120**, 1579 (2000).
2. E.S. Sheldon *et al.*, *Astronomical Journal* **127**, 2544 (2004).
3. D.J. Eisenstein *et al.*, submitted to *Astrophysical Journal*, (2005),
eprint: astro-ph/0501171.

**THE ON-GOING EFFORT TOWARDS A GLOBAL LINEAR
COLLIDER**

Carlo Pagani
INFN Sezione di Milano

Written contribution not received

LASER WAKEFIELD ACCELERATION OF HIGH ENERGY QUASI-MONOENERGETIC ELECTRON BEAMS

J. Faure, Y. Glinec, V. Malka

*Laboratoire d'Optique Appliquée, Ecole Polytechnique, ENSTA/CNRS/UMR 7639
Chemin de la Huniere, 91761, Palaiseau, France*

A. Pukhov, S. Kiselev, S. Gordienko

*Institut für Theoretische Physik, Heinrich-Heine-Universität Duesseldorf
40225 Duesseldorf, Germany*

Abstract

We demonstrate the generation of high quality electron beams resulting from the interaction of ultrashort and ultraintense laser pulses with underdense plasmas. The electron energy distribution is quasi-monoenergetic and peaks at 170 MeV.

1 Introduction

Particle accelerators are used in a tremendous variety of fields, ranging from medicine and biology to high energy physics. The accelerating fields in conventional accelerators are limited to a few tens of MeV/m due to material breakdown which occurs on the walls of the structure. Thus, the production of energetic particle beams requires large scale accelerators and expensive infrastructures. In this context, laser-plasma accelerators have been proposed for the next generation of compact accelerators ¹⁾ because of the huge electric fields they can sustain (>100 GeV/m). However, it has been difficult to use them efficiently for applications because they have produced poor quality particle beams with large energy spreads. Such beams are hard to use because it is difficult to transport them and/or to focus them, as required by numerous applications. Until now, the most widespread method for producing electron beams from plasmas has relied on the self-modulated laser wake field (SMLWF) accelerator ²⁾. In the SMLWF accelerator, the laser pulse is longer than the plasma wavelength. Under the influence of the self-modulation instability, its envelope modulates at the plasma frequency and resonantly excites a plasma wave. When the plasma wave amplitude reaches the wavebreaking level, copious amounts of plasma background electrons are trapped in the plasma wave and accelerated. Numerous experiments report on the production of electron beams with nC charge and divergence varying from a few degrees to tens of degrees and Maxwellian energy distributions. More recently, several groups have demonstrated that more compact lasers can be used to efficiently generate high repetition rate (10 Hz) electron sources which could be used for applications ³⁾. However, these beams still have very large energy spread and a low number of electrons at high energy (typically <1 pC at 200 ± 10 MeV). Previous experiments inherently produced poor quality beams: wakebreaking occurred under the laser pulse envelope and the accelerated electrons were also under the influence of the ultraintense laser field. Direct laser acceleration by transverse laser field deteriorated the spatial beam quality, causing emittance growth. In this work, we performed the experiment in a different parameter regime: the pulse duration was chosen to be shorter than the plasma period. The electron density, $n_e = 6 \times 10^{18} \text{ cm}^{-3}$, was lower than in previous experiments. Another crucial point is that at these low densities, the interaction length need to be long enough in order for the laser pulse to evolve, and for the electrons to be trapped and accelerated to high energies. Extending the interaction length to millimeter scales was done by extending the Rayleigh length to $z_R = 1.3$ mm, simply by using a long focal length optics. In this regime, the laser drives a highly nonlinear wakefield (or plasma bubble) which traps and accelerates plasma electrons, producing an extremely collimated and quasi-monoenergetic electron beam with a high charge of 0.5 nanocoulomb at 170 MeV ⁴⁾. Exper-

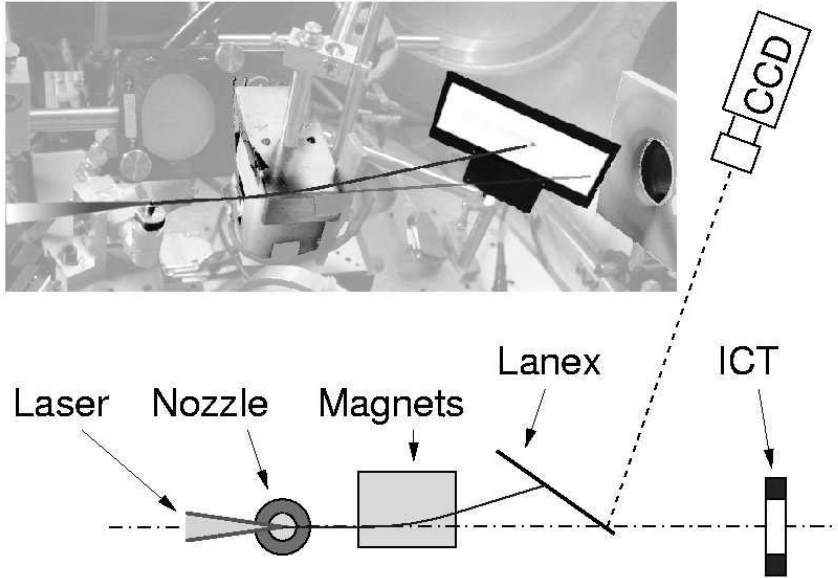


Figure 1: *Experimental set-up. Top: picture from the experiment, bottom: schematic. An ultrashort and ultraintense laser pulse is focused onto a 3 mm supersonic gas jet and produces a very collimated 170 MeV electron beam.*

iments and simulations tend to indicate that the quality of the electron beam is enhanced partly because electrons are accelerated in the plasma bubble but stay behind the laser pulse and do not interact with the laser.

2 Experiment

This regime has been reached by using the ultrashort and ultraintense laser pulse generated in a Titanium doped sapphire, chirped pulse amplification laser system. The laser pulse had a 30 fs duration at full width half maximum (FWHM), contained 1 J of laser energy at central wavelength 820 nm. It was focused onto the edge of a 3 mm long supersonic Helium gas jet using a f/18 off-axis parabola. The diffraction limited focal spot was $r_0 = 21\mu\text{m}$ at FWHM, producing vacuum-focused laser intensity of $I = 3.2 \times 10^{18} \text{ W/cm}^2$, for which the corresponding normalized potential vector is $a_0 = eA/(mc^2) = 1.3$. For these high laser intensities, the Helium gas was fully ionized by the foot of the laser

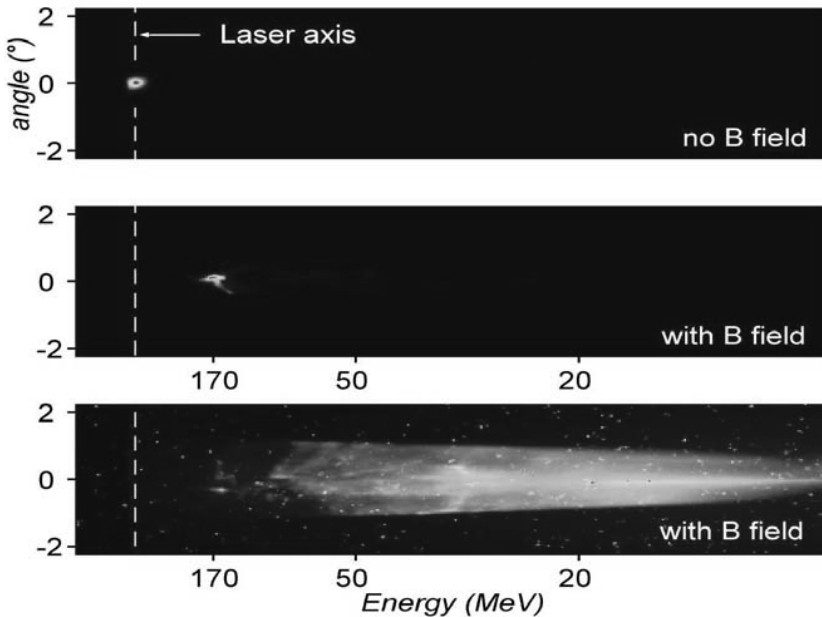


Figure 2: Raw images obtained on the LANEX screen. Top image: $n_e=61018 \text{ cm}^{-3}$, no magnetic field. Middle image: $n_e=61018 \text{ cm}^{-3}$, with magnetic field. Bottom image: $n_e = 2 \times 10^{19} \text{ cm}^{-3}$.

pulse. Monoenergetic electron distributions were observed for densities of $n_e = 6 \times 10^{18} \text{ cm}^{-3}$, for which the plasma wavelength ($\lambda_p=13.6 \mu\text{m}$) is comparable with the laser pulse length ($\tau=9 \mu\text{m}$). The diameter ($r_0=21 \mu\text{m}$) was larger than the matched one, but one may expect that self-focusing in the plasma will bring it down to the resonant value. The experimental set-up is shown on fig. 1.

Electron detection was achieved using a LANEX phosphor screen. As electrons passed through the screen, energy was deposited and reemitted into visible photons which were then imaged onto a 16 bit Charged Coupled Device (CCD) camera. When inserting a magnet ($B=0.45 \text{ T}$, on 5 cm), electrons were deflected and the image on the screen represented the electron energy distribution. The total beam charge was measured using an integrating current transformer (ICT), placed about 30 cm behind the LANEX screen. fig.2a shows a picture of the electron beam when no magnetic field is applied. The electron beam is very well collimated with a 10 mrad divergence at FWHM,

the smallest divergence ever measured for a beam emerging from a plasma accelerator. One can explain this low divergence using several arguments: (i) electrons are accelerated in the plasma bubble but they stay behind the laser pulse and do not interact with its defocusing transverse field, (ii) when electrons exit the plasma, their energy is very high and therefore, the effect of space charge is greatly diminished. Fig.2b shows the deviation of the beam when a magnetic field is applied. The image shows a narrow peak around 170 MeV, indicating efficient monoenergetic acceleration. For comparison, Fig.2c shows an image obtained at higher density ($n_e = 2 \times 10^{19} \text{cm}^{-3}$). Here, electrons are accelerated at all energies but the number of high energy electrons is low. In addition, the beam divergence is much larger than on Fig.2b. A comparison of Fig.2b and 2c shows that performances are dramatically increased when plasma bubble acceleration occurs. Fig.3 shows an electron spectrum after deconvolution. The spectrum clearly shows a quasi-monoenergetic distribution peaked at 170 MeV, with a 24spread (at FWHM). This peaked energy distribution is a clear signature of the formation of a plasma bubble as seen in computer simulations. Finally, the charge contained in this bunch can be inferred using the ICT. Without the magnet, the whole beam charge measured on the ICT is 2 ± 0.5 nC. The ICT signal can be correlated to the LANEX images to infer the charge at high energy. This shows that the charge at 170 ± 20 MeV is 0.5 ± 0.2 nC. From the above, one can deduce that the electron beam energy was 100 mJ, so that the energy conversion from the laser to the electron beam was about 10%. 2. fig. 3.

3 Discussion

To reach a deeper understanding of the experiment, we have run 3D particle-in-cell (PIC) simulations using the code Virtual Laser Plasma Laboratory ⁵). The simulation suggests that our experimental results can be explained by the following scenario. (i) At the beginning of the simulation, the laser pulse length ($9 \mu\text{m}$) is nearly resonant with the plasma wave ($lp=13.6 \mu\text{m}$); but its diameter ($21 \mu\text{m} > lp$) is larger than the matched one. (ii) As the pulse propagates in the plateau region of the gas jet, it self-focuses and undergoes longitudinal compression by plasma waves. This decreases the effective radius of the laser pulse and increases the laser intensity by one order of magnitude. (iii) This compressed laser pulse is now resonant with the plasma wave and it drives a highly non-linear wakefield: the laser ponderomotive potential expels the plasma electrons radially and leaves a cavitating region behind (this is referred to as "cavitation" or "blow-out" regime). In this regime, the three-dimensional structure of the wakefield resembles a plasma bubble. (iv) As the electron density at the walls of the bubble becomes large, wavebreaking occurs and electrons are injected and accelerated inside the bubble. (v) As the number of trapped electrons

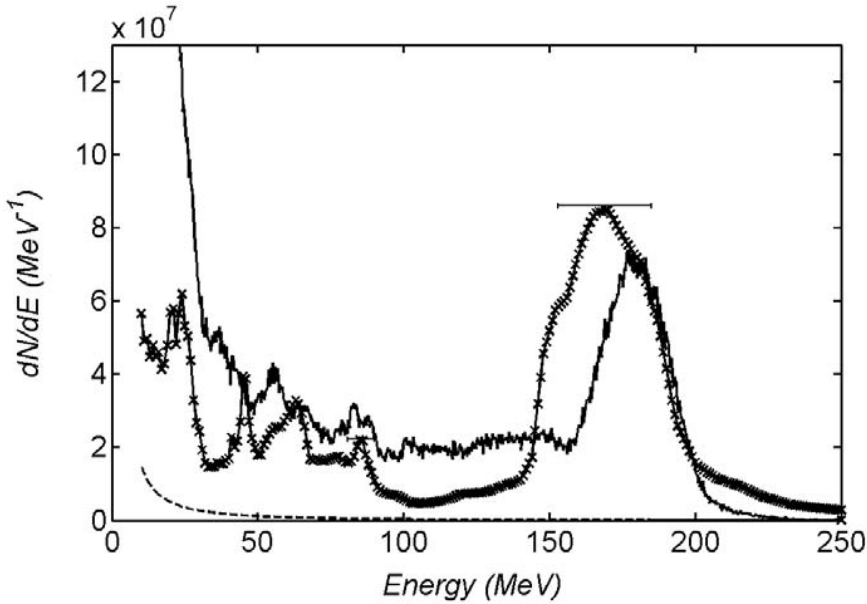


Figure 3: *Electron spectrum corresponding to the deconvolution of the image of figure 2b ($n_e = 6 \times 10^{18} \text{cm}^{-3}$). The crosses are the experimental result and the full line represents the result of 3D PIC simulations. The horizontal bars represent the spectrometer resolution.*

increases, the bubble elongates. Its effective group velocity decreases and electrons start to dephase with respect to the accelerating field. This dephasing causes electron self-bunching in the phase space. This self-bunching results in the monoenergetic peak in the energy spectrum 3. Simulations also show that the quality of the electron beam is higher when trapped electrons do not interact with the laser field. If this were to occur, the laser field would cause the electrons to scatter in phase space, degrading the low divergence as well as the monoenergetic distribution. This argument could explain why higher quality beams are obtained experimentally for shorter pulses and lower electron densities. In conclusion, the experimental results and 3D PIC simulations indicate that it is possible to generate a monoenergetic electron beam by carefully selecting laser and plasma parameters. The bunch duration (sub-50 fs), along with the present improvement on the charge (nC) and the quality of the electron beam (monoenergetic spectrum, low divergence) reinforce the major relevance

of plasma-based accelerators for many applications (such as high resolution radiography for non destructive material inspection, radiotherapy, ultrafast chemistry, radiobiology and material science). With the rapid progress of laser science, it will be possible to generate compact, monoenergetic and high quality electron beams with a tunable energy range at a reasonable cost. This source will be perfectly adapted as an injector for future GeV laser-plasma accelerator schemes. It will also be relevant for generating ultrashort X-ray sources, using undulators or lasers via Thomson scattering. Before these applications can be developed, the issue of the electron beam stability will have to be resolved. At the moment, although the beam charge and its spatial distribution are reproducible quantities, the detail of the electron energy distribution vary from shot to shot. In the future, this problem will have to be addressed: are the fluctuations due to laser fluctuations or is this regime intrinsically unstable?

4 Acknowledgements

We acknowledge the support of the European Community-Research Infrastructure Activity under the FP6 "Structuring the European Research Area" programme (CARE, contract number RII3-CT-2003-506395)

References

1. T. Tajima and J. M. Dawson *et al*, Phys. Rev. Lett. **43**, 267-270 (1979).
2. E. Esarey *et al.*, IEEE Trans. Plasma Sci. **24**, 252-288 (1996).
3. V. Malka *et al.*, Science **298**, 1596-1600 (2002).
4. J. Faure *et al.*, Nature **431**, 541-544 (2004).
5. A. Pukhov and J. Meyer-ter-Vehn, Appl.Phys.B **74**, 355-361 (2002).

PREPARING FOR PHYSICS AT THE LHC

Fabiola Gianotti

CERN, PH Department, 1211 Genève 23, Switzerland

Abstract

We discuss the strategy to prepare for physics with the ATLAS and CMS experiments at the LHC. After reviewing the various steps required to understand, calibrate and commission the detectors, from construction quality checks, to beam tests, to cosmic runs, to first collisions, we outline the approach to understand standard physics at $\sqrt{s} = 14$ TeV in the early phases of the LHC operation. Finally, we present a few examples of physics goals with the first fb^{-1} of integrated luminosity.

1 Introduction

Recently, the LHC construction has enjoyed significant achievements, with the delivery of more than half of the dipole magnets, the installation of some of them in the tunnel, and the successful beam injection test from the SPS to the LHC through the TI8 transfer line.

According to the present schedule, the machine will be cooled down in the first half of 2007, and will then be commissioned for a few months starting with single beams. A first run with colliding beams is expected in the second half of 2007, and will likely be followed by a shut-down of a few months, and then by a seven-month physics run in 2008 at instantaneous luminosities of up to $2 \times 10^{33} \text{ cm}^{-2} \text{ s}^{-1}$. There are several uncertainties on this plan (in particular because of some delays in the production of the cryogenic line) and on how the machine commissioning and performance will actually evolve. Therefore in this paper we assume that the integrated luminosity collected by ATLAS and CMS by the end of 2008 will range between a very modest 100 pb^{-1} per experiment and a very ambitious 10 fb^{-1} per experiment. These data samples will be used to commission and calibrate the detectors, and to perform first physics studies.

2 Initial detectors and initial performance

The first question in view of data taking is related to the initial detector layouts. Indeed, because of missing resources, and in some cases of construction delays, several components of ATLAS and CMS will not be fully operational at the beginning. ATLAS will start without Transition Radiation Tracker in the region $2 < |\eta| < 2.4$ and less muon chambers in the regions between the barrel and the end-cap parts. CMS will start without muon trigger chambers (RPC) in the region $1.6 < |\eta| < 2.1$ and without the fourth layer of the end-cap muon chambers. Furthermore, the CMS end-cap electromagnetic calorimeter and the whole pixel detector will be installed during the shut-down period after the 2007 run. In addition, in both experiments part of the high-level trigger and data acquisition processors will be deferred, with the consequence that the output rate of the level-1 trigger will be limited to 50 kHz (instead of 100 kHz) in CMS and to 35 kHz (instead of 75 kHz) in ATLAS.

The impact of this staging on physics will be significant but not dramatic. The main loss is a descoped B-physics programme because, due to the reduced level-1 bandwidth, the thresholds of the single-muon triggers will have to be raised from a few GeV (as originally chosen to address B-physics studies) to $p_T=14\text{-}20 \text{ GeV}$.

The second question concerns the detector performance to be expected on “day 1”, i.e. at the moment when data taking starts. Some predictions, based on construction quality checks, on the known precision of the hardware

Table 1: *Examples of expected detector performance for ATLAS and CMS at the time of the LHC start-up, and of physics samples which will be used to improve this performance.*

	expected performance on “day 1”	data samples (examples) to improve the performance
ECAL uniformity	$\sim 1\%$ ($\sim 4\%$) in ATLAS (CMS)	minimum-bias, $Z \rightarrow ee$
electron energy scale	1-2%	$Z \rightarrow ee$
HCAL uniformity	2-3%	single pions, QCD jets
jet energy scale	$\leq 10\%$	$Z(\rightarrow \ell\ell)+\text{jet}$, $W \rightarrow jj$ in $t\bar{t}$ events
tracker alignment	20-200 μm in $R\phi$	generic tracks, isolated μ , $Z \rightarrow \mu\mu$

calibration and alignment systems, on test-beam measurements and on simulation studies, are given in tab. 1 for illustration. The initial uniformity of the electromagnetic calorimeters (ECAL) should be at the level of 1% for the ATLAS liquid-argon calorimeter and 4% for the CMS crystals, where the difference comes from the different techniques and from the limited time available for test-beam measurements in CMS. Prior to data taking, the jet energy scale may be established to about 10% from a combination of test-beam measurements and simulation studies. The tracker alignment in the transverse plane is expected to be known at the level of 20 μm in the best case from surveys, from the hardware alignment systems, and possibly from some studies with cosmic muons and beam halo events.

This performance should be significantly improved as soon as the first data will be available (see last column in tab. 1) and, thanks to the huge event rates expected at the LHC, the ultimate statistical precision should be achieved in principle after a few days of data taking. Then the painful battle with the systematic uncertainties will start. This is illustrated in fig. 1 which shows that, by measuring the energy flow in about 18 million minimum-bias events (which can be collected in principle in a few hours of data taking), the non-uniformity of the CMS ECAL should be reduced from the initial 4% to about 1.5% in the barrel region. Therefore the systematic limit coming from the non-uniformity of the upstream tracker material will be hit very quickly.

3 Strategy to achieve the goal detector performance

Are the performance expectations presented in the previous section realistic? And what are the steps needed to achieve these performances?

The ATLAS and CMS detectors have been subject to stringent requirements and detailed quality controls at the various steps of the construction phase. Extensive test-beam measurements have been performed with prototypes and final modules, which have also allowed the validation of the simu-

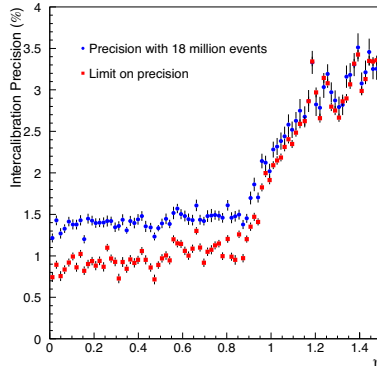


Figure 1: *Inter-calibration precision of the CMS electromagnetic calorimeter achievable with 18 million minimum-bias events*¹⁾, as a function of rapidity (dots). The squares show the limit coming from the non-uniformity of the upstream material.

lation packages (e.g. Geant4) needed for instance to extrapolate the detector response from the test-beam to the collider environment. Such detailed checks and tests represent an unprecedented culture in our field.

In addition, *in situ* commissioning and calibrations after installation in the pits will be needed to understand the experiments as a whole, to account for the presence of e.g. upstream material and magnetic field, to cure long-range effects, etc. These calibrations will be based on cosmic muons, beam-halo muons and beam-gas events during the pre-collision phase (i.e. in the first half of 2007, during the machine cool-down and single-beam commissioning). Then, as soon as first collisions will be available, well-known physics samples (e.g. $Z \rightarrow \ell\ell$ events, see tab. 1) will be used.

As a concrete example of the above procedure, and of the steps needed to prepare for physics, the case of the ATLAS electromagnetic calorimeter²⁾, which is already installed in the underground cavern, is discussed below.

One crucial performance issue for the LHC electromagnetic calorimeters is to provide a mass resolution of about 1% in the hundred GeV range, needed to observe a possible $H \rightarrow \gamma\gamma$ signal as a narrow peak on top of the huge $\gamma\gamma$ irreducible background. This requires a response uniformity, that is a total constant term of the energy resolution, of $\leq 0.7\%$ over the full calorimeter coverage ($|\eta| < 2.5$). Achieving this goal is challenging, especially at the beginning, but is necessary for a fast discovery, and can hopefully be accomplished in four steps:

- Construction quality. Test-beam measurements performed with prototypes of the ATLAS ECAL in the early '90s showed that a 1% excess in the thickness of the lead plates produces a drop of the calorimeter re-

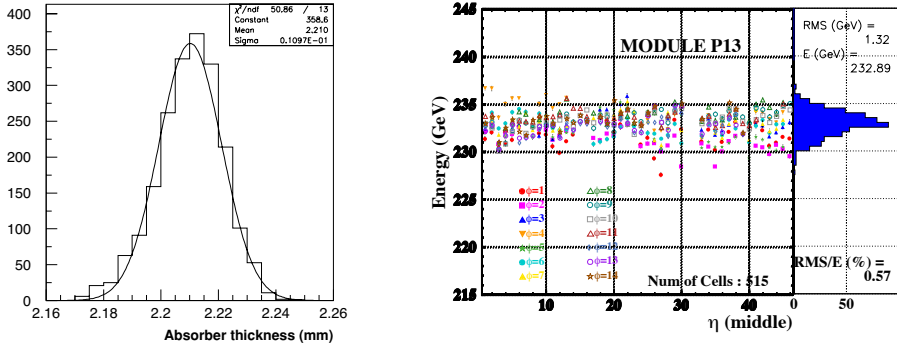


Figure 2: *Left: Distribution of the thickness of the 2048 absorber plates (3 m long and 0.5 m wide) for the ATLAS barrel ECAL, as obtained from ultrasound measurements. The mean value of the distribution is 2.2 mm and the r.m.s. is 11 μm . Right: Energy response of one module of the ATLAS barrel ECAL, as a function of rapidity, as measured from a position scan over about 500 calorimeter cells with test-beam electrons. The various symbols indicate different ϕ rows.*

sponse by 0.7%. Therefore, since the maximum response non-uniformity coming from the detector mechanics alone has to be kept below 0.3%, the thickness of the lead plates must be uniform to about 0.5%, i.e. $\sim 10 \mu\text{m}$. This goal has been achieved, as shown in the left panel of fig. 2.

- **Test-beam measurements.** About 15% of the final calorimeter modules have been exposed to electron beams, in order to verify the construction uniformity and to prepare correction factors to the detector response. The right panel in fig. 2 shows the results of a scan of one module (module size $\Delta\eta \times \Delta\phi = 1.4 \times 0.4$) performed with high-energy test-beam electrons. For all tested modules, the response non-uniformity was found to be about 1.5% before correction, i.e. at the exit of the construction chain, and better than 0.7% after calibration with test-beam data.
- **Pre-collision phase.** Before data taking starts, the calorimeter calibration can be checked *in situ* with physics-like signals by using cosmic muons. Table 2 shows the expected rates of cosmic in ATLAS³⁾, as obtained from a full simulation of the detector inside the underground cavern (including the overburden, the access shafts and the surface buildings). These results have also been validated by direct measurements of the cosmic flux in the pit made with a scintillator telescope. It can be seen that rates between 0.5 Hz and 30 Hz are expected, depending on the requirements on the muon trajectory. Therefore, in about three months of cosmic runs in 2007 during the machine cool-down and commissioning, a few million events should be collected, a data sample large enough to

Table 2: *Expected rates of cosmic muons in ATLAS for various requirements on the muon trajectory, as obtained from a full simulation of the detector in the pit.*

topology	rate (Hz)	comments
through-going muons	~ 25	muons giving hits on top and bottom RPC's and in inner detector
close to interaction vertex	~ 0.5	muons passing within $ z < 60$ cm and $R < 20$ cm from the interaction centre
useful for ECAL calibration	~ 0.5	muons with $ z < 20$ cm, $E_{\text{cell}} > 100$ MeV

catalog and fix several problems, gain operational experience, check the relative timing and position of the various sub-detectors, etc., hopefully in a more relaxed environment than during the collision phase.

In particular, for what concerns the electromagnetic calorimeter, the signal-to-noise ratio for muons is large enough ($S/N \sim 7$ from test-beam measurements) that cosmic muons can be used to check the calibration uniformity of the barrel calorimeter as a function of rapidity. The calorimeter is equipped with an electronics calibration system delivering pulses uniform to 0.25%. However, the calibration signals and the physics signals do not have exactly the same shape, and the difference depends on the rapidity of a given calorimeter cell. This induces a non-uniformity of the ECAL response to incident particles as a function of η . Test-beam studies show that the expected sample of cosmic muons is large enough to allow measurements of these effects to the 0.5% level.

- First collisions. As soon as first collider data will become available, $Z \rightarrow ee$ events, which are produced at the rate of ~ 1 Hz at a luminosity of $10^{33} \text{ cm}^{-2} \text{ s}^{-1}$, will be used to correct long-range response non-uniformities from module to module, possible temperature effects, the impact of the upstream material, etc. Full simulation studies indicate that, since the calorimeter is already quite uniform on “day 1” by construction and thanks to the previous steps, about 10^5 $Z \rightarrow ee$ events should be sufficient to achieve the goal overall constant term of 0.7%. In addition, this $Z \rightarrow ee$ sample should fix the absolute energy scale to about 0.5%. Therefore, after a few weeks of data taking the ATLAS ECAL should in principle be fairly well calibrated.

As an academic exercise, one could consider a very pessimistic (actually unrealistic...) scenario. That is, ignoring the results and expectations discussed above, one could assume that no corrections (neither based on test-beam data, nor using $Z \rightarrow ee$ events) will be applied. In this case, the intrinsic calorimeter constant term would be given by the uncorrected non-uniformity from detector

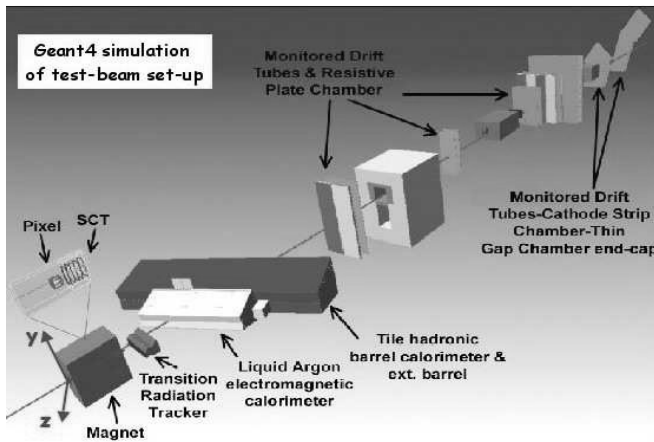


Figure 3: *Geant4* simulation of the 2004 ATLAS combined test-beam set-up, showing the beam line and the various sub-detectors.

construction (measured to be $\sim 1.5\%$, as mentioned above), to which another $\sim 1.5\%$ from uncorrected upstream material effects has to be added. This would give a total constant term of the energy resolution of about 2% instead of 0.7%. As a consequence, the significance of a $H \rightarrow \gamma\gamma$ signal would be reduced by about 30%, and factor 1.7 more integrated luminosity would be needed to achieve the same sensitivity.

4 Toward the complete experiment: the ATLAS combined test-beam

A very significant step in the preparation for data taking and physics has been made in ATLAS with the combined test-beam performed in 2004. A full vertical slice of ATLAS (see fig. 3), including the Pixel detector, the Silicon strip detector (SCT), the Transition Radiation Tracker (TRT), the liquid-argon ECAL, the Tile hadron calorimeter, muon chambers (MDT, CSC, RPC, TGC) and the trigger system, has been tested during six months on the CERN SPS H8 beam line. The set-up included magnets providing magnetic fields in the inner detector and muon chambers.

A lot of global operation experience has been gained with this test, since for the first time all ATLAS sub-detectors have been integrated, cross-timed and run together with a common data acquisition system.

Electron, pion, proton, muon, photon data have been collected over a broad energy range (from 1 GeV up to 350 GeV in some cases), for a total of 90 million events (4.5 TB of data). They are being analyzed using the common ATLAS software framework. Examples of preliminary results are presented in fig. 4. The left panel shows the correlation between the z -positions of muon

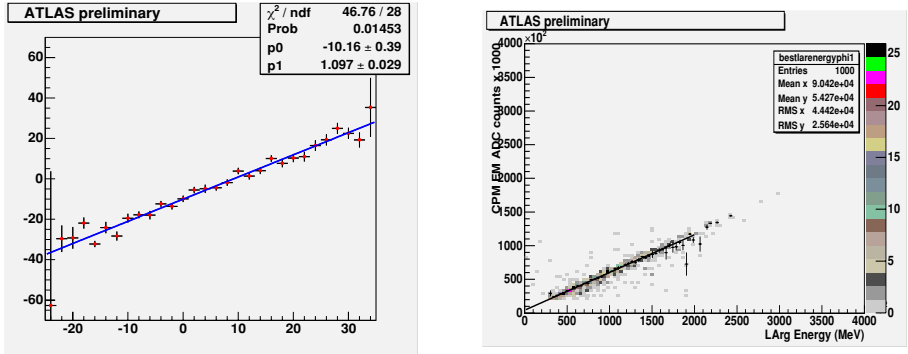


Figure 4: Preliminary results from the 2004 ATLAS combined test-beam. Left: For muon tracks, the z -position reconstructed by the muon chambers as a function of z -the position reconstructed by the inner detector (z indicates the coordinate along the LHC beam line, units are cm). Right: The energy reconstructed by the level-1 trigger cluster processor as a function of the energy reconstructed in the liquid-argon electromagnetic calorimeter.

tracks as reconstructed by the inner detector (Pixel, SCT, TRT) and the muon chambers, where z indicates the coordinate along the LHC beam line. Reconstructed muon tracks are extrapolated backward from the muon chambers over about 40 m. The right panel shows the correlation between the energy reconstructed in the ECAL and the energy reconstructed by the level-1 trigger cluster processor. These latter data were collected during a special run where the beam was delivered with a bunch spacing of 25 ns in order to emulate the LHC conditions.

5 Early physics goals and measurements

In this section we discuss the preparation for physics using the first collision data at the LHC. Table 3 shows the data samples expected in ATLAS and CMS for some example physics processes and for an integrated luminosity of 10 fb^{-1} . The trigger selection efficiencies have been included. It can be seen that already over the first year (even days in some cases) of operation, huge event samples should be available from known Standard Model (SM) processes, which will allow ATLAS and CMS to commission the detectors, the software and the physics itself, and from some new physics scenarios. We stress that this will be the case even for a very modest integrated luminosity of $\sim 100 \text{ pb}^{-1}$.

In more detail, the following goals can be addressed with such data samples¹:

¹It should be noted that the total amount of data recorded by each ex-

- Commission and calibrate the detectors *in situ* using well-known physics channels, as already mentioned. Understanding the trigger performance in as an unbiased way as possible, with a combination of minimum-bias events, QCD jets collected with various thresholds, single and di-lepton samples, is going to be one of the most challenging and crucial steps at the beginning. $Z \rightarrow \ell\ell$ is a gold-plated process for a large number of studies, e.g. to set the absolute electron and muon scales in the ECAL and tracking detectors respectively, whereas $t\bar{t}$ events can be used for instance to establish the absolute jet scale and to understand the b -tagging performance.
- Perform extensive measurements of the main SM physics processes, e.g. cross-sections and event features for minimum-bias, QCD di-jet, $W, Z, t\bar{t}$ production, etc. These measurements will be compared to the predictions of the Monte Carlo simulation, which will already be quite constrained from studies at the Tevatron and HERA energies. Typical initial precisions may be 10-20% for cross-section measurements, and 5-7 GeV on the top-quark mass, and will likely be limited by systematic uncertainties after a few weeks of data taking.
- Prepare the road to discoveries by measuring the backgrounds to possible new physics channels. Processes like W/Z +jets, QCD multijet production and $t\bar{t}$ are omnipresent backgrounds for a large number of searches and need to be understood in all details. In addition, dedicated control samples can be used to measure specific backgrounds. For instance, $t\bar{t}jj$ production, where the jets j are tagged as light-quark jets, can be used to gauge the irreducible $t\bar{t}b\bar{b}$ background to the $t\bar{t}H \rightarrow t\bar{t}b\bar{b}$ channel.

As an example of initial measurement with limited detector performance, fig. 5 shows the reconstructed top-quark signal in the gold-plated $t\bar{t} \rightarrow bj\bar{j} b\ell\nu$ semileptonic channel, as obtained from a simulation of the ATLAS detector. The event sample corresponds to an integrated luminosity of 150 pb^{-1} , which can be collected in less than one week of data taking at $L = 10^{33} \text{ cm}^{-2} \text{ s}^{-1}$. A very simple analysis was used to select these events, requiring an isolated electron or muon with $p_T > 20 \text{ GeV}$ and four and only four jets with $p_T > 40 \text{ GeV}$. The invariant mass of the three jets with the highest p_T was then plotted. No kinematic fit was made, and no b -tagging of some of the jets was required, assuming conservatively that the b -tagging performance would not have been well understood yet. Figure 5 shows that, even under these over-pessimistic conditions, a clear top signal should be observed above the background after a

periment in one year of operation corresponds to about 1 Petabyte, which represents an unprecedented challenge also for the LHC computing and offline software.

Table 3: For some physics processes, the numbers of events expected to be recorded by ATLAS and CMS for an integrated luminosity of 10 fb^{-1} per experiment.

channel	recorded events per experiment for 10 fb^{-1}
$W \rightarrow \mu\nu$	7×10^7
$Z \rightarrow \mu\mu$	1.1×10^7
$t\bar{t} \rightarrow \mu + X$	0.08×10^7
QCD jets $p_T > 150 \text{ GeV}$	$\sim 10^7$ (assuming 10% of trigger bandwidth)
minimum bias	$\sim 10^7$ (assuming 10% of trigger bandwidth)
$\tilde{g}\tilde{g}$, $m(\tilde{g}) \sim 1 \text{ TeV}$	$10^3 - 10^4$

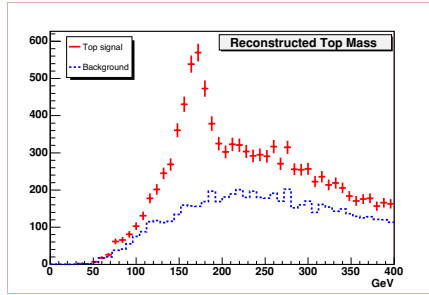


Figure 5: Three-jet invariant mass distribution for events selected as described in the text, as obtained from a simulation of the ATLAS detector. The dots with error bars show the expected signal from $t\bar{t}$ events plus the background, the dashed line shows the $W+4$ -jet background alone (ALPGEN Monte Carlo ⁴). The number of events corresponds to an integrated luminosity of 150 pb^{-1} .

few weeks of data taking (actually 30 pb^{-1} would be sufficient). In turn, this signal can be used for an early validation of the detector performance. For instance, if the top mass is wrong by several GeV, this would indicate a problem with the jet energy scale. Furthermore, top events are an excellent sample to understand the b -tagging performance of ATLAS and CMS. It should be noted that, unlike at the LHC, at the Tevatron today the statistics of $t\bar{t}$ events is not sufficient to use these samples for detector calibration purposes.

6 Early discoveries

Only after the three steps outlined in section 5 will have been fully addressed, can the LHC experiments hope to extract a convincing discovery signal from

their data. Three examples of new physics are discussed briefly below, ranked by increasing difficulty for discovery in the first year(s) of operation: an easy case, namely a possible $Z' \rightarrow e^+e^-$ signal, an intermediate case, Supersymmetry, and a difficult case, a light Standard Model Higgs boson.

6.1 $Z' \rightarrow e^+e^-$

A particle of mass 1-2 TeV decaying into e^+e^- pairs, such as a possible new gauge boson Z' , is probably the easiest object to discover at the LHC, for three main reasons. First, if the branching ratio into leptons is at least at the percent level as for the Z boson, the expected number of events after all experimental cuts is relatively large, e.g. about ten for an integrated luminosity as low as 300 pb^{-1} and a particle mass of 1.5 TeV. Second, the dominant background, di-lepton Drell-Yan production, is small in the TeV region, and even if it were to be a factor of two-three larger than expected today (which is unlikely for such a theoretically well-known process), it would still be negligible compared to the signal. Finally, the signal will be indisputable, since it will appear as a resonant peak on top of a smooth background, and not just as an overall excess in the total number of events. These expectations are not based on ultimate detector performance, since they hold also if the calorimeter response is understood to a conservative level of a few percent.

6.2 Supersymmetry

Extracting a convincing signal of Supersymmetry in the early phases of the LHC operation is not as straightforward as for the previous case, since good calibration of the detectors and detailed understanding of the numerous backgrounds are required. As soon as these two pre-requisites are satisfied, observation of a SUSY signal should be relatively easy and fast. This is because of the huge production cross-sections, and hence event rates, even for squark and gluino masses as large as $\sim 1 \text{ TeV}$ (see tab. 3), and the clear signature of such events in most scenarios. Therefore, by looking for final states containing several high- p_T jets and large missing transverse energy (E_T^{miss}), which is the most powerful and model-independent signature if R-parity is conserved, the LHC experiments should be able to discover squarks and gluinos up to masses of $\sim 1.5 \text{ TeV}$ in only one month of data taking (after the two above pre-requisites will have been satisfied) at $L = 10^{33} \text{ cm}^{-2} \text{ s}^{-1}$, as shown in the left panel of fig. 6.

Although detailed measurements of the SUSY particle masses will likely take several years, it should nevertheless be possible to obtain a first determination of the SUSY mass scale quickly after discovery. This is illustrated in the right panel of fig. 6, which shows the striking SUSY signal on top of the SM background, expected at a point in the minimal SUGRA parameter space

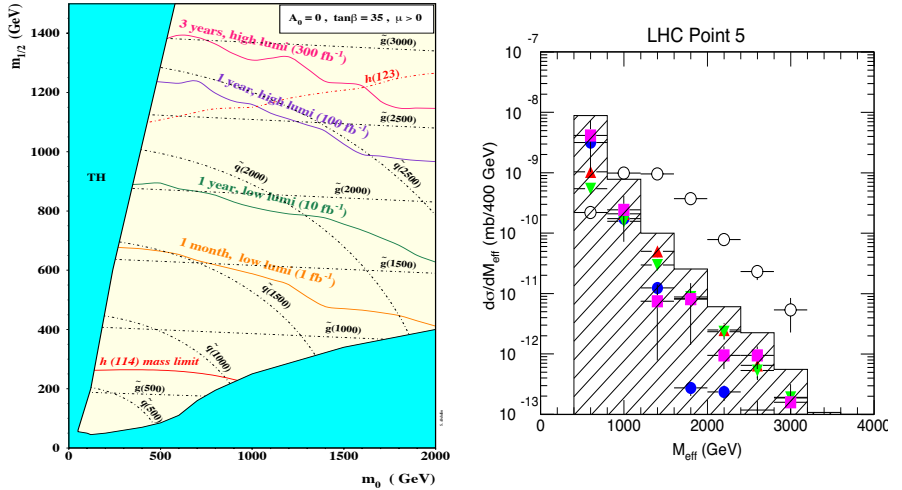


Figure 6: *Left:* The CMS discovery potential⁵⁾ for squarks and gluinos in $mSUGRA$ models, parametrized in terms of the universal scalar mass m_0 and universal gaugino mass $m_{1/2}$, as a function of integrated luminosity. Squark and gluino mass isolines are shown as dot-dashed lines (masses are given in GeV). *Right:* The expected distribution of the effective mass (see text) for the SUSY signal at “Point 5”⁶⁾ of the $mSUGRA$ parameter space (open circles), as obtained from a simulation of the ATLAS detector. The histogram shows the total SM background, which includes $t\bar{t}$ (solid circles), W +jets (triangles), Z +jets (downward triangles), and QCD jets (squares).

where squark and gluino masses are about 700 GeV. The plotted variable, called “effective mass” (M_{eff}), is defined as the scalar sum of the event E_T^{miss} and of the transverse energies of the four highest p_T jets, and thus reflects the “heaviness” of the particles produced in the final state. More precisely, the position of the peak of the M_{eff} signal distribution (see fig. 6) moves to larger/smaller values with increasing/decreasing squark and gluino masses. Therefore a measurement of the signal peak position should provide a first fast determination of the mass scale of Supersymmetry. The expected precision is about 20% for an integrated luminosity of 10 fb^{-1} , at least in minimal models like $mSUGRA$.

A crucial detector performance issue for an early SUSY discovery is a reliable reconstruction of the event missing transverse energy, which is *a priori* prone to contamination from several instrumental effects (calorimeter non-linearities, cracks in the detector, etc.). Final states with non-genuine missing transverse energy can be rejected by requiring the event primary vertex to be located close to the interaction centre (which also helps to suppress the background from cosmic and beam-halo muons), no jets pointing to detector cracks, and that the missing p_T vector is not aligned with any jet. The calorimeter response linearity can be understood to a large extent by using “calibration”

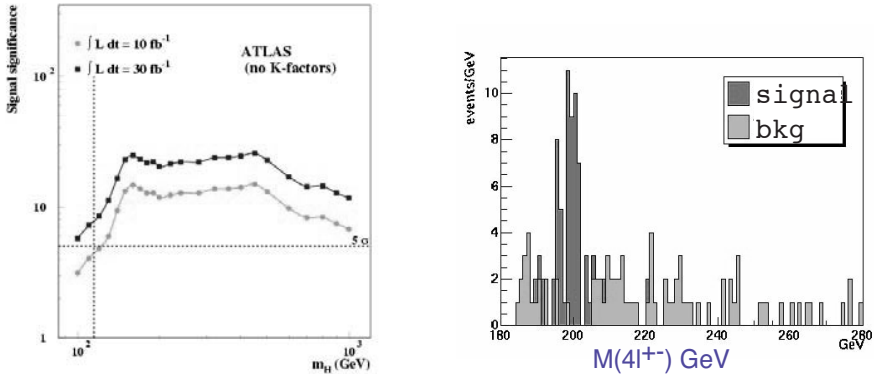


Figure 7: *Left: The expected signal significance for a SM Higgs boson in ATLAS as a function of mass, for integrated luminosities of 10 fb^{-1} (dots) and 30 fb^{-1} (squares). The vertical line shows the lower limit from searches at LEP. The horizontal line indicates the minimum significance (5σ) needed for discovery. Right: The expected $H \rightarrow ZZ \rightarrow 4\ell$ signal in CMS ⁷⁾ for a Higgs mass of 200 GeV (dark-shaded histogram) on top of the background (light-shaded histogram), for an integrated luminosity of 10 fb^{-1} .*

samples like $Z(\rightarrow \ell\ell)+\text{jet}$ events (with $\ell = e, \mu$), where the lepton pair and the jet are back-to-back in the transverse plane, so that the well-measured p_T of the lepton pair can be used to calibrate the jet p_T scale.

Concerning the physics backgrounds (e.g. $Z(\rightarrow \nu\bar{\nu})+\text{jets}$, $t\bar{t}$ production, QCD multijet events), most of them can be measured by using control samples. For instance, $Z(\rightarrow \ell\ell)+\text{jets}$ production provides a normalization of the $Z(\rightarrow \nu\bar{\nu})+\text{jets}$ background. More difficult to handle is the residual background from QCD multijet events with fake E_T^{miss} produced by the above-mentioned instrumental effects. The technique used at the Tevatron consists of normalizing the Monte Carlo simulation to the data in the (signal-free) region at low E_T^{miss} , and then use the Monte Carlo to predict the background in the (potentially “signal-rich”) region at large E_T^{miss} .

6.3 Standard Model Higgs boson

The possibility of discovering a SM Higgs boson at the LHC during the first year(s) of operation depends very much on the Higgs mass, as shown in the left panel of fig. 7. It can be seen that the most difficult case is the low-mass region close to the LEP limit and at the overlap with the Tevatron reach. The expected sensitivity for a Higgs mass of 115 GeV and for the first good (i.e. collected with well-calibrated detectors) 10 fb^{-1} is summarized in tab. 4. The total significance of about 4σ per experiment ($4_{-1.3}^{+2.2} \sigma$ including the expected

Table 4: For a Higgs boson mass of 115 GeV and an integrated luminosity of 10 fb^{-1} , expected numbers of signal (S) and background (B) events after all cuts and signal significances (S/\sqrt{B}) in ATLAS for the three dominant channels.

	$H \rightarrow \gamma\gamma$	$t\bar{t}H \rightarrow t\bar{t}b\bar{b}$	$qqH \rightarrow qq\tau\tau \rightarrow \ell + X$
S	130	15	~ 10
B	4300	45	~ 10
S/\sqrt{B}	2.0	2.2	~ 2.7

systematic uncertainties) is more or less equally shared among three channels: $H \rightarrow \gamma\gamma$, $t\bar{t}H$ production with $H \rightarrow b\bar{b}$, and Higgs production in vector-boson fusion followed by $H \rightarrow \tau\tau$. A conservative approach has been adopted in deriving these results. For instance, very simple cut-based analyses have been used, and higher-order corrections to the Higgs production cross-sections (the so-called K-factors), which are expected to increase for example the $gg \rightarrow H \rightarrow \gamma\gamma$ rate by a factor of about two compared to leading order, have not been included. Nevertheless, it will not be easy to extract a convincing signal with only 10 fb^{-1} , because the significances of the individual channels are small, and because an excellent knowledge of the backgrounds and close-to-optimal detector performances are required, as discussed below. Therefore, the contribution of both experiments, and the observation of possibly all three channels, will be crucial for an early discovery.

The channels listed in tab. 4 are complementary. They are characterized by different Higgs production mechanisms and decay modes, and therefore by different backgrounds and different detector requirements. Good uniformity of the electromagnetic calorimeters is crucial for the $H \rightarrow \gamma\gamma$ channel, as already mentioned. Powerful b -tagging is the key performance issue for the $t\bar{t}H$ channel, since there are four b -jets in the final state which all need to be tagged in order to reduce the background. Efficient and precise jet reconstruction over ten rapidity units ($|\eta| < 5$) is needed for the $H \rightarrow \tau\tau$ channel, since tagging the two forward jets accompanying the Higgs boson and vetoing additional jet activity in the central region of the detector are necessary tools to defeat the background. Finally, all three channels demand relatively low trigger thresholds (at the level of 20-30 GeV on the lepton or photon p_T), and a control of the backgrounds to a few percent. These requirements are especially challenging during the first year(s) of operation.

On the other hand, if the Higgs boson is heavier than 180 GeV early discovery should be easier thanks to the gold-plated $H \rightarrow 4\ell$ channel. As shown in the right panel of fig. 7, the expected number of events is small for 10 fb^{-1} , but these events are very pure since the background contamination is essentially negligible, and should produce a narrow mass peak. Detector requirements are

a lepton reconstruction efficiency close to 90% down to $p_T \sim 5\text{-}10$ GeV, since there are four leptons in the final state and the signal is tiny, and moderate-to-good quality of the lepton energy measurement.

It should be noted that the $H \rightarrow WW \rightarrow \ell\nu\ell\nu$ channel, which is expected to yield a much larger number of events for a Higgs mass of ~ 180 GeV, is a less convincing channel, detectable only as an overall excess of events compared to the background expectation, since no Higgs mass peak can be reconstructed due to the presence of neutrinos in the final state. Therefore it may not be a good candidate process for an early discovery.

7 Conclusions

The LHC offers the potential for very interesting physics and major discoveries right from the beginning. We note that for some standard physics processes, a single day of data taking at $L = 10^{33} \text{ cm}^{-2} \text{ s}^{-1}$ corresponds, in terms of event statistics, to ten years of operation at previous machines. Supersymmetry may be discovered quickly, a light Higgs boson will be much more difficult to observe, unexpected scenarios and surprises may well be round the corner at an unprecedented collider exploring a completely new territory.

The machine luminosity performance will be the crucial issue at the beginning. Hopefully, an instantaneous luminosity of up to $L \sim 10^{33} \text{ cm}^{-2} \text{ s}^{-1}$, and an integrated luminosity of up to 10 fb^{-1} per experiment, can be achieved by the end of 2008, as estimated by the accelerator team.

Concerning the experiments, a lot of emphasis has been given to quality checks in the various phases of the construction and to tests with beams. The results indicate that the detectors “as built” should give a good starting-point performance already on “day 1”.

However, a lot of data and time will be needed to commission the detectors, the triggers and the software *in situ*, to reach the performance required to address serious physics studies, to understand standard physics and the Monte Carlo tools at $\sqrt{s}=14$ TeV, and to measure the backgrounds to possible new physics processes.

The next challenge is therefore an efficient and timely detector commissioning, from cosmic runs to first collisions, where the experiments try to learn and fix as much as possible as early as possible. In parallel, efforts to improve and tune the Monte Carlo generators, based on theoretical developments as well as on comparisons with data from past and present experiments, should be pursued with vigor. Indeed, these two preparation activities will be crucial to reach quickly the discovery phase, and to extract a convincing signal from new physics in the first year(s) of operation.

References

1. D. Futyan, CMS Note CMS CR 2003/005.
2. ATLAS Collaboration, Liquid Argon Calorimeter Technical Design Report, CERN/LHCC/96-41.
3. M. Boonekamp *et al*, ATLAS Note ATL-GEN-2004-001.
4. M.L. Mangano, eConf **C030614** (2003) 015.
5. CMS Collaboration, Technical Proposal, CERN/LHCC/94-38.
6. ATLAS Collaboration, Detector and Physics Performance Technical Design Report, CERN/LHCC/99-15.
7. M. Sani, CMS Note 2003/046.

SPECIAL SESSION – PHYSICS AND SOCIETY
The Energy Problem

- *Duarte Borba* Energy from Fusion, from Dream to ITER

ENERGY FROM FUSION, FROM DREAM TO ITER

Duarte Borba

*EFDA Close Support Unit, Culham Science Centre, OX14 3DB, UK
Associação EURATOM/IST, Instituto Superior Técnico, Lisboa, Portugal*

Abstract

The main advantage of fusion power is in the energy available in relatively small amounts of fuel and the almost limitless worldwide resources. A successful development of fusion energy will provide a safe mean for producing electricity with low level radioactive waste and no atmospheric pollution. Significant progress has been made in fusion energy research and 22 MJ of fusion energy with 4.5 MW of steady state fusion power were produced in JET (1997) deuterium-tritium experiments. The next step fusion device, ITER, will provide plasmas with significant self heating and will test essential technologies in reactor-relevant conditions. The research and development carried out by ITER and other complementary devices will lead to demonstration fusion reactors and power plant prototypes.

1 World energy requirements and fusion energy

At present, the average world power consumption per capita is around 1.6 tons of oil equivalent per year ($2kW$), corresponding to a total energy demand of the order of 10 billion tons of oil equivalent per year (1 TOE= 42 Billion Joules) ¹⁾. However, countries like India and China, which contain a large fraction of the world population (2 Billion), are developing rapidly. This will imply a substantial increase in energy consumption as the worldwide living standards approach the western levels ^{2, 3)}. An American citizen uses on average 5-6 times more energy than a resident of developing countries. As the worldwide living standards approach western levels, the global energy consumption is expected to increase significantly ⁴⁾. In addition, the world population is increasing and may increase by up to 100% from the current value of 6 billion to 8-12 billion, in 50 years ⁵⁾. Assuming that the world population stabilises at around 10 Billion ⁶⁾ and an average energy consumption per capita of 2/3 of the current United States rate, the world energy demand will approach 50 billions tons of oil equivalent per year (approximately 350 billion barrels of oil equivalent per year) ⁷⁾. These levels of energy demand cannot be met by present sources of energy in the longer term. Conventional oil resources will be exhausted on the time scale of 40-50 years while coal ^{8, 9, 10, 11)} and gas will run out in around 100-200 years ¹²⁾. The same is true for conventional fission plants, as Uranium natural resources are also limited ¹³⁾. Longer term use of nuclear fission also requires a new generation of reactors that make use of more advanced and complex fuel cycles ¹⁴⁾. Renewable energy sources ¹⁵⁾, such as wind and solar power are important alternative means of producing energy, but their use is insufficient to meet the worldwide demands at a global scale. Currently more than 80% of the energy consumption is met by burning fossil fuels ¹⁶⁾. In addition to the limited resources, this energy source poses additional problems. Their localised supply causes political tension and this finite resource could be used in equally important chemical applications rather than just providing energy. But, more importantly, burning fossil fuels is causing important environmental damage by polluting the atmosphere with increasing amounts of Carbon dioxide. The overall concentration of Carbon dioxide in the atmosphere has increased by 40% in the last 100 years and it is predicted to at least double within the next 50 years. One of the biggest concerns related to atmospheric pollution is the possibility of significant climate change ^{17, 18)}. A global warming of the planet has been observed in the last 100 years and there is growing evidence that part of the temperature increase is due to the increase concentration of Carbon dioxide in the atmosphere via the greenhouse effect ¹⁹⁾. The potential sources of energy for the XXI century

are very restricted and they are mainly: nuclear fission, fossil fuels such as oil, gas and coal, renewable sources such as wind, solar power²⁰⁾ and Nuclear Fusion. These alternatives have some advantages, but some of them have important drawbacks that can not be discarded lightly. Nuclear fission poses long term environmental concerns due to the very long lived (10000 years) high level radioactive waste. Fossil fuels such as oil, gas and coal cause, as said, significant atmospheric pollution via the emission of greenhouse gases and significant atmospheric pollution can lead to climate change. Renewable energy sources such as wind and solar power are characterised by small (around $3 - 10W/m^2$) power densities and intermittent availability. Solar and wind power plants producing significant amounts of power (10GW) require the use of very large areas ($1000 - 3000km^2$) and also need energy storage at a large scale. On the other hand, nuclear fusion provides a safe way of producing large quantities of energy with low level radioactive waste and no atmospheric pollution. The main advantages of Nuclear Fusion are the fuel abundance and availability worldwide with almost limitless resources. The Lithium used to produce Tritium is available for thousands of years and the Deuterium for millions of years. The fuel cycle is generated inside the reactor and there is no need for transportation of activated materials. The short term radioactivity is associated mainly with plant activation which could be in principle mitigated by developing appropriate materials. Significant progress has been made regarding fusion energy research and 22 MJ of fusion energy with 4.5 MW of steady state fusion power (16 MW Fusion peak power) have been obtained. Fusion offers a great potential for future electricity production at a large scale, however, this technology has still to be demonstrated.

2 Fusion basics and magnetic plasma confinement

The most promising fusion reaction for large scale energy production is the one between heavy Hydrogen isotopes (Deuterium and Tritium) producing an Alpha particle, which carries 20% of the output energy and a Neutron with the remaining 80% of the energy. The Alpha particle is confined by the magnetic field and provides the plasma self heating. On the other hand, the Neutron escaping the magnetic field, provides the energy output and produces the Tritium by reacting with a Lithium blanket surrounding the plasma. Two main plasma magnetic confinement alternatives were explored in the early days of fusion research, with open and closed magnetic field line configurations as shown in figure 1. Since charged particles move freely along the magnetic field lines, open configurations require the pinching of the magnetic field lines at the end in order to mirror reflect the charged particles. Closed configurations lead to the development of toroidal magnetic field configurations, but a pure toroidal field is insufficient to achieve plasma confinement. Following these concepts, the Toka-

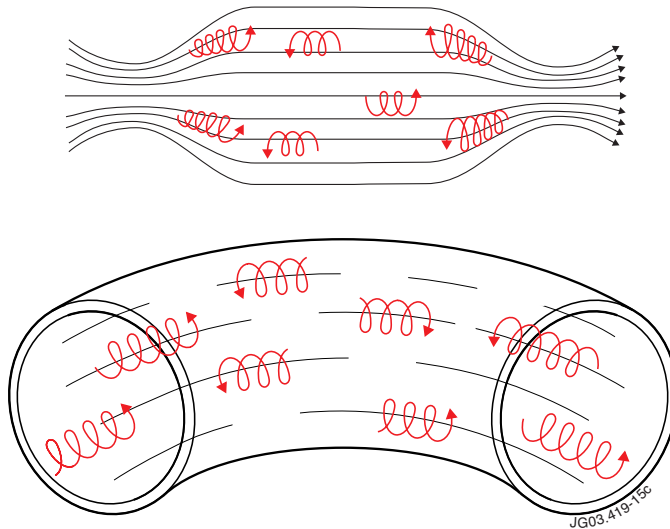


Figure 1: *Open and closed magnetic field line configurations explored in the early days of fusion research. Closed configurations lead to the development of toroidal magnetic field configurations and the development of the Tokamak, from Russian toroidalnaya kamera, magnitnaya katushka meaning toroidal chamber.*

mak device was developed and named from the Russian acronym **TO**roidalnaya **KA**mera, **MA**gnitnaya **KAT**ushka meaning toroidal chamber, where a toroidal current complements the toroidal magnetic field, resulting in a helical magnetic field configuration. In a tokamak, external coils provide the toroidal magnetic field, a transformer with an external primary winding produces the toroidal current in the secondary plasma loop. This current generates a poloidal magnetic field which makes the toroidal field lines twist, thus leading to the desired helical magnetic configuration. The plasma current, which yields the required confinement properties, also provides the basic Ohmic plasma heating (21, 22, 23). However, Ohmic heating alone is insufficient to provide the high temperatures (300 millions Kelvin) required for a fusion burning plasma. Auxiliary heating schemes, such as the injection of high energy neutral particles and radio frequency waves, have been developed and are currently used in

present Tokamaks to approach thermonuclear fusion reactor regimes.

3 Present status: JET and the bridge to ITER

Controlled fusion research has made significant progress since the 1950s, going from first small experiments to the construction of large scale experimental devices in the 1970s. The triple fusion product ²⁴⁾ of density (n), temperature (T) and energy confinement time (τ_E) has increased by 5 orders of magnitude from the early 1970s to the late 1990s, culminating in the demonstration of significant fusion power production from fusion in 1994 in the TFTR experiment (10 MW of fusion power) ²⁵⁾ and in 1997 in JET (16MW of fusion power) ²⁶⁾. This rate of progress can be compared with the increase in the accelerators energy for particle physics research (energy doubles every 3 years) and the Moores Law with the numbers of transistors in an integrated circuit doubling every 2 years. The fusion Lawson criteria ($n\tau_E$) ²⁴⁾ expressed as a function of temperature can be seen in figure 2. Ignition is achieved (yellow region $n\tau_E > f(T)$) when the fusion reaction can be sustained by the self Alpha heating without any external power. The breakeven condition is defined by $n\tau_E > f(T, Q = 1)$ where Q represents the fraction of fusion power to the external power required to sustain the plasma. A reduced form of the Lawson criterion for ignition $n\tau_E T > 10^{21}(m^{-3}s KeV)$ is obtained by taking into account the temperature dependence near its minimum, i.e. the optimal temperature regarding the deuterium-tritium (D-T) fusion cross section. The fusion deuterium-tritium performance obtained by the various fusion devices in equivalent deuterium plasmas is shown in green in figure 2, while the deuterium-tritium experiments carried out in JET and TFTR are shown in red. In this figure 2, the progress in fusion research is clearly illustrated by showing the equivalent parameters from early experiments such as the T3 tokamak (left bottom corner) up to large scale devices operating with tritium such as TFTR and JET, which are close to breakeven conditions. The operation of a large number of fusion devices has increased the understanding of plasma confinement properties ²⁷⁾, leading to a simplified expression for the confinement time (τ_E) in terms of main plasma dimensionless parameters ^{28, 29)}

$$\omega_c \tau_E = \beta^{-0.66} \rho_*^{-2.8} \nu_*^{-0.09}, \quad (1)$$

where ω_c is the cyclotron frequency, ρ_* the ion gyro radius normalised to the plasma minor radius, ν_* particle collisionality and β the plasma pressure normalised to the magnetic pressure. This global confinement scaling law leads to a confident prediction of the plasma parameters required for the next step fusion devices in terms of temperature, density and energy confinement time, based on the world wide database from 13 devices with different engineering

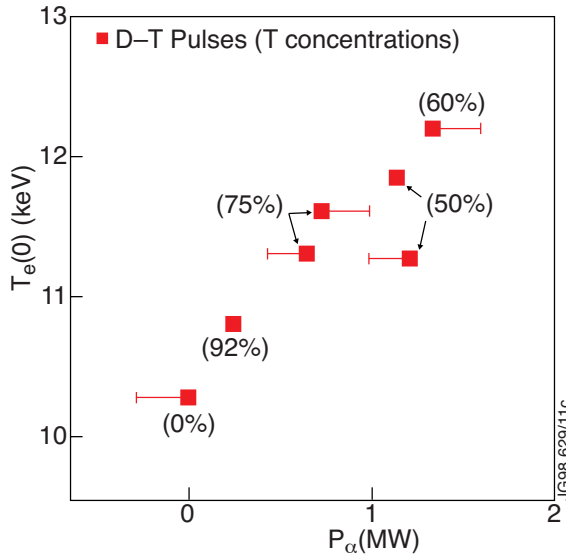


Figure 3: *The electron plasma temperature as a function of different levels of Alpha particle power, generated in similar plasma conditions by different D-T fuel plasma mixtures, demonstrating efficient plasma heating from the fusion Alphas.*

machines exist around the world able to operate at plasma currents between 1 MA and 2 MA, such as ASDEX-Upgrade (Germany) ³³), FTU (Italy) ³⁴), MAST (United Kingdom) ³⁵), TORE-SUPRA (France) ³⁶) and NSTX ³⁷), DIII-D ³⁸), C-MOD ³⁹) in the United States of America. New super conducting tokamaks are in construction in china (EAST, SUNIST) ⁴⁰) and South Korea (KSTAR) ⁴¹) in addition to the super conducting tokamak ⁴²) currently in operation in the south of France (TORE-SUPRA). One of the key areas of controlled fusion research is the ability to sustain the plasma burn via the heating deposited by the confined charged fusion products (Alpha particles). In 1997, Alpha particle heating was demonstrated for the first time on JET ⁴³) during experiments with a D-T fuel mix ⁴⁴). Figure 3 shows the electron plasma temperature as a function of different levels of Alpha particle power, generated in similar plasma conditions by different D-T fuel plasma

mixtures. The highest electron temperature under these conditions is obtained with a near optimum D-T fuel mixture, demonstrating efficient plasma heating from the fusion Alphas, as expect from classic slowing down theory. More recently, in 2003 and 2004 the first direct measurements of Alpha particle slowing down was obtained using gamma-rays spectroscopy from Alpha particle reacting with Beryllium impurities ⁴⁵⁾. This very powerful technique was used in most plasma configurations at JET, including those foreseen for the operation of the next step device (ITER) ⁴⁶⁾, to study particle slowing down. Detailed tomography imaging of the Alpha particle distribution was obtained using both the vertical and horizontal gamma-ray cameras installed at JET. Fast particles have a strong impact on the plasma stability and these measurements in combination with plasma turbulence studies carried out using magnetic and microwave diagnostics, gave a also significant contribution in this field.

4 Burning Plasma Physics: a new scientific frontier with ITER

As it was mentioned in the previous section, one of the key areas of controlled fusion research is the ability to sustain the plasma burn via the heating deposited by the confined charged fusion products (Alpha particles). The new generation of fusion devices aim to demonstrate fusion plasma operation with a dominant fraction of the plasma heating being provided by the Alpha particles. The planned International Tokamak Experimental Reactor (ITER) ⁴⁷⁾, next experimental step towards the demonstration of fusion as a potential energy source, aims to operate with a power amplification $Q > 10$; corresponding to a fraction of plasma self-heating by fusion born alpha-particles of $f_\alpha = \frac{Q}{(Q+5)} > 0.65$ ^{48, 49)}. This will represent a significant qualitative step, when compared with present machines operating space such as JET, as shown in figure 4. In addition, ITER will test nuclear components and other essential technologies in reactor-relevant conditions, such as high heat and neutron flux, and will demonstrate the safety and environmental acceptability of fusion. For this purpose, ITER has been designed with a major radius of 6.2 m and a minor radius of 2 m. Toroidal plasma currents of up to 17 MA and pulses of 2000 s duration are foreseen in ITER, leading to a predicted fusion power output of approximately 500 MW in steady state operation. The mock-ups of the main components of ITER, central solenoid, super conducting magnets, remote handling and heat load bearing divertor modules have been constructed and tested to the required specifications. The large super-conducting magnets prototypes ⁵⁰⁾ have been constructed and successfully tested using both Nb3Sn and NbTi coils. The Central Solenoid Demo Coil set a new super conducting magnet world record in terms of combined magnetic field and operating current ⁵¹⁾. The Vertical Target Medium-Scale Prototype ⁵²⁾ was constructed

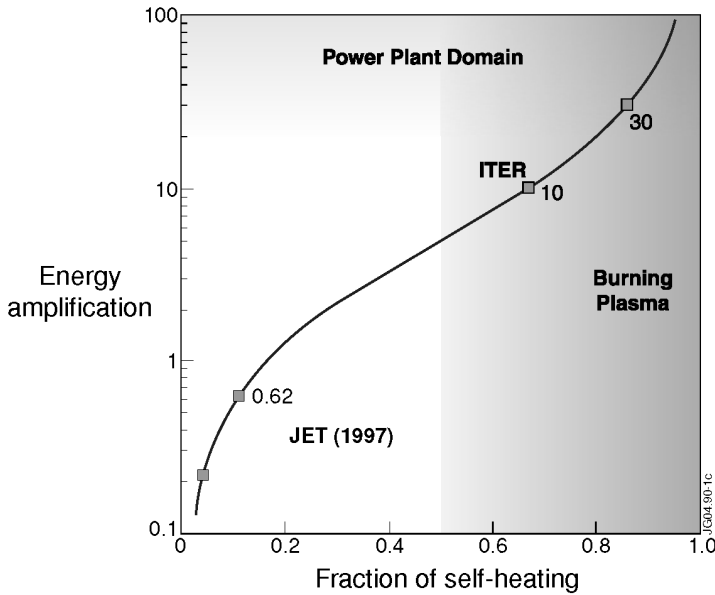


Figure 4: The ITER operation point aiming at a power amplification $Q > 10$; corresponding to a fraction of plasma self-heating by fusion born alpha-particles of $f_\alpha = \frac{Q}{(Q+5)} > 0.65$. This will represent a significant qualitative step, when compared with present machines operating space such as JET.

and tested successfully both with the Tungsten macrobrush at $15 \text{ MW/m}^2 \times 1000$ cycles and with CFC monoblock tested at $20 \text{ MW/m}^2 \times 2000$ cycles. An ITER remote handling test facility has been constructed in Italy, which includes the central cassette carrier, divertor port, dummy cassette and plug handling vehicle.

5 Fusion Reactor and Power plants

A number of specialist fusion devices are being currently operated around the world with specific tasks, as it was mentioned in section III. It is expected that concept improvement devices will operate in parallel with ITER in the next decades. In addition, further technology improvements and optimisations will also be carried out in parallel, including a dedicated material testing facility. The proposed International Fusion Material Irradiation Facility (IFMIF) 53)

jointly planned by Japan, the European Union, the United States and the Russian Federation under the direction of the IEA (International Energy Agency), is an accelerator-based deuterium-lithium (d-Li) neutron source for producing an intense beam of high energy neutrons. The main objective of this facility is to enable realistic testing of candidate materials and components to be used in fusion reactors up to full lifetime of their anticipated use. This will require sufficient irradiation volume $> 0.5L$ at the equivalent fusion reactor conditions 10^{14} neutrons/(s cm²). IFMIF will be composed by two deuterium beam 175 MHz accelerators, with 125 mA and 40 MeV each. Acceleration is achieved by Radio Frequency Quadrupoles (RFQ) and Drift Tube Linacs (DTL). The research and development carried out by ITER, IFMIF and other complementary devices will lead to demonstration fusion reactors and power plant prototypes⁵⁴). The layout of a conceptual fusion power plant is similar to other conventional plants such as oil, coal or nuclear power plants, but with different fuel and furnace. The heat exchanger, steam generator, turbines and electricity generator are similar to those used in conventional power plants. Therefore, plant auxiliaries such as water cooling systems will be used in fusion power plants. Therefore, fusion plants are expected to be similar in size to conventional power plants. The main difference is that the heat is generated by a fusion device such as the tokamak.

6 Discussion

The main advantage of fusion power is in the energy available in relatively small amounts of fuel. One hundred milligram of Deuterium, reacting with the in situ produced Tritium can yield the same amount of energy as obtained by burning one ton of gasoline. Once the power of fusion is controlled and used to produce electricity relatively small amount of fuel is required to produce significant amounts of energy. The Deuterium contained in 45 liters of water and the Lithium contained in an averaged laptop computer battery can produce 200,000 kWh of energy, sufficient for the electricity requirements of an average European citizen for 30 years. The other main advantage of fusion energy is the radioactive impact, which is much smaller than convention fission plants and is associated only with plant activation. In the long term the activation resulting from the operation of a fusion plant can be compared with the activation associated with coal power plants, due to the presence of the radioactive isotope Carbon-14. On the other hand, controlled fusion conditions are very difficult to achieve. Fusion reactions occur only at very large temperatures, which require very complex and relatively expensive devices. These two leading factors will be ultimately reflected in the final price of the electricity produced using fusion power plants. Since, the fuel price is negligible, most of the cost is associated with plant construction, maintenance and decommissioning. Recent studies,

suggest that the expected cost of fusion energy⁵⁵⁾ will be comparable with that of other sources, such as wind power and much less than solar power from present technology photovoltaic cells.

7 Conclusions

Few options exist for large scale energy production in the second half of the XXI century. They are: nuclear fission, fossil fuels such as oil, gas and coal and renewable energy sources such as solar and wind power. Both nuclear fission and fossil fuels pose serious environmental problems such as long term storage of high level radioactive waste and green house gas emissions possibly leading to climate change. Since, renewable energies cannot provide a solution for the global energy problem due to their low energy density and intermittent availability, further options need to be explored. A successful development of Fusion energy will provide a safe, with low level radioactive waste and no atmospheric pollution, mean for producing electricity. Significant progress has been made regarding fusion energy research and 22 MJ of fusion energy with 4.5 MW of steady state fusion power (16 MW Fusion peak power) was achieved in JET deuterium-tritium experiments in 1997, demonstrating alpha particle heating. The next step fusion device, ITER would provide access to plasmas with adequate self heating ($f_\alpha > 2/3$ burning fusion plasma) and test essential technologies in reactor-relevant conditions. The main ITER components have been successfully tested such as the super-conducting magnets, heat load bearing divertor modules and remote handling test facility and ITER is ready to be built. In parallel, the IFMIF neutron source for producing an intense beam of high energy neutrons will enable realistic testing of candidate materials and components to be used in fusion reactors. The research and development carried out by ITER, IFMIF and other complementary devices will lead to demonstration fusion reactors and power plant prototypes.

8 Acknowledgements

This work, carried out under the European Fusion Development Agreement, supported by the European Communities and Instituto Superior Técnico, has been carried out within the Contract of Association between EURATOM and IST. Financial support was also received from Fundação para a Ciência e Tecnologia in the frame of the Contract of Associated Laboratory. The views and opinions expressed herein do not necessarily reflect those of the European Commission, IST and FCT.

References

1. BP AMOCO, (2000), Statistical Review of World Energy June 2000, Pilians & Wilson Greenaway, London, United Kingdom.
2. Ruth A. Judson, Richard Schmalensee, and Thomas M Stoker, The Energy Journal (1999)
3. Jeffrey Chow, Raymond J. Kopp, Paul R. Portney, Science **302**, (2003) p1528-1531
4. John Asafu-Adjaye Energy, Economics **22**, (2000) p615-625
5. Wolfgang Lutz, Warren Sanderson Sergei Scherbov, Nature **387**, (1997) p805-807
6. Wolfgang Lutz, Warren Sanderson Sergei Scherbov, Nature **412**, (2001) p543-545
7. V Suri, D Chapman; International Journal of Global Energy Issues. **14** (2000) p116
8. H-H. Rogner, Annual Review of Energy and the Environment **22** (1997) p217-262
9. John D. Edwards, AAPG Bulletin, **81**, no. 8; (1997) p1292-1305
10. RC Duncan, W Youngquist, Natural Resources Research, **8**, 3, (1999) p219 232
11. KS Deffeyes, MP Silverman; American Journal of Physics, (2003)
12. World coal resources: methods of assessment and results GB Fettweis, Amsterdam; New York: New York: Elsevier Scientific Pub. Co 1979
13. NEA (OECD Nuclear Energy Agency) and IAEA (International Atomic Energy Agency), (2000), Uranium 1999 Uranium Resources, Production and Demand, OECD, Paris, France.
14. Analysis of Uranium Supply to 2050 (International Atomic Energy Agency, Vienna, 2001)
15. Renewable Energy B Soerensen, Academic Press, London and San Diego, (2000)
16. G Couch, IEACR/56. IEA Coal Research, London, (1993)
17. Peter M. Cox, Richard A. Betts, Chris D. Jones, Steven A. Spall & Ian J. Totterdell Nature **408**, 184 - 187 (2000);

18. Fortunat Joos, Gian-Kasper Plattner, Thomas F. Stocker, Olivier Marchal, Andreas Schmittner, *Science*, **284** (1999)
19. Terry L. Root, Jeff T. Price, Kimberly R. Hall, Stephen H. Schneider, Cynthia Rosenzweig, J. Alan Pounds, *Nature* **421** (2003) p57 - 60
20. "Solar and Wind Renewable energy: power for a sustainable future" G Boyle, Oxford University Press. Oxford, (1996)
21. Forrest, M J, Peacock, N J, Robinson, D C, Sannikov, V V, Wilcock, P D, *Nature* **224**, (1969) p488-490.
22. L.A. Artsimovich, *Nuclear Fusion*, **12**, (1972) p.215
23. Furth, H. P., *Nuclear Fusion*, **15**, (1975), p. 487-534.
24. JD Lawson, *Proceedings of the Physical Society Section B*, 1957
25. M.G. Bell et al, *Nuclear Fusion* **35**, (1995) p1429
26. M. Keilhacker et al, *Nuclear Fusion*, **39**, No. 2 (1999)
27. Goldstone, R.J., *Plasma Phys. Controlled Fusion* **26** (1984) p87.
28. J.P. Christiansen, J.G. Cordey, *Nuclear Fusion*, **38**, No. 12 (1998)
29. J.G. Cordey et al, Preprint of Paper to be submitted for publication in Proceedings of the 20th IAEA Conference, (Vilamoura, Portugal 1-6 November 2004); EFDAJETCP(04)07-07
30. J G Cordey et al, *Plasma Phys. Control. Fusion* **44** (2002) p19291935
31. L.D. Horton et al *Nuclear Fusion*, **39**, No. 8, (1999)
32. S. Ishida et al, *Phys. Rev. Lett.* **79**, (1997) p39173921
33. O. Gruber et al, *Nuclear Fusion*, **41**, No. 10, (2001)
34. B. Angelini, et al, *Nuclear Fusion* **43** (2003) p16321640
35. A. Sykes, et al *Nuclear Fusion*, **41**, No. 10, (2001).
36. J. Jacquinot et al *Nucl. Fusion* **43** (2003) p15831599
37. M. Ono et al, *Nuclear Fusion*, **41**, No. 10, (2001).
38. S.L. Allena, DIII-D Team, *Nuclear Fusion*, **41**, No. 10, (2001)
39. E.S. Marmor et al, *Nuclear Fusion* **43** (2003) 16101618

40. Wang Wen-Hao et al, Chinese Phys. **13**, (2004) p2091-2096
41. G.S. Lee et al, Nuclear Fusion, **41**, 10, (2001)
42. Saoutic, B., Plasma Phys. Control. Fusion, **44**, 12B, (2002), pp. 11-22
43. P. R. Thomas, et al, Phys. Rev. Lett. **80**, (1998) p55485551
44. A. Gibson and the JET Team Physics of Plasmas, **5**, 5, (2003) pp. 1839-1847
45. Kiptily V G, et al, Physical Review Letters **93**, 115001 (2004)
46. Y. Shimomura et al, Nuclear Fusion, **41**, No. 3, (2001)
47. R Aymar, P Barabaschi and Y Shimomura (for the ITER Team), Plasma Phys. Control. Fusion **44** (2002) 519565
48. Y Shimomura, Y Murakami, A R Polevoi, P Barabaschi, V Mukhovatov and M Shimada, Plasma Phys. Control. Fusion **43** (2001) A385A394
49. M. Shimada, Nuclear Fusion **44** (2004) p350356
50. Mitchell, N, Fusion Engineering and Design. **66-68**, (2003) p971-993.
51. H. Tsuji et al, Nuclear Fusion, **41**, No. 5, (2001)
52. Escourbiac, F; Chappuis, P; Schlosser, J; Merola, M; Vastra, I; Febvre, M, Fusion Engineering and Design. **56-57**, Part A, (2001) pp. 285-290.
53. A. Mslanga, Nuclear Fusion **40** (2000) p619-627
54. T C Hender P J Knight I Cook, Fusion Technology, (1996)
55. G Marbach, I Cook, D Maisonnier, Fusion Engineering and Design. **63** (2002) pp. 1-9

PARTICIPANTS

Giovanni Abbiendi	Bologna
Guido Altarelli	Roma/CERN
Fabio Ambrosino	Naples
Mario Antonelli	LNF
Anastasios Belias	Rutherford
Rita Bernabei	Roma
Ruggero Bertani	ENEL - Pisa
Duarte Borba	EFDA-CSU Culham
Davide Boscherini	Bologna
Tamas Budavari	Baltimore
Franco Cervelli	Pisa
Eugenio Coccia	LNGS
Michael Danilov	ITEP
Alvaro de Rujula	CERN
Patrick Decowski	Berkeley
Alexander Dolgov	Ferrara
Rolf Dubitzky	Heildeberg
Arnaud Duperrin	Marseille
Andreas Eckart	Kln
Daniel Elvira	Fermilab
Jerome Faure	Paris
Frank Fiedler	Munich
Francesco Forti	Pisa
Roland Garoby	CERN

Fabiola Gianotti	CERN
Alexander Glazov	Chicago
Mike Hildreth	Notre Dame
Gino Isidori	Frascati
Andrei Kataev	Moscow
Judith Katzy	DESY
Dmitri Kazakov	ITEP
Bruno Khelifi	Heidelberg
Alexander S. Kuzmin	Novosibirsk
Tom Latham	Warwick
Mats Leijon	Uppsala
Gang Li	Beijing
Vittorio Lubicz	Roma
Kaori Maeshima	Fermilab
Mario Martinez	Barcelona
Antonio Masiero	Padova
Stephanie Menzemer	MIT
Aldo Morselli	Roma
Takeshi Nakadaira	KEK
Isamu Nakamura	KEK
Victor Novikov	Moscow
Carlo Pagani	Milano
Chris Parkes	Glasgow
Pantaleo Raimondi	Frascati
Steven Robertson	Montreal
Andrea Romanino	CERN
Marco Rosa Clot	Firenze
Alan Schwartz	Cincinnati

Eugenij Shabalin	Moscow
Alex Smith	Minnesota
Amarjit Soni	Brookhaven
Marco Sozzi	Pisa
Oliver Stelzer-Chilton	Toronto
Alexander Studenikin	Moscow
Luca Trentadue	Parma
Isabel Trigger	CERN
George Velez	Fermilab
Ping Wang	Beijing
Jeanne Wilson	Oxford
Alan Wiseman	Madison
Kurt Woschnagg	Berkeley

FRASCATI PHYSICS SERIES VOLUMES**Volume I**

Heavy Quarks at Fixed Target
Eds. S. Bianco and F.L. Fabbri
Frascati, May 31–June 2, 1993
ISBN—88-86409-00-1

Volume II – Special Issue

*Les Rencontres de Physique de la Vallée d'Aoste –
Results and Perspectives in Particle Physics*
Ed. M. Greco
La Thuile, Aosta Valley, March 5 –11, 1995
ISBN—88-86409-03-6

Volume III

Heavy Quarks at Fixed Target
Ed. B. Cox
University of Virginia, Charlottesville
October 7–10, 1994, 11
ISBN—88-86409-04-4

Volume IV

Workshop on Physics and Detectors for DAΦNE
Eds. R. Baldini, F. Bossi, G. Capon, G. Pancheri
Frascati, April 4–7, 1995
ISBN—88-86409-05-2

Volume V – Special Issue

*Les Rencontres de Physique de la Vallée d'Aoste –
Results and Perspectives in Particle Physics*
Ed. M. Greco
La Thuile, Aosta Valley, March 3–9, 1996
ISBN—88-86409-07-9

Volume VI

Calorimetry in High Energy Physics
Eds. A. Antonelli, S. Bianco, A. Calcaterra, F.L. Fabbri
Frascati, June 8–14, 1996
ISBN—88-86409-10-9

Volume VII*Heavy Quarks at Fixed Target*

Ed. L. Köpke

Rhinefels Castle, St. Goar, October 3–6, 1996

ISBN—88-86409-11-7

Volume VIII*ADONE a milestone on the particle way*

Ed. V. Valente 1997

ISBN—88-86409-12-5

Volume IX – Special Issue*Les Rencontres de Physique de la Vallée d'Aoste –**Results and Perspectives in Particle Physics*

Ed. M. Greco

La Thuile, Aosta Valley, March 2–8, 1997

ISBN—88-86409-13-3

Volume X*Advanced ICFA Beam Dynamics**Workshop on Beam Dynamics Issue for e^+e^- Factories*

Eds. L. Palumbo, G. Vignola

Frascati, October 20–25, 1997

ISBN—88-86409-14-1

Volume XI*Proceedings of the XVIII International Conference on**Physics in Collision*

Eds. S. Bianco, A. Calcaterra, P. De Simone, F. L. Fabbri

Frascati, June 17–19, 1998

ISBN—88-86409-15-X

Volume XII – Special Issue*Les Rencontres de Physique de la Vallée d'Aoste –**Results and Perspectives in Particle Physics*

Ed. M. Greco

La Thuile, Aosta Valley, March 1–7, 1998

ISBN—88-86409-16-8

Volume XIII

Bruno Touschek and the Birth of the e^+e^-

Ed. G. Isidori

Frascati, 16 November, 1998

ISBN—88-86409-17-6

Volume XIV – Special Issue

Les Rencontres de Physique de la Vallée d'Aoste –

Results and Perspectives in Particle Physics

Ed. M. Greco

La Thuile, Aosta Valley, February 28–March 6, 1999

ISBN—88-86409-18-4

Volume XV

Workshop on Hadron Spectroscopy

Eds. T. Bressani, A. Feliciello, A. Filippi

Frascati, March 8–2 1999

ISBN—88-86409-19-2

Volume XVI

Physics and Detectors for DAΦNE

Eds. S. Bianco, F. Bossi, G. Capon, F.L. Fabbri,

P. Gianotti, G. Isidori, F. Murtas

Frascati, November 16–19, 1999

ISBN—88-86409-21-4

Volume XVII – Special Issue

Les Rencontres de Physique de la Vallée d'Aoste –

Results and Perspectives in Particle Physics

Ed. M. Greco

La Thuile, Aosta Valley, February 27–March 4, 2000

ISBN—88-86409-23-0

Volume XVIII

LNF Spring School

Ed. G. Pancheri

Frascati 15–20 May, 2000

ISBN—88-86409-24-9

Volume XIX*XX Physics in Collision*

Ed. G. Barreira

Lisbon June 29–July 1st. 2000

ISBN—88-86409-25-7

Volume XX*Heavy Quarks at Fixed Target*

Eds. I. Bediaga, J. Miranda, A. Reis

Rio de Janeiro, Brasil, October 9–12, 2000

ISBN—88-86409-26-5

Volume XXI*IX International Conference on Calorimetry in
High Energy Physics*

Eds. B. Aubert, J. Colas, P. Nédélec, L. Poggioli

Annecy Le Vieux Cedex, France, October 9–14, 2000

ISBN—88-86409-27-3

Volume XXII – Special Issue*Les Rencontres de Physique de la Vallée d'Aoste –
Results and Perspectives in Particle Physics*

Ed. M. Greco

La Thuile, Aosta Valley, March 4–10, 2001

ISBN—88-86409-28-1

Volume XXIII*XXI Physics in Collision*

Ed. Soo-Bong Kim

Seoul, Korea, June 28–30, 2001

ISBN—88-86409-30-3

Volume XXIV*International School of Space Science – 2001 Course on:
Astroparticle and Gamma-ray Physics in Space*

Eds. A. Morselli, P. Picozza

L'Aquila, Italy, August 30–September 7, 2000

ISBN—88-86409-31-1

Volume XXV

*TRDs for the 3rd Millennium Workshop on
Advanced Transition Radiation Detectors for
Accelerator and Space Applications*

Eds. N. Giglietto, P. Spinelli

Bari, Italy, September 20–23, 2001

ISBN—88-86409-32-X

Volume XXVI

KAON 2001 International Conference on CP Violation

Eds. F. Costantini, G. Isidori, M. Sozzi

Pisa Italy, June 12th 17th, 2001

ISBN—88-86409-33-8

Volume XXVII – Special Issue

*Les Rencontres de Physique de la Vallée d'Aoste –
Results and Perspectives in Particle Physics*

Ed. M. Greco

La Thuile, Aosta Valley, March 3–9, 2002

ISBN—88-86409-34-6

Volume XXVIII

Heavy Quarks at Leptons 2002

Eds. G. Cataldi, F. Grancagnolo, R. Perrino, S. Spagnolo

Vietri sul mare (Italy), May 27th June 1st, 2002

ISBN—88-86409-35-4

Volume XXIX

*Workshop on Radiation Dosimetry: Basic Technologies,
Medical Applications, Environmental Applications*

Ed. A. Zanini

Rome (Italy), February 56, 2002

ISBN—88-86409-36-2

Volume XXIX – Suppl.

*Workshop on Radiation Dosimetry: Basic Technologies,
Medical Applications, Environmental Applications*

Ed. A. Zanini

Rome (Italy), February 56, 2002

ISBN—88-86409-36-2

Volume XXX – Special Issue

*Les Rencontres de Physique de la Vallée d'Aoste –
Results and Perspectives in Particle Physics*

Ed. M. Greco

La Thuile, Aosta Valley, March 9–15, 2003

ISBN—88-86409-39-9

Volume XXXI

*Frontier Science 2002 – Charm, Beauty and CP,
First International Workshop on Frontier Science*

Eds. L. Benussi, R. de Sangro, F.L. Fabbri, P. Valente

Frascati, October 6–11, 2002

ISBN—88-86409-37-0

Volume XXXII

19th International Conference on x-ray and Inner-Shell Processes

Eds. A. Bianconi, A. Marcelli, N.L. Saini

Università di Roma La Sapienza June 24–28, 2002

ISBN—88-86409-39-07

Volume XXXIII

Bruno Touschek Memorial Lectures

Ed. M. Greco, G. Pancheri

Frascati, May 11, 1987

ISBN—88-86409-40-0

Volume XXXIV

*Les Rencontres de Physique de la Vallée d'Aoste –
Results and Perspectives in Particle Physics*

Ed. M. Greco

La Thuile, Aosta Valley, February 29 – March 6, 2004

ISBN—88-86409-42-7

Volume XXXV

Heavy Quarks And Leptons 2004

Ed. A. López

San Juan, Puerto Rico, 1–5 June 2004

ISBN—88-86409-43-5

Volume XXXVI*DAΦNE 2004: Physics At Meson Factories*

Eds. F. Anulli, M. Bertani, G. Capon, C. Curceanu-Petrascu,

F.L. Fabbri, S. Miscetti

Frascati, June 7–11, 2004

ISBN—88-86409-53-2

Volume XXXVII*Frontier Science 2004, Physics and Astrophysics in Space*

Eds. A. Morselli, P. Picozza, M. Ricci

Frascati, 14–19 June, 2004

ISBN—88-86409-52-4

Volume XXXVIII*II Workshop Italiano sulla Fisica di ATLAS e CMS*

Eds. Gianpaolo Carlino and Pierluigi Paolucci

Napoli, October 13 – 15, 2004

ISBN—88-86409-44-3

